



applied sciences

Special Issue Reprint

Natural-Hazards Risk Assessment for Disaster Mitigation

Edited by
Andrea Chiozzi, Elena Benvenuti and Željana Nikolić

www.mdpi.com/journal/applsci



Natural-Hazards Risk Assessment for Disaster Mitigation

Natural-Hazards Risk Assessment for Disaster Mitigation

Editors

Andrea Chiozzi
Elena Benvenuti
Željana Nikolić

MDPI • Basel • Beijing • Wuhan • Barcelona • Belgrade • Manchester • Tokyo • Cluj • Tianjin



Editors

Andrea Chiozzi
Department of Environmental
and Prevention Sciences
University of Ferrara
Ferrara
Italy

Elena Benvenuti
Engineering Department
University of Ferrara
Ferrara
Italy

Željana Nikolić
Faculty of Civil Engineering,
Architecture and Geodesy
University of Split
Split
Croatia

Editorial Office

MDPI
St. Alban-Anlage 66
4052 Basel, Switzerland

This is a reprint of articles from the Special Issue published online in the open access journal *Applied Sciences* (ISSN 2076-3417) (available at: www.mdpi.com/journal/applsci/special_issues/nhra_disaster_mitigation).

For citation purposes, cite each article independently as indicated on the article page online and as indicated below:

LastName, A.A.; LastName, B.B.; LastName, C.C. Article Title. <i>Journal Name</i> Year , <i>Volume Number</i> , Page Range.

ISBN 978-3-0365-8017-3 (Hbk)

ISBN 978-3-0365-8016-6 (PDF)

© 2023 by the authors. Articles in this book are Open Access and distributed under the Creative Commons Attribution (CC BY) license, which allows users to download, copy and build upon published articles, as long as the author and publisher are properly credited, which ensures maximum dissemination and a wider impact of our publications.

The book as a whole is distributed by MDPI under the terms and conditions of the Creative Commons license CC BY-NC-ND.

Contents

About the Editors	vii
Preface to "Natural-Hazards Risk Assessment for Disaster Mitigation"	ix
Željana Nikolić, Elena Benvenuti and Andrea Chiozzi Special Issue on Natural Hazards Risk Assessment for Disaster Mitigation Reprinted from: <i>Appl. Sci.</i> 2023 , <i>13</i> , 1940, doi:10.3390/app13031940	1
Nenad Mladineo, Marko Mladineo, Elena Benvenuti, Toni Kekez and Željana Nikolić Methodology for the Assessment of Multi-Hazard Risk in Urban Homogenous Zones Reprinted from: <i>Appl. Sci.</i> 2022 , <i>12</i> , 12843, doi:10.3390/app122412843	5
Željana Nikolić, Veljko Srzić, Ivan Lovrinović, Toni Perković, Petar Šolić and Toni Kekez Coastal Flooding Assessment Induced by Barometric Pressure, Wind-Generated Waves and Tidal-Induced Oscillations: Kaštela Bay Real-Time Early Warning System Mobile Application Reprinted from: <i>Appl. Sci.</i> 2022 , <i>12</i> , 12776, doi:10.3390/app122412776	27
Ercan Işık, Marijana Hadzima-Nyarko, Hüseyin Bilgin, Naida Ademović, Aydın Büyüksaraç and Ehsan Harirchian et al. A Comparative Study of the Effects of Earthquakes in Different Countries on Target Displacement in Mid-Rise Regular RC Structures Reprinted from: <i>Appl. Sci.</i> 2022 , <i>12</i> , 12495, doi:10.3390/app122312495	47
Jerome G. Gacu, Cris Edward F. Monjardin, Delia B. Senoro and Fibor J. Tan Flood Risk Assessment Using GIS-Based Analytical Hierarchy Process in the Municipality of Odiongan, Romblon, Philippines Reprinted from: <i>Appl. Sci.</i> 2022 , <i>12</i> , 9456, doi:10.3390/app12199456	87
Alessandra Maramai, Beatriz Brizuela and Laura Graziani A Database for Tsunamis and Meteotsunamis in the Adriatic Sea Reprinted from: <i>Appl. Sci.</i> 2022 , <i>12</i> , 5577, doi:10.3390/app12115577	119
Awais Naeem Sarwar, Muhammad Waseem, Muhammad Azam, Adnan Abbas, Ijaz Ahmad and Jae Eun Lee et al. Shifting of Meteorological to Hydrological Drought Risk at Regional Scale Reprinted from: <i>Appl. Sci.</i> 2022 , <i>12</i> , 5560, doi:10.3390/app12115560	133
Federico Da Col, Flavio Accaino, Gualtiero Böhm and Fabio Meneghini Analysis of the Seismic Properties for Engineering Purposes of the Shallow Subsurface: Two Case Studies from Italy and Croatia Reprinted from: <i>Appl. Sci.</i> 2022 , <i>12</i> , 4535, doi:10.3390/app12094535	147
Željana Nikolić, Elena Benvenuti and Luka Runjić Seismic Risk Assessment of Urban Areas by a Hybrid Empirical-Analytical Procedure Based on Peak Ground Acceleration Reprinted from: <i>Appl. Sci.</i> 2022 , <i>12</i> , 3585, doi:10.3390/app12073585	159
D. W. Shin, Steven Cocke and Baek-Min Kim A Systematic Revision of the NFIP Claims Hazard Data in Florida for Flood Risk Assessment Reprinted from: <i>Appl. Sci.</i> 2022 , <i>12</i> , 3537, doi:10.3390/app12073537	185

Mahmood Ahmad, Maaz Amjad, Ramez A. Al-Mansob, Paweł Kamiński, Piotr Olczak and Beenish Jehan Khan et al. Prediction of Liquefaction-Induced Lateral Displacements Using Gaussian Process Regression Reprinted from: <i>Appl. Sci.</i> 2022 , <i>12</i> , 1977, doi:10.3390/app12041977	199
Arianna Soldati, Andrea Chiozzi, Željana Nikolić, Carmela Vaccaro and Elena Benvenuti A PROMETHEE Multiple-Criteria Approach to Combined Seismic and Flood Risk Assessment at the Regional Scale Reprinted from: <i>Appl. Sci.</i> 2022 , <i>12</i> , 1527, doi:10.3390/app12031527	217
Ji-Yuan Lin, Jen-Chih Chao and Yung-Ming Hsu Risk Assessment of Riverine Terraces: The Case of the Chenyulan River Watershed in Nantou County, Taiwan Reprinted from: <i>Appl. Sci.</i> 2022 , <i>12</i> , 1375, doi:10.3390/app12031375	239
Diamando Vlachogiannis, Athanasios Sfetsos, Iason Markantonis, Nadia Politi, Stelios Karozis and Nikolaos Gounaris Quantifying the Occurrence of Multi-Hazards Due to Climate Change Reprinted from: <i>Appl. Sci.</i> 2022 , <i>12</i> , 1218, doi:10.3390/app12031218	259
Alessandro Rocchi, Andrea Chiozzi, Marco Nale, Zeljana Nikolic, Fabrizio Riguzzi and Luana Mantovan et al. A Machine Learning Framework for Multi-Hazard Risk Assessment at the Regional Scale in Earthquake and Flood-Prone Areas Reprinted from: <i>Appl. Sci.</i> 2022 , <i>12</i> , 583, doi:10.3390/app12020583	277
Răzvan Pîrloagă, Dragoș Ene and Bogdan Antonescu Population Bias on Tornado Reports in Europe Reprinted from: <i>Appl. Sci.</i> 2021 , <i>11</i> , 11485, doi:10.3390/app112311485	295

About the Editors

Andrea Chiozzi

Andrea Chiozzi is an Assistant Professor of Solid and Structural Mechanics at the Department of Environmental and Prevention Sciences of the University of Ferrara, Italy. Since earning his Ph.D. in 2014, he has been actively contributing to several research topics in computational mechanics, mainly addressing analysis of the mechanical behavior of curved three-dimensional masonry structures and the development of innovative numerical methods for elliptic problems in solid mechanics.

Elena Benvenuti

Elena Benvenuti is an Associate Professor of Solid and Structural Mechanics at the Engineering Department of the University of Ferrara with consolidated expertise in nonlinear computational and theoretical mechanics and civil engineering risk assessment. She has authored and co-authored more than 150 scientific contributions published in international journals and conference proceedings. Prof. Benvenuti has also directed PMO-GATE, the Italy–Croatia Interreg project focusing on risk assessment and management that has inspired many of the papers published in the present Special Issue.

Željana Nikolić

Željana Nikolić is a Professor of Structural Mechanics, Computational Mechanics, and Earthquake Engineering and head of the Laboratory for Numerical Modelling at the Faculty of Civil Engineering, Architecture and Geodesy, University of Split, Croatia. Her research focuses on the development of methodologies, advanced numerical techniques, and new non-linear numerical models for the simulation of problems of structural mechanics and earthquake engineering. She has authored and co-authored more than 230 scientific contributions and participated in numerous research projects.

Preface to “Natural-Hazards Risk Assessment for Disaster Mitigation”

Knowledge and awareness of the risks generated by natural hazards are essential requirements for the enhancement of communities’ resilience to disasters. United Nations directives have recently pointed out the necessity of undertaking actions aimed at anticipating, managing, and mitigating disaster risks to reduce their economic and social impact and protect the health, socioeconomic assets, cultural heritage, and ecosystems of communities and countries. While the increasing occurrence of disasters caused by meteorological events, such as floods, storms, and droughts, can be directly ascribed to the consequence of climate change, disasters induced by earthquakes and tsunamis are increasing even if their frequency of occurrence is historically unchanged. Therefore, other anthropogenic causes intervene to determine an increment of risk exposure and community vulnerability, such as land misuse in densely populated areas and coastal zones.

This Special Issue addresses concepts, methods, and predictive methodologies for assessing natural hazard risks. It presents fifteen articles focusing on the single-risk assessment of a broad range of natural hazards, such as earthquakes, river/sea floods, meteotsunamis, tornados, hydrological and meteorological drought, liquefaction, as well as on multirisk assessment in the presence of multiple hazards. The adopted methodologies rely on (a) quantitative, semi-quantitative, and qualitative methods for the assessment of the risks related to natural hazards; (b) risk analysis at different scales; (c) multi-hazard risk assessment techniques; (d) real-time hazard monitoring and warning systems; (e) disaster mitigation strategies; and (f) risk management and emergency planning on multiple scales.

Andrea Chiozzi, Elena Benvenuti, and Željana Nikolić
Editors

Editorial

Special Issue on Natural Hazards Risk Assessment for Disaster Mitigation

Željana Nikolić ^{1,*}, Elena Benvenuti ² and Andrea Chiozzi ²

¹ Faculty of Civil Engineering, Architecture and Geodesy, University of Split, 21000 Split, Croatia

² Engineering Department, University of Ferrara, 44121 Ferrara, Italy

* Correspondence: zeljana.nikolic@gradst.hr

Knowledge and awareness of the risks generated by natural hazards are essential requirements for the enhancement of communities' resilience to disasters. The Sendai Framework for Disaster Risk Reduction 2015–2030 has recently pointed out the necessity of undertaking actions aimed to anticipate, manage, and mitigate disaster risks, to reduce their economic and social impact and protect health, socioeconomic assets, cultural heritage, and ecosystems of communities and countries. While the increasing occurrence of disasters caused by meteorological events, such as floods, storms, and droughts, can be directly ascribed to the consequence of climate change, disasters induced by earthquakes and tsunamis are increasing even if the frequency of occurrence is historically unchanged. Therefore, other anthropogenic causes intervene to determine an increment of a risk exposure and community vulnerability, such as land misuse in densely populated areas and coastal zones.

This Special Issue addresses concepts, methods, and predictive methodologies for assessing natural hazards risks. This Special Issue presents fifteen articles focusing on the single-risk assessment of a broad range of natural hazards, such as earthquakes, river, and sea floods, meteotsunamis, tornados, hydrological and meteorological drought, liquefaction, as well as on multirisk assessment in the presence of multiple hazards. The adopted methodologies rely on: (a) quantitative, semi-quantitative, and qualitative methods for the assessment of the risks related to natural hazards; (b) risk analysis at different scales; (c) multi-hazard risk assessment techniques; (d) real-time hazard monitoring and warning systems; (e) disaster mitigation strategies; and (f) risk management and emergency planning at multiple scales.

Ahmad et al. [1] propose a Gaussian process regression (GPR) model for analyzing liquefaction-induced lateral displacement based on an impressive amount (247) of case studies of post-liquefaction events. The performance of the GPR model is assessed using statistical parameters, including the coefficient of determination, coefficient of correlation, Nash–Sutcliffe efficiency coefficient, root mean square error (RMSE), and ratio of the RMSE to the standard deviation of the measured data. It was shown that the GPR model can accurately capture the complicated nonlinear relationships between lateral displacements and their influencing factors.

Da Col et al. [2] present two case studies of the seismic surveys to estimate the elastic properties of the soil and rock in the shallow subsurface: (1) a town on the Croatian coast, near the city of Split, built on hard rock and (2) a site located in the Italian town of Ferrara, in an alluvial plain. A Multichannel Analysis of Surface Waves and a first-break tomography were carried out to obtain P-, SH-, and SV-velocity profiles. This acquisition allowed for computing the equivalent shear-wave velocity of the first 30 m of the subsurface (VS30) from the SH profiles, as well as it made it possible to deduce other useful parameters such as the VP/VS, and to estimate the soil's stratigraphy through the analysis of the VSV/VSH profiles.

Citation: Nikolić, Ž.; Benvenuti, E.; Chiozzi, A. Special Issue on Natural Hazards Risk Assessment for Disaster Mitigation. *Appl. Sci.* **2023**, *13*, 1940. <https://doi.org/10.3390/app13031940>

Received: 17 January 2023

Accepted: 28 January 2023

Published: 2 February 2023



Copyright: © 2023 by the authors. Licensee MDPI, Basel, Switzerland. This article is an open access article distributed under the terms and conditions of the Creative Commons Attribution (CC BY) license (<https://creativecommons.org/licenses/by/4.0/>).

Gacu et al. [3] studied the spatial distribution of the flood risk of the Municipality of Odiongan using the analytical hierarchy process (AHP) and the geographic information system (GIS), considering the disaster risk factors based on the data collected from various government agencies. The weights of the hazard, exposure, and vulnerability parameters were drawn from the experts' judgment. These weights were subsequently integrated into a flood risk assessment computation which resulted in a flood risk map. The study will guide local government units in developing flood management plans able to reduce flood risk and vulnerability.

Işık et al. [4] carried out a comparative study of the effects of earthquakes in different countries based on target displacement in mid-rise regular RC structures. Five different earthquakes from six countries with a high seismic risk were selected. The measured PGA for each earthquake was compared with the suggested PGA for the respective region. Target displacements specified in the Eurocode-8 were obtained for both the suggested and measured PGA values. It was concluded that both the seismic risk and target displacements were adequately represented for some earthquakes, while not adequately represented for others.

Lin et al. [5] established a method of hazard assessment for the river terraces along the Chenyulan River in Nantou County, Taiwan. Using GIS, the authors extracted nine parameters and identified the weightings by AHP analysis. Hazard assessment for the river terraces then proceeded via totaling the potential trends of the considered factors and the protected objects, as well as through comparing the historical disaster conditions and satellite images. The results showed different distributions of the relevant risks. Thus, the assessment can be used in reducing the disaster's impact induced by the risks inherent in the riverine terrace settlements.

Maramai et al. [6] developed the database of Adriatic tsunamis and meteotsunamis along the Adriatic coasts, providing an overview of the events and a detailed description of the effects observed at each affected location, and defining a picture of the geographical distribution of the effects for each tsunami and meteotsunami. The database contains 57 observations of tsunami effects related to 27 tsunamis along the Italian, Croatian, Montenegrin, and Albanian coasts and 102 observations of meteotsunami effects related to 33 meteotsunamis. The database can be accessed through a GIS WebApp, which allows the user to visualize the georeferenced information on a map.

Mladineo et al. [7] proposes a methodology for the multi-hazard risk assessment of the urban area of Kaštel Kambelovac, located on the Croatian coast of the Adriatic Sea. The procedure, based on spatial multi-criteria decision making and the PROMETHEE method, was used to assess the multi-hazard risks caused by seismic, flood due to sea level rises, and extreme sea waves impact. The multi-hazard risk is assessed for different scenarios and different levels was based on an exposure and vulnerability for each of the natural hazards and the influence of additional criteria to the overall risk in homogenous zones.

Nikolić et al. [8] developed a methodology for the seismic risk assessment of urban areas based on a hybrid empirical-analytical procedure that combines seismic vulnerability indices with critical peak ground accelerations computed through a non-linear pushover analysis. The procedure's outcomes are the computation of a relationship linking vulnerability indices to the peak ground acceleration for a series of limit states. The methodology was used to estimate the damage index and the index of seismic risk for the selected return periods for masonry buildings in the Croatian settlement Kaštel Kambelovac.

Nikolić et al. [9] present a unique procedure for the real-time assessment of the sea water elevation at the Kaštela Bay in Croatia to ensure a priori warning in the case of expected coastal flooding along the site area caused by barometric pressure, wind-generated waves, and tidal-induced oscillations. The procedure relies on relevant datasets which are site-specific and locally observed. The given information is visualized in a form of mobile application that implements the algorithm and allows end users to set the notifications based on the given ruleset.

Tornadoes are associated with damages, injuries, and even fatalities in Europe. Pîrloagă et al. [10] analyzed a problem of a population bias on tornado reporting in Europe. To account for this bias, a Bayesian modeling approach was used based on tornado observations and the population density for relatively small regions of Europe. The results indicated that the number of tornadoes could be 53% higher than are currently reported. The largest adjustments produced by the model pertain to Northern Europe and some Mediterranean regions.

Rocchi et al. [11] developed a machine learning framework for the assessment of a combined seismic and hydraulic risk at the regional scale. The machine learning techniques were used to aggregate large datasets made of many variables different in nature. The framework is applied to the case study of the Emilia Romagna region, for which the different municipalities are grouped into four homogeneous clusters ranked in terms of the relative levels of combined risk. The proposed approach proved to be robust and delivered a very useful tool for multi-hazard modeling at the regional scale.

Sarwar et al. [12] analyzed meteorological and hydrological drought risk at a regional scale in the Soan basin in Pakistan. The spatiotemporal analysis, statistical approaches, including regression analysis, trend analysis using Mann–Kendall, and moving average, were used to find a linkage between these drought types, the significance of the variations, and the lag time identification, respectively. The overall analysis indicated an increase in the frequency of both hydrological and meteorological droughts during the last three decades.

Shin et al. [13] systematically analyzed the National Flood Insurance Program (NFIP) claims hazard data in Florida. The claims with a presumably incorrect cause of loss fields were identified and revised by adding a variety of other available information. These datasets included tropical cyclone events, rainfall maxima, and distances to the nearest coast. The revised NFIP claims data will be intensively used to validate the outcomes from flood hazard (surge, wave, and inland flooding) models and to develop a flood vulnerability model in the forthcoming Florida Public Flood Loss Model (FPFLM).

Soldati et al. [14] proposes a qualitative multi-hazard risk analysis methodology in the case of combined seismic and flood risk, using PROMETHEE, a multiple-criteria decision analysis technique. The present case study is a multi-hazard risk assessment of the Ferrara province (Italy). The proposed approach provides an original and flexible methodology to qualitatively prioritize the urban centers affected by multi-hazard risks at the regional scale. It delivers a useful tool to stakeholders involved in the processes of hazard management and disaster mitigation.

Vlachogiannis et al. [15] analyzed a climatic multi-hazard risk for Greece, as the first-ever attempt to enhance scientific knowledge for the identification and definition of hazards, a critical element of risk-informed decision making. Many hazards (heatwaves, cold spells, torrential rainfall, snowstorms, and windstorms) were considered to correctly capture the country's susceptibility to climate extremes. The findings highlighted the areas that are exposed to multiple climate hazards in the country, considering the influence of the highly complex topography.

All the contributions gathered in the present special issue contribute to the crucial societal challenge of reducing human and material losses induced by natural hazards caused by extreme climate changes and earthquakes. For this purpose, the continuous upgrade of comprehensive databases of individual risks and the development of new procedures and methodologies for hazard and risk assessment are key to the implementation of effective actions. The present studies show the usefulness of modern technologies, such as multi-criteria decision-making methods coupled with GIS, machine learning, and artificial intelligence. These technologies allowed the authors of the collected contributions to provide robust solutions to several necessities, such as the implementation of numerical models for single-hazard and multi-hazard modeling with a low computational cost, fast training, validation, testing, evaluation, visualization of the results, and fast notification to end users. Furthermore, the presented approaches provide valuable operational tools which can be readily exploited by end users, whether modelers or decision makers, to

urgently allocate resources and increase the coping capacity of communities confronting catastrophic events. Therefore, the Editors believe that the Special Issue may significantly contribute to enhance the insight into technological and analytical procedures aimed to “Natural Hazards Risk Assessment for Disaster Mitigation”.

Author Contributions: Writing—original draft preparation, Ž.N., E.B. and A.C.; writing—review and editing, E.B and Ž.N. All authors have read and agreed to the published version of the manuscript.

Funding: This research was funded by the EUROPEAN UNION, Programme Interreg Italy-Croatia, Project “Preventing, managing and overcoming natural hazards risks to mitigate economic and social impact”—PMO-GATE ID 10046122. The research is also partially supported through project KK.01.1.1.02.0027, co-financed by the CROATIAN GOVERNMENT and the EUROPEAN UNION through the European Regional Development Fund—the Competitiveness and Cohesion Operational Programme.

Acknowledgments: The Editors are deeply grateful to all authors and peer reviewers for their valuable contributions to the Special Issue ‘Natural Hazards Risk Assessment for Disaster Mitigation’. Karen Men is also acknowledged for the helpful assistance in the publication process.

Conflicts of Interest: The authors declare no conflict of interest.

References

1. Ahmad, M.; Amjad, M.; Al-Mansob, R.A.; Kamiński, P.; Olczak, P.; Khan, B.J.; Alguno, A.C. Prediction of Liquefaction-Induced Lateral Displacements Using Gaussian Process Regression. *Appl. Sci.* **2022**, *12*, 1977. [CrossRef]
2. Da Col, F.; Accaino, F.; Böhm, G.; Meneghini, F. Analysis of the Seismic Properties for Engineering Purposes of the Shallow Subsurface: Two Case Studies from Italy and Croatia. *Appl. Sci.* **2022**, *12*, 4535. [CrossRef]
3. Gacu, J.G.; Monjardin, C.E.F.; Senoro, D.B.; Tan, F.J. Flood Risk Assessment Using GIS-Based Analytical Hierarchy Process in the Municipality of Odiongan, Romblon, Philippines. *Appl. Sci.* **2022**, *12*, 9456. [CrossRef]
4. Işık, E.; Hadzima-Nyarko, M.; Bilgin, H.; Ademović, N.; Büyüksaraç, A.; Harirchian, E.; Bulajić, B.; Özmen, H.B.; Aghakouchaki Hosseini, S.E. A Comparative Study of the Effects of Earthquakes in Different Countries on Target Displacement in Mid-Rise Regular RC Structures. *Appl. Sci.* **2022**, *12*, 12495. [CrossRef]
5. Lin, J.-Y.; Chao, J.-C.; Hsu, Y.-M. Risk Assessment of Riverine Terraces: The Case of the Chenyulan River Watershed in Nantou County, Taiwan. *Appl. Sci.* **2022**, *12*, 1375. [CrossRef]
6. Maramai, A.; Brizuela, B.; Graziani, L. A Database for Tsunamis and Meteotsunamis in the Adriatic Sea. *Appl. Sci.* **2022**, *12*, 5577. [CrossRef]
7. Mladineo, N.; Mladineo, M.; Benvenuti, E.; Kekez, T.; Nikolić, Ž. Methodology for the Assessment of Multi-Hazard Risk in Urban Homogenous Zones. *Appl. Sci.* **2022**, *12*, 12843. [CrossRef]
8. Nikolić, Ž.; Benvenuti, E.; Runjić, L. Seismic Risk Assessment of Urban Areas by a Hybrid Empirical-Analytical Procedure Based on Peak Ground Acceleration. *Appl. Sci.* **2022**, *12*, 3585. [CrossRef]
9. Nikolić, Ž.; Srzić, V.; Lovrinović, I.; Perković, T.; Šolić, P.; Kekez, T. Coastal Flooding Assessment Induced by Barometric Pressure, Wind-Generated Waves and Tidal-Induced Oscillations: Kaštela Bay Real-Time Early Warning System Mobile Application. *Appl. Sci.* **2022**, *12*, 12776. [CrossRef]
10. Pîrloagă, R.; Ene, D.; Antonescu, B. Population Bias on Tornado Reports in Europe. *Appl. Sci.* **2021**, *11*, 11485. [CrossRef]
11. Rocchi, A.; Chiozzi, A.; Nale, M.; Nikolic, Z.; Riguzzi, F.; Mantovan, L.; Gilli, A.; Benvenuti, E. A Machine Learning Framework for Multi-Hazard Risk Assessment at the Regional Scale in Earthquake and Flood-Prone Areas. *Appl. Sci.* **2022**, *12*, 583. [CrossRef]
12. Sarwar, A.N.; Waseem, M.; Azam, M.; Abbas, A.; Ahmad, I.; Lee, J.E.; Haq, F.u. Shifting of Meteorological to Hydrological Drought Risk at Regional Scale. *Appl. Sci.* **2022**, *12*, 5560. [CrossRef]
13. Shin, D.W.; Cocke, S.; Kim, B.-M. A Systematic Revision of the NFIP Claims Hazard Data in Florida for Flood Risk Assessment. *Appl. Sci.* **2022**, *12*, 3537. [CrossRef]
14. Soldati, A.; Chiozzi, A.; Nikolić, Ž.; Vaccaro, C.; Benvenuti, E. A PROMETHEE Multiple-Criteria Approach to Combined Seismic and Flood Risk Assessment at the Regional Scale. *Appl. Sci.* **2022**, *12*, 1527. [CrossRef]
15. Vlachogiannis, D.; Sftosos, A.; Markantonis, I.; Politi, N.; Karozis, S.; Gounaris, N. Quantifying the Occurrence of Multi-Hazards Due to Climate Change. *Appl. Sci.* **2022**, *12*, 1218. [CrossRef]

Disclaimer/Publisher’s Note: The statements, opinions and data contained in all publications are solely those of the individual author(s) and contributor(s) and not of MDPI and/or the editor(s). MDPI and/or the editor(s) disclaim responsibility for any injury to people or property resulting from any ideas, methods, instructions or products referred to in the content.

Article

Methodology for the Assessment of Multi-Hazard Risk in Urban Homogenous Zones

Nenad Mladineo¹, Marko Mladineo² , Elena Benvenuti³ , Toni Kekez¹  and Željana Nikolić^{1,*} ¹ Faculty of Civil Engineering, Architecture and Geodesy, University of Split, 21000 Split, Croatia² Faculty of Electrical Engineering, Mechanical Engineering and Naval Architecture, University of Split, 21000 Split, Croatia³ Engineering Department, University of Ferrara, 44121 Ferrara, Italy

* Correspondence: zeljana.nikolic@gradst.hr

Abstract: The multi-hazard risk assessment of urban areas represents a comprehensive approach that can be used to reduce, manage and overcome the risks arising from the combination of different natural hazards. This paper presents a methodology for multi-hazard risk assessment based on Spatial Multi-Criteria Decision Making. The PROMETHEE method was used to assess multi-hazard risks caused by seismic, flood and extreme sea waves impact. The methodology is applied for multi-hazard risk evaluation of the urban area of Kaštel Kambelovac, located on the Croatian coast of the Adriatic Sea. The settlement is placed in a zone of high seismic risk with a large number of old stone historical buildings which are vulnerable to the earthquakes. Being located along the low-lying coast, this area is also threatened by floods due to climate change-induced sea level rises. Furthermore, the settlement is exposed to flooding caused by extreme sea waves generated by severe wind. In the present contribution, the multi-hazard risk is assessed for different scenarios and different levels, based on exposure and vulnerability for each of the natural hazards and the influence of additional criteria to the overall risk in homogenous zones. Single-risk analysis has shown that the seismic risk is dominant for the whole pilot area. The results of multi-hazard assessment have shown that in all combinations the highest risk is present in the historical part of Kaštel Kambelovac. This is because the historical part is most exposed to sea floods and extreme waves, as well as due to the fact that a significant number of historical buildings is located in this area.

Keywords: risk assessment; multi hazard; multi-hazard risk assessment; multi-criteria decision-making; GIS; PROMETHEE method

Citation: Mladineo, N.; Mladineo, M.; Benvenuti, E.; Kekez, T.; Nikolić, Ž. Methodology for the Assessment of Multi-Hazard Risk in Urban Homogenous Zones. *Appl. Sci.* **2022**, *12*, 12843. <https://doi.org/10.3390/app122412843>

Academic Editor: Jianbo Gao

Received: 27 October 2022

Accepted: 9 December 2022

Published: 14 December 2022

Publisher's Note: MDPI stays neutral with regard to jurisdictional claims in published maps and institutional affiliations.



Copyright: © 2022 by the authors. Licensee MDPI, Basel, Switzerland. This article is an open access article distributed under the terms and conditions of the Creative Commons Attribution (CC BY) license (<https://creativecommons.org/licenses/by/4.0/>).

1. Introduction

Natural hazards are threatening the population throughout the world more than ever. Efficient planning and preparation are vital, since the question “will the disaster happen?”, has changed into “when will it happen?”. Enhancing the safety and resilience for disasters requires knowledge about individual territorial hazards, vulnerabilities and risks. Appropriate multi-risk methodology based on existing data and knowledge should produce an interactive and easily understanding map that will enable the visualization of individual and combined risks. Integration of this methodology into the Geographic Information System gives important information to local and regional authorities for preventing, managing and overcoming multi-hazard natural disasters [1], such as river and sea floods, meteotsunamis (or extreme sea waves) and earthquakes. To reduce the possible loss of life and damage to property caused by hazards [2], it is crucial to conduct risk assessments and make decisions pertaining to natural hazards before the hazards occur [3].

A common practice in the hazard risk assessment is to focus on the hazard frequency and intensity in combination with area vulnerability or severity of damage caused by the hazard [4]. Furthermore, the severity is not just the result of hazard intensity and area

vulnerability, but it is also influenced by the coping capacity of the emergency units in the area [5]. Hazard occurs in some periods with particular intensity and causes damage in relation to area vulnerability and coping capacity. A brief literature survey was made among scientific and professional papers to investigate what are the common factors used to calculate the risk of natural hazards (Table 1).

Table 1. Brief literature survey on factors used to calculate the risk of natural hazards.

Approach	Factors				Output	Source
	Frequency	Intensity	Vulnerability	Other		
Single hazard	Yes	No	No	Damage	Risk	Di Mauro et al. [6]
Multi-hazard	Yes	Yes	Yes	Coping capacity	Risk	Fleischhauer et al. [7]
Multi-hazard	No	Yes	Yes	Coping capacity	Integrated risk	Greiving et al. [5]
Single hazard	Yes	Yes	No	No	Risk	Kunz et al. [8]
Multi-hazard	Yes	Yes	Yes	Consequence (loss)	Risk	Liu et al. [9]
Multi-hazard	Yes	No	No	Aggregated losses	Risk	Mignan et al. [10]
Single hazard	No	No	Yes	Hazard exposure, Exposed value	Risk index	Munich Re Group [11]
Single hazard	Yes	Yes	No	Area impact	Hazard score	Odeh Engineers, Inc. [12]
Multi-hazard	Yes	Yes	Yes	Elements at risk, Temporal/Spatial probability	Risk	Van Westen [13]

Table 1 shows that hazard frequency (or probability of occurrence) is the most common factor used in risk assessment. Some approaches are focused on hazard intensity and some of them on vulnerability in combination with damage or loss. However, half of the papers dealing with multi-hazard approach are taking into account all three emphasized factors—frequency, intensity and vulnerability—including other factors. In the context of the multi-hazard risk assessment, many factors are used. Since each factor can represent one criterion, evaluation of these factors can be used as an input matrix for the Multi-Criteria Analysis (MCA). The reason for using so many criteria (factors) for multi-hazard risk assessments is due to its complexity. According to the standard for risk assessment IEC 31010:2009 [14], the risk assessment is the overall following process: risk identification, risk analysis and risk evaluation, and it is recommended to use multi-criteria analysis or multi-criteria decision-analysis method for the risk assessment.

The problem of the multi-hazard risk assessment is not just in designing a proper calculation to aggregate all hazard risks in one area [15,16], but also to take into account hazards' mutual correlation [9], since one hazard can trigger another one. For instance, fire is usually spread after earthquakes, and earthquakes can produce tsunamis, thus flooding the area.

Although the world is dealing with hazards that have an increasing frequency, like flood disasters that are caused by extreme climate and urbanization processes [17], another problem of the single-hazard or multi-hazard risk assessment lies in a specific type of hazards. There are specific hazards, earthquakes, for instance, that can be represented as low-probability/high-consequence events [10]. This issue represents a large problem, as earthquakes can have high intensity while their frequency is usually very low, so the risk calculation of multiplying intensity and frequency will result in a low risk level. Therefore, additional factors need to be taken into calculation to emphasize the risk from earthquakes and similar hazards that are low-probability/high-consequence events.

Vulnerability is one of the most important factors in the risk assessment [18]. Namely, high vulnerability of some areas can result in severe losses during a low-intensity hazard, and low vulnerability can result in minor losses during a high-intensity hazard. Many different criteria are used for vulnerability calculation, because the criteria set is also defined by the type of hazard [4]. However, assessing the vulnerability to natural hazards such as earthquakes can be characterized as an ill-structured problem or a problem without unique,

identifiable and objectively optimal solution. A review of the literature indicates a number of contrasting definitions of what vulnerability means, as well as numerous conflicting perspectives on what should or should not be included within the broad assessment of vulnerability in cities [19]. For instance, some authors also include coping capacity (emergency units) of the area in the vulnerability analysis [5]. But this is not necessarily a good approach, since coping capacity is something that can dynamically change each year, and other common vulnerability criteria (building age, building structure, building height, etc.) are less or more static. Furthermore, it is important to mention that different vulnerability analyses are used at different scales [20]. The different criteria sets (factors) are used and sometimes different methods must be used, as well.

The aim of this study is the assessment of multi-hazard risk for Kaštel Kambelovac, a small city placed along the Adriatic Sea near the city of Split, Croatia (Figure 1).



Figure 1. The City of Kaštela: (a) Historical center of Kaštel Kambelovac [21]; (b) Coastal flooding events in the City of Kaštela [22,23].

Due to its location in a zone of high seismic risk and considering the large number of stone-made and several-centuries-old historical buildings, Kaštela is a settlement with pronounced seismic vulnerability and risk [18]. The historical center, built right next to the low-lying coast, is also threatened by floods due to rising sea levels caused by climate change. Furthermore, the settlement is exposed to flooding caused by extreme sea waves generated by severe wind. Therefore, the present multi-hazard risk assessment is aimed at determining the combined risk of the settlement caused by earthquakes, sea floods and extreme sea waves. The multi-hazard risk investigation of the Kaštel Kambelovac is a part of the project “Preventing, managing, and overcoming natural-hazards risks to mitigate economic and social impact” (PMO-GATE) [24].

The main challenge in the multi-hazard risk assessment is to evaluate, use and mutually compare different mathematical variables that describe the hazard’s frequency, intensity and vulnerability. In this research, this issue is addressed by using the multi-criteria analysis that is commonly used to evaluate and compare quantitative and qualitative criteria in completely different units and the order of magnitude. However, a proper multi-criteria analysis must be selected. An additional challenge in the multi-hazard risk assessment is the data collection and evaluation, which can become complex on the settlement or regional level. Therefore, a proper spatial analysis must be used to organize and aggregate spatial thematic layers. Accordingly, the Geographic Information System is used in combination with multi-criteria analysis in order to establish a Spatial Multi-Criteria Decision Making system.

2. Methodology

The methodology used in this research relies on the combination of the Multi-Criteria Analysis/Multi-Criteria Decision-Making (MCA/MCDM) and Geographic Information System (GIS) to evaluate and visualize this risk assessment in this particular area. The advantage of GIS is in its ability to visualize spatial data (Figure 2) and enhance the spatial decision-making in the risk assessment [25–27].

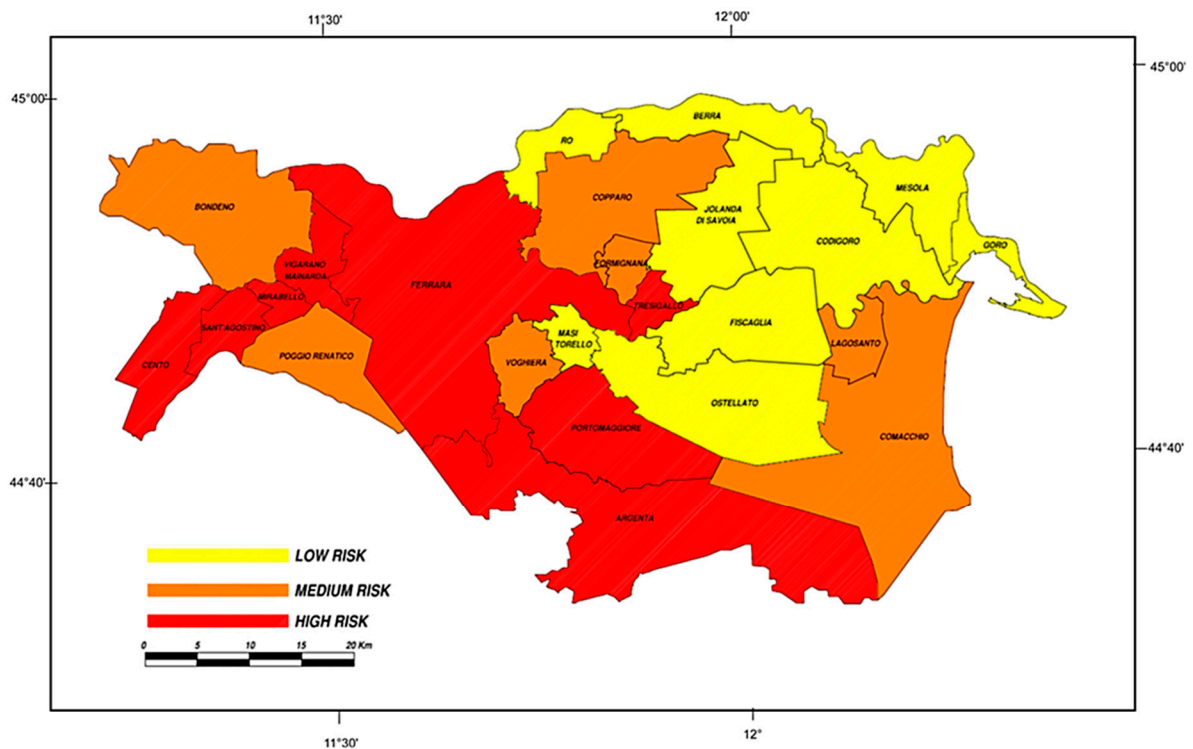


Figure 2. An example of multiple-risk map for the Ferrara province [15].

Furthermore, GIS supports the usage of the multi-scale approach and different criteria sets: the vulnerability analysis can be made for each building, the whole settlement, the settlement’s municipality, and for the whole region. The multi-scale approach was discussed in the already-mentioned paper by Vicente et al. [20], but greater contribution was given by Aubrecht et al. [28] that presented multi-level geospatial modeling of vulnerability indicators from building level to country level. Another example of a multi-level and multi-criteria approach is presented in Figure 3.

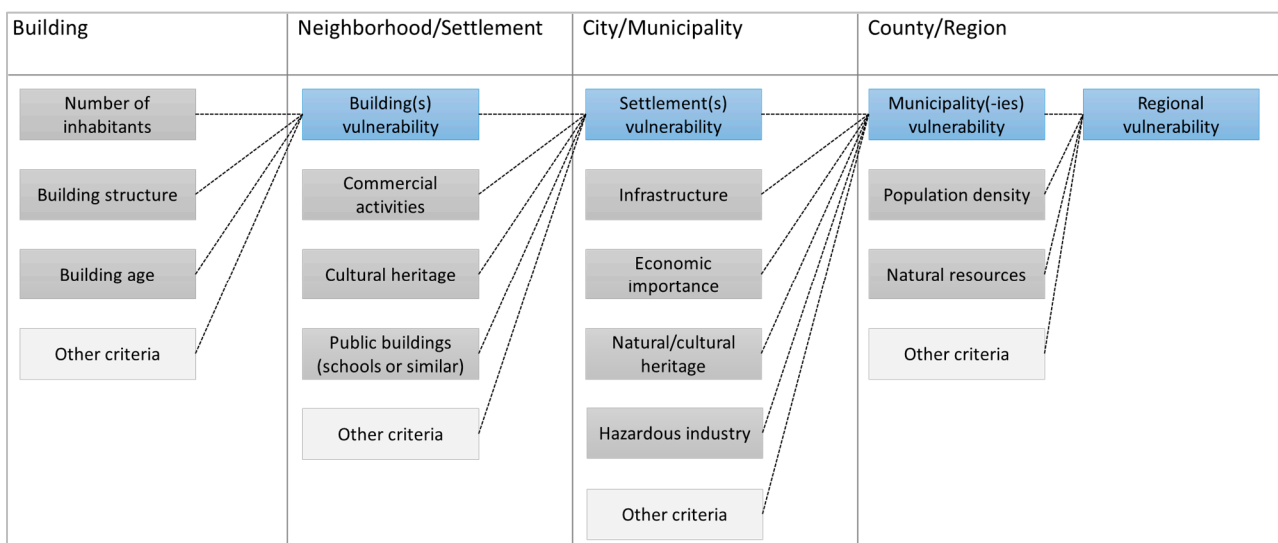


Figure 3. Vulnerability analysis at different scales with multi-criteria approach.

Regarding the risk assessment, it is usually made for a particular assessment area. These areas need to be defined by mutual spatial characteristics or by some already defined urban entity.

The first and simplest approach is to use some administrative areas as assessment areas: settlements, municipalities, provinces, counties, etc. This approach was used in the combined seismic and flood risk assessment for municipalities in the province of Ferrara [15].

The second approach is the definition of assessment areas as “working units” by using a grid of blocks. The working unit is the geographical entity in which the calculations will be computed, hereby controlling the geographical resolution of the study. The definition of the working unit depends strongly on two factors: the geographical unit in which the original data is expressed and the scale of the study. For instance, in the urban-scale seismic risk study for city Almería, a 200 m squared grid was considered appropriate to cover the entire city of Almería, totaling an amount of 400 equal cells or working units [27].

The third approach is to define assessment areas as “homogeneous zones”, which are generated by intersecting relevant thematic layers in the assessment area. The intersection of the defined number of layers becomes an assessment area (zone). This approach has been used in this research for Croatian settlement Kaštel Kambelovac, a part of Kaštela City.

2.1. Multi-Criteria Analysis and Decision-Making Approach to Risk Assessment

In the analysis of natural hazards, impacts are often expressed in terms of hazard, vulnerability and exposure. A hazard (H) presents the probability that a harmful event will appear in a particular area and in a certain time interval. Vulnerability (V) is defined as the characteristics and circumstances of a community, system or asset that make it susceptible to the damaging effects of a hazard. Exposure (E) is the totality of people, property, systems or other elements present in hazard zones that are thereby subject to potential losses.

In this research, the hazard (H) is presented by seismic hazard maps with a Peak Ground Acceleration—PGA for the earthquake, while, in the case of sea floods and extreme sea waves, it is based on a flood depth and a wave height in inundation areas, respectively. The exposure (E) that corresponds to the measure of hazard will be presented by intensity and Area Impact (e.g., area exposed to earthquake, flood or extreme waves). Furthermore, vulnerability is evaluated by vulnerability index on multiple levels (for the particular building, for the settlement, etc.) with the use of additional criteria set which is different for each level. Therefore, in this research, function f represents mathematical PROMETHEE (Preference Ranking Organisation METHod for Enrichment Evaluations) method [29] that will connect all criteria and assess the risk for the observed area.

Obviously, there are many other mathematical methods for multi-criteria analysis and decision-making, but some of them are better accepted and more widely used. Three of them have recently become the most popular: AHP [25], TOPSIS [26] and PROMETHEE [30,31]. There is also a need to decide which of the available methods is the most adequate for a particular problem, but very often, the outranking methods like PROMETHEE are the most suitable choice [32]. This is especially because PROMETHEE method can be simplified to be used by non-expert users [33,34].

Furthermore, using the concept of vulnerability makes it more explicit that the impacts of a hazard are also a function of the preventive and preparatory measures that are employed to reduce the risk. Depending on the particular risk analyzed, the measurement of risk can be carried out with a greater number of different variables and factors, depending inter alia on the complexity of the chain of impacts, the number of impact factors considered and the requisite level of precision. The scheme of assessment of single-hazard and multi-hazard exposure for the investigated coastal urban area is shown in Figure 4.

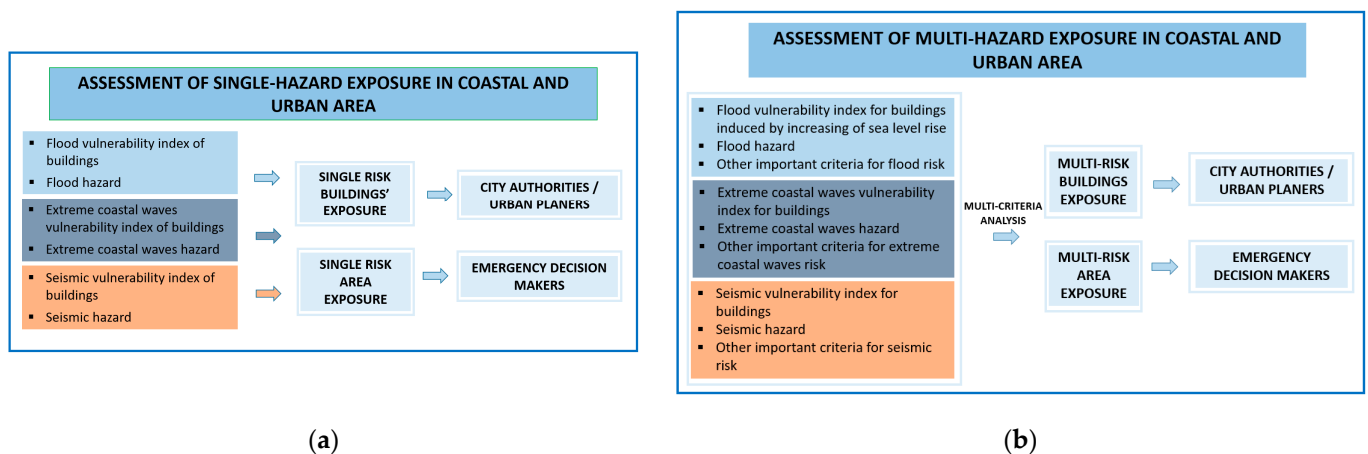


Figure 4. The scheme of the risk assessment for investigated area: (a) single-hazard exposure; (b) multi-hazard exposure.

2.2. Risk Assessment of Buildings

In this research, the risk assessment is made for different levels, starting from the lowest level (micro level), i.e., an individual building. At this micro level, the risk assessment of a single-hazard exposure is based on the calculation of vulnerability indexes of buildings for individual natural disasters:

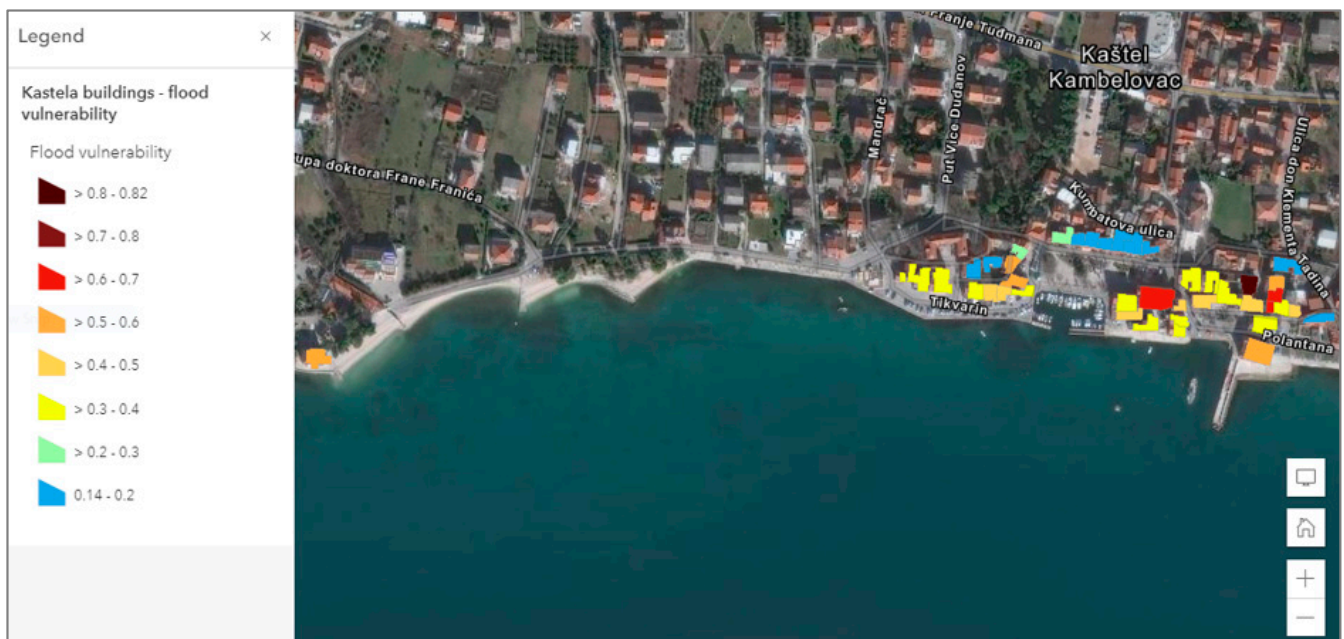
- Flood vulnerability index for buildings,
 - Extreme coastal waves vulnerability index for buildings,
 - Seismic vulnerability index for buildings,
- as well as on assessment of the single hazards:
- Flood hazard,
 - Extreme coastal waves hazard,
 - Seismic hazard.

Seismic vulnerability indexes of the buildings for investigated area are calculated according to the seismic vulnerability method [35]. The method is based on the evaluation of 11 geometrical, structural and non-structural vulnerability parameters of the building. They consider the influence of the type and quality of the structural system, the shear resistance in two horizontal directions, the position and the foundations, the properties of floors, the configuration in plan and elevation, the maximum wall spacing, the roof's typology and weight, the existence of non-structural elements, and the state of preservation. Four possibilities for each parameter were decided: from "A", indicating an optimal state, to "D", indicating a poor state. The relative importance of each parameter in the overall vulnerability is computed by using weight coefficients relating to each parameter. Finally, the vulnerability index I_v is calculated in a form $I_v = \sum_i s_{vi} w_i$, where s_{vi} is the numerical score for each class, and w_i is the weight of each parameter. The vulnerability index is normalized in a 0–100% range; a low index indicates high seismic resistance and low vulnerability, while a high vulnerability index is characteristic of the buildings with low seismic resistance and high vulnerability. Vulnerability indexes of the buildings located in the pilot area are presented in Figure 5 [35].



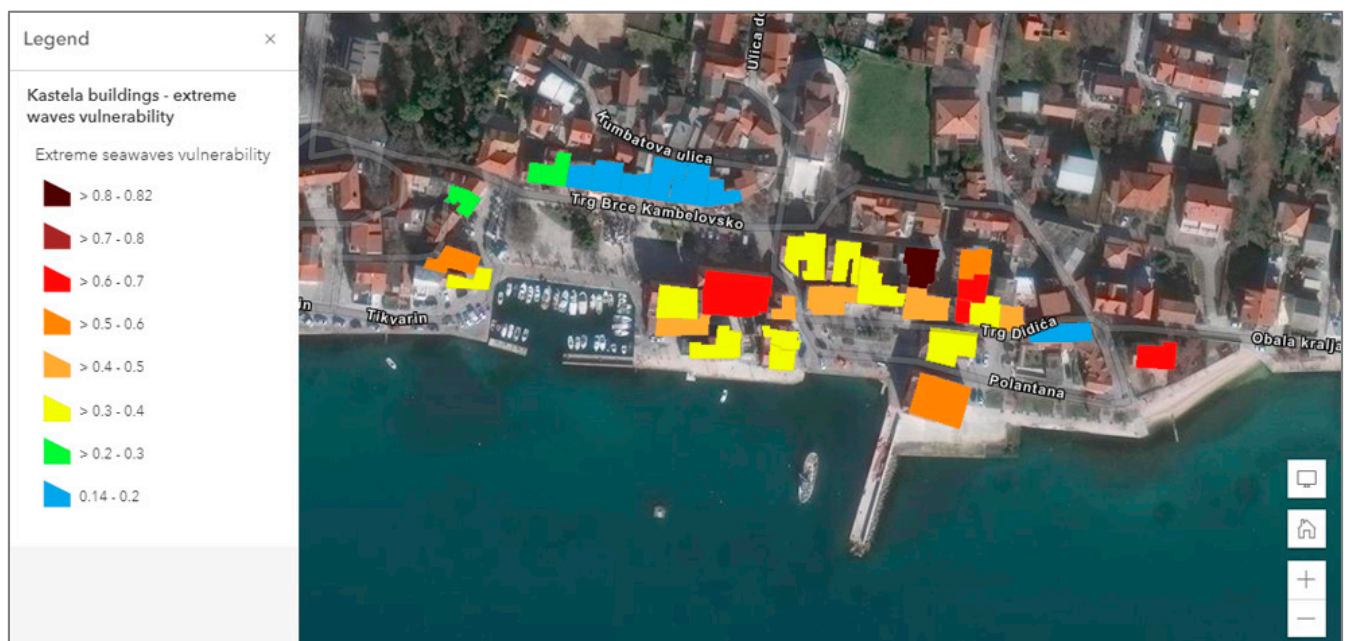
Figure 5. Seismic vulnerability index of buildings divided into 10% intervals.

The flood vulnerability index and the extreme coastal waves vulnerability index are calculated according to the methodology developed in the PMO-GATE project [25]. This methodology is based on the approach of Miranda and Ferreira [36], which takes into consideration different parameters such as building material, overall object condition, number of storeys, building age, importance of exposed objects and level of exposure. The approach has been modified for application in the multicriteria analysis, with each vulnerability index calculated as the weighted sum of set of parameters and evaluated through vulnerability classes (Figure 6).



(a)

Figure 6. Cont.



(b)

Figure 6. Vulnerability index of buildings for: (a) sea floods; (b) extreme sea waves.

The seismic hazard for Croatia is presented with two maps for return periods of 475 and 95 years, expressed in terms of the peak ground acceleration during an earthquake for a soil class A [37]. According to HRN EN 1998-1:2011 [36], the soil types A, B, C, D and E, may be used to account for the influence of local ground conditions on the seismic action. The site can be classified according to the value of the average shear wave velocity $v_{s,30}$. An investigation of the deep geology and characteristics of the terrains, performed at pilot area [38], has shown that shear wave velocity $v_{s,30}$ is higher than 800 m/s at the whole area, which define soil class A. Therefore, local ground conditions do not influence to seismic hazard in the investigated area, i.e., the seismic hazard for all buildings at the pilot area has been assumed to be constant [35].

The flood hazard caused by climate-induced sea level rise is estimated according to IPCC Fifth Assessment Report (AR5) [39] and Strategy for climate change adaptation for The Republic of Croatia [40], considering changes in the mean sea level. However, the EU Flood Directive [41] requires an analysis of a high, moderate and low probability scenario in the flood hazard assessment. The sea level in the Adriatic Sea is dominantly caused by sea tides and the effect of the barometric pressure [42]. The tidal component can be represented by the set of periodic functions [43], and the residual sea level can be represented with a probability distribution due to its randomness and stochastic behavior. In order to fulfil the Flood Directive requirements, probability scenarios are estimated from the particular probability distribution, corresponding to the return periods of 25, 100 and 250 years, respectively [44]. Finally, sea level is estimated as a superposition of mean sea level, maximum estimated tide and each probabilistic scenario. The distribution of the critical zones most prone to flood due to the impacts of climate change on sea level rise for the most critical scenario for year 2100 is shown in Figure 7 [45].

The extreme coastal waves hazard is determined based on the evaluation of wave heights and their propagation toward the coast (Figure 8). The methodology for computing the wave heights by using values of wind speeds in critical wind directions for the investigated area has been developed [46], where probability distribution function is used to fit wind speed histograms and to evaluate return period values.



Figure 7. Distribution of critical zones most prone to flood due to impact of climate changes on sea level rise: scenario for year 2100.

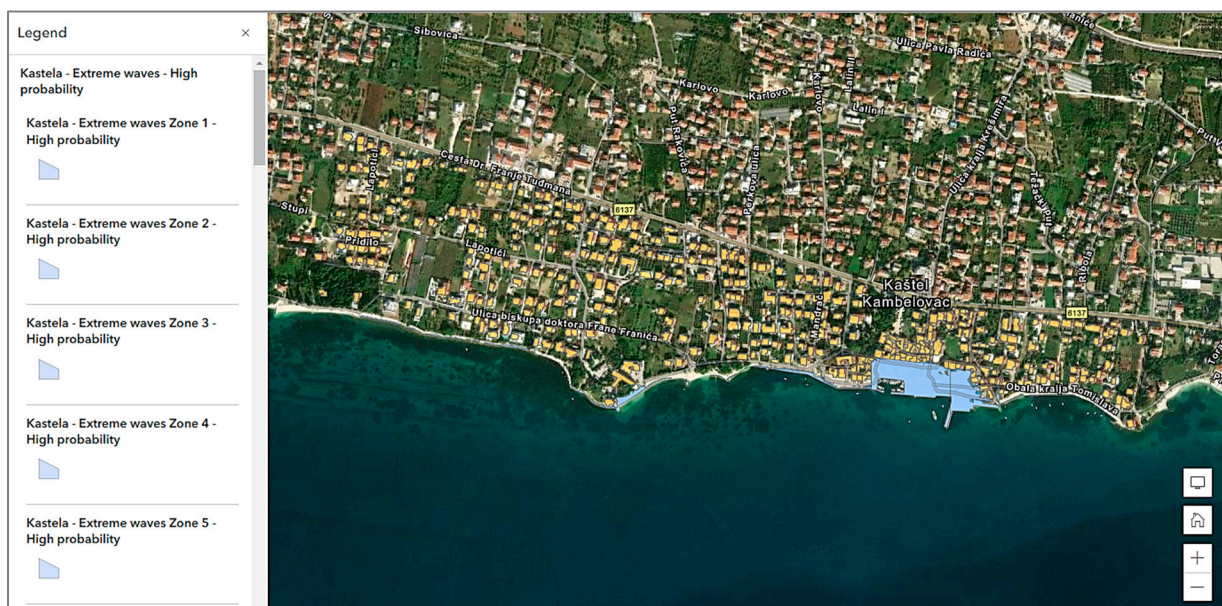


Figure 8. Distribution of critical zones most prone to extreme sea waves exposure.

Vulnerability indexes of buildings for individual natural disasters coupled by the corresponding hazards are the basis for the multi-hazard risk assessment of the area [47].

2.3. Risk Assessment of Homogenous Zones

At the higher level of analysis, which is the intermediate level, the previously-analyzed objects are grouped into spatial units (assessment area) that are called “homogenous zones” [47]. The process of creation of homogenous zones for the pilot site is presented in Figure 9. In this case, three different layers are intersected: a layer of specific urban characteristics, a layer of areas surrounded by the main roads and a layer of terrain height.

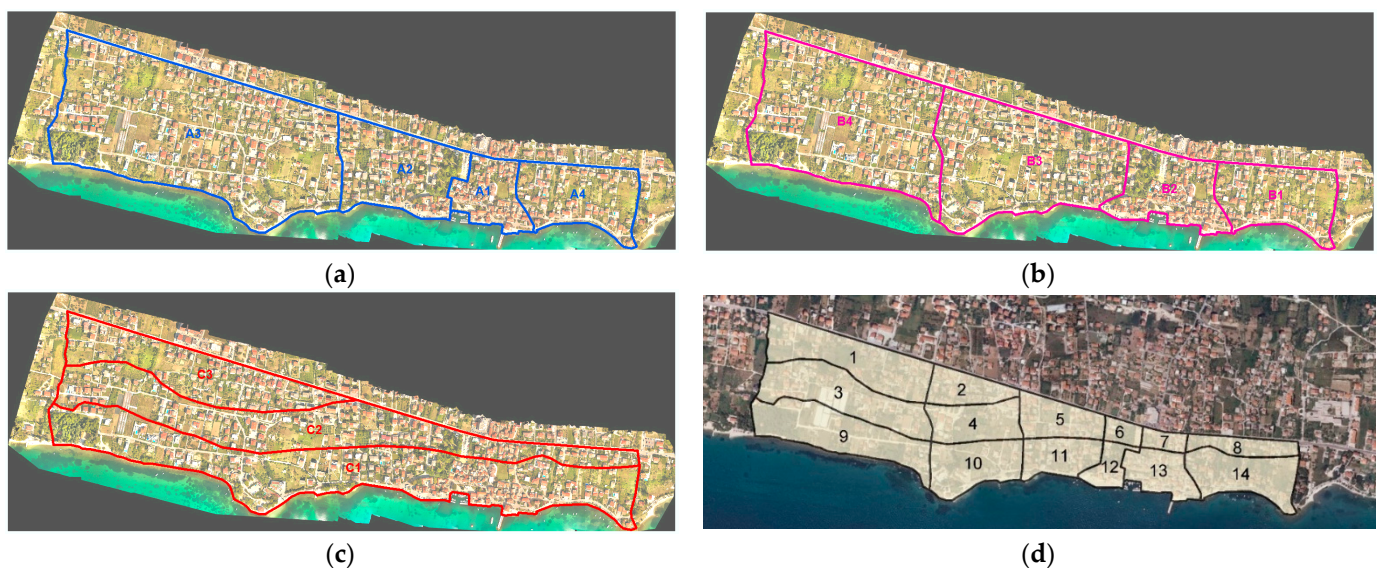


Figure 9. The creation of homogenous zones: (a) four areas defined by specific urban characteristics; (b) four areas defined by main roads; (c) three areas defined by terrain (contours 5 and 10 m); (d) intersection of layers resulted with 15 homogenous zones.

The seismic vulnerability indexes of individual buildings are used to calculate the seismic vulnerability index of a homogeneous zone. In the same way, the other vulnerabilities indexes are evaluated. However, it is important to highlight that the additional criteria are very important at this level of analysis. Since homogeneous zones have complex characteristics, additional criteria are used for both single-hazard and a multi-hazard approach, beside vulnerability and hazard.

The literature review shows that the level of risk to the community depends on a number of other parameters whose activation in a particular hazard reduces the resilience to extraordinary events. Each area due to difference in size requires a special approach in identifying the relevant parameters. For example, the most common parameters (criteria) for seismic hazard are grouped into area characteristics (geology, soil, slope, historical earthquake events, fault line, etc.), the characteristics of human intervention in space (land use, built communal infrastructure and roads, etc.), and social characteristics (housing density, social purpose of buildings, social structure, etc.).

For the pilot site at the intermediate level, additional parameters that can be quantified are detected, different for each homogeneous zone. They represent additional criteria for the risk assessment of homogenous zones: communal infrastructure, road network, construction density (distance between buildings), inhabitation density, importance factor (public building, school, etc.), and historical buildings.

3. Results

3.1. Single-Hazard Risk Assessment of Homogenous Zones

Single-hazard risk assessment is made for 14 homogeneous zones of the pilot site. Since the flood and extreme waves are affecting only a small coastal area, the seismic risk assessment will be presented here. The input data are calculated, or expert estimates are given for the following criteria:

- Seismic hazard—PGA,
- Buildings' seismic vulnerability,
- Geology,
- Communal infrastructure—electricity supply,
- Communal infrastructure—water supply and drainage,
- Road network,
- Construction density (distance between buildings),

- Inhabitation density,
- Importance factor (public, school, etc.),
- Historical buildings.

Since seismic hazard (PGA) and geology have the same values in each of the 14 homogeneous zones, they do not need be included in the numerical processing. The average seismic vulnerability has been calculated for each homogenous zone (Table 2).

Table 2. The basic data of homogenous zones and average seismic vulnerability index.

Homogenous Zone (HZ)	Area (m ²)	Number of Buildings	Seismic Vulnerability Index of Homogenous Zone
HZ1	58.627	56	0.133
HZ2	21.865	29	0.174
HZ3	57.189	54	0.116
HZ4	30.925	25	0.120
HZ5	26.972	38	0.132
HZ6	7.763	4	0.194
HZ7	7.767	20	0.435
HZ8	16.168	19	0.162
HZ9	60.068	38	0.136
HZ10	38.133	14	0.171
HZ11	24.972	35	0.156
HZ12	12.696	17	0.448
HZ13	24.903	71	0.493
HZ14	40.782	48	0.187

The criterion inhabitation density is generated from a digitized population census. For all other additional criteria a profound GIS analysis has been made, and criteria evaluations for each homogenous zone have been calculated or estimated (Figure 10).

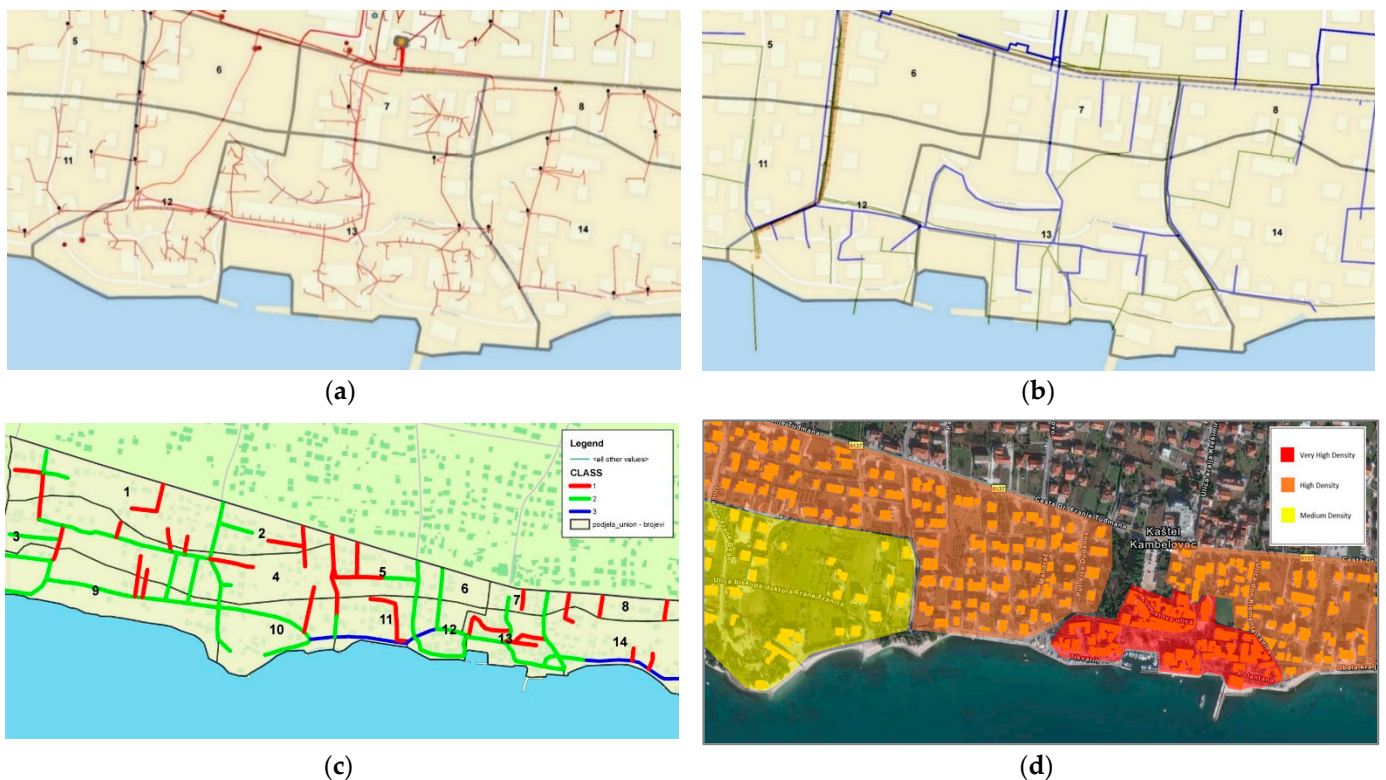


Figure 10. Cont.



Figure 10. GIS analysis of additional criteria: (a) electricity supply; (b) water supply and drainage; (c) road network; (d) construction density; (e) importance factor (public, school, etc.); (f) historical buildings.

All the above-mentioned data have been collected into the decision matrix to be used by the PROMETHEE method with the help of Visual PROMETHEE software (Figure 11).

Visual PROMETHEE Academic - PMO-GATE_Kastela.vpg (saved)

File Edit Model Control PROMETHEE-GAIA GDSS GIS Custom Assistants Snapshots Options Help

Scenario1	checkbox	checkbox	checkbox	checkbox	checkbox	checkbox	checkbox	checkbox
Criterion	checkbox	checkbox	checkbox	checkbox	checkbox	checkbox	checkbox	checkbox
Unit	unit	unit	unit	unit	unit	unit	unit	unit
Cluster/Group	◆	◆	◆	◆	◆	◆	◆	◆
Preferences								
Min/Max	max	max	max	min	max	max	max	max
Weight	40,00	10,00	8,00	8,00	14,00	10,00	4,00	6,00
Preference Fn.	Linear	Linear	Linear	Linear	Linear	Linear	Linear	Linear
Thresholds	absolute	absolute	absolute	absolute	absolute	absolute	absolute	absolute
- Q: Indifference	1,00	1,00	1,00	10,00	1,00	1,00	1,00	1,00
- P: Preference	100,00	20,00	20,00	1000,00	10,00	500,00	10,00	20,00
- S: Gaussian	n/a	n/a	n/a	n/a	n/a	n/a	n/a	n/a
Evaluations								
HZ1	13,30	11,00	8,00	-216,00	0,00	252,00	0,00	0,00
HZ2	17,40	13,00	7,00	80,00	0,00	130,00	0,00	0,00
HZ3	11,60	11,00	8,00	492,00	0,00	243,00	0,00	0,00
HZ4	12,00	9,00	11,00	-80,00	0,00	112,00	0,00	0,00
HZ5	13,20	8,00	9,00	-121,00	0,00	171,00	0,00	0,00
HZ6	19,40	2,00	2,00	60,00	0,00	18,00	0,00	0,00
HZ7	43,50	5,00	4,00	39,00	0,00	90,00	0,00	0,00
HZ8	16,20	7,00	9,00	-137,00	0,00	86,00	0,00	0,00
HZ9	13,60	9,00	7,00	633,00	0,00	171,00	0,00	0,00
HZ10	17,10	7,00	12,00	463,00	0,00	63,00	5,00	0,00
HZ11	15,60	10,00	13,00	283,00	0,00	158,00	2,00	0,00
HZ12	44,80	9,00	15,00	325,00	2,00	76,00	0,00	4,00
HZ13	49,30	15,00	18,00	211,00	9,00	319,00	7,00	15,00
HZ14	18,70	9,00	12,00	317,00	0,00	216,00	3,00	0,00

Figure 11. Homogenous zones input data for PROMETHEE method (decision matrix).

The preliminary results of the PROMETHEE method are given in Figure 12, in which better rank represents higher risk. It means that the best-ranked homogenous zone HZ13 has the highest seismic risk in this case.

Rank	action	Phi	Phi+	Phi-
1	HZ13	0,3993	0,4104	0,0111
2	HZ12	0,0975	0,1512	0,0537
3	HZ7	0,0302	0,1110	0,0808
4	HZ1	0,0025	0,0684	0,0659
5	HZ14	-0,0142	0,0518	0,0659
6	HZ2	-0,0269	0,0451	0,0720
7	HZ11	-0,0317	0,0395	0,0713
8	HZ5	-0,0318	0,0418	0,0735
9	HZ4	-0,0401	0,0387	0,0787
10	HZ8	-0,0420	0,0375	0,0795
11	HZ10	-0,0644	0,0349	0,0993
12	HZ3	-0,0654	0,0347	0,1000
13	HZ9	-0,0975	0,0166	0,1141
14	HZ6	-0,1156	0,0250	0,1407

Figure 12. Results of the PROMETHEE method for 14 homogeneous zones (better rank represents higher risk).

Visual representation of the results has been made in GIS, where green represents low risk and red represents high risk (Figure 13).

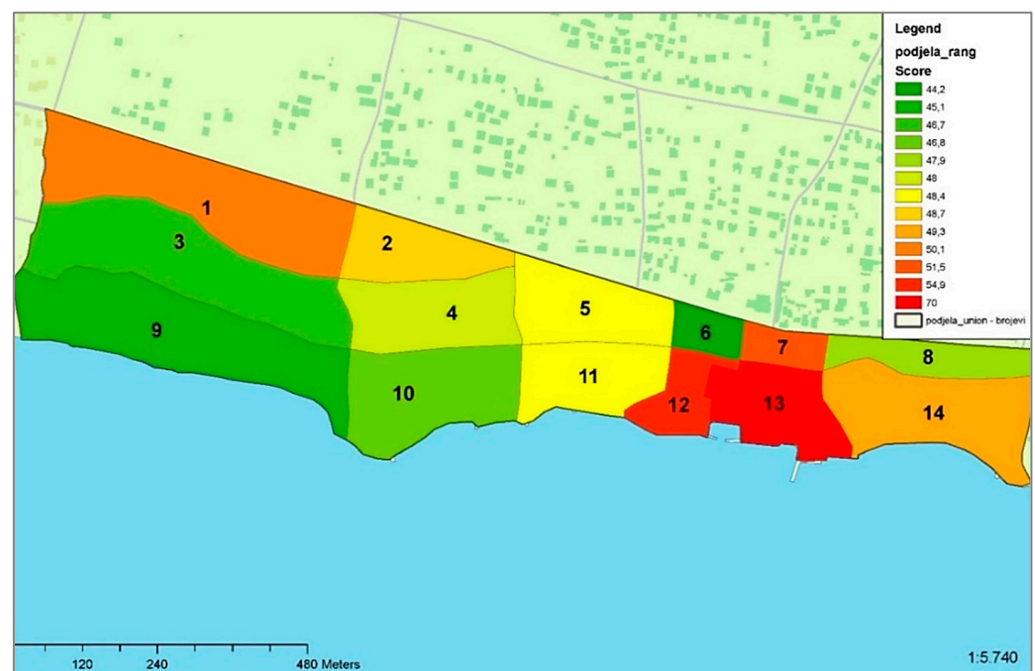


Figure 13. Seismic risk assessment for homogenous zones (green represents low risk, red represents high risk).

3.2. Multi-Hazard Risk Assessment of Homogenous Zones

Three natural-hazards—seismic, flood and extreme waves—are combined and evaluated together to assess the multi-hazard risk, and the analysis is made on the level of homogenous zones.

The two combined risk analysis are made: combination of two risks for seismic and flood hazard; and combination of three risks for seismic, flood and extreme waves hazard. Each analysis is made on three levels. The first level of analysis is based on hazard and

vulnerability data aggregated for each homogenous zone. A second and third level of analysis are using additional criteria for each homogenous zone (Table 3).

Table 3. Combined risks analysis and criteria for each level of analysis.

Level	Combined Seismic-Flood Risk: Scenario S-F	Combined Seismic-Flood-Extreme Waves Risk: Scenario S-F-EW
Level 1 criteria	Seismic hazard (1.1) Seismic vulnerability (1.2) Flood hazard (1.3) Flood vulnerability (1.4)	Seismic hazard (1.1) Seismic vulnerability (1.2) Flood hazard (1.3) Flood vulnerability (1.4) Extreme waves hazard (1.5) Extreme waves vulnerability (1.6)
Level 2 criteria	Seismic hazard (1.1) Seismic vulnerability (1.2) Flood hazard (1.3) Flood vulnerability (1.4) Construction density (2.1) Inhabitation density (2.2) Importance factor (2.3) Historical buildings (2.4)	Seismic hazard (1.1) Seismic vulnerability (1.2) Flood hazard (1.3) Flood vulnerability (1.4) Extreme waves hazard (1.5) Extreme waves vulnerability (1.6) Construction density (2.1) Inhabitation density (2.2) Importance factor (2.3) Historical buildings (2.4)
Level 3 criteria	Seismic hazard (1.1) Seismic vulnerability (1.2) Flood hazard (1.3) Flood vulnerability (1.4) Construction density (2.1) Inhabitation density (2.2) Importance factor (2.3) Historical buildings (2.4) Electrical infrastructure (3.1) Water supply infrastructure (3.2) Road network (3.3)	Seismic hazard (1.1) Seismic vulnerability (1.2) Flood hazard (1.3) Flood vulnerability (1.4) Extreme waves hazard (1.5) Extreme waves vulnerability (1.6) Construction density (2.1) Inhabitation density (2.2) Importance factor (2.3) Historical buildings (2.4) Electrical infrastructure (3.1) Water supply infrastructure (3.2) Road network (3.3)

Therefore, six multicriteria analyses are made on three different levels for each of the two scenarios. These multi-criteria analyses are classifying homogenous zones in accordance with multi-hazard risk.

The first analysis is the combined seismic-flood risk (Scenario S-F) on three different levels. Each level represents different criteria sets. Criteria are grouped in two major groups: main criteria, which are related to hazard and vulnerability and additional criteria, which are related to some important spatial data. Each criteria group has its own weight. In this case, an equal weight is given to each group—50%. An example of distribution of the criteria weights within the group are presented in Table 4. Criteria weights in this particular application are estimated comparing the estimated Expected Annual Damage values for each observed natural hazard. The Expected Annual Damage concept is based on the combination of occurrence probability and corresponding damage caused by each natural hazard [48], and it has proved to be an effective method since it enables a practical comparison of significantly different natural phenomena.

Table 4. An example of criteria weights for combined seismic-flood risk for Scenario S-F Level 2.

Criteria Group	Group Weight	Criteria	Criteria Weight
Main criteria	50%	Seismic hazard (1.1)	21.7%
		Seismic vulnerability (1.2)	21.7%
		Flood hazard (1.3)	3.3%
		Flood vulnerability (1.4)	3.3%
Additional criteria (<i>n</i> —number of additional criteria)	50%	Construction density (2.1)	50/ <i>n</i> = 12.5%
		Inhabitation density (2.2)	50/ <i>n</i> = 12.5%
		Importance factor (2.3)	50/ <i>n</i> = 12.5%
		Historical buildings (2.4)	50/ <i>n</i> = 12.5%

The input data for analysis is presented as a matrix with alternatives, in this case 14 homogenous zones (HZ) and up to 11 criteria depending on the level of analysis (Figure 14).

Short Name	1.1 Seismic vuln.	1.2 Seismic haz.	1.3 Flood vuln.	1.4 Flood haz.	2.1 Constr. dens.	2.2 Inhab. dens.	2.3 Import. fact.	2.4 Histor. build.	3.1 Comm. infr. el.	3.2 Comm. infr. wtr.	3.3 Road net.
HZ 1	13.3	0.22	0	0	0	252	0	0	11	8	-216
HZ 2	17.4	0.22	0	0	0	130	0	0	13	7	80
HZ 3	11.6	0.22	0	0	0	243	0	0	11	8	492
HZ 4	12	0.22	0	0	0	112	0	0	9	11	-80
HZ 5	13.2	0.22	0	0	0	171	0	0	8	9	-121
HZ 6	19.4	0.22	0	0	0	18	0	0	2	2	60
HZ 7	43.5	0.22	0	0	0	90	0	0	5	4	39
HZ 8	16.2	0.22	0	0	0	86	0	0	7	9	-137
HZ 9	13.6	0.22	0	0	0	171	0	0	9	7	633
HZ 10	17.1	0.22	4	1.36	0	63	5	0	7	12	463
HZ 11	15.6	0.22	0	0	0	158	2	0	10	13	283
HZ 12	44.8	0.22	18.6	1.36	2	76	0	4	9	15	325
HZ 13	49.3	0.22	15.04	1.36	9	319	7	15	15	18	211
HZ 14	18.7	0.22	1.52	1.36	0	216	3	0	9	12	317

Figure 14. Input matrix for combined seismic-flood risk (Scenario S-F) multi-criteria analysis with criteria evaluation for all three levels.

The input data (Figure 14) and criteria weights (Table 4) are imported in a multi-criteria analysis application based on the PROMETHEE method and results have been calculated for all three levels of analysis. The first analysis was made for the criteria set defined as Level 1, a second analysis for Level 2 and a third for Level 3. The criteria for each analysis were submitted to PROMETHEE method and the results for all three levels are presented in Figures 15–17, respectively. There are no significant variations in results except zone HZ 13, which becomes more exposed when additional criteria are used (Level 1 and 2). At the end, the results are exported into GIS for better visualization and a further analysis of results (Figure 18).

The second analysis is a combined seismic–flood–extreme waves risk (Scenario S-F-EW) on three different levels. Again, each level represents different criteria sets, and criteria are grouped into two groups: main criteria, which are related to hazard and additional criteria, which are related to some important spatial data. Each criteria group has its own weight. In this case, an equal weight is given to each group: 50%. Other criteria weights are presented in Table 5. The input data for analysis are presented as a matrix with alternatives, in this case 14 homogenous zones (HZ) and up to 13 criteria depending on the level of analysis (Figure 19).

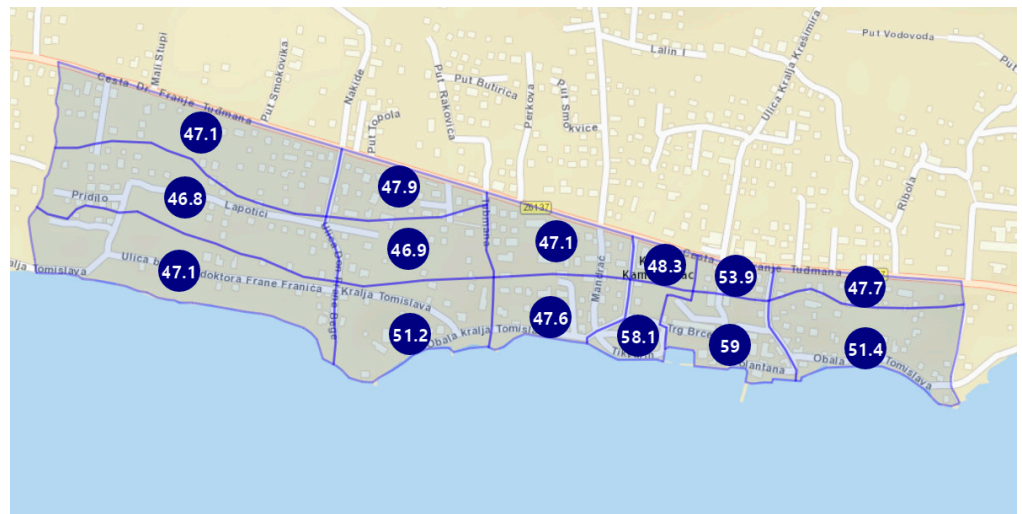


Figure 15. Results of risk analysis for seismic and flood hazard for Level 1 (Scenario S-F L1).

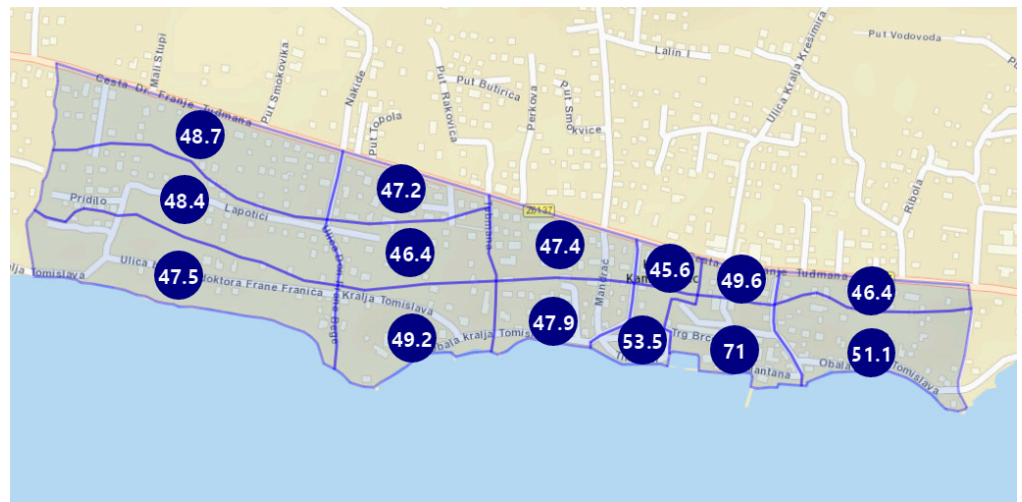


Figure 16. Results of risk analysis for seismic and flood hazard for Level 2 (Scenario S-F L2).

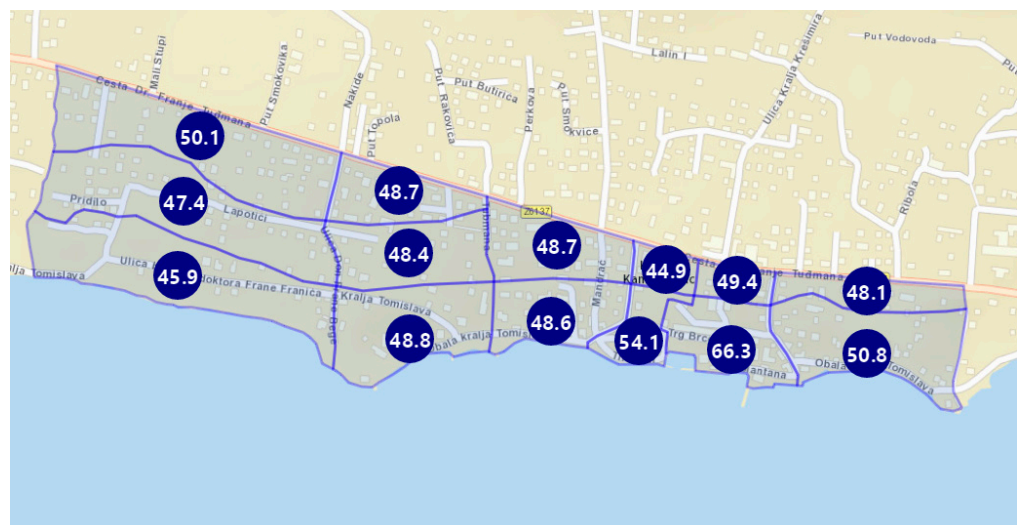


Figure 17. Results of risk analysis for seismic and flood hazard for Level 3 (Scenario S-F L3).

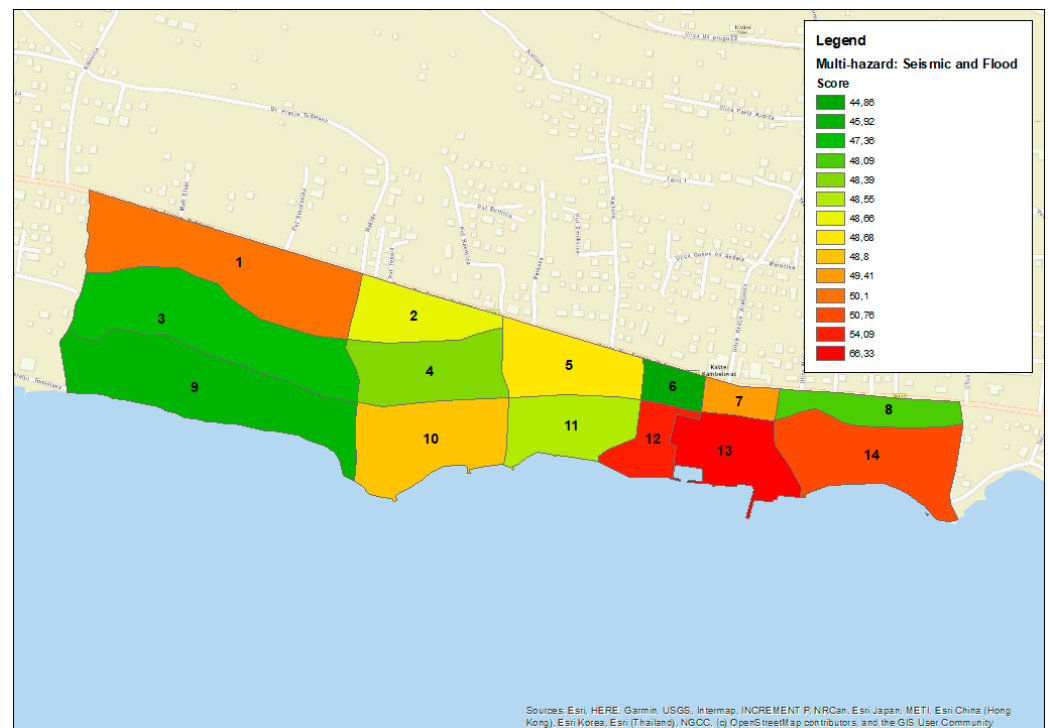


Figure 18. GIS visualization of risk for seismic and flood hazard for Level 3 (Scenario S-F L3).

Table 5. An example of criteria weights for combined seismic–flood–extreme waves risk for Scenario S-F-EW Level 2.

Criteria Group	Group Weight	Criteria	Criteria Weight
Main criteria	50%	Seismic hazard (1.1)	19.5%
		Seismic vulnerability (1.2)	19.5%
		Flood hazard (1.3)	2.5%
		Flood vulnerability (1.4)	2.5%
		Extreme waves hazard (1.5)	3.0%
		Extreme waves vulnerability (1.6)	3.0%
Additional criteria (<i>n</i> —number of additional criteria)	50%	Construction density (2.1)	50/ <i>n</i> = 12.5%
		Inhabitation density (2.2)	50/ <i>n</i> = 12.5%
		Importance factor (2.3)	50/ <i>n</i> = 12.5%
		Historical buildings (2.4)	50/ <i>n</i> = 12.5%

The input data (Figure 19) and criteria weights (Table 5) are imported in a multi-criteria analysis application based on PROMETHEE method and results have been calculated for all three levels of analysis. The first analysis was made for a criteria set defined as Level 1, a second analysis for Level 2 and a third for Level 3. The criteria for each analysis were submitted to PROMETHEE method and the results for all 3 levels are presented in Figures 20–22, respectively. Again, there are no significant variations in results except zone HZ 13, which becomes more exposed when additional criteria are used (Level 1 and 2). At the end, the results are exported into GIS for better visualization and a further analysis of results (Figure 23).

Short Name	1.1 Seismic vuln.	1.2 Seismic haz.	1.3 Flood vuln.	1.4 Flood haz.	1.5 Extr. wav. vuln.	1.6 Extr. wav. haz.	2.1 Constr. dens.	2.2 Inhab. dens.	2.3 Import. fact.	2.4 Histor. build.	3.1 Comm. infr. el.	3.2 Comm. infr. wtr.	3.3 Road net.
HZ 1	13.3	0.22	0	0	0	0	0	252	0	0	11	8	-216
HZ 2	17.4	0.22	0	0	0	0	0	130	0	0	13	7	80
HZ 3	11.6	0.22	0	0	0	0	0	243	0	0	11	8	492
HZ 4	12	0.22	0	0	0	0	0	112	0	0	9	11	-80
HZ 5	13.2	0.22	0	0	0	0	0	171	0	0	8	9	-121
HZ 6	19.4	0.22	0	0	0	0	0	18	0	0	2	2	60
HZ 7	43.5	0.22	0	0	0	0	0	90	0	0	5	4	39
HZ 8	16.2	0.22	0	0	0	0	0	86	0	0	7	9	-137
HZ 9	13.6	0.22	0	0	0	0	0	171	0	0	9	7	633
HZ 10	17.1	0.22	4	1.36	0	0	0	63	5	0	7	12	463
HZ 11	15.6	0.22	0	0	0	0	0	158	2	0	10	13	283
HZ 12	44.8	0.22	18.6	1.36	5.14	1.639	2	76	0	4	9	15	325
HZ 13	49.3	0.22	15.04	1.36	14.82	1.539	9	319	7	15	15	18	211
HZ 14	18.7	0.22	1.52	1.36	1.52	1.359	0	216	3	0	9	12	317

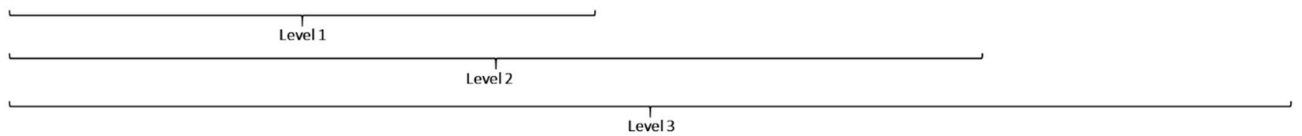


Figure 19. Input matrix for combined seismic–flood–extreme waves risk (Scenario S-F-EW) multi-criteria analysis with criteria evaluation for all three levels.



Figure 20. Results of the risk analysis for seismic, flood and extreme waves hazards for Level 1 (Scenario S-F-EW L1).

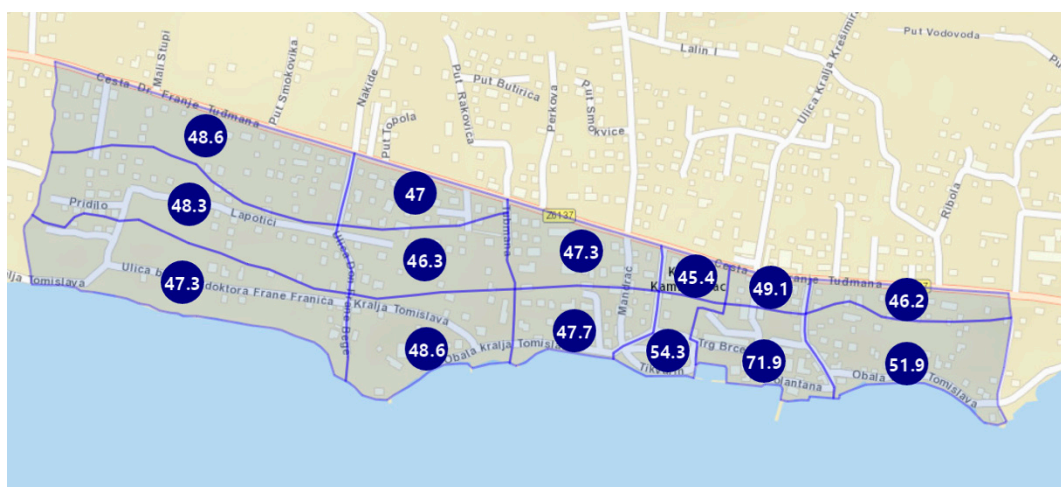


Figure 21. Results of the risk analysis for seismic, flood and extreme waves hazards for Level 2 (Scenario S-F-EW L2).



Figure 22. Results of the combined risk analysis for seismic, flood and extreme waves hazards for Level 3 (Scenario S-F-EW L3).

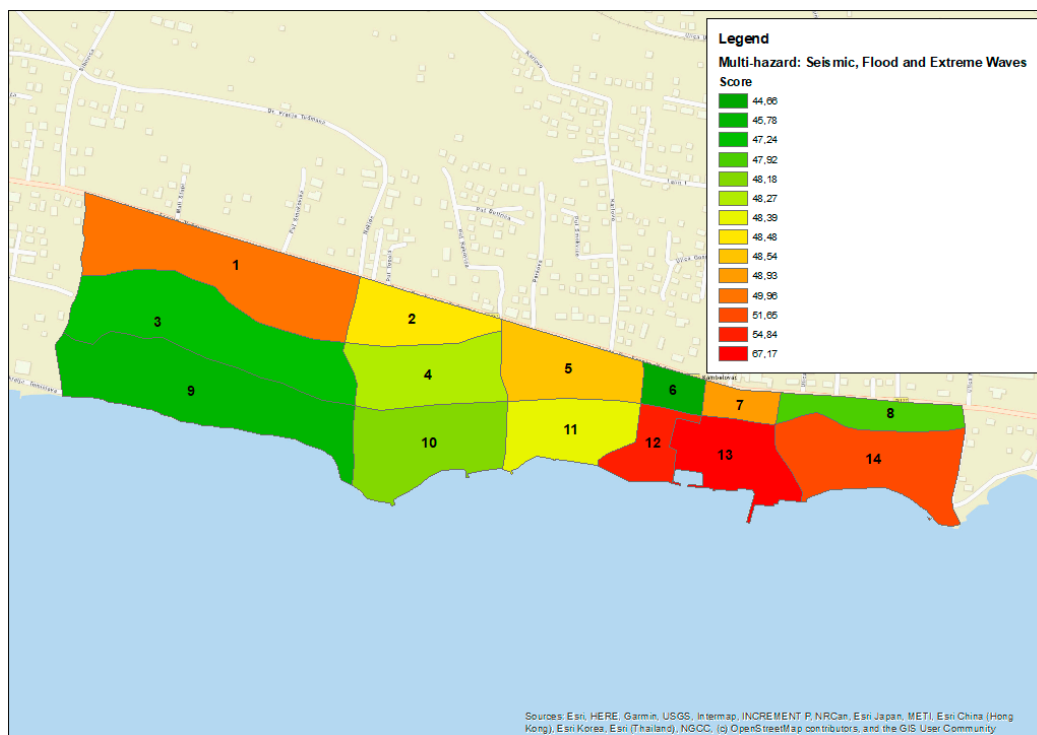


Figure 23. GIS visualization of risk for seismic, flood and extreme waves hazard for Level 3 (Scenario S-F-EW L3).

4. Conclusions

The multi-hazard risk assessment of urban areas is an important step in the risk management process. It can be used to reduce, manage and overcome the risks arising from the combination of different multiple hazards. This paper uses Spatial Multi-Criteria Decision-Making based on PROMETHEE method, coupled with the Geographic Information System, to assess the single-hazard and multi-hazard risk caused by seismic, sea floods and extreme sea waves. A case study for the application of the method is Kaštel Kambelovac, an urban settlement placed at the Croatian part of the Adriatic coast. The observed area has been divided into the homogenous zones that have been identified as areas of the test site with some mutual spatial characteristics. The homogeneity was identified by intersecting spatial

layers in the GIS. The multi-hazard risk assessment method is based on the validation of the main components of the risk caused by natural hazard phenomena, such as vulnerability expressed in terms of the vulnerability index, hazard and influence of additional criteria, to overall risk in homogenous zones. The main specificity of this research is multi-hazard risk evaluation based on a previous detailed calculation of vulnerability indexes of each building in the test area for all observed threats.

The methodology ranks the various homogenous zones in terms of the relative proneness to coupled seismic, sea floods and extreme sea waves hazards. It enables a risk analysis for different scenarios for both single and multiple hazards at the level of buildings and homogenous zones. In the case study presented here, the analysis has shown that the seismic risk is a dominant threat in all scenarios. The results of a multi-hazard analysis for the combination of seismic and sea floods hazard have shown that the area with the highest risk is related to the historical part of Kaštel Kambelovac. This is due to the fact that this area, along with high seismic risk, has the highest level of exposure to flooding. Furthermore, the vulnerability of exposed objects in the historical part is highest for both hazards. Likewise, the results of the multi-hazard analysis for the combination of seismic, sea floods and extreme waves hazard are analogous to previous ones, showing that the highest risk is again in the historical part of Kaštel Kambelovac. The vulnerability of exposed objects to extreme waves is the highest in the historical part, and this particular area is most exposed to extreme waves due its low-lying coast. Performed analyses provide useful information for decision makers and public authorities to define priorities in future interventions through the process of risk management planning.

Author Contributions: Conceptualization, Ž.N. and N.M.; data curation, M.M., N.M. and T.K.; funding acquisition, Ž.N. and E.B.; investigation, Ž.N., N.M., M.M., E.B. and T.K.; methodology, N.M. and M.M. and Ž.N.; software, N.M. and M.M.; supervision, Ž.N. and E.B.; validation, Ž.N., N.M., M.M., E.B. and T.K.; visualization, M.M. and T.K.; writing—original draft, Ž.N., N.M., M.M., E.B. and T.K. All authors have read and agreed to the published version of the manuscript.

Funding: This research was funded by the European Union, Programme Interreg Italy–Croatia, Project “Preventing, managing and overcoming natural-hazards risks to mitigate economic and social impact”—PMO-GATE ID 10046122. The research is also partially supported through project KK.01.1.1.02.0027, co-financed by the Croatian Government and the European Union through the European Regional Development Fund—the Competitiveness and Cohesion Operational Programme.

Institutional Review Board Statement: Not applicable.

Informed Consent Statement: Not applicable.

Data Availability Statement: Some of the datasets that were analyzed in this research are publicly available on the website of PMO-GATE project: <https://www.italy-croatia.eu/web/pmo-gate> (accessed on 25 October 2022).

Acknowledgments: This research was part of the Work Packages 4 and 5 of the European Union, Programme Interreg Italy–Croatia, Project “Preventing, managing and overcoming natural-hazards risks to mitigate economic and social impact”—PMO-GATE ID 10046122. The results of this research were published in the Deliverables: “4.1.1. Methodology for provision assessment indexes based on Spatial Multi-Criteria Decision-Making—Croatia” and “5.1.6. Map of spatial distribution of the critical zones most prone to flood, extreme waves and seismic risks for HR test site”.

Conflicts of Interest: The authors declare no conflict of interest.

References

1. Zerger, A. Examining GIS decision utility for natural hazard risk modelling. *Environ. Model. Softw.* **2002**, *17*, 287–294. [CrossRef]
2. Yum, S.-G.; Son, K.; Son, S.; Kim, J.-M. Identifying Risk Indicators for Natural Hazard-Related Power Outages as a Component of Risk Assessment: An Analysis Using Power Outage Data from Hurricane Irma. *Sustainability* **2020**, *12*, 7702. [CrossRef]
3. Chen, P. On the Diversity-Based Weighting Method for Risk Assessment and Decision-Making about Natural Hazards. *Entropy* **2019**, *21*, 269. [CrossRef] [PubMed]
4. Kappes, M.S.; Keiler, M.; Von Elverfeldt, K.; Glade, T. Challenges of analyzing multi-hazard risk: A review. *Nat. Hazards* **2012**, *64*, 1925–1958. [CrossRef]

5. Greiving, S.; Fleischhauer, M.; Luckenkotter, J. A methodology for an integrated risk assessment of spatially relevant hazards. *J. Environ. Plan. Manag.* **2006**, *49*, 1–19. [CrossRef]
6. Di Mauro, C.; Bouchon, S.M.; Carpignano, A.; Golia, E.; Peressin, S. Definition of Multi-Risk Maps at Regional Level as Management Tool: Experience Gained by Civil Protection Authorities of Piemonte Region. In *Atti del 5° Convegno sulla Valutazione e Gestione del Rischio negli Insediamenti Civili ed Industriali*; University of Pisa: Pisa, Italy, 2006.
7. Fleischhauer, M.; Greiving, S.; Schlusemann, B.; Schmidt-Thomé, P.; Kallio, H.; Tarvainen, T.; Jarva, J. Multi-risk assessment of spatially relevant hazards in Europe. In Proceedings of the ESPON, ESMG Symposium, Nürnberg, Germany, 11–13 October 2005.
8. Kunz, M.; Hurni, L. Hazard maps in Switzerland: State-of-the-art and potential improvements. In Proceedings of the 6th ICA Mountain Cartography Workshop, Lenk, Switzerland, 11–15 February 2008; ICA: Lenk, Switzerland, 2008.
9. Liu, B.; Siu, Y.L.; Mitchell, G. A quantitative model for estimating risk from multiple interacting natural hazards: An application to northeast Zhejiang, China. *Stoch. Environ. Res. Risk Assess.* **2017**, *31*, 1319–1340. [CrossRef]
10. Mignan, A.; Wiemer, S.; Giardini, D. The quantification of low-probability–high-consequences events: Part I. A generic multi-risk approach. *Natural Hazards* **2014**, *73*, 1999–2022. [CrossRef]
11. Munich Re Group. *Topics—Annual Review: Natural Catastrophes 2002*; Munich Re Group: Munich, Germany, 2003.
12. Odeh Engineers, Inc. Statewide Hazard Risk and Vulnerability Assessment for the State of Rhode Island. Tech. Rep., NOAA Coastal Services Center. Available online: http://www.csc.noaa.gov/rihazard/pdfs/rhdisl_hazard_report.pdf (accessed on 23 October 2019).
13. Van Westen, C.J. Multi-hazard risk assessment and decision making. *Environ. Hazards Methodol. Risk Assess. Manag.* **2017**, 31–94. [CrossRef]
14. IEC 31010:2009; Risk Management—Risk Assessment Techniques. International Organization for Standardization ISO: Geneva, Switzerland, 2009.
15. Soldati, A.; Chiozzi, A.; Nikolić, Ž.; Vaccaro, C.; Benvenuti, E. A PROMETHEE Multiple-Criteria Approach to Combined Seismic and Flood Risk Assessment at the Regional Scale. *Appl. Sci.* **2022**, *12*, 1527. [CrossRef]
16. Rocchi, A.; Chiozzi, A.; Nale, M.; Nikolic, Z.; Riguzzi, F.; Mantovan, L.; Gilli, A.; Benvenuti, E. A Machine Learning Framework for Multi-Hazard Risk Assessment at the Regional Scale in Earthquake and Flood-Prone Areas. *Appl. Sci.* **2022**, *12*, 583. [CrossRef]
17. Li, Z.; Song, K.; Peng, L. Flood Risk Assessment under Land Use and Climate Change in Wuhan City of the Yangtze River Basin, China. *Land* **2021**, *10*, 878. [CrossRef]
18. Nikolić, Ž.; Runjić, L.; Ostojić Škomrlj, N.; Benvenuti, E. Seismic Vulnerability Assessment of Historical Masonry Buildings in Croatian Coastal Area. *Appl. Sci.* **2021**, *11*, 5997. [CrossRef]
19. Rashed, T.; Weeks, J. Assessing vulnerability to earthquake hazards through spatial multicriteria analysis of urban areas. *Int. J. Geogr. Inf. Sci.* **2003**, *17*, 547–576. [CrossRef]
20. Vicente, R.; Parodi, S.; Lagomarsino, S.; Varum, H.; Silva, J.A.R.M. Seismic vulnerability and risk assessment: Case study of the historic city centre of Coimbra, Portugal. *Bull. Earthq. Eng.* **2011**, *9*, 1067–1096. [CrossRef]
21. Marinas.com. Kastel Kambelovac Harbour. Available online: https://marinas.com/view/marina/eyc39lv_Kastel_Kambelovac_Harbour_Kastel_Gomilica_Croatia (accessed on 26 October 2022).
22. Portal Grada Kaštela. Novosti. Available online: <https://www.kastela.org/novosti/aktualnosti/43639-zbog-podizanja-mora-uvitturiju-pojedinci-odustali-od-glasanja-policija-zatvorila-promet-rivom-u-sucurcu> (accessed on 26 October 2022).
23. Jutarnji List. Vijesti. Available online: <https://www.jutarnji.hr/vijesti/hrvatska/orkansko-jugo-poplavilo-kastel-stafilic-9607921> (accessed on 26 October 2022).
24. EU Interreg Italy-Croatia, PMO-GATE Project. Preventing, Managing and Overcoming Natural-Hazards Risks to Mitigate Economic and Social Impact (PMO-GATE). Available online: <https://www.italy-croatia.eu/web/pmo-gate/site> (accessed on 3 October 2022).
25. Palchadhuri, M.; Biswas, S. Application of AHP with GIS in drought risk assessment for Puruliya district, India. *Nat. Hazards* **2016**, *84*, 1905–1920. [CrossRef]
26. Nyimbili, P.H.; Erden, T.; Karaman, H. Integration of GIS, AHP and TOPSIS for earthquake hazard analysis. *Nat. Hazards* **2018**, *92*, 1523–1546. [CrossRef]
27. Rivas-Medina, A.; Gaspar-Escribano, J.M.; Benito, B.; Bernabé, M.A. The role of GIS in urban seismic risk studies: Application to the city of Almería (southern Spain). *Nat. Hazards Earth Syst. Sci.* **2013**, *13*, 2717–2725. [CrossRef]
28. Aubrecht, C.; Ozceylan, D.; Steinnocher, K.; Freire, S. Multi-level geospatial modeling of human exposure patterns and vulnerability indicators. *Nat. Hazards* **2013**, *68*, 147–163. [CrossRef]
29. Brans, J.P.; Vincke, P.; Mareschal, B. How to select and how to rank projects: The Promethee method. *Eur. J. Oper. Res.* **1986**, *24*, 228–238. [CrossRef]
30. Mladineo, N.; Margeta, J.; Brans, J.P.; Mareschal, B. Multicriteria ranking of alternative locations for small scale hydro plants. *Eur. J. Oper. Res.* **1987**, *31*, 215–222. [CrossRef]
31. Mladineo, N.; Lozic, I.; Stosic, S.; Mlinaric, D.; Radica, T. An evaluation of multicriteria analysis for DSS in public policy decision. *Eur. J. Oper. Res.* **1992**, *61*, 219–229. [CrossRef]
32. Nemery, P. On the Use of Multicriteria Ranking Methods in Sorting Problems. Ph.D. Thesis, Université Libre de Bruxelles, Brussels, Belgium, 2008.

33. Mladineo, N.; Mladineo, M.; Knezic, S. Web MCA-based decision support system for incident situations in maritime traffic: Case study of Adriatic Sea. *J. Navig.* **2017**, *70*, 1312. [CrossRef]
34. Mladineo, M.; Mladineo, N.; Jajac, N. Project Management in mine actions using Multi-Criteria-Analysis-based decision support system. *Croat. Oper. Res. Rev.* **2014**, *5*, 415–425. [CrossRef]
35. Nikolić, Ž.; Benvenuti, E.; Runjić, L. Seismic Risk Assessment of Urban Areas by a Hybrid Empirical-Analytical Procedure Based on Peak Ground Acceleration. *Appl. Sci.* **2022**, *12*, 3585. [CrossRef]
36. HRN EN 1998-1:2011; Eurocode 8: Design of Structures for Earthquake Resistance. Part 1: General Rules, Seismic Actions and Rules for Buildings. Croatian Standards Institute: Zagreb, Croatia, 2011.
37. Miranda, F.N.; Ferreira, T.M. A simplified approach for flood vulnerability assessment of historic sites. *Nat. Hazards* **2019**, *96*, 713–730. [CrossRef]
38. Da Col, F.; Accaino, F.; Bohm, G.; Meneghini, F. Characterization of shallow sediments by processing of P, SH and SV wave-fields in Kaštela (HR). *Eng. Geol.* **2021**, *293*, 106336. [CrossRef]
39. Intergovernmental Panel on Climate Change (IPCC) Fifth Assessment Report (AR5). Available online: <https://www.ipcc.ch/assessment-report/ar5/> (accessed on 26 October 2022).
40. Strategy for Climate Change Adaptation for Republic of Croatia (Official Gazette NN 46/2020; in Croatian). Available online: https://narodne-novine.nn.hr/clanci/sluzbeni/2020_04_46_921.html (accessed on 26 October 2022).
41. Directive 2007/60/EC of the European Parliament and of the Council of 23 October 2007 on the Assessment and Management of Flood Risks. Available online: <https://eur-lex.europa.eu/legal-content/EN/TXT/PDF/?uri=CELEX:32007L0060&from=EN> (accessed on 26 October 2022).
42. Srzić, V.; Lovrinović, I.; Racetin, I.; Pletikosić, F. Hydrogeological Characterization of Coastal Aquifer on the Basis of Observed Sea Level and Groundwater Level Fluctuations: Neretva Valley Aquifer, Croatia. *Water* **2020**, *12*, 348. [CrossRef]
43. Janeković, I.; Kuzmić, M. Numerical Simulation of the Adriatic Sea Principal Tidal Constituents. *Ann. Geophys.* **2005**, *23*, 3207–3218. [CrossRef]
44. EU Interreg Italy-Croatia, PMO-GATE Project. Deliverable 3.1.2. Definition of Flood Exposure Indexes for the HR Test Site. Available online: <https://www.italy-croatia.eu/web/pmo-gate/docs-and-tools-details?id=1877461&nAcc=4&file=1> (accessed on 20 October 2022).
45. EU Interreg Italy-Croatia, PMO-GATE Project. Deliverable 5.1.6. Map of Spatial Distribution of the Critical Zones Most Prone to Flood, Extreme Waves and Seismic Risks for HR Test Site. Available online: <https://www.italy-croatia.eu/web/pmo-gate/docs-and-tools-details?id=1877461&nAcc=6&file=8> (accessed on 20 October 2022).
46. EU Interreg Italy-Croatia, PMO-GATE Project. Deliverable 3.2.1. Definition of Extreme Waves Exposure Indexes for the HR Test Site. Available online: <https://www.italy-croatia.eu/web/pmo-gate/docs-and-tools-details?id=1877461&nAcc=4&file=9> (accessed on 20 October 2022).
47. EU Interreg Italy-Croatia, PMO-GATE Project. Deliverable 4.1.1. Methodology for Provision Assessment Indexes based on Spatial Multi-Criteria Decision Making. Available online: <https://www.italy-croatia.eu/web/pmo-gate/docs-and-tools-details?id=1877461&nAcc=5&file=1> (accessed on 20 October 2022).
48. Wang, Q.; Liu, K.; Wang, M.; Koks, E.E. A River Flood and Earthquake Risk Assessment of Railway Assets along the Belt and Road. *Int. J. Disaster Risk Sci.* **2021**, *12*, 553–567. [CrossRef]

Article

Coastal Flooding Assessment Induced by Barometric Pressure, Wind-Generated Waves and Tidal-Induced Oscillations: Kaštela Bay Real-Time Early Warning System Mobile Application

Željana Nikolić ^{1,*}, Veljko Srzić ¹, Ivan Lovrinović ¹, Toni Perković ², Petar Šolić ² and Toni Kekez ¹

¹ Faculty of Civil Engineering, Architecture and Geodesy, University of Split, 21000 Split, Croatia

² Faculty of Electrical Engineering, Mechanical Engineering and Naval Architecture, University of Split, 21000 Split, Croatia

* Correspondence: zeljana.nikolic@gradst.hr

Abstract: Our work presents a reliable procedure to obtain real-time assessment of the sea water elevation at the Kaštela Bay site to ensure the a priori warning in the case of expected coastal flooding along the site area. In its origin, the presented procedure relies on relevant data sets which are site-specific and locally observed. Observed data sets are used within the procedure to assess sea water surface elevation when induced by barometric pressure changes and wind-generated waves. Tidal-induced changes are introduced into the assessment procedure by a pre-learned algorithm which relies on long-term sea level oscillations from the relevant tidal gauge. Wind-generated wave heights are determined in the near shore area, following the features of the depth and reflection of the shoreline subsections. By coupling three mechanisms, this paper offers a unique real-time procedure to determine the sea water elevation and assess the possibility for coastline structure to be flooded by the sea. Given information is visualized in a form of mobile application that implements the algorithm and allows end users to set the notifications based on the given ruleset.

Keywords: coastal flooding; real-time warning system; tides; wind-generated waves; barometric pressure; mobile application

Citation: Nikolić, Ž.; Srzić, V.; Lovrinović, I.; Perković, T.; Šolić, P.; Kekez, T. Coastal Flooding Assessment Induced by Barometric Pressure, Wind-Generated Waves and Tidal-Induced Oscillations: Kaštela Bay Real-Time Early Warning System Mobile Application. *Appl. Sci.* **2022**, *12*, 12776. <https://doi.org/10.3390/app122412776>

Academic Editor: Jürgen Reichardt

Received: 31 October 2022

Accepted: 8 December 2022

Published: 13 December 2022

Publisher's Note: MDPI stays neutral with regard to jurisdictional claims in published maps and institutional affiliations.



Copyright: © 2022 by the authors. Licensee MDPI, Basel, Switzerland. This article is an open access article distributed under the terms and conditions of the Creative Commons Attribution (CC BY) license (<https://creativecommons.org/licenses/by/4.0/>).

1. Introduction

Coastal flooding events, including their occurrence and triggers for the appearance of waves, have been investigated in the past to contribute to a better understanding of flood events in coastal areas as well as efficient risk management. Recent investigations have studied the occurrence of storm and sea wave events [1,2], the numerical modelling of wave propagation in coastal areas [3], flood water movement over land areas [4], the impact of storms on coasts [5] and flood vulnerability [6].

Special attention has been given to the development of an early warning system (EWS) for the timely warning of residents in exposed areas as well. Early warning systems are also an integral part of coastal flood management plans and contribute to the development of long-term management strategies [7]. Existing sea-state monitoring technology, historical databases, numerical forecasting models and computer science have been parts of the operational coastal flood early warning system [8]. A EWS modelling framework based on a Bayesian network has been used to link coastal hazards to their socio-economic and environmental factors [9] and connect available field measurements, data obtained from numerical wave simulations and an empirical wave run-up approach [10]. An EWS that determines the total sea level height by combining predictions of tides and sea level anomalies with wave runup estimates has been presented in [11].

Technological progress in computation and communication sciences in the last decade allows for work with large databases that can store registered meteorological data that affect the occurrence of sea floods. This type of data represents a basis for developing different

forecasting platforms, which use input data and boundary conditions from global or regional scales and open sea and weather forecast databases, providing wave propagation in the ports [12]. These platforms use a number of effective hydrodynamic numerical models for the simulation of storm surge and the prediction of sea water level [13]. It is important to notice that the sea water level prediction procedure in real time is a time-consuming process which needs significant computational resources, as well as the development and monitoring of a software architecture [14] to model coupling and integration. The models based on machine learning [15] and artificial intelligence provide easy implementation of numerical models with low computational cost, as well as fast training, validation, testing and evaluation [16].

In the present study, coastal flooding caused by the simultaneous combination of several mechanisms, such as tidal-induced sea level oscillations resulting from barometric pressure changes and wind-generated waves, have been investigated in the Kaštela Bay. A special focus has been given to the area of the city of Kaštela, placed at the north part of the bay (Figure 1), with many cultural and historical buildings and/or areas located near the coastline, which are potentially endangered by coastal flooding and subject to significant consequences and damage (Figure 2).

The design of the early warning system for sea flooding risk in the city of Kaštela includes the following components:

- *A monitoring system* consisting of an installation of hardware at the site location and appropriate software for real-time data collection. This system observes the wind speed and the barometric pressure.
- *Application of mathematical and numerical models for sea level prediction on the coastline:* Numerical model is used to analyze the wave transform mechanism. A specific procedure has been established to incorporate simultaneous effects of wind-generated waves, tides and barometric pressure-induced changes in the sea level to determine sea level at the coastline based on the systematic observations of the abovementioned parameters via a real-time monitoring system (wind speed and direction and barometric pressure). Tidal-induced sea level changes have been obtained based on the past observations of the long-term sea level tidal oscillations from the relevant tidal gauge.
- *Estimation of the risk of flooding for humans:* Using a digital terrain model where each pixel is georeferenced (X, Y coordinates) and assigned altitude Z , the calculated sea heights will be compared with the altitudes, and if the sea elevation is greater than the altitude Z of a pixel, that pixel will be marked as flooded. According to the depth of the sea on land, the risk of flooding for humans will be defined based on an analytical function so that it can be easily integrated into the rest of the system. This information is necessary for the input into the early warning system. For a simple and understandable presentation of the flooding risk, the analyzed coastal area is divided into zones in order to define the total sea level. This division is made according to the criteria of the coast type and the coast height, which have a direct impact on the height of the waves.
- *Dissemination and communication of risk information by mobile application:* Flood warnings will be given to people who have the mobile application, which was developed for the purpose of the dissemination of information about flood risk in the observed area. Those that have installed the application on their mobile phone and enabled that app to send them push notifications will receive the information.

Recently, Internet of Things (IoT) systems that monitor in different scenarios to ensure a green, sustainable future have been widely used to create smart environments tailored to particular human needs [17,18]. Affordable equipment, miniaturized in its deployment, is ensured a long lifetime through solar/battery power; the communication ranges are also extremely increased and can be measured in kilometers in urban areas, which is especially pertinent in meteorological scenarios [19,20]. In this study, the established sea level monitoring system uses an IoT-based, solar-powered anemometer (Barani design—Meteo Wind) and solar-powered meteo-station (Barani design Meteo-helix) for monitoring air pressure.

The system is deployed to acquire current meteorological information used as an input for the developed model to estimate the sea level. The system is based on the LoRaWAN IoT radio, which delivers the information to The Things Network (TTN) cloud system, which is then used by the cross-platform web/mobile application called Waves, which is used as an early warning monitoring system. The multilanguage system itself implements: (1) the algorithm that defines sea level based on the tidal, wind speed/direction and air pressure information; (2) information on the shore height at the dedicated measurement and early warning zones; (3) push notification logics that can be separately activated based on user's zone of the interest.



Figure 1. (a) Location of the city of Kaštela in Kaštela Bay; (b) A view of an old historical core, Kaštel Kambelovac.



Figure 2. Coastal flooding events in the city of Kaštela.

This paper presents a methodological approach for the development of an early warning system for coastal flooding. It is based on frequently measured meteorological data and sea level predictions integrated on a single platform to provide real-time information about potential risk for the citizens of the city of Kaštela.

Novelties of the manuscript are summarized as follows: (i) to our best knowledge, the site of the application has been used for the very first time to demonstrate the application of the coastal flooding early warning system; (ii) the relevance of the selected site relies on the fact that the area is faced with coastal flooding more than 15 days per year on average, thus increasing the need for early warning system development, (iii) the manuscript couples three mechanisms contributing to the coastal flooding vulnerability assessment, those being barometric pressure-induced sea level changes, wind-generated waves and tidal-induced fluctuations, (iv) barometric- and tidal-induced sea level changes are obtained in real time, fully relying on local conditions arising from the observations, (v) wind-generated wave heights are site specific, taking into consideration bathymetric features and coastal structure type and (vi) the whole procedure has been implemented in the form of a real-time mobile application, thus resulting in a reliable tool for the end users.

Compared to relevant publications [16,21], this paper couples three of the mechanisms leading to the sea water level rise and refers to a site-specific area. Although it does not offer general findings, the procedure shows the potential to be applied to other sites all over

the Mediterranean basin after prior modifications. The latter refers to bathymetric features, the reflection of the coastline, the determination of incident deep water wave parameters and tidal observations.

The paper is structured as follows: Section 2 is the Methodology and Study area section, which couples the methodology used in the study with representative site related data. Section 3 offers Results from the study, while Section 4 consists of relevant Discussion topics and Section 5 summarizes main conclusion points.

2. Methodology and Site Description

2.1. Sea Water Elevation Prediction

Sea water level is a random process resulting from the simultaneous combination of several mechanisms, three of which are found to be dominant, those being tidal-induced oscillations and oscillations due to barometric pressure changes and wind-generated waves. Although characterized by different time scales, those three mechanisms simultaneously contribute to the absolute sea water elevation definition.

Tidal-induced sea water oscillations are driven by tidal forcing, which is induced by simultaneous inter gravity forces between the Sun, Moon and Earth. Tidal-induced changes are characterized as a mixed semidiurnal type at the location of interest, with main periodic intervals corresponding to both semi diurnal and diurnal ones. Compared to tidal oscillations, sea level changes induced by barometric pressure changes are aperiodic with time scales corresponding to two main factors: (i) daily barometric pressure changes corresponding to daily scale air temperature change and (ii) time scales corresponding to the time necessary for the air mass transfer from different geographic locations to the location of interest to occur. The latter corresponds to time scales usually equal to several hours. Wind-generated waves are characterized by very small time scales, up to 8 s in the area of interest, and these are generated as a result of the air mass kinematic energy transfer to the sea surface.

Previous research [22] has shown that tides characterizing the Adriatic Sea basin consist mainly of seven dominant constituents, of which three are diurnal (O1, P1 and K1) and four are semidiurnal (N2, M2, S2 and K2). In its origin, each constituent represents a sinusoidal function with an associated amplitude, period, and phase, contributing to the full tidal signal. To determine the unknown values of the amplitudes, periods and phases, the original signal is initially transferred from the time to frequency domain by applying the Discrete Fourier Transform (DFT) [22]. DFT results are often plotted as Amplitude Spectral Density (ASD). By normalizing magnitudes with number of samples, the amplitude of each frequency can be easily obtained. Due to the fact that DFT calculations are time demanding [23], Fast Fourier Transform (FFT) [24] incorporated in Python in SciPy library [23] has been used for faster transfer of signals from the time to frequency domain. Based on the determined tidal constituent parameters, the tidal-induced sea level can be simulated using a linear superposition of sine functions corresponding to the number of relevant constituents:

$$h_t = \sum_{i=1}^7 A_i \times \sin\left(\frac{2\pi t}{t_{pi}} + \frac{2\pi\phi_i}{360}\right), \quad t = 0, 1, \dots, M \quad (1)$$

where h_t is the simulated sea level [m], A_i is the amplitude [m], t_{pi} is the period [h] and ϕ_i phase [°] of i -th constituent, M is the sample size and t is relative time [h].

Simulated sea level h_{sea} can be calculated as a superposition of tidal harmonics from Equation (2) by adding the mean sea level value calculated from the observed sea level signal:

$$h_{sea} = h_t + \bar{h} \quad (2)$$

where h_t represents tidally induced sea level oscillations and \bar{h} represents the mean sea level value.

Increasing the barometric pressure by 1 [cm] of the saltwater column leads to a decrease in the sea level by approximately 1 [cm] and inversely, decreasing the barometric pressure by 1 [cm] raises the sea level by 1 [cm] [25]. This effect is called the Invert Barometric effect (IB). The sea level rise caused by the change of the barometric pressure can be calculated as follows:

$$h_{at} = \frac{-p_a}{\rho g} \quad (3)$$

where h_{at} is the sea level change resulting from a change in barometric pressure, p_a is the barometric pressure [Pa] change, ρ is the density of sea water [kg/m^3] and g is the gravitational acceleration [m/s^2]. Therefore, the simulated sea level incorporating both tidal oscillations and barometric pressure-induced changes is updated from Equation (2) for the value of h_{at} , as shown in Equation (3):

$$h_{sea} = h_t + h_{at} + \bar{h} \quad (4)$$

where the third right hand term (\bar{h}) represents mean sea level values as calculated from the observed signal, h_t represents tidally induced sea level oscillations and h_{at} stands for barometric pressure-induced sea level change.

To assess wind-generated wave height in front of the coastline, we start with a determination of deep water wave parameters. For the location of interest and relevant incident wave directions, fetch length has been assessed by applying the Saville method [26]. In order to determine deep water wave parameter values, data sets from the Section 2.3 climatological station have been used. Fully developed sea conditions have been checked by applying the Wilson criteria [27] prior to the determination of wave parameters. After defining relevant fetch length for a given wind duration and wind velocity, the Groen–Dorrestein nomogram is used to determine deep water wave parameters [28].

Wave transform analysis has been performed by applying SMS CGWAVE software [29]. The wave phenomena that can be simulated by CGWAVE are: bathymetric refraction, diffraction by structures (e.g., breakwaters) and bathymetry, reflection (from structures, natural boundaries (seawalls, coastlines, etc.) and bed slopes), friction, wave breaking and floating (fixed) docks influence the wave field. The model is based on the use of a triangular finite element formulation to solve the two-dimensional elliptic mild slope equation, with grid sizes varying throughout the domain based on the local wavelength [30]. The grid can be efficiently generated using the SMS graphical interface when a bathymetry file is provided. The model allows one to specify the desired reflection properties along the coastline and other internal boundaries. While the basic equation is intended for monochromatic waves, irregular (i.e., spectral) wave conditions are simulated in CGWAVE through a linear superposition of monochromatic simulations [31,32].

The procedure or the algorithm for the absolute sea water elevation assessment is based on three steps which are presented above and summarized as: (i) sea level change caused by tidal forcing prediction, (ii) sea level change caused by a barotropic pressure forcing assessment and (iii) assessment of the wind-generated wave height in front of the coastline. Sea water elevation assessment as a consequence of simultaneous effects for those three mechanisms is assessed as follows:

- From observed tidally induced oscillations, the harmonic parameters (amplitude, period and phase) are initially determined based on the Least Square Method application;
- After all harmonic parameters have been determined, tidal-induced sea level oscillation is determined by using Equation (1);
- From observed barometric pressure data, the change in sea level induced by the drop/rise of the barometric pressure is determined from Equation (3);
- Deep water wave parameters are determined depending on incident direction and wind velocity and duration parameters;
- For relevant incident directions, numerical simulation of the wave transform has been performed by incorporating shoreline reflection coefficients determined on site;

- The study area has been divided into ten zones fundamentally different with regard to reflection features;
- For each zone wave, parameters have been determined within the zone close to the shoreline (4 m away from the shoreline);
- Final determination of the sea water elevation by incorporating three abovementioned mechanisms is done by:

$$h_{sea} = h_t + h_{at} + h_{S(d=4m)} \quad (5)$$

which offers an easy-to-implement way to assess absolute sea level, where h_t represents the tidally induced component, h_{at} represents the barometric pressure-induced component and $h_{S(d=4m)}$ stands for the significant wind-generated height as found 4 m offshore. The value of h_{sea} is expressed relative to HVRS71 datum [33].

2.2. Site Description

The location of the study area with definition of the tidal gauge and meteorological stations are shown in Figure 3. The meteorological station Split with geographical coordinates $\varphi = 43^\circ 31' \text{ N}$, $\lambda = 16^\circ 26' \text{ E}$ is located northwest of the city Split, on the Marjan hill, at the altitude of 122 m a.s.l. The terrain is a slope towards the sea on the SW-W-NW-N side. To the north is the bay of Kaštela and to the east is the city of Split. At a distance of 7 km toward the north is the mountain Kozjak with the highest peak at 779 m a.s.l. The measuring system Feuss [34] is installed at a 5 m high terrace column on the building roof (12 m above ground). The only obstacles found near the meteorological station building are found to the west and northwest side (trees and terrain elevation overgrown with trees more than 10 m tall). The roughness class of the terrain is 2.5 ($z_0 = 0.2$) [34]. The wind speed and direction data obtained by the classic Feuss measurement consist of an average hourly wind speed with corresponding wind.

The nearest tidal gauge near Kaštela Bay is located within the Institute of Oceanography and Fisheries (IOR) in Split, at the western border of peninsula Marjan. The time series of measured sea surface elevations over a total duration of five years have been obtained from the Marjan tide gauge for the period from 1 January 2010 to 31 December 2014. The sampling frequency of the tide gauge was set to 1 h for the entire time series. The measured water level elevation is referred to as the HVRS71 vertical datum [33]. Due to the maintenance and malfunction of the tide gauge IOR Marjan, the observed time series are characterized by periods without recorded values of the sea level. For the purpose of this work, a continuous time series is required so the longest continuous time series has been found from 25 January 2010 at 12:00 h to 27 June 2011 at 23:00 h with a total of 12,444 h of data.

Barometric pressure data are obtained from two meteorological stations: Split-Airport and Split-Marjan. The meteorological station Split-Airport is located at 21 m a.s.l. and the barometric pressure values are recorded three times a day at 7 am, 2 pm and 9 pm. The meteorological station Split-Marjan is located at 122 m a.s.l. and has an hourly measurement frequency including barometric pressure values. Logs of barometric pressure were obtained from both meteorological stations for the period from 1 January 2010 to 31 December 2014. Due to the location of Kaštela Bay, the meteorological station Split-Airport was considered as relevant, but due to its low measurement frequency (3 times per day), the data from Split-Marjan was used for further analysis. First, the data from Split-Marjan was compared with the data from Split-Airport and a mean difference of 12.67 hPa with a standard deviation of 0.67 hPa was found. All data from Split-Marjan were corrected for the values of 12.67 hPa. The available data from the Split-Marjan station has a continuous record with no missing data for the entire 5-year period. However, since the sea level signal does not have the same continuity as the barometric pressure, the same period of barometric pressure as sea level is included in the further analysis.

Insight into bathymetric features emphasize depth values up to 37 m with a pretty uniform decrease towards the shoreline (Figure 4). A bathymetric survey for the purpose of this paper has been performed in April 2021 with a single beam setup. Shoreline

determination of the reflection coefficient has been done at the site by the inspection of both shoreline type and depth in front (Figure 5).



Figure 3. Location of the study area with the definition of the tidal gauge and meteorological stations (IOR—Institute of Oceanography and Fisheries).

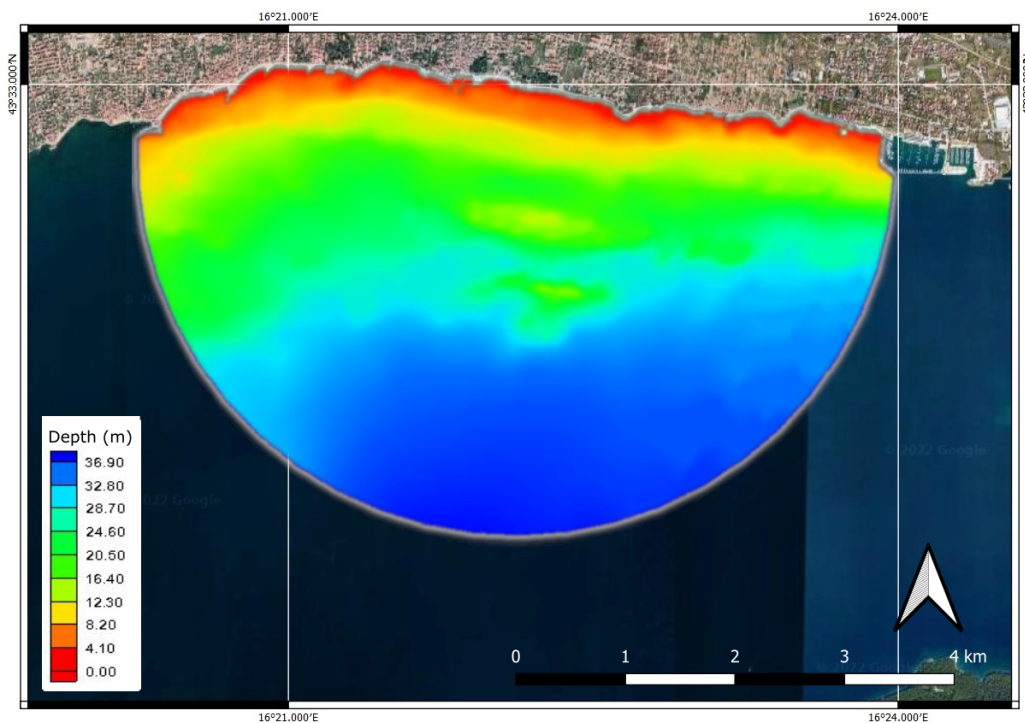


Figure 4. Bathymetric features at the location of interest.

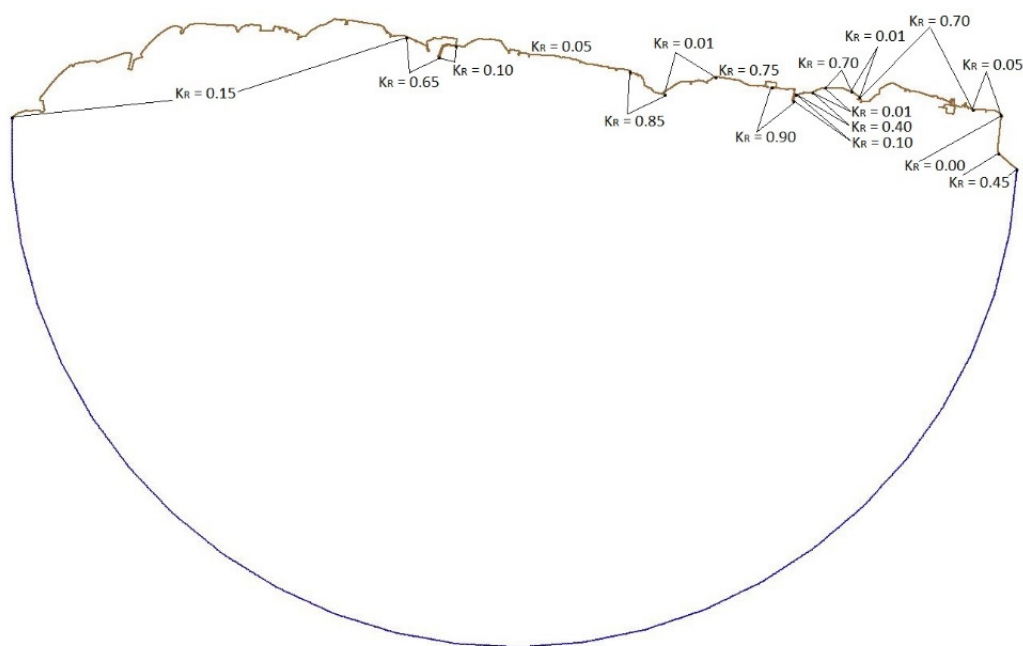


Figure 5. Shoreline reflection coefficient along the coastline.

2.3. Data Collection from LoRaWAN-Based Sensor Device

LoRaWAN is one of the most widely used Low Power Wide Area technologies that aims to collect and communicate data from an end sensor device at a large distance, making it perfect for a scenario in which sensor devices collect wind and barometric data and convey them to a centralized system. LoRaWAN employs a typical star-of-star topology where end devices communicate data in a single hop to one or more gateway devices. These messages are further forwarded to the network and application server for further processing, allowing authorized data to be forwarded to other external services (e.g., using MQTT message forwarding). LoRaWAN allows battery-operated devices to periodically transmit sensor data over large distances, while minimizing consumption during inactive periods. LoRaWAN technology finds its application in smart city/smart agriculture environments where there is no need for real-time (every second) transmission from end devices. During the inactive period, end devices simply cut off the consumption, allowing a battery lifetime up to a couple of years without any external power source.

Figure 6 depicts the architecture of the MeteoHelix weather station of Barani design that utilizes LoRaWAN as a radio technology. MeteoHelix [35] is an automatic all-in-one microweather station which is solar powered and can be active for up to 6 months without sun. It measures air temperature to WMO accuracy, air humidity to WMO accuracy with dew and frost point output, barometric pressure and solar irradiation (pyranometer). Another sensor of Barani design was also installed that utilizes LoRaWAN communication—MeteoWind IoT PRO. MeteoWind [36] is used for wind monitoring and employs two sensors: a separate wind vane and anemometer. MeteoWind allows 4+ months of battery life without sun and a maintenance-free service life with long-term measurement stability due to its elliptical cup and metal construction. As depicted in Figure 7, both devices are placed at a 10 m height without any object around within 150 m so that both the wind speed and wind direction are not distorted, while both are located in location of Kaštela Bay. Since both MeteoHelix and MeteoWind IoT PRO employ LoRaWAN communications to convey data over the air to the centralized system, The Things Network as a service provider was used to collect data for further processing. As a LoRaWAN gateway, an indoor Sentrius RG1xx LoRaWAN gateway device placed around 150 m from the sensor devices was employed that forward messages to The Things Network (TTN) cloud infrastructure. Once the message arrives at the gateway, it is forwarded to the TTN Network and Application server. Furthermore, TTN allows message forwarding from TTN infrastructure to our

dedicated Waves Seafront Monitoring app using MQTT protocol, which is described more in detail in the following section.

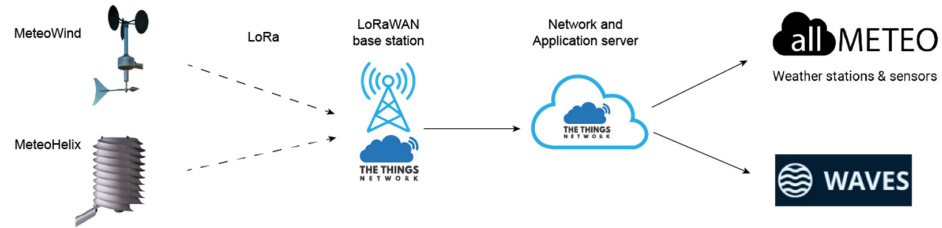


Figure 6. Architecture of LoRaWAN-enabled MeteoHelix and MeteoWind devices from Barani Design.



Figure 7. Installation of MeteoHelix and MeteoWind IoT Pro devices.

2.4. Waves Seafront Monitoring Architecture—Overview and Functionalities

Waves Seafront Monitoring is a cross-platform mobile application that allows users to access and interactively view the current sea level, discretized by coastal segments with respect to coastal height. As shown in Figure 8a, it comprises a cloud and client side. At the cloud side, the Google Firebase server component executes an evaluation algorithm based on data from the sensor it communicates with, serves as a server for these results and performs user authentication. Sensor data comprising air pressure, wind speed and direction are sent to The Things Network (TTN) cloud via the LoRaWAN communication channel, which is forwarded via MQTT protocol to the TTN microservice. Once the packet with sensor data arrives, the TTN microservice captures and stores the LoRaWAN uplink data into the database and forwards the data through the PMO algorithm to estimate sea level according to the data arriving from LoRaWAN sensors (wind speed and direction, barometric pressure and sea tide level). As can be seen, an alarm notification can be sent to the application if the sea level exceeds a predefined level.

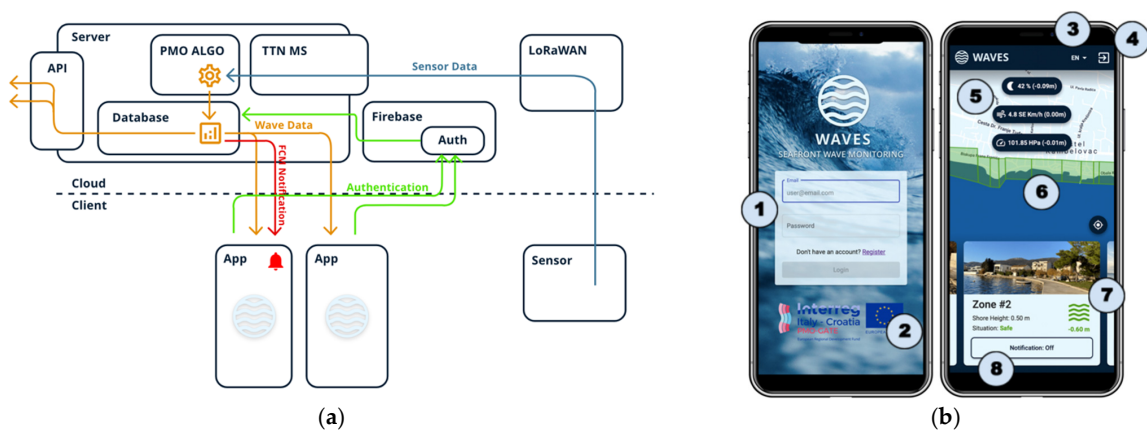


Figure 8. (a) High-level overview of the implementation of the solution, (b) Front-end interface of the mobile application.

The front-end of the application is comprised of the following elements, as depicted in Figure 8b:

- A. Login interface (Figure 8b)—initial interface for users when opening the application:
 1. Form—the user enters his login details (e-mail and password) and has the option of registration if he does not have an account by clicking on the appropriate link (Figure 8b, number 1),
 2. Prominent logo—the project was realized within the Interreg PMO GATE collaboration (Figure 8b, number 2).
- B. Registration Interface—the registration interface is analogous to the login interface, only it allows the user to create an account to access the application by entering login information. To simplify logging into the system, there is no special validation of user accounts, such as email confirmation.
- C. Map interface (Figure 8b) —the central part of the application, which contains the following basic functionalities:
 1. At the top is a drop-down menu where the user has a choice between three languages: Croatian, English and Italian. By clicking on an option, the interface text adjusts the interface language (Figure 8b, number 3).
 2. Log out button from the application (Figure 8b, number 4).
 3. Values read from the sensor are updated over time depending on how often the data from the TTN arrives. From top to bottom, sea level is the sum of altitudes caused by sea tide, wind speed and direction and barometric pressure (Figure 8b, number 5). The total amount is calculated based on the algorithm submitted by the Client.
 4. Google maps with plotted polygons that correspond to discretized segments of the coast according to their heights (Figure 8b, number 6). The color of the zone corresponds to the early warning status: green—safe, i.e., the sea level is below the coast level; yellow—warning, i.e., the sea can exceed 20 cm above the height of the shore; orange—dangerous, i.e., the sea can rise up to 50 cm above the height of the shore; red—flooded, i.e., the sea exceeds 50 cm above the height of the coast. By clicking on an individual zone, the cards will position themselves next to the corresponding zone and the map will be centered on the selected zone. Based on the coastal height data, the monitoring area is divided into 10 zones.
 5. Zone maps showing the names and photos of coastal zones. Here, the user can see exactly the height of this segment of the coast, the estimated sea level in relation to the zone and, consequently, the situation in that zone, which is coded in colors analogous to the zones on the map (Figure 8b, number 7). Each zone information contains the sea level with respect to the coastal height, where the number with the minus sign shows how much the sea level is below the coastal height. Once the number becomes positive, the zones change color since this result corresponds with estimated flood. By moving the tabs left or right, the user can focus on a specific zone, and the map will center on that zone.
 6. Notification button (Figure 8b, number 8). By clicking on this button individually for each zone, the user can indicate whether he wants to receive notifications when the situation in a particular zone changes.

3. Results

3.1. Sea Level Determination Based on the Tidal Fluctuations

To enable the assessment of tidal-induced sea level oscillations, a total of 12,444 h of observed time series data was used to perform DFT and obtain an amplitude spectrum (Figure 9). Due to the nature of the observed signal, inspection of the amplitude spectrum offers the presence of the trend, visible within the bins corresponding to the lowest frequencies. In total, seven tidal harmonics has been identified as dominant, thus ensuring the tidal-induced sea level oscillation characterization.

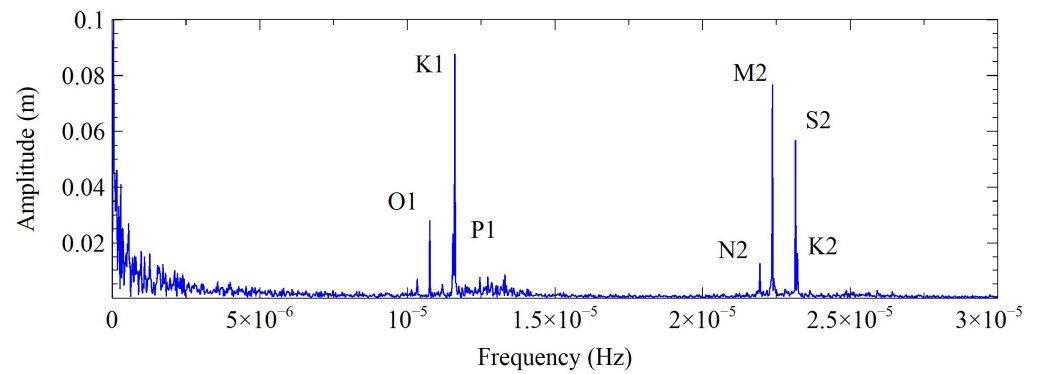


Figure 9. Amplitude Spectral Density for observed sea level reduced for the mean value.

While tidal amplitudes and periods were determined directly from the spectrum shown in Figure 9, phases were determined from the complex component of each of the seven tidal harmonics. All characteristic values for the relevant tidal constituents are shown in Table 1. The quality of the determined harmonic values were checked by the application of the correlation coefficient when applied to both the simulated and observed time series.

Table 1. Tidal constituents with corresponding values of amplitude, period and phase.

Constituent	Amplitude (m)	Period (h)	Phase (°)
O1	0.02821644	25.81743	−160.6065
K1	0.02339150	24.06963	105.3624
P1	0.08773618	23.93077	153.1416
N2	0.01279412	12.65921	65.3833
M2	0.07688095	12.41916	−31.55806
S2	0.05696792	12.00000	−126.8397
K2	0.01636003	11.96538	116.0807

Both the observed and simulated sea level signals, one for each 1000 h of the available time series, are compared by using Pearson correlation coefficient and root mean square error. When simulating the sea level by using Equation (2), the simulated signal discovers the absence of the trend within, which is incorporated in the next step as a response to long-term barometric pressure changes. The residual was determined as a difference between the observed and simulated signals. Both signals are shown relative to the HVRS71 vertical datum, as explained in the Methodology section. The same procedure was repeated for each 1000 h data of the total 12,444 h data representing the total sample. Both Pearson correlation coefficient and root mean square error values are shown in Table 2.

Table 2. Pearson coefficient and root mean square values obtained between the measured and simulated sea water elevation by Equation (2).

Data Sets (h)	0–1000	1000–2000	2000–3000	3000–4000	4000–5000	5000–6000	6000–7000	7000–8000	8000–9000	10,000–11,000	11,000–12,444	0–12,444
RMSE	0.198	0.141	0.083	0.082	0.075	0.071	0.147	0.241	0.091	0.159	0.095	0.136
Pear. Corr. Coef.	0.551	0.597	0.749	0.782	0.923	0.802	0.664	0.639	0.752	0.834	0.791	0.578

For the entire observed and simulated set of 12,444 h data, the root mean square value equals to 0.136 [m], while Pearson’s correlation coefficient equals 0.578 [-]. The high value of RMSE and low value of the correlation coefficient indicate the sea level fluctuations are not only subjected to tidal variations, but also to other factors.

3.2. Sea Level Determination Based on the Tidal Fluctuations and Barometric Pressure Changes

Figure 10 shows the effect of barometric pressure on the simulated signal with seven frequencies. The simulated sea level signal has a similar trend to the observed sea level signal with a residual remaining between the simulated and observed signal. When the sea level signal is simulated using the tidal components and the inverted barometric effect, the RMSE decreases to 0.1057 [m] and the Pearson correlation coefficient increases to 0.777 [-], further highlighting the effect of barometric pressure and its contribution to the observed sea level definition at the location of interest (Table 3). The decrease in the residual values when both the barometric pressure and tidal effects are involved in the procedure for the sea level determination implies the relevance of those two mechanisms in the vertical movement of sea surface elevation.

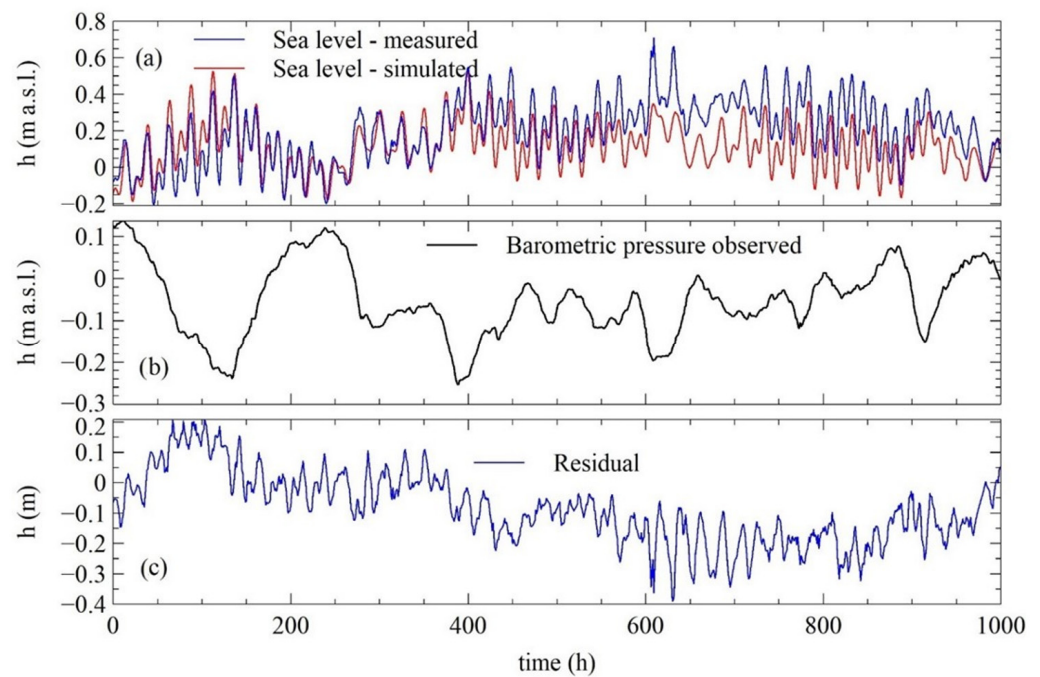


Figure 10. (a) Observed and simulated sea level by Equation (4) for the first 1000 h of observed sea level signals, (b) Observed barometric pressure, (c) Residual between simulated and observed sea level signals.

Table 3. Pearson coefficient and root mean square values obtained between the measured and simulated sea water elevation by Equation (4).

Data Sets (h)	0–1000	1000–2000	2000–3000	3000–4000	4000–5000	5000–6000	6000–7000	7000–8000	8000–9000	10,000–11,000	11,000–12,444	0–12,444
RMSE	0.144	0.103	0.061	0.062	0.083	0.061	0.113	0.189	0.091	0.126	0.076	0.106
Pear. Corr. Coef.	0.735	0.776	0.886	0.886	0.936	0.865	0.886	0.794	0.812	0.891	0.872	0.777

3.3. Wind-Generated Waves

Following the knowledge from the location of interest, two relevant wave incident directions have been identified, SE and SSW. The reason for the selection of those two incident directions relies on three facts: (i) longest possible fetch lengths compared to other incident directions, (ii) longest wind duration and wind velocities and (iii) relative position of the shoreline almost perpendicular to the incident directions. Table 4 offers the highest significant wave height equal to 2.78 m with a corresponding period of 4.76 s. For the SSW incident direction, Table 5 shows the highest wave parameters equal to 2.35 m and 4.15 s.

Table 4. Deepwater wave parameters—incident direction SE.

V (ms ⁻¹)	t (h)	F _{min} (km)	t _{min} (h)	F _{EFF} (km)	F _{MJ} (km)	H _S (m)	T _S (s)	L ₀ (m)
1.5	13	43.36	8.65	24.8	24.8			0
3.3	13	71.25	6.02	24.8	24.8			0
5.4	13	97.17	4.8	24.8	24.8	0.5	2.6	10.55
7.9	13	123.48	4.03	24.8	24.8	0.85	3.15	15.49
10.7	17	215.89	3.5	24.8	24.8	1.21	3.65	20.8
13.8	15	213.49	3.12	24.8	24.8	1.7	4	24.98
17.1	11	159.77	2.82	24.8	24.8	2.19	4.35	29.54
20.7	4	45.07	2.59	24.8	24.8	2.78	4.76	35.38

Table 5. Deepwater wave parameters—incident direction SSW.

V (ms ⁻¹)	t (h)	F _{min} (km)	t _{min} (h)	F _{EFF} (km)	F _{MJ} (km)	H _S (m)	T _S (s)	L ₀ (m)
1.5	5	11.71	6.68	17.4	11.71			0
3.3	5	19.24	4.65	17.4	17.4			0
5.4	5	26.24	3.7	17.4	17.4	0.5	2.5	9.76
7.9	5	33.35	3.11	17.4	17.4	0.77	2.95	13.59
10.7	5	40.37	2.7	17.4	17.4	1.05	3.15	15.49
13.8	5	34.91	2.41	17.4	17.4	1.41	3.6	20.23
17.1	5	26.94	2.18	17.4	17.4	1.92	3.98	24.73
20.7	5	6.75	2	17.4	6.95	2.35	4.15	26.89

The procedure for wave height determination at the distance of 4 m offshore starts with known wind velocity and duration. For the selected incident wave direction and fetch length, deep wave parameters have been selected from Tables 4 and 5. For the purpose of wave height determination in front of the shoreline, the JONSWAP spectrum is used to incorporate a real wave into the wave transform model. Spectrum parameters have been set up as shown in Table 6, where the obtained deep water wave values correspond to a 100-year return period.

Table 6. Deepwater wave parameters—JONSWAP spectrum parameters.

Incident Direction	H _s (m)	T (s)	γ	nn
SE (165°)	3.05	6.40	3.30	4.00
SSW (202.5°)	2.60	5.90	3.30	4.00

Wave height spatial distribution and direction for the SE incident wave direction is presented in Figure 11. Insight into the inner zone of interest discovers the presence of refraction as a main wave transform mechanism. The insight into significant wave height changes at 4 m offshore is shown in Figures 12 and 13. The same has been shown for the SSW incident direction in Figures 12 and 13. By comparing modeled wave heights, it is obvious the SE incident direction results in more significant wave height values.

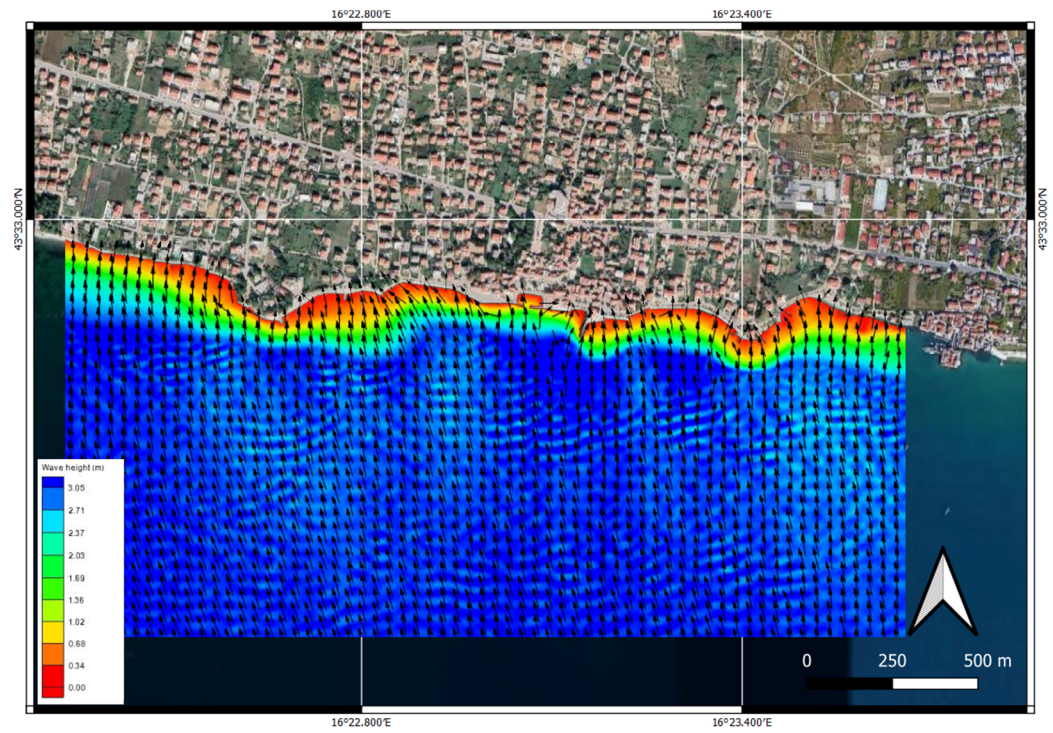


Figure 11. Wave heights and directions for the SE incident direction—local study area.

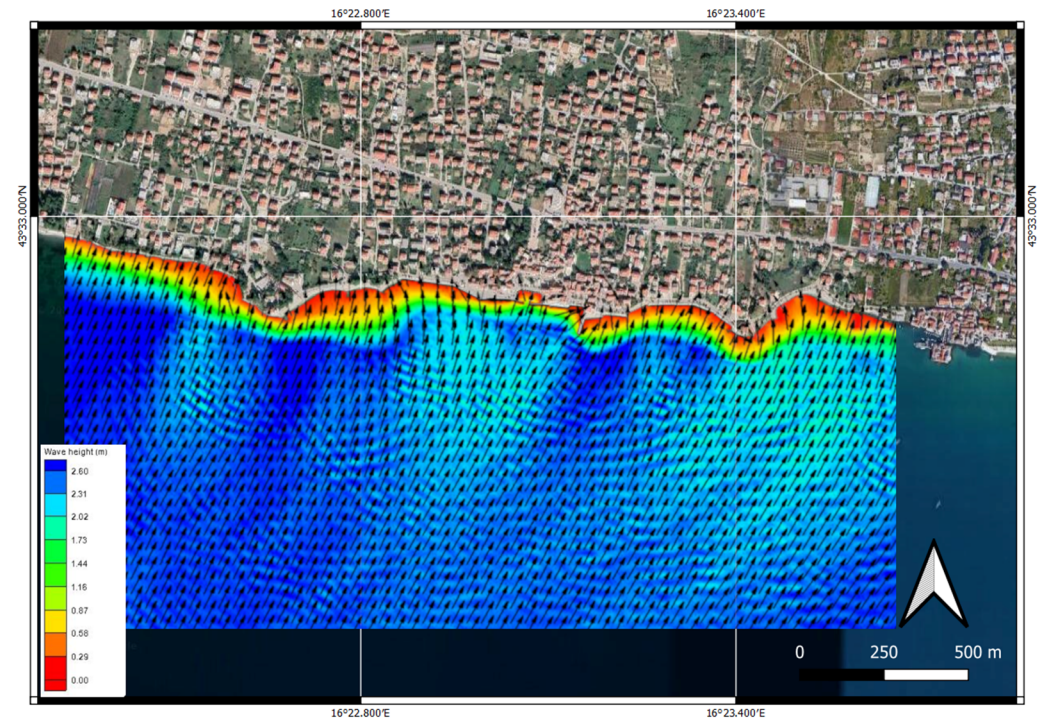


Figure 12. Wave heights and directions for the SSW incident direction—local study area.

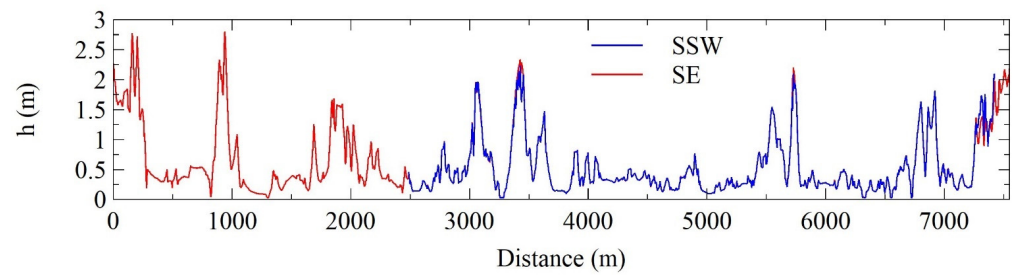


Figure 13. Modeled wave heights along the control line—incident directions: SE and SSW.

3.4. Real-Time Prediction of Sea Water Elevation and Warning

The monitoring system has been installed and put into operation at the Kaštela Bay test site to provide real-time measurement of wind speed, wind direction and barometric pressure. The observed data is used for the real-time prediction of sea level based on the developed algorithm for the estimation of sea level heights and information obtained from the monitoring system, which has been integrated into the algorithm. The real-time prediction of sea level values is obtained based on tidal fluctuations, barometric pressure values and wind characteristics.

Resulting sea level values are compared with coastline elevation in order to identify the potential danger of flooding and issue on-time warnings. Figure 14 shows wind characteristics and barometric pressure as observed during a period of 7 days during February 2022. The data containing barometric pressure along with wind direction and speed were collected into a database for the application. The data were used as an input for an algorithm to estimate sea level height.

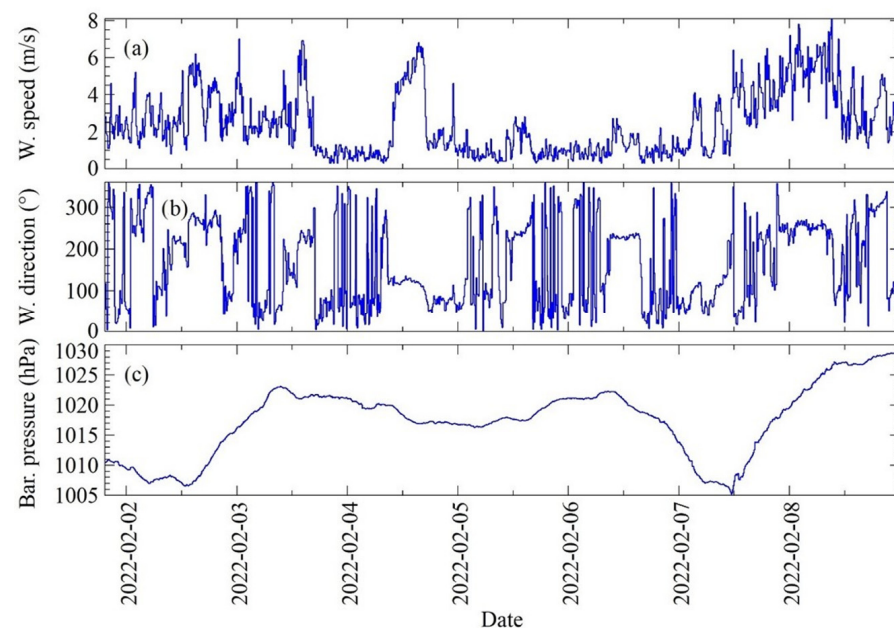


Figure 14. LoRaWAN-obtained observed time series: (a) wind speed, (b) wind direction and (c) barometric pressure.

Figure 15 shows sea water elevation as a consequence of each of the components (tidal effect, barometric pressure and wind-generated waves) as well as absolute sea water elevation as a superposition of the abovementioned components for the period from 15 December 2021–7 February 2022. The results are given for one randomly selected zone along the study area to demonstrate the capacity of the proposed procedure to assess the sea water elevation. The estimated water surface elevation is referred to the HVR571 vertical reference datum determined on the basis of mean sea level, as stated in the Methodology section.

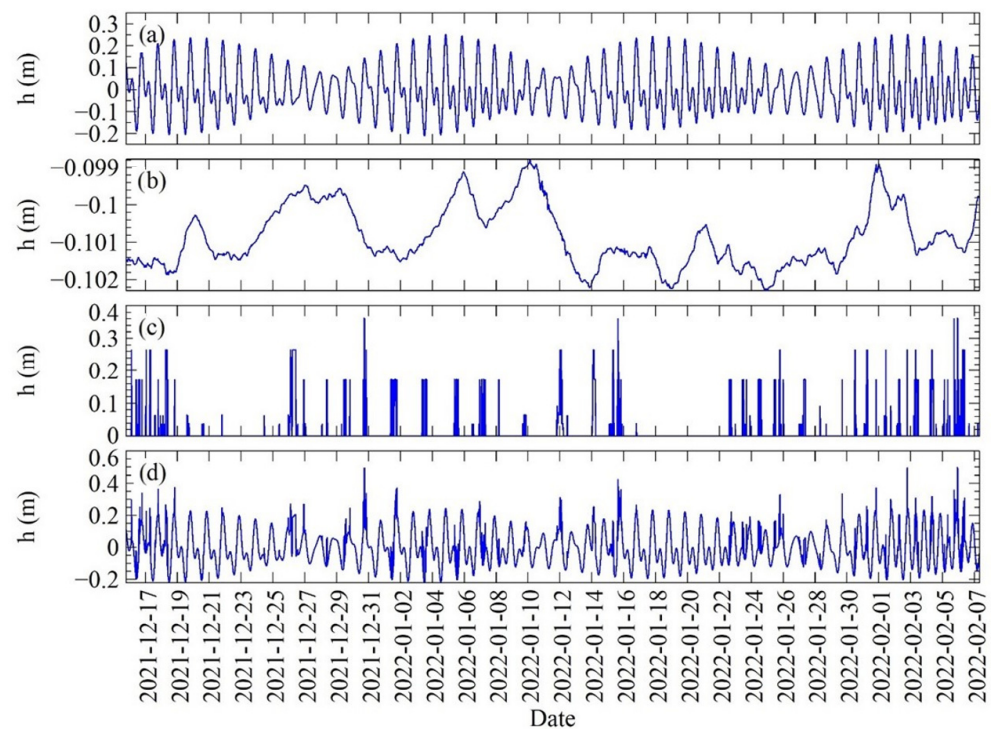


Figure 15. Calculated sea level height during the period from 15 December 2021–7 February 2022 caused by: (a) tidal effect, (b) barometric pressure-induced sea level changes, (c) wind-generated wave height and (d) absolute sea level height.

If the resulting sea level value estimated from the algorithm exceeds the coastline elevation, the warning is immediately issued by the mobile application to alert the endangered population. Flood hazard warnings in the mobile application are primarily focused on citizens' safety and their classification is based on the particular threat level. Threat levels are based on tests of the instability of a human body in floodwater and different stability thresholds [37]. Following the results of the tests, the first threat level, issuing a yellow alert, is defined for flood water depth on the coastline up to 20 cm, which is mostly threatening for children. The second level of threat corresponds to an orange warning, which is now becoming dangerous for adults and is issued when the water depth is between 20 cm and 50 cm. Finally, an exceedance of flood water depth over 50 cm on the coastline corresponds to the third threat level. In this case, severe injuries can be caused by flood water and the red warning for the population is issued.

4. Discussion

In this paper, a procedure to assess sea water elevation caused by coastal flooding at Kaštela Bay is presented, together with the monitoring system infrastructure scheme and sea water elevation prediction module. In its origin, the procedure relies on the real-time monitoring IoT-based system for sea level-relevant parameter monitoring to capture wind-generated wave heights and barometric pressure-induced sea level changes.

The latter offers the possibility to determine wind-generated wave heights in front of the coast, with an incorporation of shoreline reflection features as assessed by the sea water depth and type of structure found at the site, and long- and short-term changes in the mean sea water level. Tidal-induced sea level changes are forecasted based on the data series observation from the nearest relevant tidal gauge.

After wind speed/direction and barometric pressure sensors are installed at the site to enable real-time monitoring, a LoRaWAN-based IoT monitoring system was employed, along with the dedicated cross-platform mobile application, which was used as an early

warning notification system. Therein, registered end users can set early warning notifications based on their zone of interest.

As stated, the origin of the presented approach relies on the capability of the monitoring system to observe the wind speed/direction and barometric pressure at the site. The selection of the location of the monitoring infrastructure is performed at the location of interest to neglect spatial variations in barometric pressure variations and offer reliable input for barometric pressure-induced sea level changes.

Relevant mechanisms acting to assess the sea water elevation are selected based on the phenomena characterizing the study area and fit suitable for the pre-assumed conditions mostly found on site. The effect of barometric pressure changes and their influence on mean sea water elevation refers to the sea in a calm state and static conditions when no significant changes in the barometric pressure field are observed. In case this requirement is not met, such as when the storm is moving, a difference in predicted sea level changes compared to real ones can be obtained.

Our results demonstrate the capability of the proposed methodology to enable a realistic and reliable forecast of the sea water elevation by taking into consideration local conditions: (i) wind information, (ii) barometric pressure, (iii) tidal forcing, (iv) water depth and (v) coastal structure or type information.

When coupled with the shoreline's absolute height, one is enabled to assess flooding risk or the vulnerability of the coast to sea level-induced flooding. The developed monitoring system, coupled with data collection from LoRaWAN-based sensor device and assessment procedure, presents a unique and robust approach to be used along different coastal areas of the Adriatic Sea.

Apart from this, different coastal structures found along the specific site can easily be taken into consideration by assessing the reflectance features from the structure type and bathymetric features in front of the coastline.

5. Conclusions

This paper presents a procedure to assess the coastal flooding induced by the sea level in the Kaštela study area. In its origin, it consisted of three modes: (i) the LoRaWAN-based sensor device monitoring infrastructure located at the site to capture relevant parameters in real time, (ii) a step-by-step procedure to assess the sea water elevation and (iii) Waves Seafront Monitoring cross-platform mobile application to enable the real-time insight into coastal flooding occurrence. The main conclusions obtained from the study can be summarized as:

- The presented procedure to assess coastal flooding induced by seawater has been shown to be efficient when applied to the Kaštela study area.
- The origin of the assessment for the seawater elevation relies on three basic mechanisms: tidal oscillations, barometric pressure-induced oscillations and wind-generated waves. Despite the potential limitation, no significant deflection from the sea water elevation occurred at the site during the period from 15 December 2021 to 7 February 2022 was observed.
- The presented procedure shows robustness in the potential to incorporate other relevant mechanisms influencing sea water elevation and site-specific features. It can be extended to the relevant mechanisms acting toward the sea level definition and adjusted to the local conditions reflecting the site-specific features. In case of need, additional effects can be added: (i) submerged structures overtopping, (ii) wave run-up, (iii) seiche, (iv) beach or shoreline friction effects, (v) dynamic inverse barometric effects, (vi) coastal flooding induced by the precipitation, especially during the cyclone and its superposition with the sea-induced flooding. The latter not only contributes to enhanced capacity of the coastal flooding awareness at the Kaštela site, but also enables the procedure to be applied at other sites.

Author Contributions: Conceptualization, Ž.N., V.S. and P.Š.; Data curation, V.S., I.L., T.P., P.Š. and T.K.; Funding acquisition, Ž.N.; Investigation, Ž.N., V.S., I.L., T.P., P.Š. and T.K.; Methodology, Ž.N., V.S., P.Š. and T.K.; Software, V.S., I.L. and T.P.; Supervision, Ž.N., V.S. and P.Š.; Validation, Ž.N., V.S., I.L., T.P. and P.Š.; Visualization, I.L. and T.K.; Writing—original draft, Ž.N., V.S., I.L., T.P., P.Š. and T.K. All authors have read and agreed to the published version of the manuscript.

Funding: This research was funded by the EUROPEAN UNION, Programme Interreg Italy-Croatia, the project “Preventing, managing and overcoming natural-hazards risks to mitigate economic and social impact”—PMO-GATE ID 10046122. The research is also partially supported through project KK. 01.1.1.02.0027, co-financed by the CROATIAN GOVERNMENT and the EUROPEAN UNION through the European Regional Development Fund—the Competitiveness and Cohesion Operational Programme and the project “Internet of Things: Research and Applications”, UIP-2017-05-4206, financed by the Croatian Science Foundation.

Institutional Review Board Statement: Not applicable.

Informed Consent Statement: Not applicable.

Conflicts of Interest: The authors declare no conflict of interest.

References

- IPCC. Changes in climate extremes and their impacts on the natural physical environment. In *Managing the Risks of Extreme Events and Disasters to Advance Climate Change Adaptation*; Field, C.B., Barros, V., Stocker, T.F., Dahe, Q., Dokken, D.J., Ebi, K.L., Mastrandrea, M., Mach, K.J., Plattner, G.K., Allen, S.K., et al., Eds.; Cambridge University Press: Cambridge, UK; New York, NY, USA, 2012; pp. 109–230.
- Petroliagkis, T.I.; Voukouvalas, E.; Disperati, J.; Bidlot, J. Joint Probabilities of Storm Surge, Significant Wave Height and River Discharge Components of Coastal Flooding Events. In *Utilising Statistical Dependence Methodologies and Techniques, JCR Technical Reports*; Publications Office of the European Union: Luxembourg, 2016.
- Tsoukala, V.K.; Chondros, M.; Kapelonis, Z.G.; Martzikos, N.; Lykou, A.; Belibassakis, K.; Makropoulos, C. An integrated wave modelling framework for extreme and rare events for climate change in coastal areas—The case of Rethymno, Crete. *Oceanologia* **2016**, *58*, 71–89. [CrossRef]
- Gallien, T.; Sanders, B.; Flick, R. Urban coastal flood prediction: Integrating wave overtopping, flood defenses and drainage. *Coast. Eng.* **2014**, *91*, 18–28. [CrossRef]
- Barnard, P.L.; Van Ormondt, M.; Erikson, L.H.; Eshleman, J.; Hapke, C.; Ruggiero, P.; Adams, P.; Foxgrover, A.C. Development of the Coastal Storm Modeling System (CoSMoS) for predicting the impact of storms on high-energy, active-margin coasts. *Nat. Hazards* **2014**, *74*, 1095–1125. [CrossRef]
- Mendoza, E.T.; Jimenez, J.A. Regional vulnerability analysis of Catalan beaches to storms. In *Proceedings of the Institution of Civil Engineers—Maritime Engineering*; Thomas Telford Ltd.: London, UK, 2009; Volume 162, pp. 127–135.
- De Kleermaeker, S.; Verlaan, M.; Kroos, J.; Zijl, F. A new coastal flood forecasting system for the Netherlands. In *Proceedings of the Hydro12 Conference Proceedings: Taking Care of the Sea*, Rotterdam, The Netherlands, 13–15 November 2012; Dorst, L., van Dijk, T., van Ree, R., Boers, J., Brink, W., Kinneging, N., van Lancker, V., de Wulf, A., Nolte, H., Eds.; Hydrographic Society Benelux: Heeg, The Netherlands, 2012. [CrossRef]
- Doong, D.-J.; Chuang, L.Z.H.; Wu, L.-C.; Fan, Y.-M.; Kao, C.C.; Wang, J.-H. Development of an operational coastal flooding early warning system. *Nat. Hazards Earth Syst. Sci.* **2012**, *12*, 379–390. [CrossRef]
- Bogaard, T.; De Kleermaeker, S.; Jaeger, W.S.; Van Dongeren, A. Development of Generic Tools for Coastal Early Warning and Decision Support. In *Proceedings of the E3S Web of Conferences—3rd European Conference on Flood Risk Management (FLOODrisk 2016)*, Lyon, France, 17–21 October 2016; EDP Sciences: Paris, France, 2016; Volume 7, p. 18017. [CrossRef]
- Dreier, N.; Fröhle, P. Operational wave forecast in the German Bight as part of a sensor and risk based early warning system. *J. Coast. Res.* **2018**, *85*, 1161–1165. [CrossRef]
- Merrifield, M.A.; Johnson, M.; Guza, R.T.; Fiedler, J.W.; Young, A.P.; Henderson, C.S.; Lange, A.M.Z.; O’Reilly, W.C.; Ludka, B.C.; Okihira, M.; et al. An early warning system for wave-driven coastal flooding at Imperial Beach, CA. *Nat. Hazards* **2021**, *108*, 2591–2612. [CrossRef]
- Memos, C.; Makris, C.; Metallinos, A.; Karambas, T.; Zissis, D.; Chondros, M.; Spiliopoulos, G.; Emmanouilidou, M.; Papadimitriou, A.; Baltikas, V.; et al. Accu-Waves: A decision support tool for navigation safety in ports. In *Proceedings of the 1st International Conference Design and Management of Port, Coastal and Offshore Works (DMPCO)*, Athens, Greece, 8–11 May 2019.
- Makris, C.; Androulidakis, Y.; Karambas, T.; Papadimitriou, A.; Metallinos, A.; Kontos, Y.; Baltikas, V.; Chondros, M.; Krestenitis, Y.; Tsoukala, V.; et al. Integrated modelling of sea-state forecasts for safe navigation and operational management in ports: Application in the Mediterranean Sea. *Appl. Math. Model.* **2020**, *89*, 1206–1234. [CrossRef]

14. Spiliopoulos, G.; Bereta, K.; Zissis, D.; Memos, C.; Makris, C.; Metallinos, A.; Ka-rambas, T.; Chondros, M.; Emmanouilidou, M.; Papadimitriou, A.; et al. A Big Data framework for Modelling and Simulating high-resolution hydrodynamic models in sea harbours. In Proceedings of the Global Oceans 2020: Singapore–USA Gulf Coast, Biloxi, MS, USA, 5–30 October 2020; IEEE: New York, NY, USA, 2020; pp. 1–5.
15. Mosavi, A.; Ozturk, P.; Chau, K.-W. Flood Prediction Using Machine Learning Models: Literature Review. *Water* **2018**, *10*, 1536. [CrossRef]
16. Chondros, M.; Metallinos, A.; Papadimitriou, A.; Memos, C.; Vasiliki, T. A Coastal Flood Early-Warning System Based on Offshore Sea State Forecasts and Artificial Neural Networks. *J. Mar. Sci. Eng.* **2021**, *9*, 1272. [CrossRef]
17. Atzori, L.; Iera, A.; Morabito, G. The Internet of Things: A survey. *Comput. Netw.* **2010**, *54*, 2787–2805. [CrossRef]
18. Nižetić, S.; Šolić, P.; López-de-Ipiña González-de-Artaza, D.; Patrono, L. Internet of Things (IoT): Opportunities, issues and challenges towards a smart and sustainable future. *J. Clean. Prod.* **2020**, *274*, 122877. [CrossRef] [PubMed]
19. Reda, H.T.; Daely, P.T.; Kharel, J.; Shin, S.Y. On the application of IoT: Meteorological information display system based on LoRa wireless communication. *IETE Tech. Rev.* **2018**, *35*, 256–265. [CrossRef]
20. LÓpez-Vargas, A.; Fuentes, M.; Vivar, M. On the application of IoT for real-time monitoring of small stand-alone PV systems: Results from a new smart datalogger. In Proceedings of the 2018 IEEE 7th World Conference on Photovoltaic Energy Conversion (WCPEC) (A Joint Conference of 45th IEEE PVSC, 28th PVSEC & 34th EU PVSEC), Waikoloa, HI, USA, 10–15 June 2018; pp. 605–607. [CrossRef]
21. Idier, D.; Aurouet, A.; Bachoc, F.; Baills, A.; Betancourt, J.; Gamboa, F.; Klein, T.; López-Lopera, A.F.; Pedreros, R.; Rohmer, J.; et al. A User-Oriented Local Coastal Flooding Early Warning System Using Metamodelling Techniques. *J. Mar. Sci. Eng.* **2021**, *9*, 1191. [CrossRef]
22. Janeković, I.; Kuzmić, M. Numerical simulation of the Adriatic Sea principal tidal constituents. *Ann. Geophys.* **2005**, *23*, 3207–3218. [CrossRef]
23. Press, W.; Teukolsky, S.; Vetterline, W.T.; Flannery, B.P. *Numerical Recipes: The Art of Scientific Computing*; Cambridge University Press: Cambridge, UK, 2007.
24. Cooley, J.W.; Tukey, J.W. An algorithm for the machine calculation of complex Fourier series. *Math. Comput.* **1965**, *19*, 297–301. [CrossRef]
25. Ponte, R.M. Variability in a homogeneous global ocean forced by barometric pressure. *Dyn. Atmos. Ocean.* **1993**, *18*, 209–234. [CrossRef]
26. The Effect of Fetch Width on Wave Generation, US Corps of Engineers, Technical Memorandum No. 70. 1954. Available online: <https://usace.contentdm.oclc.org/digital/api/collection/p266001coll1/id/7549/download> (accessed on 27 July 2021).
27. Goda, J. Revisiting Wilson’s Formulas for Simplified Wind-Wave Prediction. *J. Waterw. Port Coast. Ocean Eng.* **2003**, *129*, 2003. [CrossRef]
28. World Meteorological Organization, Guide to Wave Analysis and Forecasting, Geneva, Switzerland. 2018. Available online: https://library.wmo.int/doc_num.php?explnum_id=10979 (accessed on 31 July 2021).
29. SMS 13.2 Tutorial CGWAVE Analysis, Aquaveo, v13.2. USA. 2012. Available online: <https://www.aquaveo.com/software/sms-learning-tutorials> (accessed on 17 August 2021).
30. Demirbilek, Z.; Panchang, V. *CGWAVE: A Coastal Surface Water Wave Model of the Mild Slope Equation*; Technical Report CHL-98-26; US Army Corps of Engineering: Washington, DC, USA, 1998.
31. Panchang, G.V.; Wei, G.; Pearce, R.B.; Briggs, J.M. Numerical Simulation of Irregular Wave Propagation over Shoal. *J. Waterw. Port Coast. Ocean. Eng.* **1990**, *116*, 324–340. [CrossRef]
32. Zhao, L.; Panchang, V.; Chen, W.; Demirbilek, Z.; Chhabbra, N. Simulation of wave breaking effects in two-dimensional elliptic harbor wave models. *Coast. Eng.* **2001**, *42*, 359–373. [CrossRef]
33. Brockmann, E.; Harsson, B.-G.; Ihde, J. Geodetic Reference System of the Republic of Croatia—Consultants Final Report on Horizontal and Vertical Datum Definition, Map Projection and Basic Networks for the state geodetic administration of the Republic of Croatia. 2001; 1–35.
34. Croatian Meteorological and Hydrological Service. Report of Measured Wind Properties on Gauging Station Marjan. 2011. (In Croatian)
35. BARANI DESIGN Technologies, “MeteoHelix@IoT Pro”. Available online: <https://static1.squarespace.com/static/597dc443914e6bed5fd30dcc/t/5f5f9ce8e52f900a7f1982af/1600101615389/MeteoHelix+IoT+Pro+DataSheet.pdf> (accessed on 30 March 2022).
36. BARANI DESIGN Technologies, “MeteoWind@IoT Pro”. Available online: <https://static1.squarespace.com/static/597dc443914e6bed5fd30dcc/t/5f1813e0fd8f9a4a19feb781/1595413481804/MeteoWind+IoT+Pro+DataSheet.pdf> (accessed on 30 March 2022).
37. Xia, J.; Falconer, R.A.; Xiao, X.; Wang, Y. New criterion for stability of a human body in floodwaters. *J. Hydraul. Res.* **2014**, *52*, 93–104. [CrossRef]

Article

A Comparative Study of the Effects of Earthquakes in Different Countries on Target Displacement in Mid-Rise Regular RC Structures

Ercan Işık ^{1,*}, Marijana Hadzima-Nyarko ^{2,*}, Hüseyin Bilgin ³, Naida Ademović ⁴, Aydın Büyüksaraç ⁵, Ehsan Harirchian ⁶, Borko Bulajić ⁷, Hayri Baytan Özmen ⁸ and Seyed Ehsan Aghakouchaki Hosseini ⁹

¹ Department of Civil Engineering, Bitlis Eren University, Bitlis 13100, Turkey

² Faculty of Civil Engineering and Architecture Osijek, Josip Juraj Strossmayer University of Osijek, Vladimira Preloga 3, 31000 Osijek, Croatia

³ Department of Civil Engineering, Epoka University, 1001 Tirana, Albania

⁴ Faculty of Civil Engineering in Sarajevo, University of Sarajevo, 71 000 Sarajevo, Bosnia and Herzegovina

⁵ Çan Vocational School, Çanakkale 18 Mart University, Çanakkale 17400, Turkey

⁶ Institute of Structural Mechanics (ISM), Bauhaus-Universität Weimar, 99423 Weimar, Germany

⁷ Faculty of Technical Sciences, University of Novi Sad, Trg Dositeja Obradovića 6, 21000 Novi Sad, Serbia

⁸ Department of Civil Engineering, Uşak University, Uşak 64300, Turkey

⁹ Department of Future Environments, Built Environment Engineering, Faculty of Design and Creative Technologies, Auckland University of Technology (AUT), Auckland 1010, New Zealand

* Correspondence: eisik@beu.edu.tr (E.I.); mhadzima@gfos.hr (M.H.-N.)

Citation: Işık, E.; Hadzima-Nyarko, M.; Bilgin, H.; Ademović, N.; Büyüksaraç, A.; Harirchian, E.; Bulajić, B.; Özmen, H.B.; Aghakouchaki Hosseini, S.E. A Comparative Study of the Effects of Earthquakes in Different Countries on Target Displacement in Mid-Rise Regular RC Structures. *Appl. Sci.* **2022**, *12*, 12495. <https://doi.org/10.3390/app122312495>

Academic Editors: Andrea Chiozzi and Dario De Domenico

Received: 31 October 2022

Accepted: 30 November 2022

Published: 6 December 2022

Publisher's Note: MDPI stays neutral with regard to jurisdictional claims in published maps and institutional affiliations.

Abstract: Data from past earthquakes is an important tool to reveal the impact of future earthquakes on engineering structures, especially in earthquake-prone regions. These data are important indicators for revealing the seismic loading effects that structures will be exposed to in future earthquakes. Five different earthquakes from six countries with high seismic risk were selected and were within the scope of this study. The measured peak ground acceleration (PGA) for each earthquake was compared with the suggested PGA for the respective region. Structural analyzes were performed for a reinforced-concrete (RC) building model with four different variables, including the number of storeys, local soil types, building importance class and concrete class. Target displacements specified in the Eurocode-8 were obtained for both the suggested and measured PGA values for each earthquake. The main goal of this study is to reveal whether the proposed and measured PGA values are adequately represented in different countries. We tried to reveal whether the seismic risk was taken into account at a sufficient level. In addition, target displacements have been obtained separately in order to demonstrate whether the measured and suggested PGA values for these countries are adequately represented in structural analysis and evaluations. It was concluded that both seismic risk and target displacements were adequately represented for some earthquakes, while not adequately represented for others. Comments were made about the existing building stock of the countries considering the obtained results.

Keywords: target displacement; earthquake; peak ground acceleration; reinforced-concrete; pushover



Copyright: © 2022 by the authors. Licensee MDPI, Basel, Switzerland. This article is an open access article distributed under the terms and conditions of the Creative Commons Attribution (CC BY) license (<https://creativecommons.org/licenses/by/4.0/>).

1. Introduction

Significant loss of life and property after earthquakes increases the consequence of efforts to reduce the effects of earthquakes. The studies on structural and seismic risk analyzes are carried out on both pre-earthquake and post-earthquake in order to prevent and minimize earthquake damages [1–9]. Such studies have special importance in regions with high seismic risk [10]. Ground motion parameters are needed to determine and evaluate the effects of earthquakes in a particular region [11–13]. These parameters are important in terms of both revealing earthquake characteristics and analyzing the behavior of structures under the influence of earthquakes [14–16]. Fault geometry, seismic waves,

and earthquake characteristics should be known while the determination of the ground motion parameters by considering local ground conditions. The amplitude parameter is one of the engineering aspects of ground motion parameters. The ground velocity, acceleration and displacement values are known as amplitude parameters [17,18]. Knowing that the earthquake ground motions measurements as a function of time or frequency constitutes an important database for engineering applications and scientific studies for earthquake-resistant structure design [19–21]. In this context, many different programs are used to predict earthquake threats. Openquake Engine [22], Earthquake Loss Estimation Routine (ELER) [23], HAZUS [24], Ez-Frisk [25], PSHRisk-Tool [26], FRISK [27], CRISIS2007 [28], SEISRISK III [29] and OpenSHA [30] are some of the software that are commonly used programs for predicting earthquake threat.

The obtained ground acceleration records from strong ground motion measurements can be used to both determine seismic risk and to monitor the performance of structures during earthquakes. Acceleration records can also be used for the design of earthquake-resistant structures and for the development of attenuation relationships. In addition, the expected damage estimation and intensity distribution in the settlements at different distances from the station can be determined by using attenuation relationships. Earthquake ground motions can be quite complex from this perspective. It is possible to define earthquake motion with three components of linear motion [31,32]. The Peak Ground Acceleration (PGA) is the most common measure used to determine the amplitude of strong ground motion. Any accelerometer used for acceleration records has two horizontal (EW and NS) components and one vertical component. The maximum horizontal ground acceleration is either the geometric mean of the maximum values of the component in both directions or the largest one of them regardless of direction [33–35]. Therefore, obtained PGA values from any earthquake are used to determine seismic and structural risks. Different types of analyzes can be used to decide the performance levels of structures in performance-based design [36–38].

Pushover analysis is a widely used nonlinear analysis technique to estimate the dynamic demands imposed on a structure under earthquake impact. The maximum roof displacements, known as target displacement, are one of the results obtained from this analysis [39–42]. The earthquake performances and damage estimation of the structures can be predicted using the target displacements [43–46]. It is then required to decide the structural performance by comparing the demand values to the deformation capacity for the expected performance levels [47]. Adequate demand displacement values will better reflect real values for the damage estimation of structures and building earthquake performance [48].

In this study, seismic risk and target displacements were compared, taking into account the measured and suggested PGA values for different earthquakes in different countries. Six countries with different seismicity were selected, including as Bosnia and Herzegovina, Albania, Croatia, Iran, Türkiye, and Serbia, and these were within the scope of this study. Two different country groups were selected in this study. In the first group, neighboring Bosnia and Herzegovina, Serbia, Croatia, and Albania were taken into account, while in the second group, neighboring Türkiye and Iran were taken into account. Bulgaria, Macedonia, and Greece are located between these two groups of countries. Earthquakes that occur in both groups of countries also affect other countries within the group. Therefore, seismic and structural parameters were obtained for two different country groups. For this purpose, five different earthquakes were selected for each country. The earthquakes whose data can be accessed were taken into account in the selection of these earthquakes. First, the measured and suggested PGA values were compared for selected earthquakes. Information is provided about the seismicity and the selected earthquakes for each country, respectively. Structural analyzes were made for a sample reinforced concrete (RC) structure to reveal the effect of PGA values. In order to make the structural results more understandable, the RC building has been taken into account with three different numbers of stories, including four, six, and eight-stories. In order to reveal the effect of different structural

conditions, four different variables, namely: the number of storeys, local soil class, building importance class and concrete class were selected. Within the scope of this study, regular mid-rise RC building models were taken into account. In addition, the natural fundamental periods obtained with the empirical formulas used in the earthquake regulations for each country were compared with the period values obtained from the structural analysis. The target displacement values used to determine the performance level and damage estimation of the structures were obtained separately for each number of storeys and each earthquake. In addition, information is given about the building stocks of these countries at the point of the earthquake-structure relationship. The main purpose of this study is to reveal if the suggested PGA values for the building design in seismic design codes and earthquake hazard maps meet the measured PGA values. The novelty of the study is the detailed comparison of both seismic parameters and structural analysis results for six different countries. This study will contribute to the development of seismic hazard maps and seismic design codes for the selected countries. This study will make important contributions to this and similar studies in many different countries and earthquakes.

2. Seismicity of the Selected Countries

Within the scope of this study, six different countries with different seismic characteristics, including Albania, Bosnia and Herzegovina, Croatia, Serbia, Türkiye, and Iran were selected. Comparisons were made by considering the suggested and measured peak acceleration values for the five different earthquakes in each country. In addition to the information about the selected earthquakes, brief information about the seismicity of these countries is given in this section. The locations of selected countries in the active tectonic map were shown in Figure 1.

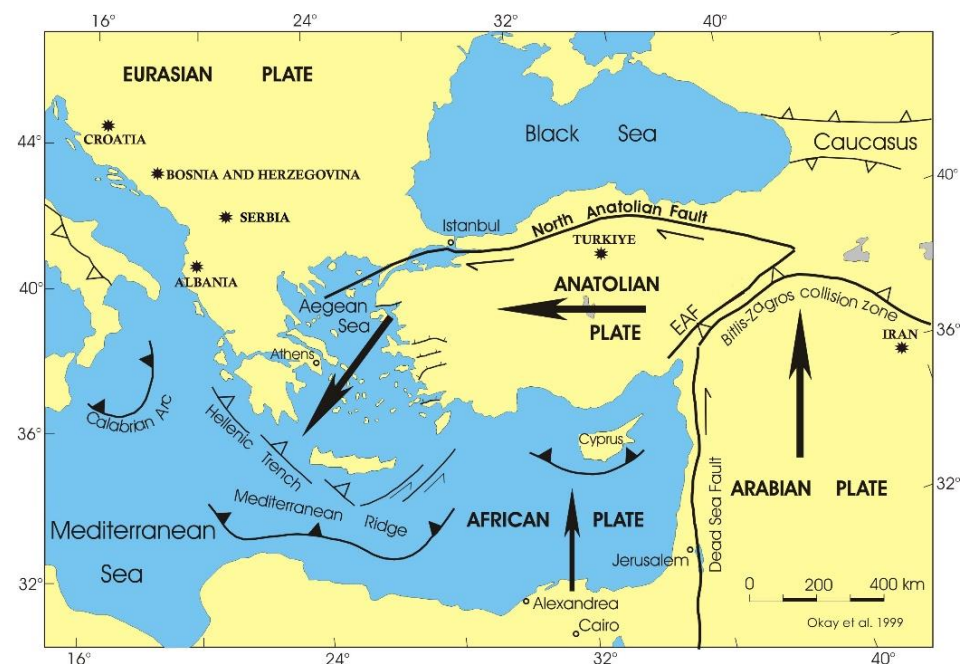


Figure 1. Location of selected countries in the active tectonic map (adopted from [49,50]).

2.1. Albania

Albania is a country with moderate seismicity in the Western Balkans. Located on the Alpine-Mediterranean plate, this region has historically been affected by high-intensity earthquakes. Albanian seismic activity is characterized by intense seismic microactivity ($3.0 > M > 1.0$) by lots of small earthquakes ($5.0 > M > 3.0$), few mid-sized earthquakes ($7.0 > M > 5.0$) and very rarely by large earthquakes ($M > 7.0$). The most important tremors in the last century are given in Table 1.

Table 1. Major earthquakes in Albania [51].

Date	Area affected	M_w	Depth (km)	Causalities	
				Dead	Injured
26.11.2019	Durres	6.4	20	52	3000+
21.09.2019	Durres	5.6	10	-	108
09.01.1988	Tirana	5.4	24	-	-
16.11.1982	Fier	5.6	22	1	12
15.04.1979	Shkoder	6.9	10	136	1000+
30.11.1967	Diber	6.6	20	12	174
18.03.1962	Fier	6.0	-	5	77
26.05.1960	Korce	6.4	-	7	127
01.09.1959	Fier	6.2	20	2	-
27.08.1942	Diber	6.0	33	43	110
21.11.1930	Vlore	6.0	35	30	100
26.11.1920	Tepelene	6.4	-	36	102
06.01.1905	Shkoder	6.6	-	200	500

Albania and its neighborhood are in a rather complicated seismotectonic region and are prone to earthquakes. A high frequency of earthquakes has been experienced, resulting in loss of life and property destruction in the region (Table 1). According to available records, this region sits in a high rate of seismicity, ranging from moderate to a high seismic risk level. It is characterized by noticeable micro-seismicity (a high number of small earthquakes), sparse mid-sized earthquakes, and very rare large earthquakes. Considering the recorded earthquakes from the accessible data, the earthquakes given in Table 1 were selected by the authors [51].

The first seismic zone intensity map of Albania dates back to 1952. Since then, it has been updated many times until 1979, which is at the moment that the map for seismic evaluation is enforced by the law. The KTP-1963 and KTP-1978 seismic guides were based on the pre-1979s map, which had lower seismic load requirements than the updated values due to a lack of information at the time. Few authors have studied this issue [52]. The largest earthquake in Albania occurred on June 1, 1905, in the North-Western part of Albania with a magnitude of $M_s = 6.6$. The duration of the tremor was 10–12 s and caused extensive damage to the built environment. In Shkodra alone, around 1500 residential buildings were completely destroyed and all other buildings were severely damaged. In addition, the walls of the historical Shkodra fortress were damaged and partially destroyed. The 15.04.1979 earthquake is one of the strongest earthquakes to occur in the Balkan Peninsula with a moment magnitude of 6.9. The epicenter of this tremor was the coastal area near Petrovac/Montenegro. Several tremors occurred about two weeks before the main shock, and aftershocks lasted for more than nine months. A strong aftershock of $M_s = 6.3$ occurred on May 24 [53]. This earthquake was one of the main reasons that led to amendments to the earthquake code and seismic zoning maps. Today's seismic zonation map is still based on regions of maximum intensity, not peak ground acceleration. Another strong earthquake occurred in Durrës on November 26, 2019, with a magnitude of $M_s = 6.4$ [14]. The fact that the epicenter of the earthquake was so close to Albania's most populated and urban area increased the loss of life and injuries. In particular, the old masonry structures in the region were severely damaged and some of them were completely demolished. In this study, this earthquake and its losses will be examined and the results of all analyzes will be compared with the actual damage to the buildings.

The seismic source zones of Albania, characterized by active faults and tectonic regimes, are the essential primary inputs for the estimation of seismic hazards [53]. The following nine earthquake zones have been defined in and around Albania:

- | | |
|---------------------------------|----------------------------------|
| 1. Zone of Lezha-Ulqin | 2. Zone of Peri-Adriatic Lowland |
| 3. Zone of Ionian Coast | 4. Zone of Korca-Ohrid |
| 5. Zone of Elbasan-Diber/Tetova | 6. Zone of Kukës-Peshkopi |
| 7. Zone of Shkodra-Tropoja | 8. Zone of Peja-Prizren |
| 9. Zone of Skopje | |

The compiled Albania earthquake catalog comprises earthquakes of magnitude $M_s > 4.5$ that struck the territory between 39.0° N and 43.0° N and between 18.5° E and 21.5° E spanning a timeline 1958–2005 [53]. The best assessments of maximum magnitude are done by taking into account the biggest seismic activity identified and observed in similar tectonic locations. All this data input is processed by utilizing a probabilistic methodology and appropriate attenuation relationships to develop the Probabilistic Hazard Map of Albania.

The seismic zonation map of Albania is based on the intensity values [54], whereas new modern seismic guidelines like Eurocode 8 use probabilistic seismic hazard maps utilizing the peak ground acceleration values derived by probabilistic approaches with different return periods. In many modern codes, Damage Limitation (DL) is expected to be satisfied for an earthquake with peak ground acceleration for a return period of 95 years. Meanwhile, for an earthquake with PGA within the return period of 475 years, buildings should perform as per the limit state of Significant Damage (SD). Seismic hazard maps for maximum horizontal ground acceleration with recurrence periods of 95 and 475 years, respectively, are given for hard rock conditions (Figure 2).

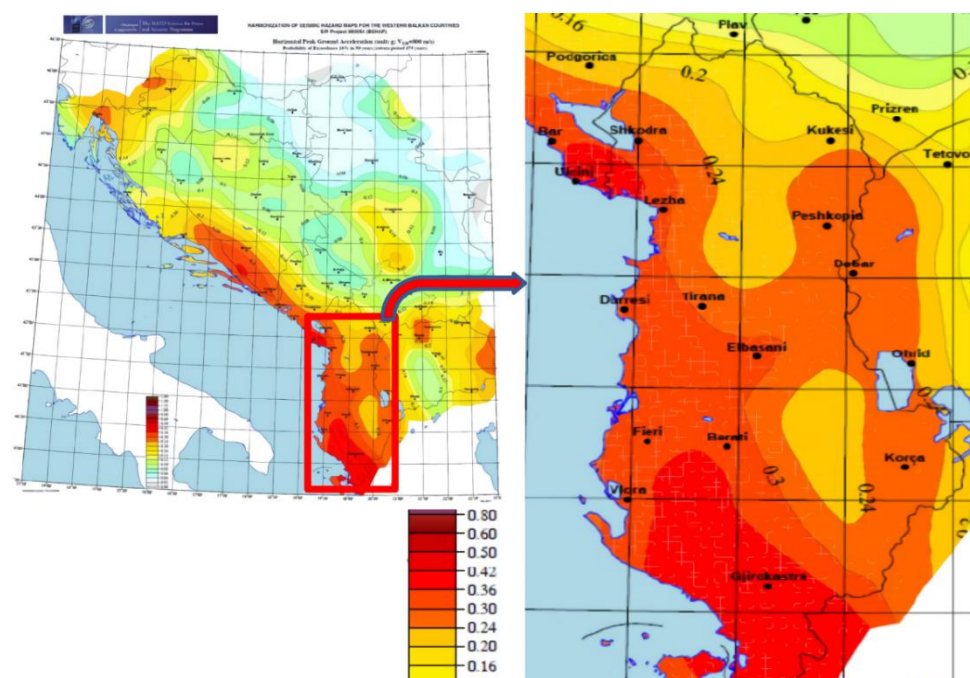


Figure 2. Horizontal peak ground acceleration values for a return period of 475 years (probabilistic seismic hazard map of Albania [55]).

As shown in Figures 2 and 4, in many cities with dense masonry structures, such as Durrës, Shkodra, Elbasan, Tirane, and Vlora, the expected PGA for an earthquake with a recurrence period of 95 years is around 0.20 g, whereas this value is around 0.30–0.40 g with a recurrence period of 475 years. If these values are compared to the recordings of the 26 November 2019 shakings, in most of the regions these values are near the values of a 95 year return period. The data for the selected earthquakes in Albania is shown in Table 2.

Table 2. Data of selected earthquakes in Albania.

No	Date	Lat.	Lon.	Magnitude			Loss of Life	Damaged Buildings	Loss of Life/Damaged Buildings	Location
				Mb	Ms	Mw				
1	26/11/2019	41.51°	19.52°			6.4	52	~90,000	0.0006	Durrës/Albania
2	26/11/2019	41.51°	19.52°			6.4	52	~90,000	0.0006	Durrës/Albania
3	21/09/2019	41.43°	19.71°			5.6	-	120	-	Durrës/Albania
4	09/01/1988	41.20°	19.80°			5.9	-	188	-	Tirana/Albania
5	15/04/1979	42.096°	19.209°			6.9	136	~1000	0.14	Shkoder/Albania

A comparison of the measured and suggested PGA values of the selected earthquakes for Albania are given in Table 3.

Table 3. Comparison of the measured and suggested PGA values of the selected earthquakes for Albania.

No	Earthquake Location	Station Name	Year	Earthquake Magnitude (Mw)	PGA(g)	Seismic Risk Zone	A(g)
						Seismic Risk Zone (As Per KTP-N.2-89)	(A(g) (Expected Design Base Acceleration) (from the Probabilistic Map of Albania)
1	Albania	Tirana	2019	6.4	0.11	High	0.30
2	Albania	Durrës	2019	6.4	0.12	High	0.28–0.30
3	Albania	Tirana	2019	5.6	0.18	High	0.32–0.36
4	Albania	Tirana	1988	5.4	0.40	High	0.28–0.30
5	Albania	Shkoder	1979	6.9	0.46	High	0.30

While the number of damaged buildings in the first two earthquakes considered for Albania was quite high, the loss of life was quite low. In addition, the highest loss of life/damaged buildings ratio for this country was obtained for the fifth earthquake, and this ratio was 0.14. The measured PGA values in these earthquakes that have occurred in these regions with high earthquake risk were considerably lower than the suggested PGA values for the first three earthquakes. However, the measured PGA values for the third and fourth earthquakes are considerably higher than the recommended PGA values. For this country, the seismic risk can be expressed adequately by considering the earthquake ground motion levels for different probabilities of exceedance.

2.2. Bosnia and Herzegovina

Bosnia and Herzegovina is located in the central part of the Dinaridic Mountain System [56]. The location of Mediterranean is characterized by various types of faults that have been identified in this region. The Adriatic coast and the Dinarides are specific for reverse faults, while normal faults are mainly identified in the Apennine Peninsula. The fault plane solution for major earthquakes in Adria has been presented by Slejko et al. [57], while obtaining data from various sources; Gasparini et al. [58], Herak et al. [59], Louvari et al. [60], Sulstarova et al. [61], and Harvard [62].

As stated in the article in [63], quote: “It is evident that with the increase of population in seismically prone areas, urban areas are becoming more vulnerable to seismic risk. Record losses were registered in 2011 [64] after earthquakes that hit Japan and New Zealand, for developed countries with a high degree of earthquake disaster awareness and preparedness. In absolute terms, the costliest disasters happen in the most developed countries, however, with respect to their GDP, it was limited to a few percentage points [65]. The analysis showed that countries of middle income in the last two decades were at a higher risk in comparison to the countries with low and high GDP. From the available data [65], Bosnia and Herzegovina falls into lower-middle-income.”

Taking into account the high density of the population, high level of vulnerability of buildings, and moderate to high in some locations PGA results in a high risk of earthquakes in Bosnia and Herzegovina. After the Zagreb 2020 earthquakes, the engineering community awakened regarding the potential risk and level of devastation to the existing building stock in Bosnia and Herzegovina. It should be mentioned that the last devastating earthquake that hit Zagreb was in 1880. Then, 140 years later, the Zagreb 2020 earthquake and Petrinja earthquake occurred and had a major effect on the building and clearly showed the high vulnerability of the existing stock. It is important to state that the Pokupsko-Petrinja Fault is oriented in the NW-SE direction within the Eurasian plate. This is the strongest earthquake that occurred since the 1880 Great Zagreb earthquake (magnitude of 6.3). The seismicity of this region (Croatia and the upper part of Bosnia and Herzegovina-Banja Luka region) is given in Figure 4. Looking at the map, it is believed that the Petrinja fault is the same as the Banja Luka fault, as indicated in Figure 3 and indicated as PKBL = Pokuplje-Kostajnica-Banja Luka right-lateral fault.

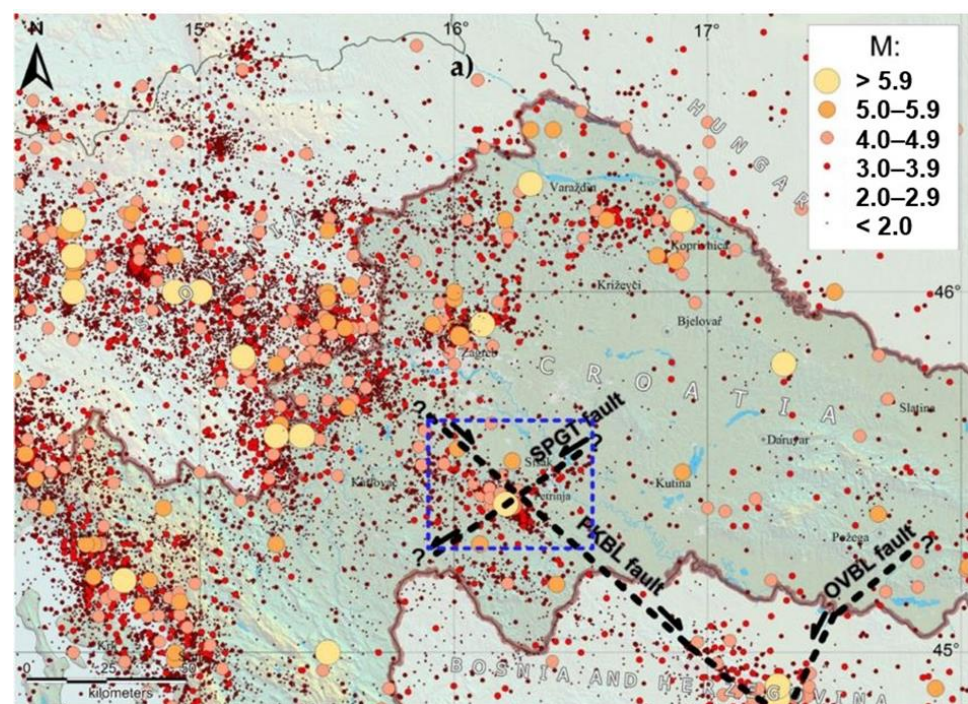


Figure 3. The spatial distribution of earthquakes in Croatia (373 BC–2019, according to the Croatian Earthquake Catalogue (CEC), of which an updated version was first described in [67], with the Pokupsko-Petrinja epicentral area indicated (blue rectangle). Thick, black-dashed lines mark regional active faults: PKBL = Pokuplje-Kostajnica-Banja Luka right-lateral fault, SPGT = Sisak-Petrinja-Glina-Topusko left-lateral fault, and OVBL = Orljava-Vrbas-Banja Luka left-lateral fault.

After the Petrinja earthquake, a quick field inspection revealed that fresh fault planes in the outcrops on the Hrastovička gora appeared mostly along the longitudinal NW–SE-striking Pokupsko–Kostajnica–Banja Luka Fault and showed clear dextral coseismic strike-slip displacements and a 20 km long section of the Pokupsko Fault was (re)activated. It is assumed by Markušić et al. [68] that the creeping sinistral Sisak–Petrinja–Glina–Topusko Fault is locking the dextral Pokupsko–Kostajnica–Banja Luka Fault and a similar complex fault mechanism is also proposed for the Banja Luka area. According to Markušić et al. [68], the dextral Pokupsko–Banja Luka Fault could be one of the main inherited active faults between the crustal segments of Adria.

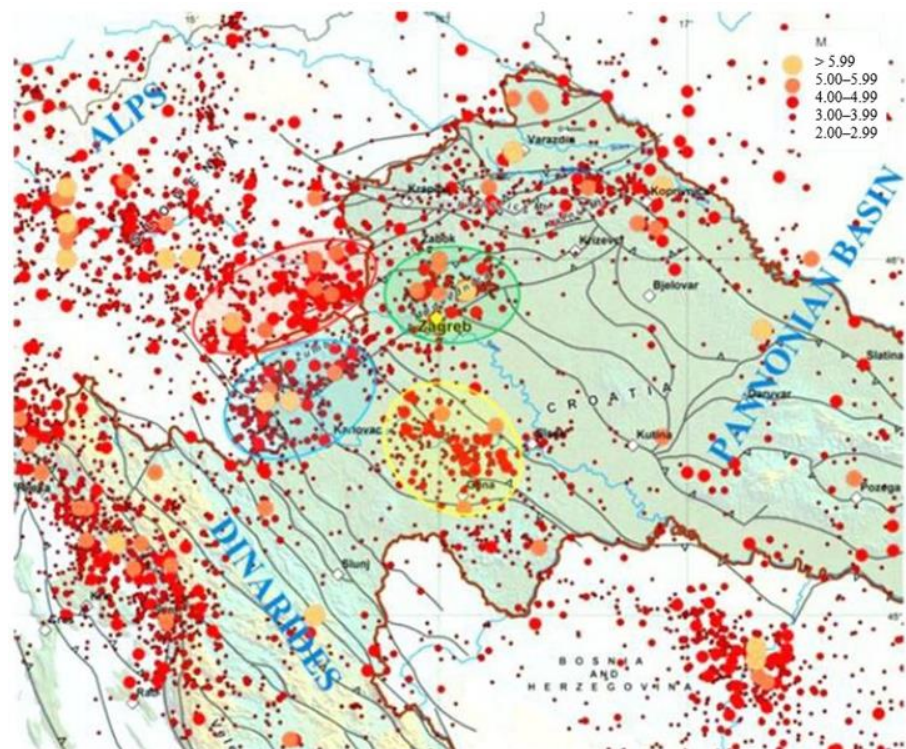


Figure 4. Map of earthquake epicenters in Croatia and part of Bosnia and Herzegovina in the period from BC to 2015 according to the Catalog of Earthquakes in Croatia and the neighboring areas [66–71].

Taking this all into account, it is of the utmost importance to take Bosnia and Herzegovina into account regarding the effects of earthquakes on target displacement in RC structures and other structures as well. Other than the Peak Ground Acceleration, it is necessary to take into account the vulnerability of structures and the exposure of the population during the assessment of the seismic risk. After the Petrinja earthquake, the seismic community in Bosnia and Herzegovina discussions started, and at the moment, there are initiatives for a revision of the interactive seismic map of Bosnia and Herzegovina.

Papeš [72] gave the most comprehensive picture of the tectonic structure in Bosnia and Herzegovina. The longest fault is the Sarajevo Fault, which spreads in the direction of NW-SW, followed by the Banja Luka fault and Konjic Fault. Sarajevo fault with a low to moderate seismic activity level is under-passed by all the transversal deep faults, where the highest seismic motions are noted. Ademović et al. [73] presented that 64% of all earthquakes have a focal depth of up to 10 km and that this is one of the causes of the damaging impact on the structures. Bosnia and Herzegovina in the last 50 years was hit by more than a few medium-sized earthquakes of magnitude M_w up to 6.1 [74]. The earthquake, which had the most devastating impact on the structures, was the 1969 Banja Luka earthquake. According to the MSK-64, the Banja Luka earthquake was marked as a VIII intensity scale [75]. The aftermath of this earthquake was 15 fatalities, 1117 injured people, and over \$300 million in damage [74,76].

The second-largest earthquake that should be mentioned is the 1962 Treskavica earthquake with a magnitude $M_w = 5.9$, and a focal depth of 15 km. As the epicenter of the earthquake was in an abandoned area of Mount Treskavica, there were no major casualties, nor significant damage to the buildings due to the low level of population and construction in this region at that time [77]. Several structures have been damaged in Sarajevo by this earthquake activity (Building of the Executive Council, the Main Post Office, Faculty of Medicine) [73]. The damage caused by this earthquake in the financial means was equal to 396 million dinars [78]. Looking at the period from 306 to 2015, 66.9% of all earthquakes had a magnitude between 3.6–4.5, while 20.5% of the earthquakes had a magnitude in the

range of 4.6 to 6. This region was not often hit (4.2% of all earthquakes) by an earthquake of larger magnitudes, while only 8.5% of all earthquakes that hit this region had a magnitude between 3.1 to 3.5 [73].

Figure 5 shows epicentres of regional north-western Balkan earthquakes observed between 1900 and April 2021 with $M_w \geq 3.0$ [79], as well as the boundaries of Croatia, Bosnia and Herzegovina, and Serbia. It also shows epicentres of the earthquakes from which PGA values have been recorded on rock, as well as the recording sites. In 2018, new seismic hazard maps were compiled for Bosnia and Herzegovina and incorporated into the National Annex to Eurocode 8 [80]. It should be noted that the reference PGA values in these maps are given for ground type A, i.e., for the rock sites. Recently, in all three countries (Croatia, Bosnia and Herzegovina, and Serbia), current official seismic hazard maps are part of the respective National Annexes to Eurocode 8 and the PGA values for rock sites (ground type A) are used to express the hazard. Hence, in Table 5, we have presented only the PGA values recorded on rock (i.e., sites with shear wave velocity in the top 30 m of the soil larger than or equal to 800 m/s). This has unfortunately posed a challenge, since for some devastating historical earthquakes there were very few accelerograph stations on rock sites, while for others we could not find any available data.

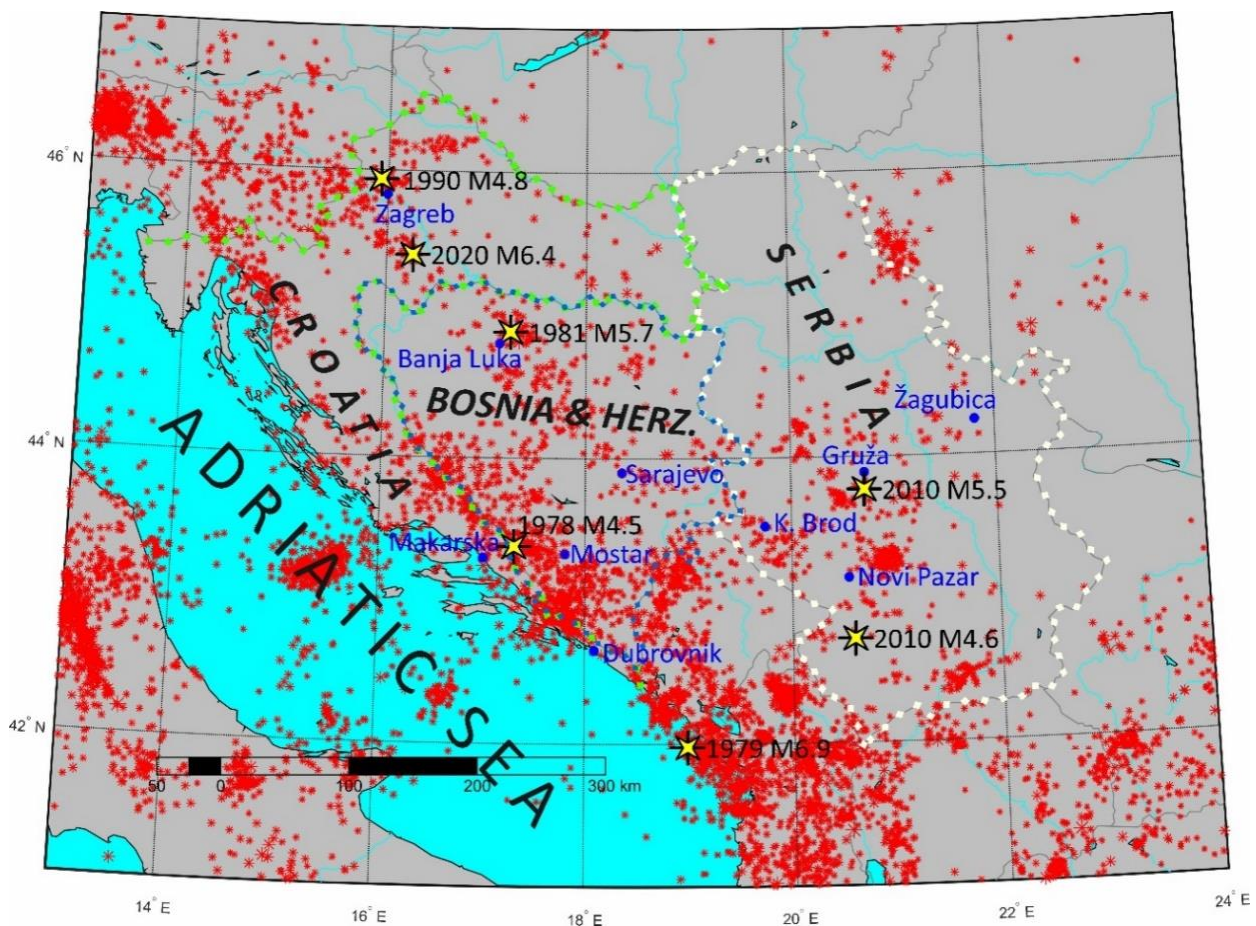


Figure 5. Epicentres of the north-western Balkan earthquakes observed between 1900 and 2021 [79], including the epicentres of the earthquakes that were recorded in Croatia, Bosnia and Herzegovina, and Serbia on rock (blue circles show locations of the corresponding recording stations).

During the analysis, we have chosen the countries of the Balkan as two years ago several earthquakes hit Croatia, which, even though not of “extreme” magnitude, had a major impact on the building stock and community as a whole. The data on the 1981 Banja Luka earthquake are shown in Table 4.

Table 4. Data of the selected earthquake in Bosnia and Herzegovina [81,82].

No	Date	Lat.	Lon.	Magnitude			Loss of Life	Damaged Buildings	Loss of Life/ Damaged Buildings	Location
				Mb	Ms	Mw				
1	13.08.1981	44.82	17.26	5.3	5.5	5.7	-	-	-	Banja Luka (Bosnia and Herzegovina)

The comparison of the PGA values for selected earthquakes in Bosnia and Herzegovina is shown in Table 5. In Table 5, all PGA values were taken from the EQINFOS database [83]. All given PGA values were recorded at rock sites (corresponding to ground type A according to Eurocode 8).

Table 5. Comparison of the measured and suggested PGA values of selected earthquakes for Bosnia and Herzegovina [83].

No	Earthquake Location	Station Name	Year	Earthquake Magnitude (Mw)	Distance to Epicentre to Station (km)	PGA(g)	Seismic Risk Zone	A(g)
							Seismic Risk Zone	(A(g) (Expected Design Base Acceleration) (from the Probabilistic Map of B&H)
1	Banja Luka, B&H	Banja Luka	1981	5.7	7.1	0.29	High	0.17
2	Banja Luka, B&H	Banja Luka	1981	5.7	7.4	0.36	High	0.17
3	Banja Luka, B&H	Banja Luka	1981	5.7	6.5	0.43	High	0.17
4	Montenegro	Sarajevo	1979	6.9	215	0.01	High	0.18
5	Montenegro	Mostar	1979	6.9	177	0.04	High	0.26

For Bosnia and Herzegovina, the loss of life/damaged buildings ratio for the first earthquake, whose data can be accessed, was 0.09. The measured PGA values for the three earthquakes were considerably higher than the predicted PGA values, however, it should be noted that these values were recorded at very short epicentral distances—7.1, 7.4, and 6.5 km, respectively—while the hypocentral depth was only 10 km. Smaller measured PGA values are recorded at large distances of 215 and 177 km, respectively.

2.3. Croatia

As part of the Mediterranean–Trans-Asian belt, the territory of the Republic of Croatia is located in a seismically active area. The territory of Croatia consists of several tectonic units: The Pannonian basin in the north, the eastern part of the Alps in the northwest, the Dinarides, the transition zone between the Dinarides and the Adriatic plate, and the Adriatic plate [84,85]. Structural-geological data on recently active faults, combined with data on seismic activity, form the basis for the interpretation of seismotectonic activity, seismic hazard, and risk in seismically active areas.

The majority of earthquakes in Croatia occur around the Adriatic coast due to the interaction (collision) of the Adriatic Platform and the Dinarides (see Figure 6). However, the north-east parts of Croatia are located in an intraplate low to moderate seismicity region of the Pannonian Basin [85]. Moho depths in Croatia range from 25 km beneath the Pannonian Basin to 45 km beneath the Dinarides [86,87]. Since 2011, current official seismic hazard maps (for a return period of 95 and 475 years) for Croatia are part of

the Croatian National Annex to Eurocode 8 [88]. Hazard maps for the return period of 475 years for Croatia are presented in Figure 6. In Table 6, data on selected earthquakes in Croatia are given. All given PGA values were recorded at rock sites (corresponding to ground type A according to Eurocode 8). The ratio of loss of life/damaged buildings was 0.01 for the first earthquake and 0.09 for the third earthquake. Here, the first earthquake is the 6.4 Mw earthquake that devastated the village of Petrinja on 29 December 2020, with the epicentre 40 km south of the capital of Croatia, Zagreb [89]. The focal depth of the earthquake was around 10 km. Another earthquake that should be mentioned here, and which caused damages in Bosnia and Herzegovina as well as in Croatia and even Albania, is the 1979 Montenegro earthquake, which was the strongest earthquake recorded in the area of the former Yugoslavia, with the epicentre offshore in the Adriatic Sea (see Figure 5). While this earthquake was felt up to 900 km from the epicentre, it had destructive consequences only in a 100 km coastal zone and a 25 km stretch from the shore to the mountains [90]. Montenegro suffered 101 and Albania 35 fatalities as a result of the earthquake [90]. This earthquake contributed to the last two PGA values in Table 5, and the third and fourth PGA values in Table 6.

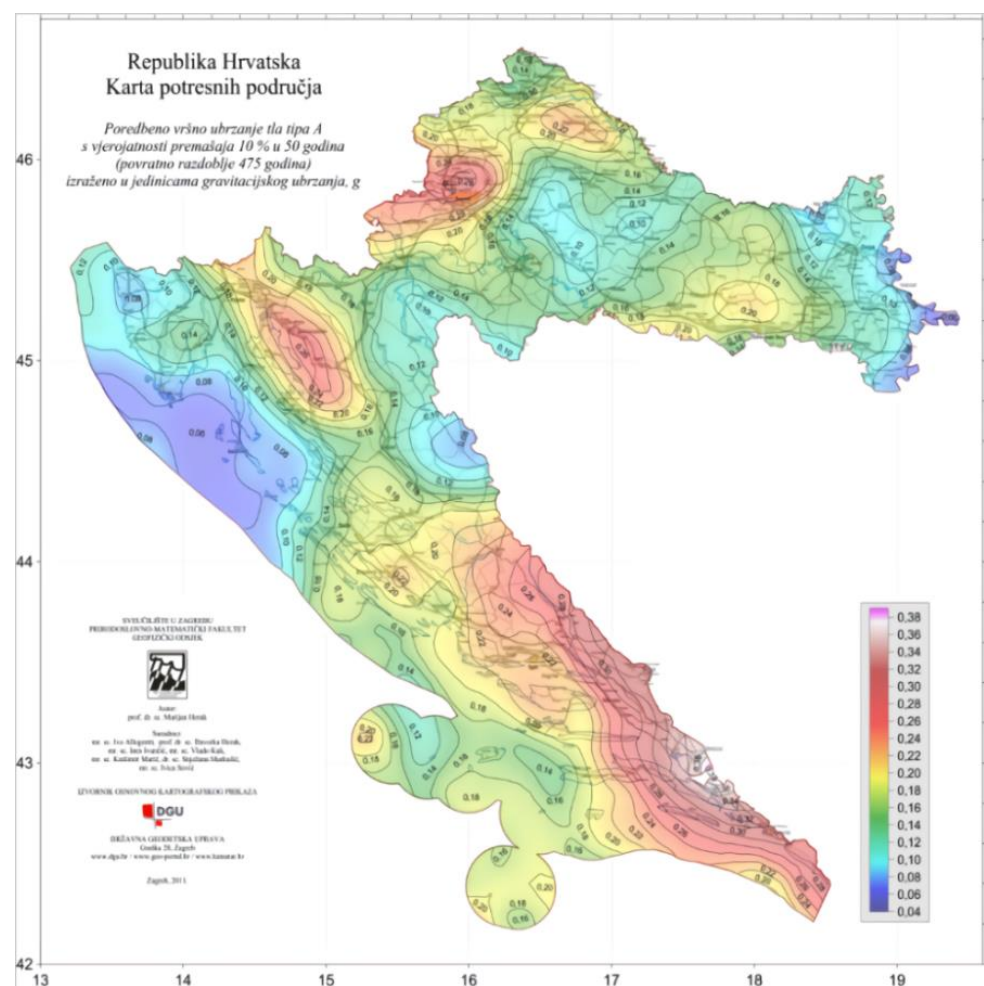


Figure 6. Seismic hazard maps for Croatia for a return period of 475 years (<http://seizkarta.gfz.hr/karta.php>, accessed 30 August 2022) [91].

Table 6. Data of selected earthquakes in Croatia [79,82,83].

No	Date	Lat.	Lon.	Magnitude			Loss of Life	Damaged Buildings	Loss of Life/ Damaged Buildings	Location
				Mb	Ms	Mw				
1	29.12.2020	45.40	16.22	6.0		6.4	7	8300*	0.01	Petrinja, Croatia
2	03.09.1990	45.92	15.92	4.8	4.7	4.9	-	-	-	Kraljev Vrh, Croatia
3	17.12.1978	43.38	17.29	4.5	3.7	4.7	-	-	-	Imotski, Croatia

* UNICEF Country Office for Croatia, Earthquake Situation Report #5, 3 February 2021 [92].

The comparison of measured and suggested PGA of the selected earthquakes for Croatia is given in Table 7.

Table 7. Comparison of the measured and suggested PGA values of the selected earthquakes for Croatia [82,83,93,94].

No	Earthquake Location	Station Name	Year	Earthquake Magnitude (Mw)	Distance to Epicentre to Station (km)	PGA(g)	Seismic Risk Zone	A(g)
								(A(g) (Expected Design Base Acceleration) (from the Probabilistic Map of Croatia))
1	Petrinja, Croatia	Zagreb-Puntijarka	2020	6.4	60	0.04	High	0.279
2	Kraljev Vrh, Croatia	Zagreb	1990	4.9	12	0.06	High	0.259
3	Montenegro	Dubrovnik	1979	6.9	105	0.08	High	0.305
4	Montenegro	Makarska	1979	6.9	208	0.04	High	0.276
5	Imotski, Croatia	Makarska	1978	4.7	24	0.03	High	0.276

Table 7 shows all the PGA values recorded on rock sites in Croatia that could be found at the moment. The first PGA value corresponds to the 2020 Petrinja earthquake [94]. The second PGA value was taken from the ISESD database [81,83]. The last three PGA values were taken from the EQINFOS database [82]. It is interesting to see from Table 5 that, although there were no casualties in Croatia, the PGA values recorded from this earthquake on rock sites at distances of 105 and 218 km are very similar to those recorded in Croatia at much smaller distances, but during moderate size events. From what can be seen from Table 7, the presented PGA values are very, very low compared to the corresponding PGA values given in the Croatian hazard map. However, it should be noted that some of these values were recorded at relatively large epicentral distances. For example, the first value was recorded at a distance of 60 km, while the third and fourth PGA values were recorded at distances of 105 and 218 km, respectively (the hypocentral depth was 12 km). The second value was recorded at the epicentral distance of 12 km while the epicentral depth was 13 km. The fifth value was recorded at the epicentral distance of 24 km, while the epicentral depth was 10 km.

2.4. Serbia

The major part of Serbia is located in intraplate low to moderate seismicity regions. To the north, Serbia comprises the Pannonian Basin's southern part, with a rare occurrence of larger earthquakes [95]. To the southwest, Serbia is surrounded by Dinaric Alps and borders the Mediterranean-Trans-Asian belt, known for its frequent occurrence of stronger earthquakes. To the northeast, Serbia is surrounded by the Carpathian Mountains, and to

the southeast by the Balkan Mountains and Rhodopes. The range of the Moho depths is similar to that in Croatia (shallowest beneath the Pannonian Basin and deepest beneath the Dinarides) [86,87]. Normal faults are, however, more common in Serbia than thrusts and strike-slip faults, which do account for practically all occurrences in the External Dinarides.

A series of earthquakes struck central Serbia in the twentieth century, causing largely rural devastation, such as the 1922 M6.0 Lazarevac, 1927 M = 5.9 Rudnik, 1980 M = 5.8 Kopaonik, and 1998 M = 5.7 Mionica earthquakes. The most recent devastating earthquake in Serbia was the M = 5.5 Kraljevo Earthquake, which occurred on 3 November 2010, with an epicentral intensity of VII-VIII °MCS. Two individuals died, 180 people were injured, and numerous buildings were damaged [96].

Data of selected earthquakes that are available for Serbia [97] is given in Table 8 and the comparison of PGA's is given in Table 10. All given PGA values were recorded at rock sites (corresponding to ground type A according to Eurocode 8).

Table 8. Data of selected earthquakes in Serbia [97].

No	Date	Lat.	Lon.	Magnitude			Loss of Life	Damaged Buildings	Loss of Life/ Damaged Buildings	Location
				Mb	Ms	Mw				
1	03.11.2010	43.76	20.73	5.3	5.0	5.5	2	1689	0.01	Kraljevo, Serbia
2	10.03.2010	42.77	20.56	5.0	4.0	4.6	-	-	-	Peć

In 2018, new seismic hazard maps were compiled for Serbia and incorporated into the National Annex to Eurocode 8. Similar to Croatia and Bosnia and Herzegovina, for Serbia, it was also a challenge to find PGA records on rock sites, especially because Serbia did not experience an event with Mw larger than 5.9 in the past 100 years. The values presented in Table 9 are the only ones we could find for the rock sites, and which were recorded by the Seismological Survey of Serbia's (2021) [98] accelerograph network in Serbia.

Table 9. Comparison of the measured and suggested PGA values of the selected earthquakes for Serbia [98].

No	Earthquake Location	Station Name	Year	Earthquake Magnitude (Mw)	Distance to Epicentre to Station (km)	PGA(g)	Seismic Risk Zone	A(g)
							(A(g) (Expected Design Base Acceleration) (from the Probabilistic Map of Serbia))	
1	Kraljevo, Serbia	Gruža	2010	5.5	13	0.06	High	0.20
2	Kraljevo, Serbia	Novi Pazar	2010	5.5	69	0.01	High	0.20
3	Kraljevo, Serbia	Radoinja, Kokin Brod	2010	5.5	83	0.01	Medium	0.15
4	Kraljevo, Serbia	Žagubica	2010	5.5	102	0.01	Medium	0.15
5	Peć	Novi Pazar	2010	4.6	46	0.01	High	0.20

Data of selected earthquakes that are available for Serbia is given in Table 8 and the comparison of PGA's is given in Table 9. All given PGA values were recorded at rock sites (corresponding to ground type A according to Eurocode 8).

For Serbia, the ratio of loss of life to damaged buildings was 0.01 for the first earthquake. The recorded PGA values considered for Serbia are very, very low compared to the corresponding PGA values given in the Serbian official seismic hazard map. However, most

of these values shown here were also recorded at relatively large epicentral distances. The epicentral distances for the last four PGA values were 69, 83, 102, and 46 km, respectively, while for the first value the distance was 13 km (the hypocentral depth was 13 km for the first four records and 12 km for the last record).

2.5. Türkiye

Türkiye is situated within the Alpine-Himalayan orogenic belt and is among the most seismically active areas in the world [99,100]. The distribution of seismicity is focused on high-strain regions, many of which are major strike-slip faults, such as the North Anatolian Fault Zone (NAFZ), the East Anatolian Fault Zone (EAFZ), and the Western Anatolian Graben Zones (WAGZ). The NAFZ is a 1200 km long strike-slip fault zone that connects the East Anatolian convergent zone to the Hellenic subduction zone [101–103]. The distribution of earthquakes that dominate the seismic pattern of the northern part of Türkiye is mostly parallel to the NAFZ [104–106]. The NAFZ is a continuous and narrow fault system that cuts the Anatolian Peninsula in an E-W direction from Karlıova in the east to the northern Aegean in the west. The NAFZ, which is the northern plate boundary of the Anatolian Plate with the N-S extensional regime of the Aegean region, spreads as a complex fault system in the eastern part of the Marmara region, in contrast to the simple structure of the NAFZ (Figure 7).

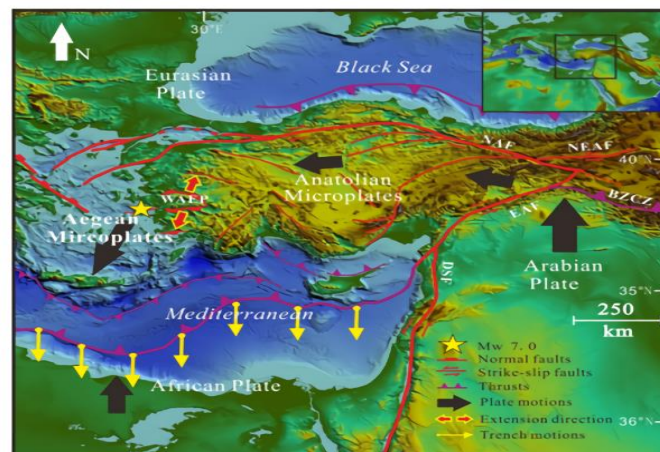


Figure 7. Main tectonics elements for Türkiye [107].

Distribution of the epicenters ($M \geq 3.0$) and main fault zones in Türkiye was given in Figure 8.

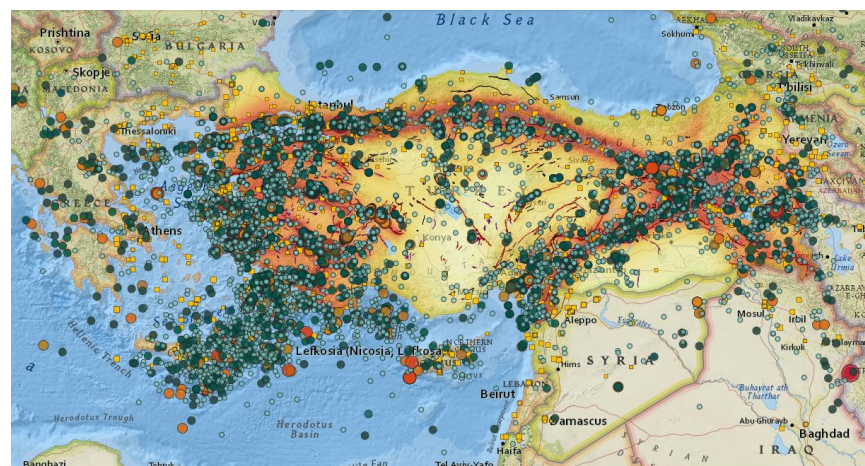


Figure 8. Distribution of epicenters ($M \geq 3.0$) and main fault zones in Türkiye.

The earthquakes taken into account for Türkiye are the 1992 Erzincan, 1999 Kocaeli, 1999 Düzce, 2003 Bingöl, and 2011 Van. The 1992 Erzincan earthquake occurred in the eastern half of the Erzincan basin, and two days after this earthquake, the largest aftershock occurred in Pülümür [108]. After this 6.8 magnitude earthquake, many engineering structures were damaged [109]. The 1999 Gölcük (Kocaeli) earthquake, which was felt in and around the Marmara region, caused different levels of structural damage in these settlements. This earthquake, which occurred on the northern branch of the North Anatolian Fault Zone (NAFZ), is associated with a 145 km long surface rupture extending from the southwest of Düzce in the east to the west of the Hersek delta in the west [110]. The 1999 Düzce earthquake, which took place three months after the 1999 Gölcük earthquake, was felt in many different settlements and caused huge structural damage [111]. The surface rupture of this earthquake, which occurred on the Düzce Fault, which is an extension of the North Anatolian Fault Zone in the Bolu Basin, was 40 km long and the maximum right lateral deviation was measured as 500 ± 5 cm [112]. The 2003 earthquake that occurred in Bingöl, one of Türkiye's provinces with high seismicity, occurred approximately 60 km southwest of the triple junction near Karlıova, where the North Anatolian Fault Zone (NAFZ) and the East Anatolian Fault Zone (EAFZ) intersect [113]. The earthquake-causing fault is a right-lateral strike-slip fault and it is stated that the earthquake depth is in the range of 5–15 km [114]. The last earthquake considered in the study is the 2011 Van earthquake that happened in the Lake Van Basin. The epicentral depth of this earthquake, which was centered in Tabanlı village between Van and Erçiş, was measured as 5 km [115]. The large aftershock of 9.11. 2011 ($M_W = 5.7$) was caused by additional damage, especially in the city center of Van, and more than 40 fatalities [116,117]. The settlements where the epicentres of these five different earthquakes, which are considered for Türkiye, have high seismic risk.

The loss of life and property of a total of selected earthquakes and their locations are shown in Table 10. Data on these earthquakes were obtained from the databases of two main institutions that record instrumental earthquakes in Türkiye such as the Republic of Türkiye Prime Ministry Disaster and Emergency Management Presidency (DEMP) and the Kandilli Observatory Earthquake Research Institute of Bogaziçi University (KOERI) and [118,119].

Table 10. Data of selected earthquakes in Türkiye [118,119].

No	Date	Lat.	Lon.	Magnitude			Loss of Life	Damaged Buildings	Loss of Life/ Damaged Buildings	Location
				Mb	Ms	Mw				
1	13.03.1992	39.72	39.63	6.1	6.8		653	8057	0.08	Erzincan
2	17.08.1999	40.76	29.96	6.1	7.4		17,480	73,342	0.24	Gölcük (Kocaeli)
3	12.11.1999	40.81	31.19	6.2	7.2		763	35,519	0.02	Düzce
4	01.05.2003	39.00	40.46	5.7	6.3		176	6000	0.03	Bingöl
5	23.10.2011	38.76	43.36			7.2	644	17,005	0.04	Van

Among the selected earthquakes in this study, the greatest damage occurred in the 1999 Kocaeli (Gölcük) earthquake. The loss of life per building was obtained as 0.24 for this earthquake. The lowest loss of life per building occurred in the 1999 Düzce earthquake. These five different earthquakes caused a total of 19,716 deaths in a total of 139,923 damaged buildings. This data is sufficient to clearly demonstrate Türkiye's earthquake hazard. The loss of life per building for five earthquakes was calculated as 0.14. The measured and recommended PGA values for these earthquakes are given in Table 11. The standard design earthquake ground motion level was selected to determine the suggested PGA values. This level is opposed to probabilities of exceedance of 10% in 50 years, which has a 475-year repetition period.

Table 11. Comparison of the measured and suggested PGA values of the selected earthquakes for Türkiye.

No	Earthquake Location	Station Name	Year	Earthquake Magnitude	Magnitude Type	PGA(g)	Seismic Risk Zone	PGA(g)
							As Per TSDC-2007	As Per TBEC-2018
1	Türkiye	Van	2011	7.2	Mw	0.182	High	0.399
2	Türkiye	Bingöl	2003	6.3	Ms	0.511	Very High	0.633
3	Türkiye	Düzce	1999	7.2	Ms	0.823	Very High	0.588
4	Türkiye	Erzincan	1992	6.8	Ms	0.485	Very High	0.432
5	Türkiye	Kocaeli	1999	7.4	Ms	0.399	Very High	0.690

Except for the third and fourth Düzce earthquakes, the recommended PGA values for the design earthquake were not exceeded for the other three earthquakes. For Türkiye, the recommended PGA values for the first, second and fifth earthquake locations are lower than the predicted PGA values, and the seismic risk for these locations has been adequately taken into account. All earthquake hazard maps used in Türkiye until 2018 were prepared on a regional basis. However, the earthquake hazard is specified specifically for the geographical location with the map currently used after this date. In addition, while there was only one earthquake ground motion level in the previous seismic design code, four different exceedance probabilities are taken into account with the updated code. With the earthquake hazard specific to the geographical location, the expected target displacements from the structures under the effect of the earthquake could be obtained more realistically. Considering the earthquake ground motion levels for different probabilities of exceedance, it is possible for the structures to provide the desired performance levels under the influence of larger earthquakes.

2.6. Iran

The Iranian plateau is located on the Alpine–Himalayan seismic belt, which is considered to be one of the most seismic zones of the world [120,121] and the source of major and destructive earthquakes that occurred in this country throughout history. Some of the most catastrophic earthquakes recorded in the seismic history of Iran include 1960 Lar ($M_s = 6.5$), 1962 Buin-Zahra ($M_s = 7.2$), 1978 Tabas ($M_w = 7.35$), 1990 Manjil ($M_w = 7.37$), and 2003 Bam ($M_w = 6.6$) [122]. One of the first elaborate attempts at research on the tectonics and seismicity of Iran was conducted by Ambraseys and Melville (1982) [123]. Berberian (1994) [124] published the first earthquake catalogue of Iran. Updated earthquake catalogues and seismic zoning maps of Iran are regularly published by the seismic zoning sub-committee of the Iranian Seismic Code's permanent committee and are provided by the Iranian Strong Motion Network (ISMN) as the major source of seismology and earthquake engineering in Iran [125]. Figure 9 shows the epicenter of earthquakes that occurred in Iran in 2017 recorded by ISMN (ISMN, 2017) [126], while Figure 10 represents records of large earthquakes that occurred in Iran and adjacent countries from 1900 up to recent years [127]. This figure shows 17 earthquakes with $M_w > 7$, 103 earthquakes with $6 < M_w < 7$, and more than 1700 earthquakes with $M_w > 5$ that have occurred in the recorded seismic history of Iran [125]. It is also demonstrated from Figure 10 that the Zagros zone in the western and southwestern part of Iran is the most seismically active zone which also confirms the major seismic zone categorization proposed by Shoja-Taheri and Niazi (1981) [128]. Based on Figures 11 and 12, as well as the earthquake zonation map of Iran, most of the provinces with large populations are located within high or very high seismic zone areas. As mentioned in the study by Izadkhah and Amini [129], more than 70 percent of cities in Iran are in the vicinity or within the route of active faults, which poses a great risk of seismic hazards to such cities.

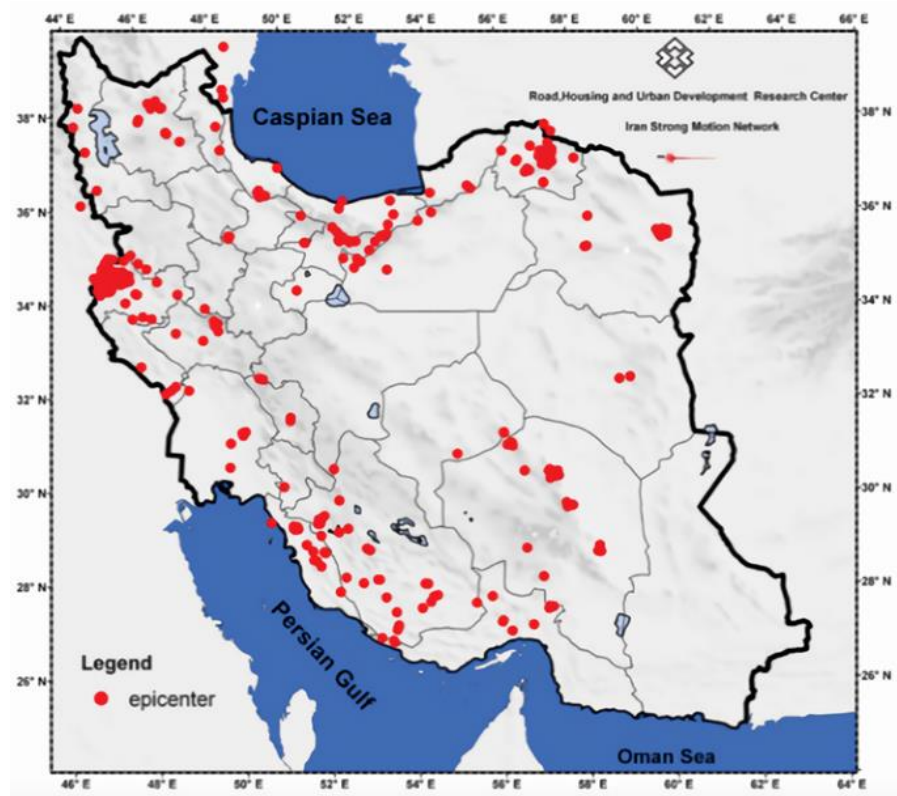


Figure 9. Epicentre of earthquakes occurred in Iran in 2017, recorded by ISMN [126].

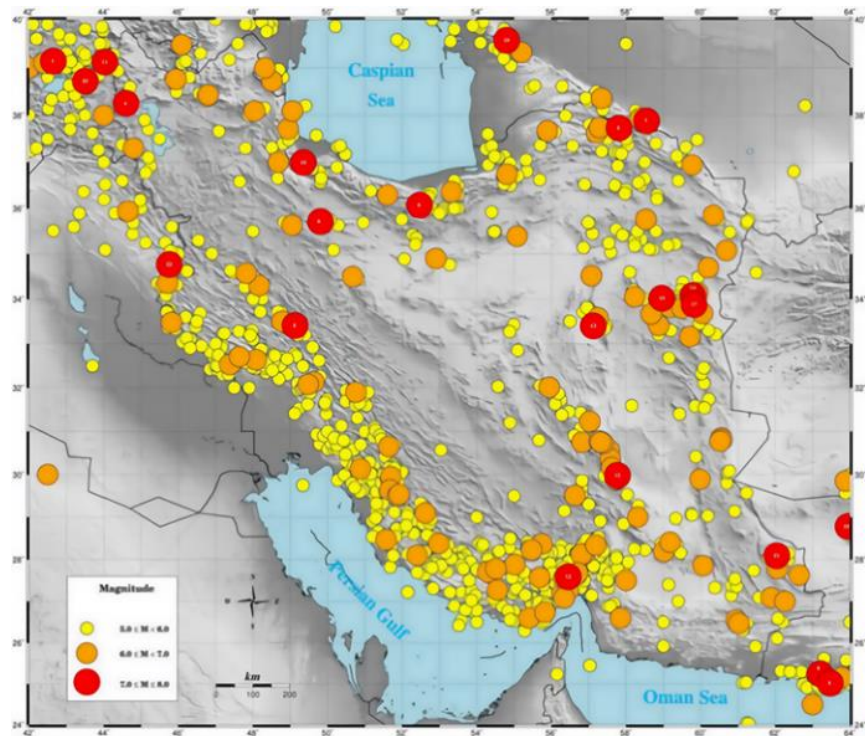


Figure 10. Large earthquakes in Iran and adjacent countries (1900–2019) [126].

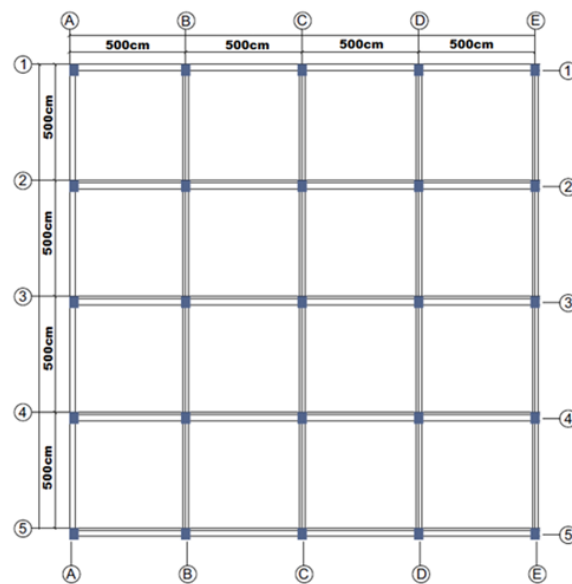


Figure 11. The blueprint of the sample RC building.

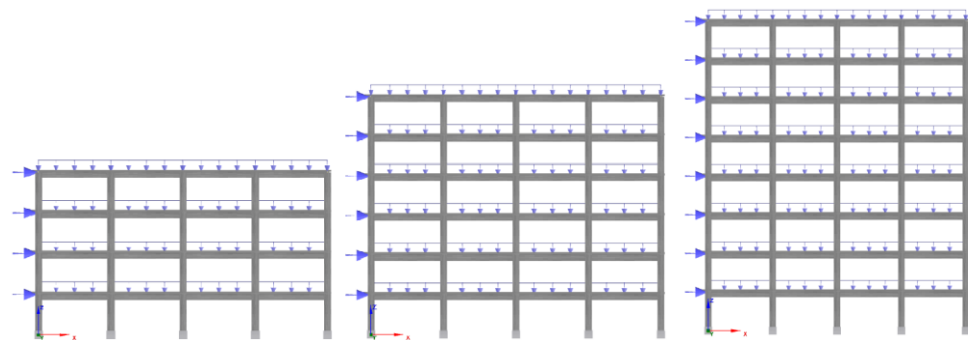


Figure 12. 2D models of the sample RC building for different numbers of stories.

Epicentre locations, loss of life and properties, and magnitudes for some of the most destructive earthquakes that occurred in the seismic history of Iran have been presented in Table 12. Major sources of these data include USGS, ISMN, IIEES, and IRIS.

Table 12. Data of the selected earthquakes in Iran [130–135].

No	Date	Lat.	Lon.	Magnitude			Loss of Life	Damaged Buildings	Loss of Life/ Damaged Buildings	Location
				Mb	Ms	Mw				
1	2003/12/26	29.04	58.33	-	-	6.6	35,000	85%	-	Bam, Iran
2	1990/06/20	36.96	49.41	6.4	7.7	-	40,000–50,000	Nearly all buildings	-	Manjil-Rudbar, Iran
3	1978/09/16	33.37	57.44	6.4	7.4	-	11,000–13,000	>15,000	-	Tabas, Iran
4	1968/08/31	34.02	58.96	-	-	7.2	15,000	>12,000	-	Dasht-e Bayaz, South Khorasan, Iran

Table 13 shows magnitudes, PGA values, and Design Base Accelerations ($A(g)$) for the calculation of base shear for building structures recommended by the Iranian Code of Practice for Earthquake Resistant Design of Buildings, Standard 2800 [136] for some of the most destructive earthquakes and corresponding seismic zones of Iran.

Table 13. Measured magnitude, PGA values, seismic risk zones, and recommended design base acceleration of selected earthquakes for Iran [126,130–135].

No	Earthquake Location	Station Name	Year	Earthquake Magnitude	Magnitude Type	PGA(g)	Seismic Risk Zone	A(g)
							(As Per IS-2800)	(Design Base Acceleration) (As Per IS-2800)
1	Manjil, Iran	Qazvin	1990	7.37	Mw	0.130	Very High	0.35
2	Manjil, Iran	Rudsar	1990	7.37	Mw	0.086	Very High	0.35
3	Manjil, Iran	Rudsar	1990	7.37	Mw	0.538	Very High	0.35
4	Tabas, Iran	Tabas	1978	7.35	Mw	0.641	Very High	0.35
5	Bam, Iran	Bam	2003	6.60	Mw	0.970	High	0.30

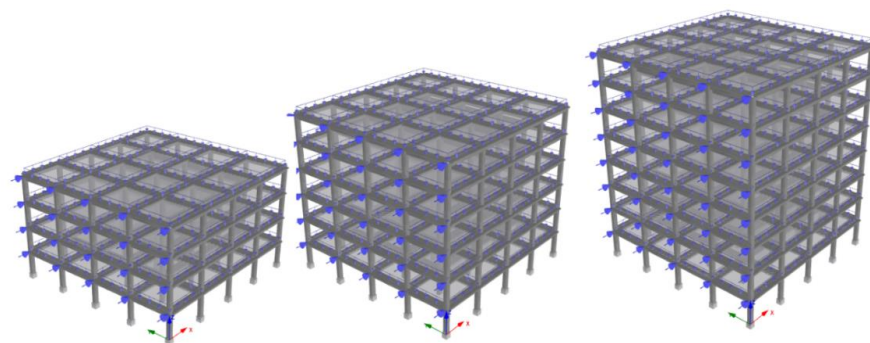
The measured PGA values for the first two recorded earthquakes in the considered stations for Iran are considerably lower than the recommended PGA values, and it can be said that the seismic risk for these locations represents a sufficient level. However, the measured PGA values for the last three earthquakes exceeded the recommended PGA values considerably. This clearly reveals Iran's high potential for seismic risk, taking into account the high population of the selected cities.

3. RC Building Models for Numerical Analysis

Earthquake-resistant rules aim to construct buildings that do not experience damage under an expected ground motion level. Structural analyses for a total of five earthquake locations from each country, whose PGA values can be reached. The Seismostruct software was used for numerical analysis [137]. Pushover analyses were used in these analyses for the sample RC building models with four-storey, six-storey, and eight-storey using obtained data. The story plan was taken in the same way in all analyzed buildings and is shown in Figure 11.

The infrmFBPH (force-based plastic hinge frame elements) were used for structural elements such as beams and columns while creating all building models. These elements model force-based extensional flexibility and limit plasticity to only a finite length. The ideal number of fibers in the section should be sufficient to model the stress-strain distribution in the section [138]. A total of 100 fiber elements are defined for the selected sections. This value is sufficient for such partitions. Plastic-hinge length (L_p/L) was selected as 16.67%. The boundary conditions of the column were set in accordance with the cantilever boundary conditions, which resulted in a fully fixed column footing and a free top end. The boundary condition of the footings was fixed on the ground.

The storey height in all building models is considered as 3 m. The sample RC building was chosen symmetrically in the X and Y directions, and each of this span is 5 m in each direction was considered. The applied loads and 2D and 3D building models are shown for four-storey, six-storey, and eight-storey in Figures 12 and 13, respectively.

**Figure 13.** 3D models of the RC building for different numbers of stories.

The structural properties of the RC building model are shown in Table 14.

Table 14. Analysis of input data for the structural models.

Parameter	Value	
Concrete Grade	C20	
Reinforcement Grade	S420	
Beams	250 × 600 mm	
Floor height	120 mm	
Cover thickness	25 mm	
Columns	400 × 500 mm	
Longitudinal reinforcement	Corners	4Φ20
	Top bottom side	4Φ16
	Left right side	4Φ16
Transverse reinforcement	Φ10/100	
Material model (steel)	Menegotto-Pinto [139]	
Material model (Concrete)	Mander et al. nonlinear [140]	
Constraint type	Rigid diaphragm	
Local soil class	ZD	
Incremental loads	5.0 kN	
Permanent loads	5.0 kN/m	
Target-displacement (4-storey)	0.24 m	
Target-displacement (6-storey)	0.36 m	
Target-displacement (8-storey)	0.48 m	
Importance class	IV	
Damping ratio	5%	

In performance-based earthquake engineering, it is critical to estimate target displacements for damage estimation when certain performance limits of structural members are reached. The limit states envisaged in Eurocode 8 (Part 3) [141,142] were taken into account for damage estimation in this study. The target displacements are presented in Figure 14 and the description of these states are shown in Table 15.

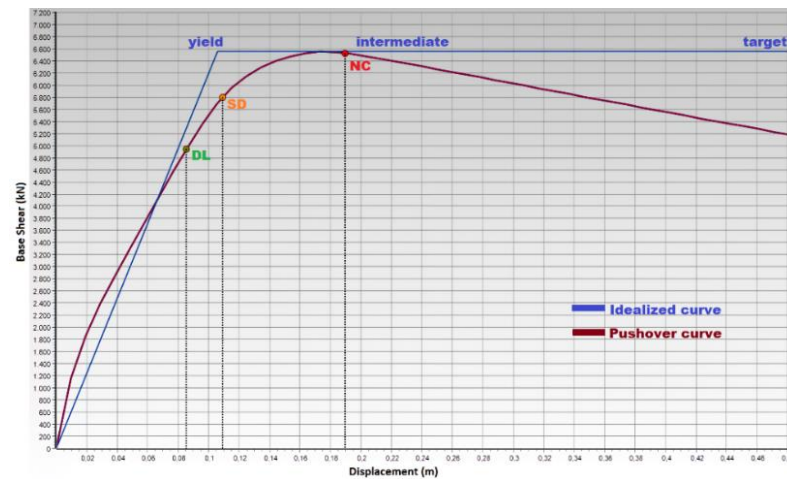


Figure 14. Target displacements on idealized curves/typical pushover.

Table 15. Suggested limit states in Eurocode 8 (Part 3) [141,142].

Limit State	Description	Return Period (Year)	Probability of Exceedance (in 50 Years)
Damage Limitation (DL)	Only lightly damaged, damage to non-structural components is economically repairable	225	0.20
Significant Damage (SD)	Uneconomic to repair, significantly damaged, some residual strength and stiffness, non-structural components damaged,	475	0.10
Near collapse (NC)	Very low residual strength and stiffness, large permanent drift but still standing, heavily damaged	2475	0.02

4. Structural Analyses Results

Within the scope of this study, firstly, the natural fundamental periods for the sample building models were obtained from the eigenvalue analysis. The target displacements and base shear forces for all the structural models were obtained for each country, respectively.

4.1. Comparison of Natural Fundamental Periods

In this part, the period values obtained according to the eigenvalue analyses were compared with the empirical ones predicted for each country. The time required for the undamped system to complete one vibration cycle is called the natural vibration period of the system. The more rigid one of the same mass with a single degree of freedom system will have a shorter natural period and a higher natural frequency. Similarly, of two structures of the same stiffness, the heavier (greater mass) has a lower natural frequency and a longer natural period. This value can be obtained both with approximate formulas and as a result of numerical analysis [143–146]. The empirical relations and explanations stipulated in the corresponding design code for each country are given in Table 16. The comparison of these periods with the ones obtained from structural analyses is shown in Table 16. The empirical formulas used in Table 16 are directly taken from the seismic design codes currently used by countries.

Table 16. Comparison of the natural fundamental periods for selected countries.

Country	Number of Storey	Empirical Formula	Empirical Period (s)	Structural Analyses Period (s)	Description
Albania	4	$T_1 = (0.09 \cdot h)/b^{1/2}$	0.242	0.402	h—the height of the structure (in meters). b—dimension of the building in parallel to the applied forces (in meters).
	6		0.362	0.597	
	8		0.483	0.796	
Bosnia and Herzegovina	4	$T = C_t \cdot H^{3/4}$	0.484	0.402	C_t is 0.075 for RC frame structures and H is the total height of the building
	6		0.655	0.597	
	8		0.813	0.796	
Croatia	4	$T = C_t \cdot H^{3/4}$	0.484	0.402	C_t is 0.075 for RC frame structures and H is the total building height
	6		0.655	0.597	
	8		0.813	0.796	
Iran	4	$T = 0.05H^{0.9}$	0.468	0.402	H is the total building height
	6		0.674	0.597	
	8		0.873	0.796	
Serbia	4	$T = C_t \cdot H^{3/4}$	0.484	0.402	C_t is 0.075 for RC frame structures and H is the total building height
	6		0.655	0.597	
	8		0.813	0.796	
Türkiye	4	$T_{PA} = C_t \cdot H_N^{3/4}$	0.645	0.402	H_N is the building's total height; C_t is the correction coefficient. $C_t = 0.1$ for RC building frames that built only beams and columns
	6		0.874	0.597	
	8		1.084	0.796	

The fundamental periods obtained from the structural analyses for all countries were constant since the structural characteristics of the sample RC buildings models did not change. Empirically, the smallest period values were obtained for Albania, while the highest periods were obtained for Türkiye. The empirical periods suggested for Albania were lower than the periods obtained from the structural analysis. For the other five countries,

the empirically suggested period values were higher than the period values obtained from the structural analyses.

4.2. Comparisons of Limit States

In this study, the target displacement values for the different number of storeys were obtained from the structural analyses for each country, considering the limit states in Eurocode 8 for six different countries. The comparison of target displacements of sample RC models for Albania is given in Table 17.

Table 17. The obtained target displacements of sample RC models for Albania.

No	Date	Location	Number of Storeys	Code Suggested			Measured		
				DL (m)	SD (m)	NC (m)	DL (m)	SD (m)	NC (m)
1	26 November 2019	Tirana	4	0.115	0.157	0.295	0.035	0.045	0.088
			6	0.203	0.262	0.459	0.071	0.092	0.164
			8	0.272	0.348	0.604	0.099	0.128	0.221
2	26 November 2019	Durrës	4	0.115	0.157	0.295	0.039	0.049	0.099
			6	0.203	0.262	0.459	0.078	0.101	0.179
			8	0.272	0.348	0.604	0.109	0.139	0.242
3	21 September 2019	Tirana	4	0.135	0.182	0.338	0.058	0.082	0.164
			6	0.231	0.298	0.521	0.119	0.155	0.272
			8	0.308	0.395	0.685	0.163	0.209	0.362
4	9 January 1998	Tirana	4	0.115	0.157	0.295	0.164	0.219	0.403
			6	0.203	0.262	0.459	0.273	0.351	0.614
			8	0.272	0.348	0.604	0.362	0.465	0.805
5	15 April 1979	Shkoder	4	0.115	0.157	0.295	0.193	0.257	0.468
			6	0.203	0.262	0.459	0.314	0.405	0.707
			8	0.272	0.348	0.604	0.416	0.534	0.926

The target displacements suggested by the seismic design code for the first three earthquakes in Albania provide target displacements in which the acceleration values measured in earthquakes are taken into account. However, the target displacements predicted for the structure for the last two earthquakes and the target displacements obtained under the effect of the earthquake were exceeded. This suggests that the target displacements are adequately represented for some earthquakes, while it is not sufficient for others.

The comparison of target displacements of sample RC models for Bosnia and Herzegovina is given in Table 18.

Table 18. The obtained target displacements of sample RC models for Bosnia and Herzegovina.

No	Date	Location	Number of Storeys	Suggested			Measured		
				DL (m)	SD (m)	NC (m)	DL (m)	SD (m)	NC (m)
1	1969	Bosnia and Herzegovina	4	0.055	0.076	0.154	0.111	0.151	0.284
			6	0.112	0.146	0.257	0.196	0.253	0.443
			8	0.154	0.197	0.342	0.263	0.337	0.584
2	1962	Bosnia and Herzegovina	4	0.055	0.076	0.154	0.145	0.194	0.360
			6	0.112	0.146	0.257	0.245	0.316	0.552
			8	0.154	0.197	0.342	0.326	0.418	0.725
3	1981	Bosnia and Herzegovina	4	0.055	0.076	0.154	0.179	0.237	0.436
			6	0.112	0.146	0.257	0.293	0.378	0.661
			8	0.154	0.197	0.342	0.389	0.499	0.866
4	1969	Bosnia and Herzegovina	4	0.058	0.082	0.164	0.003	0.004	0.007
			6	0.119	0.155	0.272	0.006	0.008	0.014
			8	0.163	0.209	0.362	0.009	0.012	0.020
5	2019	Bosnia and Herzegovina	4	0.096	0.132	0.251	0.013	0.016	0.029
			6	0.175	0.226	0.397	0.026	0.033	0.058
			8	0.235	0.302	0.524	0.036	0.046	0.081

The target displacements suggested by the seismic design code for the first three earthquakes in Bosnia and Herzegovina do not provide target displacements in which the acceleration values measured in earthquakes are taken into account. However, the target displacements predicted for the structure for the last two earthquakes and the target displacements obtained under the effect of the earthquake were not exceeded. This suggests that the target displacements are adequately represented for some earthquakes, while it is not sufficient for others.

The comparison of target displacements of sample RC models for Croatia is given in Table 19.

Table 19. The comparison of target displacements of sample RC models for Croatia.

No	Date	Location	Number of Storeys	Suggested			Measured		
				DL (m)	SD (m)	NC (m)	DL (m)	SD (m)	NC (m)
1	2020	Petrinja	4	0.105	0.144	0.272	0.013	0.016	0.029
			6	0.188	0.243	0.426	0.026	0.033	0.058
			8	0.253	0.324	0.562	0.036	0.046	0.081
2	1990	Kraljev Vrh	4	0.095	0.131	0.250	0.019	0.025	0.043
			6	0.174	0.225	0.395	0.039	0.050	0.087
			8	0.234	0.301	0.522	0.054	0.070	0.121
3	1979	Montenegro	4	0.112	0.160	0.300	0.026	0.033	0.057
			6	0.206	0.266	0.467	0.052	0.067	0.118
			8	0.276	0.352	0.614	0.072	0.093	0.161
4	1979	Montenegro	4	0.104	0.142	0.269	0.013	0.016	0.029
			6	0.186	0.241	0.422	0.026	0.033	0.058
			8	0.250	0.321	0.556	0.036	0.046	0.081
5	1978	Imotsk	4	0.104	0.142	0.269	0.010	0.012	0.021
			6	0.186	0.241	0.422	0.019	0.025	0.043
			8	0.250	0.321	0.556	0.027	0.035	0.060

The target displacements suggested by the seismic design code for all earthquakes in Croatia provide target displacements in which the acceleration values measured in earthquakes are taken into account. It shows that the seismic hazard is adequately taken into account in the structural analysis for all the selected earthquakes.

The comparison of target displacements of sample RC models for Serbia is given in Table 20.

The target displacements suggested by the seismic design code for all earthquakes in Serbia provide target displacements in which the acceleration values measured in earthquakes are taken into account. It shows that the seismic hazard is adequately taken into account in the structural analysis for all selected earthquakes.

The comparison of target displacements of sample RC models for Türkiye is given in Table 21. As seen in Table 21, the target displacements suggested by the seismic design code for the first, second, and fifth earthquakes for Türkiye provide target displacements in which the acceleration values measured in earthquakes are taken into account. However, the target displacements predicted for the other earthquakes for these structures were exceeded. This suggests that the target displacements are adequately represented for some earthquakes, while it is not sufficient for others.

Table 20. The obtained target displacements of sample RC models for Serbia.

No	Date	Location	Number of Storeys	Suggested			Measured		
				DL (m)	SD (m)	NC (m)	DL (m)	SD (m)	NC (m)
1	2010	Gruža	4	0.067	0.094	0.186	0.019	0.025	0.043
			6	0.133	0.173	0.304	0.039	0.050	0.087
			8	0.181	0.232	0.403	0.054	0.070	0.121
2	2010	Novi Pazar	4	0.067	0.094	0.186	0.003	0.004	0.007
			6	0.133	0.173	0.304	0.006	0.008	0.014
			8	0.181	0.232	0.403	0.009	0.012	0.020
3	2010	Kokin Brod	4	0.048	0.063	0.132	0.003	0.004	0.007
			6	0.098	0.128	0.226	0.006	0.008	0.014
			8	0.136	0.174	0.302	0.009	0.012	0.020
4	2010	Žagubica	4	0.048	0.063	0.132	0.003	0.004	0.007
			6	0.098	0.128	0.226	0.006	0.008	0.014
			8	0.136	0.174	0.302	0.009	0.012	0.020
5	1990	Novi Pazar	4	0.067	0.094	0.186	0.003	0.004	0.007
			6	0.133	0.173	0.304	0.006	0.008	0.014
			8	0.181	0.232	0.403	0.009	0.012	0.020

Table 21. The obtained target displacements of sample RC models for Türkiye.

No	Date	Location	Number of Storeys	TBEC-2018, Suggested			Measured		
				DL (m)	SD (m)	NC (m)	DL (m)	SD (m)	NC (m)
1	23 October 2011	Van	4	0.164	0.219	0.402	0.058	0.083	0.167
			6	0.272	0.351	0.612	0.121	0.156	0.276
			8	0.361	0.463	0.803	0.165	0.211	0.366
2	1 May 2003	Bingöl	4	0.278	0.365	0.656	0.218	0.289	0.524
			6	0.435	0.560	0.975	0.350	0.451	0.786
			8	0.573	0.735	1.275	0.463	0.594	1.029
3	12 November 1999	Düzce	4	0.256	0.337	0.607	0.371	0.484	0.862
			6	0.404	0.520	0.906	0.568	0.730	1.270
			8	0.532	0.683	1.184	0.745	0.956	1.657
4	13 March 1992	Erzincan	4	0.180	0.239	0.439	0.206	0.273	0.495
			6	0.295	0.380	0.664	0.332	0.428	0.746
			8	0.391	0.502	0.870	0.439	0.563	0.977
5	17 Augst 1999	Kocaeli	4	0.306	0.401	0.718	0.164	0.219	0.402
			6	0.475	0.611	1.064	0.272	0.351	0.612
			8	0.625	0.801	1.389	0.361	0.463	0.803

The comparison of target displacements of sample RC models for Iran is shown in Table 22.

The target displacements suggested by the seismic design code for the first two earthquakes for Iran provide target displacements in which the acceleration values measured in earthquakes are taken into account. However, the target displacements predicted for the structure for the last three earthquakes and the target displacements obtained under the effect of the earthquake were exceeded. This suggests that the target displacements are adequately represented for some earthquakes, while it is not sufficient for others.

In addition to the structural analysis according to the number of stories, the local soil class change was taken into account. The structural analyzes were carried out only for the four-storey RC building model since it is aimed to reveal the soil class effects. In the previous structural analyses, the ZD soil class envisaged in Eurocode-8 was taken into account. In this section, structural analyzes were made separately for each earthquake by choosing the ZA class in the same code. The recommended properties in the code for these

two soil types are given in Table 23. The target displacements for selected earthquakes for each country for the ZA soil class type were given in Table 24.

Table 22. The obtained target displacements of sample RC models for Iran.

No	Date	Location	Number of Storeys	IS-2800 (Suggested)			Measured		
				DL (m)	SD (m)	NC (m)	DL (m)	SD (m)	NC (m)
1	1990	Qazvin	4	0.140	0.188	0.349	0.031	0.039	0.072
			6	0.238	0.307	0.536	0.062	0.079	0.141
			8	0.317	0.407	0.705	0.086	0.110	0.191
2	1990	Rudsar	4	0.140	0.188	0.349	0.028	0.035	0.062
			6	0.238	0.307	0.536	0.056	0.072	0.127
			8	0.317	0.407	0.705	0.078	0.100	0.173
3	1990	Rudsar	4	0.140	0.188	0.349	0.231	0.306	0.553
			6	0.238	0.307	0.536	0.369	0.475	0.828
			8	0.317	0.407	0.705	0.487	0.625	1.083
4	1978	Tabas	4	0.140	0.188	0.349	0.282	0.370	0.665
			6	0.238	0.307	0.536	0.441	0.567	0.988
			8	0.317	0.407	0.705	0.580	0.745	1.291
5	2003	Bam	4	0.115	0.157	0.294	0.442	0.576	1.022
			6	0.203	0.262	0.459	0.670	0.861	1.498
			8	0.272	0.348	0.604	0.878	1.127	1.953

Table 23. The characteristics of local soil types considered in this study [147].

Ground-Type	Description of Stratigraphic Profile	Parameters		
		$V_{s,30}$ (m/s)	N_{SPT} (Blows/30 cm)	C_u (kPa)
A	Rock or other rock-like geological formation, including at most 5 m of weaker material at the surface	>800	—	—
D	Deposits of loose-to-medium cohesionless soil (with or without some soft cohesive layers), or of predominantly soft-to-firm cohesive soil.	<180	<15	<70

Table 24. Comparison of target displacements for the ZA soil class type.

Earthquake No	Country	Location	Number of Storeys	Suggested			Measured		
				DL (m)	SD (m)	NC (m)	DL (m)	SD (m)	NC (m)
1	Albania	Tirana	4	0.054	0.070	0.121	0.020	0.025	0.044
2		Durres	4	0.054	0.070	0.121	0.022	0.028	0.048
3		Tirana	4	0.061	0.079	0.137	0.033	0.042	0.072
4		Tirana	4	0.054	0.070	0.121	0.072	0.093	0.161
5		Shkoder	4	0.054	0.070	0.121	0.083	0.107	0.185
1	Bosnia and Herzegovina	Banja Luka,	4	0.030	0.040	0.068	0.052	0.067	0.117
2		Banja Luka	4	0.030	0.040	0.068	0.065	0.083	0.145
3		Banja Luka,	4	0.030	0.040	0.068	0.078	0.100	0.173
4		Montenegro	4	0.033	0.042	0.072	0.002	0.002	0.004
5		Montenegro	4	0.047	0.060	0.104	0.007	0.009	0.016
1	Croatia	Petrinja	4	0.050	0.065	0.112	0.007	0.009	0.016
2		Kraljev Vrh	4	0.047	0.060	0.104	0.011	0.014	0.024
3		Montenegro	4	0.055	0.071	0.123	0.014	0.019	0.032
4		Montenegro	4	0.050	0.064	0.111	0.007	0.009	0.016
5		Imotsk	4	0.050	0.064	0.111	0.005	0.007	0.012
1	Serbia	Gruža	4	0.036	0.046	0.080	0.011	0.014	0.024
2		Novi Pazar	4	0.036	0.046	0.080	0.002	0.002	0.004
3		Kokin Brod	4	0.027	0.035	0.060	0.002	0.002	0.004
4		Žagubica	4	0.027	0.035	0.060	0.002	0.002	0.004
5		Novi Pazar	4	0.036	0.046	0.080	0.002	0.002	0.004
1	Türkiye	Van	4	0.072	0.092	0.160	0.033	0.042	0.073
2		Bingöl	4	0.114	0.147	0.254	0.092	0.118	0.205
3		Düzce	4	0.106	0.136	0.236	0.149	0.191	0.331
4		Erzincan	4	0.078	0.100	0.174	0.087	0.112	0.195
5		Kocaeli	4	0.125	0.160	0.277	0.072	0.092	0.160
1	Iran	Qazvin	4	0.063	0.081	0.141	0.023	0.030	0.052
2		Rudsar	4	0.063	0.081	0.141	0.016	0.020	0.035
3		Rudsar	4	0.063	0.081	0.141	0.097	0.125	0.216
4		Tabas	4	0.063	0.081	0.141	0.116	0.149	0.258
5		Bam	4	0.054	0.070	0.121	0.175	0.225	0.390

Another parameter chosen in order to put the effect of different structural conditions in common was the importance class of the structure. While the IV class was selected in the previous analysis, it was considered as the II class in the new analysis. The only difference in the initial analysis is the building importance class, all other features remained the same. Selected building importance class characteristics are given in Table 25. The target displacements for selected earthquakes for each country for the II class were given in Table 26.

Table 25. Selected importance classes for buildings [147].

Importance Class	Buildings
II	Ordinary buildings, not belonging to the other categories.
IV	Buildings whose integrity during earthquakes is of vital importance for civil protection, e.g., hospitals, fire stations, power plants, etc

Table 26. Comparison of target displacements for building important class II.

Earthquake No	Country	Location	Number of Storeys	Suggested			Measured		
				DL (m)	SD (m)	NC (m)	DL (m)	SD (m)	NC (m)
1	Albania	Tirana	4	0.074	0.103	0.202	0.025	0.032	0.056
2		Durres	4	0.074	0.103	0.202	0.027	0.035	0.062
3		Tirana	4	0.088	0.121	0.233	0.041	0.053	0.109
4		Tirana	4	0.074	0.103	0.202	0.109	0.147	0.279
5		Shkoder	4	0.074	0.103	0.202	0.129	0.175	0.326
1	Bosnia and Herzegovina	Banja Luka,	4	0.039	0.05	0.101	0.07	0.099	0.194
2		Banja Luka	4	0.039	0.05	0.101	0.094	0.130	0.248
3		Banja Luka,	4	0.039	0.05	0.101	0.119	0.161	0.302
4		Montenegro	4	0.041	0.053	0.109	0.002	0.003	0.005
5		Montenegro	4	0.06	0.085	0.171	0.009	0.011	0.02
1	Croatia	Petrinja	4	0.066	0.094	0.185	0.009	0.011	0.02
2		Kraljev Vrh	4	0.059	0.085	0.170	0.014	0.018	0.031
3		Montenegro	4	0.075	0.105	0.205	0.018	0.024	0.041
4		Montenegro	4	0.065	0.093	0.183	0.009	0.011	0.02
5		Imotsk	4	0.065	0.093	0.183	0.007	0.009	0.015
1	Serbia	Gruža	4	0.046	0.059	0.124	0.014	0.018	0.031
2		Novi Pazar	4	0.046	0.059	0.124	0.002	0.003	0.005
3		Kokin Brod	4	0.034	0.044	0.085	0.002	0.003	0.005
4		Žagubica	4	0.034	0.044	0.085	0.002	0.003	0.005
5		Novi Pazar	4	0.046	0.059	0.124	0.002	0.003	0.005
1	Türkiye	Van	4	0.108	0.147	0.278	0.042	0.054	0.11
2		Bingöl	4	0.190	0.252	0.46	0.147	0.198	0.365
3		Düzce	4	0.174	0.232	0.425	0.256	0.337	0.607
4		Erzincan	4	0.12	0.162	0.304	0.138	0.186	0.345
5		Kocaeli	4	0.21	0.278	0.504	0.108	0.147	0.278
1	Iran	Qazvin	4	0.091	0.126	0.240	0.030	0.038	0.700
2		Rudsar	4	0.091	0.126	0.240	0.020	0.025	0.044
3		Rudsar	4	0.091	0.126	0.24	0.157	0.21	0.386
4		Tabas	4	0.091	0.126	0.240	0.192	0.256	0.466
5		Bam	4	0.074	0.103	0.202	0.307	0.403	0.721

In addition to all these different structural conditions, the concrete class is also considered as a variable. While previous analyzes were performed for the C20 concrete class, new structural analyzes considered the C12 concrete class with lower properties for all load-bearing elements. The target displacements for selected earthquakes for each country for the C12 concrete class were given in Table 27.

Table 27. Comparison of target displacements for the C12 concrete class.

Earthquake No	Country	Location	Number of Storeys	Suggested			Measured		
				DL (m)	SD (m)	NC (m)	DL (m)	SD (m)	NC (m)
1	Albania	Tirana	4	0.124	0.167	0.311	0.038	0.049	0.096
2		Durres	4	0.124	0.167	0.311	0.042	0.054	0.107
3		Tirana	4	0.144	0.193	0.356	0.063	0.089	0.175
4		Tirana	4	0.124	0.167	0.311	0.175	0.232	0.424
5		Shkoder	4	0.124	0.167	0.311	0.205	0.272	0.492
1	Bosnia and Herzegovina	Banja Luka,	4	0.059	0.082	0.164	0.119	0.161	0.3
2		Banja Luka	4	0.059	0.082	0.164	0.154	0.206	0.379
3		Banja Luka,	4	0.059	0.082	0.164	0.19	0.252	0.458
4		Montenegro	4	0.063	0.088	0.175	0.004	0.005	0.008
5		Montenegro	4	0.104	0.141	0.266	0.014	0.018	0.031
1	Croatia	Petrinja	4	0.113	0.153	0.287	0.014	0.018	0.031
2		Kraljev Vrh	4	0.103	0.14	0.264	0.021	0.027	0.047
3		Montenegro	4	0.126	0.17	0.316	0.028	0.036	0.062
4		Montenegro	4	0.112	0.151	0.284	0.014	0.018	0.031
5		Imotsk	4	0.112	0.151	0.284	0.01	0.013	0.023
1	Serbia	Gruža	4	0.073	0.102	0.198	0.021	0.027	0.047
2		Novi Pazar	4	0.073	0.102	0.198	0.004	0.005	0.008
3		Kokin Brod	4	0.052	0.069	0.141	0.004	0.005	0.008
4		Žagubica	4	0.052	0.069	0.141	0.004	0.005	0.008
5		Novi Pazar	4	0.073	0.102	0.198	0.004	0.005	0.008
1	Turkey	Van	4	0.174	0.232	0.423	0.064	0.09	0.177
2		Bingöl	4	0.293	0.385	0.688	0.231	0.305	0.55
3		Düzce	4	0.271	0.355	0.637	0.39	0.509	0.903
4		Erzincan	4	0.191	0.253	0.46	0.218	0.288	0.52
5		Kocaeli	4	0.322	0.422	0.752	0.174	0.232	0.423
1	Iran	Qazvin	4	0.149	0.2	0.367	0.045	0.058	0.118
2		Rudsar	4	0.149	0.2	0.367	0.03	0.039	0.069
3		Rudsar	4	0.149	0.2	0.367	0.245	0.323	0.58
4		Tabas	4	0.149	0.2	0.367	0.297	0.389	0.697
5		Bam	4	0.124	0.167	0.311	0.465	0.605	1.069

4.3. Evaluation of Existing Building Stocks

4.3.1. Albania

According to the Albanian Institute of Statistics (INSTAT) 2001, the Albanian building stock primarily consists of four typologies, namely brick and stone, prefabricated, wood, and other building materials. However, when referring to the recent census of 2011 (INSTAT), information on building materials is not included and houses are classified based on their heights and construction period. Table 28 presents a summary of the Albanian building stock based on existing information (INSTAT 2001) [148]. Accordingly, the ‘RC and masonry’ type represents the biggest part of the current building stock.

Table 28. Albanian building stock [147].

Material Type	<1945	1945–1960	1961–1980	1981–1990	1991–1995
RC and masonry structures	37416	63870	141170	102198	43324
Prefabricated concrete	-	-	4601	5993	4575
Wooden	462	-	1821	1273	743
Other types	2560	3393	7105	6263	4238

According to the Albanian Institute of Statistics (INSTAT) 2011, one-storey buildings account for 85% of the total building stock corresponding to the accommodation of the half population of the country. They were mostly built with unreinforced masonry and

reinforced concrete frames with infill walls. However, the total number of multi-storey houses in Albania is significantly lower compared to one-storey houses, but they shelter the remaining half of the population. During the recent earthquake sequences in 2019, multi-storey buildings were significantly affected, resulting in higher damage in the stricken areas. While the available data given in Table 24 is outdated, they highlight an important indicator (design code) on the construction year of the housings. An important portion of the current building stock was built before 1990 showing a lack of adequacy to the modern code requirements [17]. Therefore, it is likely that there were deficiencies affecting the seismic performance of buildings constructed in this time period.

4.3.2. Bosnia and Herzegovina

According to the available data for Bosnia and Herzegovina (CBS 2013) [149], it is noted that, from the total of 1,078,156 buildings, 60.72% are structures made of brick, stone, and concrete, 35.08% of reinforced concrete and steel frames and only 4.20% of wood and light material [73]. The majority of the structures are either confined masonry buildings or RC buildings constructed according to the regulations from 1981 (35%), considering age distribution from 1981–1990. Since 1991 Prestandards (ENV) have been applied and this accounts for 18.9% of all buildings being either RC buildings or confined masonry buildings. The application of Eurocode 8 started after 2006 accounting for 2.0% of all buildings (as well as RC buildings or confined masonry buildings). Masonry structures with rigid floors were mainly constructed in the period from 1971 to 1980, amounting to 33.6% of all structures built in Bosnia and Herzegovina. Brick masonry structures with rigid RC slabs were built in the period from 1946 to 1970, amounting to 6.6% of all the structures built in Bosnia and Herzegovina. The remaining 4% is devoted to stone masonry buildings with wooden floors constructed before 1945. Seismic vulnerability assessment of structures in Bosnia and Herzegovina is mainly done by individual researchers [150–153]. At the moment, Bosnia and Herzegovina does not have a well-organized and efficient database of structures and building's typologies. Several studies were conducted to determine the vulnerability of buildings in several cities of Bosnia and Herzegovina, like Banja Luka and Sarajevo [74]), Visoko [154], and Tuzla [155]. For the first time, the specific site and its influence on the vulnerability were taken into consideration in the Tuzla region [155]. Currently, 700 structures in the city of Sarajevo are being examined and a database is being created [156]. Based on all this preliminary analysis, it is clear that most of the existing building stock in Bosnia and Herzegovina does not possess sufficient resistance to ground motions that may be expected in this region. It is necessary to construct a detailed database taking into account all the data required to conduct adequate seismic assessments and perform a seismic risk assessment. Without this database and conducted calculations, it is not possible to construct an effective disaster management plan.

4.3.3. Croatia

According to the 2011 Census, the total number of dwellings in Croatia by year of construction was 1,496,558. Of that, 13.2% were built before 1945, which means that they did not follow any building codes. Building design and construction in Croatia did not follow earthquake-resistant building rules until 1948 [157].

Masonry houses used timber floor constructions until 1920. Most of these structures were constructed between 1860 and 1920 and are now part of Croatia's historic town centers, most of which are categorized as historical heritage. These structures were not intended to withstand significant horizontal ground motions (e.g., earthquakes). After 1930, the first semi-prefabricated RC floors were installed, followed by monolithic RC floors in 1964. After the Skopje earthquake in 1963, the first seismic building codes were developed and later modified. In addition, following the earthquake in Skopje in 1963, masonry structures throughout the former Yugoslavia were erected systematically using horizontal tie-beams and vertical tie-columns to achieve confined masonry. The load-bearing system in reinforced concrete structures (RC frames and RC shear walls) was built in accordance with

the seismic regulations enacted in 1964 (following the 1963 Skopje earthquake) and 1981 (following the 1979 Montenegro (coast) earthquake). Eurocodes were gradually adopted as voluntary structural design norms between 1992 and 1998. Due to the challenges associated with the harmonization of new standards with old national legislation at the time, they kept a pre-standards status (ENV label). The final version was introduced in 1998, with the European standard (EN label), but the ultimate implementation began in 2005 with the adoption of the technical standards for concrete buildings (NN 101/05). Eurocodes were ultimately made a requirement in official usage in 2011, however, pre-standards were still used until the end of 2012 [147].

Predominant structural systems for the buildings in one of the Croatian cities (Osijek) can be summarized as follows [147]: Unreinforced masonry buildings made of old bricks with flexible floors, unreinforced masonry structures with rigid floors, confined masonry structures, RC frame structures, RC shear walls, and RC dual structures. For RC structures, the level of earthquake resistance design should be taken into account.

On December 29, 2020, an earthquake of magnitude 6.4 MW hit Sisak-Moslavina county with an epicentre 3 km southwest of the Croatian city of Petrinja. In the preliminary report on the consequences of the earthquake, a detailed description of the damage to residential low-rise and multi-family residential buildings is presented [158]. The following are the primary sources of damage and failure in low-rise residential buildings: Excessive lateral displacements of flexible timber flooring caused out-of-plane damage or failure of exterior masonry walls at the upper/top levels of older URM structures (built before World War II). Recent masonry structures have rigid floors, but they also suffered damage owing to the lack of vertical reinforcement at the bottom floor level. Due to the extremely high seismic demand, the in-plane damage pattern took the form of diagonal tension cracks in the walls. The major tensile stresses in the walls created by the earthquake surpassed the masonry tensile strength, resulting in the formation of inclined cracks (diagonal tension cracks). In certain situations, the quality of masonry materials and construction appeared to be poor, which was also a source of damage. The primary sources of damage and failure in multi-family residential buildings can be summarized as follows: Excessive lateral displacements of flexible timber flooring caused out-of-plane damage or failure of exterior masonry walls at the upper/top levels of older URM structures (built before World War II). In general, the failure process in low-rise and mid-rise structures is relatively similar.

Many older URM buildings were not properly maintained, and as a result, their condition was poor before the earthquake [159]. The level of damage is thought to have been impacted by the degradation of building materials and components (such as wooden floors and roofing) as well as the use of weak mortar.

Due to extremely high seismic demand, masonry structures with rigid floors built in the 1960s developed in-plane shear cracking at the building's base. The major tensile stresses in the walls created by the earthquake surpassed the masonry tensile strength, resulting in the formation of inclined cracks (diagonal tension cracks). The earthquake caused no structural damage to RC structures; nevertheless, minor damage to non-structural components such as chimneys occurred in several buildings.

4.3.4. Serbia

According to the 2011 Serbian Census of population, household, and dwellings, 85% of all dwellings in Serbia were constructed after 1945, i.e., in the period when there were at least some seismic design codes. Before 2019, the seismic design codes created and implemented in the former Yugoslavia were used. The first seismic design code was published in 1948, but it lacked detailed detailing guidelines for RC and masonry construction. The disastrous earthquakes that struck Skopje in 1963 and Montenegro in 1979 served as turning points in the creation of Yugoslavian seismic design codes. Following the 1963 Skopje Earthquake, the first complete seismic design code was published in 1964. Two years after the 1979 Montenegro earthquake, a new, much more advanced code was published. The seismic design of new structures in Serbia must comply with Eurocode 8—Part 1 [147]

as of 2019 [160]. However, although most buildings were constructed after 1945, a recent moderate-size $M_w = 5.5$ 2010 Kraljevo earthquake revealed the vulnerability of the Serbian building stock. It should be noted that reinforced-concrete structures accounted for only 10% of the building stock in the affected area. As expected, buildings with unreinforced brick masonry walls and flexible diaphragms sustained notable damages while properly constructed modern confined masonry buildings remained undamaged. However, numerous one- or two-storey masonry buildings with rigid RC floors and horizontal ring beams suffered severe damage and/or partial collapse due to the inadequate design and construction and/or low-quality building materials and many multi-storey masonry buildings were damaged due to poorly planned and executed renovations and extensions [161]. These findings call for increased efforts toward a more realistic estimation of the vulnerability of the existing building stock in Serbia if one would like to obtain a realistic estimate of the seismic risk.

4.3.5. Türkiye

Most of the existing building stock in Türkiye does not have sufficient resistance to earthquakes. This is clearly seen from the observed damage caused by the recent earthquakes in Türkiye. Earthquake regulations are renewed over time and put into effect, especially after the large-scale loss of life and property [162–164]. Insufficient structural features of the existing building stock play an active role in losses in earthquakes. For this reason, these uninspected buildings, which constitute the majority of the building stock, should be examined, some of them should be strengthened and others should be evaluated within an urban transformation project. The need for low-cost housing as a result of unplanned urbanization due to population growth and migration to big cities in Türkiye has caused both the shift from residential areas to areas with high earthquake hazards and the growth of building stock with weak earthquake safety. Knowing the characteristics of both new buildings and relatively old buildings with weak earthquake safety is of great importance in order to make accurate earthquake risk and loss calculations of settlements. To reduce the damage caused by earthquakes and for effective disaster management, the earthquake risks of existing structures should be calculated realistically. In this context, it is of great importance to know the properties of the building stock that affect the earthquake behavior well, to make the risk and loss calculations correctly. In this respect, examining the Turkish building stock in terms of time and space is of great importance in earthquake risk calculations.

4.3.6. Iran

After the 1990 Manjil mega-earthquake, one of the biggest and most fatal incidents in the seismic history of Iran that claimed the lives of more than 40,000 people, several investigations were initiated by many researchers on the analysis of the damages and vulnerability of the building stocks in the similar earthquake-stricken areas. The catastrophe caused a turning point in the analysis and design approaches of buildings and several modifications to the Iranian Code of Practice for Earthquake Resistant Design of Buildings, Standard 2800, and the definition of many research programs [165]. A study was conducted on three earthquakes in Iran, including the 2003 Bam earthquake, the 2005 Zarand earthquake, and the 2006 Silakhor earthquake by Mahdi and Mahdi [166]. The Bam earthquake has been the biggest earthquake with the highest rate of fatalities in the country after the 1990 Manjil earthquake, in which more than 53,000 buildings were destroyed while the remaining structures were severely damaged [167]. Damage analysis of buildings after the 2003 Bam earthquake by Mostafaei and Kabeyasawa [168] showed that building stock in this city at the time of the earthquake was comprised of adobe, masonry (reinforced and unreinforced), steel, and concrete buildings. As shown in this study, the major building system type has been unreinforced masonry (for around 68% of the buildings), and only 24% of the buildings in the city had been designed seismic-resistant, having a structural system as per the Iranian seismic design code of practice. This is while even the remaining steel or

reinforced concrete (RC) damaged buildings suffered from inappropriate structural design, low-quality construction practices, and insufficient implementation controls. Buildings that have been destroyed or heavily damaged in the other two earthquakes have been mostly adobe or unreinforced masonry buildings, while inadequate seismic-resistant structural systems or unsuitable construction practices were recognized as the main reason for damages. According to the 2016 national census conducted by the Statistical Centre of Iran (SCI) on the residential building stock and different building types, it is understood that the five main types of building systems, i.e., concrete, steel, masonry, adobe, and wooden, could be recognized in Iran. The census shows that masonry, steel, and concrete structures contain 39%, 30%, and 27% of the building stock, respectively. The remaining building types were either wooden or adobe, with 0.14% and 4%, respectively, while the remaining 0.26% had no recognizable system [169]. The study by Bastami et al. [169] which proposes new seismic vulnerability models for building stocks in Iran, shows a considerable change in newer versions of the Iranian Code of Practice for Earthquake Resistant Design of Buildings, Standard 2800, in terms of response factor for calculating base shear in the equivalent static method. These revisions as well as other stricter regulations and modifications for the design and construction of seismic-resistant buildings are in line with the above-mentioned started programs and initiatives for more protection of structures in Iran.

5. Results and Conclusions

Both the seismic parameters and the expected target displacements from the structures have been obtained by considering five earthquakes that occurred in six different countries with different seismic risks within the scope of the study. The highest PGA value for all considered earthquakes was obtained in the 2003 Bam (Iran) earthquake and is 0.970 g. The lowest measured PGA was obtained as 0.01 g for the Serbian earthquakes. While the measured PGA's for Croatia and Serbia provided the recommended PGA's, the recommended PGA values for Türkiye, Bosnia and Herzegovina, Iran and Albania were exceeded. PGA values were compared, considering the standard design earthquake with a 10% exceedance of probability in 50 years (repetition period of 475 years). Therefore, it is possible that these values can be met with the consideration of earthquakes with a larger repetition period. Considering the largest earthquake data as the ground motion level in regions with high seismicity risk means that the seismicity risk can be adequately represented.

The selected earthquake range in Albania is between 5.4–6.9. Medium-sized earthquakes are mostly in the range of 0.1–0.2 g. However, the acceleration of the 5.4 magnitude earthquake that occurred in Tirana in 1988 was recorded as very high (0.4 g), exceeding the expected acceleration value (0.28–0.3 g). Two earthquakes, one moderate (5.7) and the other large (6.9) were selected in Bosnia and Herzegovina. The first selected earthquake exceeded the expected acceleration value (0.17 g) at nearby stations and took values in the range of 0.29–0.43 g. However, the 6.9 magnitude earthquake created an acceleration value (0.01–0.4 g) far below the expected acceleration value (0.18–0.26 g) at stations approximately 200 km away. In three different earthquakes selected in Croatia, a small (4.9) earthquake, however, close to the recording station (6.4 km) created an acceleration of 0.0 g. The acceleration value created by the 6.4 magnitude earthquake 60 km away from the station was 0.04 g. The 6.9 magnitude earthquake that occurred in Montenegro in 1979 had an acceleration of 0.08 g in Dubrovnik, 105 km away, and 0.04 g in Makarska, 208 km away. All of the recorded accelerations are considerably lower than the expected acceleration values. The earthquakes considered in Serbia are medium-sized, and the distances of the earthquakes to the acceleration stations are also high. Moreover, the places where the stations are located are rocky. For this reason, the acceleration values formed were quite low. The lowest of the five earthquakes selected that occurred in Türkiye is 6.3 and the highest is 7.4. It is quite interesting that three earthquakes greater than 7 produce very different accelerations from each other. The lowest acceleration was recorded in Van ($M_w = 7.2$) with 0.182 g and Düzce ($M_w = 7.2$) with 0.823 g. However, very high accelerations were observed in Erzincan ($M_w = 6.8$) earthquakes in 1992 and Bingöl ($M_w = 6.3$) earthquakes in 2003 (Bingöl 0.511 g

and Erzincan 0.485 g). One of the main factors in recording very high acceleration values is the proximity of the recording station to the earthquake focus and the other is ground conditions. It is seen that very high acceleration values were recorded in three different earthquakes in Iran. The 7.37 magnitude earthquake that occurred in Manjil in 1990 was recorded differently at different stations. Accordingly, the acceleration value of 0.13 g in Qazvin, 0.086 g in Rudsar, and 0.538 g at the other station in Rudsar show how different geological conditions affect the acceleration value. The acceleration of the 7.35 magnitude earthquake that occurred in Tabas in 1978 was recorded as 0.64 g, and the acceleration of the 6.6 magnitude earthquake that occurred in Bam in 2003 was recorded as an extraordinarily large 0.97 g. It is clear that the very loose soil structure of the city of Bam played the most important role in such magnification of the acceleration value.

The highest loss of life/damaged buildings ratio was found as 0.24 for 17.08.1999 Türkiye (İzmit) and the lowest value was determined as 0.0006 for 26.11.2019 Albania (Durrës). While the highest loss of life among all earthquakes was 17,480 in the 17.08.1999 Türkiye (İzmit) earthquake, the most building damage occurred in the Albania (Durrës) earthquake of 26.11.2019 with ~90000 buildings.

In order to reveal the effect of different structural conditions within the scope of this study, the number of storeys, local soil class, building importance class, and concrete class were chosen as variables. There is complete agreement between the target displacements obtained for all variables. The target displacements increased for three different limit conditions as the number of storeys in the building increased. In the case of weak local soil properties, the target displacements were obtained larger. The values obtained for ZA are lower than the values obtained for ZD. At the same time, target displacements were found to be larger in buildings that were required to be used after the earthquake. The displacements obtained for the building importance class IV are larger than those obtained for the II. class. As the strength of the concrete decreased, the target displacements expected from the structure increased. This once again reveals that buildings with weak earthquake vulnerability require larger displacements.

However, it was examined whether the seismic risks taken into account for different countries are adequately represented. In this context, since the seismicity elements of each country differ, the losses resulting from the earthquakes vary. Therefore, it is obvious that the realistic determination of the seismic risk will result in a more realistic result with the performance levels expected from the structures. In this respect, the building stock characteristics and local ground conditions also directly affect the losses. The vulnerability of the existing building stock increases the structural damage.

Earthquakes occur in fragile parts of the earth's crust due to their formation mechanism. Loose layers near the surface cannot be a source of earthquakes in this sense. However, since such areas are areas of weakness, they allow the incoming tremor to reach the surface easily and stand out because they are geologically highly impacted areas. In this study, it is observed that the earthquakes selected in countries other than Bosnia and Herzegovina and Croatia occur under the influence of geological conditions. Selected earthquakes in Albania are mostly in Durrës, Shkoder, and Tirana. The depression areas formed with the neotectonic uplift that started in the Pliocene period in Albania led to the formation of Quaternary lakes and plains. In these grabens, the thickness of which reaches 200 m, unstable soil formations at the swamp level cause earthquakes to be more effective [170]. In Serbia, mainly earthquakes occurred in Kraljevo. This area is in the current alluvial and Tertiary flysch structure. The second important earthquake zone is the Pec zone, which is also the flysch zone. Therefore, it can be said that earthquakes occurring in these regions are based on weak geological conditions. Almost all the earthquakes selected in Türkiye have occurred in the current alluvial areas (Erzincan, Kocaeli, Düzce, Bingöl, Van). Plain regime areas created by very thick alluvial structures and active tectonism continue to be sources of earthquakes. The Bam and Manjil earthquakes, which were selected from the earthquakes that occurred in Iran, were effective in the current alluvial basin-type areas.

The reason for the occurrence of earthquakes in these areas can be considered as specific geological conditions.

Buildings constructed in loose and unstable ground conditions are the most vulnerable to earthquakes. For this purpose, it is necessary to choose the soil-building interaction correctly. Almost all the earthquakes selected in this article, which are considered important in the country where they occurred due to the damage caused, have resulted in severe damage due to incompatibility. One of the main purposes of this study is to show that the damages caused by earthquakes without borders are based on similar faults.

It is important to construct buildings in accordance with earthquake-resistant building design guidelines in earthquake-prone regions against the possibility of the recurrence of earthquakes that cause significant damage. This depends on the correct application of earthquake-resistant building design principles during the design and construction stages. The application of earthquake-resistant building design principles together with adequate supervision can be seen as the first step in minimizing the problems, both during the project and construction phases. In addition, the existing building stock should be determined quickly and reliably, and then strengthening and demolition procedures should be decided in buildings that do not have sufficient earthquake performance. At this point, the number of weak buildings under the effect of earthquakes should be minimized by utilizing urban transformation.

Author Contributions: Conceptualization, E.I., M.H.-N., H.B., N.A., A.B., E.H., B.B., H.B.Ö. and S.E.A.H.; methodology, E.H., S.E.A.H., E.I., A.B. and E.H.; software, E.I., N.A., H.B. and M.H.-N.; validation, E.H., A.B., H.B.Ö. and S.E.A.H.; formal analysis, B.B.; investigation, E.I., M.H.-N., H.B., N.A., A.B., E.H., B.B., H.B.Ö. and S.E.A.H.; resources, E.I., M.H.-N., H.B., N.A., A.B., E.H., B.B., H.B.Ö. and S.E.A.H.; data curation, E.I., M.H.-N., H.B., N.A., A.B., E.H., B.B., H.B.Ö. and S.E.A.H.; writing—original draft preparation, N.A., A.B., E.I., B.B. and M.H.-N.; writing—review and editing, S.E.A.H., N.A., M.H.-N., E.I. and E.H.; visualization, H.B.; supervision, E.I., N.A., M.H.-N. and B.B.; project administration, E.I.; funding acquisition, M.H.-N. All authors have read and agreed to the published version of the manuscript.

Funding: This research received no external funding.

Institutional Review Board Statement: Not applicable.

Informed Consent Statement: Not applicable.

Data Availability Statement: Data sharing is not applicable.

Conflicts of Interest: The authors declare no conflict of interest.

References

1. Kumar, S.; Gupta, V.; Kumar, P.; Sundriyal, Y.P. Coseismic landslide hazard assessment for the future scenario earthquakes in the Kumaun Himalaya, India. *Bull. Eng. Geol. Environ.* **2021**, *80*, 5219–5235. [CrossRef]
2. Işık, M.F.; Işık, E.; Harirchian, E. Application of IOS/Android rapid evaluation of post-earthquake damages in masonry buildings. *Gazi Mühendislik Bilimleri Derg.* **2021**, *7*, 36–50.
3. Sandhu, M.; Sharma, B.; Mittal, H.; Chingtham, P. Analysis of the site effects in the North East region of India using the recorded strong ground motions from moderate earthquakes. *J. Earthq. Eng.* **2022**, *26*, 1480–1499. [CrossRef]
4. Halder, L.; Dutta, S.C.; Sharma, R.P.; Bhattacharya, S. Lessons learnt from post-earthquake damage study of Northeast India and Nepal during last ten years: 2021 Assam earthquake, 2020 Mizoram earthquake, 2017 Ambasa earthquake, 2016 Manipur earthquake, 2015 Nepal earthquake, and 2011 Sikkim earthquake. *Soil Dyn. Earthq. Eng.* **2021**, *151*, 106990. [CrossRef]
5. Işık, E.; Sağır, Ç.; Tozlu, Z.; Ustaoglu, Ü.S. Determination of Urban Earthquake Risk for Kırşehir, Turkey. *Earth Sci. Res. J.* **2019**, *23*, 237–247. [CrossRef]
6. Hoveidae, N.; Fathi, A.; Karimzadeh, S. Seismic damage assessment of a historic masonry building under simulated scenario earthquakes: A case study for Arge-Tabriz. *Soil Dyn. Earthq. Eng.* **2021**, *147*, 106732. [CrossRef]
7. Tabrizikahou, A.; Hadzima-Nyarko, M.; Kuczma, M.; Lozančić, S. Application of shape memory alloys in retrofitting of masonry and heritage structures based on their vulnerability revealed in the Bam 2003 earthquake. *Materials* **2021**, *14*, 4480. [CrossRef] [PubMed]
8. Ertuncay, D.; Malisan, P.; Costa, G.; Grimaz, S. Impulsive signals produced by earthquakes in Italy and their potential relation with site effects and structural damage. *Geosciences* **2021**, *11*, 261. [CrossRef]

9. Ditommaso, R.; Iacovino, C.; Auletta, G.; Parolai, S.; Ponzio, F.C. Damage detection and localization on real structures subjected to strong motion earthquakes using the curvature evolution method: The Navelli (Italy) case Study. *Appl. Sci.* **2021**, *11*, 6496. [CrossRef]
10. Ozmen, H.B. A view on how to mitigate earthquake damages in turkey from a civil engineering perspective. *Res. Eng. Struct. Mater.* **2021**, *7*, 1–11. [CrossRef]
11. Zuo, H.; Bi, K.; Hao, H.; Ma, R. Influences of ground motion parameters and structural damping on the optimum design of inerter-based tuned mass dampers. *Eng. Struct.* **2021**, *227*, 111422. [CrossRef]
12. Felicetta, C.; Mascandola, C.; Spallarossa, D.; Pacor, F.; Hailemikael, S.; Di Giulio, G. Quantification of site effects in the Amatrice area (Central Italy): Insights from ground-motion recordings of the 2016–2017 seismic sequence. *Soil Dyn. Earthq. Eng.* **2021**, *142*, 106565. [CrossRef]
13. Mase, L.Z.; Likitlersuang, S.; Tobita, T. Ground motion parameters and resonance effect during strong earthquake in northern Thailand. *Geotech. Geol. Eng.* **2021**, *39*, 2207–2219. [CrossRef]
14. Bilgin, H.; Shkodrani, N.; Hysenliu, M.; Ozmen, H.B.; Isik, E.; Harirchian, E. Damage and performance evaluation of masonry buildings constructed in 1970s during the 2019 Albania earthquakes. *Eng. Fail. Anal.* **2022**, *131*, 105824. [CrossRef]
15. Kamal, M.; İnel, M. Correlation between Ground motion parameters and displacement demands of mid-rise rc buildings on soft soils. *Buildings* **2021**, *12*, 125. [CrossRef]
16. Gijini, A.; Cullufi, H.; Deneko, E.; Xhika, P. Behavior of structure type 82/2 (RC frame), during the earthquake of 26 November 2019 in Durrës, Albania. *Res. Eng. Struct. Mater.* **2021**, *7*, 595–615. [CrossRef]
17. Bulajić, B.Đ.; Pavić, G.; Hadzima-Nyarko, M. PGA vertical estimates for deep soils and deep geological sediments—A case study of Osijek (Croatia). *Comput. Geosci.* **2022**, *158*, 104985. [CrossRef]
18. Işık, E. Comparative investigation of seismic and structural parameters of earthquakes ($M \geq 6$) after 1900 in Turkey. *Arab. J. Geosci.* **2022**, *15*, 971. [CrossRef]
19. Nayak, C.B. A state-of-the-art review of vertical ground motion (VGM) characteristics, effects and provisions. *Innov. Infrastr. Solut.* **2021**, *6*, 124. [CrossRef]
20. Bhanu, V.; Chandramohan, R.; Sullivan, T.J. Influence of ground motion duration on the dynamic deformation capacity of reinforced concrete frame structures. *Earthq. Spectra* **2021**, *37*, 2622–2637. [CrossRef]
21. Todorov, B.; Billah, A.M. Seismic fragility and damage assessment of reinforced concrete bridge pier under long-duration, near-fault, and far-field ground motions. *Structures* **2021**, *31*, 671–685. [CrossRef]
22. Silva, V.; Crowley, H.; Pagani, M.; Monelli, D.; Pinho, R. Development of the OpenQuake engine, the Global Earthquake Model's open-source software for seismic risk assessment. *Nat. Hazards* **2014**, *72*, 1409–1427. [CrossRef]
23. Hancilar, U.; Tuzun, C.; Yenidogan, C.; Erdik, M. ELER software—a new tool for urban earthquake loss assessment. *Nat. Hazards Earth Syst. Sci.* **2010**, *10*, 2677–2696. [CrossRef]
24. Crowley, H.; Pinho, R.; Bommer, J.J. A probabilistic displacement-based vulnerability assessment procedure for earthquake loss estimation. *Bull. Earthq. Eng.* **2004**, *2*, 173–219. [CrossRef]
25. EZ-FRISK. Available online: <https://www.ez-frisk.com/> (accessed on 13 November 2022).
26. Nahar, T.T.; Rahman, M.M.; Kim, D. Effective safety assessment of aged concrete gravity dam based on the reliability index in a seismically induced site. *Appl. Sci.* **2021**, *11*, 1987.
27. McGuire, R.K. FRISK: Computer program for seismic risk analysis using faults as earthquake sources. *US Geol. Surv.* **1978**, *78*, 1007.
28. Ordaz, M.; Martinelli, F.; D'Amico, V.; Meletti, C. CRISIS2008: A flexible tool to perform probabilistic seismic hazard assessment. *Seismol. Res. Lett.* **2013**, *84*, 495–504. [CrossRef]
29. Bender, B.; Perkins, D.M. *SEISRISK III: A Computer Program for Seismic Hazard Estimation*; (No. 1772); US Government Printing Office: Washington, DC, USA, 1987.
30. Field, E.H.; Jordan, T.H.; Cornell, C.A. A developing community-modeling environment for seismic hazard analysis. *Seismol. Res. Lett.* **2003**, *74*, 406–419. [CrossRef]
31. Özener, P. Dinamik Yükler, Yer Hareketi Parametreleri ve İvme Spektrumları, Yıldız Tenk Üniversitesi, Ders Notları. Available online: <https://studylibtr.com/doc/1406240/ders-2.1-dinamik-y%C3%BCKler--yer-hareketi-parametreleri-ve-i%C3%87vme> (accessed on 11 November 2022).
32. Büyüksaraç, A.; Över, S.; Geneş, M.C.; Bikçe, M.; Kacin, S.; Bektaş, Ö. Estimating shear wave velocity using acceleration data in Antakya (Turkey). *Earth Sci. Res. J.* **2004**, *18*, 87–98.
33. Pejovic, J.R.; Serdar, N.N.; Pejovic, R.R. Optimal intensity measures for probabilistic seismic demand models of RC high-rise buildings. *Earthq. Struct.* **2017**, *13*, 221–230.
34. Tao, D.; Ma, Q.; Li, S.; Xie, Z.; Lin, D.; Li, S. Support vector regression for the relationships between ground motion parameters and macroseismic intensity in the Sichuan–Yunnan Region. *Appl. Sci.* **2020**, *10*, 3086. [CrossRef]
35. Işık, E.; Peker, F.; Büyüksaraç, A. The effect of vertical earthquake motion on steel structures behaviour in different seismic zones. *J. Adv. Res. Nat. Appl. Sci.* **2022**, *8*, 527–542. [CrossRef]
36. Liu, J.; Wang, W.; Dasgupta, G. Pushover analysis of underground structures: Method and application. *Sci. China Technol. Sci.* **2014**, *57*, 423–437. [CrossRef]

37. Elnashai, A.S. Advanced inelastic static (pushover) analysis for earthquake applications. *Struct. Eng. Mech.* **2001**, *12*, 51–69. [CrossRef]
38. Shendkar, M.R.; Kontoni, D.P.N.; Işık, E.; Mandal, S.; Maiti, P.R.; Harirchian, E. Influence of masonry infill on seismic design factors of reinforced-concrete buildings. *Shock Vib.* **2022**, *2022*, 5521162. [CrossRef]
39. Chopra, A.K.; Goel, R.K. A modal pushover analysis procedure for estimating seismic demands for buildings. *Earthq. Eng. Struct. Dyn.* **2002**, *31*, 561–582. [CrossRef]
40. Rofooeil, F.; Attari, N.K.; Shodja, A.; Rasekh, A. Comparison of static and dynamic pushover analysis in assessment of the target displacement. *Int. J. Civ. Eng.* **2006**, *4*, 212–225.
41. Krawinkler, H.; Seneviratna, G.D.P.K. Pros and cons of a pushover analysis of seismic performance evaluation. *Eng. Struct.* **1998**, *20*, 452–464. [CrossRef]
42. Işık, E.; Karaşin, İ.B.; Karaşin, A. The effect of different earthquake ground motion levels on the performance of steel structures in settlements with different seismic hazards. *Struct. Eng. Mech.* **2022**, *84*, 85–100.
43. Tso, W.K.; Moghadam, A.S. Pushover procedure for seismic analysis of buildings. *Prog. Struct. Eng. Mater.* **1998**, *1*, 337–344. [CrossRef]
44. Pinho, R.; Casarotti, C.; Antoniou, S. A comparison of single-run pushover analysis techniques for seismic assessment of bridges. *Earthq. Eng. Struct. Dyn.* **2007**, *36*, 1347–1362. [CrossRef]
45. Kim, S.; D’Amore, E. Push-over analysis procedure in earthquake engineering. *Earthq. Spectra.* **1999**, *15*, 417–434. [CrossRef]
46. Papanikolaou, V.K.; Elnashai, A.S. Evaluation of conventional and adaptive pushover analysis I: Methodology. *J. Earthq. Eng.* **2005**, *9*, 923–941. [CrossRef]
47. Işık, E.; Kutanis, M. Determination of local site-specific spectra using probabilistic seismic hazard analysis for Bitlis Province, Turkey. *Earth Sci. Res. J.* **2015**, *19*, 129–134. [CrossRef]
48. Kutanis, M.; Ulutaş, H.; Işık, E. PSHA of Van province for performance assessment using spectrally matched strong ground motion records. *J. Earth Syst. Sci.* **2018**, *127*, 99. [CrossRef]
49. Available online: https://seismo.berkeley.edu/gifs/blog_20200126_Figure1.jpg (accessed on 16 November 2022).
50. Okay, A.I.; Kaşlılar-Özcan, A.; İmren, C.; Boztepe-Güney, A.; Demirbağ, E.; Kuşçu, İ. Active faults and evolving strike-slip basins in the Marmara Sea, northwest Turkey: A multichannel seismic reflection study. *Tectonophysics* **2000**, *321*, 189–218. [CrossRef]
51. Bilgin, H.; Hysenliu, M. Comparison of near and far-fault ground motion effects on low and mid-rise masonry buildings. *J. Build. Eng.* **2020**, *30*, 101248. [CrossRef]
52. Fundo, A.; Ll, D.; Kuka, S.; Begu, E.; Kuka, N. Probabilistic seismic hazard assessment of Albania. *Acta Geod. Geophys. Hung.* **2012**, *47*, 465–479. [CrossRef]
53. Sulstarova, E.; Peçi, V.; Shuteriqi, P. Vlora-Elbasan-Diber transversal fault and its seismic activity. In *29th General Assembly of IASPEI*; Abstract; P. Ziti & Co. Thessaloniki: Thessaloniki, Greece, 1997; p. 115.
54. *KTP-1978 Kusht Teknike te Projektimit. KTP-1978, Technical Design Code KTP*; Akademia e Shkencave: Tirana, Albania, 1978.
55. *NATO Sfp Project 983054, Harmonization of Seismic Hazard Maps for the Western Balkan Countries (BSHAP), Final Report*; NATO: Ankara, Türkiye, 2011.
56. Miošić, N.; Samardžić, N.; Hrvatović, H. The current status of geothermal energy use and development in Bosnia and Herzegovina. In *Proceedings of the Proceedings World Geothermal Congress, Bali, Indonesia, 25–29 April 2010*; pp. 25–29.
57. Slejko, D.; Camassi, R.; Cecic, I.; Herak, D.; Herak, M.; Kociu, S.; Kouskouna, V.; Lapajine, J.; Makropoulos, K.; Meletti, C.; et al. Seismic hazard assessment for Adria. *Ann. Geofis.* **1999**, *42*, 1085–1107. [CrossRef]
58. Gasparini, C.; Iannaccone, G.; Scarpa, R. Fault-plane solution and seismicity of the Italian peninsula. *Tectonophysics* **1985**, *117*, 59–78. [CrossRef]
59. Herak, M.; Herak, D.; Markušić, S. Fault-plane solutions for earthquakes (1956–1995) in Croatia and neighbouring regions. *Geofizika* **1995**, *12*, 43–56.
60. Louvari, H.K.; Kiratzi, A.A.; Papazachos, B.C. Further evidence for strike-slip faulting in the Ionian Islands: The Lefkada fault. In *Proceedings of the IASPEI 29th General Assembly, Thessaloniki, Greece, 18–28 August 1997*; pp. 18–29.
61. Sulstarova, E.; Peçi, V.; Shuteriqi, P. Vlora-Elbasani-Dibra (Albania) transversal fault zone and its seismic activity. *J. Seismol.* **2000**, *4*, 117–131. [CrossRef]
62. Harvard. CMT Focal Mechanisms. 1998. Available online: <http://www.seismology.harvard.edu> (accessed on 20 October 2022).
63. Šipoš, T.K.; Hadzima-Nyarko, M. Rapid seismic risk assessment. *Int. J. Dis. Risk Reduct.* **2017**, *24*, 348–360. [CrossRef]
64. MunichRe. *Topics Geo: Natural Catastrophes 2011 Analyses Assessments Positions*, Munich. Germany. 2012. Available online: <http://www.munichre.com/natcatservice/> (accessed on 20 September 2022).
65. Cummins, J.D.; Mahul, O. *Catastrophe Risk Financing in Developing Countries: Principles for Public Intervention*; World Bank Publications: Washington DC, USA, 2009.
66. Archives of the Department of Geophysics, Faculty of Science, University of Zagreb. Available online: <https://www.pmf.unizg.hr/geof/en> (accessed on 12 November 2022).
67. Herak, M.; Herak, D.; Markušić, S. Revision of the earthquake catalogue and seismicity of Croatia, 1908–1992. *Terra Nova* **1996**, *8*, 86–94. [CrossRef]
68. Markušić, S.; Herak, D.; Ivančić, I.; Sović, I.; Herak, M.; Prelogović, E. Seismicity of Croatia in the period 1993–1996 and the Ston-Slano earthquake of 1996. *GEOFIZIKA* **1998**, *15*, 83–102.

69. Ivančić, I.; Herak, D.; Markušić, S.; Sović, I.; Herak, M. Seismicity of Croatia in the period 1997–2001. *Geofizika* **2002**, *18*, 17–29.
70. Ivančić, I.; Herak, D.; Markušić, S.; Sović, I.; Herak, M. Seismicity of Croatia in the period 2002–2005. *Geofizika* **2006**, *23*, 87–103.
71. Markušić, S.; Stanko, D.; Penava, D.; Ivančić, I.; Bjelotomić Oršulić, O.; Korbar, T.; Sarhosis, V. Destructive M6. 2 petrinja earthquake (Croatia) in 2020—Preliminary multidisciplinary research. *Remote Sens.* **2021**, *13*, 1095. [CrossRef]
72. Papeš, *Tektonska Građa Teritorije SR BiH, Report*; Geoinstitut Ilidža: Sarajevo, Bosnia and Herzegovina, 1998.
73. Ademović, N.; Kalman Šipoš, T.; Hadzima-Nyarko, M. Rapid assessment of earthquake risk for Bosnia and Herzegovina. *Bull. Earthq. Eng.* **2020**, *18*, 1835–1863. [CrossRef]
74. Ademović, N.; Hadzima-Nyarko, M.; Zagora, N. Seismic vulnerability assessment of masonry buildings in Banja Luka and Sarajevo (Bosnia and Herzegovina) using the macroseismic model. *Bull. Earthq. Eng.* **2020**, *18*, 3897–3933. [CrossRef]
75. Lee, V.W.; Manić, M.I.; Bulajić, B.Đ.; Herak, D.; Herak, M.; Trifunac, M.D. Microzonation of Banja Luka for performance-based earthquake-resistant design. *Soil Dyn. Earthq. Eng.* **2015**, *78*, 71–88. [CrossRef]
76. Trukulja, D. Seizmogenetska obilježja oblasti zahvaćene zemljotresima u Banjoj Luci. Međunarodni simpozijum povodom 30 godina zeljotresa u Banjoj Luci. International Symposium on the 30 years 1969 Banja Luka Earthquake. *Univ. Banja Luci* **1999**, 28–41.
77. Janković, M. *Quelques Observations sur les Consé-Quences du Tremblement de terre du 11 juin 1962. Rapport Multigraphié, une Carte*; Sarajevo, Bosnia and Herzegovina, 1963.
78. Petković, K.V. Neue Erkenntnisse über den Bau der Dinariden. Jahrbuch der Geol. Bundesanstalt.(Wien). *Bundesanstalt* **1963**, *101*, 1–24.
79. USGS. Earthquake Catalogue for all Earthquakes with $M_w \geq 3$ in the Period between 1900 and April 2021 for the Geographic Region between 41.0° N and 47.0° N, and 12.5° E and 23.0° E, as Reported by the United States Geological Survey. 2021. Available online: <https://earthquake.usgs.gov/earthquakes/search/> (accessed on 23 May 2021).
80. *BAS EN 1998-1/NA: 2018 Eurocode 8: Design of Structures for Earthquake Resistance—Part 1: General Rules, Seismic Actions and Rules for Buildings—National Annex*; Institut za standardizaciju Bosne i Hercegovine: Istočno Sarajevo, Bosnia and Hercegovina.
81. Jordanovski, L.R.; Lee, V.W.; Manić, M.I.; Olumčeva, T.; Sinadnovski, C.; Todorovska, M.I.; Trifunac, M.D. *Strong Earthquake Ground Motion Data in EQINFOS: Yugoslavia. Part I*; Report No. 87-05; Department of Civil Engineering, University of Southern California: Los Angeles, CA, USA, 1987.
82. Ambraseys, N.; Douglas, J.; Margaris, B.; Sigbjörnsson, R.; Smit, P.; Suhadolc, P. Internet site for European strong motion data. In Proceedings of the 12th European Conference on Earthquake Engineering, London, UK, 9–13 September 2002; p. 837.
83. Ambraseys, N.; Douglas, J.; Margaris, B.; Sigbjörnsson, R.; Berge-Thierry, C.; Suhadolc, P.; Costa, G.; Smit, P. Dissemination of European strong-motion data. In Proceedings of the 13th World Conference on Earthquake Engineering, Vancouver, BC, Canada, 1–6 August 2004; Volume 2, p. 32.
84. Markušić, S.; Herak, M. Seismic zoning of Croatia. *Nat. Hazards* **1998**, *18*, 269–285. [CrossRef]
85. Prevolnik, S. Analiza Akcelerograma Petrinjskih Potresa (Accelerogram Analysis of Petrinja Earthquakes). Available online: https://www.pmf.unizg.hr/geof/seizmoloska_sluzba/potresi_kod_petrinje_2020 (accessed on 11 June 2022).
86. Medak, D.; Pribičević, B.; Prelogović, E. Recent geodynamical GPS-project in Croatia, raziskave s područja geodezije in geofizike 2006. In Proceedings of the 12th Strokovno Srečanje Slovenskega Združenja za Geodezijo in Geofiziko, Ljubljana, Slovenija, 18 January 2007.
87. Morales-Esteban, A.; Martinez-Alvarez, F.; Scitovski, S.; Scitovski, R. A fast partitioning algorithm using adaptive Mahalanobis clustering with application to seismic zoning. *Comput. Geosci.* **2014**, *73*, 132–141. [CrossRef]
88. Skoko, D.; Prelogović, E.; Aljinović, B. Geological structure of the Earth's crust above the Moho discontinuity in Yugoslavia. *Geophys. J. Int.* **1987**, *89*, 379–382. [CrossRef]
89. Bielik, M.; Makarenko, I.; Csicsay, K.; Legostaeva, O.; Starostenko, V.; Savchenko, A.; Šimonová, B.; Dérerová, J.; Fojtíková, L.; Pašteka, R.; et al. The refined Moho depth map in the Carpathian-Pannonian region. *Contrib. Geophys. Geod.* **2018**, *48*, 179–190.
90. *Hrvatski zavod za norme: HRN EN 1998-1:2011/NA:2011. Eurocode 8: Design of Structures for Earthquake Resistance—Part 1: General Rules, Seismic Actions and Rules for Buildings—National Annex*; Hrvatski Zavod za Norme: Zagreb, Croatia, 2011.
91. Ganas, A.; Elias, P.; Valkaniotis, S.; Tsironi, V.; Karasante, I.; Briole, P. Petrinja earthquake moved crust 10 feet. *Tembler* **2021**. [CrossRef]
92. ZHMS. 35 Godina od Katastrofalnog Zemljotresa u Crnoj Gori (35 Years since the Catastrophic Earthquake in Montenegro). Seismological Survey of Montenegro, Podgorica. 2014. Available online: <http://www.seismo.co.me/documents/35%20GODINA%20OD%20KATASTROFALNOG%20ZEMLJOTRESA%20U%20CRNOJ%20GORI.pdf> (accessed on 15 August 2022).
93. Available online: <http://seizkarta.gfz.hr/karta.php> (accessed on 30 August 2022).
94. UNICEF Country Office for Croatia. *Earthquake Situation Report #5*. Croatia, 2021. Available online: [https://www.unicef.org/media/92246/file/UNICEF%20Croatia%20Situation%20Report%20No.%205%20\(Earthquake\)](https://www.unicef.org/media/92246/file/UNICEF%20Croatia%20Situation%20Report%20No.%205%20(Earthquake)) (accessed on 31 October 2022).
95. Morales-Esteban, A.; Martinez-Alvarez, F.; Scitovski, S.; Scitovski, R. Mahalanobis clustering for the determination of incidence-magnitude seismic parameters for the Iberian Peninsula and the Republic of Croatia. *Comput. Geosci.* **2021**, *156*, 104873. [CrossRef]
96. RTS. 2012. Available online: <https://www.rts.rs/page/stories/sr/story/125/drustvo/1204516/dve-godine-od-zemljotresa-u-kraljevu.html> (accessed on 20 April 2022).





97. SSS. Catalog of $M \geq 3$ Earthquakes of the Republic of Serbia. Seismological Survey of Serbia, Belgrade, Serbia, 2013. Available online: <https://www.seismo.gov.rs/Seizmichnost/Katalog-zemljotresa.pdf> (accessed on 10 November 2022).
98. Seismological Survey of Serbia. Accelerograms Recorded during 10 March 2010 Peć and 3 November 2010 Kraljevo Earthquakes. Seismological Survey of Serbia, Republic of Serbia; 2021. Available online: <http://www.seismo.gov.rs/O%20zavodu/Infol.htm> (accessed on 21 May 2021).
99. Bozkurt, E. Neotectonics of Turkey—A synthesis. *Geodin. Acta* **2001**, *14*, 3–30. [CrossRef]
100. Işık, E.; Büyüksaraç, A.; Ekinci, Y.L.; Aydın, M.C.; Harirchian, E. The effect of site-specific design spectrum on earthquake-building parameters: A case study from the Marmara region (NW Turkey). *Appl. Sci.* **2020**, *10*, 7247. [CrossRef]
101. Tatar, O.; Poyraz, F.; Gürsoy, H.; Cakir, Z.; Ergintav, S.; Akpınar, Z.; Koçbulut, F.; Sezen, F.; Türk, T.; Hastaoğlu, K.Ö.; et al. Crustal deformation and kinematics of the Eastern Part of the North Anatolian Fault Zone (Turkey) from GPS measurements. *Tectonophysics* **2012**, *518–521*, 55–62. [CrossRef]
102. Şengör, A.M.C.; Grall, C.; Imren, C.; Le Pichon, X.; Görür, N.; Henry, P.; Karabulut, H.; Siyako, M. The geometry of the North Anatolian transform fault in the Sea of Marmara and its temporal evolution: Implications for the development of intracontinental transform faults. *Can. J. Earth Sci.* **2014**, *51*, 222–242. [CrossRef]
103. Alkan, H.; Büyüksaraç, A.; Bektaş, Ö.; Işık, E. Coulomb stress change before and after 24.01. 2020 Sivrice (Elazığ) Earthquake ($M_w = 6.8$) on the East Anatolian Fault Zone. *Arab. J. Geosci.* **2021**, *14*, 2648. [CrossRef]
104. Örgülü, G. Seismicity and source parameters for small-scale earthquakes along the splays of the North Anatolian Fault (NAF) in the Marmara Sea. *Geophys. J. Int.* **2011**, *184*, 385–404. [CrossRef]
105. Bohnhoff, M.; Martínez-Garzón, P.; Bulut, F.; Stierle, E.; Ben-Zion, Y. Maximum earthquake magnitudes along different sections of the North Anatolian Fault Zone. *Tectonophysics* **2016**, *674*, 147–165. [CrossRef]
106. Poyraz, F. Determining the strain upon the eastern section of the North Anatolian fault zone (NAFZ). *Arab. J. Geosci.* **2015**, *8*, 1787–1799. [CrossRef]
107. Meng, J.; Sinoplu, O.; Zhou, Z.; Tokay, B.; Kusky, T.; Bozkurt, E.; Wang, L. Greece and Turkey Shaken by African tectonic retreat. *Sci. Rep.* **2021**, *11*, 6486. [CrossRef]
108. Barka, A.; Eyidoğan, H. The Erzincan earthquake of 13 March 1992 in eastern Turkey. *Terra Nova* **1993**, *5*, 190–194. [CrossRef]
109. Saatcioglu, M.; Bruneau, M. Performance of structures during the 1992 Erzincan earthquake. *Can. J. Civ. Eng.* **1993**, *20*, 305–325. [CrossRef]
110. Barka, A.; Akyuz, H.S.; Altunel, E.; Sunal, G.; Cakir, Z.; Dikbas, A.; Page, W. The surface rupture and slip distribution of the 17 August 1999 Izmit earthquake ($M 7.4$), North Anatolian fault. *Bull. Seismol. Soc. Am.* **2002**, *92*, 43–60. [CrossRef]
111. Ghasemi, H.; Cooper, J.D.; Imbsen, R.A.; Piskin, H.; Inal, F.; Tiras, A. *The November 1999 Duzce Earthquake: Post-Earthquake Investigation of the Structures on the TEM (No. FHWA-RD-00-146)*; Federal Highway Administration: Washington, DC, USA, 2000.
112. Akyuz, H.S.; Hartleb, R.; Barka, A.; Altunel, E.; Sunal, G.; Meyer, B.; Armijo, V.R. Surface rupture and slip distribution of the 12 November 1999 Duzce earthquake ($M 7.1$), North Anatolian fault, Bolu, Turkey. *Bull. Seismol. Soc. Am.* **2002**, *92*, 61–66. [CrossRef]
113. Öztürk, S.; Çinar, H.; Bayrak, Y.; Karsli, H.; Daniel, G. Properties of the aftershock sequences of the 2003 Bingöl, $M_D = 6.4$, (Turkey) earthquake. *Pure Appl. Geophys.* **2008**, *165*, 349–371. [CrossRef]
114. Aydan, Ö.; Ulusay, R.; Miyajima, M. *The Bingöl Earthquake of May 1, 2003*; Japan Society of Civil: Tokyo, Japan, 2003.
115. Erdik, M.; Kamer, Y.; Demircioğlu, M.; Şeşetyan, K. 23 October 2011 Van (Turkey) earthquake. *Nat. Hazards* **2012**, *64*, 651–665. [CrossRef]
116. Utkucu, M.; Durmus, H.; Yalçın, H.; Budakoglu, E.; Isik, E. Coulomb static stress changes before and after the 23 October 2011 Van, eastern Turkey, earthquake ($MW = 7.1$): Implications for the earthquake hazard mitigation. *Nat. Hazards Earth Syst. Sci.* **2013**, *13*, 1889. [CrossRef]
117. Toker, M.; Sengor, A.C.; Schluter, F.D.; Demirbag, E.; Cukur, D.; Imren, C. The structural elements and tectonics of the Lake Van basin (Eastern Anatolia) from multi-channel seismic reflection profiles. *J. Afr. Earth Sci.* **2017**, *129*, 165–178. [CrossRef]
118. Anonymous. Historical Earthquakes. 2021. Available online: <http://www.koeri.boun.edu.tr> (accessed on 15 May 2022).
119. Anonymous. Historical Earthquakes. 2021. Available online: <http://www.deprem.afad.gov.tr> (accessed on 15 May 2022).
120. Gupta, H.K. Seismic hazard assessment in the Alpide belt from Iran to Burma. *Ann. Geofis.* **1993**, *36*, 61–82.
121. Hamzehloo, H.; Alikhanzadeh, A.; Rahmani, M.; Ansari, A. Seismic hazard maps of Iran. In Proceedings of the 15th World Conference on Earthquake Engineering, Lisbon, Portugal, 24–28 September 2012; pp. 24–28.
122. Moinfar, A.A.; Naderzadeh, A.; Nabavi, M.H. New Iranian seismic hazard zoning map for new edition of seismic code and its comparison with neighbor countries. In Proceedings of the 15th World Conference on Earthquake Engineering, Lisbon, Portugal, 24–28 September 2012.
123. Ambraseys, N.; Melville, C. *A History of Persian Earthquakes*; Cambridge University Press: New York, NY, USA, 1982.
124. Berberian, M. *Natural Hazards and the First Earthquake Catalogue of Iran. Volume 1: Historical Hazards in Iran Prior to 1900*; Internationaonal Institute of Earthquake Engineering and Seismology: Tehran, Iran, 1994; 603p.
125. Shahvar, M.P.; Farzanegan, E.; Eshaghi, A.; Mirzaei, H. i1-net: The Iran Strong Motion Network. *Seismol. Res. Lett.* **2021**, *92*, 2100–2108. [CrossRef]
126. ISMN. Catalogue of Earthquake Strong Motion Records, Iran Strong Motion Network. Road, Housing, and Urban Development Research Center. 2017. Available online: <https://ismn.bhrc.ac.ir/en> (accessed on 4 July 2022).

127. IRSC. Iranian Seismological Center, Institute of Geophysics, University of Tehran. 2022. Available online: <https://irsc.ut.ac.ir/seismicity.php> (accessed on 4 July 2022).
128. Shoja-Taheri, J.; Niazi, M. Seismicity of the Iranian plateau and bordering regions. *Bull. Seismol. Soc. Am.* **1981**, *71*, 477–489.
129. Izadkhah, Y.O.; Hosseini, K.A. An evaluation of disaster preparedness in four major earthquakes in Iran. *J. Seismol. Earthq. Eng.* **2010**, *12*, 61.
130. Ambraseys, N.N.; Tchalenko, J.S. The Dasht-e Bayāz (Iran) earthquake of August 31, 1968: A field report. *Bull. Seismol. Soc. Am.* **1969**, *59*, 1751–1792. [CrossRef]
131. Berberian, M. Tabas-e-Golshan (Iran) catastrophic earthquake of 16 September 1978; a preliminary field report. *Disasters* **1979**, *2*, 207–219. [CrossRef] [PubMed]
132. USGS. United States Geological Survey (USGS), Bam Earthquake, Impact. 2022. Available online: <https://earthquake.usgs.gov/earthquakes/eventpage/usp0004arq/impact> (accessed on 6 July 2022).
133. ISMN. *Iran Strong Motion Network*; Road, Housing, and Urban Development Research Center: Tehran, Iran, 2022.
134. IIEES. International Institute of Earthquake Engineering and Seismology (IIEES): Tabas Earthquake of 16 September 1978 Mw=7.4. 2022. Available online: <https://www.iiees.ac.ir/en/tabas-earthquake-of-16-september-1978-mw7-4-2/> (accessed on 6 July 2022).
135. IRIS. 1968 Dasht-e-Bayaz (Iran) Earthquake Archive, Incorporated Research Institutions for Seismology (IRIS). 2022. Available online: <https://ds.iris.edu/seismo-archives/quakes/1968dasht-e-bayaz/> (accessed on 6 July 2022).
136. ICSRDB. *Iranian Code of Practice for Earthquake Resistant Design of Buildings (Standard 2800)*, 4th ed.; PN S 253; Building and Housing Research Center of Iran: Tehran, Iran, 2014.
137. Seismosoft. SeismoStruct 2021—A Computer Program for Static and Dynamic Nonlinear Analysis of Framed Structures. 2021. Available online: <http://www.seismosoft.com> (accessed on 10 June 2022).
138. Antoniou, S.; Pinho, R. *Seismostruct—Seismic Analysis Program by Seismosoft*; Technical Manual and User Manual; Seismosoft: Pavia, Italy, 2022.
139. Menegotto, M.; Pinto, P.E. Method of analysis for cyclically loaded RC plane frames including changes in geometry and non-elastic behavior of elements under combined normal force and bending. In *Symposium on the Resistance and Ultimate Deformability of Structures Acted on by Well-defined Repeated Loads*; International Association for Bridge and Structural Engineering: Zurich, Switzerland, 1973; pp. 15–22.
140. Mander, J.B.; Priestley, M.J.N.; Park, R. Theoretical stress-strain model for confined concrete. *J. Struct. Eng.* **1998**, *114*, 1804–1825. [CrossRef]
141. EN 1998-3; Eurocode-8: Design of Structures for Earthquake Resistance-Part 3: Assessment and Retrofitting of Buildings. European Committee for Standardization: Bruxelles, Belgium, 2005.
142. Pinto, P.E.; Franchin, P. Eurocode 8-Part 3: Assessment and retrofitting of buildings. In *Proceedings of the Eurocode 8 Background and Applications, Dissemination of Information for Training*, Lisbon, Portugal, 10–11 February 2011.
143. Kutanis, M.; Boru, E.O.; Işık, E. Alternative instrumentation schemes for the structural identification of the reinforced concrete field test structure by ambient vibration measurements. *KSCE J. Civ. Eng.* **2017**, *21*, 1793–1801. [CrossRef]
144. Aksoylu, C.; Mobark, A.; Arslan, M.H.; Hakkı Erkan, İ. A comparative study on ASCE 7-16, TBEC-2018 and TEC-2007 for reinforced concrete buildings. *Rev. Construcción* **2020**, *19*, 282–305. [CrossRef]
145. Hadzima-Nyarko, M.; Morić, D.; Draganić, H.; Štefić, T. Comparison of fundamental periods of reinforced shear wall dominant building models with empirical expressions. *Teh. Vjesn.* **2015**, *22*, 685–694. [CrossRef]
146. Aksoylu, C.; Arslan, M.H. Çerçeve+ perde türü betonarme binalarin periyod hesaplarının TBDY-2019 yönetmeliğine göre ampirik olarak değerlendirilmesi. *Uludağ Univ. J. Fac. Eng.* **2019**, *24*, 365–382. [CrossRef]
147. CEN. *Eurocode 8-Design of Structures for Earthquake Resistance-Part 1: General Rules, Seismic Actions and Rules for Buildings*, EN 1998-1:2005; European Committee for Standardization: Bruxelles, Belgium, 2005.
148. INSTAT. *Population and Housing Census of Albania, 2011—Regjistrimi në Harta—Albania 2001 Census Atlas*; Seria e Studimeve: Tirana, Albania, 2011; p. 11.
149. Bureau of Statistics [CBS]. *National Population and Housing Census 2013 (National Report)*; Agency for Statistics of Bosnia and Herzegovina: Sarajevo, Bosnia and Herzegovina, 2013.
150. Ademović, N. Structural and Seismic Behavior of Typical Masonry Buildings from Bosnia and Herzegovina. Master Thesis, The University of Minho, Guimaraes, Portugal, 2011.
151. Ademovic, N.; Hrasnica, M.; Oliveira, D.V. Pushover analysis and failure pattern of a typical masonry residential building in Bosnia and Herzegovina. *Eng. Struct.* **2013**, *50*, 13–29. [CrossRef]
152. Ademović, N.; Oliveira, D.V. (2017)—Damage Indicators for Unreinforced Masonry Building Walls Subjected to Seismic Actions, UDK: 692.2.042.7. *Građevinski Mater. I Konstr.* **2017**, *60*, 17–32. [CrossRef]
153. Ademović, N.; Oliveira, D.V.; Lourenco, P.B. Seismic evaluation and strengthening of an existing masonry building in Sarajevo, BiH. *Buildings* **2019**, *9*, 30. [CrossRef]
154. Ademovic, N.; Zagora, M.; Hadzima-Nyarko, M. Seismic Vulnerability Analysis in Urban and Rural Regions of Visoko, BiH, The International Symposium on Civil Engineering—ISCE 2018 TLTH (12th) days of Bhaaas in Bosnia and Herzegovina mostar 2021, Advanced Technologies, Systems, and Applications VI. In *Proceedings of the International Symposium on Innovative and Interdisciplinary Applications of Advanced Technologies (IAT) 2021, Lecture Notes in Networks and Systems*, Sarajevo, Bosnia and Herzegovina, 24–27 June 2021; pp. 421–4299.

155. Ademovic, N.; Hadzima-Nyarko, M.; Zagora, N. Influence of site effects on the seismic vulnerability of masonry and reinforced concrete buildings in Tuzla (Bosnia and Herzegovina). *Bull. Earthq. Eng.* **2022**, *20*, 2643–2681. [CrossRef]
156. Piljug, A.; Medanović, Ć.; Ademović, N.; Hadzima-Nyarko, M.; Zagora, N. Quick visual seismic assessment of existing buildings in Sarajevo (BiH). In Proceedings of 3rd European Conference on Earthquake Engineering & Seismology, pp-1300-1306, Bucharest, Romania, 4–9 September 2022.
157. Pavić, G.; Hadzima-Nyarko, M.; Bulajić, B.; Jurković, Ž. Development of seismic vulnerability and exposure models—A case study of Croatia. *Sustainability* **2020**, *12*, 973. [CrossRef]
158. Miranda, E.; Brzev, S.; Bijelic, N.; Arbanas, Ž.; Bartolac, M.; Jagodnik, V.; Robertson, I. *Petrinja, Croatia December 29, 2020, Mw 6.4 Earthquake Joint Reconnaissance Report (JRR)*; ETH Zurich: Zurich, Switzerland, 2021.
159. Pavić, G.; Hadzima-Nyarko, M.; Bulajić, B. A contribution to a uhs-based seismic risk assessment in Croatia—A Case Study for the City of Osijek. *Sustainability* **2020**, *12*, 1796. [CrossRef]
160. SRPS EN 1998-1/NA:2018; *Evrokod 8-Projektovanje Seizmički Otpornih Konstrukcija Dio 1: Opsta Pravila, Seizmicka Dejstva i Pravila za Zgrade (Eurocode 8-Design of Structures for Earthquake Resistance-Part 1: General Rules, Seismic Actions and Rules for Buildings)*; Institute for Standardization of Serbia: Belgrade, Serbia, 2018.
161. Manić, M.I.; Bulajić, B. Examples of typical damages to masonry buildings for individual housing in Kraljevo region during the November 03, 2010 earthquake (in Serbian with English abstract). In Proceedings of the Fourth International Conference Earthquake Engineering and Engineering Seismology, Tehran, Iran, 19–21 May 2014; Association of Civil Engineers of Serbia: Belgrad, Serbia, 2014; pp. 315–324.
162. Işık, E.; Karaşin, İ.B.; Demirci, A.; Büyüksaraç, A. Seismic risk priorities of site and mid-rise RC buildings in Turkey. *Chall. J. Struct. Mech.* **2020**, *6*, 191–203. [CrossRef]
163. Dogan, G.; Ecemis, A.S.; Korkmaz, S.Z.; Arslan, M.H.; Korkmaz, H.H. Buildings damages after Elazığ, Turkey earthquake on 24 January 2020. *Nat. Hazards* **2021**, *109*, 161–200. [CrossRef]
164. Yel, N.S.; Arslan, M.H.; Aksoylu, C.; Erkan, İ.H.; Arslan, H.D.; Işık, E. Investigation of the Earthquake Performance Adequacy of Low-Rise RC Structures Designed According to the Simplified Design Rules in TBEC-2019. *Buildings* **2022**, *12*, 1722. [CrossRef]
165. Ghafoory-Ashtlany, M.; Jafari, M.K.; Tehranizadeh, M. Earthquake hazard mitigation achievement in Iran. In Proceedings of the 12th World Conference on Earthquake Engineering, Auckland, New Zealand, 30 January–4 February 2000; Volume 30.
166. Mahdi, T.; Mahdi, A. Reconstruction and retrofitting of buildings after recent earthquakes in Iran. *Procedia Eng.* **2013**, *54*, 127–139. [CrossRef]
167. Astaneh-Asl, A.; Saeedikia, M.; Havaii, M.H.; Fathi, M.; Fatemi-Aghda, S.M.; Mir Ghaderi, S.R.; Heidarinejad, G. Reconstruction of housing destroyed in the 2003 Bam-Iran Earthquake. In Proceedings of the 100th Anniversary Earthquake Conference: Commemorating the 1906 San Francisco Earthquake, California, CA, USA, 18–22 April 2006.
168. Mostafaei, H.; Kabeyasawa, T. Investigation and analysis of damage to buildings during the 2003 Bam earthquake. *Bull. Earthq. Res. Inst.* **2004**, *79*, 107–132.
169. Bastami, M.; Abbasnejadfad, M.; Motamed, H.; Ansari, A.; Garakaninezhad, A. Development of hybrid earthquake vulnerability functions for typical residential buildings in Iran. *Int. J. Disaster Risk Reduct.* **2022**, *77*, 103087. [CrossRef]
170. Aliaj, S.H.; Baldassarre, G.; Shkupi, D. Quaternary subsidence zones in Albania: Some case studies. *Bull. Eng. Geol. Environ.* **2001**, *59*, 313–318. [CrossRef]

Article

Flood Risk Assessment Using GIS-Based Analytical Hierarchy Process in the Municipality of Odiongan, Romblon, Philippines

Jerome G. Gacu ^{1,2,3} , Cris Edward F. Monjardin ^{1,2,4,*} , Delia B. Senoro ^{1,2,4}  and Fibor J. Tan ^{1,2,4} 

¹ Masters Program in Civil Engineering, School of Graduate Studies, Mapua University, Manila 1002, Philippines

² School of Civil, Environmental and Geological Engineering, Mapua University, Manila 1002, Philippines

³ Civil Engineering Department, College of Engineering and Technology, Romblon State University, Liwanag, Odiongan, Romblon 5505, Philippines

⁴ Resiliency and Sustainable Development Center, Yuchengco Innovation Center, Mapua University, Manila 1002, Philippines

* Correspondence: cefmonjardin@mapua.edu.ph

Abstract: The archipelagic Romblon province frequently experiences typhoons and heavy rains that causes extreme flooding, this produces particular concern about the severity of damage in the Municipality of Odiongan. Hence, this study aimed to assess the spatial flood risk of Odiongan using the analytical hierarchy process (AHP), considering disaster risk factors with data collected from various government agencies. The study employed the geographic information system (GIS) to illustrate the spatial distribution of flooding in the municipality. Sendai Framework was the basis of risk analysis in this study. The hazard parameters considered were average annual rainfall, elevation, slope, soil type, and flood depth. Population density, land use, and household number were considered parameters for the exposure assessment. Vulnerability assessments considered gender ratio, mean age, average income, number of persons with disabilities, educational attainment, water usage, emergency preparedness, type of structures, and distance to evacuation area as physical, social, and economic factors. Each parameter was compared to one another by pairwise comparison to identify the weights based on experts' judgment. These weights were then integrated into the flood risk assessment computation. The results led to a flood risk map which recorded nine barangays (small local government units) at high risk of flooding, notably the Poblacion Area. The results of this study will guide local government units in developing prompt flood management programs, appropriate mitigation measures, preparedness, and response and recovery strategies to reduce flood risk and vulnerability to the population of Odiongan.

Keywords: AHP; digital elevation model; flood; GIS; risk assessment

Citation: Gacu, J.G.; Monjardin, C.E.F.; Senoro, D.B.; Tan, F.J. Flood Risk Assessment Using GIS-Based Analytical Hierarchy Process in the Municipality of Odiongan, Romblon, Philippines. *Appl. Sci.* **2022**, *12*, 9456. <https://doi.org/10.3390/app12199456>

Academic Editors: Andrea Chiozzi, Željana Nikolić and Elena Benvenuti

Received: 17 August 2022

Accepted: 19 September 2022

Published: 21 September 2022

Publisher's Note: MDPI stays neutral with regard to jurisdictional claims in published maps and institutional affiliations.



Copyright: © 2022 by the authors. Licensee MDPI, Basel, Switzerland. This article is an open access article distributed under the terms and conditions of the Creative Commons Attribution (CC BY) license (<https://creativecommons.org/licenses/by/4.0/>).

1. Introduction

Floods are caused by the failure of natural paths and drainage systems to hold excess water during and immediately following excessive rainfall [1]. This condition is among the disastrous natural hazards that can cause tremendous economic loss, damage to infrastructures and natural ecosystems, as well as death. The Organization for Economic Cooperation and Development (OECD) reported that floods trigger more than USD 40 billion in destruction worldwide [2]. The United States loses about USD 8 billion a year due to flooding. Recently, casualties have risen to roughly 100 deaths annually [3] and about 6.8 million were adversely affected by excessive flooding in the northeastern part of India. Nepal, Indonesia, and Japan [4].

According to a study by Monjardin et al. [5], flooding is a dangerous natural phenomenon that has taken numerous lives and caused enormous economic damage in the Philippines. Flood is considered the second most frequent calamity in the Philippines, representing 31.9% of annual natural disasters [6]. The National Council for Disaster Risk

Reduction and Management (NDRRMC) of the Philippines reported on 19 April 2021 that 68,490 individuals were evacuated in Bicol and Eastern Visayas regions due to risk from Tropical Cyclone Surigae (Bising) [7]. Additionally, the Mindanao Island that was formerly considered as a region free from typhoons was devastated by consecutive typhoons, e.g., Sendong (international name, Washi) and Pablo (international name, Bopha). These typhoons altered the usual typhoon pathway and made a new typhoon route. These two typhoons landed in 2011 and 2012, respectively, and caused devastation that killed more than 1000 individuals and 100 people went missing [8]. Further, as mentioned in the study of Siddayao et al. [9], Typhoon Haiyan distressed the Philippines telecommunication signals, power, and water lines on 8 November 2013. In the province of Romblon, floods frequently occur, resulting in losses to the affected municipalities. All rivers and tributaries in the Romblon province overflowed [10] during typhoons. Flood occurrences are frequent in the Municipality of Odiongan, being a low-lying area of Tablas Island, Romblon province.

In the Philippines, flood risk maps are essential for the safety of communities and ecosystems [11]. Decision-makers are looking for longer-term mitigation of the adverse effects of floods and some natural tragedies; hence, confidence criteria in engineered solutions such as flood protection systems are important [8]. Furthermore, the assessment and evaluation of flood hazards must be constructed on accurate flood hazard guides to show the real impact of urban development [12]. Risk assessment is vital in formulating decisions guidelines, policies, and mitigations based on meteorological, hydrological, and socioeconomic factors [13]. Comprehensive flood risk assessment and the enhancement of efficient flood mitigation actions need systematic information regarding flood occurrences at points in a catchment basin [14]. However, specific factors of population, society, economy, environment, transportation, and other disaster-bearing elements in different parts of mountain cities are remarkably varied, which increases the doubt of risk assessment index weight and risk assessment reliability [15]. Hence, accurate hazard maps and least-error indices are important tools in risk assessment.

The GIS tool plays a vital component of flood risk assessment due to the evaluation process that needs spatial information. The practice of a standard approach for evaluation and merging distinctive data affect the precision and comparability of assessment outcomes. Some nations have established national guidelines to assess flood risk potential [16]. In addition, GIS can be utilized to study international, regional, and local flood risks and guide the implementation of a risk mitigation plan [17]. GIS in the Philippines is a primary distinctive tool used in countrywide flood risk modeling. However, existing high-resolution flood risk models have come to be very important. These tools can be used for flood readiness by improving these maps' data levels [18]. ArcGIS, developed by ESRI, is a GIS-based tool that can produce standard Web Services and make numerous network GIS uses [19].

The Digital Elevation Model (DEM) is widely used in GIS modeling, and the enhancement, development, and processing of DEMs are vital in many environmental aspects. It is in the form of a grid as a digital illustration of land with a corresponding pixel value equal to an elevation from the datum [20,21]. According to Suguruman et al. [22], DEMs are used more often in flood risk management, including flood plain models, visualization, flood hazard assessment, and identification of floodplain altitudes. There are numerous sources of DEM information, including Advanced Space Borne Thermal Emission and Reflection Radiometer (ASTER), Synthetic Aperture Radar (SAR), Global Positioning System (GPS), and Light Detection and Ranging (LiDAR) [23]. In the Philippines, hydraulic and hydrologic tools for flood risk analysis are very limited in line with topographic, geometric, and hydrologic river information [24]. The Philippines assimilated geospatial data LiDAR and IfSAR (Interferometric Synthetic Aperture Radar) with excellent resolution Digital Terrain Models (DTMs) covering 300,000 square kilometers of the terrestrial area [25]. This is to deal the insufficient high-resolution topographic maps.

Flooding needs considerable attention, studies have evaluated the connection between urban/rural services, flood history, and disaster readiness in local communities living in

safety [26]. The Sendai Framework acknowledged the critical role played by the community in disaster risk reduction [27]. This framework is used in disaster risk management delivers quantifiable parameters for a national and local scale to calculate the reduction in disaster damages. The compilation and evaluation of disaster damages under the Sendai Framework enhance our knowledge of the efficiency of disaster risk reduction approaches [28].

There is a need to understand the spatial extent of flood zones by utilizing multiple data to show a possible baseline for consistent flood risk management and mitigation measures [29]. The methodology using multicriteria analysis (MCA), also known as multicriteria decision-making (MCDM), supports a basis that can hold distinctive assessment on determining the factors of a composite decision, arrange the aspects into a hierarchical configuration, and analyze the relations amid elements of the identified hazard [30]. All MCA methods make the options and their influence on the different criteria clear. They vary, however, in how they associate all the data needed. The method's primary role is to solve the difficulties that decision-makers have encountered when handling a large quantity of complex information. MCA can be used to recognize a single most preferred option, rank options, shortlist a limited number of options for subsequent detailed evaluation, or differentiate conventional from unconventional possibilities [31].

Several approaches have been suggested for MCA, but the Analytical Hierarchy Process (AHP) is being used most frequently to resolve different flood risk assessments [32]. The AHP provides the same advantage as MCA models in focusing decision-maker consideration on developing a structure to gather all the significant factors expected to differentiate the best option [31,33]. AHP represents the problem in three parts where the first part is the matter that needs to be fixed, and the second part is the alternative solutions available to resolve the problem. The third and most important process is the criteria expended to assess the alternative solutions [34]. Studies on flood risk assessment in Thailand [26,35], Bangladesh [36], and Indonesia [37] used GIS and AHP. Additionally, in the Philippines, identified relevant flood factors and judgments of decision-makers were analyzed using AHP judgments to weigh each parameter in estimating flood hazards in the study [38] at the central business district of Tuguegarao City, Philippines. Another study was conducted in Infanta, Quezon Province, Philippines, aiming to give the municipality options and models for flood mitigation. The drainage system in said municipality is at risk of causing flood-related problems deliberating identified relative factors via AHP [6]. The evaluation of flood zones and flood problems for Davao Oriental, Philippines, were analyzed by the AHP and Maxent tool which reduce the subjectivity and uncertainty in selecting and weighting criteria [8]. The rareness of using AHP-based research made it easier to make a model of indecision without compromising the subjective and objective aspects of the assessment process [29]. Hence, the number of flood events in the Municipality of Odiongan that caused property damage to the community explicitly need the output of this research study. The results of this assessment will be used as the basis for the municipality's flood mitigation and risk management. Additionally, the information will useful in areas with similar topography and weather conditions.

2. Materials and Methods

2.1. Study Area

The study area is the Municipality of Odiongan located in the middle west portion of Tablas Island, Romblon province with coordinated of 22°04' East Longitude and 12°19' North Latitude. Odiongan has a land area of 185.67 square kilometers representing 12.11% of Romblon province. The town proper lies in the low-lying plains, and the interior part of the municipality is composed of hills and mountainous forests. Odiongan consists of 25 barangays and 1 anchorage, which is linked to other neighboring islands. Figure 1 shows the imagery map of Odiongan with barangay boundaries.

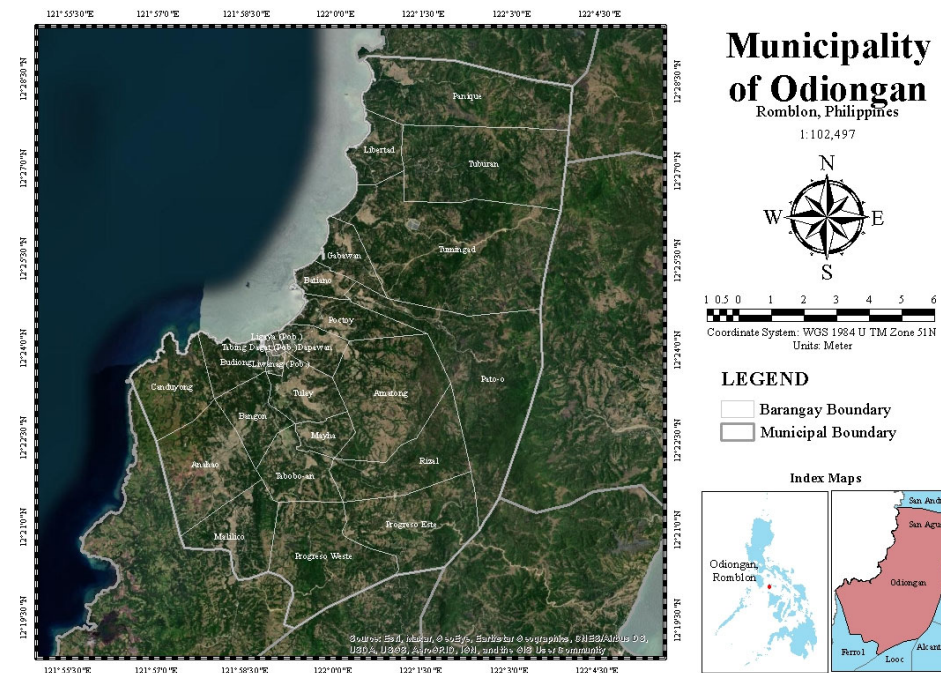


Figure 1. Imagery map with barangay and municipal boundaries of the study area.

2.2. Data Collection and Identification of Factors

The Sendai Framework was followed to identify flood indicators in assessing flood disaster risk, hence identifying the parameters and the data that need to be collected. There were three identified categories of flood risks parameters, such as (a) hazard, (b) vulnerability, and (c) exposure. The hazard parameters considered were: Average annual rainfall, slope, elevation, soil type, and flood depth. The parameters for vulnerability that were considered were: Gender ratio, age, average income, physical health of the individual, educational attainment, water usage, emergency preparedness, types structures, and proximity to the evacuation center. The parameters for flood exposure were: Population density, number of households, and land use/details are shown in Table 1.

Table 1. Parameters with the type of data used, duration/year, and source used for hazard, vulnerability, and exposure assessment.

References	Parameter	Data Type	Duration/Year	Source
Flood Hazard Parameters				
[8,17,35,39–41]	Average Annual Rainfall	Interpolated Climatological Normal using Isohyetal Method	2020	PAGASA and web search for weather station coordinates
[8,17,26,32,35,41]	Slope	Derived from IfSAR Data using Slope Tool in ArcMap	2013	(NAMRIA-DENR)
[6,8,26,32,35,41]	Elevation	Derived from IfSAR Data using Field Contour Tool in ArcMap	2013	(NAMRIA-DENR)
[8,9,17,42]	Soil Type	Shapefile from the archive of CLUP	2011	Municipality of Odiongan, Romblon—(CLUP)
[37,43–45]	Flood Depth	100-year period of flood model simulated in HEC-HMS and HEC-RAS and MGB Flood Susceptibility Map	2018	MGB
Flood Vulnerability Parameters				
[39,43]	Gender Ratio	Men to women gender ratio	2020	Barangay Profile
[43]	Average Age	Mean age of the individual	2020	Barangay Profile
[31,43]	Average Income	Annual average income per household	2020	Barangay Profile
[39,46]	Number of Persons with Disabilities	Number of PWD in barangay	2022	Barangay Management System (BMS)
[43,46]	Highest Educational Attainment	Average educational attainment of individuals in barangay	2020	Barangay Profile

Table 1. Cont.

References	Parameter	Data Type	Duration/Year	Source
[46–48]	Water Usage	Primary source of water	2022	Survey Questionnaire
	Emergency Preparedness	Emergency preparedness during unexpected situations like natural disasters	2022	Survey Questionnaire
[29]	Types of Built-up Structures	Classification of structures of every household	2020	Barangay Profile
	Distance from the nearest Evacuation Area	Distance of identified evacuation area using buffer tool in Arcmap	2022	Site Investigation and Survey Questionnaire
Flood Exposure Parameters				
[9,29,40,42,49]	Population Density	Computed from the population over the covered area of the barangay	2020	PSA
[43]	Household Number	Number of households of every barangay	2020	PSA
[6,17,26,35,40,41]	Land Use/Land Cover	Land cover map from CLUP	2011	Municipality of Odiongan, Romblon—(CLUP)

2.2.1. Flood Hazard Parameters

Flood management cannot be adequately completed without assessing flood hazards [48]; therefore, details of indicators are elaborated below.

1. Average Annual Rainfall

Precipitation values were plotted on a suitable base map at their respective stations using isohyetal method, and isohyets were drawn to create an isohyetal map. The study used the climatological normal records [50] from long-term averages over 30 years of PAGASA weather stations (Figure 2) with corresponding coordinates. Spatial interpolation employing the isohyetal method was applied to obtain dimensional rainfall patterns for projections of Romblon.

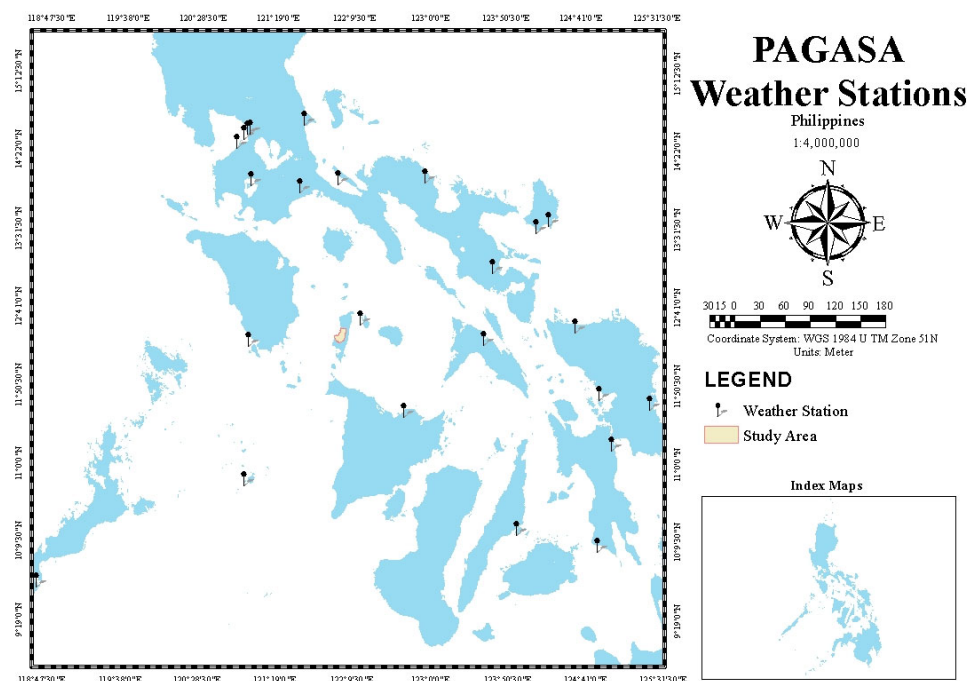


Figure 2. Weather stations considered in the interpolation for average annual rainfall using the Isohyetal Method.

2. Slope

The slope is a critical factor contributing to the intensity of destructive forces of floods in a particular area. The study prepared the slope map using the IfSAR DTM from National Mapping and Resource Information Authority (NAMRIA) and the spatial tool in the GIS application platform.

3. Elevation

Ground elevation is one of the main factors that should be considered in assessing flood hazards. IfSAR data were utilized and processed in the GIS tool.

4. Soil Type

The study used the soil map based on the map of NAMRIA stipulated in the Comprehensive Land Use Plan (CLUP) [51] of the Municipality of Odiongan. These data were correlated to the soil's water holding capacity and infiltration rate.

5. Flood Depth

ArcGIS, HEC-HMS (Hydrologic Engineering Center's—Hydrologic Modeling System) [52] and HEC-RAS (Hydrologic Engineering Center's—River Analysis System) [53] were the tools used for flood hazard simulation. The most important data used in the simulation were the DEM, which were provided by NAMRIA with a resolution of five-by-five (5×5) meters. A combination of simulated maps and Flood Susceptibility Maps [54] from the Mines and Geoscience Bureau (MGB) were used in the study.

2.2.2. Flood Vulnerability Parameters

The vulnerability factor includes social, economic, and personal safety [44]. Demographics and disaster risk reduction data of the Municipality of Odiongan were gathered through actual surveys (questionnaire) and existing records of the local government of Odiongan.

1. Demographics

The demographic data were gathered from the database of Philippine Statistics Authority (PSA). The period considered was 2015 to 2020. The on-site survey was conducted in every barangay of the Municipality of Odiongan.

2. Disaster Risk Reduction Data

All data were extracted from the survey conducted in every barangay and CLUP of the Municipality of Odiongan. The barangay identified evacuation facilities where coordinates and floor areas were recorded using GPS and area measuring tools.

2.2.3. Flood Exposure Parameters

The exposure analysis was aimed at identifying the life and property elements exposed in flooding events [41]. The identified exposure elements were population density, number of households, and land use/cover. The data were taken from the PSA record and municipal zoning maps archived from CLUP of the Municipality of Odiongan.

2.3. Modeling, GIS Mapping, and Validation

Generated models and maps from ArcGIS were the primary basis in the computation and analysis of final flood risk indices.

2.3.1. Basin Model Pre-Processing

In creating a basin model of Odiongan River channels (Bangon River), IfSAR-DEM with a $5 \text{ m} \times 5 \text{ m}$ resolution was used. Data were processed using the GeoHMS10.7 tool plugin in ArcGIS 10.7. This is to generate a basin model and incorporated with the available soil and land cover data of 2004 from NAMRIA to assign curve numbers (CN) for each sub-basin. Soil type and land cover classification were represented as CN for each sub-basin. Initial abstraction (IA), time of concentration (TC), Storage Coefficient (SC), River Length, and sub-watershed area were derived during the pre-processing of the basin model.

2.3.2. Basin Model Calibration and RIDF Simulations

The pre-processing output of the HMS Basin Model was calibrated under the HEC-HMS 4.9 software to model the hydrologic response of the watershed to a specified hy-

drometeorological input. The parameters' values were tuned to attain an at least acceptable result in all the statistical measures recommended for model evaluation. As the model was calibrated, the simulations of rainfall scenarios of 25-, 50-, and 100-year followed. The rainfall intensity duration frequency (RIDF) data were acquired from PAGASA Romblon, Romblon province rain gauge station with 48-year rainfall records. These data were entered as the meteorological model file using the frequency storm precipitation method in HEC-HMS performed with calibrated basin model. The outputs of the simulations were then calibrated basin model with precipitation and outflow data of the three (3) return periods.

2.3.3. Two-Dimensional (2D) RAS Model Simulations

The processed DEM was used to create the river analysis model (RAS) model using the HEC-RAS 6.2, a practical river hydraulic simulation and analysis software. The RAS model was processed through unsteady flow analysis, and the boundary conditions used were flow hydrograph in the upstream and normal depth in the downstream which considers both the frictional resistance and slope of the channel. The calibrated outflow in HMS and precipitation were incorporated into the model. Flood depth considering a 100-year return period was regarded as one of the parameters in hazard mapping; this was exported as raster files and translated into spatial data in the GIS.

2.4. Evaluation and Assessment of Parameters Using AHP

Contributing factors were identified and assessed in which the weights of each parameter were determined using AHP based on the knowledge of experts composed of end-users, hydrologists, meteorologists, water resource engineers, and persons with comprehensive expertise in disaster risk reduction. Experts from government agencies such as PAGASA, Bureau of Soils and Water Management (BSWM), and MGB participated in the survey. A specialist from academic institutions (University of the Philippines, Mapúa University, Central Luzon State University, and Asian Institute of Technology) and an end-user (LGU-Odiongan) also responded to the survey. The survey for pairwise comparison was delivered and requested thru an online and printed-out questionnaire. A risk assessment was proceeded using the weights of each factor derived in AHP through a pairwise comparison questionnaire.

2.4.1. Determination of the Priorities among the Decision Elements of the Hierarchy

The feature weights were assigned parameters, where levels were reclassified and normalized into 1 for the least priority and 5 for the most focused. This step gathered the weight for each criterion and option using a pairwise comparison technique. Ten (10) experts on-field and end-users participated in determining the relevance of one alternative over the other with a pairwise comparison method presented in a matrix.

Each comparison was graded by experts and end-users using the pairwise comparison technique scale. The procedure usually contains a questionnaire for comparing all the elements and a geometric mean to arrive at a final solution [32] specifying the nine points intensity matrix, as shown in Table A1 of Appendix A.

2.4.2. Derivation of the Overall Relative Weights

The relative significance or weight of the factor after a pairwise comparison matrix was computed based on systematic AHP assessment and expert's inputs. This step was conducted by calculating the normalized values for each criterion and alternative, and choosing the normalized main priority vectors. Normalized values for each criterion and alternative in their respective matrices were derived by dividing each cell into its column and producing a total column of 1 for each criterion and alternative. Weights were calculated by averaging the rows of the matrix. The resulting value will give relative weight to every criterion concerning the best goal, and provide relative weight for the alternatives with respect to the criteria. The final relative weights of the alternatives were defined by computing the product's linear combination (LC) between the relative weight

of each criterion and the alternative for the specific criterion. The decision-makers choose the best according to the alternatives' overall weights if the experts' judgments are proven consistent. This is mathematically expressed using Equation (1).

$$C = \{C_j | j = 1, 2, \dots, n\} \tag{1}$$

The pairwise comparison on the criteria can be generalized using an evaluation matrix A , as shown as Equation (2), in which every element is the quotient of weights of the criteria given in Equation (3) [32].

$$A = \begin{bmatrix} a_{11} & a_{12} & \dots & a_{1n} \\ a_{21} & a_{22} & \dots & a_{2n} \\ \dots & \dots & \dots & \dots \\ a_{n1} & a_{n2} & \dots & a_{nn} \end{bmatrix}, a_{ii} = 1, a_{ji} = \frac{1}{a_{ij}}, a_{ij} \neq 0 \tag{2}$$

2.4.3. Verification of the Consistency of Judgments and Conclusions according to Results

AHP's quality output was related to the consistency of the pairwise comparison judgments. This step was essential to identify the consistency of the assessment by computing the consistency ratio (CR) before a decision was completed. However, if the problem was expected during deliberation for choosing the best alternative, the CRs for matrices were computed initially before the alternatives' overall relative weights were calculated. After which, calculations were performed to obtain the largest eigenvalue, consistency index (CI), CR, and normalized values for each criterion and alternative.

The last mathematical process normalized and identified the relative weights per matrix. The right eigenvector gave the relative weights (w) conforming to the highest eigenvalue (λ_{max}), as shown in Equation (3).

$$Aw = \lambda_{max}w \tag{3}$$

If the pairwise comparisons were consistent, the matrix A was ranked one and $\lambda_{max} = n$, so the weights can be taken by normalizing any of the rows or columns of A [32]. The relativeness between the entries determines the consistency, and the CI was calculated using the equation below:

$$CI = (\lambda_{max} - n) / (n - 1) \tag{4}$$

The final CR , which enables the decision-maker to accomplish whether the assessments were adequately coherent, was computed as the CI 's and the random index (RI) quotient using Equation (5).

$$CR = CI / RI \tag{5}$$

One recommendation for this step was: if the proportion exceeds 0.1, the judgment was considered inconsistent. Therefore, a consistency ratio must be below 0.1 or 10%. The process was reiterated if the evaluation was unpredictable until the CR was within the wanted scale. The user formulated a conclusion according to the assessment results [32].

2.5. Development of Flood Risk Map

In this study, Sendai Framework was the basis to evaluate the flood risk by integrating the three (3) criteria, e.g., hazard, vulnerability, and exposure. The result of the flood risk assessment was laid into a map for a better comprehension of it. The last phase of the methodology was to overlay the analysis technique using ArcGIS. The GIS tool generated two or more different thematic maps of a similar area. It overlapped them on top of one another resulting in a new map using the weighted overlay tool. This technique results in a calculation matrix that defined the primary change forms in a study location [26]. The weighted overlay analysis results were developed employing equal intervals with four (4) levels (very low, low, moderate, and high). Flood risk map results were also validated by

doing actual ground assessment of the localities in Odiongan, Romblon, and by reviewing identified flood zones in the area using records of historical flood events.

3. Results

3.1. Data Analysis for Identified Parameter

The result of data collection gathered through related literature, and past research studies were put into maps and analyzed. Each map has a scale of 1:100,000 and mainly focuses on identified parameters enumerated in Table 1 and detailed in Section 2.2. Subsequent sections elaborated the results.

3.1.1. Flood Hazard Parameters

Figure 3 shows the maps for every parameter of the Municipality of Odiongan, Romblon province, based on hazard criteria. It was noted that 2203.9 mm was the recorded average annual rainfall by the Romblon Weather Station. The average annual rainfall of the municipality was classified according to interpolation. Figure 3a shows the generated map from ArcMap using the Isohyetal Method with an average annual rainfall ranging from 2200 to 2250 mm. The amount of rain intensifies from the eastern part to the western part of the municipality.

The result of the reclassified slope layer was presented in Figure 3b and categorized in degrees where the green color means the lowest elevation. At the same time, the red part indicates the highest slope. Most maps show a higher slope ranging from 18 degrees to 50 and above. Residential areas were located in the plain areas (green part) where water accumulated during excessive rainfall.

Figure 3c shows the elevation map of the study location extracted using the IfSAR DTM. The elevation was classified into five (5) levels ranging from 0 to 600 m. Most of the map shows a high elevation of 21 to 600 m. The eastern part of the municipality, where the residential and commercial area was located, has the lowest elevation value, varying from 0 to 20 m. These elevations affect how rapidly stormwater could be drained into the catchment based on its slopes.

The slope map shown in Figure 3d was prepared as a shapefile from the Odiongan CLUP 2015. The map was sorted according to its Hydrologic Soil Group (HSG). Soils were classified by the Natural Resource Conservation Service based on the soil's runoff potential. Group A-class (sand, loamy sand, or sandy loam types of soils) has low runoff potential and high infiltration levels, even when fully saturated. They contain chiefly deep, well-drained to excessively drained sands or gravels, and have a high rate of water transmission. Group B is silt loam or loam. It has a moderate penetration rate when fully saturated and consists of moderately deep to deep, well-drained soils with relatively fine to coarse textures. Group C soils are sandy clay loam. They have low infiltration levels when thoroughly wetted. They consist chiefly of soils with a layer that impedes the downward movement of water and soils with moderately fine to fine structure. It is observed that most of the map falls under Group C. The eastern part of the municipality is mainly silt loam or loam. The map shown in Figure 3e is the overlaid flood depth map combined with the MGB Flood Susceptibility Map (see Figure A1) and further discussed below.

In the simulation or modeling process, as a result of delineation, there were 32 watersheds, 16 junctions, and 16 reaches extracted, as shown in Figure 4.

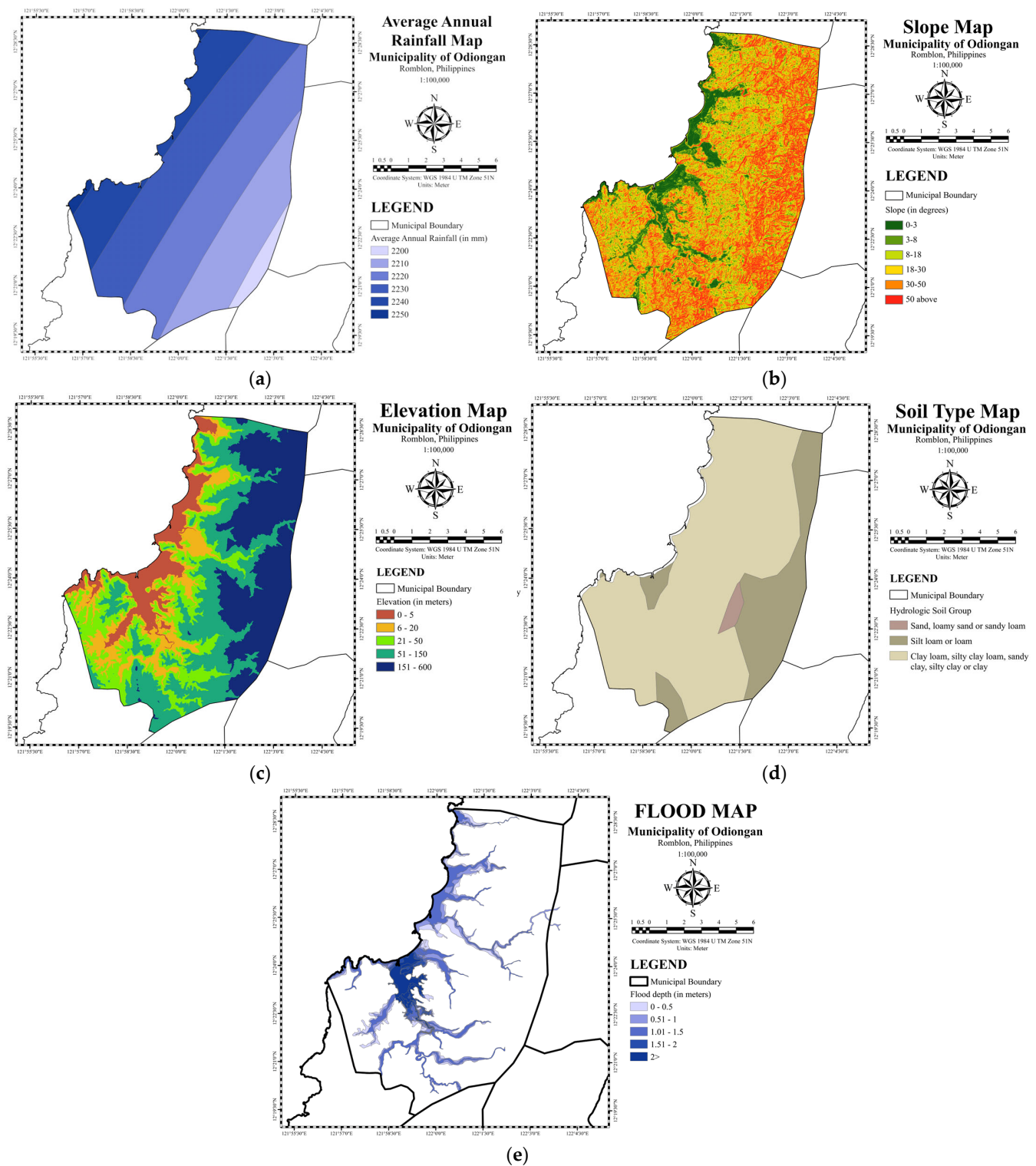


Figure 3. Maps generated using ArcGIS in flood hazard parameters: (a) Average Annual Rainfall Map; (b) Slope Map; (c) Elevation Map; (d) Soil Type Map; and (e) Flood Depth map of Odiongan, Romblon.

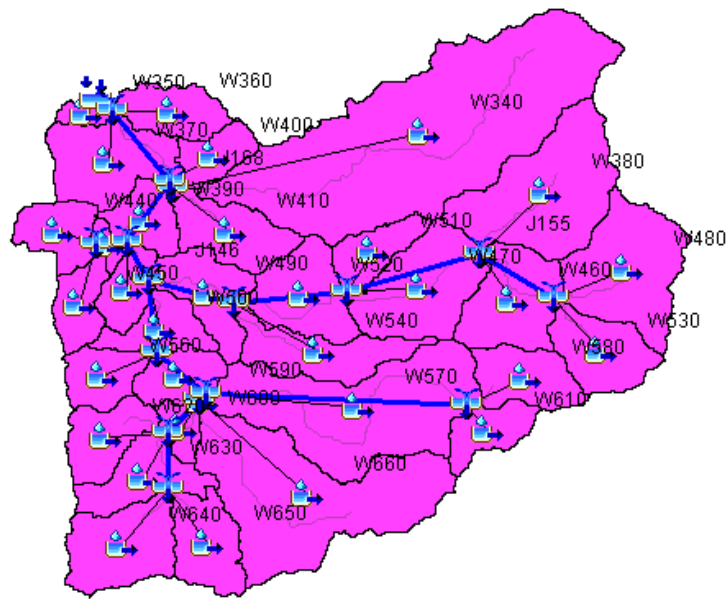


Figure 4. Extracted Basin Model of Odiongan, Romblon using GeoHMS10.7 tool in ArcpMAP.

The results from the basin model for 25-, 50-, and 100-year (Figure 5) simulation were exported to excel for the data preparation for hydraulic modeling in HEC-RAS and recorded 2.9 m³/s as its total highest inflow.

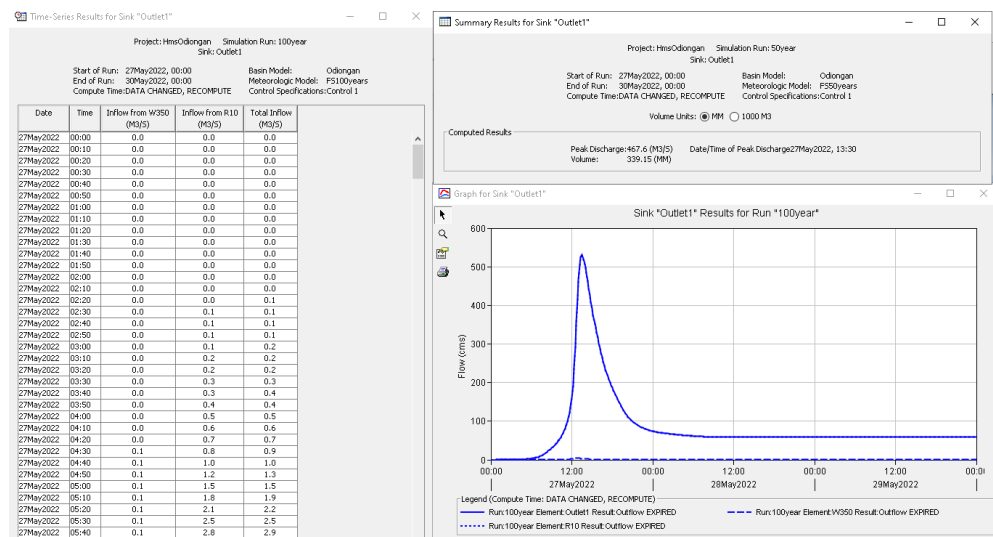


Figure 5. Simulation of total inflow results in 100-year using HEC-HMS.

Figure 6 shows that flood depth for all the periods led to a drastic result in a possible flood for the Poblacion area and nearby barangays from the watershed. Based on the simulation, about 5.87 m of flood height were recorded in the worst-case scenario of a 100-year return period. Flood depth with the 100-year model, considered one of the parameters, was exported as raster files from HEC-RAS and mapped to the layers in GIS.

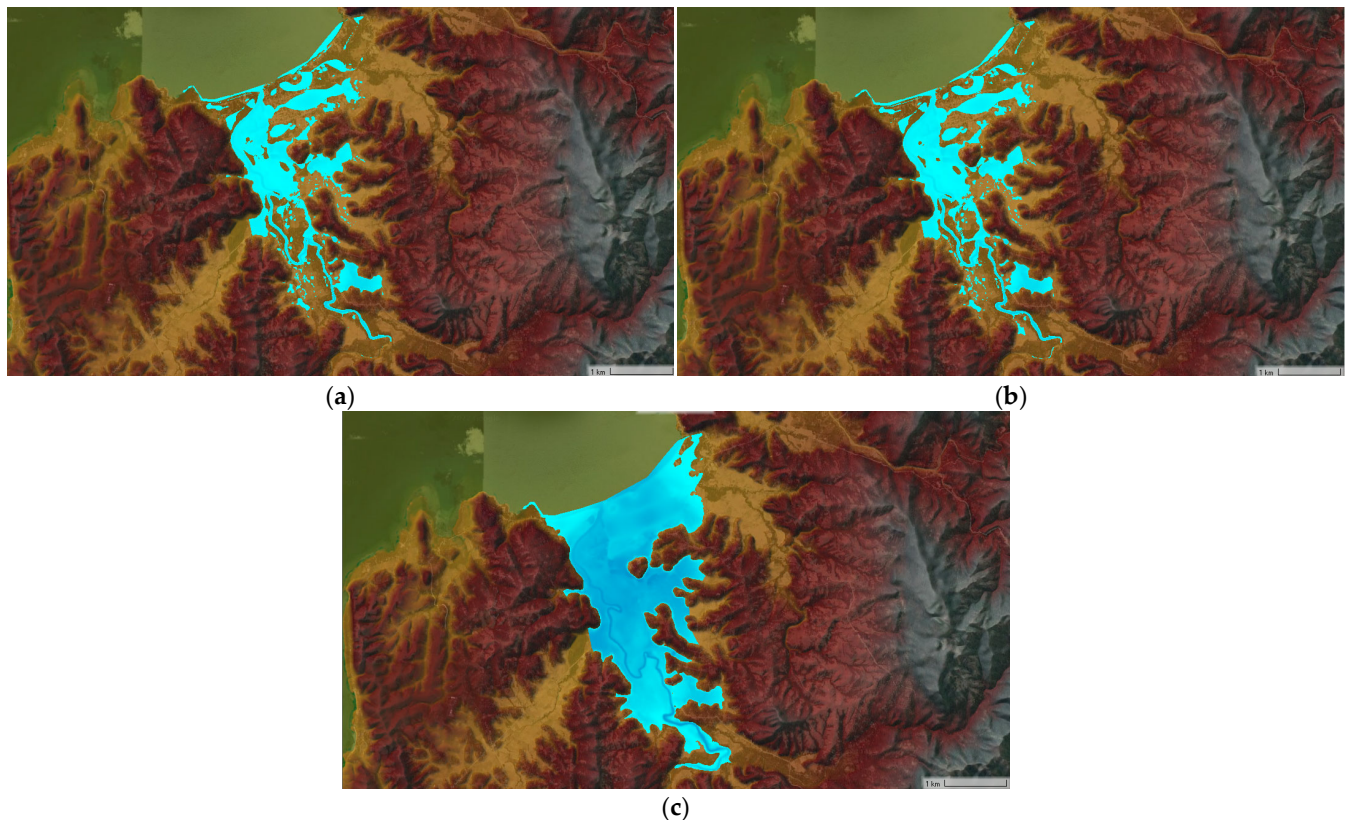


Figure 6. Simulation of maximum flood depth in the main river (Bangon River) of Odiongan, Romblon using HEC-RAS for (a) 25 years, (b) 50 years, and (c) 100-year period.

Modeled flood depths were categorized into five (5), e.g., (1) 0–0.5 m (low), (2) 0.5–1 m (moderate), (3) 1.01–1.5 m (high), (4) 1.51–2 m very high, and (5) 2 m and above is considered extremely high. These ranges were based on the Mines and Geosciences Bureau’s Flood Susceptibility maps wherein low susceptibility can experience flood heights of less than 0.5 m and a flood duration of less than one (1) day. These included low hills and gentle slopes. It has also spared moderate drainage density. Moderate susceptibility areas were expected to experience flood depths of 0.5 m to 1 m. These spaces are prone to widespread inundation (flooding) throughout long and extensive heavy rainfall and extreme weather conditions. In areas of high susceptibility, where flood height is 1 meter or more with a time of recession of 3 days, are immediately flooded during heavy rains of several hours. The map indicated that most of the area has an adequate slope where only exposure to flood happens in the low-lying zone. Based on the 100-year flood model, the flood surge was concentrated in the town proper of Odiongan with a depth of 3 m for rainfall that occurred in two (2) days based on simulations.

3.1.2. Flood Vulnerability Parameters

This study considered the demographics and disaster risk reduction data of the Municipality of Odiongan. Figure 7 shows the maps from the available archival and survey data showing the population age, gender ratio, average income, physical health of the individual, educational attainment, emergency preparedness, and variety of built-up structures.

The men to women gender ratio in the Municipality of Odiongan, as shown in Figure 7a, has recorded more women than men. Barangay Amatong, Rizal and Progreso Este showed only a majority number of men to women. For the total men-to-women gender ratio of Odiongan, it was recorded that the population of women and men is almost the same with a ratio of 0.99991.

The mean age of an individual was considered a parameter. The numbers were taken from each barangay database. Mean age was calculated for all the group data as per age category. As per the results, as shown in Figure 7b, the majority of participants were between 30 and 39. Barangay Pato-o, Amatong, Dapawan, and Bangon have the lowest age range of 29 to 30, while Anahao obtained the highest mean age with 37 to 38 age level.

The average income of individuals was mapped per barangay stipulated in each barangay profile. As shown in Figure 7c, the average annual income per barangay was classified under six (6) levels. Most of the average income ranges from 100,000 to 500,000. However, Barangay Amatong, Bangon, Anahao, Malilico, and Progreso Este have the lowest income, having 40,000 and below.

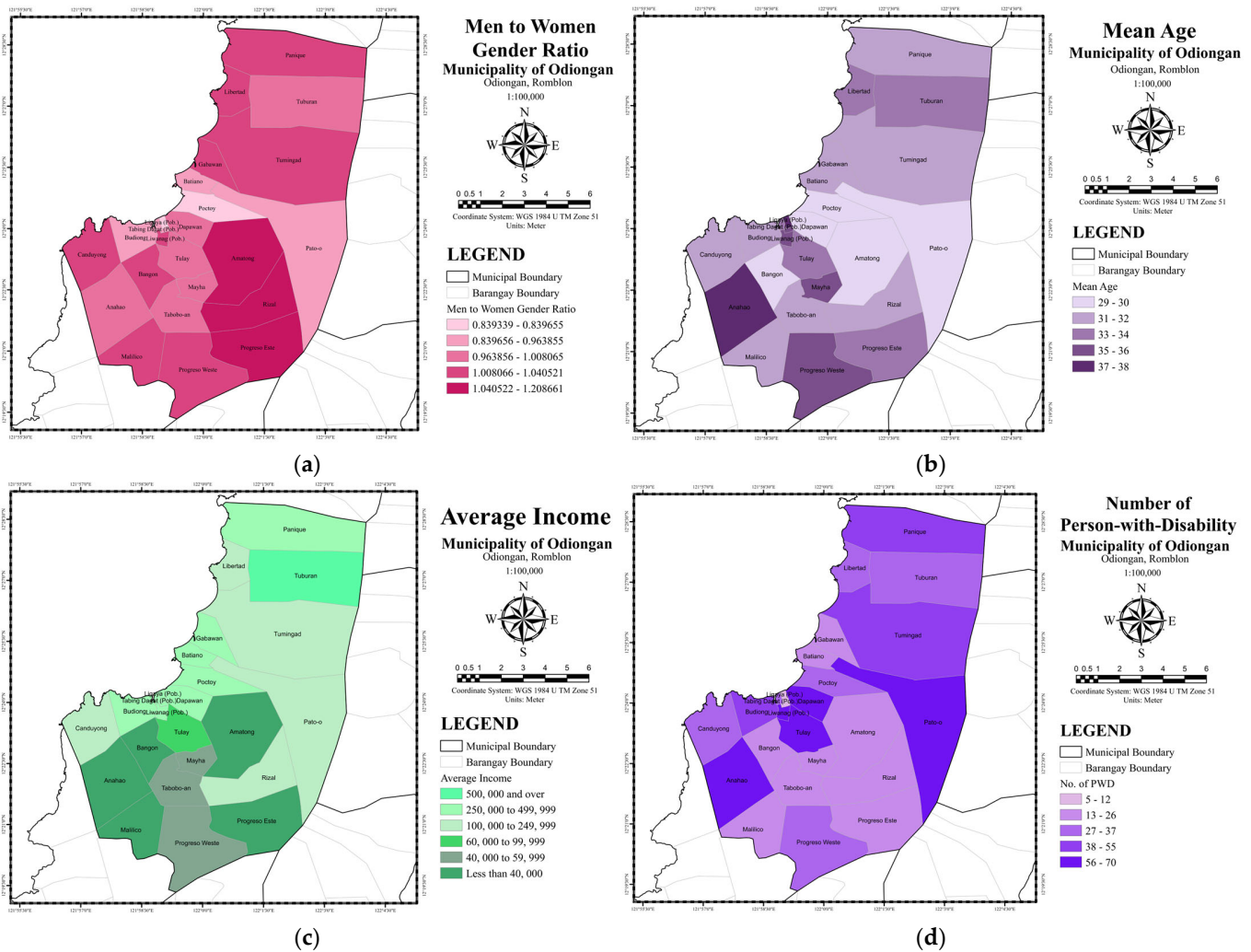


Figure 7. Cont.

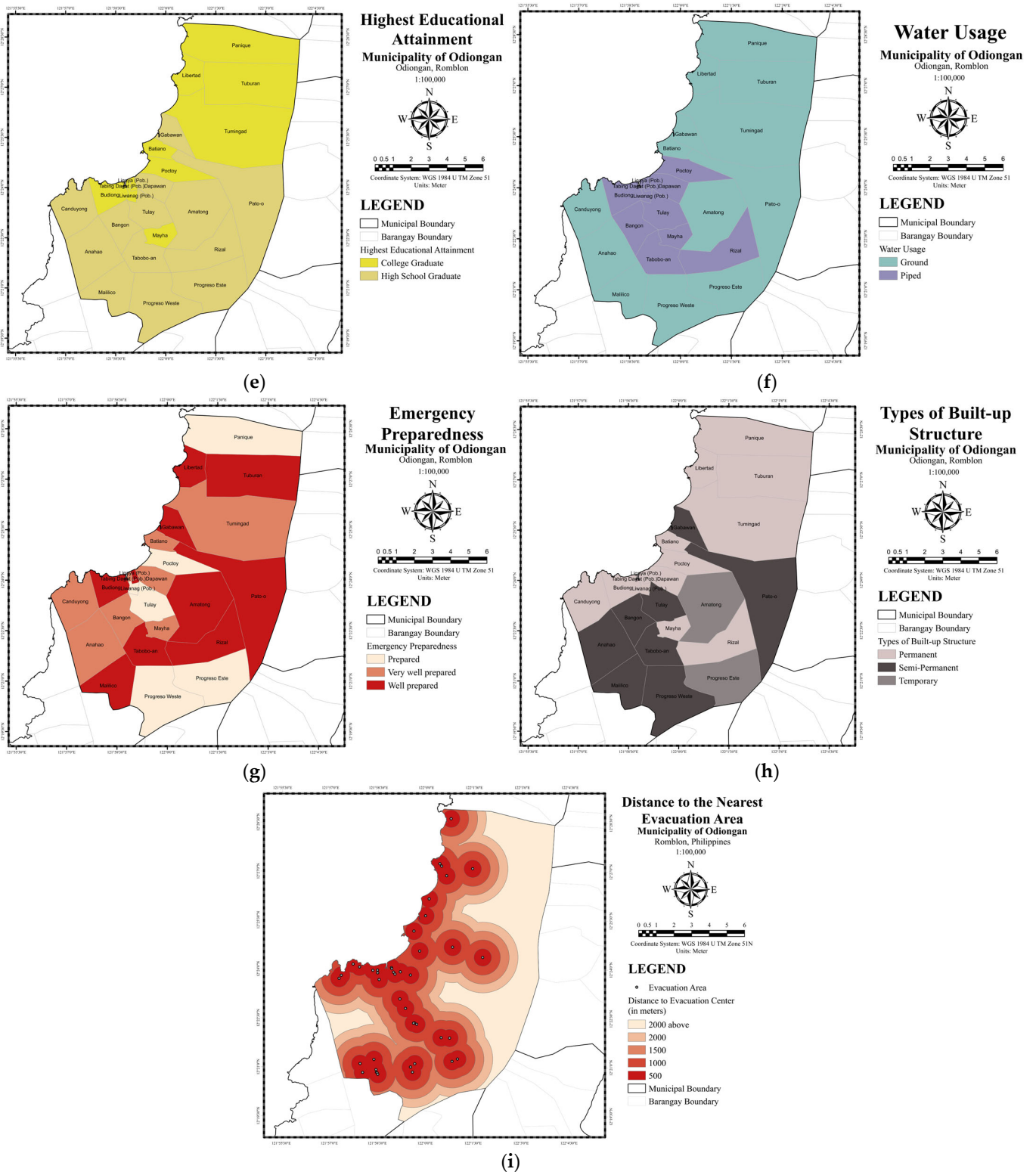


Figure 7. Result maps for flood vulnerability parameters in Odiongan, Romblon using ArcMap: (a) Gender Ratio; (b) Mean Age; (c) Average Annual Income; (d) Number of PWD; (e) Highest Educational Attainment; (f) Water Usage; (g) Emergency Preparedness; (h) Types of Built-up Structure; and (i) Distance to the Nearest Evacuation Center.

1. The floods that hit the areas have disrupted public health and are a subject that has become increasingly important daily due to society’s reactions to hazards [55,56].

With a lack of health information, the study considered the number of PWD in each barangay. Under RA 10524, it refers to individuals who agonize long-term physical, mental, intellectual, or sensory impairments that may obstruct their full and practical involvement in society on an equal basis upon interaction with various barriers. The seven types of disabilities mentioned in RA No. 7277 are psychosocial disability, disability due to chronic illness, learning disability, mental disability, visual disability, orthopedic disability, and communication disability [56]. The number of PWD was based on the Barangay Management System (BMS). Records of the number of PWD in Odiongan, Romblon, as shown in Figure 7d, signify a risk in flood events or other natural disasters. The highest number of PWD are in Barangay Anahao, Pato-o, Tulay, and Dapawan, where Tulay and Dapawan experience flood events every year. However, many PWDs were observed in the southern and northern parts of the municipality, excluding barangay Anahao.

2. The higher the level of education a respondent from a household has, the more likely the individual evacuates [57]. The data used in the study were based on a questionnaire survey conducted in each barangay. Only two categories recorded the highest educational attainment in Odiongan, Romblon, as shown in Figure 7e. More than half of the barangays indicate some high school graduate, and almost half were categorized as college graduates.

The research also incorporated water usage (Figure 7f) as a vulnerability parameter as an additional parameter in disaster risk reduction information. The source of information was a questionnaire survey where the head of barangays was asked for the primary source of water supply. Information was also verified in the records and data of Odiongan Water District. From Barangay Rizal down to the Poblacion (Dawapan, Liwanag, Liwayway, Ligay, Tabin-Dagat) area have access to pipe water. According to the data validated from the Odiongan Water District, 11 out of 25 barangays were supplied by piped water, where the main tank and reservoir are from Barangay Rizal. However, as Romblon is given such a water source, water supply from electric pumps and wells was installed for some barangays.

The emergency prepared data were based on a survey questionnaire's knowledge and input from the head of barangays. The emergency preparedness map is shown in Figure 7g and was classified into three (3) categories, e.g., prepared, well prepared, and very well prepared. It was noticed that only 5 out of 25 barangays, namely, Progreso Weste, Progreso Este, Tulay, Poctoy, and Panique, have been categorized as "prepared" barangays during calamities.

3. Type of Built-up Structures

The combination of information was taken from the barangay profile as of 2018, and a questionnaire survey was conducted. Figure 7h shows the types of built-up structures and are classified into three (3) categories. These are the (a) permanent, (b) semi-permanent, and (c) temporary shelters. Permanent buildings are structures with concrete foundations and walling, GI sheets as roofing, and other solid materials. Semi-permanent structures are a combination of lumber and concrete elements. Temporary shelters use sawali, bamboo, nipa, and cogon as construction materials. The map shows that most of the barangay have permanent and semi-permanent structures. This indicated that most of the homes in Odiongan are more resilient in terms of flood events. However, eight (8) barangays in the elevated area have residential structures categorized as temporary shelter. Consistent findings were proven in the previous research regarding households' housing types as a significant factor in flood vulnerability [43].

Coordinates were noted and listed during site investigations and measured the floor area to estimate the capacity of every room area during calamity (see Figure A2). Figure 7i shows the ideal coverage of every evacuation area in the municipality on which 500 to 2000 m circles around each evacuation center were drawn and categorized into five (5) levels. The map shows the number of people who can reach the facility within an acceptable

walking distance. In this map, the ideal number of people have been identified for each evacuation center during a disaster.

The Sphere standards imply that in the instant aftershock of a disaster, particularly in dangerous climatic conditions where quarter materials are not readily available, an area of no less than 3.5 square meters per person is suitable to save lives and provide adequate short-term shelter. As an evacuation center is utilized preferably only for a short duration, a center’s maximum ‘event sheltering’ capacity should permit no less than 1.5 square meters per person [55].

3.1.3. Flood Exposure Parameters

There were three (3) identified parameters for flood exposure assessment. Figure 8 shows the population density data, land use map, and household numbers from the CLUP Odiongan and PSA Database.

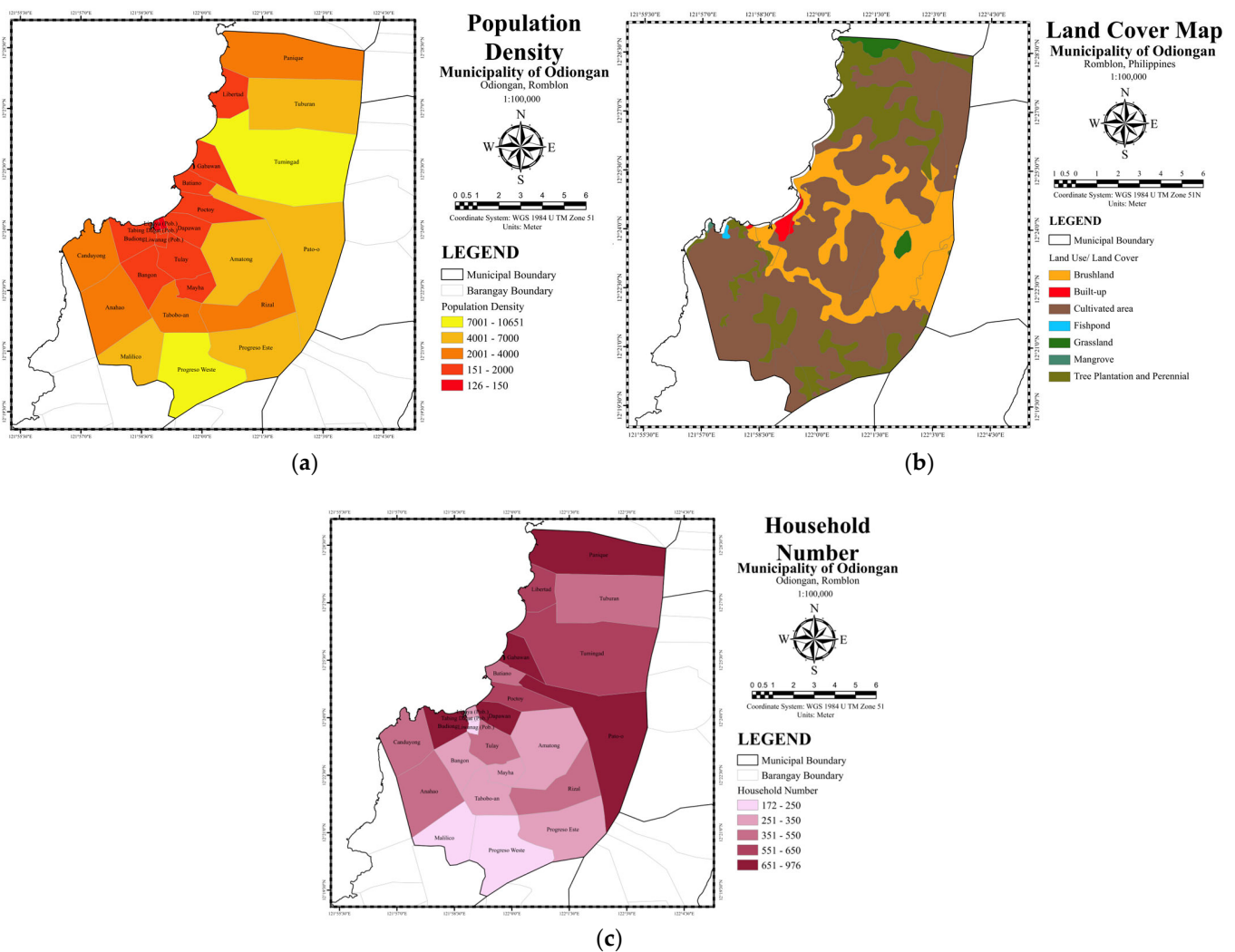


Figure 8. Result maps for flood exposure parameters in using ArcMap: (a) Population Density; (b) Land Use Map; and (c) Household Number.

Figure 8a shows the Population Density in the Municipality of Odiongan. The map demonstrates that population density is low in the nearby Poblacion area or where the center of the municipality is located. Barangay Ligaya and Liwayway as the lowest population density followed by Tabin-Dagat, Dapawan, Budiong, Liwanag, Bangon, Tulay,

Mayha, Batiano, Gabawan, and Libertad. However, Barangay Tumingad and Progreso Weste displayed a high population density.

Land use and land cover type are vital factors responsible for flood incidence. The land cover represents the physical (water, bare ground, and artificial structures) and biological (grass and trees) land cover. In contrast, land use describes how men utilized the land to improve their state of living [58,59]. The occurrence of flooding was inversely related to vegetation density. The study area's land cover classes were prepared from the municipal's CLUP. The land cover map was reassigned by categorizing the land-use types into seven (7) general categories. The map shown in Figure 8b indicates that most of the municipality's land area was cultivated. Brushland is observed in the center part of the map, while the scattered site of tree plantation and perennial were seen on the map. The built-up zone is located in the town proper of the municipality.

Evacuation decision before (preemptive) or during (forced) a disaster indicates the choice of households to evacuate or stay in the area at risk of impending hazard [43]. The household number was considered one of the parameters in assessing exposure. The study obtained the data from PSA's last 2020 census. Presented in Figure 8c is the range of the number of households for every barangay in the municipality. It was recorded that a high number of households in Baranagay, Panique, Pato-o, Gabawan, Dapawan, and Tabin-Dagat were exposed to flood events. Between 172 and 250 households, which was the least number, were observed in Liwanag, Liwayway, Barangay Malilico, and Progreso Weste. However, Liwanag and Liwayway have small land areas that cater only to some houses.

3.2. Evaluation and Assessment of Parameters

Contributing factors were evaluated and assessed.

The decision was segregated into its independent components. It was presented in a hierarchy diagram of at least three levels: goal, criteria, and indicators. The study structure using AHP was shown in Figure 9, wherein the uppermost place of the hierarchy is the primary goal of having a flood risk map. The lower level of the order contains the criteria contributing to attaining the goal: flood hazard map, flood vulnerability map, and flood exposure map. Finally, the lowest level included the indicators: average annual rainfall, elevation, slope, flood depth, soil type, gender ratio, individual age, average income, number of PWD, highest educational attainment, water usage, emergency preparedness, types of built-up structures, distance to evacuation area, population density, land cover, and number of households. The featured weight was assigned for each parameter, where were reclassified and normalized. Assigned values depend on the type of level or category. Table 2 indicates the feature weight of every indicator. The results of the weights computed using the AHP based on experts' inputs are shown in Table 3. These are the final weights of each parameters identified through AHP and was ensured to pass the consistency index requirement for it to be considered as valid.

Table 2. Standard matrix for hazard parameters.

	AAR	E	S	ST	FD	Weights	Percentage Weights
AAR	0.224979	0.221826	0.259802	0.194982	0.228034	0.225925	23%
E	0.208256	0.205338	0.197392	0.202930	0.208920	0.204567	20%
S	0.154522	0.185622	0.178439	0.193329	0.188299	0.180042	18%
ST	0.196749	0.172539	0.157384	0.170516	0.156328	0.170703	17%
FD	0.215493	0.214675	0.206983	0.238243	0.21842	0.218763	22%
							100%

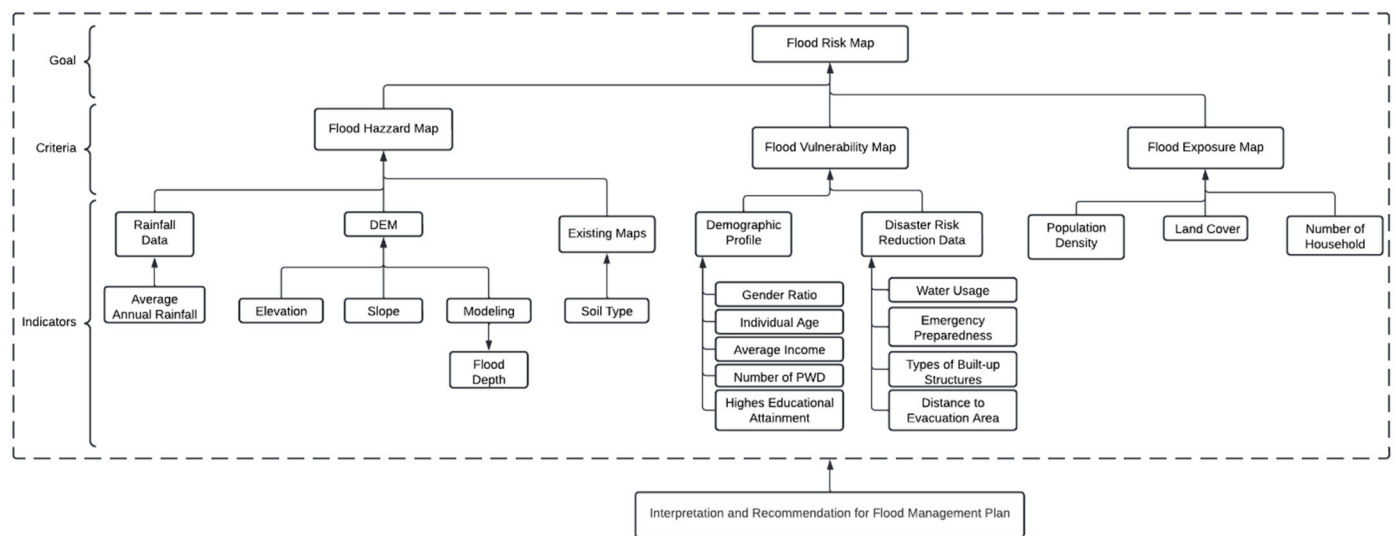


Figure 9. Multicriteria data analysis for flood risk assessment in AHP framework.

Table 3. Standard matrix vulnerability parameters.

	GR	MA	AI	NPWD	HEA	WU	EP	TBS	DEA	Weights	Percentage Weights
GR	0.091812	0.072630	0.083258	0.095499	0.093304	0.088862	0.116943	0.095699	0.080989	0.091000	9%
MA	0.136601	0.108062	0.134171	0.116910	0.076277	0.083485	0.110578	0.090066	0.125462	0.109068	11%
AI	0.124171	0.090691	0.112602	0.090232	0.105573	0.129437	0.126444	0.135126	0.096882	0.112351	11%
NPWD	0.101895	0.097966	0.132265	0.105988	0.102919	0.107756	0.086492	0.107974	0.106007	0.105474	11%
HEA	0.078704	0.113313	0.085309	0.082368	0.079983	0.095524	0.073935	0.096588	0.092532	0.088695	9%
WU	0.109121	0.136708	0.091879	0.103882	0.088433	0.105616	0.085829	0.111776	0.117633	0.105653	11%
EP	0.108148	0.134616	0.122671	0.168801	0.149019	0.169508	0.137751	0.134197	0.130969	0.139520	14%
TBS	0.114932	0.143735	0.099830	0.117594	0.099203	0.113196	0.122971	0.119798	0.130779	0.118004	12%
DEA	0.134616	0.102279	0.138016	0.118726	0.205288	0.106616	0.139056	0.108777	0.118748	0.130236	13%
											100%

The final relative weights of the alternatives which were defined by computing the product’s linear combination (LC) between the relative weight of each criterion and the alternative for that specific criterion are shown in Tables 2–4, whereas Tables 5–7 are the computation of CI and CR for hazard, vulnerability, and exposure, respectively. A consistency ratio of 1.32%, 3.31%, and 6.85% were noticed in the hazard, vulnerability, and exposure below 10%. The experts made repeated responses to obtain the acceptable CR for all judgments. Further, final weights for hazard, vulnerability, and exposure are shown in Table 8. These weights are integrated into ArcGIS to generate hazard, vulnerability, and exposure maps with the corresponding index value.

Table 4. Standard matrix for exposure parameters.

	PD	LC	NH	Weights	Percentage Weights
PD	0.326245	1/3	1/3	0.327369	33%
LC	0.37159	0.34364	0.31783	0.344357	34%
NH	0.302161	0.354651	0.328012	0.328274	33%
					100%

Table 5. Computation of CR and CI of hazard parameters for consistency of AHP.

	AAR	E	S	ST	FD	Sum	Crit. Weights
AAR	0.225925	0.244066	0.328938	0.258341	0.235870	1.293139	5.72376382
E	0.189362	0.204567	0.226295	0.243454	0.195670	1.059347	5.17847996
S	0.123658	0.162756	0.180042	0.204129	0.155214	0.825800	4.58669759
ST	0.149284	0.143437	0.150561	0.170703	0.122176	0.736161	4.31251769
FD	0.209539	0.228710	0.253757	0.305653	0.218763	1.216422	5.56046026
						<i>y_{max}</i>	5.07238386
						CI	0.018095966
						CR	0.016157112

Table 6. Computation of CR and CI of vulnerability parameters for consistency of AHP.

	GR	MA	AI	NPWD	HEA	WU	EP	TBS	DEA	Sum	Crit. Weights
GR	0.091000	0.061162	0.067285	0.081994	0.106155	0.076564	0.077254	0.072694	0.062064	0.696171	7.650275
MA	0.162276	0.109068	0.129960	0.120308	0.104014	0.086214	0.087554	0.081999	0.115235	0.996628	9.137668
AI	0.151949	0.094290	0.112351	0.095649	0.148296	0.137692	0.103129	0.126726	0.091663	1.061744	9.450256
NPWD	0.117057	0.095620	0.123891	0.105474	0.135719	0.107612	0.066225	0.095063	0.094157	0.940818	8.919941
HEA	0.076032	0.093005	0.067196	0.068929	0.088695	0.080220	0.047605	0.071511	0.069114	0.662308	7.467245
WU	0.125572	0.133660	0.086208	0.103554	0.116815	0.105653	0.065829	0.098578	0.104661	0.940530	8.902074
EP	0.164345	0.173804	0.151996	0.222206	0.259944	0.223923	0.139520	0.156289	0.153880	1.645906	11.79692
TBS	0.147721	0.156959	0.104619	0.130927	0.146361	0.126474	0.105343	0.118004	0.129960	1.166368	9.884114
DEA	0.190954	0.123266	0.159630	0.145889	0.334267	0.131470	0.131470	0.118254	0.130236	1.465436	11.25217
										<i>y_{max}</i>	9.384519
										CI	0.048065
										CR	0.033148

Table 7. Computation of CR and CI of exposure parameters for consistency of AHP.

	PD	LC	NH	Sum	Crit. Weights
PD	0.327369	0.287416	0.353462	0.968247	2.957665
LC	0.392224	0.344357	0.33367	1.070251	3.10797
NH	0.30404	0.338789	0.328274	0.971104	2.958207
				<i>y_{max}</i>	3.007947
				CI	0.003974
				CR	0.006851

Table 8. Final weights and percentage weights of every parameter for hazard, vulnerability, and exposure.

Parameters	Weights	Percentage Weights
Hazard Parameters		
Average Annual Rainfall (AAR)	0.225925	22.59%
Elevation (E)	0.204567	20.46%
Slope (S)	0.180042	18.0%
Soil Type (ST)	0.170703	17.07%
Flood Depth (FD)	0.218763	21.88%
Vulnerability Parameters		
Gender Ratio (GR)	0.091000	9.1%
Mean Age (MA)	0.109068	10.91%
Average Income (AI)	0.112351	11.24%
Number of PWD (NPWD)	0.105474	10.55%
Highest Educational Attainment (HEA)	0.088695	8.87%

Table 8. Cont.

Parameters	Weights	Percentage Weights
Water Usage (WU)	0.105653	10.57%
Emergency Preparedness (EP)	0.139520	13.95%
Types of Build-up Structures (TBS)	0.118004	11.8%
Distance to the nearest Evacuation Area (DEA)	0.130236	13.02%
Exposure Parameters		
Population Density (PD)	0.327369	32.74%
Land Use/Land Cover (LULC)	0.344357	34.44%
Household Number (HN)	0.328274	32.83%

3.3. Development of Flood Risk Map

The visualization outputs for hazard, vulnerability, and exposure are shown in Figure 10. These maps were generated after computing the criteria weights using AHP and incorporating these weights with a GIS-based process consisting of overlays, raster conversion, and layer clipping.

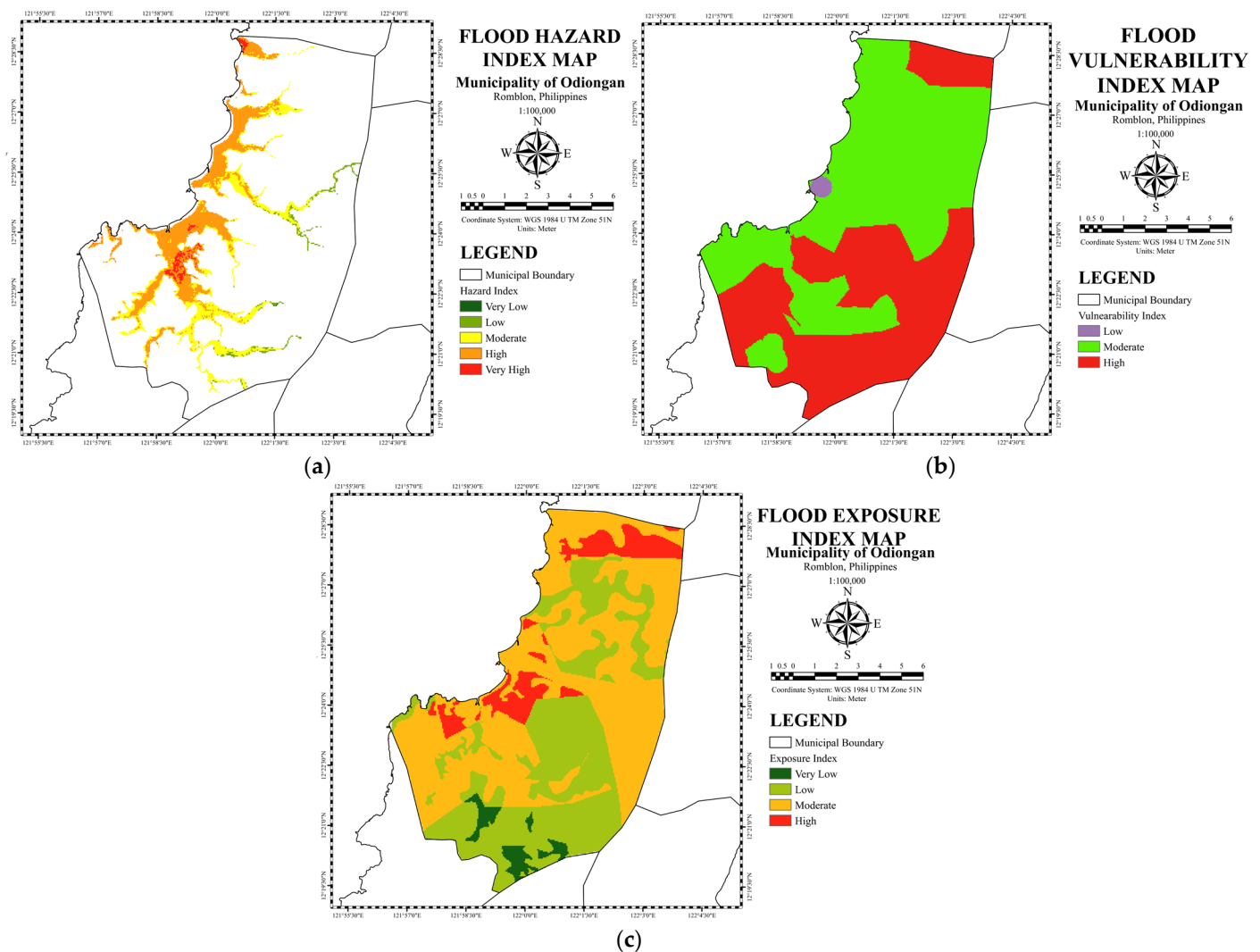


Figure 10. (a) Flood Hazard, (b) Flood Vulnerability, (c) Flood Exposure Index Maps of the Odiongan, Romblon, integrating all parameters in ArcGIS.

As shown in Figure 10a, the flood hazard index map, which combined all five (5) factors, was developed using the overlay tool in ArcGIS. The hazard map was classified into five (5) levels: very low (green), low (yellow-green), moderate (yellow), high (orange), and very high (red) and covers 0.009, 1.07, 8.74, 11.71, and 0.76 square kilometers, respectively. It was observed that areas with hazard index values were mostly affected according to the flood depth map, where river bodies are also located. Moderate to very high hazard is seen in areas of Poblacion, including Poctoy, Bangon, and Anahao. However, a moderate to high index was presented in some parts of Batiano, Gabawan, Libertad, and Paniques.

The vulnerability index map obtained by combining all nine (9) parameters highlights five areas (low, moderate, and high), as shown in Figure 10b, using the overlay tool. The flood vulnerability map generated from ArcGIS determines the degree of susceptibility of the flood-prone zone [29]. Purple connotes low vulnerability, yellow-green for moderate, and red for high vulnerability. Low, moderate, and high classes cover 0.56%, 54.52%, and 44.92% of Odiongan. As can be seen, only barangay Batiano is in low vulnerability and barangays Mayha, Tabobo-an, Canduyong, Malilico, Poctoy, Gabawan, Tumingad, Tuburan, Libertad, and a portion of Poctoy and Budiong is in moderate vulnerability. Tulay, Amatong, Pato-o, Rizal, Progreso Este, Progreso Weste, Anahao, Bangon, Tulay, and Panique is observed as highly vulnerable.

Exposure parameters (population density, number of households, and land cover) were overlaid in ArcGIS to develop a Flood Exposure Index Map. The resulting map derived four categories (very low, low, moderate, and high) in flood exposure using experts' weights, as shown in Figure 10c. The green symbolizes very low exposure, yellow-green for low, orange for moderate, and red for high exposure, which covers 2.61%, 36.39, 53%, and 8.01%, respectively, of the total land area of Odiongan. The Poblacion area and parts of Budiong, Gabawan, Batiano, and Panique were at high exposure to flood. However, more than half of the map is scattered orange illustrating moderate exposure.

The result of the flood risk assessment is laid into a map for a better comprehension. As shown in Figure 11, the analysis result was a map combining flood hazard, flood vulnerability, and flood exposure index maps utilizing ArcGIS. Equal weights were employed in three (3) maps. The flood risk map is categorized using equal intervals with four (4) levels (very low, low, moderate, and high). In total, 93.92 square kilometers (green) are classified as very low risk, comprising 83.78% of the total land area. The yellow-green color as low risk covers approximately 0.198 square kilometers (0.15% of land area) and is seen in a small part of Barangay Rizal and Tumingad. Overall, 12.86% of the total area was categorized as moderate risk (yellow) and noted on the map as 17.56 square kilometers. A portion of barangays Rizal, Progreso Este, Progreso Weste, Malilico, Amatong, Anahao, Canduyong, Pato-o, Tumingad, Mayha, Tuburan, and Panique were observe with moderate risk. Gabawan, Batiano, Tabobo-an, and Libertad were also at moderate risk, with more than half of their respective barangay boundaries. The Poblacion area, Tulay, Bangon, Anahao, Dapawan, and Poctoy were at high risk to flood occurrence, covering 3.26% of land area (4.46 square kilometers). Parcels with high risk were also sighted in Canduyong, Gabawan, and Panique. Through this flood risk map, the municipal councils, planning agencies, and other stakeholders can prepare Flood Management Plan to reduce the threat to lives due to flooding and anticipate future infrastructure development in the municipality.

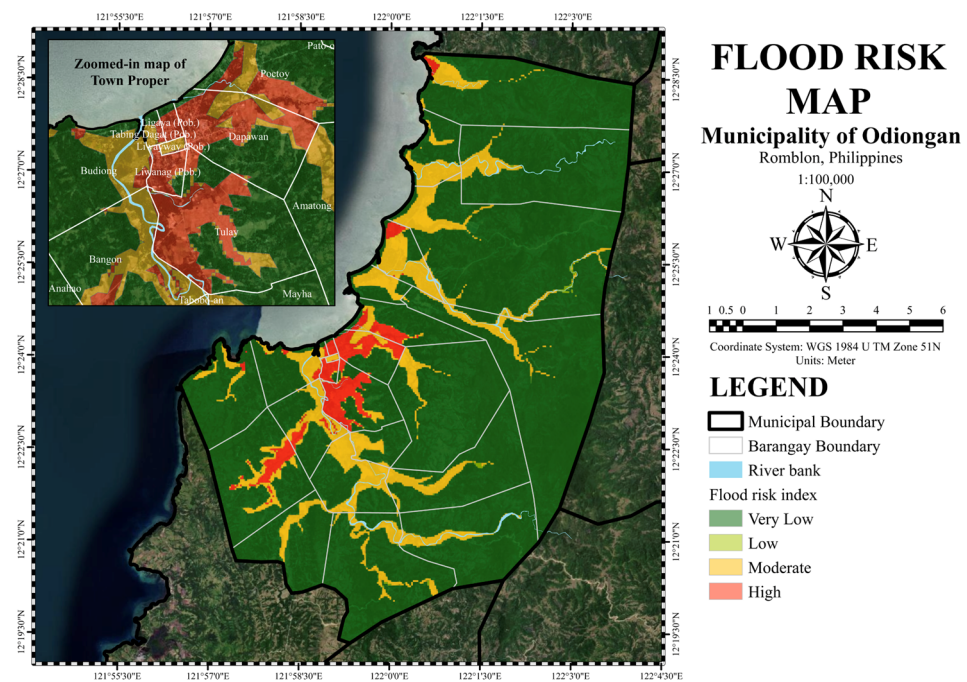


Figure 11. Imagery and flood risk map (50% transparency) with 1:50,000 scale zoomed-in map of town proper of the Municipality of Odiongan.

4. Discussion

The harmful effects of disasters in flood-prone areas have amplified in severity over the years. The damage ensuing from these events are also exponentially growing, where serious land use and climate change impacts are alarming. The development of a flood risk map utilizing elevation models, demographics, awareness, and disaster-risk-related data integrated into GIS and analyzed using AHP is an effective tool for evaluating risk. Integrating available data through the archival, automated process, and survey data were possible in deriving each criterion. It is noted in the flood risk map that approximately 83.78% of the total area map is at very low risk, 0.15% is at low, 12.86% at moderate, and 3.26% for high flood risk. 93.92, 0.198, 17.56, and 4.46 square kilometers are very low, low, moderate, and high risk to flood. A small portion of Barangay Rizal and Tumingad are at low risk (yellow-green). Moderate risk was noted on the map covering a part of barangays Rizal, Progreso Este, Progreso Weste, Malilico, Amatong, Anahao, Canduyong, Pato-o, Tumingad, Mayha, Tuburan, and Panique. Then, Gabawan, Batiano, Tabobo-an, and Libertad were at moderate risk covering half of their respective barangay boundaries. Moreover, based on the zoomed-in map of the town proper, the Poblacion area, Tulay, Bangon, Anahao, Dapawan, and Poctoy are at high risk to flood occurrence. The possible reason for this is the rapid urbanization and infrastructure development in the town proper of Odiongan, as shown in Figure 11. In addition, moderate to high-risk indexes were observed along the riverbanks of Odiongan. In validation, areas at high risk are known to have flood events. The results of the risk maps urge the municipality to plan for flood mitigation or develop a comprehensive flood management plan as a countermeasure during for future flood events. Flood risk assessment is required for the flood management and mitigation of cities and municipalities. However, the specific parameters available in such areas are significantly different, which differs the risk assessment index weight. The study of Cai et al. [15] adopted the frequency of rainstorms and average annual precipitation of counties as hazard parameters, similar to what were used in this study. Average annual rainfall represented 22.59% of the weight of the total hazard parameters which showed its importance or role in identifying hazard level in a certain area. For vulnerability factors, the study considered the following: population density, average area GDP, per capita disposable income, road network density, and land use type. Average income was

basically identified to have the highest weight among all other factors considered in the vulnerability index with 11.24%, this just shows that the capability to spend affects how people could prepare and protect themselves during a disaster. A risk assessment could also be performed, even in mega-cities, as based on the study of Lyu et al. [60]. Parameters such as rainy season, average rainfall, average rainy day for hazard and elevation, slope, river proximity, river density as exposure parameters; and land use, metro line proximity, metro line density, road network proximity and road network density as vulnerability indicators were considered, similarly to what was considered in this study. This shows that methodology used in this study could also be applied in mega-cities here in the Philippines with some revision of factors to be considered which will be based on the city's characteristics. A local study [46] used Confirmatory Factor Analysis (CFA) to simultaneously investigate the interrelationship between vulnerability to natural hazards composed of exposure, sensitivity, and resilience. Additionally, a study [61] developed a comprehensive framework for vulnerability assessment to determine vulnerability that would deliver a transparent understanding and improve community competency leading to the development of methodologies to assess factors and indicators of vulnerability. For this assessment, the combination of hazard, vulnerability, and exposure assessment established a clear definition of risk levels [36,62]. Compared to other related studies, the evaluation used the Sendai Framework to clear out the true meaning of disaster risk based on all dimensions of vulnerability, exposure, and hazard characteristics of the environment. Regarding hazard assessment, many studies used factors such as topographical [63], natural, and anthropogenic [62] factors. In this study, factors used were average annual rainfall, slope, elevation, soil type, and simulated flood depth, which were decided according to the data availability. In terms of vulnerability assessment, flood vulnerability is affected by factors such as settlement conditions, infrastructure, policy and capacities of the authorities, social inequities, and economic patterns. The study effectively generated a vulnerability map integrating age, gender ratio, average income, individual physical health, educational attainment, emergency preparedness, and types of built-up structures as factors. Exposure assessment of the study is based on the analysis of [64], which used land use and population density as parameters. The study added the additional factor, household number, to justify the flood exposure.

The accuracy of generating flood hazard maps is highly dependent on the quality of topographical data [62]. Topographical information such as DEMs is an excellent source to derive topographic factors responsible for flood activity [65]. Although local studies [63,64] utilized LiDAR-derived DEM due to its inherent high vertical accuracy and resolution, If-SAR DTM from NAMRIA, as one of the highest resolution available DEM in the location, is used in the study, which showed reasonably consistent with the generated maps.

The flood risk assessment map demonstrates flood risk areas that must be managed on a priority basis. In some studies, different methodologies were established for assessing flood risk. One uses a hybrid intelligence model [14], probability [66,67], polygon approach [68], Quantitative risk assessment methods (e.g., Fine Kiney [55] and Maxent model [8]), and MCDA techniques, such as fuzzy majority approach [30], fuzzy variable set theory [44], multi-attribute value, frequency ratio, artificial neural network [65], fuzzy analytical hierarchy process (FAHP) [41], and decision tree [69] to assess the flood risk. Most government units, municipal planners, and other concerned agencies use AHP as an MCA in terms of disaster risk reduction, land use plans, and decisions requiring a comprehensive judgment and recommendation from experts to benefit the community. Using the AHP decision-making method for the multiple flood-related factors is extensively adopted. From the result of the study, it is noticed that AHP proposes a flexible, stepwise, and precise process of analyzing complicated problems in an MCDA environment. In addition, the resolution of complications in multicriteria methods is realized as the primary use of AHP. In this research, where three (3) criteria (hazard, vulnerability, and exposure) with multiple parameters (5, 9, 3, respectively) have different dimensions, it makes a simple MCDA dilemma more complicated. In this study, the AHP-based flood risk assessment

method is considered relatively practical, convenient, and promotes interactive usage by flood managers for continuing improvement. AHP is a useful method for selecting contending options in light of a range of objectives to be convened. The computations were not complex, and the MCA did not need to understand the calculation to use the procedure. Nonetheless, the AHP has established considerations because it highlights the knowledge of decision-makers' preferences [32].

Compared to other flood maps available online and offline, the study highlighted how comprehensive the methodology is. Government agencies' flood maps consider only one to two criteria (hazard, susceptibility, or only topographical related data) that limit the assessment's accuracy. For this research, several social, economic, environmental, and technical factors were considered to develop a comprehensive flood risk map. Future studies could be performed to improve this risk map where environmental quality could be incorporated [70], such as flooding, was found to be correlated with the increasing concentration of manganese in Marinduque. Considering environmental quality in risk assessment would be useful.

5. Conclusions

The number of flooding events in the Municipality of Odiongan caused property damage to the community and has put lives at risk based on historical documents. This showed how vital flooding risk assessments using GIS-based, and multi-criteria decisions are. The results of this study are useful for improving the municipality's flood mitigation and risk management strategies.

This study assessed the flood risk in the Municipality of Odiongan, Romblon, considering relevant factors in floods using AHP and following the Sendai Framework. The study used ArcGIS, HEC-RAS, and HEC-HMS to map and model the primary and secondary data as parameters that mainly contribute to flooding. The study considered the following parameters: average annual rainfall, elevation, slope, soil type, and flood depth for hazard criteria; gender ratio, mean age, average income, PWD, educational attainment, water usage, emergency preparedness, type of built-up structures, and distance to evacuation area in vulnerability and population density, land cover and household number for exposure, respectively. Each parameter was compared to one another by pairwise comparison to identify its weights based on experts' judgment and integrate these weights of factors into AHP. Weights were computed as follows: average annual rainfall with 23%, elevation—20%, slope—18%, soil type—17%, and flood depth—22% for hazard criteria; gender ratio—9%, mean age—11%, average income—11%, PWD—11%, educational attainment—9%, water usage—11%, emergency preparedness—14%, type of built-up structures—12%, and distance to evacuation area—13% in vulnerability and population density with 33%, land use—34% and household number—33% for exposure. It was noted that approximately 83.78% of the total area map was at very low risk, 0.15% is at low, 12.86% at moderate, and 3.26% for high flood risk. Then, 93.92, 0.198, 17.56, and 4.46 square kilometers were very low, low, moderate, and high risk to flood. The risk assessment results derived a flood risk map which found out the nine (9) barangays were at high risk of flooding, notably the Poblacion Area, Tulay, Bangon, Tabobo-an, Dapawan, and Anahao. The flood risk map developed in this study considered the social, economic, environmental, and technical factors that represent those factors in actual scenarios. Highlighting its difference compared to the flood depth map or available flood maps online and released by the different concerned agencies incorporating the topographic aspect of the area.

In conclusion, the result of this flood risk assessment is essential for the municipality to improve their flood management strategies considering the risk factors: hazard, vulnerability, and exposure. It can help the planning agencies and other stakeholders anticipate flood risk, especially the LGU, by integrating the output into their CLUP. This technique can also be employed by other local government units to come up with more practical and effective strategies. Moreover, future studies must be conducted to enhance and update the flood risk assessment methods and management.

Author Contributions: Conceptualization, J.G.G. and C.E.F.M.; methodology, J.G.G. and C.E.F.M.; software, J.G.G.; validation, J.G.G.; formal analysis, J.G.G., C.E.F.M. and D.B.S.; investigation, J.G.G.; resources, J.G.G. and C.E.F.M.; data curation, J.G.G. and C.E.F.M.; writing—original draft preparation, J.G.G.; writing—review and editing, J.G.G., C.E.F.M., D.B.S. and F.J.T.; visualization, J.G.G. and C.E.F.M.; supervision, C.E.F.M., D.B.S. and F.J.T.; project administration, J.G.G. and C.E.F.M. All authors have read and agreed to the published version of the manuscript.

Funding: The study was funded by the Department of Science and Technology—Engineering Research and Development for Technology and Mapúa University.

Informed Consent Statement: Informed consent was obtained from all subjects involved in the study.

Data Availability Statement: All data are contained in the manuscript.

Acknowledgments: The author would like to acknowledge the in-kind support of Romblon State University, Local Government of Odiongan, National Mapping and Resource Information Authority (NAMRIA), Philippine Atmospheric, Geophysical, and Astronomical Services Administration (PAGASA), Mines and Geosciences Bureau (MGB), Bureau of Soils and Water Management (BSWM), and the Philippine Statistics Authority (PSA) for the conduct of the study.

Conflicts of Interest: The authors declare no conflict of interest.

Appendix A

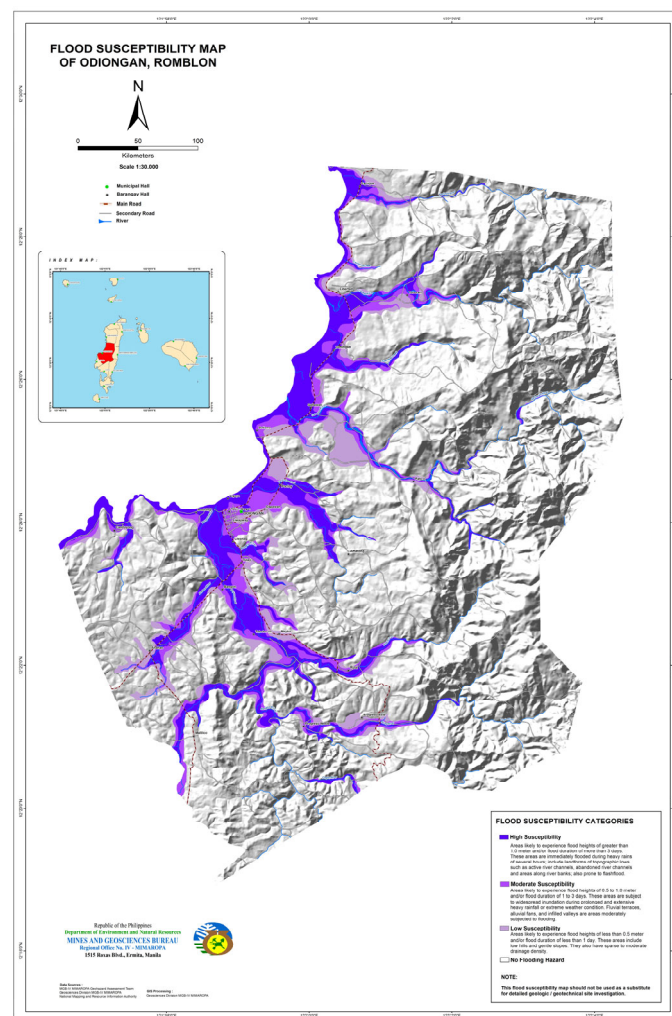


Figure A1. Flood Susceptibility Map from MGB-DENR.

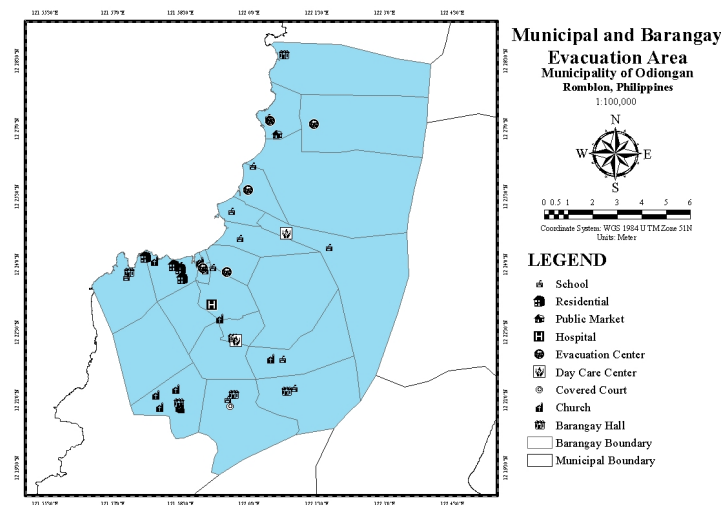


Figure A2. Identified evacuation area of barangay in Odiongan, Romblon, during emergency events.

In identifying the weights of factors, the pairwise comparison procedure usually contains a questionnaire for comparing all the elements and a geometric mean to arrive at a final solution. Psychologists conclude that the nine points shown in Table A1 are the most used comparison matrix individuals can compare simultaneously and consistently rank.

Table A1. The nine-point intensity of importance scale was modified from Schoenherr. Copyright 2008 Elsevier.

Intensity of Importance	Definition	Description
1	Equally important	Two factors contribute equally to the objective
3	Moderately more important	Experience and judgment slightly favor one over the other
5	Strongly more important	Experience and judgment strongly favor one over the other
7	Very strong, more important	Experience and judgment very strongly favor one over the other. Its importance is demonstrated in practice.
9	Extremely more important	The evidence favoring one over the other is of the highest possible validity.
2, 4, 6, 8	Intermediate values	When compromise is needed.
Reciprocals of above	If an element <i>i</i> has one of the above numbers assigned to it when compared with element <i>j</i> , then <i>j</i> has the reciprocal value when compared with <i>i</i>	
Ratios (1.1–1.9)	If the activities (elements) are very close.	It may be challenging to assign the best value, but when compared with other contrasting activities (elements), the size of the small numbers would not be too noticeable, yet they can still indicate the relative importance of the activities (elements)

The feature weight was assigned to each parameter, where levels were reclassified and normalized into 1, 2, 3, 4, and 5 (1 for the least priority and 5 for the most prior). Assigned values depend on how primary the level or category is. Table A2 indicates the feature weight of every indicator.

Table A2. Parameters with their designated feature weight.

Indicators	Feature Class	Feature Weight
Flood Hazard Parameters		
Average Annual Rainfall (in mm)	2200	1
	2210	1
	2220	2
	2230	3
	2240	4
	2250	5
Elevation (in meters)	0–5	5
	6–20	4
	21–50	3
	51–150	1
	151–600	0
Slope (in degrees)	0–3	5
	3–8	4
	8–18	3
	18–30	2
	30–50	1
	50 above	0
Soil Type	Sandy, loamy sand, or sandy loam	1
	Silt loam or loam	3
	Clay loam, silty clay loam, sandy clay, or clay	5
Flood Depth (in meters)	0–0.5	1
	0.51–1	2
	1.01–1.5	3
	1.51–2	4
	2>	5
Flood Vulnerability Parameters		
Gender Ratio (men to women ratio)	0.839339–0.839655	1
	0.839656–0.963855	2
	0.963856–1.008065	3
	1.008066–1.040521	4
	1.040522–1.208661	5
Mean Age	29–30	1
	31–32	2
	33–34	3
	35–36	4
	37–38	5
Average Income	500,000 and over	1
	250,000 to 499,999	1
	100,000 to 249,999	2
	60,000 to 99,999	3
	40,000 to 59,999	4
Less than 40,000	5	
Number of PWD	5–12	1
	13–26	2
	27–37	3
	38–55	4
	56–70	5
Highest Educational Attainment	College Graduate	3
	High School Graduate	5

Table A2. Cont.

Indicators	Feature Class	Feature Weight	
Water Usage	Ground	4	
	Piped	5	
Emergency Preparedness	Prepared	5	
	Well prepared	4	
	Very well prepared	3	
Types of Build-up Structures	Permanent	3	
	Semi-permanent	4	
	Temporary	5	
Distance to the nearest Evacuation Area (in meters)	2000 above	5	
	2000	4	
	1500	3	
	1000	2	
500		1	
	Flood Exposure Parameters		
	Population Density	7001–10,651	1
		4001–7000	2
2001–4000		3	
151–2000		4	
126–150		5	
Land Use and Land Cover	Brushland	1	
	Built-up	4	
	Cultivated Area	3	
	Fishpond	5	
	Grassland	2	
	Mangrove	0	
Tree Plantation and Perennial	0		
Household Number	172–250	1	
	251–350	2	
	351–550	3	
	551–650	4	
	651–976	5	

Pairwise comparison was based on adequate information, expert knowledge, and experience using a questionnaire. Ten (10) experts on-field and end-users determined the relevance of one alternative over the other with a pairwise comparison method presented in a matrix. Gathered weight for each criterion and option used a pairwise comparison technique. Then, each comparison is graded by expert respondents and end-user using the nine-point scale of importance. Eligible respondents and their credentials are shown in Table A3.

Table A3. Respondent's credentials for pairwise comparison technique.

Respondent	Field of Expertise/Project Involvement	Agency/Institution/Project	Years in Service
1	Water Resource Engineering/Disaster Risk	Mapua University	10
2	Meteorology/Hydrology	PAGASA-DOST	30
3	Project Staff	FRAMER—Mapua University	4
4	Researcher	FRA Project—Asian Institute of Technology	3
5	Disaster Risk/Municipal Engineer	LGU—Odiongan	30

Table A3. Cont.

Respondent	Field of Expertise/Project Involvement	Agency/Institution/Project	Years in Service
6	Meteorology/Hydrology	Visayas State University—Department of Meteorology	8
7	Meteorology/Hydrology	Central Luzon State University	3
8	Senior Research Specialist	UP Training Center for Applied Geodesy and Photogrammetry	5
9	Agriculturist II/Regional Head	Department of Agriculture—Bureau of Soil and Water Management	3
10	Supervising Geologist/Expert in Landslide and flood susceptibility mapping	Department of Environment and Natural Resources—Mines and Geosciences Bureau MIMAROPA	15

References

- Osei, B.K.; Ahenkorah, I.; Ewusi, A.; Fiadonu, E.B. Assessment of flood prone zones in the Tarkwa mining area of Ghana using a GIS-based approach. *Environ. Chall.* **2021**, *3*, 100028. [CrossRef]
- Flood—UN-SPIDER Knowledge Portal. Available online: <https://www.un-spider.org/category/disaster-type/flood> (accessed on 7 September 2022).
- Nunez, C. Floods—Facts and Information. Available online: <https://www.nationalgeographic.com/environment/article/floods> (accessed on 27 June 2021).
- Malhotra, S. Flooded Cities and Millions Displaced in Pictures—Greenpeace International. Available online: <https://www.greenpeace.org/international/story/44296/flooded-cities-and-millions-displaced-in-pictures/> (accessed on 27 June 2021).
- Monjardin, C.E.F.; Tan, F.J.; Uy, F.A.A.; Bale, F.J.P.; Voluntad, E.O.; Batac, R.M.N. Assessment of the existing drainage system in Infanta, Quezon province for flood hazard management using analytical hierarchy process. In Proceedings of the 2020 IEEE Conference on Technologies for Sustainability (SusTech), Santa Ana, CA, USA, 23–25 April 2020. [CrossRef]
- ESCAP IDD. *Disasters in Asia and the Pacific: 2015 Year in Review*; ESCAP IDD: Bangkok, Thailand, 2015.
- Davies, R. Philippines—Thousands Hit by More Floods in Central Regions—FloodList. Available online: <http://floodlist.com/asia/philippines-negros-occidental-floods-january-2021> (accessed on 27 June 2021).
- Cabrera, J.S.; Lee, H.S. Flood risk assessment for Davao Oriental in the Philippines using geographic information system-based multi-criteria analysis and the maximum entropy model. *J. Flood Risk Manag.* **2020**, *13*, e12607. [CrossRef]
- Siddayao, G.P.; Valdez, S.E.; Fernandez, P.L. Analytic Hierarchy Process (AHP) in Spatial Modeling for Floodplain Risk Assessment. *Int. J. Mach. Learn. Comput.* **2014**, *4*, 450–457. [CrossRef]
- Teves, C. Romblon Waterways at Risk of Overflow due to ‘Quinta’ Rains—Philippine News Agency. Available online: <https://www.pna.gov.ph/articles/1119823> (accessed on 27 June 2021).
- Alfonso, C.D.Q.; Sundo, M.B.; Zafra, R.G.; Velasco, P.P.; Aguirre, J.J.C.; Madlangbayan, M.S. Flood risk assessment of major river basins in the philippines. *Int. J. GEOMATE* **2019**, *17*, 201–208. [CrossRef]
- Rahman, M.Z.A.; Alkema, D. Digital surface model (DSM) construction and flood hazard simulation for Development Plans in Naga City, Philippines. *GIS Dev. Malaysia* **2006**, 1–15.
- Ali, K.; Bajracharya, R.M.; Koirala, H.L. A Review of Flood Risk Assessment. *Int. J. Environ. Agric. Biotechnol.* **2016**, *1*, 1065–1077. [CrossRef]
- Pham, B.T.; Luu, C.; Phong, T.V.; Nguyen, H.D.; Le, H.V.; Tran, T.Q.; Ta, H.T.; Prakash, I. Flood risk assessment using hybrid artificial intelligence models integrated with multi-criteria decision analysis in Quang Nam Province, Vietnam. *J. Hydrol.* **2021**, *592*, 125815. [CrossRef]
- Cai, S.; Fan, J.; Yang, W. Flooding Risk Assessment and Analysis Based on GIS and the TFN-AHP Method: A Case Study of Chongqing, China. *Atmosphere* **2021**, *12*, 623. [CrossRef]
- Eleutério, J.; Martinez, D.; Rozan, A. Developing a GIS tool to assess potential damage of future floods. *WIT Trans. Inf. Commun. Technol.* **2010**, *43*, 381–392. [CrossRef]
- Noamen, B.; Taoufik, H.; Arfa, S.B. Flood risk assessment and mapping using multi-criteria analysis (AHP) model and GIS: Case of the Jendouba Governorate—Northwestern Tunisia. *Int. J. Water Sci. Environ. Technol.* **2020**, *2*, 139–149.

18. Santillan, J.R.; Makinano-Santillan, M. Vertical accuracy assessment of 30-M resolution ALOS, ASTER, and SRTM global DEMS over Northeastern Mindanao, Philippines. *Int. Arch. Photogramm. Remote Sens. Spat. Inf. Sci.—ISPRS Arch.* **2016**, *41*, 149–156. [CrossRef]
19. Chen, B.; Ge, Y. The building of network geographic information system based on ArcGIS. In Proceedings of the International Conference on Computer Application and System Modeling, Taiyuan, China, 22–24 October 2010; Volume 14, pp. 90–93. [CrossRef]
20. Hawker, L.; Bates, P.; Neal, J.; Rougier, J. Perspectives on Digital Elevation Model (DEM) Simulation for Flood Modeling in the Absence of a High-Accuracy Open Access Global DEM. *Front. Earth Sci.* **2018**, *6*, 3389. [CrossRef]
21. Jeon, Y.W.; Bae, Y.; Ra, J.B. Error detection in digital elevation model using a camera image. In Proceedings of the International Geoscience and Remote Sensing Symposium, Melbourne, VIC, Australia, 21–26 July 2013; pp. 2517–2519. [CrossRef]
22. Sugumaran, R.; Davis, C.H.; Meyer, J.; Prato, T. High resolution digital elevation model and a web-based client-server application for improved flood plain management. In Proceedings of the International Geoscience and Remote Sensing Symposium, Honolulu, HI, USA, 24–28 July 2000; Volume 1, pp. 334–335. [CrossRef]
23. Ballado, A.H.; Bentir, S.A.P.; Lazaro, J.B.; Macawile, M.J.P. Depth perception analysis of LiDAR digital elevation model for low lying areas using delaunay triangulation algorithm. In Proceedings of the HNICEM 2017—9th International Conference on Humanoid, Nanotechnology, Information Technology, Communication and Control, Environment and Management, Manila, Philippines, 1–3 December 2017; pp. 1–5. [CrossRef]
24. Ternate, J.R.; Celeste, M.I.; Pineda, E.F.; Tan, F.J.; Uy, F.A.A. Floodplain Modelling of Malaking-Ilog River in Southern Luzon, Philippines Using LiDAR Digital Elevation Model for the Design of Water-Related Structures. *IOP Conf. Ser. Mater. Sci. Eng.* **2017**, *216*, 012044. [CrossRef]
25. Lagmay, A.M.F.A.; Racoma, B.A.; Aracan, K.A.; Alconis-Ayco, J.; Saddi, I.L. Disseminating near-real-time hazards information and flood maps in the Philippines through Web-GIS. *J. Environ. Sci.* **2017**, *59*, 13–23. [CrossRef] [PubMed]
26. Kittipongvises, S.; Phetrak, A.; Rattanapun, P.; Brundiars, K.; Buizer, J.L.; Melnick, R. AHP-GIS analysis for flood hazard assessment of the communities nearby the world heritage site on Ayutthaya Island, Thailand. *Int. J. Disaster Risk Reduct.* **2020**, *48*, 101612. [CrossRef]
27. Abe, Y.; Zodrow, I.; Johnson, D.A.K.; Silerio, L. Risk informed and resilient development: Engaging the private sector in the era of the Sendai Framework. *Prog. Disaster Sci.* **2019**, *2*, 100020. [CrossRef]
28. Wilkins, A.; Pennaz, A.; Dix, M.; Smith, A.; Vawter, J.; Karlson, D.; Tokar, S.; Brooks, E. Challenges and opportunities for Sendai framework disaster loss reporting in the United States. *Prog. Disaster Sci.* **2021**, *10*, 100167. [CrossRef]
29. Danumah, J.H.; Odai, S.N.; Saley, B.M.; Szarzynski, J.; Thiel, M.; Kwaku, A.; Kouame, F.K.; Akpa, L.Y. Flood risk assessment and mapping in Abidjan district using multi-criteria analysis (AHP) model and geoinformation techniques, (cote d’ivoire). *Geoenvirom. Disasters* **2016**, *3*, 10. [CrossRef]
30. Boroushaki, S.; Malczewski, J. Using the fuzzy majority approach for GIS-based multicriteria group decision-making. *Comput. Geosci.* **2010**, *36*, 302–312. [CrossRef]
31. Dodgson, J.S.; Spackman, M.; Pearman, A.; Phillips, L.D. *Multi-Criteria Analysis: A Manual*; Department for Communities and Local Government: London, UK, 2009; Volume 11, pp. 1–16. ISBN 978-1-4098-1023-0.
32. Ouma, Y.O.; Tateishi, R. Urban flood vulnerability and risk mapping using integrated multi-parametric AHP and GIS: Methodological overview and case study assessment. *Water* **2014**, *6*, 1515–1545. [CrossRef]
33. Juneja, P. What Is Analytical Hierarchy Process (AHP) and How to Use It? Available online: <https://www.managementstudyguide.com/analytical-hierarchy-process.htm> (accessed on 30 June 2021).
34. Siddayao, G.P.; Valdez, S.E.; Fernandez, P.L. Modeling Flood Risk for an Urban CBD Using AHP and GIS. *Int. J. Inf. Educ. Technol.* **2015**, *5*, 748–753. [CrossRef]
35. Rahadianto, H.; Fariza, A.; Hasim, J.A.N. Risk-level assessment system on Bengawan Solo River basin flood prone areas using analytic hierarchy process and natural breaks: Study case: East Java. In Proceedings of the 2015 International Conference on Data and Software Engineering, ICODSE 2015, Yogyakarta, Indonesia, 25–26 November 2015; pp. 195–200. [CrossRef]
36. Lyu, H.M.; Zhou, W.H.; Shen, S.L.; Zhou, A.N. Inundation risk assessment of metro system using AHP and TFN-AHP in Shenzhen. *Sustain. Cities Soc.* **2020**, *56*, 102103. [CrossRef]
37. Weerasinghe, K.M.; Gehrels, H.; Arambepola, N.M.S.I.; Vajja, H.P.; Herath, J.M.K.; Atapattu, K.B. Qualitative Flood Risk assessment for the Western Province of Sri Lanka. *Procedia Eng.* **2018**, *212*, 503–510. [CrossRef]
38. Seejata, K.; Yodying, A.; Wongthadam, T.; Mahavik, N.; Tantanee, S. Assessment of flood hazard areas using Analytical Hierarchy Process over the Lower Yom Basin, Sukhothai Province. *Procedia Eng.* **2018**, *212*, 340–347. [CrossRef]
39. Cabrera, J.S.; Lee, H.S. Impacts of climate change on flood-prone areas in Davao Oriental, Philippines. *Water* **2018**, *10*, 893. [CrossRef]
40. Lim, M.B.B.; Lim, H.R.; Piantanakulchai, M. Flood evacuation decision modeling for high risk urban area in the Philippines. *Asia Pac. Manag. Rev.* **2019**, *24*, 106–113. [CrossRef]
41. Cai, T.; Li, X.; Ding, X.; Wang, J.; Zhan, J. Flood risk assessment based on hydrodynamic model and fuzzy comprehensive evaluation with GIS technique. *Int. J. Disaster Risk Reduct.* **2019**, *35*, 101077. [CrossRef]
42. Robielos, R.A.C.; Lin, C.J.; Senoro, D.B.; Ney, F.P. Development of vulnerability assessment framework for disaster risk reduction at three levels of geopolitical units in the Philippines. *Sustainability* **2020**, *12*, 8815. [CrossRef]

43. Prasetyo, Y.T.; Senoro, D.B.; German, J.D.; Robielos, R.A.C.; Ney, F.P. Confirmatory factor analysis of vulnerability to natural hazards: A household Vulnerability Assessment in Marinduque Island, Philippines. *Int. J. Disaster Risk Reduct.* **2020**, *50*, 101831. [CrossRef]
44. Chen, Y.R.; Yeh, C.H.; Yu, B. Integrated application of the analytic hierarchy process and the geographic information system for flood risk assessment and flood plain management in Taiwan. *Nat. Hazards* **2011**, *59*, 1261–1276. [CrossRef]
45. Gigović, L.; Pamučar, D.; Bajić, Z.; Drobnjak, S. Application of GIS-interval rough AHP methodology for flood hazard mapping in Urban areas. *Water* **2017**, *9*, 360. [CrossRef]
46. Cabrera, J.S.; Lee, H.S. Flood-prone area assessment using GIS-based multi-criteria analysis: A case study in Davao Oriental, Philippines. *Water* **2019**, *11*, 2203. [CrossRef]
47. PAGASA. Climatological Normals. Available online: <https://www.pagasa.dost.gov.ph/climate/climatological-normals> (accessed on 10 September 2022).
48. LGU Odiongan. *Comprehensive Land Use Plan (CLUP)*; LGU Odiongan: Romblon, Philippines, 2017.
49. HEC-HMS. Available online: <https://www.hec.usace.army.mil/software/hec-hms/> (accessed on 10 September 2022).
50. HEC-RAS. Available online: <https://www.hec.usace.army.mil/software/hec-ras/> (accessed on 10 September 2022).
51. GEOHAZARD MAPS. Available online: <https://region4b.mgb.gov.ph/28-geohazard-maps/98-geohazard-maps#romblon-2> (accessed on 10 September 2022).
52. Kokangül, A.; Polat, U.; Dağsuyu, C. A new approximation for risk assessment using the AHP and Fine Kinney methodologies. *Saf. Sci.* **2017**, *91*, 24–32. [CrossRef]
53. Employment of PWDs. Available online: <https://www.pwc.com/ph/en/taxwise-or-otherwise/2017/employment-of-pwds.html> (accessed on 2 June 2022).
54. Febrianto, H.; Fariza, A.; Hasim, J.A.N. Urban flood risk mapping using analytic hierarchy process and natural break classification (Case study: Surabaya, East Java, Indonesia). In Proceedings of the 2016 International Conference on Knowledge Creation and Intelligent Computing, KCIC 2016, Manado, Indonesia, 15–17 November 2016; pp. 148–154. [CrossRef]
55. National Disaster Management Office (NDMO). *Republic of Vanuatu National Guidelines for the Selection and Assessment of Evacuation Centres*; National Disaster Management Office: Port Vila, Vanatu, 2016.
56. Engay-Gutierrez, K.G. Land cover change in the silang-santa rosa river subwatershed, Laguna, Philippines. *J. Environ. Sci. Manag.* **2015**, *18*, 34–46. [CrossRef]
57. Stefanidis, S.; Stathis, D. Assessment of flood hazard based on natural and anthropogenic factors using analytic hierarchy process (AHP). *Nat. Hazards* **2013**, *68*, 569–585. [CrossRef]
58. Shrestha, B.B.; Okazumi, T.; Miyamoto, M.; Sawano, H. Development of flood risk assessment method for data-poor river basins: A case study in the Pampanga River Basin, Philippines. In Proceedings of the 6th International Conference on Flood Management, Sao Paulo, Brazil, 16–18 September 2014; Volume ii, pp. 1–12.
59. Shrestha, B.B.; Sawano, H.; Ohara, M.; Nagumo, N. Improvement in flood disaster damage assessment using highly accurate IfSAR DEM. *J. Disaster Res.* **2016**, *11*, 1137–1149. [CrossRef]
60. Lyu, H.M.; Sun, W.J.; Shen, S.L.; Arulrajah, A. Flood risk assessment in metro systems of mega-cities using a GIS-based modeling approach. *Sci. Total Environ.* **2018**, *626*, 1012–1025. [CrossRef]
61. Bera, R.; Maiti, R. Multi hazards risk assessment of Indian Sundarbans using GIS based Analytic Hierarchy Process (AHP). *Reg. Stud. Mar. Sci.* **2021**, *44*, 101766. [CrossRef]
62. Puno, G.R.; Amper, R.A.L.; Talisay, B.A.M. Flood simulation using geospatial models in Manupali Watershed, Bukidnon, Philippines. *J. Biodivers. Environ. Sci.* **2018**, *12*, 294–303.
63. Kia, M.B.; Pirasteh, S.; Pradhan, B.; Mahmud, A.R.; Sulaiman, W.N.A.; Moradi, A. An artificial neural network model for flood simulation using GIS: Johor River Basin, Malaysia. *Environ. Earth Sci.* **2012**, *67*, 251–264. [CrossRef]
64. Talisay, B.A.M.; Puno, G.R.; Amper, R.A.L. Flood hazard mapping in an urban area using combined hydrologic-hydraulic models and geospatial technologies. *Glob. J. Environ. Sci. Manag.* **2019**, *5*, 139–154. [CrossRef]
65. Pornasodoro, K.P.; Silva, L.C.; Munárriz, M.L.T.; Estepa, B.A.; Capaque, C.A. Flood Risk of Metro Manila Barangays: A GIS Based Risk Assessment Using Multi-Criteria Techniques. *J. Urban Reg. Plan.* **2014**, *1*, 51–72.
66. Clark, C. Flood risk assessment. *Int. Water Power Dam Constr.* **2007**, *59*, 1–25. [CrossRef]
67. Åström, H.L.A. *An Urban Flood Risk Assessment Method Using the Bayesian Network Approach*; DTU Environment, Technical University of Denmark: Lyngby, Denmark, 2015.
68. Feloni, E.; Mousadis, I.; Baltas, E. Flood vulnerability assessment using a GIS-based multi-criteria approach—The case of Attica region. *J. Flood Risk Manag.* **2020**, *13*, e12563. [CrossRef]
69. Tehrany, M.S.; Pradhan, B.; Jebur, M.N. Spatial prediction of flood susceptible areas using rule based decision tree (DT) and a novel ensemble bivariate and multivariate statistical models in GIS. *J. Hydrol.* **2013**, *504*, 69–79. [CrossRef]
70. Monjardin, C.E.F.; Senoro, D.B.; Magbanlac, J.J.M.; de Jesus, K.L.M.; Tabelin, C.B.; Natal, P.M. Geo-Accumulation Index of Manganese in Soils Due to Flooding in Boac and Mogpog Rivers, Marinduque, Philippines with Mining Disaster Exposure. *Appl. Sci.* **2022**, *12*, 3527. [CrossRef]

Article

A Database for Tsunamis and Meteotsunamis in the Adriatic Sea

Alessandra Maramai *, Beatriz Brizuela and Laura Graziani

Istituto Nazionale di Geofisica e Vulcanologia, 00143 Rome, Italy; beatriz.brizuela@ingv.it (B.B.); laura.graziani@ingv.it (L.G.)

* Correspondence: alessandra.maramai@ingv.it; Tel.: +39-06-51860210

Abstract: In the frame of the Interreg Italy-Croatia program, the EU has funded the PMO-GATE project, focusing on the prevention and mitigation of the socioeconomic impact of natural hazards in the Adriatic region. The Database of Adriatic Tsunamis and Meteotsunamis (DAMT) is one of the deliverables of this project. DAMT is a collection of data documenting both meteotsunami and tsunami effects along the Eastern and Western Adriatic coasts, and it was realized by starting from the available database and catalogues, with the inclusion of new data gained from recent studies, newspapers and websites. For each tsunami and meteotsunami, the database provides an overview of the event and a detailed description of the effects observed at each affected location and gives a picture of the geographical distribution of the effects. The database can be accessed through a GIS WebApp, which allows the user to visualize the georeferenced information on a map. The DAMT WebApp includes three layers: (1) Adriatic Tsunami Sources, (2) Adriatic Tsunami Observation Points and (3) Adriatic Meteotsunamis Observation Points. The database contains 57 observations of tsunami effects related to 27 tsunamis along the Italian, Croatian, Montenegrin and Albanian coasts and 102 observations of meteotsunami effects related to 33 meteotsunamis.

Keywords: Adriatic Sea; database; tsunami; meteotsunami; ArcGis; WebApp

Citation: Maramai, A.; Brizuela, B.; Graziani, L. A Database for Tsunamis and Meteotsunamis in the Adriatic Sea. *Appl. Sci.* **2022**, *12*, 5577. <https://doi.org/10.3390/app12115577>

Academic Editors: Andrea Chiozzi, Željana Nikolić and Elena Benvenuti

Received: 31 March 2022

Accepted: 25 May 2022

Published: 31 May 2022

Publisher's Note: MDPI stays neutral with regard to jurisdictional claims in published maps and institutional affiliations.



Copyright: © 2022 by the authors. Licensee MDPI, Basel, Switzerland. This article is an open access article distributed under the terms and conditions of the Creative Commons Attribution (CC BY) license (<https://creativecommons.org/licenses/by/4.0/>).

1. Introduction

Due to the increasing number of extreme events that are being experienced around the world, the interest of the scientific community in natural hazards has grown significantly in recent years, and one of the main targets is the prevention and reduction of risks related to natural events. The Sendai Framework for Disaster Risk Reduction (2015–2030) outlines the overall objectives to substantially reduce disaster risk and losses of lives, livelihoods, and health. It clearly states that in order to diminish the frequency and impact of disasters, it is required to better understand disaster risk (exposure to hazards, vulnerability and capacity and the hazard's characteristics) and furthermore to improve risk governance and increase resilience.

In this regard, many international projects related to the reduction of risk have been funded in the last decade, and the European Union has supported and financed some projects as well. In particular, a wide-ranging cross-border cooperation program between Italy and Croatia called Interreg has been established, focusing on the sea basin, coastal landscapes, green areas and urban areas as well.

The Adriatic Sea is the core center of the Italy-Croatia cooperation area, and it is a joint economic and environmental asset and a natural platform for combined efforts. The coastal area, both in Italy and in Croatia, is exposed to a range of natural hazards, particularly floods, strong winds, drought, earthquakes, tsunamis and meteotsunamis. Taking into account the coastal vulnerability, disaster risk reduction is a critical factor for the social and economic development of the involved countries.

In the framework of the Interreg Italy-Croatia program, Preventing, Managing and Overcoming Natural-Hazards Risks to mitiGATE economic and social impact (PMO-GATE)

has been funded, and it aims at increasing safety from natural and man-made disasters along both the Italian and Croatian coasts of the Adriatic Sea. Making the most of the capitalization on the expertise gained by all partners in previous projects, and using the data and the results available from previous studies, PMO-GATE's purpose is to enhance the level of protection and resilience against natural disasters specific of the region, such as river and sea floods, earthquakes, meteotsunamis and tsunamis. In particular, the project addresses the vulnerability of the Adriatic Sea system with its coasts and islands, implementing cross-border actions in the field of prevention and management regarding the exposure to floods and meteotsunamis in a seismically vulnerable context.

The final outcome of the project is an innovative methodology for preventing, managing and overcoming multi-hazard natural disasters, and climate-induced hazards (such as floods and meteotsunamis) will be combined with non-climate-induced hazards (earthquakes and tsunamis).

PMO-GATE addresses the general public, local and national public authorities, emergency services, education and training centers, universities and research institutes. An effective communication strategy to increase awareness and perception of risk in the population and public authorities is one of the pillars of the project, and the dissemination of results is one of the main goals of the project.

Among the different deliverables of PMO-GATE is the realization of a database for tsunamis and meteotsunamis occurring in the Adriatic region. The Database of Adriatic Tsunamis and Meteotsunamis (DAMT) is the result of the analysis of tsunami and meteotsunami databases existing in the literature for the Adriatic area. Although the two phenomena have different origins, they affect the coasts with similar characteristics and effects, and therefore, in terms of coastal hazard, similar prevention measures must be taken. The two phenomena have always been treated separately, and the creation of a single database is, therefore, important to optimize the hazard and risk studies in the area.

DAMT contains the Adriatic tsunamis present in the Italian Tsunami Effect Database (ITED) [1] and in the Euro-Mediterranean Tsunami Catalogue (EMTC) [2], while as far as meteotsunamis are concerned, the data are essentially those of the Catalogue of Meteorological Tsunamis in Croatian coastal waters (CMTC) [3], integrated with the results of new studies conducted during the PMO-GATE project. Therefore, DAMT is a tool that can be a starting point for a better understanding of the characteristics of such phenomena in the Adriatic area, and it can contribute to hazard and risk assessment for natural events.

PMO-GATE is also a contribution to delivering new data to educational initiatives in the future. In this frame, DAMT is a tool that has also been used for educational purposes during special events addressed to both the general public and scholars, such as World Earth Day [4] and the National Conference in Science Communication 2021 [5], in order to enhance risk perception, which is one of the main aims of the project.

2. Tsunamis and Meteotsunamis in the Adriatic Region

Among the various natural hazards to which the Adriatic coasts are exposed, the Istituto Nazionale di Geofisica e Vulcanologia (INGV), as a partner of PMO-GATE, has focussed its efforts on tsunamis and meteotsunamis with the aim of developing and implementing a database of these events: DAMT.

The geographical position of the Adriatic region is peculiar. It lies between the Apennine and Dinaric mountain chains, and it is mostly surrounded by active fold-and-thrust belts and strike-slip faults [6–8]. The presence of microplates and the complex system of faults in the area explain the seismicity which affects the Adriatic region.

Both Italy and Croatia experienced several earthquakes in the past, and a large number of studies were carried out with the aim of better assessing the seismicity of this region. It has been underlined that historical seismicity is poorly documented, and the Adriatic Sea is characterized by quite low seismic activity mainly consisting of earthquakes of moderate magnitudes, but important seismic sequences with main shocks of relevant magnitudes have also been observed [9–16]. Frequent earthquakes occur along the well-known fault

zones, most of which run close to the coastlines or in the open sea and are thus potential sources for tsunamis [17].

In the Adriatic region, the strongest earthquakes ($M > 7$) have occurred near the eastern margin of the central Adriatic Sea and at the southern end of the basin near the Ionian Islands. The majority of the remaining structures are potentially capable of generating earthquakes of magnitudes $6 \leq M \leq 7$, therefore having significant potential for causing tsunamis [6].

Tsunami is a well-known term mainly used in reference to earthquakes generated ocean waves, and they have a typical period range from a few to tens of minutes to hours. As they approach the coast, these waves can produce severe damage to coastal structures and can cause loss of human life.

Tsunamis are usually generated by submarine earthquakes. However, as the literature demonstrates, in the Adriatic region, as well as along the other Italian coasts, tsunamigenic sources are located both offshore and very close to the coast [1,18]. In this region, a number of tsunamis related to earthquake activity were observed [1,2,18–26]. Most of them had low intensities, but a few events, such as the 1627 Gargano and 1930 Ancona tsunamis, were classified as “very strong”.

Italian tsunamis are quite well-documented, and tsunami effects have been observed in many places from the northern to the southern Adriatic region, while in Croatia, tsunami effects have been reported along the northern and southern coasts, with no evidence along the central coast of the country. In Montenegro, tsunamis have been located along the whole coast, and along the Albanian coast, they were mainly located in the area of Valona. Twelve Adriatic tsunamis originated along the Italian coasts, being observed from 1348 to 1930 [18].

Tsunamis generated in the eastern Adriatic region are less frequent; four tsunamis, mainly of low intensities, were ascertained to have occurred since 1667 along the Croatian coast, while the Montenegro coast has been affected by three events since 1667. Six tsunamis have occurred along the Albanian coasts since 1833, all of which were concentrated in the coastal area of Valona. The Croatian coast is much more prone to meteotsunamis, which are meteorologically generated long ocean waves with characteristics similar to those of tsunamis, and they represent a significant hazard for the eastern Adriatic coast [23–25].

Meteotsunamis are formed by storm systems moving rapidly across the water, such as a squall line, and their development depends on several factors such as the intensity, direction and speed of the disturbance as it travels over a water body [23–25]. They can affect localized areas when they reach land. The wave heights and spatial extent of meteotsunamis are smaller compared with tsunamis, but they can cause sea level oscillations of several meters and human losses and injuries. Although meteotsunamis are not catastrophic to the extent of major seismically induced events, their occurrence in time and space are higher than those of seismic tsunamis, as the atmospheric disturbances responsible for the generation of meteotsunamis are much more common.

According to recent studies [26], extreme weather has been a common result of the planet’s rising temperature, and climate change, like global warming and the sea level rising, may have an impact on the future occurrence and likelihood of meteotsunamis.

The meteotsunami phenomenon is a relatively recent scientific discovery, considering that the first description of tsunami-like effects produced by atmospheric disturbances appeared only in 1931 [27] and that the term “meteotsunamis” was introduced only in 1961 [27].

Thus far, it has been shown that Mediterranean meteotsunamis tend to be stronger in summer. Despite calm conditions at ground level, fast winds of dry air from Africa in the atmosphere 1500 m up seem to trigger atmospheric waves. Mostly during summertime, small-scale strong atmospheric disturbances take place in the Adriatic area, and the coast has a quite complex topography, with a large number of funnel-shaped bays and harbors which have high amplification factors. In fact, the strength of a meteotsunami is also largely dependent on both the topography and the bathymetry of the affected area, and in the

Adriatic Sea, recurrent meteotsunami events are known to strongly impact the lifestyles of the coastal communities, particularly in the Dalmatian islands, where meteotsunamis can generate serious flooding. Several destructive events affected the eastern Adriatic shore in the last few decades, mainly involving Mali Lošinj, Ist, Stari Grad, Vela Luka and Mali Ston. The strongest event hit Vela Luka in Croatia in June 1978, with a wave height of 6 m (crest to trough) and a period of 18 min. This meteotsunami, the most powerful recorded in the Mediterranean, lasted several hours and caused USD 7 million in damage [28,29]. Siroka Bay in the island of Ist and Mali Losinj Bay in the island of Losinj are the two bays in the northern Adriatic where destructive meteotsunamis have occurred recently. Four-meter waves struck Siroka Bay on 22 August 2007, injuring one person and damaging local infrastructure [26]. This locality also experienced meteotsunami effects on 4 October 1984. Mali Losinj Bay was hit on 15 August 2008 by 2-m waves, flooding a forefront of the most populated town of the Adriatic Sea islands and causing a panic during tourist season [30,31].

3. The Database of the Adriatic Meteotsunamis and Tsunamis (DAMT)

The understanding of natural phenomena, including tsunamis and meteotsunamis, is essentially based on the deep knowledge of past events. In fact, knowing how many events occurred in the past in a specific region and studying their characteristics help to encourage the study of the more prone coastal areas to assess the hazard and to calibrate models of propagation and inundation. A proper and systematic dissemination of the acquired knowledge is also fundamental to increase the awareness of people living in vulnerable areas.

From this perspective, the availability of a database of events is very important because it is a useful tool for increasing public awareness and, when robust information is available, to validate hazard and risk assessments. In the frame of the PMO-GATE project, one of the deliverables is the creation of the database of Adriatic Tsunamis and Meteotsunamis (DAMT), which was carried out by starting from the catalogs available in the literature, particularly the Italian Tsunami Effects Database (ITED) [1], the Euro-Mediterranean Tsunami Catalogue [2] and the Catalogue of Meteorological Tsunamis in Croatian coastal waters [3].

DAMT was created by selecting and analyzing the information already available in both of the above-mentioned catalogs, as well as including new data acquired in the frame of the PMO-GATE project from the analysis of recent studies, newspapers and websites. As far as tsunamis are concerned, the data available in the catalogues cover a period of time ranging from 1348 to present day [1,2], while for meteotsunamis, the first information is only available from 1931 onward because for previous events, usually only the year of occurrence was known, and therefore, they were not verifiable or reliable [3]. For each tsunami and meteotsunami observation, the database provides a general description of the event, together with a detailed georeferenced description of the effects observed in each affected location, and offers a complete picture of the geographical distribution of the effects on the coast. In Table 1, the list of tsunamis and meteotsunamis included in DAMT is presented, reporting the main parameters for each event.

The data included in DAMT can be retrieved by the public through a web application similar to that used for ITED [1] which allows the user to visualize the georeferenced information on a map. The WebApp, developed in a freely accessible ESRI ArcGIS online environment, is accessible through this link (<https://ingv.maps.arcgis.com/apps/webappviewer/index.html?id=0f465d51001146d79a6c89884a8e5d8c>) (accessed on 20 May 2022) without the need for an Esri user account.

The DAMT WebApp includes three layers: (1) Adriatic Tsunami Sources (ATS), containing the information on the tsunamis that occurred in the Adriatic Basin, (2) Adriatic Tsunami Observation Points (ATOPs), namely the localities where tsunami effects were observed, and (3) Adriatic Meteotsunami Observation Points (AMOPs), which are the localities where meteotsunami effects were observed. In Figure 1, the main screen of the

DAMT WebApp is visible, showing the geographical distribution of the whole dataset contained in the database: tsunamis, where the location coincides with the epicenter of the earthquake that triggered the tsunami (blue squares), tsunami observation points (colored dots in shades of beige) and meteotsunami observation points (red points). Using the layers widget at the top right of the screen, the user can choose the layers to be displayed (*Layer List*).

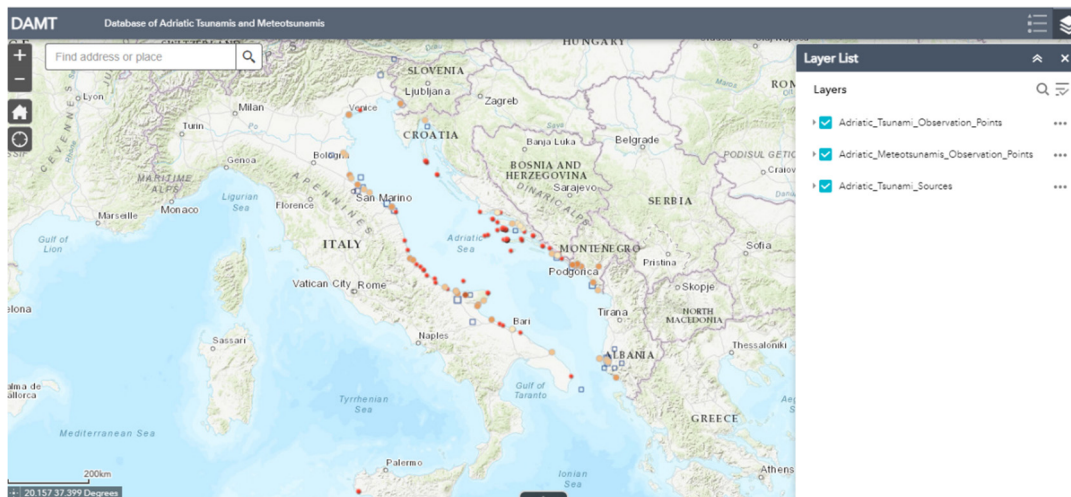


Figure 1. Main screen of the DAMT WebApp. On the right, the layer list is shown. Check marks indicate that all levels are highlighted in the map. Blue squares are tsunamigenic sources. Beige-shaded points are tsunami observation points. Red points are meteotsunami observation points.

The data contained in DAMT also populates an attribute table, which can be retrieved through the arrow located at the bottom of the main screen (Figure 2). The tabular information contained in each layer of the WebApp can be exported in csv format, and it can also be filtered by using user-customized expressions in the tab options of the database table (i.e., selecting data from the extent viewed, by date, reliability, cause, region, etc. or by a combination of several of these parameters).

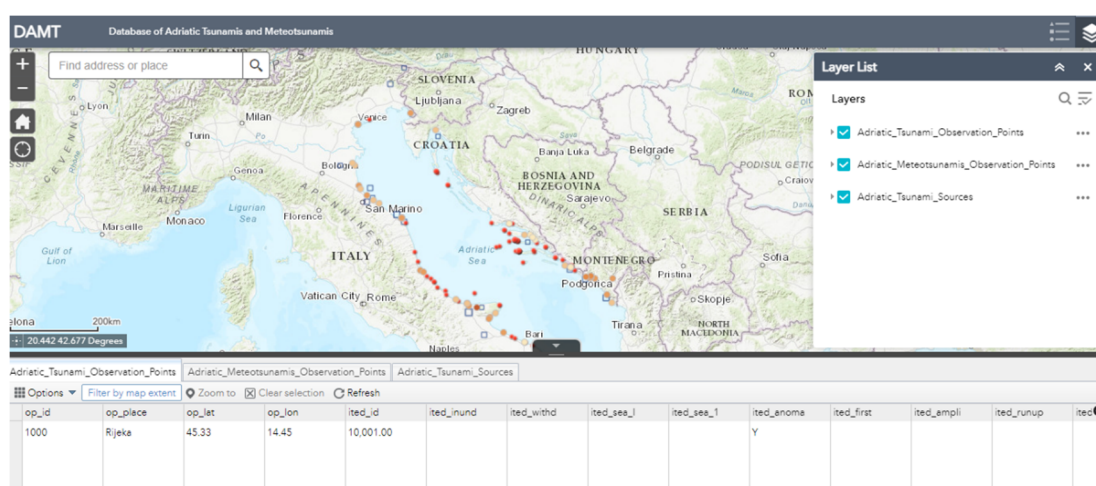


Figure 2. The attribute table allows the user to filter the data contained in the layers of the WebApp according to different selections.

As far as tsunamis are concerned, the ATS layer contains the 24 events with the general description of the effects, mainly taken from the EMTC [2].

Twelve tsunamis were located in the Italian coasts, four in the Croatian ones, three in Montenegro and six along the Albanian coasts. By clicking on one of the blue squares on the screen, a pop-up allows the user to obtain general information on the main parameters of the selected tsunami (earthquake parameters and tsunami intensity), and it can link to the general description of the event. In Figure 3a,b, the example of the 30 October 1930 Ancona tsunami is reported.

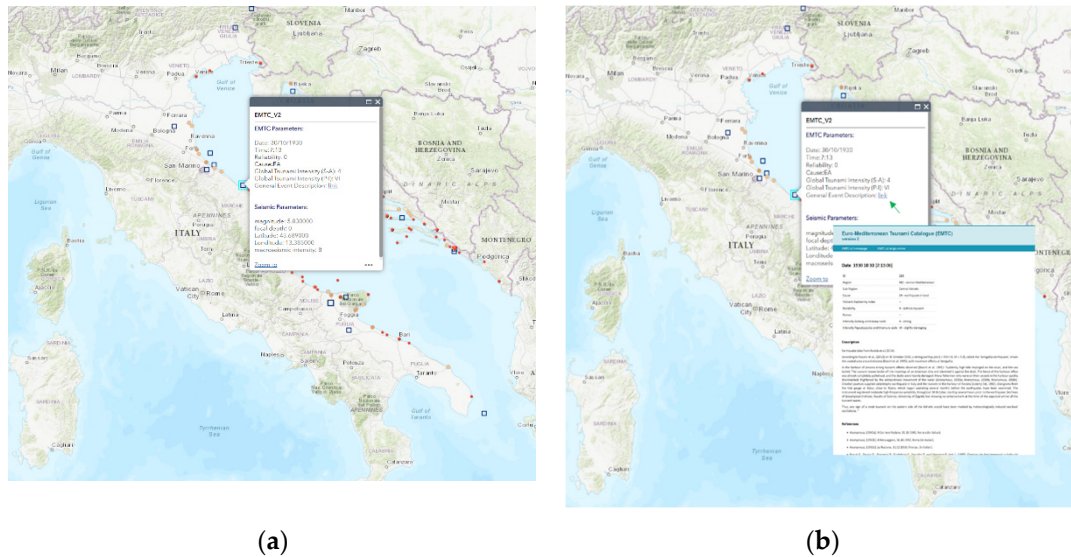


Figure 3. (a) Example of pop-up of the ATS layer, showing the main parameters of the 30 October 1930 Ancona tsunami. (b) Example of the 30 October 1930 Ancona tsunami, where the green arrow indicates the link to click on for the general description of the event.

With regard to the Adriatic Tsunami Observation Points (ATOPs) layer, it hosts 57 observation points where tsunami effects were observed: 28 on the Italian coast, 10 in Croatia, 9 in Montenegro and 9 in Albania, respectively (Figure 4a). The Italian ATOPs came from ITED [1], while ATOPs located on the eastern coasts of the Adriatic Sea came from the analysis of the descriptions of the tsunamis contained in EMTC [2]. Additional information has enriched the knowledge on the tsunamis reported in the catalogue. For eastern coast events, additional information was included, and for each observation point, a “local” tsunami intensity value was assessed as “ex novo” on both the Ambraseys–Sieberg [32] and Papadopoulos–Imamura [33] scales. The beige-shaded points are the locations where tsunami effects were observed, while the darker points correspond to more severe effects. For each point, descriptive and, when available, quantitative information (inundation, run-up and wave height values) is provided, along with the corresponding bibliographical references. By clicking on each point, through a pop-up window, the user can obtain information about the effects observed, as well as the main info on the generating tsunami (Figure 4b). Among the Adriatic tsunamis, the maximum run-up observed was 2.5 m at Manfredonia (Apulia region in Italy) during the event on 30 July 1627, while the largest inundation was 50 m at Boka Kotorska (Montenegro) for the event on 15 April 1979, during which one person died [1].

The Adriatic Meteotsunami (AM) layer contains 33 meteotsunami events observed or recorded in 54 places along both the eastern and western Adriatic coasts. Most of the data came from [3], with new information, new events and images being added. Among these 54 places, 8 experienced meteotsunami effects more than once. In particular, from 1931 to the present, Vela Luka has been affected by 18 events, and Stari Grad has been affected by 11 events. In Figure 5, the geographical distribution of the places where meteotsunami effects have been observed is visible. As already mentioned above, meteotsunamis are mainly localized along the coasts of Croatia. As for the northern Adriatic region, although

it is a region prone to Proudman resonances, due to the lack of bays or harbors with high amplification factors, no major meteotsunamis occur in that area [23]. Conversely, the Croatian coast of the central Adriatic, characterized by many islands, channels and narrow bays, is the area where the most meteotsunamis occur (Figure 4), most of which are very powerful. On the Italian coasts, most of the effects were due to the 21 June 1978 event, the strongest in the Mediterranean, but some locations were also affected by the 25 June 2014 event.

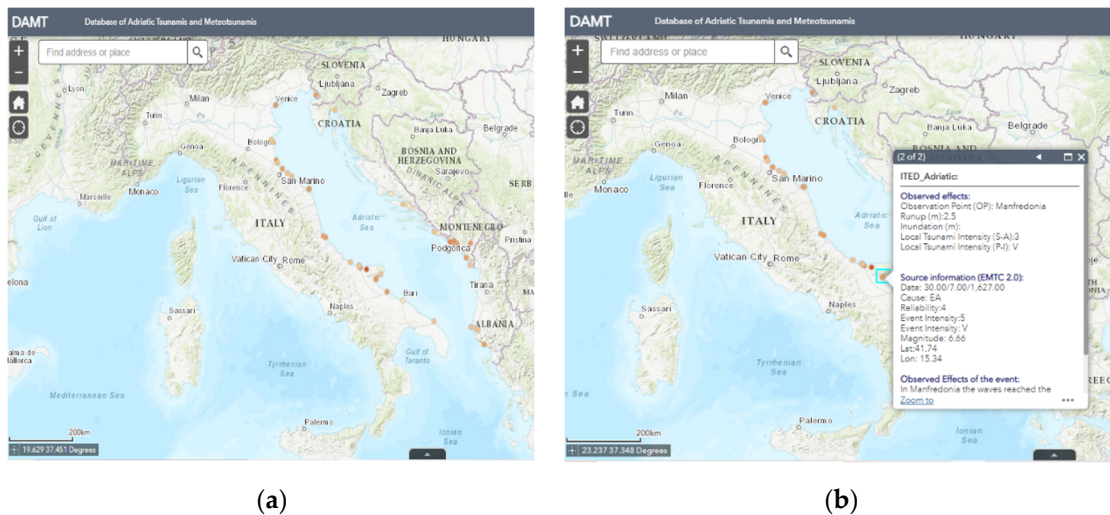


Figure 4. (a) Geographical distribution of the Tsunami Observation Points (ATOP layer). (b) An example of the pop-up for the Manfredonia (Apulia) observation point.

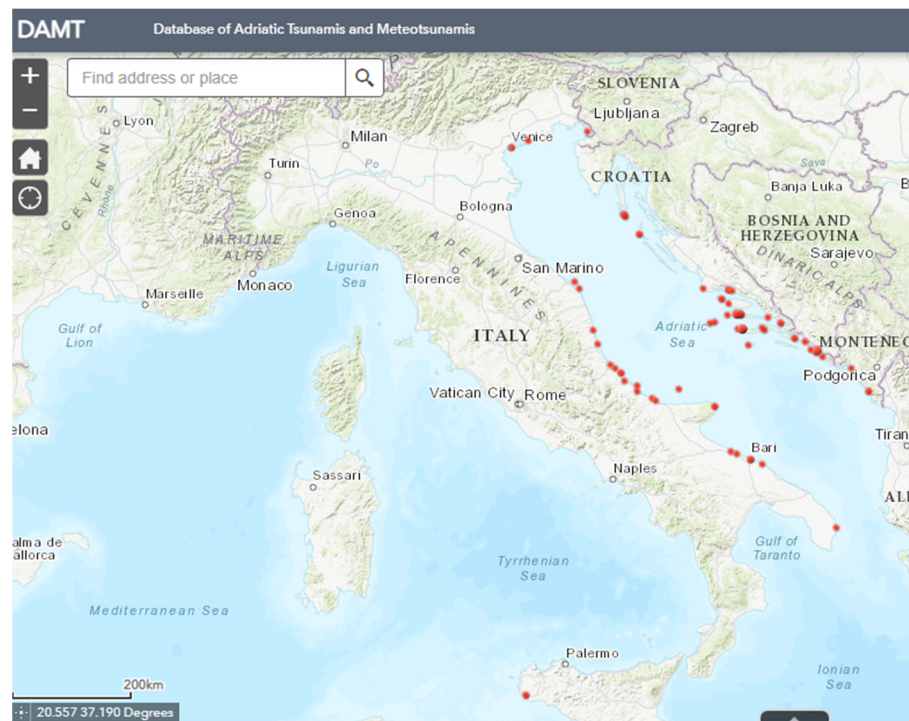


Figure 5. Geographical distribution of the meteotsunami effects.

As for tsunamis, and also for meteotsunamis reported in the WebApp, the user can click on each point where the effects were observed. The pop-up window shows the date of the event (or several dates if there is more than one event at the same point), a short description of the observed effects, a link to the general description of the event and the intensity. Since

meteotsunamis are a very complex phenomenon involving meteorological, hydrological and bathymetric factors, for their classification, Orlić and Šepić [3] introduced a value, the QIndex, that indicates how detailed the information about the event is. The QIndex ranges from 1 (elementary description of sea-level variability) to 5 (analysis of oceanographic and meteorological data combined with both oceanographic and meteorological modeling), depending on what kind of bibliographic sources support the available data. In DAMT, the same type of classification has been used, maintaining the QIndex values assigned by [3] and assigning the QIndex to the new events inserted. Figure 6 shows an example of the pop-up for the 11 May 2020 event.

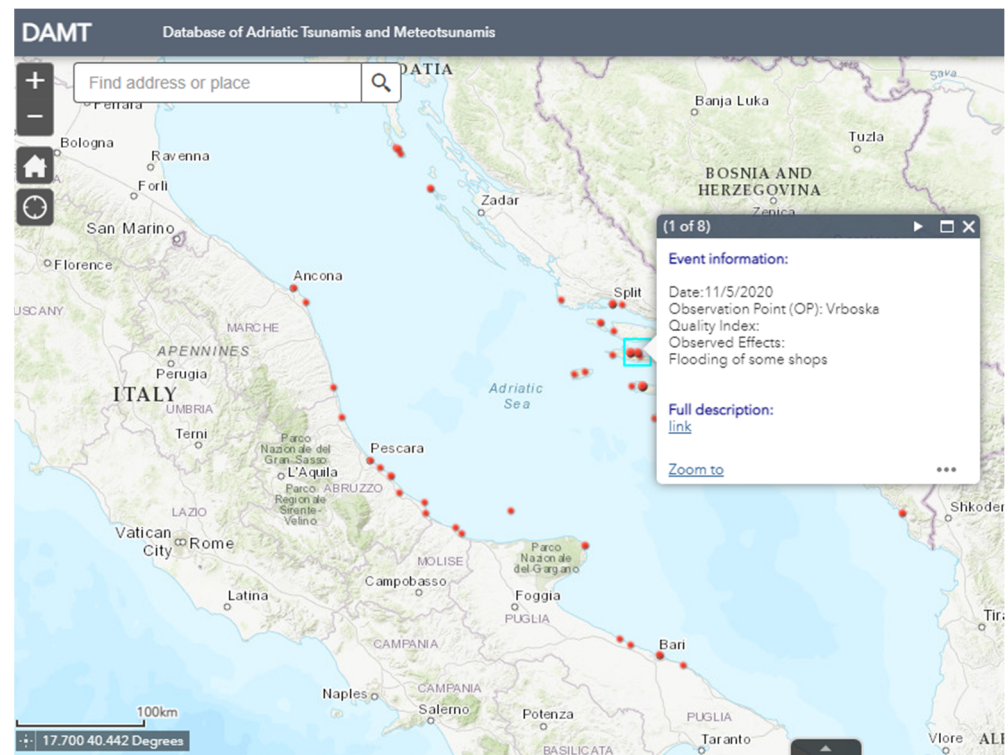


Figure 6. Example of a pop-up of the AM layer, showing the 15 May 2020 at Vrboska observation point. By clicking on the full description link, the user can retrieve detailed information on all effects observed at that location over time.

4. Discussion

The analysis of the characteristics of past events provides clues to what might happen in the future. In this perspective, a database can be an important and useful starting point to better characterize a region in terms of these phenomena. In the frame of the PMO-GATE project, the realization of a database which includes tsunamis and meteotsunamis in the Adriatic region aims at providing a comprehensive picture of the events in order to highlight that the Adriatic region is prone to these events.

DAMT, for the first time, brings together two phenomena, tsunamis and meteotsunamis, which although originating from different causes produce very similar effects when they hit the coast. Therefore, the measures to be implemented for the prevention and reduction of coastal hazards could be similar.

DAMT was built by starting from the data included in the ITED database [1], in the Euro-Mediterranean Tsunami Catalogue [2] and in the Catalogue of Meteorological Tsunamis in Croatian coastal waters by Orlić and Šepić [3], with the insertion of new events and new info and parameters for the events which had already been catalogued. In Table 1, short descriptions of the events included in the database are reported. DAMT aims to enhance the usability of data and is displayed by means of an ESRI WebApp that allows

the user to query the database in order to retrieve general and detailed information about events, select the events of interest and know the tsunami and meteotsunami history for each observation point. As far as tsunamis, DAMT contains observations of 24 events that have been reported from 1348 to present day, all of which were caused by earthquakes. The analysis of the database puts forth the evidence that in the Adriatic region, the most affected coasts are the Italian ones, which have been affected by 12 events since 1348. Among them, the central northern coast (Emilia Romagna) and the southern one (Apulia) experienced the most relevant events. Four tsunamis have occurred on the coasts of Croatia from 1667 to 1962, three events have affected the coasts of Montenegro in 1667, 1780 and 1979, and finally, the coasts of Albania experienced six tsunamis from 1833 to 1920.

The tsunamis included in DAMT are classified by a *reliability index*, a value indicating the quality and reliability of the data [21]. Fourteen events (about 60%) have the maximum reliability (four = definite tsunami), and only three events, all of which occurred in Albania in the 1800s, have a reliability of one (very improbable tsunami). Inserting in the database events with low reliability as well allows for keeping a record of those for which little information is available and of which one could otherwise lose track. At the same time, it allows the user to know that the information available for that event is not sufficiently robust to attribute a high reliability value to the event, and therefore, it must be considered with due attention.

Regarding tsunami intensity, to each observation point was assigned a local intensity value based on both the Ambraseys–Sieberg and Papadopoulos–Imamura scales. Most of the events (80%) had intensities that were medium-low, light (2) or rather strong (3), but there were four events with strong (4) and very strong (5) intensities. Two of these tsunamis occurred in Italy in 1627 and 1930, one which took place in Albania in 1920 while the other occurred on the Croatian coast in 1979.

As highlighted by a detailed study of Adriatic tsunamis [34], the analysis of DAMT confirmed that there is no evidence of tsunami effects on the eastern Adriatic side related to the western Adriatic events. However, during two events in the eastern Adriatic region, light effects were observed on the Italian coasts. In particular, after the devastating 1667 Dubrovnik earthquake, anomalous movements were observed in the waters of the canals of Venice, while the tsunami generated by the 1979 Montenegro earthquake was recorded by the tide gauge of Bari in Apulia.

Modeling studies of tsunami propagation from different source areas and tsunami hazards in the Adriatic Sea have shown that earthquakes in the northern Adriatic Sea are not very efficient in generating tsunamis due to the shallow water depth, while the central Adriatic Sea has low seismicity and shallow water, and tsunami waves arriving from the southern Adriatic Sea are partly reflected by the Palagruža rocks [6,34]. Furthermore, the Croatian island chain protects both coasts from tsunami waves propagating from the opposite side of the Adriatic. According to [20], earthquakes located in front of the Montenegrin coast are more efficient at generating tsunamis, and the seismically active region in front of the Albanian coast can generate severe tsunamis, but the modeling results are contradictory as to whether or not tsunamis generated in this area can propagate toward the Italian coasts [6,34]. At the moment, the evidence of the recording of sea level variation during the 1979 Montenegro earthquake in the tide gauge of Bari suggests a possible propagation from the eastern to the western coasts [34]. However, further studies are recommended.

Concerning meteotsunamis, DAMT reports 33 events that occurred from 1931 to the present date, with 103 observations related to 58 places. Compared with tsunamis, for meteotsunamis, the time interval covered by DAMT is much shorter, since the first meteotsunami included occurred in 1931. This is essentially due to two factors: (1) as highlighted in [3], for previous events, usually only the year of occurrence was known, and therefore, they were not verifiable or reliable, and (2) meteotsunamis as a phenomenon are a recent discovery. Just think that the first description of tsunami-like effects produced by

atmospheric disturbances appeared only in 1931 [27], and the term “meteotsunami” was introduced only in 1961 [27].

As also highlighted in [31], for the characterization and proper definition of a meteotsunami event, long-term, high-frequency measurements are necessary. Unfortunately, as mentioned above, historical observations of meteotsunamis in the Adriatic region were extremely scarce and poorly detailed until the early 1930s. In addition, only in recent decades have instruments capable of analyzing such phenomena been installed.

Gathering the information and cataloguing these events is crucial to identify “hot-spots”, which intensify observational networks in order to obtain, in the future, a robust dataset number to characterize these events, both in terms of effects produced and generated characteristics.

Although the number of events present in DAMT does not allow for performing statistical analysis, it enables us to make general observations.

The exam of the meteotsunami events included in DAMT shows that all of them originated from the Croatian coasts, mainly in the central part of the region. Unlike the tsunamis, the effects of three of them—the 19 September 1977, 21 June 1978 and 25 June 2014 events—were also clearly observed along the Italian coasts. The latter, the strongest meteotsunami in the Mediterranean that was destructive in Vela Luka, affected 14 locations along the Italian coast from Ancona to Otranto, causing serious damage in some places and some injuries in Vieste.

For the classification of meteotsunamis, in the DAMT, we used the criterion proposed by the authors of [3], who assigned a QIndex to each event based on how detailed the bibliographic sources were according to different parameters. In addition, considering the description of meteotsunami effects as if they were tsunami descriptions, in the DAMT, a local intensity value was also assigned for each observation point (OP) according to both Ambraseys–Sieberg [32] and Papadopoulos–Imamura [33] scales. During this process, it was pointed out that the two scales, created for a very similar but nonetheless different phenomenon, are not properly suited for meteotsunami intensity assessment. This is particularly evident for the Papadopoulos–Imamura scale, which has a higher number of degrees (12) with respect to the Ambraseys–Sieberg scale (6 degrees), and the more devastating effects that are described in the higher degrees cannot be produced by meteotsunamis. In fact, even in the case of a very strong meteotsunami, such as the one on 21 June 1978, the observed effects reached a maximum of five on the Ambraseys–Sieberg scale, while they reached a maximum of seven on the Papadopoulos–Imamura scale.

The DAMT contains several reliable data, and it is a tool that can contribute to improving the knowledge of tsunami and meteotsunami activity in the Adriatic area and to increase public awareness along these coasts which, especially in the peak season, are some of most densely populated areas in the Mediterranean. The database has already been used several times for educational purposes to increase the awareness of public authorities, citizens and students toward coastal hazards, and it will be one of the main tools for dissemination of the PMO-GATE project results.

As mentioned earlier, the availability of long-term observations is essential to characterizing the events in a region. Therefore, particularly with regard to meteotsunamis, in the Adriatic area, two factors could be beneficial in the near future: an increase in tide gauge and barometric instrumentation, especially in “hot-spots” that are particularly prone to meteotsunamis on one hand, and on the other hand, in-depth research of bibliographic sources on events that occurred in the past, mainly before 1931. Regarding the latter, a collaboration with Croatian and Albanian researchers is going to start in order to consult local archives and libraries.

Table 1. List of the events included in DAMT with the main parameters. Y = year, M = month, D = day of the event, Ev = type of event (T = tsunami; M = meteotsunami), Lat-Lon. = coordinates of the tsunamigenic earthquake, Description = short description of the main effects, OP = number of observation points where effects were observed; Int. = maximum intensity of the event, where the first number is the value according to the Ambraseys–Sieberg scale and the roman number is the value according to the Papadopoulos–Imamura scale, QI/Rel. = quality index (meteotsunami) and reliability (tsunami), and Source = catalogue from which the data were mainly derived.

Y	M	D	Ev	Lat.	Lon.	Description	OP	Int.	QI/Rel.	Source
1348	1	25	T	46.500	13.580	Agitation in canals in Venice	1	2/III	2	EMTC and ITED
1511	3	26	T	46.210	13.220	Large sea level rise at Trieste	2	3/V	2	EMTC and ITED
1624	3	19	T	44.640	11.850	Strong agitation in Po River and coastal lagoons	3	2/III	4	EMTC and ITED
1627	7	30	T	41.740	15.340	Large sea withdrawal and flooding in Lesina	7	5/V	4	EMTC and ITED
1667	4	6	T	42.600	18.100	Sea withdrawal at Dubrovnik	3	3/V	4	EMTC and ITED
1672	4	14	T	43.940	12.580	Sea withdrawal and flooding at Rimini	1	3/IV	4	EMTC and ITED
1690	12	23	T	43.550	13.590	Boats stranded in Ancona	1	3/IV	2	EMTC and ITED
1731	3	20	T	41.270	15.760	Sea rise at Siponto and Barletta	2	3/IV	4	EMTC and ITED
1743	2	20	T	39.850	18.770	Sea withdrawal at Brindisi	1	2/III	2	EMTC and ITED
1780	9	21	T	42.400	18.500	Sea withdrawal in Kotor	2	3/IV	4	EMTC and ITED
1833	1	19	T	40.400	19.900	Tsunami at Saseno Island	1	2/V	1	EMTC and ITED
1838	8	10	T	45.200	14.500	Sea oscillations at Fiume	1	2/III	2	EMTC and ITED
1845	8	16	T	42.640	18.110	Sea level rise at Gruž	2	3/IV	4	EMTC and ITED
1851	10	12	T	40.700	19.700	Sea level rise at Valona	1	2/IV	4	EMTC and ITED
1866	1	2	T	40.300	19.400	Tsunami at Valona and Kanina	2	2/VII	3	EMTC and ITED
1866	3	3	T	40.400	19.500	Tsunami at Valona, Kanina and Himara	3	3/IV	1	EMTC and ITED
1875	3	17	T	44.210	12.660	Sea flooding at Rimini and Cervia	5	3/IV	4	EMTC and ITED
1889	12	8	T	41.830	15.690	Sea agitation in Termoli and Mattinata	2	2/III	2	EMTC and ITED
1893	6	14	T	40.300	19.700	Tsunami at Valona	1	2/V	1	EMTC and ITED
1916	8	16	T	44.020	12.740	At Tavollo, tsunami waves observed	1	2/IV	4	EMTC and ITED
1920	12	18	T	40.500	19.500	Tsunami at Saseno Island	1	5/VIII	4	EMTC and ITED
1930	10	30	T	43.690	13.380	Sudden high tide at Ancona	1	4/VI	4	EMTC and ITED
1931	7	21	M			Flooding and ebb at Vela Luka	1	3/IV	1	CMCT
1935	5	28	M			Strong seiches at Vela Luka	1	3/IV	1	CMCT
1937	9	12	M			Large seiches at Vela Luka	1	3/IV	1	CMCT
1951	11	11	M			Strong flood of houses and shops	4	4/VII	1	CMTC
1956	7	21	M			Large flood at Vela Luka	1	2/IV	1	CMTC
1962	1	11	T	43.150	16.940	Sea level oscillation at Split	4	2/II	4	EMTC and ITED
1966	8	27	M			Flooding, boats damaged at Korčula	1	4/V	2	CMTC
1972	2	10	M			Flooding of roads at Vela Luka	1	3/IV	2	CMTC and DAMT
1977	8	21	M			Severe flooding, boats damaged at Vela Luka	1	4/V	2	CMTC
1977	9	19	M			Severe flooding, damage, 5 injured at Jesolo	4	4/VI	2	CMTC and DAMT
1978	6	21	M			Inundation, heavy damage, injured people	30	5/VII	5	CMTC and DAMT
1978	7	6	M			Damage on the waterfront at Vela Luka	1	4/V	2	CMTC
1979	2	12	M			Flooding of roads in Vela Luka	1	3/IV	2	CMTC
1979	4	15	T	42.020	19.070	Damaging wave at Kotor Bay	9	4/VII	4	EMTC and ITED

Table 1. Cont.

Y	M	D	Ev	Lat.	Lon.	Description	OP	Int.	QI/Rel.	Source
1980	7	10	M			Strong inundation and heavy damage	2	4/VI	2	CMTC and DAMT
1984	10	5	M			Big waves in Siroka Bay	1	3/IV	2	CMTC
1987	7	26	M			No description	3	1/I	1	CMTC
2003	6	27	M			Large inundation and damage to shops at Stari Grad	6	4/VI	2	CMTC and DAMT
2006	5	24	M			Strong waves at Vrboska	1	2/III	1	CMTC
2007	8	22	M			Damaging wave in Siroka Bay	2	4/V	2	CMTC and DAMT
2008	8	15	M			Flood and damage at Mali Lošinj	1	4/VI	2	CMTC and DAMT
2010	2	19	M			Severe damage to houses and shops at Stari Grad	1	4/VI	2	CMTC and DAMT
2014	6	25	M			Inundation and many boats destroyed	20	4/V	5	CMTC and DAMT
2017	6	28	M			Inundation of the waterfront at Stari Grad	1	3/IV	2	CMTC and DAMT
2017	6	30	M			Inundation of the promenade, slight damage	2	4/V	2	CMTC and DAMT
2017	7	11	M			Flooding of streets and shops	3	4/VI	2	CMTC and DAMT
2018	3	31	M			Flooding of buildings and shops at Stari Grad	1	4/V	2	CMTC and DAMT
2018	10	29	M			Tide gauge record	1	1/II	2	CMTC
2019	7	9	M			Inundation of piers	2	2/II	2	DAMT
2019	11	12	M			Strong flooding of the quays at Vrboska	1	3/III	2	DAMT
2020	2	16	M			Some boats stranded in the Bay of Stobreč	1	3/IV	2	DAMT
2020	2	23	M			No description	3	1/I	1	DAMT
2020	5	11	M			Flooding of shops in Vrboska	3	3/V	5	DAMT
2020	5	14	M			Flooding of the waterfront at Vela Luka	2	3/V	5	DAMT
2020	5	16	M			Flooding of shops and cafes at Vela Luka	1	3/V	3	DAMT

Author Contributions: Conceptualization, A.M. and L.G.; methodology, A.M.; software, B.B.; validation, A.M.; formal analysis, A.M.; investigation, A.M.; resources, A.M.; data curation, A.M.; writing—original draft preparation, A.M.; writing—review and editing, A.M., B.B. and L.G.; visualization, A.M.; supervision, A.M.; project administration, A.M.; funding acquisition, A.M. All authors have read and agreed to the published version of the manuscript.

Funding: This research was funded by the EUROPEAN UNION, Programme Interreg Italy-Croatia, Project “Preventing, managing and overcoming natural-hazards risks to mitigate economic and social impact” PMO-GATE ID 10046122.

Institutional Review Board Statement: Not applicable.

Informed Consent Statement: Not applicable.

Data Availability Statement: The datasets presented in this study can be found in online repositories. The name of the repository and accession number can be found below: <https://ingv.maps.arcgis.com/apps/webappviewer/index.html?id=0f465d51001146d79a6c89884a8e5d8c> (accessed on 20 May 2022).

Acknowledgments: The authors thank Mario Locati, (INGV, Milan) for the technical support during the realization of the DAMT database.

Conflicts of Interest: The authors declare no conflict of interest.





References

- Maramai, A.; Graziani, L.; Brizuela, B. *Italian Tsunami Effects Database (ITED): The First Database of Tsunami Effects Observed along the Italian Coasts*; Istituto Nazionale di Geofisica e Vulcanologia: Milan, Italy, 2019. [CrossRef]
- Maramai, A.; Brizuela, B.; Graziani, L. The Euro-Mediterranean Tsunami Catalogue. *Ann. Geophys.* **2014**, *57*, S0435. [CrossRef]
- Orlić, M.; Šepić, J. Meteorological Tsunamis in the Adriatic Sea—Catalogue of Meteorological Tsunamis in Croatian Coastal Waters. Available online: http://jadran.izor.hr/~sepic/meteotsunami_catalogue/ (accessed on 15 March 2022).
- The Meteotsunami Risk in the Adriatic Sea. Available online: https://www.youtube.com/watch?v=xJaxMxTsu_s (accessed on 26 April 2022).
- Italian Conference on Science Communication, SISSA Trieste. 17–20 November 2021. Available online: <https://www.facebook.com/pmogate> (accessed on 26 April 2021).
- Tiberti, M.M.; Lorito, S.; Basili, R.; Kastelic, V.; Piatanesi, A.; Valensise, G. Scenarios of Earthquake-Generated Tsunamis for the Italian Coast of the Adriatic Sea. *Pure Appl. Geophys.* **2008**, *165*, 2117–2142. [CrossRef]
- Ollier, C.D.; Pain, C.F. The Apennines, the Dinarides, and the Adriatic Sea: Is the Adriatic microplate a reality? *Geogr. Fis. Dinam. Quat.* **2009**, *32*, 167–175.
- Piccardi, L.; Sani, F.; Moratti, G.; Cunningham, D.; Vittori, E. Present-day geodynamics of the circum-Adriatic region: An overview. *J. Geodynam.* **2011**, *51*, 81–89. [CrossRef]
- Bada, G.; Horvath, F.; Gemer, P.; Fejes, I. Review of the present-day geodynamics of the Pannonian basin: Progress and problems. *J. Geodynam.* **1999**, *27*, 501–527. [CrossRef]
- Babbucci, D.; Tamburelli, C.; Viti, M.; Mantovani, E.; Albarello, D.; D’Onza, F.; Cenni, N.; Mugnaioli, E. Relative motion of the Adriatic with respect to the confining plates: Seismological and geodetic constraints. *Geophys. J. Int.* **2004**, *159*, 765–775. [CrossRef]
- Battaglia, M.; Murray, M.H.; Serpelloni, E.; Bürgmann, R. The Adriatic region: An independent microplate within the Africa Eurasia collision zone. *Geophys. Res. Lett.* **2004**, *31*, L09605. [CrossRef]
- Venisti, N.; Calcagnile, G.; Pontevivo, A.; Panza, G.F. Tomographic Study of the Adriatic Plate. *Pure Appl. Geophys.* **2005**, *162*, 311–329. [CrossRef]
- Pinter, N.; Grenczy, G. Recent advances in Peri-Adriatic geodynamics and future research directions. In *The Adria Microplate: GPS Geodesy, Tectonics and Hazards*, 1st ed.; Pinter, N., Grenczy, G., Weber, J., Stein, S., Medak, D., Eds.; Springer: Dordrecht, The Netherlands, 2006; pp. 1–20. [CrossRef]
- Altiner, Y.; Bačić, Z.; Bačić, T.; Cotichia, A.; Medved, M.; Mulić, M.; Nurçe, B. Present-day tectonics in and around the Adria plate inferred from GPS measurements. In *Postcollisional Tectonic and Magmatism in the Mediterranean Region and Asia*; Dilek, Y., Pavlides, S., Eds.; The Geological Society of America: Boulder, CO, USA, 2006; pp. 43–55. [CrossRef]
- Thouvenot, F.; Fréchet, J. Seismicity along the northwestern edge of the Asia Microplate. In *The Asia Microplate: GPS Geodesy, Tectonics and Hazards*, 1st ed.; Pinter, N., Grenczy, G., Weber, J., Stein, S., Medak, D., Eds.; Springer: Dordrecht, The Netherlands, 2006; pp. 335–349. [CrossRef]
- Muço, B. Seismicity of the Adriatic Microplate and a possible triggering: Geodynamic implication. In *The Asia Microplate: GPS Geodesy, Tectonics and Hazards*, 1st ed.; Pinter, N., Grenczy, G., Weber, J., Stein, S., Medak, D., Eds.; Springer: Dordrecht, The Netherlands, 2006; pp. 351–367. [CrossRef]
- Lorito, S.; Tiberti, M.M.; Basili, R.; Piatanesi, A.; Valensise, G. Earthquake-generated tsunamis in the Mediterranean Sea: Scenarios of potential threats to Southern Italy. *J. Geophys. Res.* **2008**, *113*, B01301. [CrossRef]

18. Maramai, A.; Graziani, L.; Tinti, S. Investigation on tsunami effects in the central Adriatic Sea during the last century—A contribution. *Nat. Hazards Earth Syst. Sci.* **2007**, *7*, 15–19. [CrossRef]
19. Caputo, M.; Fatta, G. Primo catalogo dei maremoti delle coste italiane. *Atti Accad. Naz. Lincei Mem. Cl. Sci. Fis. Mat. Nat. Rend.* **1986**, *80*, 213–356.
20. Bedosti, B.; Caputo, M. Primo aggiornamento del catalogo dei maremoti delle coste italiane. *Atti Accad. Naz. Lincei Rend. Cl. Sci. Fis. Mat. Nat.* **1987**, *80*, 570–584.
21. Tinti, S.; Maramai, A.; Graziani, L. The New Catalogue of Italian Tsunamis. *Nat. Hazards* **2004**, *33*, 439–465. [CrossRef]
22. Paulatto, M.; Pinat, T.; Romanelli, F. Tsunami hazard scenarios in the Adriatic Sea domain. *Nat. Hazards Earth Syst. Sci.* **2007**, *7*, 309–325. [CrossRef]
23. Monserrat, S.; Vilibić, I.; Rabinovich, A.B. Meteotsunamis: Atmospherically induced destructive ocean waves in the tsunami frequency band. *Nat. Hazards Earth Syst. Sci.* **2006**, *6*, 1035–1051. [CrossRef]
24. Rabinovich, A.B.; Vilibić, I.; Tinti, S. Meteorological tsunamis: Atmospherically induced destructive ocean waves in the tsunami frequency band. *Phys. Chem. Earth* **2009**, *34*, 891–893. [CrossRef]
25. Vilibić, I.; Denamiel, C.; Zemunik, P.; Monserrat, S. The Mediterranean and Black Sea meteotsunamis: An overview. *Nat. Hazards* **2021**, *106*, 1223–1267. [CrossRef]
26. Bechle, A.J.; Wu, C.H.; Kristovich, D.A.R.; Anderson, E.J.; Schwab, D.J.; Rabinovich, A.B. Meteotsunamis in the Laurentian Great Lakes. *Sci. Rep.* **2016**, *6*, 37832. [CrossRef]
27. Pattiaratchi, C.B.; Wijeratne, E.M.S. Are meteotsunamis an underrated hazard? *Philos. Trans. A Math. Phys. Eng. Sci.* **2015**, *373*, 20140377. [CrossRef]
28. Vučetić, T.; Vilibić, I.; Tinti, S.; Maramai, A. The Great Adriatic flood of 21 June 1978 revisited: An overview of the reports. *Phys. Chem. Earth* **2009**, *34*, 894–903. [CrossRef]
29. Orlić, M.; Belusić, D.; Janekivić, I.; Pasarić, M. Fresh evidence relating the great Adriatic surge of 21 June 1978 to mesoscale atmospheric forcing. *J. Geophys. Res.* **2010**, *115*, C06011. [CrossRef]
30. Sepić, J.; Vilibić, I.; Monserrat, S. Teleconnections between the Adriatic and the Balearic meteotsunamis. *Phys. Chem. Earth* **2009**, *34*, 928–937. [CrossRef]
31. Belušić, D.; Strelec Mahović, N. Detecting and following atmospheric disturbances with a potential to generate meteotsunamis in the Adriatic. *Phys. Chem. Earth* **2009**, *34*, 918–927. [CrossRef]
32. Ambraseys, N.N. Data for the investigation of seismic sea waves in the Eastern Mediterranean. *Bull. Seism. Soc. Am.* **1962**, *52*, 895–913.
33. Papadopoulos, G.A.; Imamura, F. A proposal for a new tsunami intensity scale. *Environ. Sci.* **2001**, *5*, 569–577.
34. Pasarić, M.; Brizuela, B.; Graziani, L.; Maramai, A.; Orlić, M. Historical tsunamis in the Adriatic Sea. *Nat. Hazards* **2012**, *61*, 281–316. [CrossRef]

Article

Shifting of Meteorological to Hydrological Drought Risk at Regional Scale

Awais Naeem Sarwar¹, Muhammad Waseem^{1,*}, Muhammad Azam², Adnan Abbas³, Ijaz Ahmad¹,
Jae Eun Lee^{4,*} and Faraz ul Haq¹

- ¹ Centre of Excellence in Water Resources Engineering, University of Engineering & Technology, GT-Road, Lahore 54890, Pakistan; ranaawais094@gmail.com (A.N.S.); ijaz.ahmad@cewre.edu.pk (I.A.); engraraz@uet.edu.pk (F.u.H.)
- ² Faculty of Agricultural Engineering and Technology, PMAS Arid Agriculture University, Rawalpindi 46000, Pakistan; mazammakram@gmail.com
- ³ Land Science Research Center, Nanjing University of Information Science & Technology, Nanjing 210044, China; adnanabbas@nuist.edu.cn
- ⁴ National Crisisonomy Institute, Chungbuk National University, Cheongju 28644, Korea
- * Correspondence: waseem.jatoi@cewre.edu.pk (M.W.); jeunlee@chungbuk.ac.kr (J.E.L.)

Abstract: The drought along with climate variation has become a serious issue for human society and the ecosystem in the arid region like the Soan basin (the main source of water resources for the capital of Pakistan and the Pothohar arid region). The increasing concerns about drought in the study area have brought about the necessity of spatiotemporal analysis and assessment of the linkage between different drought types for an early warning system. Hence, the streamflow drought index (SDI) and standard precipitation index (SPI) were used for the analysis of the spatiotemporal variations in hydrological and meteorological drought, respectively. Furthermore, statistical approaches, including regression analysis, trend analysis using Mann Kendall, and moving average, have been used for investigation of the linkage between these drought types, the significance of the variations, and lag time identification, respectively. The overall analysis indicated an increase in the frequency of both hydrological and meteorological droughts during the last three decades. Moreover, a strong linkage between hydrological and meteorological droughts was found; and this relationship varied on the spatiotemporal scale. Significant variations between hydrological and meteorological droughts also resulted during the past three (3) decades. These discrepancies would be because of different onset and termination times and specific anthropogenic activities in the selected basin for the minimization of hydrological drought. Conclusively, the present study contributes to comprehending the linkage between hydrological and meteorological droughts and, thus, could have a practical use for local water resource management practices at the basin scale.

Citation: Sarwar, A.N.; Waseem, M.; Azam, M.; Abbas, A.; Ahmad, I.; Lee, J.E.; Haq, F.u. Shifting of Meteorological to Hydrological Drought Risk at Regional Scale. *Appl. Sci.* **2022**, *12*, 5560. <https://doi.org/10.3390/app12115560>

Academic Editors: Andrea Chiozzi, Željana Nikolić and Elena Benvenuti

Received: 24 March 2022

Accepted: 27 May 2022

Published: 30 May 2022

Publisher's Note: MDPI stays neutral with regard to jurisdictional claims in published maps and institutional affiliations.



Copyright: © 2022 by the authors. Licensee MDPI, Basel, Switzerland. This article is an open access article distributed under the terms and conditions of the Creative Commons Attribution (CC BY) license (<https://creativecommons.org/licenses/by/4.0/>).

Keywords: drought SDI; SPI; linkage; propagation

1. Introduction

Drought is a condition considered as the deficit of water, including surface, ground, or atmospheric water, for a long period [1]. Irrespective of climatic sites, the drought could occur worldwide even in humid and wet environments [2]. Drought is generally classified into meteorological, hydrological, socioeconomic, and agricultural drought [3]. Among these four types of droughts, hydrological is the most important form as sustainable water resources management is heavily dependent on hydro-meteorological information. Various numbers of factors are associated with the onset of hydrological drought, and meteorological drought is one of the main influencing factors. The root cause of drought onset is the deficiency of rainfall across a large area for a very long period and is notated as a meteorological drought [4]. A meteorological drought can develop quickly because it is primarily caused by a lack of precipitation [5], and if the lack of precipitation spreads

to specific regions, the meteorological drought can be transformed into a hydrological drought, and then into an agricultural drought. The drought propagation process refers to the transition of different types of droughts.

The relationships between different types of droughts are studied by several authors, for example, [6] resulted that hydrological drought events occurred approximately seven months after meteorological drought events. The streamflow drought can be investigated using meteorological drought information at the annual time scale [7]. The interrelationship between runoff and meteorological drought has also been investigated and it was concluded that the significant dependency of hydrological drought on meteorological drought [8]. The impact of meteorological forcing on hydrological droughts has been computed [9]. A copula-based joint meteorological-hydrological drought index has been used to model the relationship between meteorological and hydrological droughts upstream and downstream of the Kasilian basin [10]. The transmission of meteorological droughts to hydrological droughts and the influence factors have been explored and investigated [11]. The entropy theory was used to create a hybrid drought index that combines hydrological, meteorological, and agricultural data and was used to investigate the drought condition in Northwest China [12]. In literature, the relationships between hydro-meteorological droughts, climatic variables, and human activities were also explored [13,14]. For example, [15] examined the relationship between various hydrologic and meteorological drought indices considering natural and human factors for different basins in the contiguous United States. Similarly, [16–19] studied the dependence structure between meteorological drought and hydrological drought using different approaches and resulted that the occurring time lag between meteorological and hydrological droughts is critical for sustainable drought management.

Most studies in the literature focused on determining hydro-meteorological drought and drought propagation; however, it remains unexplored. Besides that, the lack of understanding considering hydrological drought response to meteorological drought in different regions raises an unanswered question for basin-scale drought risk management [20]. To find answers to these questions, a comprehensive study of droughts that span multiple geographic areas and last for extended periods is required. Strategic water resources can be implemented more efficiently with accurate water-based information based on regional drought characteristics. Furthermore, given Pakistan's erratic, scarce, unstable climate and current drought situation [20–29], drought propagation information is critical at the regional and national levels, as it can provide the appropriate and consistent information required for efficient water management and drought early warning systems. Drought propagation information can aid in the prevention of significant economic losses as well as decision-making. Early warning systems are estimated to save hundreds of lives, save 2.7 billion Euros in natural disaster losses, and generate billions of supplementary benefits per year in Europe based on the optimization of economic production in the energy and agriculture sectors. In the near past, Pakistan has also experienced recurrent droughts and more severe droughts are anticipated in near future due to climate change [22].

The Soan River is a tributary of Pakistan's mighty Indus River Basin. It flows from the Murree Mountains into the Indus via the Dhoke Pathan hydrological station. It is the main hydrological unit for the Pothohar arid region of Pakistan. The importance of the Pothohar region cannot be repudiated as the region of Pothohar is rich in agriculture and agriculture is the backbone of the country's economy [30]. However, there are canal irrigation resources in this area and the crop production depends entirely on rainfall at suitable timings. Pothohar region gets rainfall during both the winter and summer seasons, which is the main source of crop germination, flowering, and maturity. If any of the seasons fail to bring rain, then soil moisture depletes resulting in drought and ultimately significant crop damage. More specifically, the crops in these areas depend on monsoon rains in summer and on western rains in winter. If the summer season fails to bring rains in the area, then it will cause huge crop yield loss in that specific year. Similarly, if the westerly system also fails to bring rains to the area, crops are affected badly, resulting in severe

droughts. Historically, this Pothohar region was severely affected by substantial variation in the rainfall and prolonged rain shortage especially from 1999 to 2002 [31]. Hence, the objectives of the present study include the exploration of spatiotemporal evolutions of meteorological and hydrological droughts in the study basin, evaluation of the link between meteorological and hydrological droughts, identifying the lag time, and the investigation of the differences between hydrological and meteorological droughts.

2. Materials and Methods

2.1. Study Area

The Soan River, initiating from the Murree highlands, is a major tributary of the Indus River and a key hydrological entity of the Potohar region of Pakistan. The Soan River flows through Chirah and Dhoke Pathan hydrological gauging stations (Figure 1) before being a part of the Indus River. The total drainage area of the Soan River basin is 6842 km² with an elevation ranging from 265 to 2274 m. The Soan basin is characterized by gentle to the steep slope and monsoon fed streams which generate almost all of the basin flow with mean annual precipitation of 1465 mm, and the mean annual temperature ranges from 8 to 22 °C. The Simly Dam, which spans the Soan River, provides drinking water to Islamabad, Pakistan's capital, as well as water for irrigation activities in the Pothohar region [32]. Furthermore, for a better understanding and evaluation of the spatial variation of drought, the study area was divided into two sub-basins: Chirah (hereafter sub-basin 1) and Dhoke Pathan (hereafter sub-basin 2). In the current study, monthly precipitation data of five meteorological stations within the basin (Murree, Zero Point, airport, Dhamial, and SAWCRI) from 1983 to 2015 was collected from Pakistan Meteorological Department (PMD). The average value of four stations lying in sub-basin 2 was used to estimate the meteorological drought in sub-basin 2, whereas the data of the remaining one station, i.e., Murree was used for meteorological drought analysis at sub-basin 1. Similarly, the monthly streamflow data of two hydrological gauging stations, i.e., Chirah and Dhoke Pathan was collected from Water and Power Development Authority (WAPDA) for the same period.

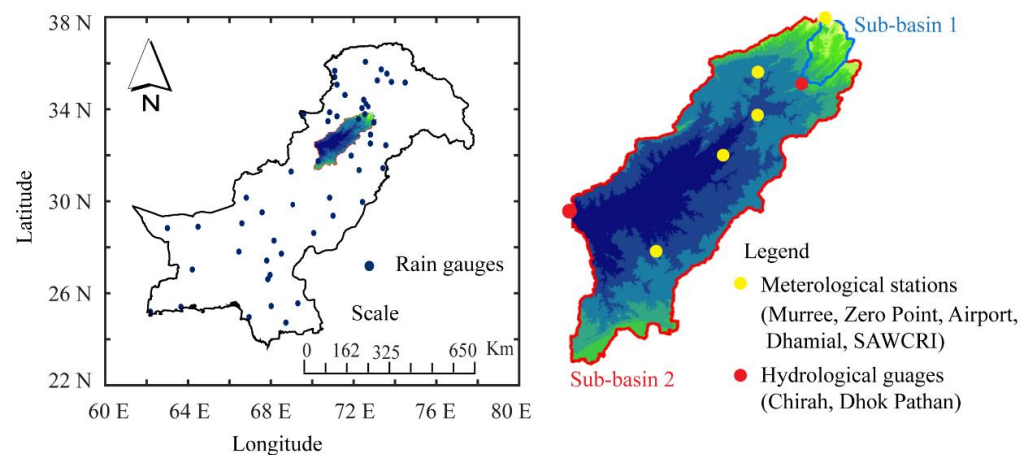


Figure 1. Location map of the study area.

2.2. Spatiotemporal Analysis of Drought

2.2.1. Meteorological Drought Assessment

For the assessment of meteorological drought, the Standardized Precipitation Index (SPI) was used due to its effectiveness, applicability, and suitability at different time scales for many case studies, e.g., [28,33,34]. Considering the hydrological year (October to September), SPI was calculated at four different time scales, i.e., SPI-3 (October–December), SPI-6 (October–March), SPI-9 (October–June), and SPI-12 (October–September). Further-

more, for the calculation of SPI at different time scales, the following expression was used for cumulative precipitation ($R_{i,K}$).

$$R_{i,K} = \sum_{j=1}^{3k} P_{i,j} \quad i = 1, 2, 3, \dots, n \quad j = 1, 2, \dots, 12 \quad \text{and} \quad k = 1, 2, 3, 4 \quad (1)$$

where ($P_{i,j}$) corresponds to monthly precipitation, j denotes the particular month of the hydrological year, i indicates the hydrological year, and k reveals the timescale (e.g., SPI-3, $k = 1$ indicating 3-month time scale October-December, and similarly $k = 4$ is for October to September).

SPI computation includes fitting distributions to precipitation data ($R_{i,K}$) and estimating a probability density function (PDF) and cumulative distribution function (CDF). These functions are further transformed into standardized distributions with unit standard deviations and zero means yielding the SPI value using the expression below (Equation (2)). The SPI value could range from <-2 to $>+2$ [35], whereas the positive value of SPI indicates a wet condition while the negative value represents a drought condition. Moreover, in this study, the drought thresholds were as follows: weak drought ($-1.0 \leq \text{index} < 0$), moderate drought ($-1.49 \leq \text{index} < -1.0$), severe drought ($-1.99 \leq \text{index} < -1.50$), and extreme drought ($\text{index} \leq -2$).

$$\text{SPI}_{i,k} = \frac{R_{i,k} - \bar{R}_k}{S_k} \quad (2)$$

where S_k and \bar{R}_k are the standard deviation and average value of the precipitation, respectively.

2.2.2. Hydrological Drought Assessment

The Streamflow Drought Index (SDI) was developed by [36] and is widely used to characterize hydrological drought events. SDI computation also includes fitting distributions to runoff data and estimation of PDF and CDF and then transforming into a standardized distribution, yielding the SDI value [13]. Similarly, the positive SDI value represents wet conditions, while the negative value represents drought conditions. Furthermore, SPI thresholds were adopted for hydrological drought analysis.

$$V_{i,k} = \sum_{j=1}^{3k} Q_{i,j} \quad i = 1, 2, 3, \dots, n \quad j = 1, 2, 3, \dots, 12 \quad \text{and} \quad k = 1, 2, 3, 4 \quad (3)$$

$$\text{SDI}_{i,k} = \frac{V_{i,k} - \bar{V}_k}{S_k} \quad (4)$$

where $V_{i,k}$ the cumulative runoff for reference period k and the i is the hydrological year; S_k is the standard deviation and \bar{V}_k is the mean value of runoff.

The SDI can also be calculated at various time scales, such as one, three, six, and twelve months. For the estimation of SPI-3, SDI-3, SPI-6, SDI-6, SPI-9, SDI-9, SPI-12, and SDI-12, the cumulative sums of precipitation and runoff for 3, 6, 9, and 12-month timescales were used. When calculating SPI-3 and SDI-3, for example, the cumulative sum for October was obtained by adding the following two-month data (November and December) to the October data [20]. SPI-6 and SDI-6 cumulative sums were calculated by adding six months from October to March.

Furthermore, the Mann-Kendall method [37] was used to estimate the trend in SPI-3, SPI-6, SPI-9, and SPI-12 at a significance level of 5% and similarly for SDI values at different time scales.

2.3. Identification of Linkage between Meteorological and Hydrological Drought and Lag Time

A regression analysis is a statistical technique for estimating the magnitude of the effect of any independent time series (hereafter the meteorological drought index) on any dependent time series (hereafter the hydrological drought index) [38]. In particular,

regression analysis is used to better understand the relationships between independent and dependent time series. As a result, a linear regression was used to evaluate the relationship and temporal changes in drought. Coefficient of determination (R^2), slope, and p -value were calculated for each relationship using the two-tailed t -test, and R^2 was used to indicate the best relationship between SDI and SPI [38]. Equation (5) depicts the mathematical expression of regression between any independent and any dependent time. In the current study, several simple linear regression models were developed between SPI and SDI of the same time scale, e.g., SPI-3 versus SDI-3; SPI-6 versus SDI-6; and similarly for other time scales.

$$Y = \beta_0 + aX + \varepsilon \quad (5)$$

where Y is the dependent time series, a is the regression coefficient, X is the independent time series, β_0 is the intercept, and ε is an error term.

Furthermore, in this study, moving average (running average) analysis was performed at multiple time scales to better assess the correlation between SPI and SDI. It is a quite simple statistical analysis tool used as the fluctuation, trend, or lagging indicator. For a given time series and a fixed size subset, the first value of the moving average is calculated by averaging the fixed subset of the given time series. After this, the subset is shifting forward by including the next number and excluding the first number in the subset. For example, Let $(X_1, t_1), (X_2, t_2), \dots, (X_n, t_n)$ represents SPI or SDI time series, X_1, X_2, \dots, X_n are the values of SPI or SDI; against time periods t_1, t_2, \dots, t_n , respectively. The first two moving averages of order k (here 2) can be calculated as given in Equations (6) and (7). A similar procedure was adopted up to the n th value.

$$\text{For 1st MA :} \\ MA_K = \frac{X_1 + X_2 + \dots + X_k}{K} \quad (6)$$

$$\text{For 2nd MA :} \\ MA_K = \frac{X_2 + X_3 + \dots + X_{k+1}}{K} \quad (7)$$

3. Results

3.1. Spatiotemporal Analysis of Droughts

3.1.1. Analysis of Meteorological Drought

Figure 2 illustrates the meteorological drought index calculated at selected time scales for both sub-basins of the study area. Based on the analysis, it was observed that there was an increase in the frequency of drought after 1998 specifically in the case of sub-basin-1 when SPIs mostly remained negative. These results are in good agreement with the results previously published on droughts in Pakistan [19,20,23,29,39]. The variations in drought between both sub-basins are due to the more relative decrease in precipitation in subbasin-1, compared to sub-basin-2 [30,32]. Moreover, the numbers of drought events were different at different computed time scales. Significant inconsistencies were found when the 3-month time scale was compared with the 6-month time scale, and a comparison between the 6-month and 12-month time scales gave slight variations in results. Results reveal the frequent occurrence of severe drought events at each sub-basin of the study area, and these were more sensitive to short-term drought compared to long-term droughts. According to the results, the recurrence of drought is more frequent and consecutive at 1 to 6 months' timescale in sub-basin 1 and during the 12-month timescale, there exists a sharp difference between wet and dry episodes. while the sub-basin 2 is found to be more sensitive to drought (mild to severe) at a 1-month timescale as compared to 3, 6, and 12-month timescales. The results also specified that the drought events state varied with the increase in SPI time scales, mostly a declining trend in sub-basin 2. This is due to the reason that computation of 12-month time scale SPI involves the aggregation of total precipitation from October to September and includes both wet and dry seasons. However, the 3-month SPI time scale considers only the sum of three-month precipitation, and the 3-month time scale (March-May) of the study basin was normally a dry season.

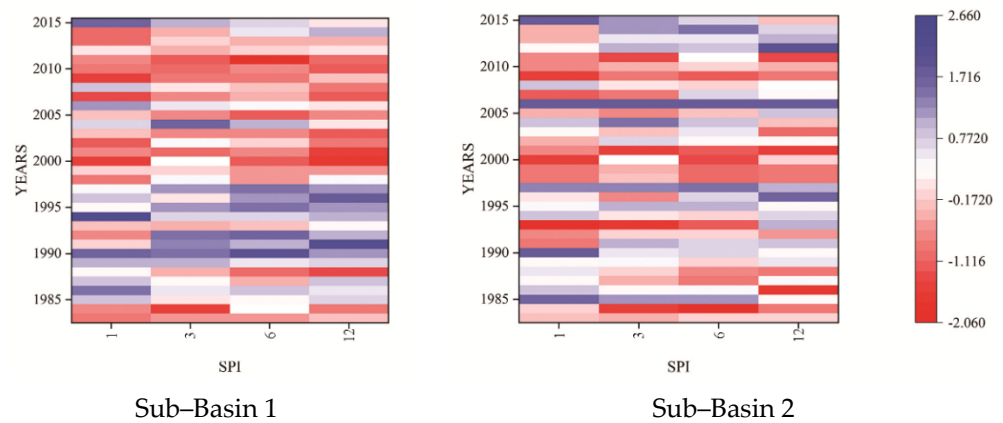


Figure 2. Temporal variations of meteorological drought periods during 1983–2015 in sub-basins 1 and 2.

Figure 3 illustrates the severity of meteorological drought based on the 12-month time scale for both hydrological sub-basins and the difference in their SPI-12 values during the study period (i.e., 1983–2015). Based on the analysis, it resulted that the years from 1998 to 2004 were the driest years of the selected time series. Moreover, the difference in meteorological drought (SPI-12) severity at both sub-basins represents the notable spatial variations across the Soan river basins. The Mann-Kendall test was also used on SPI-12 to figure out the trend in meteorological drought at sub-basin 1 and sub-basin 2. The analysis showed an increase in meteorological drought severity during the past 33 years, and a significant decreasing trend in SPI-12 values was observed downstream, i.e., sub-basin 2. The Z-value of the Mann-Kendall test was 1.78 at upstream sub-basin 1, and 1.71 at downstream sub-basin 2.

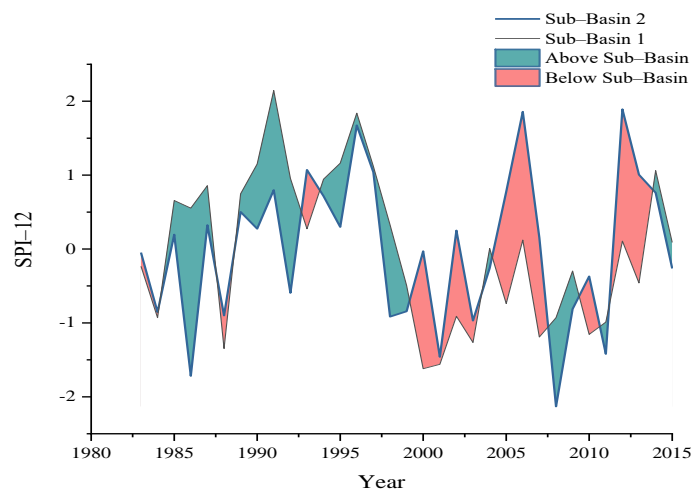


Figure 3. Difference in meteorological drought (SPI-12) severity at both sub-basins representing the spatial variations across the Soan river basins.

3.1.2. Analysis of Hydrological Droughts

Figure 4 depicts the temporal variations of hydrological drought periods in sub-basins 1 and 2 at different time scales, indicating the occurrence of hydrological drought over the last three decades. Hydrological drought, like meteorological drought, was more sensitive to short-term droughts than long-term droughts. Drought events occurred continuously from 1983 to 2015, with the driest period for the study area being 1998–2004. Drought patches were also randomly observed in 1993, 1998–2004, and 2009. Sub-basin 1 was stressed by hydrological drought, and the number of drought events was high from 1985 to 2004, with a slight wet condition from 2005-to 2015. However, in the case of sub-basin 2,

the results showed that the frequency of hydrological drought events was increasing in the basin from 1983 to 2015. Figure 5 shows the illustration of the difference in hydrological drought severity (SDI-12) for two sub-basins and indicates notable variations across the two sub-basin. Furthermore, based on the MK test, a statistically significant trend was observed for downstream sub-basins 2 with a Z-value of 1.83, whereas, upstream sub-basin 1 showed opposite behavior with an insignificant statistical trend. However, there still exists an increasing trend of drought at upstream sub-basin 1.

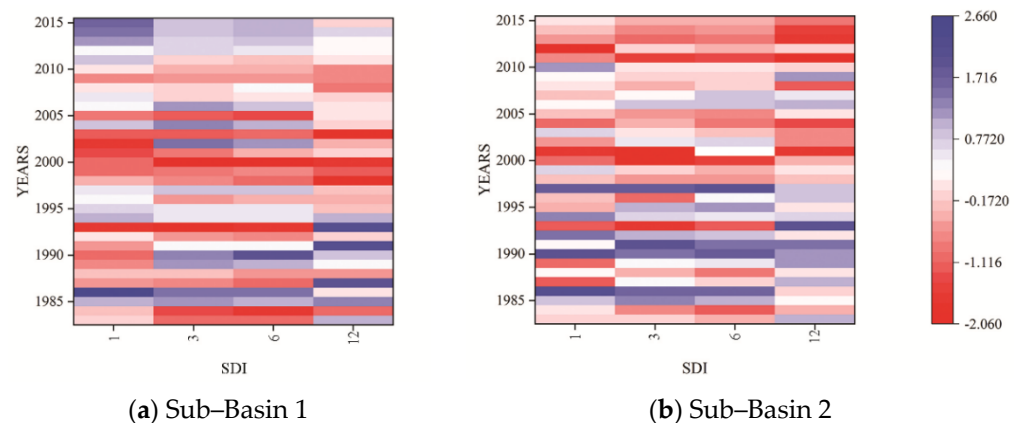


Figure 4. Temporal variation of hydrological drought periods in sub-basins 1 and 2 at different time scales.

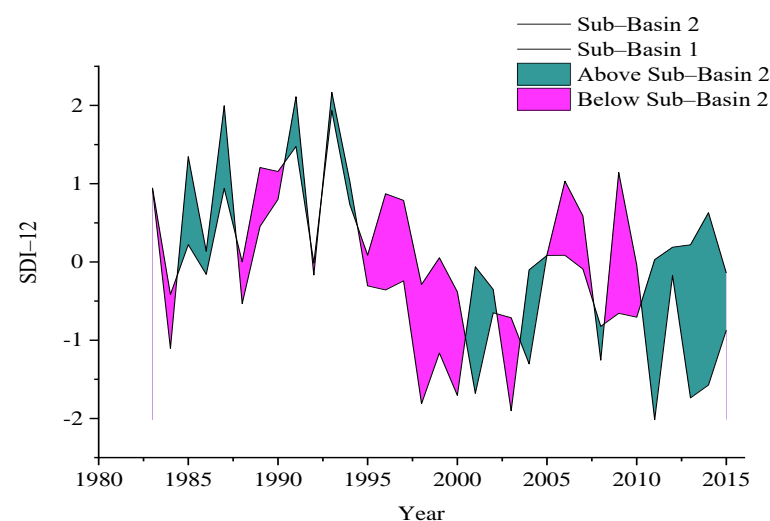


Figure 5. Difference in Hydrological drought (SDI-12) severity at both sub-basins representing the spatial variations across the Soan river basin.

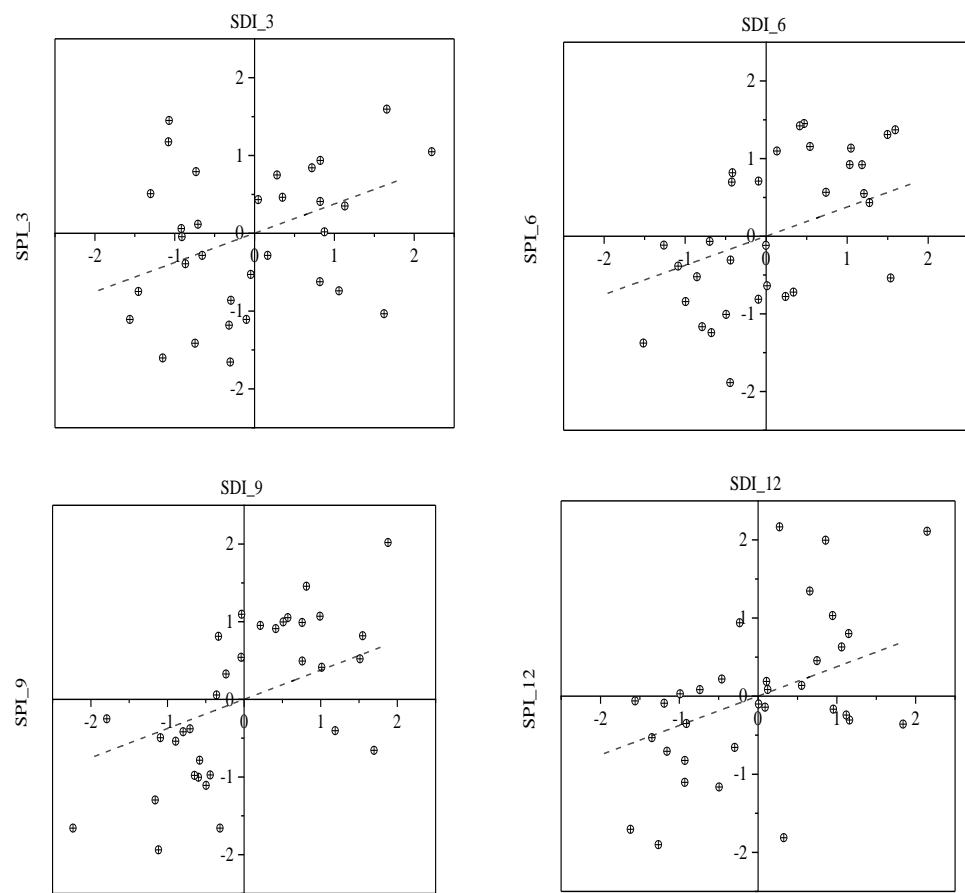
3.2. Link between Meteorological and Hydrological Droughts

3.2.1. Establishing Regression Function

The coefficient of determination (R^2) and regression coefficient (a) extracted from linear regression equations (Table 1) showed that a significant relationship existed between SDI and SPI, and it increased up to the 9-month time scale and then decrease in the case of the 12-month time scale. The coefficient of determination (R^2) of the 6-months and the 9-month time scale was relatively higher as compared to the other two time scales. Moreover, the correlation of SPI and SDI was higher at upstream sub-basin 1 of the Soan River Basin as compared to downstream. For instance, sub-basin 1 and sub-basin 2 had 0.66 and 0.63 values of R^2 based on a 9-month time scale respectively. The regression lines with the related data points are shown in Figure 6 which may be utilized for the prediction of hydrological droughts using the meteorological droughts information.

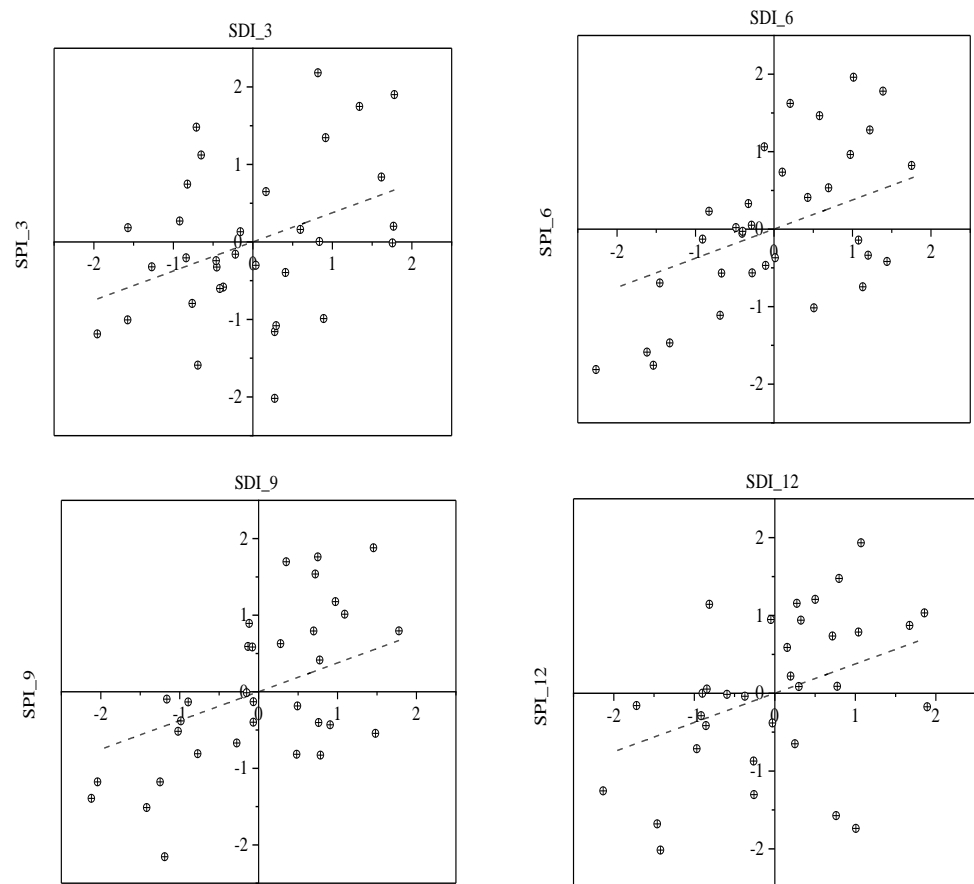
Table 1. Results of Regression modeling developed between SDI on SPI.

K		Sub-Basin 1	Sub-Basin 2
3-Months	a	0.35	0.37
	R ²	0.125	0.14
6-months	a	0.67	0.64
	R ²	0.45	0.4
9-Months	a	0.66	0.63
	R ²	0.44	0.4
12-Months	a	0.54	0.45
	R ²	0.29	0.21



(a) For Sub-Basin 1

Figure 6. Cont.



(b) For Sub-Basin 2

Figure 6. The linear relationship between SDI and SPI at the four selected time scales.

3.2.2. Moving Average Analysis and Lag Time Identification

A moving average analysis was performed at multiple time scales to better assess the correlation between SPI and SDI, see Figure 7. Results show that the variations of SPI and SDI were quite comparable; however, the differences between them do exist. In general, a strong correlation was observed between SPI and SDI at the upstream sub-basin 1, i.e., $CC = 0.66$. Overall based on the correlation analysis with different lag times, it was observed that at both sub-basins, the SDI was 1 month lagging behind SPI at 3-month and 12-month time scales and 2 months lagging for 6-month and 9-month time scales. This period of lagging time was in accordance with the prior study [7].

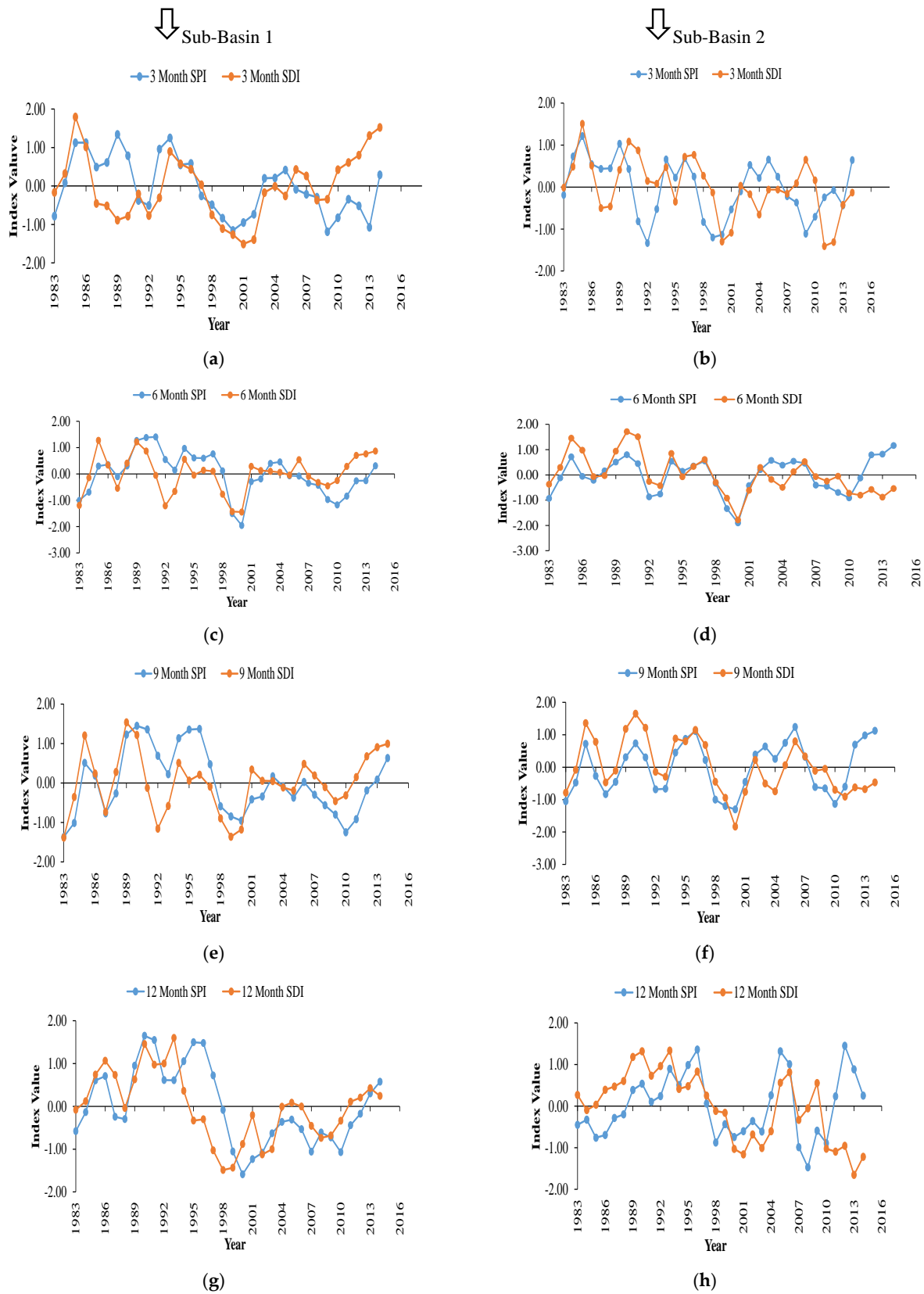


Figure 7. Moving average analysis for lag time identification between SPI and SDI at sub-basins 1 and 2 for different time scales. (a,b) 3 months, (c,d) 6 months, (e,f) 9 months, (g,h) 12 months.

4. Discussion

Climate change includes the variations in the behavior of climatic parameters, e.g., precipitation, evapotranspiration, etc. [40]. Whereas anthropogenic activities include land-use/land cover changes, irrigation area expansion, increased water diversion, water conservation practices, etc. During the last decades, the Soan basin experienced precipitation and runoff variation (with a change point in 1998 [30]) due to both climate change and anthropogenic activities [30,32]. Based on the drought analysis performed in the current study, notable variations between SPI and SDI values were found over the past three decades. It could be mainly because of major changes in agricultural land, forest, settlement, water bodies, and bare land in addition to natural climate variability [41].

To further justify, a trend analysis of precipitation, runoff, and runoff coefficient had been performed. The analysis resulted, in the case of sub-basin 1 a declining trend in precipitation was observed during the years 1983–2015, as shown in Figure 8a. For instance, the average annual precipitation decreased from 1983–1997 (1950 mm) to 1998–2015 (1570.50 mm). This decline in precipitation was significant in sub-basin 1, while little variation (no significant trend) was found in the case of sub-basin 2 with an average value of 1115 mm and 1065 mm for 1983–1997 and 1998–2015 respectively. For sub-basin 1, the annual runoff depth had a decreasing trend (i.e., an average of 174.44 mm for 1983–1997, and 84.00 mm for 1998–2015) during the study period (left panel Figure 8b) and, the runoff coefficient had no significant trend (left panel Figure 8c). Similarly, in the case of sub-basin 2, runoff depth has a decreasing trend, while runoff coefficient has no significant trend as the p -value is greater than alpha. The variations in the trend direction of runoff, and runoff coefficient in the case of sub-basins 1 and 2 could be mainly due to land-use changes, e.g., 71 km² and 1611 km² increase in agriculture land was observed in sub-basins 1 and 2 respectively from 1983–1997 to 1998–2015 [30].

Moreover, the higher decreasing rate in runoff compared to precipitation and change point showed the possible effect of anthropogenic activities [32]. It was anticipated because of a significant increase in the intensity of crops and the construction of large numbers of small dams from 1998- onward [27]. These significant variations were also anticipated due to the significant number of development projects under the Government of Punjab, Pakistan, which comprises the development of ponds and mini-dams for rainwater harvesting and to increase the intensity of agriculture. The initiative of these developments was to increase the storage for crop and drinking purposes, which might have caused the increase in evaporation, and water use for the growing population, ultimately decrease in surface runoff and increasing in probability of drought occurrence. In addition to that, a reservoir could decrease the frequency, duration, and severity of drought events downstream of the dam, and irrigation practices can primarily influence hydrological droughts by consuming streamflow and groundwater, which typically results in a decrease in streamflow and groundwater levels [16,42]. Hence, the Simly reservoir operation, as well as seasonal irrigation practices, could have an impact on the statistical relationship among drought indices.

The difference in SPI and SDI trends could be due to evapotranspiration or lag time between rainfall and runoff, which could predict the propagation of meteorological to hydrological droughts. Drought propagation may also be influenced by basin characteristics such as soil moisture, land use, and the relationships between streamflow and groundwater. A time lag was used to perform cross-correlation between SPI and SDI, which acknowledged the sequence between SPI and SDI and demonstrated that meteorological drought events could be used to predict hydrological droughts in relatively small watersheds with less anthropogenic activities.

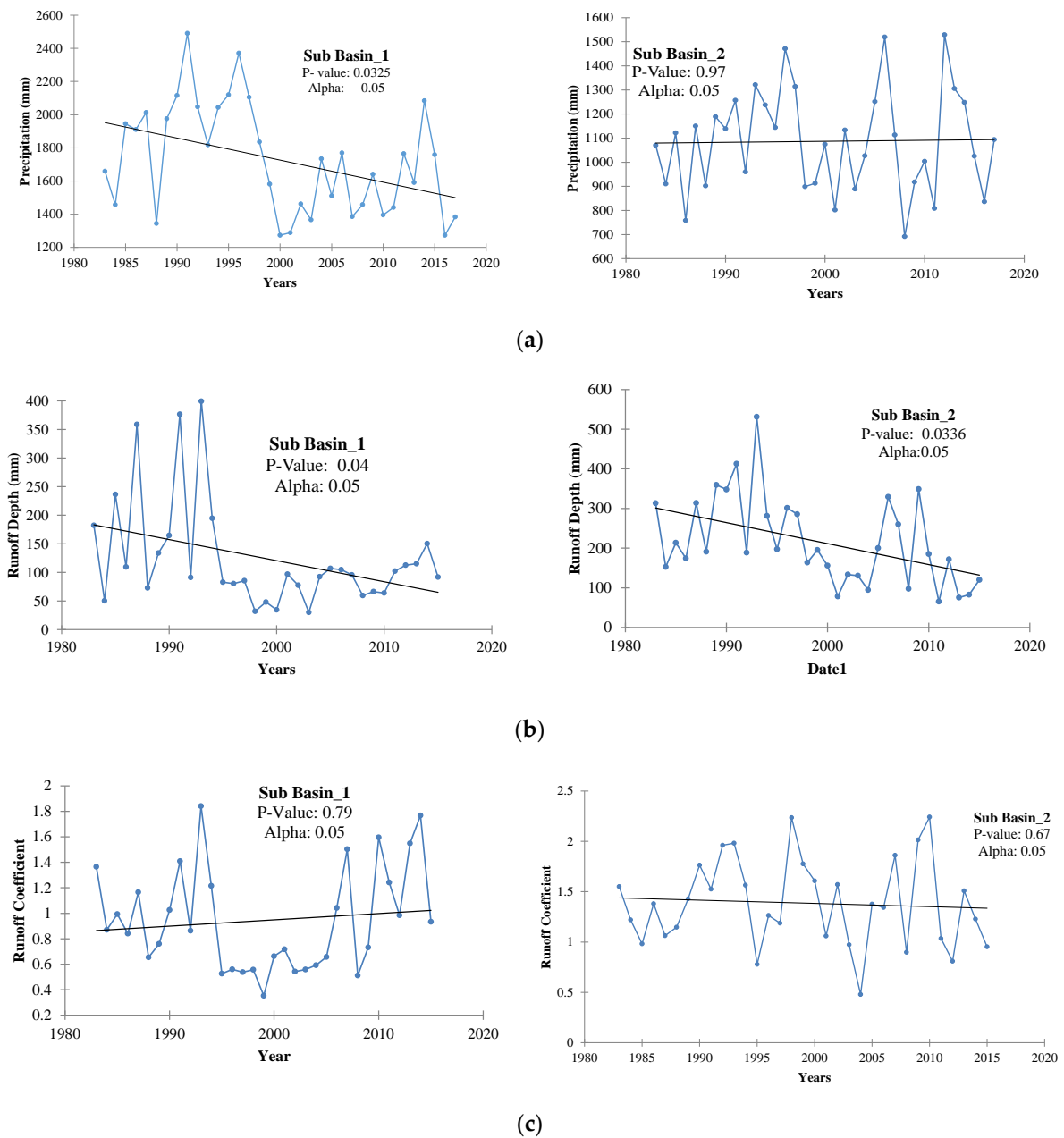


Figure 8. Temporal Variation of (a) Precipitation, (b) Runoff depth, and (c) Runoff Coefficient at sub-basin 1 and 2.

5. Conclusions

This study concludes that the frequency of both hydrological and meteorological droughts increased in the Soan River Basin during the study period. At various time scales, Sub-basin 1 was subjected to more frequent meteorological moderate drought and hydrological drought events. The current study was also designed to investigate the relationship between meteorological and hydrological drought events and SPI and SDI by developing a simple linear function between them. The results of a linear regression between SPI and SDI show an increase in regression coefficients with increasing time scale and became stronger until the ninth month. Climate change and anthropogenic activities (i.e., land use/land cover changes) are the main reasons that cause the variations between these two types of droughts. Moreover, the hydrological drought events commonly lagged 1–3 months (subject to the time scale and sub-basin) from the meteorological drought events. The dissimilarities between these two types of droughts became larger due to

climatic variation and might be due to human activities as well. Conclusively, this study provided drought propagation and the basis for long-term drought forecasting and, thus, can be employed for early warning water resources management and as an extension of this current study can be to assess the climate change impacts on hydrological drought at the basin scale.

Author Contributions: Conceptualization, A.N.S. and M.W.; methodology, M.A. and A.A.; software, M.A.; validation, M.W., J.E.L. and M.A.; formal analysis, I.A. and A.A.; investigation, F.u.H.; data curation, A.N.S. and M.W.; writing—original draft preparation, J.E.L.; funding acquisition. All authors have read and agreed to the published version of the manuscript.

Funding: This work was supported by the Ministry of Education of the Republic of Korea and the National Research Foundation of Korea (NRF-2020S1A5B8103910).

Institutional Review Board Statement: Not applicable.

Informed Consent Statement: Not applicable.

Data Availability Statement: All data is provided in the form of tables and figures.

Acknowledgments: The Authors appreciate the NRPU-HEC projects.

Conflicts of Interest: The authors declare no conflict of interest.

References

- Dai, A. Drought under Global Warming: A Review. *Wiley Interdiscip. Rev. Clim. Chang.* **2011**, *2*, 45–65. [CrossRef]
- Van Loon, A.F.; Stahl, K.; Di Baldassarre, G.; Clark, J.; Rangelcroft, S.; Wanders, N.; Gleeson, T.; Van Dijk, A.I.J.M.; Tallaksen, L.M.; Hannaford, J. Drought in a Human-Modified World: Reframing Drought Definitions, Understanding, and Analysis Approaches. *Hydrol. Earth Syst. Sci.* **2016**, *20*, 3631–3650. [CrossRef]
- Willhite, D.A. Drought as a Natural Hazard. In *Droughts*; Routledge: London, UK, 2021; p. 33.
- Vidal, J.-P.; Martin, E.; Franchistéguy, L.; Habets, F.; Soubeyroux, J.-M.; Blanchard, M.; Baillon, M. Multilevel and Multiscale Drought Reanalysis over France with the Safran-Isba-Modcou Hydrometeorological Suite. *Hydrol. Earth Syst. Sci.* **2010**, *14*, 459–478. [CrossRef]
- Peters, E.; Bier, G.; Van Lanen, H.A.J.; Torfs, P. Propagation and Spatial Distribution of Drought in a Groundwater Catchment. *J. Hydrol.* **2006**, *321*, 257–275. [CrossRef]
- Edossa, D.C.; Babel, M.S.; Das Gupta, A. Drought Analysis in the Awash River Basin, Ethiopia. *Water Resour. Manag.* **2010**, *24*, 1441–1460. [CrossRef]
- Tabrizi, A.A.; Khalili, D.; Kamgar-Haghighi, A.A.; Zand-Parsa, S. Utilization of Time-Based Meteorological Droughts to Investigate Occurrence of Streamflow Droughts. *Water Resour. Manag.* **2010**, *24*, 4287–4306. [CrossRef]
- Haslinger, K.; Koffler, D.; Schöner, W.; Laaha, G. Exploring the Link between Meteorological Drought and Streamflow: Effects of Climate-catchment Interaction. *Water Resour. Res.* **2014**, *50*, 2468–2487. [CrossRef]
- Jörg-Hess, S.; Griessinger, N.; Zappa, M. Probabilistic Forecasts of Snow Water Equivalent and Runoff in Mountainous Areas. *J. Hydrometeorol.* **2015**, *16*, 2169–2186. [CrossRef]
- Cheraghalizadeh, M.; Ghameshlou, A.N.; Bazrafshan, J.; Bazrafshan, O. A Copula-Based Joint Meteorological–Hydrological Drought Index in a Humid Region (Kasilian Basin, North Iran). *Arab. J. Geosci.* **2018**, *11*, 300. [CrossRef]
- Huang, S.; Li, P.; Huang, Q.; Leng, G.; Hou, B.; Ma, L. The Propagation from Meteorological to Hydrological Drought and Its Potential Influence Factors. *J. Hydrol.* **2017**, *547*, 184–195. [CrossRef]
- Zhu, J.; Zhou, L.; Huang, S. A Hybrid Drought Index Combining Meteorological, Hydrological, and Agricultural Information Based on the Entropy Weight Theory. *Arab. J. Geosci.* **2018**, *11*, 91. [CrossRef]
- Gumus, V.; Algin, H.M. Meteorological and Hydrological Drought Analysis of the Seyhan–Ceyhan River Basins, Turkey. *Meteorol. Appl.* **2017**, *24*, 62–73. [CrossRef]
- Huang, S.; Huang, Q.; Leng, G.; Liu, S. A Nonparametric Multivariate Standardized Drought Index for Characterizing Socioeconomic Drought: A Case Study in the Heihe River Basin. *J. Hydrol.* **2016**, *542*, 875–883. [CrossRef]
- Tijdeman, E.; Barker, L.J.; Svoboda, M.D.; Stahl, K. Natural and Human Influences on the Link between Meteorological and Hydrological Drought Indices for a Large Set of Catchments in the Contiguous United States. *Water Resour. Res.* **2018**, *54*, 6005–6023. [CrossRef]
- Wu, J.; Chen, X.; Gao, L.; Yao, H.; Chen, Y.; Liu, M. Response of Hydrological Drought to Meteorological Drought under the Influence of Large Reservoir. *Adv. Meteorol.* **2016**, *2016*, 2197142. [CrossRef]
- Wong, G.; Van Lanen, H.A.J.; Torfs, P. Probabilistic Analysis of Hydrological Drought Characteristics Using Meteorological Drought. *Hydrol. Sci. J.* **2013**, *58*, 253–270. [CrossRef]

18. Sattar, M.N.; Lee, J.-Y.; Shin, J.-Y.; Kim, T.-W. Probabilistic Characteristics of Drought Propagation from Meteorological to Hydrological Drought in South Korea. *Water Resour. Manag.* **2019**, *33*, 2439–2452. [CrossRef]
19. Abbas, A.; Waseem, M.; Ullah, W.; Zhao, C.; Zhu, J. Spatiotemporal Analysis of Meteorological and Hydrological Droughts and Their Propagations. *Water* **2021**, *13*, 2237. [CrossRef]
20. Waseem, M.; Khurshid, T.; Abbas, A.; Ahmad, I.; Javed, Z. Impact of Meteorological Drought on Agriculture Production at Different Scales in Punjab, Pakistan. *J. Water Clim. Chang.* **2022**, *13*, 113–124. [CrossRef]
21. Ahmed, K.; Shahid, S.; Harun, S.B.; Wang, X. Characterization of Seasonal Droughts in Balochistan Province, Pakistan. *Stoch. Environ. Res. Risk Assess.* **2016**, *30*, 747–762. [CrossRef]
22. Sheikh, M.M. Drought Management and Prevention in Pakistan. In Proceedings of the COMSATS 1st Meeting on Water Resources in the South: Present Scenario and Future Prospects, Islamabad, Pakistan, 1–2 November 2001; Volume 1.
23. Ahmed, K.; Shahid, S.; Nawaz, N. Impacts of Climate Variability and Change on Seasonal Drought Characteristics of Pakistan. *Atmos. Res.* **2018**, *214*, 364–374. [CrossRef]
24. Ahmed, K.; Shahid, S.; Wang, X.; Nawaz, N.; Khan, N. Spatiotemporal Changes in Aridity of Pakistan during 1901–2016. *Hydrol. Earth Syst. Sci.* **2019**, *23*, 3081–3096. [CrossRef]
25. Zahid, M.; Rasul, G. Frequency of Extreme Temperature and Precipitation Events in Pakistan 1965–2009. *Sci. Int.* **2011**, *23*, 313–319.
26. Usman, M.; Nichol, J.E. A Spatio-Temporal Analysis of Rainfall and Drought Monitoring in the Tharparkar Region of Pakistan. *Remote Sens.* **2020**, *12*, 580. [CrossRef]
27. Adnan, S.; Ullah, K.; Gao, S.; Khosa, A.H.; Wang, Z. Shifting of Agro-climatic Zones, Their Drought Vulnerability, and Precipitation and Temperature Trends in Pakistan. *Int. J. Climatol.* **2017**, *37*, 529–543. [CrossRef]
28. Xie, H.; Ringler, C.; Zhu, T.; Waqas, A. Droughts in Pakistan: A Spatiotemporal Variability Analysis Using the Standardized Precipitation Index. *Water Int.* **2013**, *38*, 620–631. [CrossRef]
29. Lee, J.E.; Azam, M.; Rehman, S.U.; Waseem, M.; Anjum, M.N.; Afzal, A.; Cheema, M.J.M.; Mehtab, M.; Latif, M.; Ahmed, R. Spatio-Temporal Variability of Drought Characteristics across Pakistan. *Paddy Water Environ.* **2022**, *20*, 117–135. [CrossRef]
30. Shahid, M.; Cong, Z.; Zhang, D. Understanding the Impacts of Climate Change and Human Activities on Streamflow: A Case Study of the Soan River Basin, Pakistan. *Theor. Appl. Climatol.* **2018**, *134*, 205–219. [CrossRef]
31. Shahid, M.; Dumat, C.; Khalid, S.; Schreck, E.; Xiong, T.; Niazi, N.K. Foliar Heavy Metal Uptake, Toxicity and Detoxification in Plants: A Comparison of Foliar and Root Metal Uptake. *J. Hazard. Mater.* **2017**, *325*, 36–58. [CrossRef]
32. Muhammad, W.; Muhammad, S.; Khan, N.M.; Si, C. Hydrological Drought Indexing Approach in Response to Climate and Anthropogenic Activities. *Theor. Appl. Climatol.* **2020**, *141*, 1401–1413. [CrossRef]
33. Liu, C.; Yang, C.; Yang, Q.; Wang, J. Spatiotemporal Drought Analysis by the Standardized Precipitation Index (SPI) and Standardized Precipitation Evapotranspiration Index (SPEI) in Sichuan Province, China. *Sci. Rep.* **2021**, *11*, 1280. [CrossRef] [PubMed]
34. Qin, Y.; Yang, D.; Lei, H.; Xu, K.; Xu, X. Comparative Analysis of Drought Based on Precipitation and Soil Moisture Indices in Haihe Basin of North China during the Period of 1960–2010. *J. Hydrol.* **2015**, *526*, 55–67. [CrossRef]
35. Zhao, P.; Lü, H.; Wang, W.; Fu, G. From Meteorological Droughts to Hydrological Droughts: A Case Study of the Weihe River Basin, China. *Arab. J. Geosci.* **2019**, *12*, 364. [CrossRef]
36. Nalbantis, I.; Tsakiris, G. Assessment of Hydrological Drought Revisited. *Water Resour. Manag.* **2009**, *23*, 881–897. [CrossRef]
37. Waseem, M.; Ahmad, I.; Mujtaba, A.; Tayyab, M.; Si, C.; Lü, H.; Dong, X. Spatiotemporal Dynamics of Precipitation in Southwest Arid-Agriculture Zones of Pakistan. *Sustainability* **2020**, *12*, 2305. [CrossRef]
38. Waseem, M.; Ajmal, M.; Kim, T.-W. Improving the Flow Duration Curve Predictability at Ungauged Sites Using a Constrained Hydrologic Regression Technique. *KSCE J. Civ. Eng.* **2016**, *20*, 3012–3021. [CrossRef]
39. Waseem, M.; Ajmal, M.; Ahmad, I.; Khan, N.M.; Azam, M.; Sarwar, M.K. Projected Drought Pattern under Climate Change Scenario Using Multivariate Analysis. *Arab. J. Geosci.* **2021**, *14*, 544. [CrossRef]
40. Fu, Q.; Johanson, C.M.; Warren, S.G.; Seidel, D.J. Contribution of Stratospheric Cooling to Satellite-Inferred Tropospheric Temperature Trends. *Nature* **2004**, *429*, 55–58. [CrossRef]
41. He, Y.; Wang, F.; Mu, X.; Yan, H.; Zhao, G. An Assessment of Human versus Climatic Impacts on Jing River Basin, Loess Plateau, China. *Adv. Meteorol.* **2015**, *2015*, 478739. [CrossRef]
42. Wu, J.; Chen, X.; Yao, H.; Gao, L.; Chen, Y.; Liu, M. Non-Linear Relationship of Hydrological Drought Responding to Meteorological Drought and Impact of a Large Reservoir. *J. Hydrol.* **2017**, *551*, 495–507. [CrossRef]

Article

Analysis of the Seismic Properties for Engineering Purposes of the Shallow Subsurface: Two Case Studies from Italy and Croatia

Federico Da Col , Flavio Accaino , Gualtiero Böhm  and Fabio Meneghini Istituto Nazionale di Oceanografia e di Geofisica Sperimentale-OGS, 34010 Sgonico, Italy;
faccaino@ogs.it (F.A.); gbohm@ogs.it (G.B.); fmeneghini@ogs.it (F.M.)

* Correspondence: fdacol@ogs.it

Featured Application: Civil Engineering, Seismic Characterization.

Abstract: We present two case studies of the application of seismic surveys to estimate the elastic properties of soil and rock in the shallow subsurface. The two sites present very different geological characteristics. The first test site is a town on the Croatian coast, not far from the city of Split, built on hard rock, where we acquired three seismic lines. The second site is located in the outskirts of the city of Ferrara, in Italy, in an alluvial plain, where two lines were acquired. In both sites, for detailed characterization, we acquired surface-, compressional- and shear-waves, further distinguishing the latter between horizontally (SH) and vertically (SV) polarized wavefields. We processed the data by performing a Multichannel Analysis of Surface Waves to compute a preliminary one-dimensional shear wave velocity profile. Then, we performed first-break tomography to compute P-, SH- and SV-velocity profiles. Such unusual acquisition allowed us to compute not only basic engineering parameters such as the equivalent shear-wave velocity of the first 30 m of subsurface (V_{S30}) from the SH profiles but also other useful parameters such as the V_P/V_S and estimate the anisotropy of the medium thanks to the V_{SV}/V_{SH} . Given the level of detail of the results and their engineering value, we conclude that the method of investigation we applied in the two test sites is a valuable tool for characterizing the shallow subsurface.

Keywords: geophysical surveying; seismic tomography; geotechnical characterization

Citation: Da Col, F.; Accaino, F.; Böhm, G.; Meneghini, F. Analysis of the Seismic Properties for Engineering Purposes of the Shallow Subsurface: Two Case Studies from Italy and Croatia. *Appl. Sci.* **2022**, *12*, 4535. <https://doi.org/10.3390/app12094535>

Academic Editors: Andrea Chiozzi, Elena Benvenuti and Željana Nikolić

Received: 30 March 2022

Accepted: 21 April 2022

Published: 29 April 2022

Publisher's Note: MDPI stays neutral with regard to jurisdictional claims in published maps and institutional affiliations.



Copyright: © 2022 by the authors. Licensee MDPI, Basel, Switzerland. This article is an open access article distributed under the terms and conditions of the Creative Commons Attribution (CC BY) license (<https://creativecommons.org/licenses/by/4.0/>).

1. Introduction

Geotechnical characterization of the shallow geological structures of a site is an essential tool to evaluate the response of the terrain to a macroseismic event. Typically, the geotechnical properties can be estimated by analyzing samples in a laboratory [1] or with in situ measurements such as the core penetration test and the load-bearing test.

However, these have the main disadvantage that they only provide a punctual estimation of the parameters. For this reason, geophysical surveys are becoming increasingly popular in seismic engineering thanks to their ability to accurately compute the main geotechnical parameters of the terrain and therefore its ability to amplify the seismic waves over a relatively wide area [2]. Specifically, the seismic method is able to evaluate the seismic velocities of the medium, which are a proxy for its elastic moduli [3]. More precisely, the seismic velocities are related to the bulk and shear moduli of the terrain, which describe the stiffness of the medium and therefore its ability to amplify seismic waves [4]. Based on this, in the past several decades, seismologists have established the vital importance of near-surface shear-wave velocity characterization both from a theoretical [5] and observational point of view [6]. Legislation followed these studies, and currently, the most commonly used geotechnical parameter is the equivalent shear-wave velocity of the first 30 m of subsoil (V_{S30}) [7–9]. The most widely used geophysical method to compute V_{S30} is

the Multichannel Analysis of Surface Waves (MASW) [10]. Technically, MASW relies on the dispersive behavior of the surface waves and consists in extracting a dispersion curve from a recorded seismogram and inverting it, obtaining a 1D shear-wave velocity profile. Yust et al. (2018) [11] show that the method is able to estimate accurately V_s profiles and therefore compute the V_{S30} with a relatively small error. Another method that relies on the surface waves is the Horizontal to Vertical Spectral Ratio (HVSr, [12]). The method consists in processing the data from 3C single-station data by computing the ratio between the horizontal and vertical spectra and thereby extracting a 1D shear-wave velocity profile together with the resonant frequency of the terrain.

A method that is gaining popularity is the travel-time tomography of first breaks on an SH active seismic survey [13,14]. The main advantage of this method is that it provides a 2D (potentially even 3D) S-wave velocity profile and therefore a computation of the V_{S30} along the entire seismic line.

A more accurate characterization of the shallow subsurface, beyond the computation of the V_{S30} , can be of high interest for engineers. For instance, from the computation of Poisson's ratio or V_P/V_S , information regarding the fracturing of the rocks [1] and its fluid saturation [15] can be inferred.

In this work, we present the application of an innovative survey technique in two case studies from two very different sites. The first was recorded along the roads of a small town lying on hard rock in the area of Split in Croatia. The second case study consists of a dataset recorded in an alluvial plain in an intensively cultivated countryside close to the city of Ferrara. The novelty of the method proposed lies in the fact that we recorded separately compressional- and shear-wavefields, distinguishing in the latter between the components orthogonal (SH) and parallel (SV) to the seismic line. In fact, while integrating P- and SH-waves is increasingly popular in the near-surface geophysics community [16,17], the distinction between SH- and SV-wavefields is much rarer. Seismologists performed several numerical simulations [18] and analyzed field data [19] aiming at the study of shear-wave splitting and anisotropy, but hardly any field example using controlled sources can be found in the literature.

In the same surveys, data specifically for surface-wave analysis was also recorded. The final aim of our analyses is to provide detailed engineering information of the shallow subsurface without invasive tests at a relatively large scale. Successful testing of the method in two such different locations should allow us to confirm whether the method is replicable in most situations.

2. Geological Context

The Croatian site lies in the village of Kaštela Kambelovac, which is a town lying on the shores of the homonymous bay, just northwest of the city of Split. Geologically, the Bay lies in a compressional environment [20], where the rocks are subject to strong thrusting and folding. This caused the thrusting of the Senonian limestone on top of the Eocene flysch [21,22]. The town therefore is built on top of such flysch, the thickness of which has been estimated to be several hundreds of meters and the composition of which is known to be mainly of alternating layers of marls and calcarenites/calcurudites [23]. Previous geological and geotechnical investigations in the area showed that the bedding of the flysch is subvertical because of the tectonic compressional context. More detailed geological information about the Croatian site can be found in [24].

As for the Italian site, the acquisition took place in the southeastern suburbs of the city of Ferrara, in the central Po Valley, an alluvial, subsiding plain. Specifically, the area where the studies were carried out lies at the heart of such a plain, filled with olocenic sediments of marine, lagunal and riverine origin [25]. These are horizontally layered and composed of sand mixed with clay and silt, the proportion of which is variable both depending on the location and on the depth. These sediments are often not consolidated, giving place to phenomena of liquefaction during macroseismic events [26]. At the base of the olocenic sediments, located at approximately 1000 m depth, lie the so-called "Ferrara folds", pre-

pleistocene rocks folded by the Appennine orogeny (“Buried Appennine” [27]). In fact, tectonically, the area lies at the margin of the compressional environment that created the Appennine mountain range.

3. Data Acquisition

In both sites, we acquired three wavefields separately (P, SH and SV). To do this, we used as source a wheelbarrow-mounted vibrator, which is capable of generating both P- and S-waves, reorienting it orthogonal and parallel to the line to generate SH- and SV-waves, respectively. As for the receivers, we used 10 Hz vertical geophones to record the P-waves and 14 Hz horizontal geophones to record the S-waves. The latter were re-oriented to record SH and SV, respectively, orthogonal and parallel to the survey line. We vibrated twice at each shot point, to perform stacking of the seismograms and therefore increase the signal–noise ratio.

3.1. Ferrara Site

We acquired two high-resolution seismic lines, the location of which can be seen in Figure 1a, while the UTM coordinates of the two lines are reported in Table 1. For both lines, we deployed 150 active channels, spaced every 2 m, and we shot every 4 m. The length of both lines is therefore approximately 300 m.

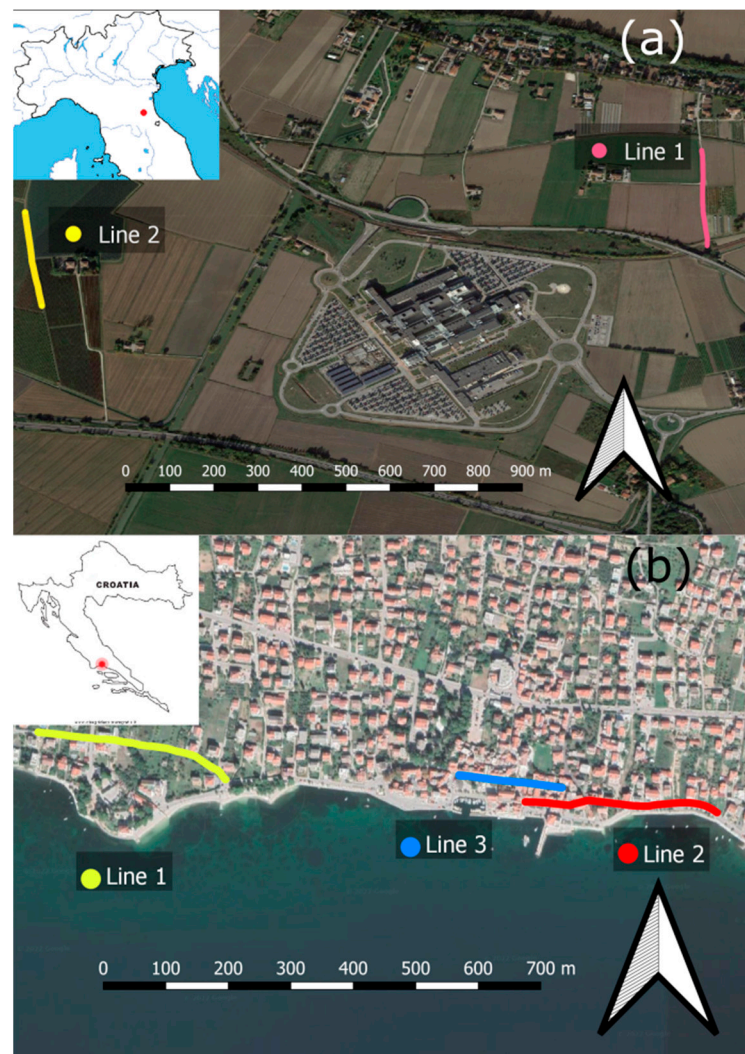


Figure 1. (a) Location of the lines acquired in the area of Ferrara, Italy. (b) Location of the lines acquired in Kaštela, Croatia. Images created on Google Earth Pro on 30 March 2022.

Table 1. UTM coordinates of the first and last receiver of each acquired seismic line.

Line Name	First Rec. N	First Rec. E	Last Rec. N	Last Rec. E	UTM Zone
Ferrara Line 1	4964800	713828	4964503	713850	32
Ferrara Line 2	4964552	712300	4964258	712347	32
Kastela Line 1	4822696	611466	4822770	611167	33
Kastela Line 2	4822643	612232	4822660	611943	33
Kastela Line 3	4822683	611984	4822703	611821	33

Along Line 1 (highlighted in red in Figure 1a), we acquired surface-wave data by deploying 48 4.5 Hz receivers, which were spaced every 4 m. As a source, we used a 100 kg weight-drop. We shot four times: twice at the beginning and twice at the end of the line.

The data of Line 1 were acquired along a gravel road. The main sources of noise were the agricultural activities ongoing in the nearby fruit farms (tractors, walking, irrigation pumps) and the car traffic.

The data of Line 2 were acquired in a fruit farm along a line of pear trees. Therefore, the geophones were planted in the soft soil. The main sources of noise are, similarly to Line 1, the activities going on in the fruit farm, including tractors and irrigation pumps.

3.2. Kaštela Site

We acquired three seismic lines along the roads of the village, planting the sensors in holes drilled in the tarmac. The details of the survey are outlined in [14], and the location of the lines can be seen in Figure 1b, while the UTM coordinates are reported in Table 1. Line 1 and 2 are 300 m long, while Line 3 is 150 m long. The receiver spacing in all lines is 2 m, and the shot spacing is 4 m. It is to be noted that during the acquisition of Line 1 and Line 2, traffic was quite intense in the village, and the weather was windy and even rainy at times. On the other hand, Line 3 was less affected by traffic noise, and the weather was fine.

4. Processing Methods

Multichannel Analysis of Surface Waves [10] provided information only on the Ferrara site, as no dispersive event could be identified in the Kaštela dataset, which was probably due the presence of tubes or other voids just below the road.

In Figure 2a, we show the frequency-wavenumber (f - k) spectrum of the Ferrara dataset, from which we picked the most energetic linear (i.e., dispersive) event to compute the dispersion curve shown in Figure 2b. The frequency range is from 3.5 to 15 Hz, giving a maximum wavelength of 58 m, i.e., a penetration depth of 29 m ($\lambda/2$, where λ is the wavelength). Finally, we inverted such a dispersion curve using the neighborhood algorithm in the GeoPsy software [27]. The initial model consists of three layers + Halfspace, the properties of which are described in Table 2. One million profiles were computed; in Figure 2c, we show the 500 best—that is, those generating a synthetic dispersion curve having the lowest misfit with respect to the picked one.

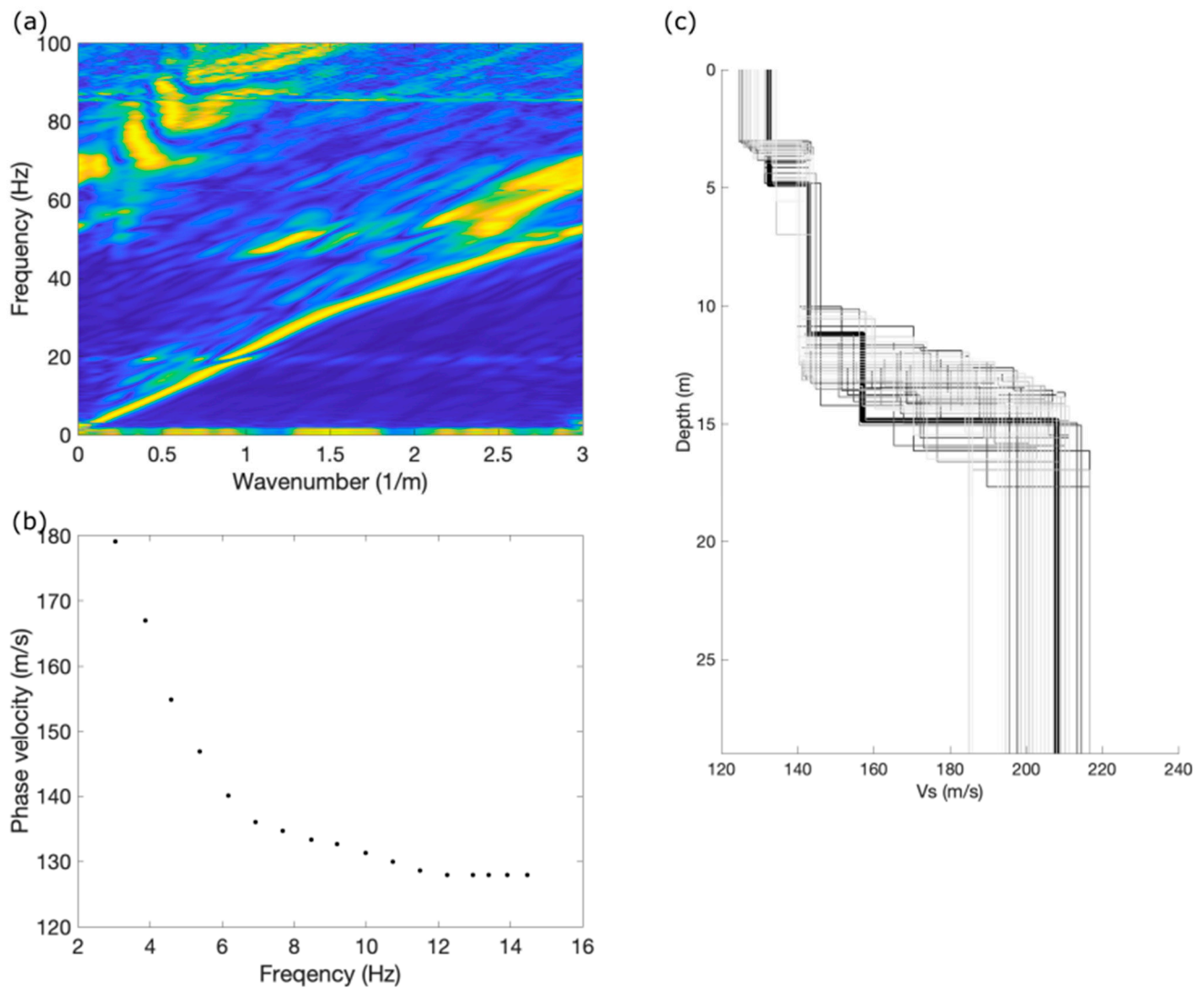


Figure 2. (a) f-k spectrum. (b) Dispersion curve. (c) The 1000 best fitting S-wave velocity profiles. The color of the lines represents the misfit, as indicated in the color bar.

Table 2. Properties of the initial model used for the inversion of the surface waves.

Layer Number	Thickness	Vs	Density
1	3–15 m	100–200 m/s	2000 kg/m ³
2	3–15 m	120–220 m/s	
3	3–15 m	140–240 m/s	
Halfspace		150–250 m/s	

We performed first break tomography on all the lines for all of the wavefields. Before this, some pre-processing was performed. Specifically, to increase the signal-to-noise ratio, for each shot, we applied a predictive deconvolution to the uncorrelated signals as in [28]. Furthermore, to remove random noise, we stacked in the time domain the seismograms relative to the same shot point.

The first breaks were manually picked on the seismograms. Examples of first-break picking can be seen in Figure 3.

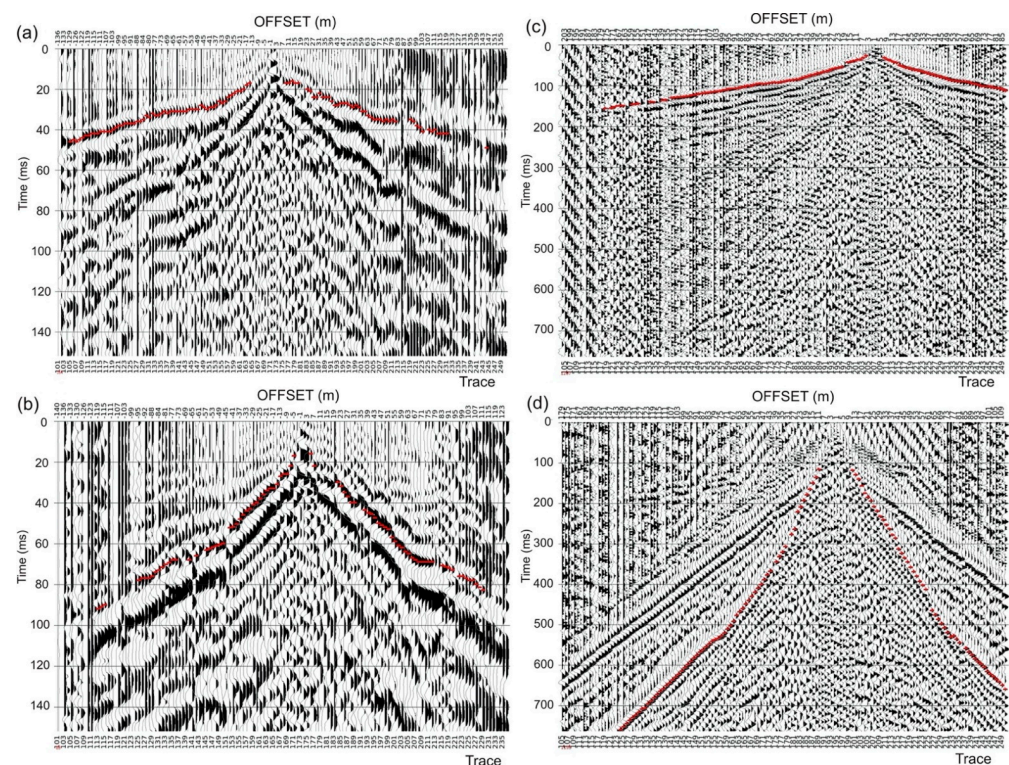


Figure 3. Examples of first-break picking on common shot gathers. Highlighted in red are the picked travel times. (a) P-waves from the Croatian site. (b) SH-waves from the Croatian site. (c) P-waves from the Italian site. (d) SH-waves from the Italian site.

Then, the travel times were inverted with Cat3D software [29], which is a tomographic package developed at the National Institute of Oceanography and Applied Geophysics-OGS that uses a ray-tracing algorithm based on a minimum time principle and SIRT (Simultaneous Iterative Reconstruction Technique) as an inversion method [30].

5. Results and Discussion

In Figure 4, we show the velocity profiles from the tomographic inversion of all wavefields relative to the three lines acquired in Kaštela, while in Figure 5, we show those relative to the two lines acquired in Ferrara. The two velocity profiles show very different features. In Kaštela, below a slower weathered layer, the velocity rapidly increases to 4.5 km/s and 3.0 km/s for P- and S-waves, respectively. Furthermore, we observe an overall increase in the velocities in the eastern lines (Lines 2 and 3) compared to the western line 1. In Figure 4d–f, we show the SH-velocity profiles and the corresponding V_{S30} . Since the velocity is >800 m/s along all three profiles, we conclude that the soil can be classified as A-class following the Eurocode-8 provisions [9]. In the bottom-right corner of each velocity profile, the mean RMS error is reported. All profiles present a mean RMS lower than 5%, except for the P-wave profile of line 2. This is probably due to the low signal-to-noise ratio of the data caused by the rainfall during the acquisition. Having said this, all other profiles show low mean RMS and can therefore be considered reliable.

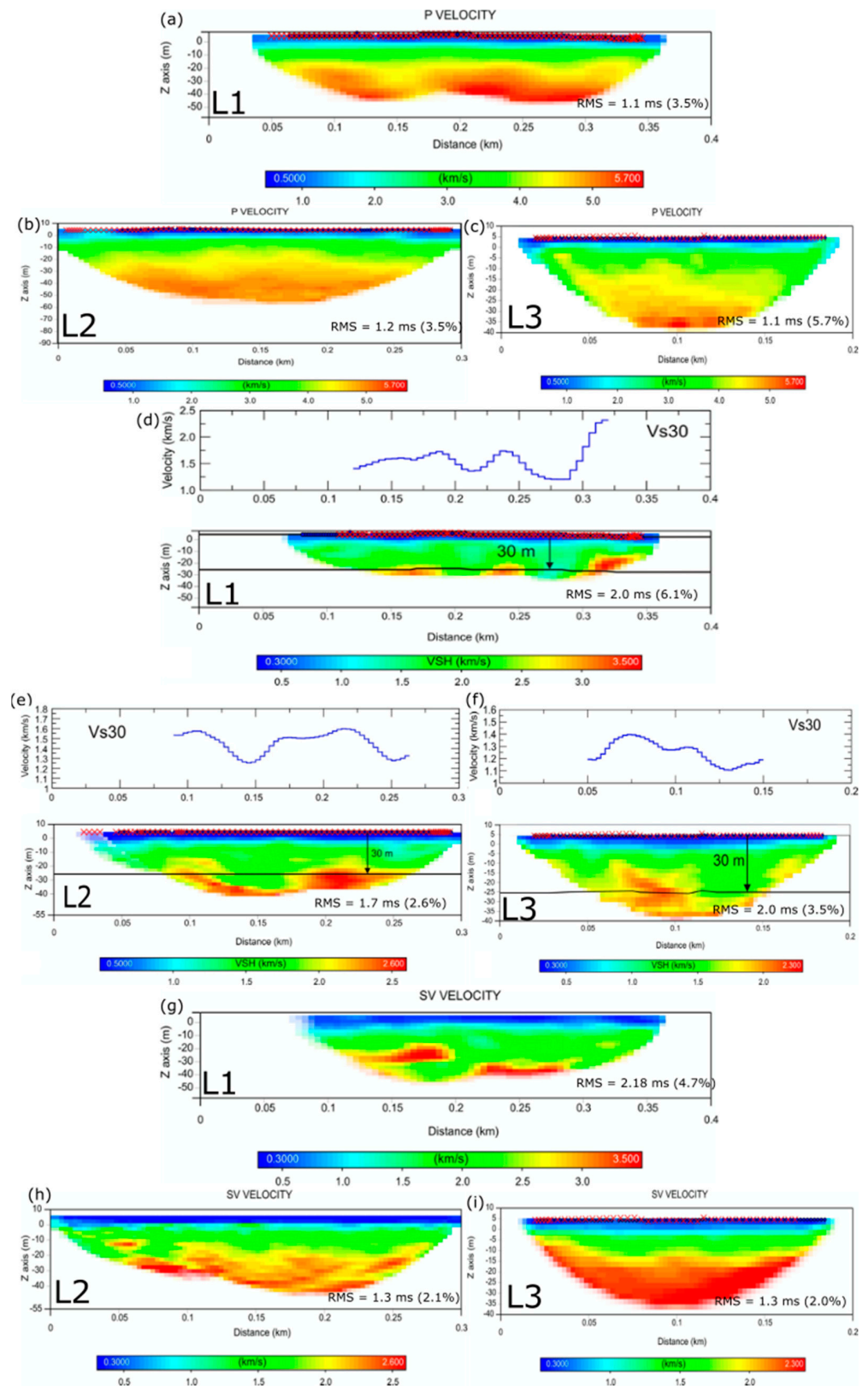


Figure 4. Results of the tomographies in Croatia; in the bottom-right corner, the value of the mean RMS error is shown. (a) Line 1, P-waves, (b) Line 2, P-waves, (c) Line 3, P-waves, (d) Line 1, SH-waves and VS30, (e) Line 2 SH-waves and VS30, (f) Line 3 SH-waves and VS30, (g) Line 1 SV-waves, (h) Line 2 SV-waves, (i) Line 3 SV-waves.

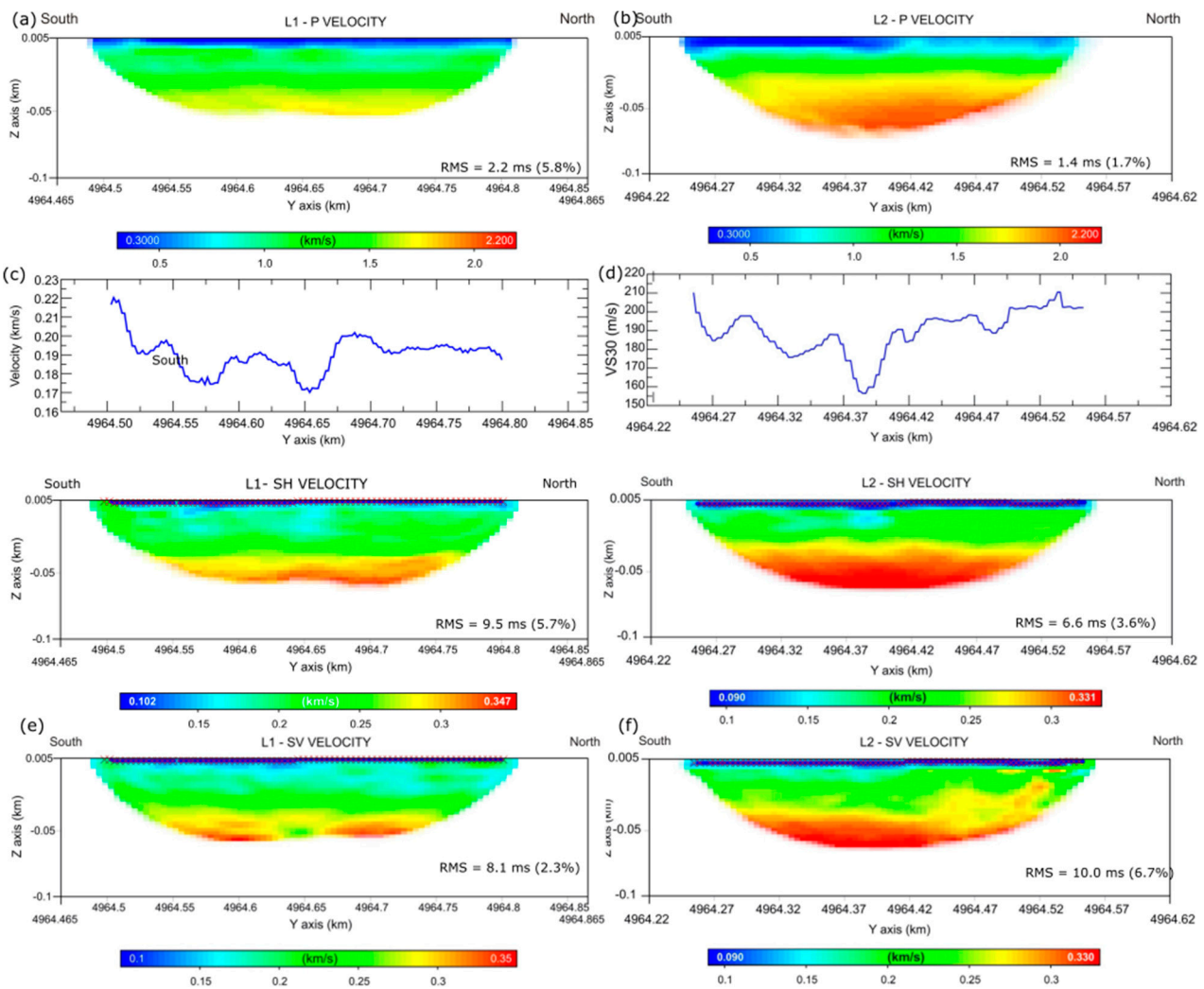


Figure 5. Velocity profiles from the Italian site; in the bottom-right corner, the value of the mean RMS error is shown. (a) Line 1 P-waves, (b) Line 2 P-waves, (c) Line 1 SH-waves with V_{S30} , (d) Line 2 SH-waves with V_{S30} , (e) Line 1 SV-waves, (f) Line 2 SV-waves.

In Figure 4, we show the velocity profiles relative to all wavefields for the two lines acquired in Ferrara. We observe a horizontal layering of the sediments, which is typical of alluvial plains. The highest velocities are reached in Line 2, where they exceed 2 km/s and 0.3 km/s for P- and S-waves, respectively. The V_{S30} is shown in Figure 4c,d, and it shows values for which the soil can be identified as C-class ($V_{S30} > 180$ m/s) following the Eurocode-8 provisions [9], matching the estimates performed in the area by previous large-scale studies [31]. This value and the velocity profile at the center of the line (where the 1D S-wave velocity profile from the MASW is ideally located) is compatible with the results of the inversion of the surface waves, confirming the reliability of our results. The sharp transition at approximately 3 m depth from blue to green in both P-wave velocity profiles most likely indicates the water table. This is consistent with previous geotechnical investigations in the area [32]. Similarly to Figure 4, the mean RMS error is shown in the bottom-right corner of each velocity profile. The values are quite variable, depending on the signal-to-noise ratio of the datasets, which depended on the amount of activities ongoing in the fields. Having said this, they usually show quite a low value, in the range of 5%, and therefore, the velocity profiles can be considered reliable.

Further information about the sites can be obtained by computing the V_P/V_S ratio (proxy for Poisson's ratio). In Figure 6a–c, we show the V_P/V_S profiles relative to the three lines acquired in Croatia, while in Figure 6d,e, we show those relative to the lines acquired

in Italy. The profiles acquired in Croatia show an overall increase in the V_P/V_S ratio in the eastern lines (especially Line 3) compared to the western line. This indicates a more fractured medium that is possibly saturated with water. As for the Italian site, the V_P/V_S ratio is very high in both profiles, reaching a maximum in Line 2. The sharp increase in both lines at a depth of approximately 3 m confirms the position of the water table. Furthermore, such high V_P/V_S probably indicate the presence of water-saturated unconsolidated clay sediments.

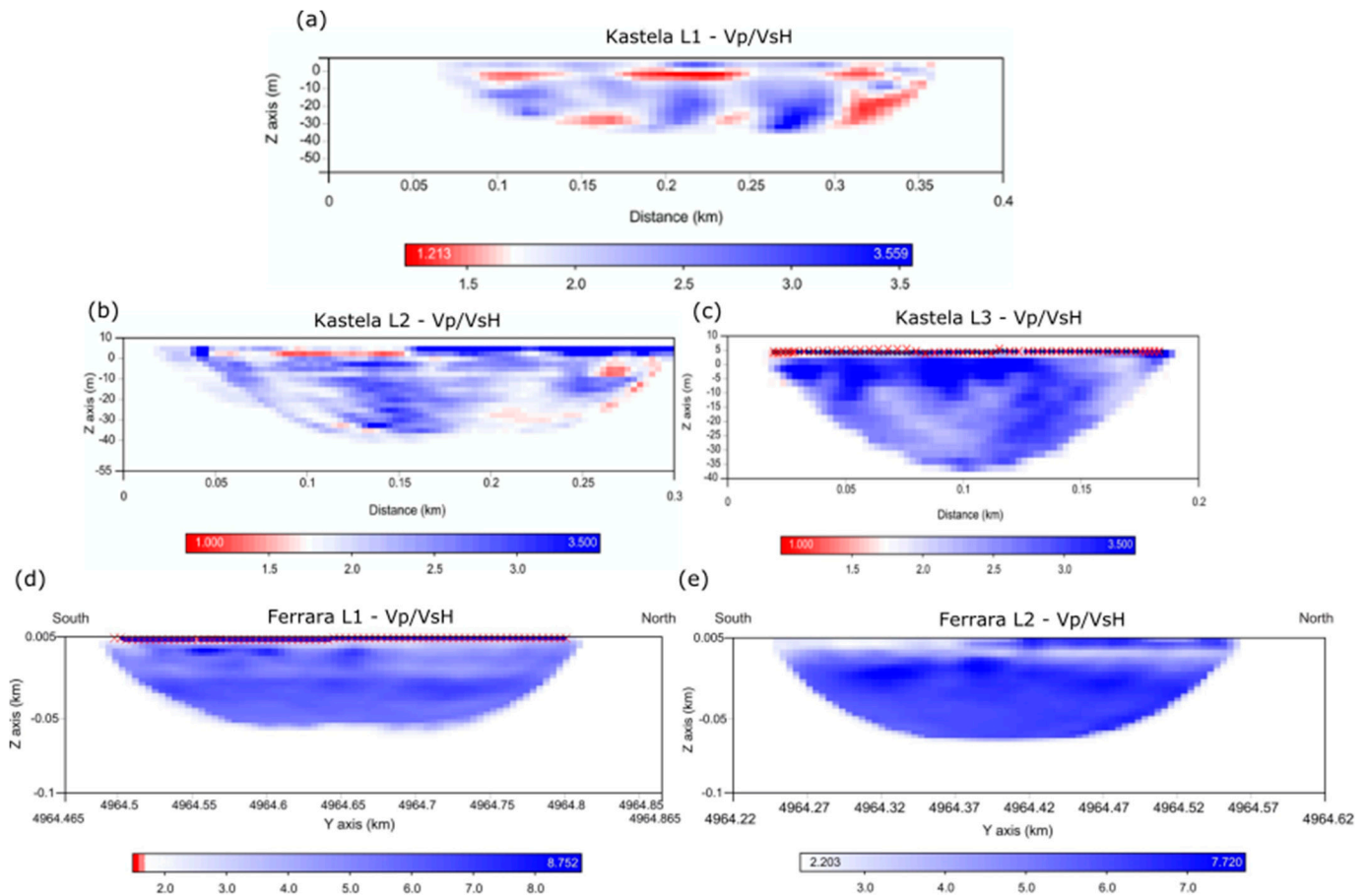


Figure 6. V_P/V_{SH} (a) Kaštela Line 1. (b) Kaštela Line 2. (c) Kaštela Line 3. (d) Ferrara Line 1. (e) Ferrara Line 2.

In Figure 7, we show profiles of the V_{SV}/V_{SH} . In the Croatian site, shown in Figure 7a–c, the presence of anisotropy is due to the layering of the Eocene flysch [14]. From the geometrical considerations applied to the raypaths, it is possible to estimate the bedding angles (dip and strike), as shown in [14]. As for the Italian site, shown in Figure 7d,e the presence of anisotropy confirms that the sediments are composed of horizontal layers of clay and silt, which are known for producing anisotropy [33,34]

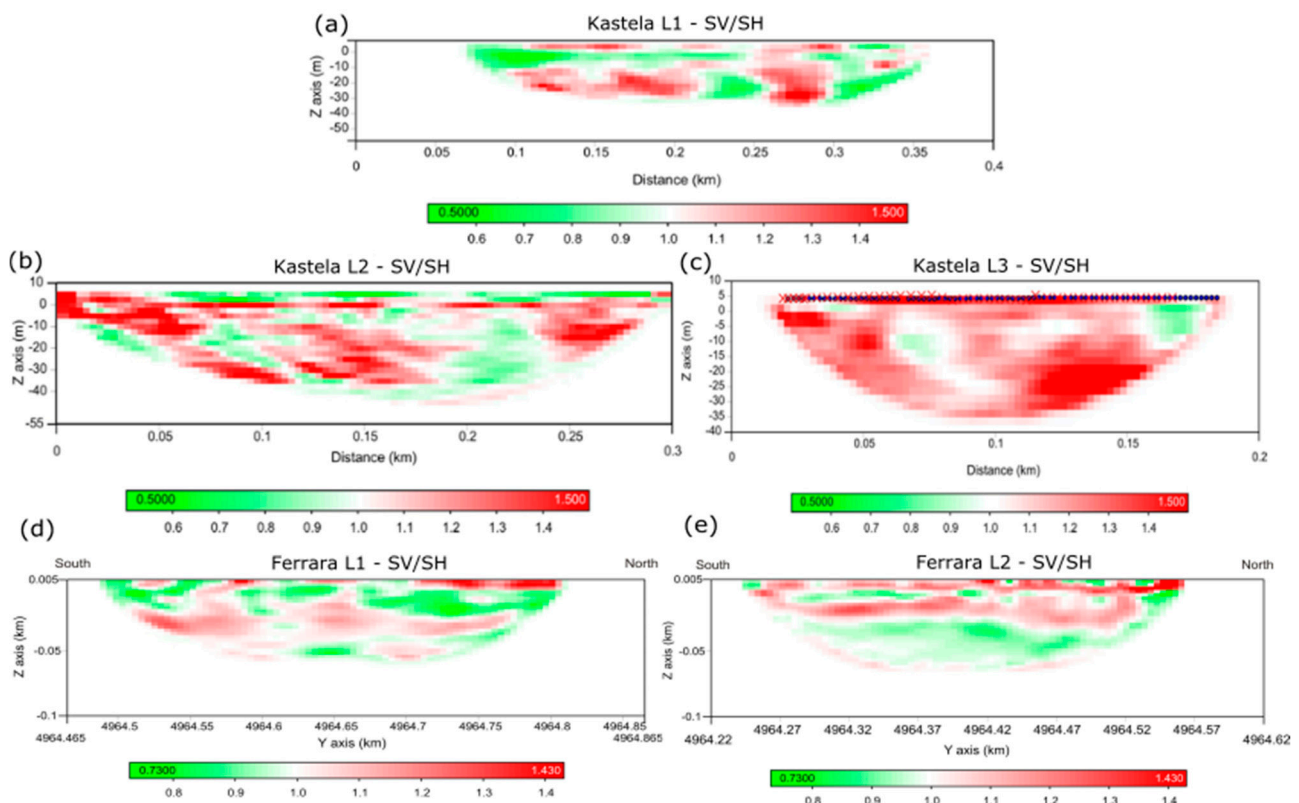


Figure 7. V_{SV}/V_{SH} (a) Kaštelna Line 1. (b) Kaštelna Line 2. (c) Kaštelna Line 3. (d) Ferrara Line 1. (e) Ferrara Line 2.

6. Conclusions

We presented two case studies from two very different sites in order to validate the method in such different circumstances. The first consisted of three high-resolution seismic lines acquired along the roads of a village built on hard rock in Croatia. The second consisted of two high-resolution seismic lines acquired in a cultivated area in northern Italy. In both cases, we acquired P-waves as well as S-waves, the latter in two different polarizations: parallel (SV) and orthogonal (SH) to the seismic line. Furthermore, surface-waves were acquired in the two sites. However, in Croatia, no dispersive event could be identified and therefore no results could be obtained. This highlights the importance of acquiring SH-waves. We then performed first break tomography on all lines, for all wavefields.

The results output by the presented survey method are of high value for engineering purposes, as well as for the overall geological and geotechnical characterization of the investigated areas. Specifically, from an engineering point of view, the sites were classified based on their V_{S30} as required by the current legislation. The method allows to investigate also other important properties of the subsoil, such as the V_P/V_S and the anisotropy of the medium. From the former, it is possible to infer the fracturing of the medium and its water saturation (i.e., the position of the water table). From the latter in the Croatian site, it was possible to compute the dip and strike angles of the bedding of the flysch, providing therefore a geologically valuable information, while in the Italian site, it confirmed the silty/clay composition of the sediments and their horizontal layering.

The method proposed is non-invasive, replicable and relatively cheap, as the acquisition required only 2–3 days for each seismic line. Furthermore, it provides an in-depth characterization of the composition of the subsurface up to a depth of several tens of meters without the need for expensive procedures such as drilling and coring. Finally, these parameters are given along entire profiles, a few hundred meters long, making it attractive for the extensive characterization of geologically heterogeneous areas.

Given the value of the results and all the above considerations, we conclude that the method proposed is an optimal tool to perform an in-depth characterization of the shallow layers of the subsurface.

Author Contributions: Conceptualization, F.A., F.D.C. and G.B.; methodology, F.A. and G.B.; software, F.D.C. and G.B.; validation, F.D.C., G.B. and F.A.; formal analysis, G.B. and F.D.C.; investigation, F.A., F.D.C. and G.B.; resources, F.A. and F.M.; data curation, F.M.; writing—original draft preparation, F.D.C.; writing—review and editing, F.D.C.; visualization, F.D.C., G.B. and F.M.; supervision, F.A.; project administration, F.A.; funding acquisition, F.A. All authors have read and agreed to the published version of the manuscript.

Funding: The research presented in this paper has been carried out within the PMO-GATE (Preventing, Managing and Overcoming Natural-Hazards Risks to mitiGATE economic and social impact) project. Such project falls in the Interreg Italy-Croatia programme of the European Commission under project id 10046122.

Institutional Review Board Statement: Not applicable.

Informed Consent Statement: Not applicable.

Data Availability Statement: The data presented in this study are available on request from the corresponding author.

Acknowledgments: We thank the crew involved in the two data acquisitions, in the names of Stefano Maffione, Gino Cristofano, Massimo Lovo and Andrea Schleifer. Special thanks also to Zeljana Nikolic of the University of Split, who gave us important feedback on the results we obtained. A final thank to the Municipalities both of Ferrara and Kaštela, who gave important help with the logistics.

Conflicts of Interest: The authors declare no conflict of interest.

References

1. Lancellotta, R. *Geotechnical Engineering*; CRC Press: London, UK, 2008.
2. Cardarelli, E.; Cercato, M.; De Donno, G. Characterization of an earth-filled dam through the combined use of electrical resistivity tomography, P-and SH-wave seismic tomography and surface wave data. *J. Appl. Geophys.* **2014**, *106*, 87–95. [CrossRef]
3. Ansal, A.; Kurtulus, A.; Tönük, G. Seismic microzonation and earthquake damage scenarios for urban areas. *Soil Dyn. Earthq. Eng.* **2010**, *30*, 1319–1328. [CrossRef]
4. Aki, K.; Richards, P.G. *Quantitative Seismology*; W.H. Freeman: San Francisco, CA, USA, 1980; Volume 1.
5. Stein, S.; Wysession, M. *An Introduction to Seismology, Earthquakes and Earth Structure*; Blackwell Publishing Ltd.: Malden, MA, USA, 2009.
6. Borcherdt, R.D. Estimates of site-dependent response spectra for design (methodology and justification). *Earth Spectra* **1994**, *10*, 617–654. [CrossRef]
7. Borcherdt, R.D. Simplified site classes and empirical amplification factors for site-dependent code provisions: NCEER, SEADC, BSSC. In Proceedings of the Workshop on Site Response during Earthquakes and Seismic Code Provisions, Los Angeles, CA, USA, 18–20 November 1992.
8. Dobry, R.; Borcherdt, R.D.; Crouse, C.B.; Idriss, I.M.; Joyner, W.B.; Martin, G.R.; Seed, R.B. New site coefficients and site classification system used in recent building seismic code provisions. *Earthquake Spectra* **2000**, *16*, 41–67. [CrossRef]
9. Sabetta, F.; Bommer, J. Modification of the spectral shapes and subsoil conditions in Eurocode 8. In Proceedings of the 12th European Conference on Earthquake Engineering, London, UK, 9–13 September 2002.
10. Park, C.B.; Miller, R.D.; Xia, J. Multichannel analysis of surface waves. *Geophysics* **1999**, *64*, 800–808. [CrossRef]
11. Yust, M.B.S.; Cox, R.B.; Cheng, T. Epistemic Uncertainty in Vs Profiles and Vs30 Values Derived from Joint Consideration of Surface Wave and H/V Data at the FW07 TexNet Station. In *Geotechnical Earthquake Engineering and Soil Dynamics V: Seismic Hazard Analysis, Earthquake Ground Motions, and Regional-Scale Assessment*; American Society of Civil Engineers: Reston, VA, USA, 2018; pp. 387–399.
12. Nakamura, Y. A method for dynamic characteristics estimation of subsurface using microtremor on the ground surface. *Railway Tech. Res. Inst. (Q. Rep.)* **1989**, *30*.
13. Chan, J.H.; Catchings, R.D.; Goldman, M.R.; Criley, C.J. VS30 at Three Strong-motion Recording Stations in Napa and Napa County, California—Main Street in Downtown Napa, Napa Fire Station Number 3, and Kreuzer Lane—Calculations Determined From s-Wave Refraction Tomography and Multichannel Analysis of Surface Waves (Rayleigh and Love); US Geological Survey: Reston, VA, USA, 2018.
14. Da Col, F.; Accaino, F.; Böhm, G.; Meneghini, F. Characterisation of shallow sediments by processing of P, SH and SV wavefields in Kaštela (HR). *Eng. Geol.* **2021**, *293*, 106336. [CrossRef]

15. Uhlemann, S.; Hagedorn, S.; Dashwood, B.; Maurer, H.; Gunn, D.; Dijkstra, T.; Chambers, J. Landslide characterization using P- and S-wave seismic refraction tomography—The importance of elastic moduli. *J. Appl. Geophys.* **2016**, *134*, 64–76. [CrossRef]
16. Chen, J.; Zelt, C.A.; Jaiswal, P. Detecting a known near-surface target through application of frequency-dependent traveltimes tomography and full-waveform inversion to P- and SH-wave seismic refraction data. *Geophysics* **2017**, *82*, R1–R17. [CrossRef]
17. Wang, C.; Shi, Z.; Yang, W.; Wei, Y.; Huang, M. High-resolution shallow anomaly characterization using cross-hole P- and S-wave tomography. *J. Appl. Geophys.* **2022**, *201*, 104649. [CrossRef]
18. Fishman, K.L.; Ahmad, S. Seismic response for alluvial valleys subjected to SH, P and Sv waves. *Soil Dyn. Earthq. Eng.* **1995**, *14*, 249–258. [CrossRef]
19. Yong-Gang, L. Seismic wave propagation in anisotropic rocks with applications to defining fractures in earth crust. In *Rock Anisotropy, Fracture and Earthquake Assessment*; Walter de Gruyter: Berlin, Germany, 2016.
20. Herak, M. *A New Concept of Geotectonics of the Dinarides*; Jugoslavenska Akademija Znanosti i Umjetnosti: Zagreb, Croatia, 1986.
21. Marincic, S.; Magas, N.; Borovic, I. *Osnovna Geoloska Karta SFRJ 1: 100.000, List Split i Pripadaju i Tumac Karte, K33-21*; Institute of Geology: Zagreb, Croatia, 1973.
22. Buljan, R.; Pollack, D.; Pest, D. Engineering geological properties of the rock mass along the Kastela Bay sewage system. *Geol. Soc. Lond.* **2006**, *740*, 467–477.
23. Babic, L.; Zupancic, J. Evolution of a river-fed foreland basin fill: The north Dalmatia flysch revisited (Eocene, outer dinarides). *Nat. Croat.* **2008**, *17*, 357–374.
24. Gargini, A.; Bondesan, M.; Pasini, M.; Messina, A.; Piccinini, L.; Zanella, A.; Oddone, E. *Supporto Tecnico Geologico-Idrologico Alla Procedura di Valutazione e Sostenibilità Ambientale per Il Nuovo Piano Regolatore del Comune di Ferrar—Zona via Bologna—Direttrice per Cona. Relazione n. 1/03.01*; Comune di Ferrara: Ferrara, Italy, 2003.
25. Fontana, D.; Lugli, S.; Marchetti Dori, S.; Caputo, R.; Stefani, M. Sedimentology and composition of sands injected during the seismic crisis of May 2012 (Emilia, Italy): Clues for source layer identification and liquefaction regime. *Sediment. Geol.* **2015**, *325*, 158–167. [CrossRef]
26. Pieri, M.; Groppi, G. *Subsurface Geological Structure of the Po Plain, Italy. Pubbl.414. P.F. Geodinamica*; C.N.R.: Milano, Italy, 1981; pp. 1–23.
27. Wathelet, M. An improved neighborhood algorithm: Parameter conditions and dynamic scaling. *Geophys. Res. Lett.* **2008**, *35*, L09301. [CrossRef]
28. Baradello, L.; Accaino, F. Vibroseis deconvolution: A comparison of pre and post correlation vibroseis deconvolution data in real noisy data. *J. Appl. Geophys.* **2013**, *92*, 50–56. [CrossRef]
29. Böhm, G.; OGS Research Group. *Cat3D. Computer Aided Tomography for 3-D Models. User Manual*; OGS: Trieste, Italy, 2014.
30. Stewart, R. Exploration Seismic Tomography: Fundamentals. In *Course Note Series*; Domenico, S.N., Ed.; SEG—Society of Exploration Geophysicists: Tulsa, OK, USA, 1993; Volume 3.
31. Condotta, M. *Progetto di Adeguamento Funzionale del Sistema Irriguo Della Valli Giralda, Gaffaro e Falce in Comune di Codigoro (FE). Relazione Geologica e Geotecnica. Elaborato 1.2*; Consorzio di Bonifica Pianura di Ferrara: Ferrara, Italy, 2011.
32. Rossi, F.; Tumiati, D.; Bassi, A.; Perelli, P. *Piano Particolareggiato di Iniziativa Pubblica—Sottozona F2—Polo Ospedaliero di Cona. Rapporto di Valutazione Ambientale del Piano Particolareggiato in Località Cona di Ferrara*; Comune di Ferrara: Ferrara, Italy, 2011.
33. Wang, Z. Seismic anisotropy in sedimentary rocks. Part 2, Laboratory tests. *Geophysics* **2002**, *67*, 1348–1672. [CrossRef]
34. Sayers, C.M.; Den Boer, L.D. The elastic anisotropy of clay minerals. *Geophysics* **2016**, *81*, C193–C203. [CrossRef]

Article

Seismic Risk Assessment of Urban Areas by a Hybrid Empirical-Analytical Procedure Based on Peak Ground Acceleration

Željana Nikolić ^{1,*} , Elena Benvenuti ²  and Luka Runjić ³¹ Faculty of Civil Engineering, Architecture and Geodesy, University of Split, 21000 Split, Croatia² Engineering Department, University of Ferrara, 44121 Ferrara, Italy; bnvln@unife.it³ Projektni Biro Runjić, 21000 Split, Croatia; lrunjic.ured@gmail.com

* Correspondence: zeljana.nikolic@gradst.hr

Abstract: The seismic risk assessment of existing urban areas provides important information for the process of seismic risk reduction in different phases of planning and emergency management. Between different large-scale assessment approaches, a vulnerability index method is often used for the first screening of the buildings and vulnerability classification. However, this method cannot fully predict the effects of a specific seismic action on buildings. This paper fully extends the scale of the settlement and properly upgrades a methodology previously proposed by authors to predict seismic damage and the risk to a restricted number of masonry buildings in the Croatian settlement Kaštel Kambelovac located along the Adriatic coast. The proposed approach is based on a hybrid empirical-analytical procedure that combines seismic vulnerability indices with critical peak ground accelerations for different limit states computed through a non-linear pushover analysis. The procedure's outcomes are the computation of a relationship linking vulnerability indices to peak ground acceleration for a series of states, corresponding to damage limitation, significant damage, and near collapse. The described methodology is used to estimate seismic risk in terms of damage and the index of seismic risk for selected return periods. The general methodology has allowed a full seismic vulnerability assessment of the whole Croatian settlement of Kaštel Kambelovac.

Keywords: seismic risk assessment; pushover analysis; vulnerability index; damage index; index of seismic risk; masonry buildings

Citation: Nikolić, Ž.; Benvenuti, E.; Runjić, L. Seismic Risk Assessment of Urban Areas by a Hybrid Empirical-Analytical Procedure Based on Peak Ground Acceleration. *Appl. Sci.* **2022**, *12*, 3585. <https://doi.org/10.3390/app12073585>

Academic Editor: Amadeo Benavent-Climent

Received: 12 March 2022

Accepted: 30 March 2022

Published: 1 April 2022

Publisher's Note: MDPI stays neutral with regard to jurisdictional claims in published maps and institutional affiliations.



Copyright: © 2022 by the authors. Licensee MDPI, Basel, Switzerland. This article is an open access article distributed under the terms and conditions of the Creative Commons Attribution (CC BY) license (<https://creativecommons.org/licenses/by/4.0/>).

1. Introduction

The main reason for excessive human losses and material damage during a seismic event is the insufficient seismic resistance of buildings. The assessment of seismic performance of buildings in an existing urban area is a demanding task for civil engineers, especially in old cities that have been gradually growing and expanding over the course of centuries. The heterogeneous distribution of buildings with different architectural, material and structural characteristics, accompanied by different ages of buildings, material degradation over time, various structural and non-structural interventions and, generally, the lack of knowledge about the performance of the structure, lead to numerous uncertainties in the analysis of such structures. Given the complexity of the problem, the assessment of seismic vulnerability and the risk to large areas is usually performed by simplified methods.

The approaches for the evaluation of structural vulnerability can be generally classified as empirical, analytical, or hybrid. Among them, empirical methods are often used for the first screening of buildings and vulnerability classification. The vulnerability index method [1,2] and the damage probability index method [3] are the most common approaches to assess a building's vulnerability at the urban scale. Different versions of the vulnerability index method have been derived from the approach developed by the Italian Defense National Group against Earthquakes (GNDT) for the seismic vulnerability

assessment of masonry and RC buildings located in historical centers [2] by calibrating the weights of vulnerability parameters using information about the damage induced from past earthquakes [4–6]. The damage probability index method predicts the damage pattern caused by the given intensity of an earthquake using different macroseismic scales [7–9]. The advantage of empirical methods is primarily to reduce the computational efforts in comparison with more complex detailed approaches. Empirical methods are based on qualitative evaluations and can be used for setting priorities in reconstruction or undertaking measures of prevention, mitigation, preparedness, and response as part of a seismic risk management.

Analytical methods aim to represent seismic vulnerability through the analysis of the mechanical behavior of the structure. These methods result in the quantitative evaluation of the seismic performance of buildings based on models of different complexity. Among them, the most detailed are the models based on non-linear methods such as non-linear static (pushover) [10] or incremental dynamic analysis [11], which are very demanding even for a single building and cannot be exploited to assess seismic vulnerability on a wider, urban scale. However, these methods can be used to derive fragility curves for certain typologies of buildings, which can, in turn, be used as starting points to subsequently proceed with the evaluation of seismic vulnerability and damage scenarios at the urban scale [12–20].

Finally, seismic vulnerability at the urban scale can be assessed by hybrid methods, namely methods combining empirical approaches with detailed analytical ones, and leading to the quantitative representation of the behavior of buildings under certain seismic actions.

In this regard, most state-of-the-art contributions containing assessment methodologies, and their related case studies, rely upon the concept that the levels of vulnerability and damage shall depend on the earthquake intensity [21–23]. In particular, a reference can be performed by the study [24] for a thorough discussion of the most relevant vulnerability assessment methods applicable at different scales. Essentially, the choice of the approach should depend on a series of aspects. In addition to the area of study, as settlements will require methods that cannot be used to analyse cities or entire regions, a discriminant comes from data availability about the building stock. A further important aspect is the purpose of the study, while information of the utmost importance will afford a better understanding of both the actual seismic hazard and the structural damage caused by previous earthquakes.

The study of seismic vulnerability and risk proposed in the present paper is based on the vulnerability index method derived from the original Italian GNDT approach [2]. The method provides a vulnerability index as a sum of vulnerability scores, representing a main material and structural and non-structural characteristics important for the seismic behavior of building. Thus, the vulnerability of an urban area can be represented by the vulnerability index map, which informs civil protection bodies of territorial vulnerability and contributes to the planning and managing of emergency actions.

More information about seismic capacity and risk of the buildings can be obtained by linking the vulnerability indices with the intensity of a seismic event. The knowledge about seismic capacity expressed by intensity, peak ground acceleration, or damage is especially important in the prevention of activities aimed to determine priorities in structural interventions and reconstructions. There have been several studies that established vulnerability–damage–peak ground acceleration relationships on an observational basis starting from information about the pre-existing damage levels triggered by past earthquakes [1,25]. The main problem with the application of this relationships is the scarcity of data on previous earthquakes, which are needed to calibrate the model in another area. Non-linear computational approaches, such as the static non-linear (pushover) method and the incremental dynamic analysis, can compute the critical states of the structure, both in terms of capacity represented by peak ground acceleration and associated damage. Therefore, using these non-linear analytical approaches, post earthquake damage data can be replaced with those obtained from the numerical tests. The consequence is that empirical information from the form of the vulnerability index can be linked with quantita-

tive numerical results obtained by means of a non-linear approach. This is an important step in the calibration of the vulnerability model and in establishing relationships between the vulnerability index based on qualitative empirical estimation and the quantitative indicators of structural capacities. A few recent investigations have been performed to assess seismic capacity and/or damage based on vulnerability indices and critical peak ground acceleration obtained by pushover analyses [26,27]. One such hybrid approach has been developed for establishing seismic vulnerability in the Mediterranean urban center of Lampedusa Island in Italy [27]. The procedure combined experimental data and numerical results obtained for a class of buildings representative of the most widespread typology with the purpose of calibrating the vulnerability curves previously obtained by Guagenti and Petrini [4]. Peak ground accelerations corresponding to the life safety limit state have been also analyzed by pushover analysis and used for the seismic fragility assessment of masonry buildings [17].

The hybrid seismic risk assessment procedure adopted in the present paper combines the vulnerability index method with the non-linear pushover analysis of buildings. The methodology has been applied to the entire settlement of Kaštel Kambelovac, a small Mediterranean urban settlement along the Croatian side of the Adriatic Sea and consisting of a historical core constituted by stonemasonry. The historical core was erected between the 15th and the 19th century, while the periphery outside of the historical core includes more modern buildings. In particular, five main categories of construction data of the modern buildings have been recognized: before 1948, 1949–1964, 1964–1982, 1982–2005, and modern buildings erected from 2005 onwards. All these buildings exhibit different seismic performance depending on the period of construction and applied technical regulation.

It should be noted that there are only a few published studies focusing on the seismic behavior of buildings typical of the Adriatic coastal area. They concern experimental research about the behavior of protected buildings inside Diocletian's Palace in Split [28,29] or propose their numerical modeling using finite-discrete element models [30]. Lattice models are also being developed for the precise modeling of energy dissipation under dynamic actions [31,32] which, due to the possibility of modelling heterogeneity in materials, can be highly suitable for the numerical simulation of masonry buildings, whether of regular or irregular blocks. Although complex, all these models are not yet suitable for the analysis of the complex geometries featuring the buildings placed in the area chosen as the test site.

While the aforementioned studies analyzed single buildings in the Adriatic coastal area, a first version of the present hybrid procedure [33] was recently applied by the authors for the assessment of seismic vulnerability and damage of a limited number of stonemasonry buildings in the historical core of Kaštel Kambelovac. With respect to the previous contribution [33], where only two limit states were considered, the hybrid methodology in the present paper is fully generalized and extended to define vulnerability-peak ground acceleration relations for three limit states of the buildings of the entire settlement, which comprises 400 buildings. In particular, the investigation of vulnerability indices and capacities of the buildings obtained by nonlinear pushover analyses has been extended from the historical part of the test site, with stone masonry buildings, to the whole test site including more recent buildings constructed in the 20th and 21st centuries. Furthermore, a general procedure to define seismic risk in terms of damage index and seismic risk index is hereby presented. In fact, the vulnerability curves in terms of the relationships damage index, vulnerability index, and peak ground accelerations, have been generalized in order to account for the influence of the peripheral modern buildings. The damage index has been computed for three return periods for the whole test site and a damage map for convenient visualization is provided. Finally, in the present paper, an entirely new index of seismic risk has been defined and computed for three return periods for the considerable number of 111 buildings.

A massive campaign of field investigations has been purposely performed to gain a full understanding of the material and structural characteristics, including analyzing the available technical documentation and examining the influence of building codes on

the design and construction of the buildings. A sample of eighteen masonry buildings representative of the typical buildings located in the test site has been analyzed by a pushover analysis. The critical peak ground accelerations for three limit states (damage limitation, significant damage, and near collapse) have been determined and used to calibrate vulnerability curves at the test site. The described methodology has been used to estimate the damage index and the index of seismic risk for the selected return periods.

2. Methodology for Seismic Risk Evaluation

The seismic risk of buildings is usually defined as a function of seismic hazard of the area, vulnerability of buildings, and exposure. The seismic hazard of the area expresses the probability of the occurrence of a certain intensity earthquake in a given area and at a certain period of time. The vulnerability of buildings represents the susceptibility of the structure to suffer damage due to a seismic event of a given intensity. The exposure measures the quality and quantity of elements exposed to the risk.

In order to completely understand vulnerability and risk of the urban area exposed to seismic action, the comprehensive procedure for seismic risk evaluation and visualization in this paper is structured as follows:

- Documentation of architectural, structural and material features by examining building codes, historical and archival sources, on-site visual inspection, and thermographic imaging;
- Creation of a database of buildings and visualization of input data by the web map in the GIS environment;
- Geophysical survey of the soil type;
- Definition of seismic hazard for the test site using available seismic hazard maps of Croatia and the results of geophysical survey;
- Seismic vulnerability assessment by vulnerability index method for the sample of the buildings;
- Extrapolation of the results for the seismic vulnerability index for the entire test site;
- Non-linear static analysis of the relevant buildings located in the test site and determination of the peak ground accelerations for damage limitation, significant damage and near collapse states;
- Development of vulnerability–peak ground acceleration curves for three limit states (damage limitation, significant damage, and near collapse) for the test site;
- Development of vulnerability curves that establish relations between damage, vulnerability and peak ground acceleration for the test site, and serve to estimate the structural damage for a given seismic action;
- Risk evaluation in terms of seismic damage for three return periods;
- Risk evaluation in terms of the index of seismic risk for three return periods;
- Visualization of hazard, vulnerability indices, damage indices and indices of seismic risk of the buildings in the web map.

3. Investigation of the Test Site

3.1. Architectural, Material, and Structural Characteristics of Buildings

The proposed method has been applied to Kaštel Kambelovac, one of the seven settlements forming the City of Kaštela (Figure 1a). The structure of each settlement from the aspect of architectural, urban and construction feature is similar. Each settlement was formed around an old historical center built between the 15th and the 19th century. The settlements gradually expanded over the years to the surrounding area. In the course of their development, the settlements merged and the entire area forms today's agglomeration of the City of Kaštela. Nowadays, the city has seven separated historical centers, each composed of stone masonry buildings, which are represented by the combination of smaller family houses, old mansions and public facilities.

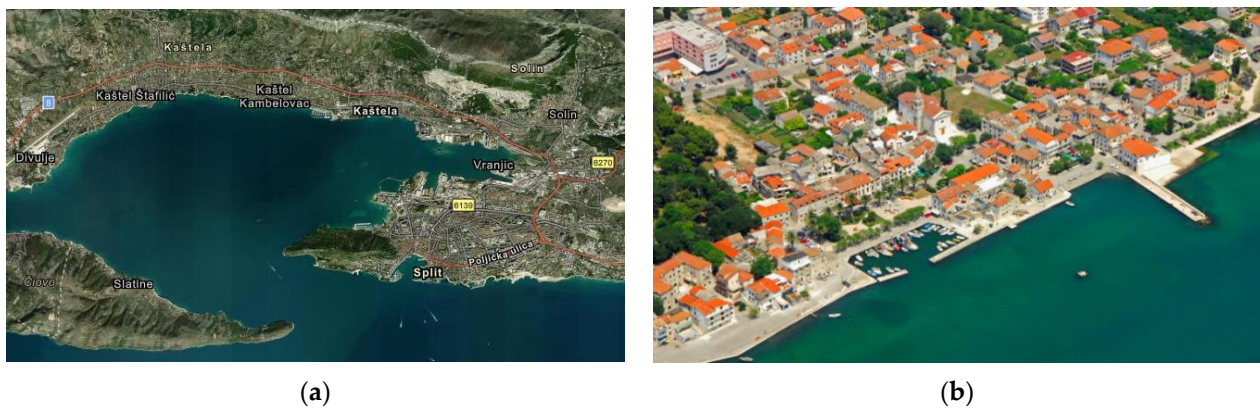


Figure 1. City of Kaštela: (a) geographical position of the city in the Kaštela Bay; (b) historical center of Kaštel Kambelovac [34].

The test site of Kaštel Kambelovac (Figure 1b) consists of an old historical center dating from the 15th and the 19th century, while the peripheral buildings were built from the beginning of the 20th century to the present day (Figure 2). The relevant area includes more than 400 buildings.

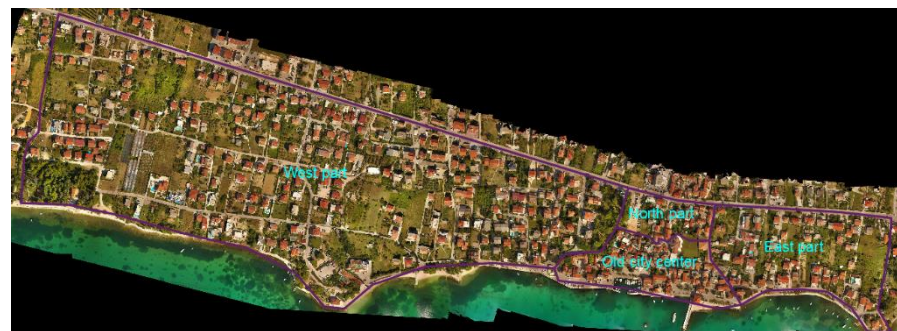


Figure 2. Characteristic parts of the test site.

The masonry walls of the more ancient buildings, located in the historical center (Figure 3), are made of stone blocks and mortar joints, and are from 45 cm to 75 cm thick. The wall textures are variable: roughly shaped stone blocks of various size arranged in a haphazard way alternate to masonry consist of blocks of homogeneous size, well-shaped or cut [33]. The quality of mortar is overall poor. Floors are made of timber beams and wooden floor coverings. Confining elements are lacking, and connections between the walls and floors are generally weak. Some of these buildings were reconstructed and, astypically happens, monolithic reinforced concrete plates replaced the wooden floors.



Figure 3. Buildings in the historical center.

Outside of the historical center (the northern, eastern, and western parts shown in Figure 2), the buildings (Figure 4) were mostly made as masonry structures consisting of

stone, concrete, or brick blocks, unreinforced or reinforced with RC confining elements (only with ties or with ties and columns) depending on the construction period and technical regulations.

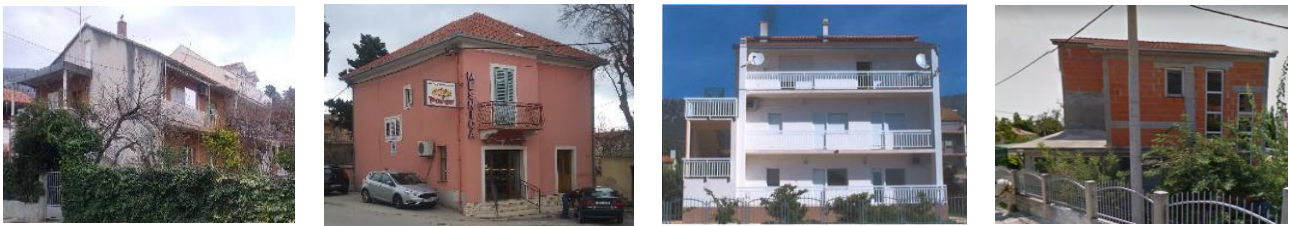


Figure 4. Buildings outside of the historical center.

In fact, the masonry buildings constructed before 1964 are not earthquake-resistant because they have been built as unreinforced masonry structures [35]. Since 1964, seismic regulations required that all buildings have horizontal confining elements and rigid horizontal diaphragms or horizontal and vertical confining elements and rigid horizontal diaphragms depending on the seismic zone and the number of floors. After 1980, stricter regulations for the construction in earthquake areas were applied and the use of unreinforced masonry was not allowed in the areas of medium and high seismicity. In the Kaštela area, it is allowed to build a two-story masonry structure without vertical confining elements and a three-story structure with vertical and horizontal confining elements. Buildings erected from 2005 onwards are seismically resistant structures due to the application of modern design standards based on the European regulations (Eurocode 8), firstly implemented through the pre-standards (HRN ENV 1998-1:2005 [36]) and finally by introducing the full European standard (Eurocode 8) in 2011 in the Croatian national legislation (HRN EN 1998-1:2011 [37]). They are made as confined masonry.

In addition to the analysis of technical regulations, material and structural characteristics have been investigated using historical documentation and literature [38], archival documentation of the City of Kaštela, field survey by a visual inspection, and thermographic examination in a conspicuous number of cases where, due to non-documented reconstructions and external plaster covering the walls, it was impossible to identify material and structural characteristics of the building. In fact, the texture of the walls, the presence of horizontal and vertical confinement, floor covering material and roof structures, and heterogeneities of materials can be successfully detected by thermographic examination. An example of such an investigation is shown in Figure 5.

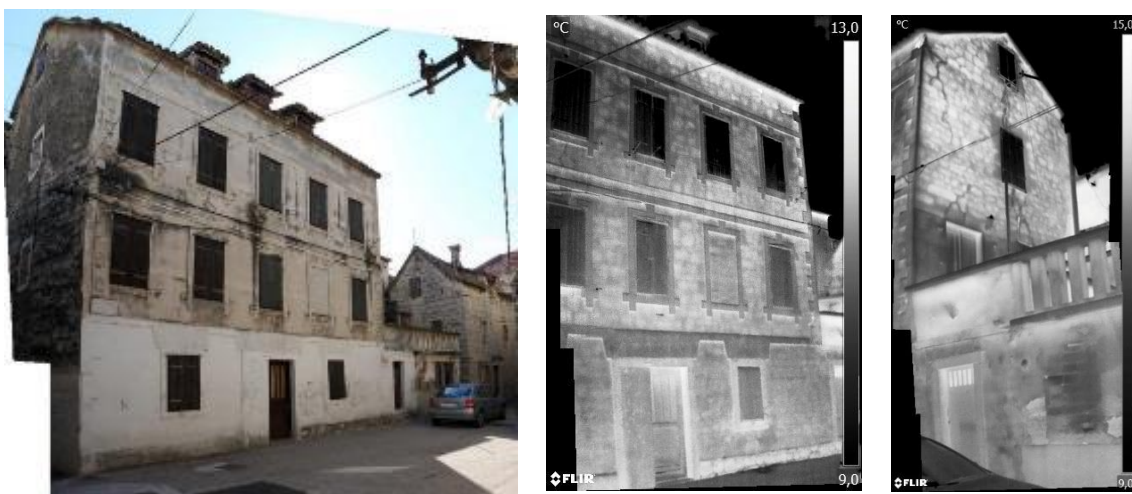


Figure 5. Thermographic examination of unreinforced stone masonry building partially covered with plaster, and significant cracks in a gable wall [39].

The mechanical properties of materials for stone masonry buildings (stone blocks, walls, and mortar) were deduced from the literature [40]. Past design rules were exploited to estimate the mechanical properties of buildings erected from 1900 to nowadays.

Additional assistance was obtained from precise geodetic map of the test site that allowed identification of planimetric dimensions, from Google Maps, Street View, as well as from a map dating back to 1968 that made it possible to identify the subsequently reconstructed sites.

3.2. Geophysical Survey of the Test Site

The characterization of soil type has been determined by a geophysical survey. A detailed description of investigation, performed in May 2019, is presented in [41]. The investigation aims to determine shear wave velocity $V_{S,30}$ of the shallow subsurface along three seismic lines in Kaštel Kambelovac. The velocity $V_{S,30}$ was calculated as the average of the V_{sH} velocities, measured from the surface to a depth of 30 m. The $V_{S,30}$ velocity, higher than 800 m/s, allows us to classify the soil as A class according EN 1998-1:2011 [37] in all three lines. Considering that the investigated test site is relatively small, the soil type A was considered for all buildings in the test area.

4. Seismic Hazard of the Area

The seismic hazard for Croatia is presented in terms of the horizontal peak ground acceleration with two maps for the return periods of 475 and 95 years. The maps have been accepted as a part of the Croatian National Annex of HRN EN 1998-1:2011 [37]. Recently, a new hazard map for $T = 225$ years has been developed. According these maps, the peak ground acceleration a_g in the Kaštela area, is equal to 0.22 g, 0.17 g, and 0.11 g for the return periods of 475, 225, and 95 years, respectively, and ground type A.

The seismic hazard for soil types different from A increases. A simple engineering way to calculate the hazard for local ground conditions is by multiplying the peak ground acceleration for ground type A with the soil factor S [37] for observed location.

Considering the results of the geophysical survey which indicated the ground type A at the investigated area, the seismic hazard for all buildings at the test site has been assumed to be constant.

5. Seismic Vulnerability Assessment of the Area

5.1. Vulnerability Index Method

We perform a vulnerability assessment analysis by the vulnerability index method developed from GNDT in collaboration with the Italian National Research Council from 1984 onwards [1,2]. The present study further includes the modifications of the GNDT method proposed for the Tuscany region in [42] and considers the replacement of light timber floors with heavier RC floors, which are often used in the reconstruction of old masonry buildings. In fact, such replacement induces a significant increase in the mass at the top of the floors, consequently enhancing the overall in-plane stiffness and causing a different dynamic behavior of the modified structures [33].

The vulnerability index method is here used to calculate the vulnerability index for the building based on the calculation of 11 geometrical, structural and non-structural vulnerability parameters of the building. They consider the influence of the type and quality of the structural system, the shear resistance in two horizontal directions, the position and the foundations, the properties of floors, the configuration in plan and elevation, the maximum wall spacing, the roof's typology and weight, the existence of non-structural elements, and the state of preservation. Four possibilities for each parameter were decided: from "A", indicating an optimal state, to "D", indicating a poor state. Furthermore, the method numerically scores each option. The relative importance of each parameter in the

overall vulnerability is computed by using weight coefficients relating to each parameter. Ultimately, a vulnerability index I_V is obtained as follows:

$$I_V = \sum_i s_{vi}w_i \tag{1}$$

where s_{vi} is the numerical score for each class, and w_i is the weight of each parameter. The vulnerability index is normalized in a 0–100% range; the low index indicates high seismic resistance and low vulnerability, while a high vulnerability index is characteristic of the buildings with low seismic resistance and high vulnerability.

Table 1 displays the vulnerability parameters and their weight coefficients used in this paper. The upper value of the vulnerability index I_V is 438.75.

Table 1. Vulnerability parameters and their weights.

Parameter	Score (s_{vi})				Weight (w_i)
	A	B	C	D	
Type and organization of the resistant system (P1)	0	5	20	45	1.50
Quality of the resistant system (P2)	0	5	25	45	0.25
Conventional resistance (P3)	0	5	25	45	1.50
Position of the building and foundation (P4)	0	5	25	45	0.75
Typology of floors (P5)	0	5	15	45	0.50–1.25
Planimetric configuration (P6)	0	5	25	45	0.50
Elevation configuration (P7)	0	5	25	45	0.50–1.00
Maximum distance among the walls (P8)	0	5	25	45	0.25
Roof (P9)	0	15	25	45	0.5–1.5
Non-structural elements (P10)	0	0	25	45	0.25
State of conservation (P11)	0	5	25	45	1.00

5.2. Application of Vulnerability Index Method at the Test Site

The vulnerability indices for 111 buildings with known architectural, structural, and material features (75 in the old city center and 35 outside of the center) were calculated by the vulnerability index method. The distribution of the vulnerability index is shown in Figure 6. The vulnerability indices were included into a web map based on the geographical information system (GIS).

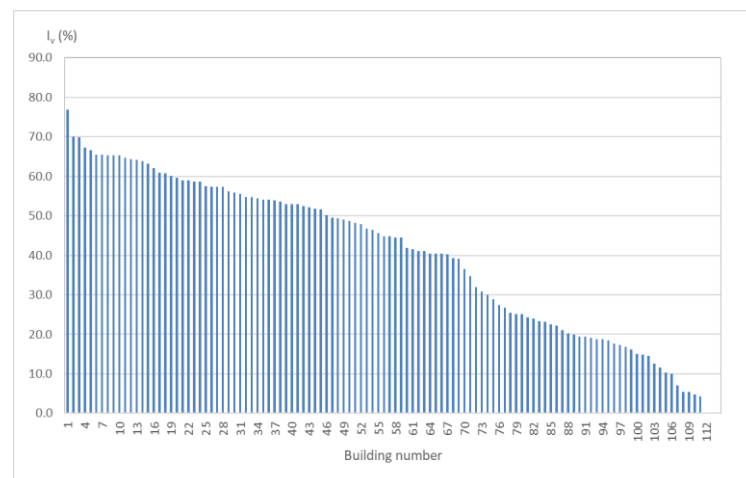


Figure 6. Distribution of I_V for a sample of 111 buildings.

The vulnerability index map is shown in Figure 7. Figure 7a shows the buildings divided into four vulnerability classes: low vulnerability for $I_V < 30$, from medium to low

vulnerability for $30 < I_v < 45$, from medium to high vulnerability for $45 < I_v < 60$, and high vulnerability for $I_v > 60$. The range of the values of vulnerability indices are taken according to the GNDT vulnerability classification used in the study of reconstruction of the Municipality of Arsita following the seismic event of 6 April 2009 [2,43]. More insight into the vulnerability of buildings erected in the period 1950 to 2000 can be obtained from the division of the vulnerability index map into 10% intervals (Figure 7b). The lowest vulnerability index, equal to 2.6, belongs to a two-story house with regular layout and elevation, made as a confined masonry structure with horizontal and vertical confining elements (RC ties and RC columns) and rigid horizontal diaphragms, all designed according to EC-8. The highest vulnerability index, equal to 76.9, was obtained for the Cambi Tower, a stone masonry building dating from the 15th century. The Cambi Tower is characterized by having poorly connected walls, flexible floors, an irregular layout and elevation. A vulnerability index of 45 and beyond is ascribed to medium-high and high vulnerability buildings, respectively. Typically, high vulnerability buildings turn out being mainly located in the old city center and made of stonemasonry.

In the northern part of the settlement, which does not belong to the historical center, there is a number of stone masonry buildings. Therefore, most of the buildings belong to high, medium-high and medium-low vulnerability classes. Only two buildings belong to the low vulnerability class.

In the eastern and western parts of the test site, the buildings are built with concrete or clay blocks, with different confining methods: (1) without confinement; (2) with horizontal tie beams, (3) with horizontal and vertical confinement. They mostly belong to the low vulnerability class ($I_v < 30\%$). Within this class, however, there are visible differences in vulnerability. Newer buildings with brick blocks and horizontal and vertical confinement generally have the lowest vulnerability (less than 10%). Older buildings with concrete blocks and horizontal confinement approximately have an index between 10% and 20%. Buildings without confinement or the aforementioned ones, but irregular in elevation and/or layout and with several annexes and additions, have an index mostly between 20% and 30%.

The vulnerability indices have been computed in detail for 111 buildings with known geometry, structural system, and types of material. The vulnerability of other buildings at the test site without the available technical documentations was determined based on the estimated geometric and structural characteristics of the building using a geodetic survey of the area, a street view map, and a visual inspection of the area. Therefore, a lower precision of vulnerability index results can be expected for these buildings.

5.3. Vulnerability Index Method as a Basis for Seismic Risk Evaluation

Although the vulnerability index is an important indicator of seismic risk, it should be noted that it is useful for a relative comparison of the seismic performance of buildings in the case of equal seismic action. According to modern seismic regulations, such as Eurocode 8 [37], seismic action varies even for constant seismic hazard of the area because it depends on the soil type and the importance factor of the building. More precise information on the behavior of the building subjected to a certain earthquake action can be obtained either by evaluating the damage or by assessing the risk induced by an earthquake of a specific intensity. The former approach establishes a relation between the vulnerability index, the intensity of seismic action and structural damage using the post-earthquake damage observations [1,25] or, alternatively, performing non-linear pushover analyses [27,33]. Seismic risk can also be expressed in terms of the index of seismic risk (or index of seismic safety), expressed as the ratio of the peak ground acceleration achieved to the structural collapse and the demand ground acceleration.



(a)



(b)

Figure 7. Vulnerability index map of the test site. (a) Division into four vulnerability classes. (b) 10% division intervals.

The present study aims to evaluate seismic risk both in terms of the damage index and the index of seismic risk using information about vulnerability of the buildings obtained by vulnerability index method. In order to calculate the damage index, the relation between the vulnerability index and the seismic capacity represented by peak ground acceleration for the sample of 18 buildings has been established. Non-linear static (pushover) analysis has been applied for the calculation of peak ground acceleration for different limit states of buildings (early damage, significant damage, and near collapse). Vulnerability index—peak ground relations enable the calculation of the damage index of the building, but also the calculation of the index of seismic risk for each limit states.

6. Evaluation of PGA Values for Specific Limit States by Pushover Analysis

6.1. Detection of Specific Limit States

A static non-linear pushover method [10,37] is used to evaluate seismic behavior and the capacity of the building for three limit state (LS) conditions that have been taken into account according to Eurocode 8, part 3 [44], as follows:

- Near collapse NC—global capacity of the building is taken to be equal to the ultimate displacement capacity;
- Significant damage SD—global capacity of the building is taken to be equal to $\frac{3}{4}$ of the ultimate displacement capacity;
- Damage limitation DL—the capacity for global assessment is defined as a yield point of the idealized elasto-perfectly plastic force-displacement relationship of the equivalent SDOF.

The pushover analysis has been performed by applying the gradually increasing load up to the structural collapse, using a uniform and modal pattern, according to the N2 method of Eurocode 8 [37]. The analysis allows the determination of capacity curves and collapse load as well as damage monitoring, which continuously increases because of the non-linear deformation.

Pushover analysis results in the MDOF capacity curve, which is transformed into the SDOF capacity curve, and a bilinear force-displacement curve is obtained. Peak ground accelerations for three mentioned limit states have been determined as follows.

We specify that henceforth, the forthcoming equations have been modified with respect to the homologous ones reported in [33] to consider three damage levels.

Given that the displacement in the yield point d_y^* of SDOF is linked with the DL state, the ultimate displacement d_u^* with the NC state and SD state with the displacement equal to $\frac{3}{4} d_u^*$, the corresponding ductilities are expressed as:

$$\mu_{DL} = \mu_y = 1; \mu_{SD} = \frac{3}{4} \frac{d_u^*}{d_y^*}; \mu_{NC} = \mu_u = \frac{d_u^*}{d_y^*} \quad (2)$$

where $\mu_{DL} = \mu_y$, μ_{SD} and $\mu_{NC} = \mu_u$ represents damage limitation, significant damage, and near collapse ductility coefficients.

The associated elastic spectral displacements can be calculated as follows:

$$S_{de,i}(T^*) = \frac{d_y^* \bar{R}_\mu(\mu_i)}{[\bar{R}_\mu(\mu_i) - 1] \frac{T_c}{T^*} + 1}, \quad i = DL, SD, NC \quad (3)$$

where \bar{R}_μ is a reduction factor depending on the ductility coefficient μ of SDOF system [35].

The spectral accelerations are given as:

$$S_{ae,i}(T^*) = \frac{4\pi}{T^{*2}} S_{de,i}(T^*), \quad i = DL, SD, NC \quad (4)$$

The periods T_B , T_C , and T_D divide the elastic response spectrum [37] into four spectral acceleration branches represented with the functions f_i ($i = 1, \dots, 4$). Therefore, it can be expressed as follows:

$$S_{ae}(T) = PGA \cdot f_i(T) \quad (5)$$

where $PGA = a_g$ is peak ground acceleration and T is the period of the structure. Each limit state (DL, SD, and NC) is characterized with the following peak ground accelerations:

$$PGA_{DL} = \frac{S_{ae,DL}(T^*)}{f_i(T)}; \quad PGA_{SD} = \frac{S_{ae,SD}(T^*)}{f_i(T)}; \quad PGA_c = \frac{S_{ae,NC}(T^*)}{f_i(T)} \quad (6)$$

Eighteen buildings in the settlement were modelled using 3MURI software [45] following the equivalent frame model approach. Thus, the structural response is checked along

two horizontal axes, in the positive and the negative direction. Accidental eccentricity equal to $\pm 5\%$ of the maximum floor dimension is considered to model the non-regular mass distribution.

Pushover analysis provides reliable results for the structures that oscillate predominantly in the first mode. In the presence of both horizontal and vertical irregularities, multi-modal non-linear static analysis can be applied [46]. Due to significant irregularities of buildings, a threefold lateral load distribution, namely uniform, linear, and modal, has been applied in this study. Considering the eccentricities in positive and negative directions, this resulted in a total of 36 analyses.

The evaluation procedure of peak ground accelerations for three limit states is shown for the Cambi Tower (Figure 8).

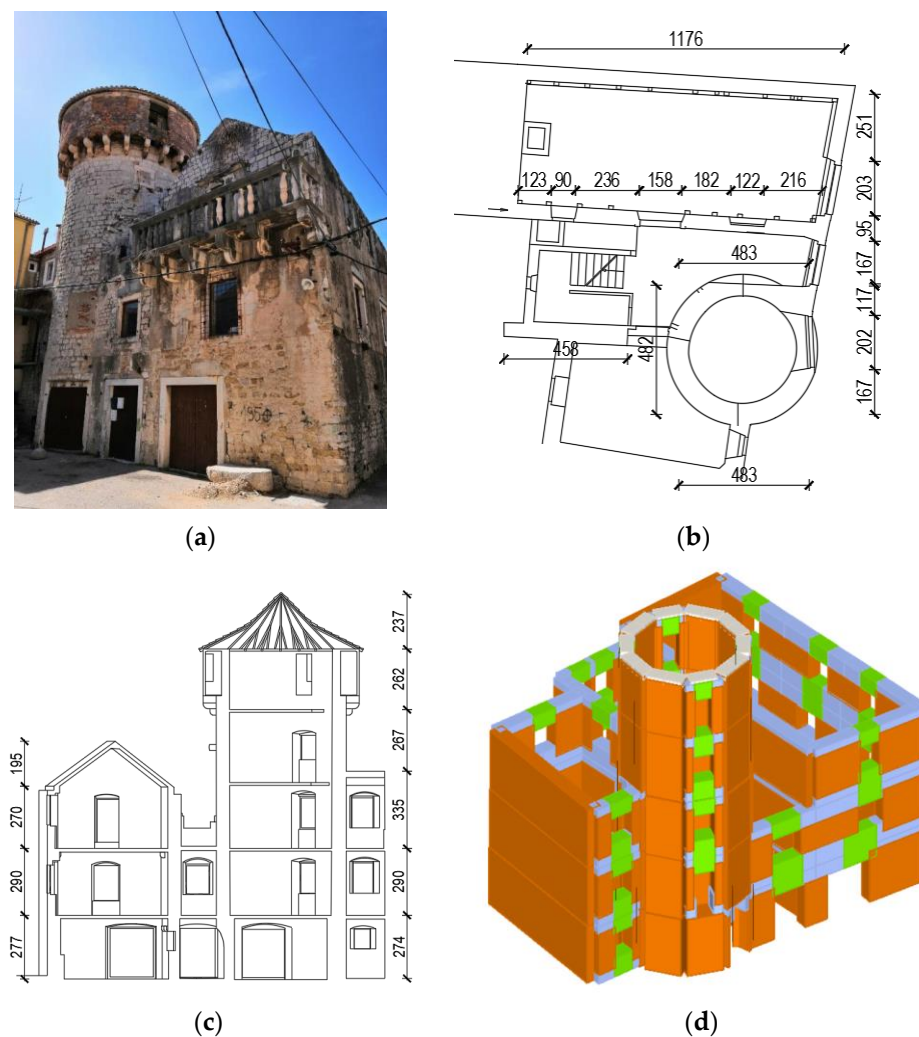
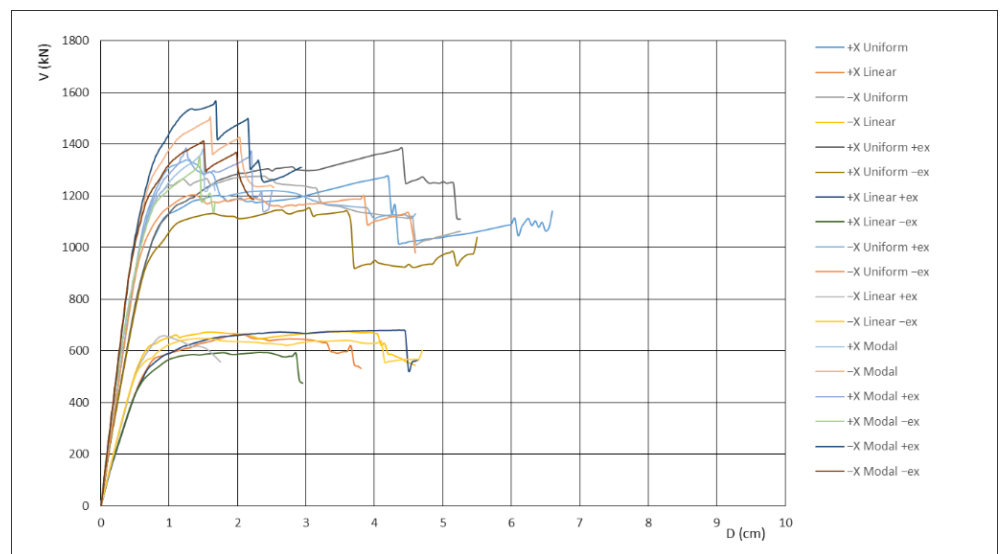


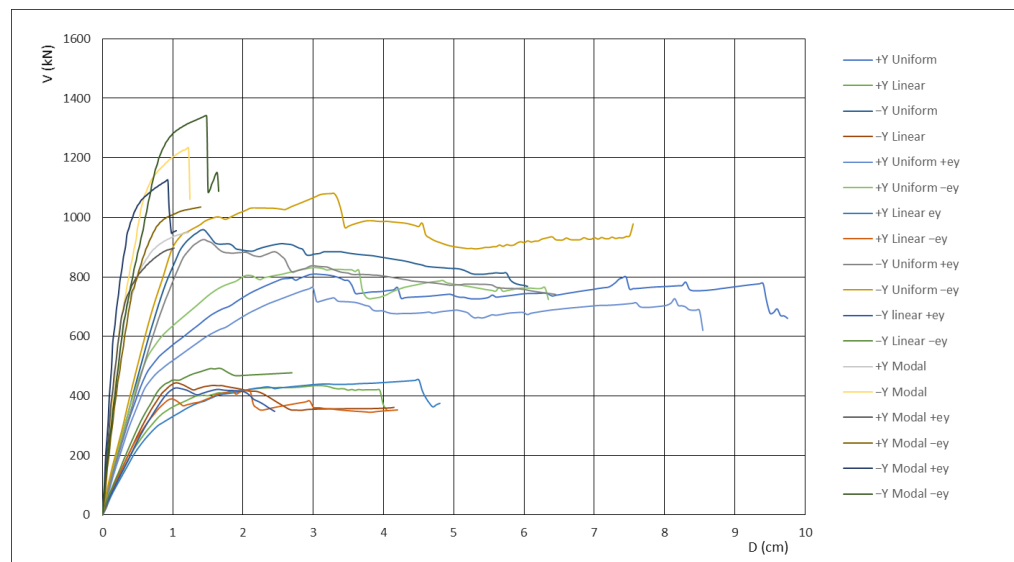
Figure 8. Cambi Tower: (a) photo of the building; (b) ground floor plan; (c) section view; (d) structural model.

The floors were modeled as flexible. The walls' mechanical properties were taken according to [40] as follows: compressive strength of 3.20 MPa, tensile strength of 0.10 MPa, modulus of elasticity of 1700 MPa, shear modulus of 580 MPa, and specific weight of 21 kN/m³.

Seismic demand was deduced from the elastic response acceleration spectrum. A soil class A and type 1 response spectrum [37] have been adopted. Other assumptions include the importance factor $\gamma_1 = 1.2$ and the design ground acceleration $a_g = 0.22$ g. Figure 9 illustrates the results of the pushover analyses for x and y direction.



(a)



(b)

Figure 9. Pushover curves for the Cambi Tower: (a) x-direction; (b) y-direction.

Seismic capacity for two orthogonal directions was evaluated by a pushover analysis, comparing the displacement capacity and the displacement demand for the same control point. The calculation was repeated for all of the 36 loading cases.

The critical peak ground accelerations associated with the DL, SD, and NC limit states were computed as follows: (a) x direction— $PGA_{DL} = 0.093 \text{ g} = 0.422a_g$, $PGA_{SD} = 0.116 \text{ g} = 0.527a_g$, $PGA_{NC} = 0.147 \text{ g} = 0.668a_g$; (a) y direction— $PGA_{DL} = 0.030 \text{ g} = 0.136a_g$, $PGA_{SD} = 0.059 \text{ g} = 0.268a_g$, $PGA_{NC} = 0.078 \text{ g} = 0.355a_g$. For completeness, the design ground acceleration $a_g = 0.22 \text{ g}$ has been obtained based on the seismic hazard map for the return period of 475 years.

6.2. Results of Pushover Analysis of the Buildings

A static non-linear (pushover) method is used for a detailed analysis of 18 buildings at the test site: 10 stone masonry buildings in the historical center (Figure 10) and 8 masonry buildings outside of the historical center (Figure 4).

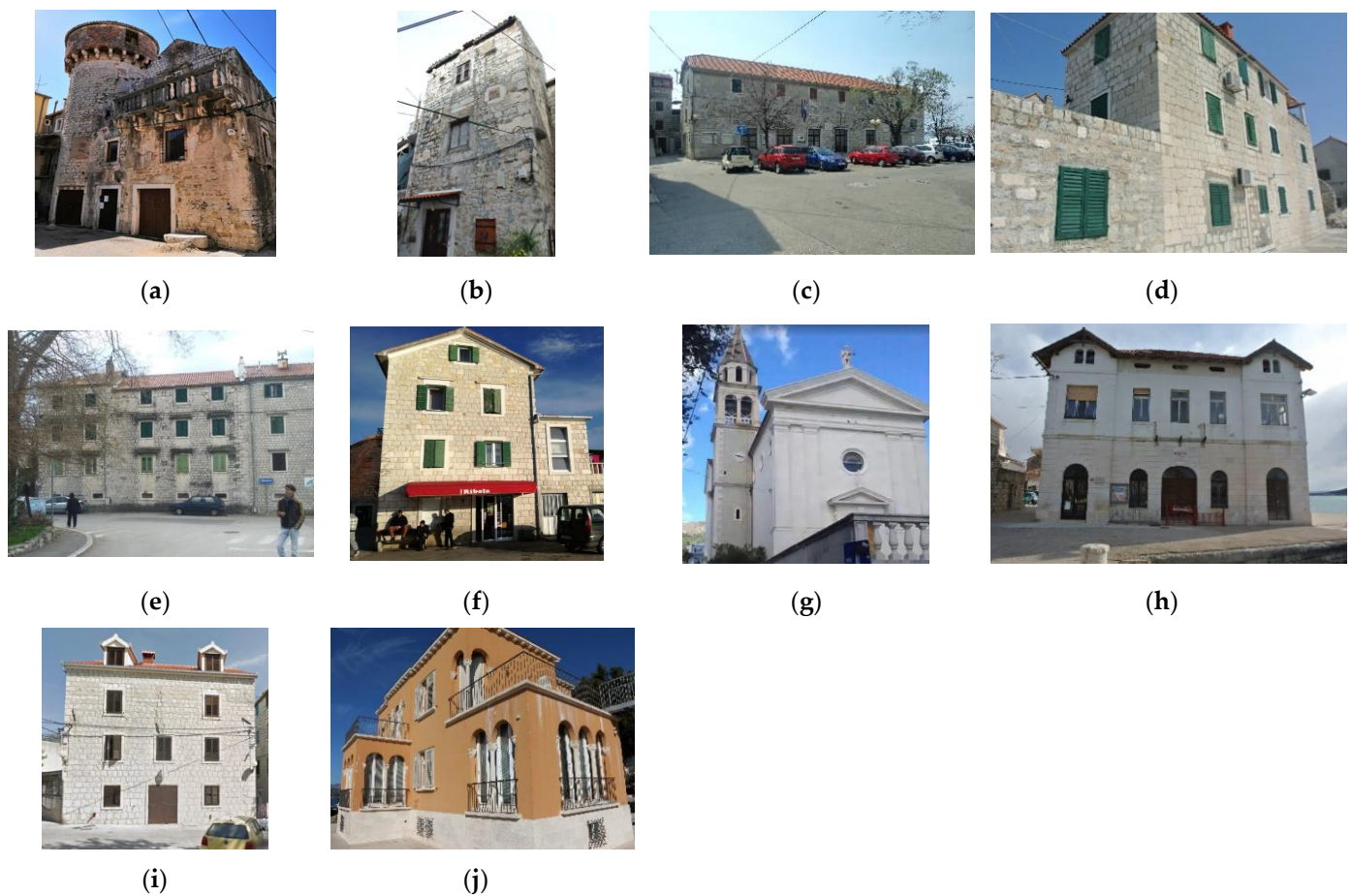


Figure 10. Analyzed buildings in the historical centre: (a) Cambi Tower; (b) Cumbat Towers; (c) Public Library; (d) Folk Castle; (e) Dudan Palace; (f) Perišin house; (g) St. Mihovil Church; (h) rowing club; (i) residential building; (j) ballet school.

The buildings in the historical center have different floor plans and height configurations, dimensions, and number of floors. Many have been upgraded over time. Their common feature is that they are all built of stone blocks. Pushover analysis was conducted on ten buildings that have historical or cultural value. Today they are intended for public use or housing. Some of the buildings have very poor mechanical properties, while the others have been reconstructed and show higher seismic resistance. The basic idea in the selection was to include as many different types of buildings as possible.

The masonry buildings outside of historical center are typical for the constructions built of concrete or brick hollow blocks after 1948 and can be classified according to the construction period. They belong to the following categories: (1) Type 1—unreinforced concrete masonry built before the first seismic regulation in 1964; (2) Type 2—concrete masonry with horizontal RC confining elements typical for the period between 1964 and 1980; (3) Type 3—confined concrete masonry with horizontal RC ties and RC columns built between 1980 and 2005, and (4) Type 4—confined brick masonry with horizontal RC ties and RC columns, which are seismically resistant structures due to the applications of modern design standards based on Eurocode 8. The buildings have rigid RC slabs, while the roof is mainly wooden with roof tiles. A large number of buildings, especially the older ones, have a similar floor plan and the ratio of the shear surface area of the walls to the floor area. Since two configurations of buildings prevail in terms of height, with two floors and a roof and three floors and a roof, two buildings of different storeys were selected for each period of construction for detailed pushover analysis. Therefore, two different elevation

configurations have been analyzed: (a) P + 1 which consists of ground, one floor, and a roof; and (b) P + 2 which consists of ground, two floors, and a roof (Figure 11).

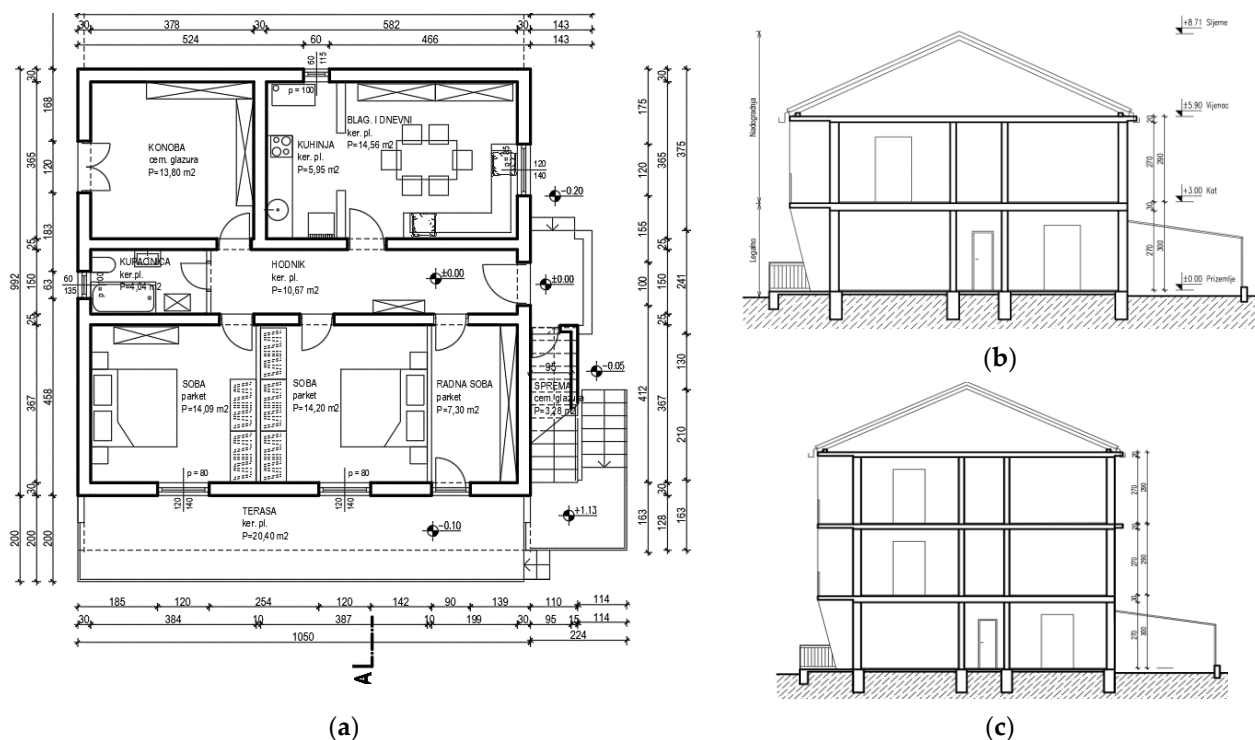


Figure 11. Typical configurations outside of the historical center: (a) plan; (b) section view P + 1; (c) section view P + 2.

Peak ground accelerations for the DL, SD, and NC limit states were computed in the x and y directions. The lowest PGA values were identified for each building and limit state. The critical PGA results and vulnerability indices for the considered buildings are presented in Table 2.

Table 2. Vulnerability index and critical peak ground accelerations of the buildings.

No.	Building	I _v [%]	PGA _{DL} [g]	PGA _{SD} [g]	PGA _{NC} [g]
1	Cambi Tower	76.9	0.030	0.059	0.078
2	Kumbat Towers	65.2	0.057	0.087	0.103
3	Public Library	59.0	0.028	0.061	0.079
4	Folk Castle	58.7	0.081	0.061	0.080
5	Dudan Palace	50.1	0.051	0.068	0.083
6	Perišin house	48.7	0.058	0.061	0.121
7	St. Mihovil Church	40.5	0.057	0.086	0.102
8	Rowing club	40.2	0.064	0.110	0.141
9	Residential building	34.8	0.081	0.095	0.152
10	Ballet school	23.9	0.103	0.142	0.183
11	Type 1 building P + 2	29.1	0.083	0.114	0.142
12	Type 1 building P + 1	29.1	0.061	0.144	0.173
13	Type 2 building P + 2	13.4	0.098	0.145	0.175
14	Type 2 building P + 1	13.4	0.115	0.187	0.220
15	Type 3 building P + 2	6.0	0.065	0.158	0.189
16	Type 3 building P + 1	6.0	0.075	0.175	0.206
17	Type 4 building P + 2	4.3	0.103	0.188	0.243
18	Type 4 building P + 1	2.6	0.130	0.218	0.270

The distribution of vulnerability index I_v is shown in Figure 12, while peak ground accelerations for the NC, SD, and DL limit states calculated by the pushover analysis for 18 buildings are presented in Figure 13.

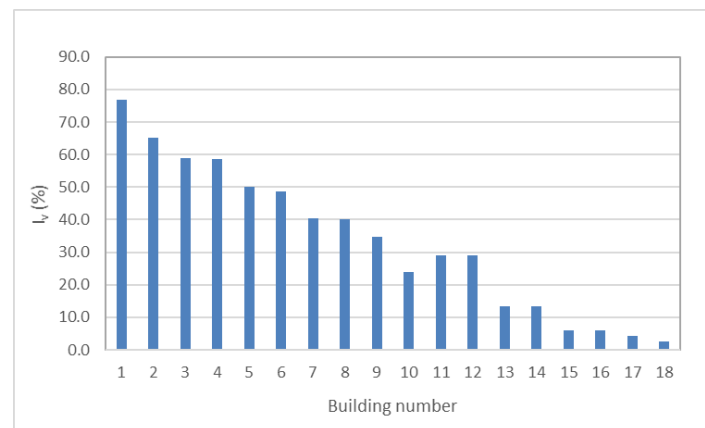


Figure 12. Distribution of I_v for 18 buildings analyzed by pushover analysis.

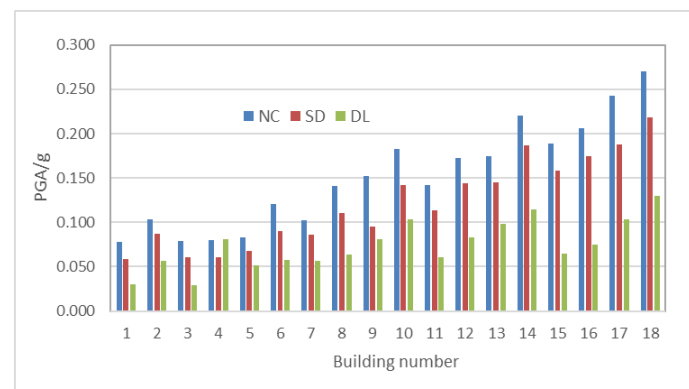


Figure 13. Peak ground accelerations for NC, SD, and DL limit states calculated by pushover analysis.

7. Vulnerability Index—PGA Relations

The emphasis of this part of the paper is to investigate whether the seismic behavior of the building can be estimated from the vulnerability index parameters. Therefore, 18 buildings, which represent 16% of total 111 buildings with calculated vulnerability indices, were analyzed by the non-linear static (pushover) method. The buildings have been chosen considering different material and structural characteristics as well as the period of construction. Additionally, there are buildings among them with different number of the floors and regular and non-regular layout and elevation.

The non-linear pushover analysis carried out on the stone masonry buildings in the old city center indicated a low global capacity in terms of the collapse peak ground acceleration, as well as low global accelerations of significant damage and damage limitation states. Numerical predictions of the acceleration achieved for structural collapse have indicated that no building meets the seismic demand of $a_g = 0.22$ g for $T = 475$ years in both the x and y directions. Moreover, in the simulations, a conspicuous number of buildings reached the collapse at accelerations that are lower than the demand acceleration of $a_g = 0.11$ g for a return period $T = 95$ years. The local mechanism failure induced by a lack of connection among perpendicular walls, and poor connections between floors/roofs and walls, was also analyzed for few stone masonry buildings in the old city center, where out-of-plane effect can be expected. The lowest acceleration was achieved for the global response of the buildings [33]. Buildings outside of the center are made of concrete or brick masonry with horizontal RC confining elements or both with horizontal and vertical confining elements

and rigid horizontal diaphragms. Therefore, the failure of the structure caused by local mechanisms is not expected and the behavior of the buildings represented by capacity accelerations will be analyzed assuming the global failure of the structure.

The results for 18 analyzed buildings (10 in the historical center and 8 outside of the center) presented in Table 2 and Figures 12 and 13, are used to establish the vulnerability index—peak ground acceleration relation for the DL, SD, and NC limit states at the entire test site. Figure 14 shows a cloud of points representing the relationship between the vulnerability index calculated on the basis of 11 parameters I_v and the critical peak ground accelerations associated with the DL, SD, and NC limits. The trend lines I_v – PGA_{DL} , I_v – PGA_{SD} and I_v – PGA_{NC} for three limit states were obtained and are shown in Figure 14. The exponential functions were chosen as the most representative. They are used to approximate the yield, significant damage, and collapse peak ground accelerations for the entire test site. The values of yield and collapse accelerations are the basis for deriving vulnerability curves.

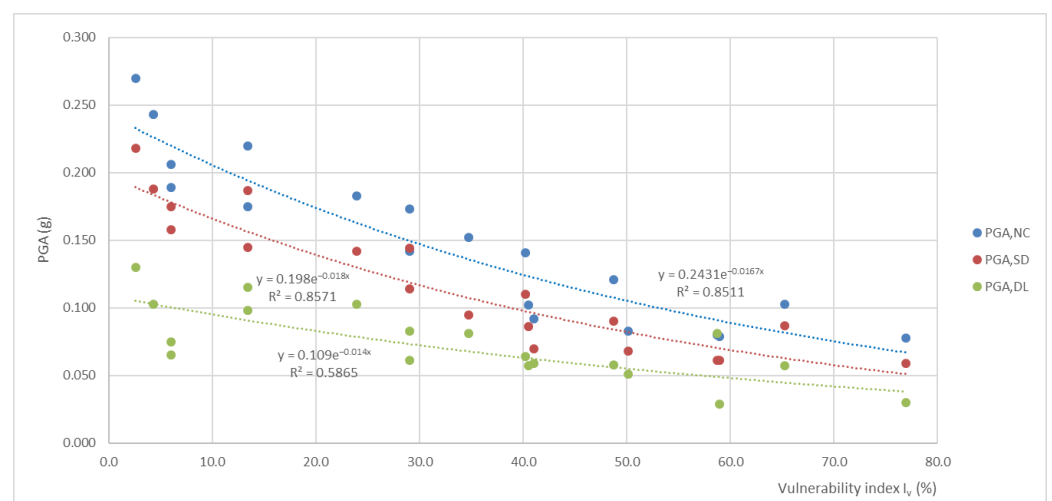


Figure 14. Trend lines I_v – PGA_{DL} , I_v – PGA_{SD} , and I_v – PGA_{NC} .

The quality of the approximation of the results obtained by the pushover analysis and those represented by trend lines for the three limit states are validated by standard deviation. The comparison shows a significantly better quality of peak ground acceleration approximations for the NC and SD limit states than for the DL state. It is obvious that the most vulnerable buildings have a certain seismic load-bearing capacity expressed with peak acceleration. The derived trend lines are used to estimate peak ground accelerations for three limit states of the buildings using their vulnerability index. It should be noted that the results for near collapse and significant damage states approximate critical accelerations much better than the state of damage limitation.

8. Vulnerability Curves and Damage Index Distribution

The vulnerability curve allows to correlate the vulnerability index, damage index, and peak ground acceleration. Two limit-levels of acceleration are key to the analysis of damage: the acceleration associated to the beginning of the damage and the acceleration associated to the structural collapse. We recall that the damage value varies in the (0, 1) interval. The present investigation relies upon the study devised by Guagenti and Petrini [4], who obtained a relation between vulnerability index, acceleration, and damage, by observing the damage levels of masonry buildings subjected to real earthquakes. Corresponding acceleration/damage relation can be modelled with a smooth vulnerability curve (Figure 15). For simplicity purposes, Guagenti and Petrini, instead of using a vulnerability curve, proposed to exploit a tri-linear law parametrized in terms of the values that the peak ground acceleration takes at early damage, PGA_i , and at the collapse, PGA_c . In this study, instead

of a post-earthquake damage observation, the acceleration for the yield and collapse states were calculated by the pushover analysis [27,33]. Then, using the vulnerability indices and yield and collapse accelerations, a new damage–vulnerability–peak ground acceleration relationship was derived. The damage index is expressed in the (0–1) interval via a tri-linear law, analogously to [4] though defined through two parameters: yield acceleration PGA_y , which corresponds the beginning of the damage ($d = 0$), and collapse acceleration PGA_c ($d = 1$).

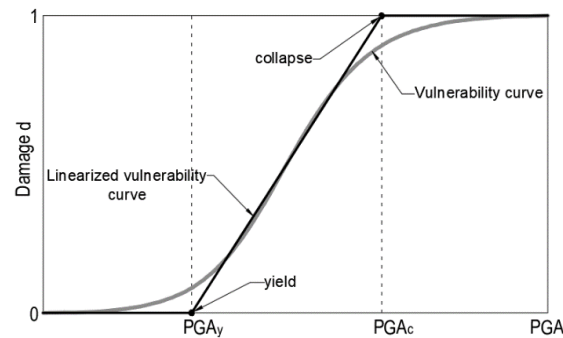


Figure 15. Vulnerability curve and its idealization.

The developed procedure has been applied to the observed test site. The basis for defining vulnerability curves are vulnerability indices, yield peak ground acceleration PGA_y , and collapse peak ground acceleration PGA_c , obtained by the pushover analysis for 18 analyzed buildings, as shown in Table 2. Yield acceleration PGA_y is assigned to PGA_{DL} and collapse acceleration PGA_c to PGA_{NC} limit states, respectively. As PGA_y and PGA_c depend on the vulnerability index I_v , the values of PGA_y , associated with damage $d = 0$, and PGA_c , associated with damage $d = 1$, can be calculated for each value of I_v .

Figure 16 shows the vulnerability curves used for the estimation of the damage index of the buildings at the investigated area. These vulnerability curves are partially changed in comparison to those derived from the authors for the sole historical center [31], as here the study was extended to the entire test site. In fact, the influence of the buildings outside of the historical center with vulnerability indices mainly up to 30% changed the relationships between vulnerability index and peak ground accelerations, as well as the vulnerability curves for the low vulnerability buildings.

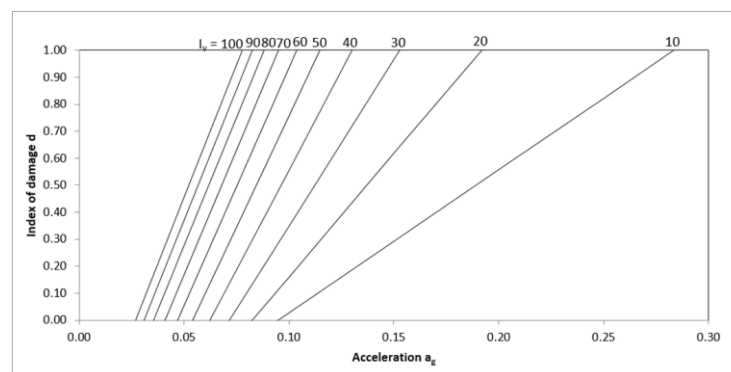
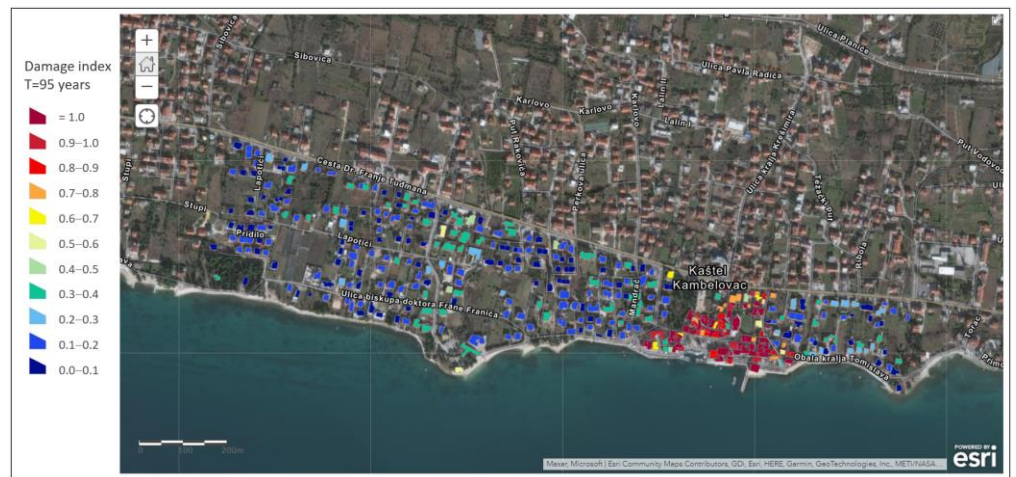


Figure 16. Vulnerability curves for the test site.

The spatial distribution of the damage is represented by the damage index maps of the investigated area for the given intensity of the earthquake. Three seismic scenarios corresponding to return periods of 95, 225, and 475 years and demand peak ground accelerations of 0.11 g, 0.17 g, and 0.22 g, respectively, have been chosen. The damage to the buildings for different scenarios is presented in Figure 17.



(a)



(b)



(c)

Figure 17. Damage index distribution at the test site: (a) T = 95 years; (b) T = 225 years; (c) T = 475 years.

9. Seismic Risk Distribution in Terms of the Index of Seismic Risk

In this section, the methodology for the assessment of seismic risk in terms of the index of seismic risk is presented. The methodology uses vulnerability index–peak ground acceleration relations for the DL, SD, and NC limit states, as presented in Figure 14, to estimate critical peak ground accelerations from the vulnerability index.

The index of seismic risk is calculated as the ratio of the peak ground acceleration PGA_C associated to the structural capacity and the demand ground acceleration PGA_D . It is expressed in the following form:

$$\alpha_{PGA,C} = \frac{PGA_C}{PGA_D} \tag{7}$$

The capacity of the structure represents the minimum value of PGA for which a certain limit state is achieved. In the further analysis, capacity of the structure leading to the structural collapse (i.e., NC limit state) is analyzed. Therefore, PGA_C is equal to PGA_{NC} .

Seismic hazard is defined according to EC-8 with the following parameters:

- a_g —peak ground horizontal acceleration on type A soil, $a_g = \gamma_I a_{gR}$, where γ_I depends on the importance of the building;
- S —soil parameter.

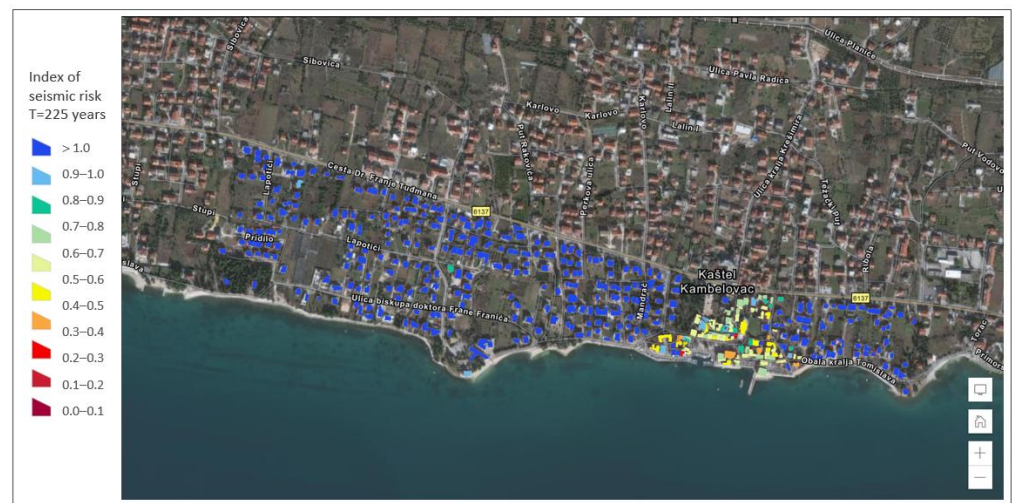
Demand ground acceleration PGA_D obtained from the seismic hazard map for the selected return period is given as $PGA_D = a_g S$.

Indices of seismic risk are used to validate the safety of the structure. The values $\alpha_{PGA} > 1$ refer to safe structures, while the values $\alpha_{PGA} < 1$ refer to non-safe structures. The indices of seismic risk that evaluate safety for the NC limit state of the buildings for three return periods are presented in Figure 18. Indices of seismic risk for other limit states can be calculated in a similar manner.



(a)

Figure 18. Cont.



(b)



(c)

Figure 18. Risk maps in terms of index of seismic risk: (a) $T = 95$ years; (b) $T = 225$ years; (c) $T = 475$ years.

10. Discussion

The methodology for large-scale seismic vulnerability and risk assessment has been developed and applied to Kaštel Kambelovac, one of seven settlements of the City of Kaštela. The hybrid procedure combining the vulnerability index method with the pushover analysis of the selected buildings has been used to calculate vulnerability indices, critical peak ground accelerations for three limit states (early damage, significant damage, and near collapse), seismic risk in terms of damage, and indices of seismic risk. Vulnerability and risk of the test site have been demonstrated through the vulnerability index map, damage index map and map of indices of seismic risk. All results have been integrated into a web-map based on the GIS tool.

The main findings of the study are summarized below.

Vulnerability indices have been calculated for 111 buildings with known geometrical, structural, and material characteristics (75 in the old city center and 35 outside of the center). The vulnerability of other buildings at the test site without the available technical documentations was estimated using geometric and structural characteristics of the buildings obtained from a geodetic survey of the area, a street view map, and a visual inspection of the area. The distribution of vulnerability indices shows the medium-high and high vulnerability of the historical center and the part north of the center. Such high vulnerability

is associated with stone masonry buildings built between the 16th and the beginning of the 20th century, which are mostly made with walls poorly connected, flexible floors, and irregular layout and elevation. The medium-low and low vulnerability has been achieved for the buildings outside of the historical center, which were built starting from the second half of the 20th century to the present day. They are made of concrete or brick blocks. Some of them are unreinforced, while the others are confined with horizontal RC ring ties or both with horizontal RC ring ties and RC columns which, together with rigid RC floors, contributed to high seismic resistance and low vulnerability.

The pushover analysis has been conducted on 18 typical buildings (10 in the historical center and 8 outside of the center). The buildings in the historical center have reached the collapse for a low peak ground acceleration (between 0.078 g and 0.183 g). The acceleration for significant damage ranges from 0.059 g to 0.142 g, while the lowest acceleration has been achieved for the early damage state (between 0.028 g and 0.103 g). No buildings in the center meet the seismic requirement of $a_g = 0.22$ g for $T = 475$ years in either directions. Moreover, several buildings reached the structural collapse at peak ground accelerations that are lower than the demand acceleration of $a_g = 0.11$ g for a return period $T = 95$ years. It should be noted that capacity accelerations have been obtained for the global structural response. Although local failure mechanisms can be critical for the buildings with flexible floors and weak connection between the walls, the analysis of local mechanisms of many buildings showed that the lowest accelerations have been reached for the global analysis of the buildings. Considering that the aim of the study is a vulnerability assessment of the settlement, critical acceleration has been determined on all buildings for the global response of the structure. The capacity of the buildings typical for the structures outside of the historical center varied depending on the applied materials and construction rules. Unreinforced concrete masonry buildings built before the first seismic regulation in 1964, concrete masonry with horizontal RC ring ties typical for the period between 1964 and 1980, and confined concrete masonry both with horizontal and vertical RC confining elements built between 1980 and 2005 do not meet seismic demands of $a_g = 0.22$ g for $T = 475$ years. Only the buildings made of confined brick masonry, designed according to Eurocode 8, meet the seismic demand.

Vulnerability index–PGA accelerations for the DL, SD, and NC limit states according to EC8-3 have been derived and validated by standard deviation. Satisfactory approximations have been obtained for the NC and SD limit states, while the deviations for the DL state had low accuracy.

The seismic risk has been formulated in terms of the damage index and the index of seismic risk. Damage indices have been calculated from derived vulnerability curves for the test site. Spatial distribution of the damage, represented by the damage index maps, shows a high level damage of the historical center already for the return period of 95 years. High-level damage spreads well beyond the center by increasing peak acceleration. Therefore, almost the entire area is damaged in the return period of 475 years.

Indices of seismic risk have been defined as a ratio of the peak ground acceleration associated to the NC, SD, or DL states, respectively, and the demand ground acceleration. Maps of seismic risk index indicate a number of non-safe buildings in the historical center already for the return period of 95 years. With the increase in peak ground accelerations, the number of non-safe buildings also increases. For $T = 475$ years, all buildings in the historical center and many buildings outside of the center are considered non-safe.

The developed methodology for seismic risk assessment is a demanding process that carries a number of uncertainties, due to the diversity of materials and performance, a series of construction interventions and upgrades over time, and, generally, a lack of knowledge about the buildings. Additional problems arise from the limitations of vulnerability index method and the non-linear static pushover analysis in predicting the behavior of the buildings under seismic action. Despite these shortcomings, the approach presented in this study gives valuable information on the vulnerability and risk of the area, which can

be applied to preventive activities for improving the seismic resistance of buildings and emergency situations in the case of seismic action.

11. Conclusions

This paper presents a comprehensive hybrid approach to large-scale seismic vulnerability and risk assessment of existing urban areas. The methodology combines the advantages of the vulnerability index method in assessing the vulnerability of a large number of buildings with a detailed analytical approach based on the nonlinear static pushover method, which allows determination of the capacity curves and detection of the specific limit states of the buildings.

The proposed methodology includes all phases leading to the final risk estimation, starting from data collection and detecting characteristics of buildings and ground type, vulnerability index evaluation, non-linear analysis of the selected buildings, defining vulnerability–peak ground acceleration curves, deriving vulnerability curves for the selected urban area and, finally, risk representation in terms of the damage index and the index of seismic risk.

The methodology has been applied to a whole urban settlement placed along the Croatian Adriatic coast, which has expanded over past centuries, resulting in a heterogeneous distribution of the buildings with different architectural, material, and structural characteristics. The present study covered various types of masonry buildings, ranging from stone masonry buildings several centuries old to the buildings made of concrete and brick blocks built from the mid-20th century to the present day in compliance with the technical regulations or common building rules during the construction period.

The findings of the present research are crucial for several reasons.

Firstly, the paper presents a methodological approach for a full consideration of seismic risk that can be applied to any settlement. It is not necessary to dispose with the data on damage from the previous earthquakes to conduct the research, although it can, if any, be used to calibrate the results. The methodology provides the relationship between the vulnerability index and peak ground accelerations of early damage, significant damage, and near collapse states. It also allows the derivation of vulnerability curves that serve to determine the damage index of the buildings for a specific seismic action.

Secondly, the pushover analysis conducted on 18 buildings with different characteristics provided valuable results of their behavior up to the failure, as well as peak ground accelerations for specific limit states, contributing to scientific knowledge of the behavior of such buildings. This is of particular importance given the seismic vulnerability of Croatia, and especially the southern part of the Croatian coast affected by devastating earthquakes (Dubrovnik, Ston, Makarska) in the past, and the similarity of the presented test area with many settlements and cities along the Adriatic coast.

Finally, the outcomes of the developed methodology are important for the observed test site and can be immediately applied to improve the seismic risk-coping capacity of the community of the relevant municipality. Indeed, the present procedure has resulted in seismic vulnerability indices, damage indices, and critical accelerations for different limit states, and indices of seismic risk for three return periods (95, 225, and 475 years). The results have been presented in a web map made in the GIS environment, which enables the visualization of vulnerability and risk of the area. Therefore, the developed vulnerability, damage, and risk maps have important operational outcomes in the seismic risk management of the investigated area.

Author Contributions: Conceptualization, Ž.N.; Data curation, L.R.; Funding acquisition, Ž.N. and E.B.; Investigation, Ž.N., E.B. and L.R.; Methodology, Ž.N. and E.B.; Software, L.R.; Supervision, Ž.N. and E.B.; Validation, Ž.N., E.B. and L.R.; Visualization, L.R.; Writing—original draft, Ž.N., E.B. and L.R. All authors have read and agreed to the published version of the manuscript.

Funding: This research was funded by the EUROPEAN UNION, Programme Interreg Italy–Croatia, Project “Preventing, managing and overcoming natural-hazards risks to mitigate economic and

social impact”—PMO-GATE ID 10046122. The research is also partially supported through project KK.01.1.1.02.0027, co-financed by the CROATIAN GOVERNMENT and the EUROPEAN UNION through the European Regional Development Fund—the Competitiveness and Cohesion Operational Programme.

Institutional Review Board Statement: Not applicable.

Informed Consent Statement: Not applicable.

Data Availability Statement: Not applicable.

Conflicts of Interest: The authors declare no conflict of interest.

References

- Benedetti, D.; Petrini, V. Vulnerability of masonry buildings: Proposal of a method of assessment (in Italian). *L'industria Delle Costr.* **1984**, *149*, 66–74.
- GNDT-SSN. *Scheda di Esposizione e Vulnerabilità e di Rilevamento Danni di Primo e Secondo Livello (Muratura e Cemento Armato)*; GNDT-SSN: Rome, Italy, 1994. Available online: https://protezionecivile.regione.abruzzo.it/files/rischio%20sismico/verificheSism/Manuale_e_scheda_GNDT_II_livello.pdf (accessed on 26 April 2021).
- Whitman, R.V.; Reed, J.W.; Hong, S.T. Earthquake Damage Probability Matrices. In Proceedings of the 5th World Conference on Earthquake Engineering, Rome, Italy, 25–29 June 1973; Volume II, pp. 2531–2540.
- Guagenti, E.; Petrini, V. The case of old buildings: Towards a new law damage-intensity (in Italian). In Proceedings of the IV ANIDIS Convention, Milan, Italy, 1989; Volume I, pp. 145–153.
- Bernardini, A. *The Vulnerability of Buildings-Evaluation on the National Scale of the Seismic Vulnerability of Ordinary Buildings*; CNR-GNDT: Rome, Italy, 2000.
- Giovinazzi, S. The Vulnerability Assessment and the Damage Scenario in Seismic Risk Analysis. Ph.D. Thesis, Faculty of Engineering Department of Civil Engineering of University of the Florence, Florence, Italy, 2005.
- Di Pascuale, G.; Orsini, G.; Romeo, R.W. New developments in seismic risk assessment in Italy. *Bull. Earthq. Eng.* **2005**, *3*, 101–128. [CrossRef]
- Lagomarsino, S.; Giovinazzi, S. Macroseismic and mechanical models for the vulnerability and damage assessment of current buildings. *Bull. Earthq. Eng.* **2006**, *4*, 415–443. [CrossRef]
- Grunthall, G. *European Macroseismic Scale 1998 (EMS-98)*; Cahiers du Centre Européen de Géodynamique et Séismologie: Luxembourg, 1998; Volume 15.
- Fajfar, P.; Eeri, M. A nonlinear analysis method for performance based seismic design. *Earthq. Spectra* **2000**, *16*, 573–592. [CrossRef]
- Vamvatsikos, D.; Cornell, C.A. Incremental Dynamic Analysis. *Earthq. Eng. Struct. Dyn.* **2002**, *31*, 491–514. [CrossRef]
- Rossetto, T.; Elnashai, A. Derivation of vulnerability functions for European-type RC structures based on observational data. *Eng. Struct.* **2003**, *25*, 1241–1263. [CrossRef]
- Maniyar, M.M.; Khare, R.; Dhakal, R.P. Probabilistic seismic performance evaluation of non-seismic RC frame buildings. *Struct. Eng. Mech.* **2009**, *33*, 725–745. [CrossRef]
- Ripepe, M.; Lacanna, G.; Deguy, P.; De Stefano, M.; Mariani, V.; Tanganelli, M. Large-Scale Seismic Vulnerability Assessment Method for Urban Centres. An Application to the City of Florence. *Key Eng. Mater.* **2014**, *628*, 49–54. [CrossRef]
- Salgado-Galvez, M.A.; Zuloaga, R.D.; Velasquez, C.A.; Carreno, M.L.; Cardona, O.D.; Barbat, A.H. Urban seismic risk index for Medellín, Colombia, based on probabilistic loss and casualties estimations. *Nat. Hazards* **2016**, *80*, 1995–2021. [CrossRef]
- Salazar, L.G.F.; Ferreira, T.M. Seismic Vulnerability Assessment of Historic Constructions in the Downtown of Mexico City. *Sustainability* **2020**, *12*, 1276. [CrossRef]
- Battaglia, L.; Ferreira, T.M.; Lourenço, P.B. Seismic fragility assessment of masonry building aggregates: A case study in the old city Centre of Seixal, Portugal. *Earthq. Eng. Struct. Dyn.* **2021**, *50*, 1358–1377. [CrossRef]
- Lagomarsino, S.; Cattari, S.; Ottonelli, D. The heuristic vulnerability model: Fragility curves for masonry buildings. *Bull. Earthq. Eng.* **2021**, *19*, 3129–3163. [CrossRef]
- Giordano, N.; De Luca, F.; Sextos, A. Analytical fragility curves for masonry school building portfolios in Nepal. *Bull. Earthq. Eng.* **2021**, *19*, 1121–1150. [CrossRef]
- Capanna, I.; Aloisio, A.; Di Fabio, F.; Fragiaco, M. Sensitivity Assessment of the Seismic Response of a Masonry Palace via Non-Linear Static Analysis: A Case Study in L'Aquila (Italy). *Infrastructures* **2021**, *6*, 8. [CrossRef]
- Vicente, R.; Parodi, S.; Lagomarsino, S.; Varum, H.; Da Silva, M. Seismic vulnerability and risk assessment: Case study of the historic city centre of Coimbra, Portugal. *Bull. Earthq. Eng.* **2011**, *9*, 1067–1096. [CrossRef]
- Achs, G.; Adam, C. Rapid seismic evaluation of historic brick-masonry buildings in Vienna (Austria) based on visual screening. *Bull. Earthq. Eng.* **2012**, *10*, 1833–1856. [CrossRef]
- Hadzima-Nyarko, M.; Mišetić, V.; Morić, D. Seismic vulnerability assessment of an old historical masonry building in Osijek, Croatia, using Damage Index. *J. Cult. Herit.* **2017**, *28*, 140–150. [CrossRef]
- Ferreira, T.M.; Mendes, N.; Silva, R. Multiscale Seismic Vulnerability Assessment and Retrofit of Existing Masonry Buildings. *Buildings* **2019**, *9*, 91. [CrossRef]

25. Angeletti, P.; Bellina, A.; Guagenti, E.; Moretti, A.; Petrini, V. Comparison between vulnerability assessment and damage index, some results. In Proceedings of the 9th World Conference on Earthquake Engineering, Tokyo, Japan, 2–9 August 1988.
26. Ciavattone, A.; Vignoli, A.; Matthies, H.G. Seismic vulnerability analysis for masonry hospital structures: Expedient and detailed methods. In *Brick and Block Masonry—Trends, Innovations and Challenges*; da Porto, M., Valluzzi, Eds.; Taylor & Francis Group: London, UK, 2016; ISBN 978-1-138-02999-6.
27. Cavaleri, L.; Di Trapani, F.; Ferrotto, M.F. A new hybrid procedure for the definition of seismic vulnerability in Mediterranean cross-border urban areas. *Nat. Hazards* **2017**, *86*, 517–541. [CrossRef]
28. Nikolić, Ž.; Krstevska, L.; Marović, P.; Smoljanović, H. Experimental investigation of seismic behaviour of the ancient Protiron monument model. *Earthq. Eng. Struct. Dyn.* **2019**, *48*, 573–593. [CrossRef]
29. Krstevska, L.; Nikolić, Ž.; Kustura, M. Shake table testing of two historical masonry structures for estimation of their seismic stability. *Int. J. Archit. Herit.* **2021**, *15*, 45–63. [CrossRef]
30. Smoljanović, H.; Živaljić, N.; Nikolić, Ž.; Munjiza, A. Numerical Simulation of the Ancient Protiron Structure Model Exposed to Seismic Loading. *Int. J. Archit. Herit.* **2021**, *15*, 779–789. [CrossRef]
31. Nikolić, M.; Do, X.N.; Ibrahimbegovic, A.; Nikolić, Ž. Crack propagation in dynamics by embedded strong discontinuity approach: Enhanced solid versus discrete lattice model. *Comput. Methods Appl. Mech. Eng.* **2018**, *340*, 480–499. [CrossRef]
32. Čarija, J.; Nikolić, M.; Ibrahimbegovic, A.; Nikolić, Ž. Discrete softening-damage model for fracture process representation with embedded strong discontinuities. *Eng. Fract. Mech.* **2020**, *236*, 107211. [CrossRef]
33. Nikolić, Ž.; Runjić, L.; Ostojić Škomrlj, N.; Benvenuti, E. Seismic Vulnerability Assessment of Historical Masonry Buildings in Croatian Coastal Area. *Appl. Sci.* **2021**, *11*, 5997. [CrossRef]
34. Available online: https://marinas.com/view/marina/eyc39lv_Kastel_Kambelovac_Harbour_Kastel_Gomilica_Croatia (accessed on 21 November 2020).
35. Stepinac, M.; Lourenço, P.B.; Atalić, J.; Kišiček, T.; Uroš, M.; Baniček, M.; Šavor Novak, M. Damage classification of residential buildings in historical downtown after the ML5.5 earthquake in Zagreb, Croatia in 2020. *Int. J. Disaster Risk Reduct.* **2021**, *56*, 102140. [CrossRef]
36. HRN ENV 1998-1 Eurocode 8: Design Provisions for Earthquake Resistance of Structures—Part 1: General Rules, Seismic Actions and General Requirements for Structures; Croatian Standards Institute: Zagreb, Croatia, 2005.
37. HRN EN 1998-1:2011. Eurocode 8: Design of Structures for Earthquake Resistance. Part 1: General Rules, Seismic Actions and Rules for Buildings; Croatian Standards Institute: Zagreb, Croatia, 2011.
38. Marasović, K. Kaštel Kambelovac. *Kaštela J.* **2003**, *7*, 35–61. (In Croatian)
39. Opara, L.K. *Termographic Report—Buildings in Kaštel Kambelovac*; University of Split, Faculty of Electrical Engineering, Mechanical Engineering and Naval Architecture: Split, Croatia, March 2020.
40. Uranjek, M.; Žarnić, R.; Bokan-Bosiljkov, V.; Bosiljkov, V. Seismic resistance of stone masonry building and effect of grouting. *Grđevinar* **2014**, *66*, 715–726.
41. Da Col, F.; Accaino, F.; Bohm, G.; Meneghini, F. Characterization of shallow sediments by processing of P, SH and SV wave-fields in Kaštela (HR). *Eng. Geol.* **2021**, *293*, 106336. [CrossRef]
42. Ferrini, M.; Melozzi, A.; Pagliuzzi, A.; Scarparolo, S. Rilevamento della vulnerabilità sismica degli edifici in muratura. In *Manuale per la Compilazione Della Scheda GNDT/CNR di II Livello*; Versione modificata dalla Regione Toscana. S.I.; Direzione Generale delle Politiche Territoriale e Ambientali, Settore—Servizio Sismico Regionale: Regione Toscana, Italy, 2003.
43. Piano di Ricostruzione del Comune di Arsita (TE), a Seguito Dell’evento Sismico del 6/04/2009, Document: 3A_01_f_Aspetti Strutturali e di Vulnerabilità_Rev.2. Available online: http://www.pdr-arsita.bologna.enea.it/wordpress/wp-content/uploads/arsita/pdr_finale/terza_fase/3A_01_Elaborati%20tecnici/3A_01_f_Aspetti%20strutturali%20e%20di%20vulnerabilit%C3%A0/3A_01_f_Aspetti%20strutturali%20e%20di%20vulnerabilit%C3%A0%20Rev.%20202.pdf (accessed on 26 March 2019).
44. HRN EN 1998-3 Eurocode 8: Design of Structures for Earthquake Resistance—Part 3: Assessment and Retrofitting of Buildings; Croatian Standards Institute: Zagreb, Croatia, 2011.
45. 3MURI Software, Professional version; S.T.A. DATA: Torino, Germany, 2019.
46. Kreslin, M.; Fajfar, P. The extended N2 method considering higher mode effects in both plan and elevation. *Bull. Earthq. Eng.* **2012**, *10*, 695–715. [CrossRef]

Article

A Systematic Revision of the NFIP Claims Hazard Data in Florida for Flood Risk Assessment

D. W. Shin¹, Steven Cocke¹ and Baek-Min Kim^{2,*}

¹ Center for Ocean-Atmospheric Prediction Studies, Florida State University, Tallahassee, FL 32306-2840, USA; shin@coaps.fsu.edu (D.W.S.); scocke@fsu.edu (S.C.)

² Department of Environmental Atmospheric Sciences, Pukyong National University, Busan 48513, Korea

* Correspondence: baekmin@pknu.ac.kr; Tel.: +82-10-4194-9404

Abstract: The hazard components of National Flood Insurance Program (NFIP) claims data in Florida were systematically analyzed and revised in the current study. The provided fields in NFIP claims data are not always complete or accurate and are often missing. The authors associated each claim to a proper flood hazard event by updating the provided catastrophe number using the National Hurricane Center HURDAT2 (best track data). The claims with presumably incorrect *cause of loss* fields were identified and revised by adding a variety of other available information to claims data. These datasets included tropical cyclone events, rainfall maxima, and distances to the nearest coast. The enhanced information assisted in identifying the cause or likelihood of a hazard event or attributing a particular hazard event to a loss claim. The revised NFIP claims data will be intensively used to validate the outcomes from flood hazard (i.e., surge, wave and inland flooding) models and to develop a flood vulnerability model in the forthcoming Florida Public Flood Loss Model (FPFLM).

Keywords: NFIP claims; flood risk; flood insurance; flood cause of loss; HURDAT; catastrophe model

Citation: Shin, D.W.; Cocke, S.; Kim, B.-M. A Systematic Revision of the NFIP Claims Hazard Data in Florida for Flood Risk Assessment. *Appl. Sci.* **2022**, *12*, 3537. <https://doi.org/10.3390/app12073537>

Academic Editor: Andrea Chiozzi

Received: 18 February 2022

Accepted: 29 March 2022

Published: 30 March 2022

Publisher's Note: MDPI stays neutral with regard to jurisdictional claims in published maps and institutional affiliations.



Copyright: © 2022 by the authors. Licensee MDPI, Basel, Switzerland. This article is an open access article distributed under the terms and conditions of the Creative Commons Attribution (CC BY) license (<https://creativecommons.org/licenses/by/4.0/>).

1. Introduction

The Florida Commission on Hurricane Loss Projection Methodology (FCHLPM), under legislative direction, published Flood Standards Reports of Activities [1] similar in concept to the current hurricane wind hazard standards [2]. Accordingly, the Florida Office of Insurance Regulation (FLOIR) requested the Florida Public Hurricane Loss Model (FPHLM) [3] group to undertake a project to develop a flood risk model officially called the Florida Public Flood Loss Model (FPFLM). The flood catastrophe model is to estimate and/or predict aggregated insured losses for properties in the form of annual expected losses and probable maximum losses, which can be employed by Florida state regulators and insurance companies to help evaluate premium rate filings. A developed model will be delivered to the FCHLPM, which would be acceptable under the current flood standards. The FPFLM (a catastrophe model) is to estimate possible losses caused by coastal and inland flood events. It includes three main components: (1) hazard, (2) vulnerability, and (3) actuarial components. During the development process of a risk model, flood claim (and/or exposure) data are necessary for calibration and validation of flood model outputs.

Because the Department of Homeland Security's (DHS's)/Federal Emergency Management Agency's (FEMA's) National Flood Insurance Program (NFIP) claim data have not been publicly available, there have not been many in-depth analysis studies on flood insurance claims until recently. Kousky and Michel-Kerjan [4] examined the NFIP flood insurance claims in the continental United States and found six claim characteristics (e.g., claims are lower for elevated properties and higher from storm surges). A series of studies have also concentrated on flood losses, all of which involved a translation from inundation depth to its economic impacts, e.g., [5]. Wing et al. [6] used over two million NFIP claims to assess flood depth and damage functions (or curves) for economic evaluation. They showed that the NFIP damage data could partially remedy the uncertainties in the currently employed

flood depth and damage functions, which involve disparate relationships that match poorly with observations. However, these studies used the original NFIP claim data without any modification attempts in their analysis and/or development of vulnerability curves.

The widely used standard flood depth and damage curves were compiled by the United States Army Corps of Engineers (USACE) [7]. The USACE developed these curves beginning in 1970 using early NFIP loss data, local Corps studies, and the collective judgment of experts [8]. They were assumed to be well calibrated and universally applicable when used in the majority of engineering communities, even though their simple relationships do not match well with observations. Therefore, Pinelli et al. [9,10] developed a better set of flood vulnerability curves using some modified NFIP claim data for the FPFLM project. However, they did not present the detailed analysis and revision process for the NFIP loss data in their paper.

The FLOIR provided the FPFLM group with the NFIP claim data in Florida. Benefiting from this special access, the authors analyzed the NFIP claims filed between 19 July 1975 and 10 January 2014 in the current study. The claim data contained flood hazard information (e.g., date and type of event, cause of loss) and building information (e.g., house location, values, elevation, age). However, the provided NFIP claim data were not always complete or accurate. Thus, it was necessary to make significant modifications to the NFIP claim data to properly assess the risk of all significant hazard events leading to flooding. The authors undertook a major task to identify the hazard event associated with each claim in the NFIP database. While the NFIP claim data included a *catastrophe number* that purports to identify the event, it was found that this information was often incorrect or identified as unknown. Furthermore, the NFIP database listed a *cause of loss*, which the authors also found to be inaccurate or unknown.

The paper is organized as follows: the provided NFIP claim data and additional data used to revise the claims hazard information are presented in Section 2; Section 3 shows the revision process of the NFIP claim hazard data, the results thereof, and further analyses for flood risk assessments; and the conclusions follow in Section 4.

2. Materials and Methods

2.1. NFIP Claim Data in Florida

Florida accounts for roughly 37% of all NFIP policies according to FEMA. The number of total claims in the provided NFIP loss data was 240,469 for the period of 19 July 1975 to 10 January 2014. Among them, only 153,751 (63.9%) were paid claims and were hence used in the current study. The paid claim locations are shown in Figure 1.

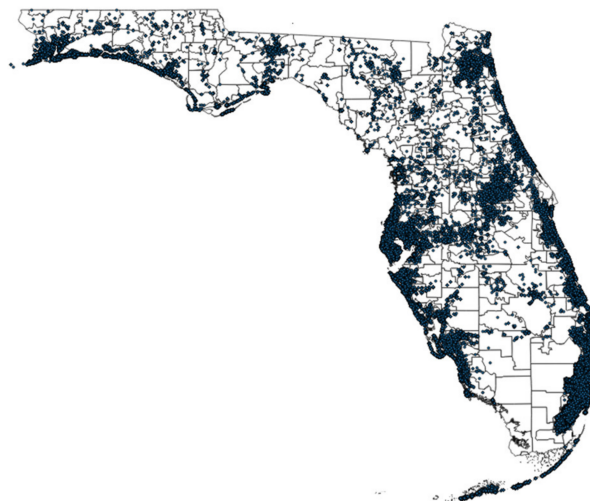


Figure 1. The NFIP paid claim data in Florida (claims period: 19 July 1975–10 January 2014).

The majority of flood damages were claimed along coastal and urban areas (e.g., Miami, Orlando, Jacksonville, and Tampa) as expected, partly because of the high frequency of storm surge hazards and partly because of the high density of the population. Although tropical cyclones are the major natural hazards, other frequently occurring intensive nontropical storm events can cause inundation damages in both coastal and inland areas of Florida.

The provided NFIP flood damage claim data contained 100 fields for hazard-, building, and actuarial-related information. These fields included *date of loss*, policy number, address (*latitude and longitude*), flood risk zone, occupancy type, *catastrophe number*, *cause of loss*, lowest floor elevation, base flood elevation, building claim payment, contents claim payment, etc. The hazard-related fields (italic font) were the main target fields to be assessed in the current study. To respect privacy, sensitive information (e.g., homeowner's address) was neither exposed nor explicitly used.

Brief descriptions of several claim fields are as follows:

- occupancy type: single-family homes or other type;
- catastrophe number: the flood event with which it is associated;
- base flood elevation (BFE): 100 year flood elevation (i.e., 1% chance of flooding);
- building and contents claim payment: how much was paid by the NFIP;
- flood risk zone: to indicate the risks in different parts of the United States, FEMA has assigned a character from the alphabet to each zone. The most hazardous flood zones are V (usually the first row of beachfront properties) and A (usually, but not always, properties near a lake, river, stream, or other body of water). Any building located in an A or V zone is considered to be in a Special Flood Hazard Area and lower than the BFE;
- cause of loss: the natural hazard cause identification for the claimed loss, as follows—0: other causes, 1: tidal water overflow, 2: stream, river, or lake overflow, 3: alluvial fan overflow, 4: accumulation of rainfall, 7: erosion—demolition, 8: erosion—removal, 9: earth movement, landslide, land subsidence, sinkholes, etc.

2.2. Additional Data to Claims

To revise inaccurate flood hazard information in the provided NFIP claim data, additional hazard-related information and land surface characteristics were added to the claim data for each claim location from a variety of resources. This information could help in identifying the cause or likelihood of a hazard event or attributing a particular hazard event to a loss claim.

2.2.1. HURDAT2

Atlantic HURDAT2 comprises the best track data available from the National Oceanic and Atmospheric Administration National Weather Service National Hurricane Center (NOAA NWS NHC; available at <http://www.nhc.noaa.gov/data/#hurdat>, 11 February 2022). This dataset has a comma-delimited text format with six-hourly information on the location, maximum winds, central pressure, and size of all known tropical cyclones and subtropical cyclones. It is updated at least once per year to include the previous year's best tracks and/or historical reanalysis tracks [11].

Since many of the NFIP claims are due to tropical storms or hurricanes, HURDAT2 might be the best resource for matching historical storms to loss claims properly in Florida. The date and time of the storm track positions can be compared to the claim location and time of loss using spatial and temporal metrics to determine possible storm influence. Additional information concerning the storm intensity level (depression, tropical storm, or hurricane) can be added to the provided claims as well.

2.2.2. PRISM Rainfall

The PRISM (Parameter-Elevation Regression on Independent Slopes Model) analysis, from the PRISM climate group at Oregon State University, is particularly interesting because of its high spatial resolution (800 m to 4 km). It provides daily rainfall from 1 January 1981

to recent [12]. As a demonstration of the quality of the PRISM, rainfall total and frequency statistics for the period of 1981–2014 are shown in Figure 2. The area averaged rainfall total amount was approximately 46,000 mm for these 34 years. The right panel shows a frequency count map of rainfalls of more than 100 mm/day (i.e., ~4 inches; extremely high chance of flooding events). The Western Panhandle region of Florida appeared to be most susceptible to heavy rainfall events, along with coastal areas. Indeed, one notable recent event was heavy rain around Pensacola in 2014. In addition, Hurricane Ivan (2004) made landfall around this area, producing a strong inundation event by surge and inland flooding. Figure 3 shows the total rainfall for the Hurricane Ivan event.

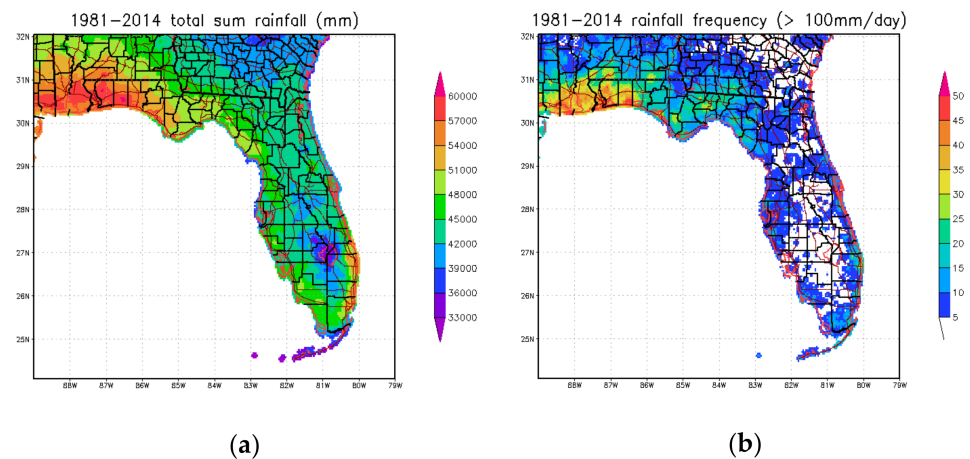


Figure 2. Rainfall total (a, unit is mm) and frequency (b) statistics for the period of 1981 to 2014 derived from the PRISM dataset.

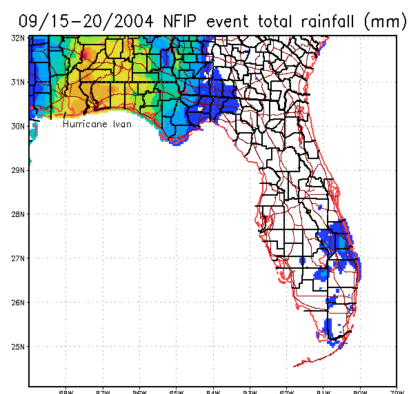


Figure 3. Cumulative rainfall for the Hurricane Ivan (2004) heavy rain event near Pensacola, Florida based on the PRISM dataset. Unit is mm. The provided event period of NFIP claims was from 15 to 20 September 2004.

Precipitation maximum data were derived from the 4 km PRISM daily rainfall database. The largest precipitation amount that occurred with ± 1 day and within 10 km of the claim property location was recorded. This information helped determine whether the cause of loss could have been accumulation of rainfall.

2.2.3. NLCD Distances

The distance to coast was the distance of each claim location to the nearest coast. This information was helpful to decide whether a coastal surge flood was likely to occur. The distance was calculated using the 2011 Multiresolution Land Characteristics Consortium (MRLC) National Land Cover Database (NLCD) [13] to identify water and land locations. The NLCD has approximately 30 m resolution, allowing for a reasonably accurate calcula-

tion. Figure 4 demonstrates the quality of computed distance to coast for the Florida coastal lines, the area around Tampa, and the area around Miami.

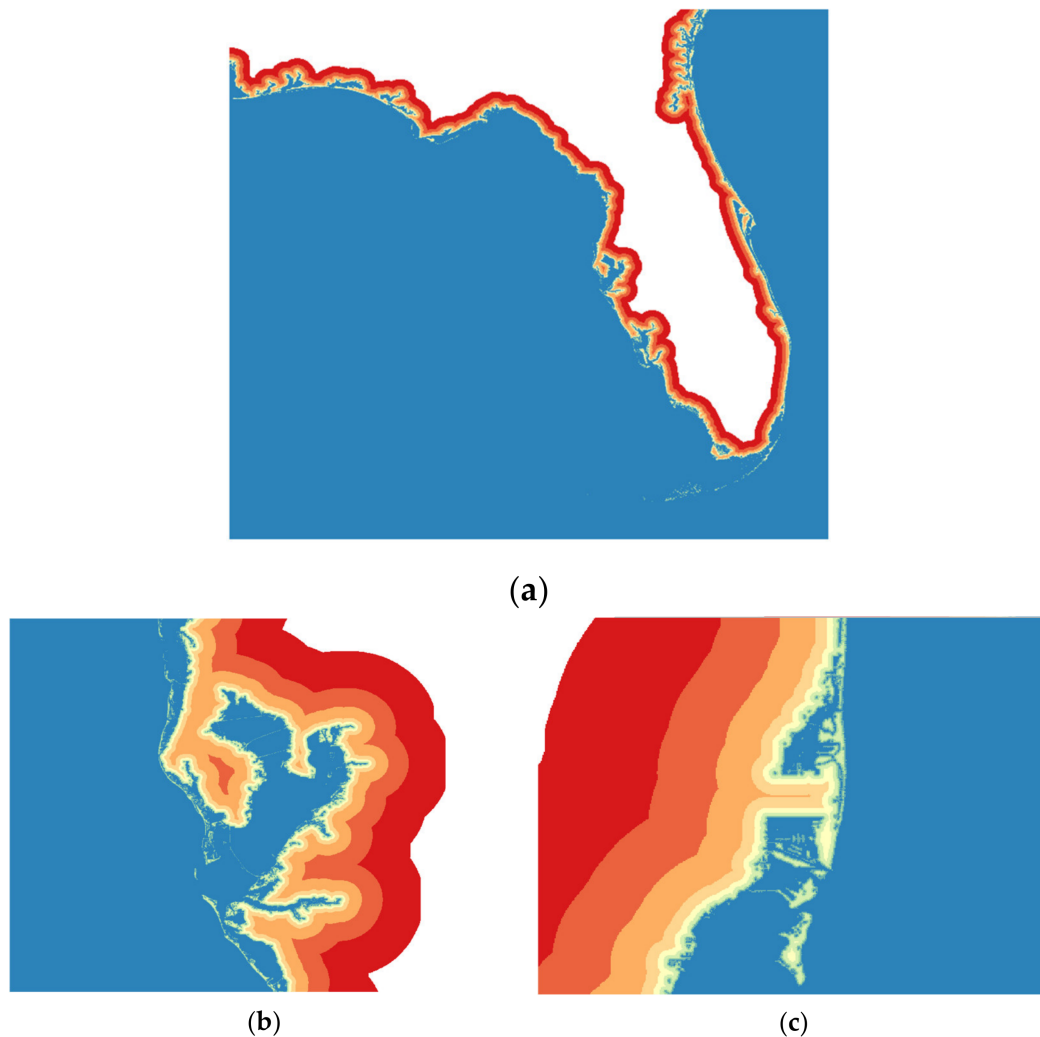


Figure 4. Distance to coast maps for the Florida coastline (a), the area around Tampa (b), and the area around Miami (c). Intervals: 20 m, 100 m, 500 m, 1 km, and 2 km.

The distance to the nearest body of water was computed in the same manner as the distance to the coast, but the distance was to the nearest body of water, regardless of water body type. This computed distance data could help to determine whether flooding could be due to river, stream, or lake overflow. However, these data were not explicitly used in the current analysis.

3. Results and Discussion

3.1. NFIP Claims Hazard Revision

The NFIP claim data had several fields that contained information that could be used to associate each claim to a flood hazard event. Among these fields were the *date of loss*, *property location*, *catastrophe number*, and *cause of loss*. The information provided by these fields was not always complete or accurate and often did not provide sufficient detail concerning the flood hazard event. For example, the catastrophe number was often missing, or multiple hazard events may have been assigned the same number if they occurred around the same time period. The cause of loss often appeared to be incorrect based on other information. There were cases, for example, in which the loss was listed as *tidal water overflow* even though the property was too far from the coast to be affected by tidal water.

The claim data often did not provide important details of the hazard, such as the flood elevation or wave conditions.

3.1.1. Catastrophe Event Number Matching

Our first task was to attribute meteorological events to claim data that were grouped by a *catastrophe number* or *date of loss*. Using a summary table provided by NFIP, the authors were able to determine the causative event for most of the groups of claim data. The results of this work were used to determine which historical events should be focused on in our modeling studies. These results, however, did not provide details of the cause of loss on the individual claims level. Our initial focus was on determining the types of events that we may need to consider in order to update the FPFLM hazard models.

Among the paid claims, 34,257 (22.3%; money-wise USD 498,827,000 (13.4%)) did not include catastrophe event numbers. The HURDAT2 tropical cyclone information was used to match tropical events to the NFIP claim data. If loss claims were located within 700 km of a storm center during the event date, it was considered that the claims belonged to that storm event. Of the 153,751 claims studied, 108,244 were detected by the HURDAT2 storm name check within claim event dates to keep and/or modify the original catastrophe event number. In addition to the provided claim count and paid amount, the revised statistics are shown in Table 1 for selected catastrophe events. The event number zero was assigned for the unidentified events. While the distinguishable number of claims were now attributed to several of the last century's hurricanes (Major Hurricane (MH) Frederic (1979), MH Georges (1998), MH Mitch (1998), etc.), not many claims were modified for recent hurricanes, perhaps because of a better collection system for claim data in the NFIP. An example of catastrophe event number updates is shown in Figure 5.

Table 1. NFIP catastrophe event number revision (selected events among total 158 events).

Catastrophe Event Number	Provided		Revised		Event
	Claim Count	Paid Amount (Thousands of USD)	Claim Count	Paid Amount (Thousands of USD)	
0	34,257	498,828	27,080	374,330	
22	32	814	897	8686	MH Frederic (1979)
131	3248	40,163	4258	51,425	MH Georges (1998)
133	1466	20,518	854	14,323	
134	8	51	206	2471	MH Mitch (1998)
182	2492	49,429	2515	49,656	MH Charley (2004)
564	3247	139,821	3278	140,967	MH Andrew (1992)
615	241	3386	779	11,787	H Earl (1998)
641	3278	106,816	4789	139,913	MH Frances (2004)
643	10,353	945,500	10,619	959,392	MH Ivan (2004)
646	3800	90,497	3918	93,128	MH Jeanne (2004)
649	3375	109,045	3698	116,507	MH Dennis (2005)
659	9411	355,267	9616	363,625	MH Wilma (2005)

H: hurricane, MH: major hurricane.

Many claims around Miami and Keys were attributed to the event of MH Mitch (1998). The majority of claims were assigned to more reliable and accurate meteorological events in the NFIP flood loss data.

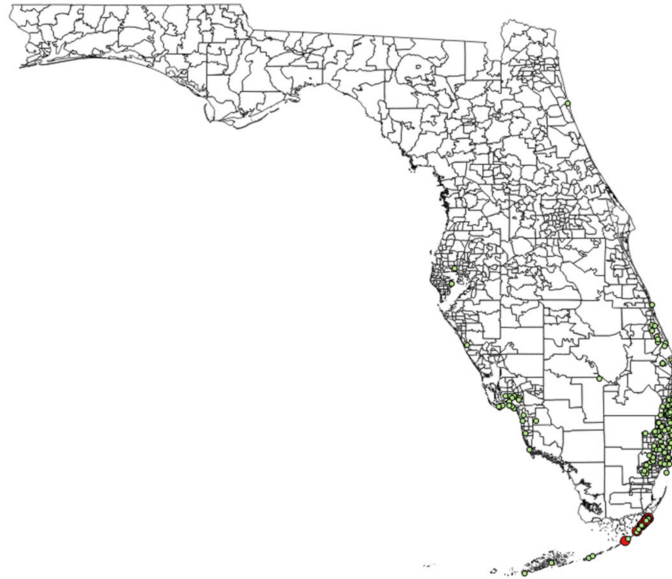


Figure 5. NFIP catastrophe event number update: Major Hurricane Mitch (period: 4 November 1998–6 November 1998); event number = 134 (see Table 1). Provided claim count = 8 (**red dots**) vs. revised claim count = 206 (**green dots**).

3.1.2. Cause of Loss Revision

The following fields were added to the original NFIP claim data: HURDAT2 storm identification, storm flag (tropical depression (TD), tropical storm (TS), hurricane (HU) or nontropical storm (NA)), revised catastrophe number, rainfall maximum, and distances to the nearest coast and body of water. Using these collected information permitted a revision of the cause of loss when the original loss cause was in clear error or ambiguous.

The algorithms for the revision were as follows:

- if the provided cause of loss was tidal water overflow (surge; cause number 1), but the distance to coast was greater than 20 km (based on personal communication with surge modeling experts), the rainfall maximum for the location was checked. If it was greater than 25 mm/day, the cause was revised to be accumulation of rainfall (cause number 4). Otherwise, it was designated as questionable, likely wrong address (see Figure 6);
- for hurricane events, if the original cause of loss was unknown for a property that was less than 20 km to the coast, and the precipitation maximum was greater than 25 mm/day, the cause of loss was marked as undetermined (cause number 5) but was either tidal water overflow or accumulation of rainfall, and further investigation was warranted. Otherwise, the cause of loss was marked as cause number 1;
- for nonhurricane events, if the original cause of loss was unknown for a property that was greater than 20 km to the coast and the precipitation maximum was greater than 25 mm/day, the cause of loss was marked as cause number 4;
- if the original cause of loss was 4 in inland areas, but the precipitation maximum was less than 5 mm/day, then the cause of loss was marked as questionable, possible error in address or date;
- for hurricane-only events, if the distance to the coast was less than 1 km, claims with cause numbers 2, 3, and 4 were revised to tidal water overflow (cause number 1). Figure 7 shows why this might be a practical revision algorithm. Hurricane Ivan (2014) hit the northwest coast of Florida (see Figure 3) and caused widespread surge damages according to FEMA. However, the cause of loss in many NFIP paid claims was marked as accumulation of rainfall (cause number 4), even in the apparent isolated island areas. All these areas were damaged by the storm surge according to the FEMA observed flood estimates.

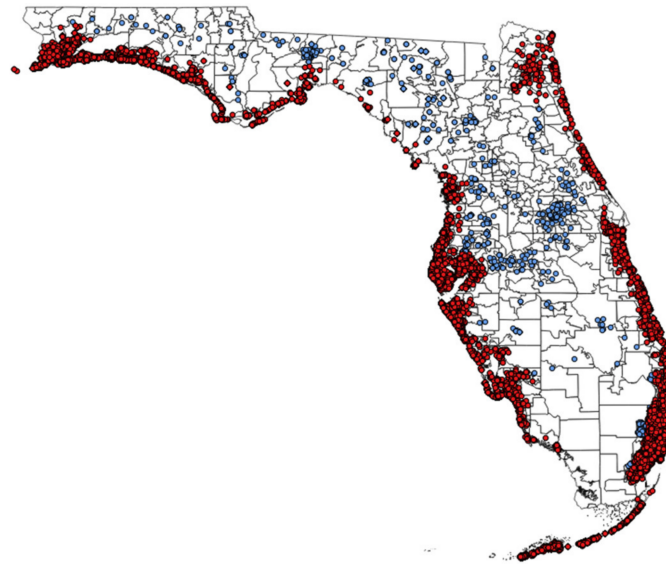


Figure 6. NFIP cause of loss revision—incorrect surge claims. All circles denote the provided NFIP surge claims. Red circles denote revised surge loss claims, while blue circles denote incorrect surge claims.

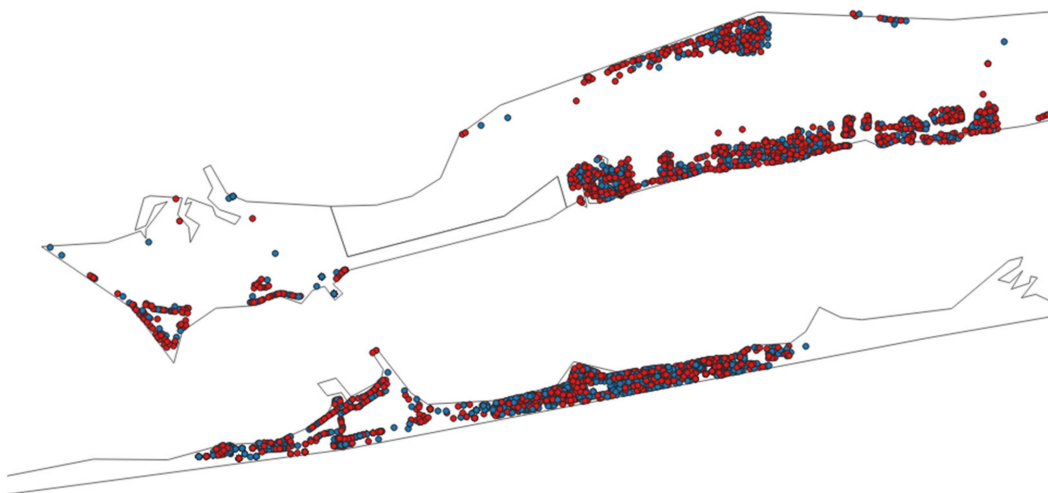


Figure 7. NFIP cause of loss—Hurricane Ivan (2004). Red dots denote surge claims, and blue dots denote accumulation of rainfall claims. Domain: -87.21 W to -87.04 W and 30.3 N to 30.4 N.

3.1.3. Summary of Revised Claims

The provided and revised NFIP claim counts and paid loss amounts with percentages are shown in Tables 2 and 3, respectively. Before our revision, the majority of flood loss causes in Florida were considered due to the accumulation of rainfall (53.1% in claim count and 46.6% in paid loss), followed by surges (29.4% in claim count and 36.6% in paid loss). Hence, it can be misinterpreted that the main flood cause of loss in Florida was accumulation of rainfall. After our systematic revision, this misinformation was dramatically changed to the following: the main cause of flood loss in Florida was storm surge events. Tidal water overflow now explained 46.4% of claims by count and 65.0% of paid losses. While there was just a ca. 17% increase in claim count, there was an increase of more than USD 1 billion (USD 2415 million out of 3714 million) in the paid loss amount.

Table 2. The NFIP claims count summary in accordance with the cause of loss.

Cause	Provided		Revised	
	Count	%	Count	%
0	11,069	7.2	215	0.1
1	45,222	29.4	71,386	46.4
2	11,303	7.4	7401	4.8
3	1919	1.2	1522	1.0
4	81,614	53.1	59,364	38.6
5	0	0	9596	6.2
6	2624	1.7	4267	2.8
all	153,751	100	153,751	100

0: other causes; 1: tidal water overflow; 2: stream, river, or lake overflow; 3: alluvial fan overflow; 4: accumulation of rainfall; 5: indeterminate, cause 1 or 4; 6: all other causes.

Table 3. The NFIP claims paid loss amount summary in accordance with the cause of loss (see Table 2 for the cause number reference).

Cause	Provided		Revised	
	Paid Loss (Thousands of USD)	%	Paid Loss (Thousands of USD)	%
0	318,190	8.6	4046	0.1
1	1,358,612	36.6	2,414,944	65.0
2	260,414	7.0	132,077	3.6
3	42,905	1.2	32,738	0.9
4	1,729,295	46.6	810,876	21.8
5	0	0	286,971	7.7
6	4770	0.1	32,534	0.9
all	3,714,186	100	3,714,186	100

A summary of the general types of meteorological events and their respective portions of the claim data is provided in Table 4 for the revised NFIP events. In this table, it can be seen that hurricanes were by far the primary cause of flooding damage in Florida, accounting for 72.1% of the revised claim losses and 54.5% of claims by count. The losses labeled tropical storm and depression did not reach hurricane strength while damage occurred. These events accounted for approximately 13% of the losses in the revised claims. While the losses for tropical storms were lower than for hurricanes, the number of potential events that may need to be considered could be larger. Tropical storms may produce lower surges than hurricanes, but the rainfall from such storms can often be quite significant. The third class of general flood hazard events in Table 4 was nontropical systems. These events are usually heavy rainfall events that are not caused by tropical systems. These events, however, do include nontropical cyclones, such as the *Storm of the Century* (March, 1993). These cyclones can cause surges as well as heavy rain. Currently, the FPFLM does not have any model to take these types of events into account.

Table 5 shows the detailed breakdown of NFIP paid losses due to each type of meteorological events and cause of loss. For hurricane events, approximately 80% of paid losses were due to storm surges. Meanwhile only 21.6% were due to surges in tropical storm events. The accumulation of rainfall explained 9.5% for hurricane, 58.5% for tropical storms, 81.9% for tropical depressions, and 49.1% for nontropical events. The importance of nontropical cyclone events to storm surges and associated coastal inundation was examined through the NFIP claim data. Based on the revised NFIP, the number of nontropical surge claims was 10,564 (~7% of the paid claims and ~15% of storm surge claims), accounting for paid losses of USD 179,719,000 (~5% of the paid claims and ~7.6% of storm surge claims). The Storm of the Century accounted for 5875 surge claims out of total 8846 claims, amounting to paid losses of USD 132,764,000 (79%) for coastal surge claims.

Table 4. The revised NFIP paid loss amounts and corresponding claim counts in accordance with the type of meteorological event.

Cause	Revised NFIP Events			
	Paid (Thousands of USD)	%	Claim Count	%
Nontropical	574,612	15.5	38,733	25.2
Tropical Depression	160,431	4.3	9467	6.2
Tropical Storm	302,267	8.1	21,733	14.1
Hurricane	2,676,876	72.1	83,818	54.5
All	3,714,186	100	153,751	100

Table 5. Breakdown of the NFIP claim paid loss amounts due to each type of event as a function of cause of loss (see Table 2 for the cause number reference).

Cause	Hurricane Only		Tropical Storm Only	
	Paid Loss (Thousands of USD)	%	Paid Loss (Thousands of USD)	%
0	182	0	61	0
1	2,128,099	79.5	65,284	21.6
2	42,602	1.6	38,657	12.8
3	1106	0	920	0.3
4	253,644	9.5	176,714	58.5
5	247,293	9.2	19,970	6.6
6	3950	0.1	661	0.2
all	2,676,876	100	302,267	100

Cause	Tropical Depression Only		Nontropical Only	
	Paid Loss (Thousands of USD)	%	Paid Loss (Thousands of USD)	%
0	9	0	3794	0.7
1	1207	0.8	179,719	31.3
2	7633	4.8	50,562	8.8
3	184	0.1	30,933	5.4
4	131,427	81.9	282,374	49.1
5	19,709	12.3	0	0
6	262	0.2	27,230	4.7
all	160,431	100	574,612	100

3.2. Further Analyses for Flood Risk Assessments

3.2.1. Nontropical Flood Claims

In order to determine an appropriate method or model for estimate losses due to nontropical inland rainfall flood events, the analysis of the revised NFIP claim data was expanded. It was previously reported that approximately USD 574 million in losses were due to nontropical events (Table 4), specifically events that could not be directly attributed to an event in the HURDAT2 database. The authors further broke down the losses by excluding non-rainfall-related events, such as surges, and determining whether the claims were within 1 km (0.6 miles) of the coast. The results are summarized in Table 6. As shown in Table 6, the losses due to nontropical rainfall for inland locations totaled about USD 228 million. These were losses due to events that could be potentially modeled by a nontropical rainfall model (or set of models).

Table 6. Breakdown of the revised NFIP paid loss amount due to nontropical events.

	Loss (Millions of USD)	% of NFIP	Remarks
Nontropical flood	574	15	Includes surge due to nontropical cyclones
Nontropical nonsurge	394	11	Excludes all surge
Nontropical rain-related	372	10	Excludes surge and other/unknown
Nontropical rain—inland	228	6	Greater than 1 km to coast
Total NFIP all causes	3714	100	

To gain further insight into these types of only-rainfall-related losses, the authors show the top five loss events in Table 7. The largest loss, USD 29.7 million, was due to a heavy frontal rainfall event in December, 2009. The second largest event was due to the record El Nino winter of 1997–1998. That event lasted several months, and there were claims with dates of loss for nearly every day from 24 December 1997 to 10 April 1998. The fourth largest loss, about USD 12 million, was due to the *Storm of the Century* in March, 1993, which was a very unusually strong nontropical cyclone that entered Florida from the Gulf. Note that these losses did not include surge losses, which were larger. The third and fifth largest losses were possibly due to remnants of tropical disturbances or storms that were not fully recorded in the HURDAT2 database.

Table 7. The top five NFIP nontropical loss events in order of paid loss amount.

Claim Count	Loss (Thousands of USD)	Event Duration		Remarks
		Begin	End	
702	29,671	9 December 2009	20 December 2009	17 December 2009 heavy rain
1154	14,302	24 December 1997	10 April 1998	El Nino record event
558	13,618	28 October 2011	2 November 2011	Possible related to tropical disturbance
529	11,999	12 March 1993	24 March 1993	Storm of the Century
467	11,244	12 May 2009	29 May 2009	Possible remnant of tropical depression 1

Examination of these losses indicated that there were a number of unique and varied meteorological conditions that lead to these heavy rainfall events. This presents a challenge in terms of developing a robust rainfall model. Since the total rainfall-related losses that can be modeled accounted for less than 6% of the NFIP losses historically, a decision needs to be made as to whether these types of losses should be explicitly modeled as opposed to making an actuarial adjustment of the losses to include them implicitly.

3.2.2. Loss Convergence in 30 Zones

The Flood Standards [1] require that modelers create a minimum of 30 geographic zones and verify that any Monte Carlo simulations required by the flood model to estimate losses converge to within a standard error of 5% in each zone of Florida (unless otherwise justified). The authors developed a preliminary set of zones based on the nearest coastal target location using a carefully selected set of 30 target coastal city locations. All zones were developed to have coastal exposure, so that storm surge risk affected every zone. The zones were made somewhat smaller in more vulnerable regions and larger in less vulnerable regions, to ensure a sufficient loss in all zones, while maintaining a reasonable size and structure, so that risk convergence was suitably ensured over all of Florida. These zones are subject to revision once stochastic losses are available and we have better understanding of the distribution of the vulnerability. As stochastic losses had not become available, the NFIP claims data was used for guidance. Figure 8 shows the preliminary set of 30 zones, along with the target coastal locations that define the zones. In addition, the NFIP losses are

shown for each zone in millions of USD (paid losses). The Pensacola zone had the largest loss, at USD 592 million, mainly due to Hurricane Ivan (2004). Next were Miami (USD 423 million) and Navarre (USD 415 million). The least vulnerable zone was St. Augustine Beach, at USD 11 million. Note that these losses were heavily influenced by singular events and thus should not be interpreted as an overall measure of risk. If a zone were to have no or negligible losses, then convergence may not be possible.

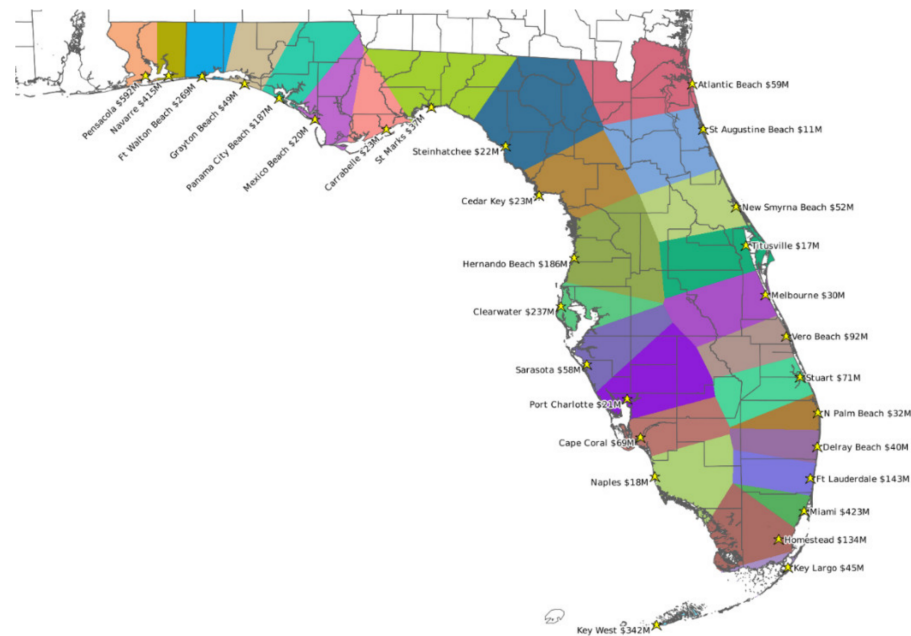


Figure 8. Preliminary creation of 30 zones to be used for Monte Carlo convergence tests. Yellow stars indicate target locations that define the zones. Losses for each zone were based on the analysis of NFIP claim data.

3.2.3. Historical Reconstruction

In general, observations of flood elevations and wave conditions are not available or very limited. To obtain estimates of these data, the authors used the FPFLM hazard models and other data to reconstruct select historical flood events. For storm surges, the Coastal Estuarine Storm Tide (CEST) model [14] was used. The CEST is forced by estimated observed winds from the H*Wind hurricane wind analyses [15] where available; otherwise, modeled winds are used. Wave conditions were determined by a wave model from the FPFLM that was based on the STWAVE (steady-state spectral wave) model [16]. For inland flooding, a simple two-dimensional modeling framework [17] was used. The modeled hazard data was interpolated to the claim locations, taking into account very-high-resolution 5 m DEM (Digital Elevation Model) elevation data. Based on the modeled results, each claim in the revised NFIP portfolio could be assigned to one of four hydrological states: inland flood with no waves; coastal flood with minor waves; coastal flood with moderate waves; and coastal flood with severe waves. A better set of flood vulnerability curves can be developed based on these hydrological states and can be validated using the modified NFIP claim data for the FPFLM project [9,10].

4. Conclusions

The NFIP claim data constitute an essential resource for developing, calibrating, and validating a flood risk model. They can be intensively used, for example, in the assessment of the flood outcomes from hazard (i.e., surge, wave and inland flooding) models and in the development process of a set of vulnerability curves. The provided original (especially hazard) fields in NFIP claim data are not always complete or accurate and often missing. In order to determine significant types of meteorological events that can cause flooding, the

authors tackled the revision of the NFIP claim data in Florida filed between 19 July 1975 and 10 January 2014. The hazard fields in the NFIP claim data were systematically revised using existing meteorological and geographical data in Florida. Tropical cyclone events, rainfall maxima, and distance to coast information permitted revisions of the cause of loss when the provided claim loss causes were in clear error or ambiguous. After our revision, the number and paid loss amount of surge claims in Florida increased dramatically, while those of accumulation of rainfall claims decreased. Sample usages of the revised NFIP claim data are presented in this study as well in the analyses of nontropical flood claims, loss convergence, and historical reconstruction of hydrological states.

The types of meteorological events that can lead to flooding are varied. For hurricane events, the currently developing FPFLM has both a surge model and an inland flood model that have been implemented and are now being evaluated using the revised NFIP claim data. However, for nonhurricane events, we do not have such models. There are unusual cases, such as the tropical disturbance in southeast Florida in 2000 (2 October 2020–6 October 2000). At that time, there was no tropical cyclone present, but heavy rain from a disturbance caused significant flooding. A tropical storm later developed from this disturbance after it left the region. Based on the NFIP claim data, the damage due to these rainfall events appeared to exceed the flood damage due to Hurricane Andrew (1992), which impacted the same region. Since the event was not a cyclone at that time, we could not model this event.

It should be noted that our criteria used for the revision of cause of loss in the current paper were somewhat arbitrary, such as the radius of hurricane influence (700 km), rainfall criteria (25 or 5 mm/day), distance to coast for surge influence (20 km), and surge assignment for hurricane event (<1 km). If these criteria were selected more scientifically, the reliability of revised claim counts and loss amounts might be improved. For example, in lieu of a <1 km rule for surge assignment, we could use Florida DEM surge zones based on NHC SLOSH model runs with FEMA observed flood estimates. If there is still doubt about the revised cause of loss, individual claims should be checked manually with added meteorological and georeferencing information to attain a proper selection of cause of loss.

Author Contributions: Conceptualization, D.W.S. and S.C.; methodology, D.W.S. and S.C.; software, D.W.S. and B.-M.K.; validation, D.W.S., S.C. and B.-M.K.; formal analysis, D.W.S. and S.C.; investigation, B.-M.K.; resources, S.C. and B.-M.K.; data curation, D.W.S.; writing—original draft preparation, D.W.S.; writing—review and editing, S.C. and B.-M.K.; visualization, D.W.S. and S.C.; supervision, S.C.; project administration, S.C. and B.-M.K.; funding acquisition, S.C. and B.-M.K. All authors have read and agreed to the published version of the manuscript.

Funding: This research was funded by the Florida Office of Insurance Regulation (FLOIR). B.K. was partially supported by “Investigation and prediction system development of marine heatwave around the Korean peninsula originated from the sub-Arctic and western Pacific” project supported by the Ministry of Ocean (No. 2019044).

Institutional Review Board Statement: Not applicable.

Informed Consent Statement: Not applicable.

Data Availability Statement: Data used in this study are not available for public use. However, redacted NFIP claim data can be obtained from the FEMA website (<https://www.fema.gov/openfema-data-page/fima-nfip-redacted-claims>, accessed on 11 February 2022).

Acknowledgments: FLOIR provided the authors with the NFIP claim data. The views expressed in this paper are those of the authors and do not necessarily reflect the views of FLOIR or any of its associated agencies.


Conflicts of Interest: The authors declare no conflict of interest.

References

1. Florida Commission on Hurricane Loss Projection Methodology. Flood Standards Report of Activities. Available online: www.sbafla.com/methodology (accessed on 15 January 2022).
2. Florida Commission on Hurricane Loss Projection Methodology. Hurricane Standards Report of Activities. Available online: www.sbafla.com/methodology (accessed on 15 January 2022).
3. Hamid, S.; Pinelli, J.P.; Cheng, S.C.; Gurley, K. Catastrophe model based assessment of Hurricane risk and estimates of potential insured losses for the State of Florida. *Nat. Hazard Rev.* **2011**, *12*, 171–183. [CrossRef]
4. Kousky, C.; Michel-Kerjan, E. Examining flood insurance claims in the United States: Six key findings. *J. Risk Insur.* **2015**, *84*, 819–850. [CrossRef]
5. McGrath, H.; El Ezz, A.A.; Nastev, M. Probabilistic depth-damage curves for assessment of flood-induced building losses. *Nat. Hazards* **2019**, *87*, 1–14. [CrossRef]
6. Wing, O.E.J.; Pinter, N.; Bates, P.D.; Kousky, C. New insights into US flood vulnerability revealed from flood insurance big data. *Nat. Commun.* **2020**, *11*, 1444. [CrossRef] [PubMed]
7. Davis, S.A.; Skaggs, L.L. *Catalog of Residential Depth-Damage Functions Used by the Army Corps of Engineers in Flood Damage Estimation*; IWR-92-R-3; USACE Institute for Water Resources: Fort Belvoir, VA, USA, 1992.
8. Skaggs, L.L.; Davis, S.A. *Variations in Residential Depth-Damage Functions Used by the US Army Corps of Engineers in Flood Damage Estimation*; Association of State Floodplain Managers: Atlanta, GA, USA, 2014.
9. Pinelli, J.-P.; Rodriguez, D.; Roueche, D.; Gurley, K.; Baradaranshoraka, M.; Cocke, S.; Shin, D.W.; Lapaiche, L.; Gay, R. Data management for the development of a flood vulnerability model. In *Safety and Reliability—Safe Societies in a Changing World*; Taylor & Francis: Boca Raton, FL, USA, 2018; pp. 2781–2788. [CrossRef]
10. Pinelli, J.-P.; Cruz, J.D.; Gurley, K.; Paleo-Torres, A.S.; Baradaranshoraka, M.; Cocke, S.; Shin, D.W. Uncertainty reduction through data management in the development, validation, calibration, and operation of a hurricane vulnerability model. *Int. J. Disaster Risk Sci.* **2020**, *11*. [CrossRef]
11. Landsea, C.W.; Franklin, J.L. Atlantic hurricane database uncertainty and presentation of a new database format. *Mon. Weather Rev.* **2003**, *141*, 3576–3592. [CrossRef]
12. Daly, C.; Halbleib, M.; Smith, J.I.; Gibson, W.P.; Doggett, M.K.; Taylor, G.H.; Curtis, J.; Pasteris, P.P. Physiographically sensitive mapping of climatological temperature and precipitation across the conterminous United States. *Int. J. Climatol.* **2008**, *28*, 2031–2064. [CrossRef]
13. Homer, C.G.; Dewitz, J.; Yang, L.; Jin, S.; Danielson, P.; Xian, G.Z.; Coulston, J.; Herold, N.; Wickham, J.; Megown, K. Completion of the 2011 national land cover database for the conterminous United States—Representing a decade of land cover change information. *Photogramm. Eng. Remote Sens.* **2015**, *81*, 345–354.
14. Zhang, K.; Xiao, C.; Shen, J. Comparison of the CEST and SLOSH models for storm surge flooding. *J. Coast. Res.* **2008**, *24*, 489–499. [CrossRef]
15. Powell, M.D.; Houston, S.H.; Amat, L.R.; Morisseau-Leroy, N. The HRD real-time hurricane wind analysis system. *J. Wind. Eng. Ind. Aerodyn.* **1998**, *77–78*, 53–64. [CrossRef]
16. Massey, T.C.; Anderson, M.E.; Smith, J.M.; Gomez, J.; Jones, R. *STWAVE: Steady-State Spectral Wave Model. User's Manual for STWAVE, Version 6.0*; Report ERDC/CHL SR-11-1; US Army Corps of Engineers: Washington, DC, USA, 2011.
17. Jamali, B.; Bach, P.M.; Cunningham, L.; Deletic, A. A cellular automata fast flood evaluation (CA-ffe) model. *Water Resour. Res.* **2019**, *55*, 4936–4953. [CrossRef]

Article

Prediction of Liquefaction-Induced Lateral Displacements Using Gaussian Process Regression

Mahmood Ahmad ^{1,2}, Maaz Amjad ³, Ramez A. Al-Mansob ^{1,*}, Paweł Kamiński ⁴, Piotr Olczak ⁵, Beenish Jehan Khan ⁶ and Arnold C. Alguno ⁷

- ¹ Department of Civil Engineering, Faculty of Engineering, International Islamic University Malaysia, Jalan Gombak, Selangor 50728, Malaysia; ahmadm@iium.edu.my
- ² Department of Civil Engineering, University of Engineering and Technology Peshawar (Bannu Campus), Bannu 28100, Pakistan
- ³ Department of Civil Engineering, University of Engineering and Technology, Peshawar 25120, Pakistan; maazamjad.civ@uetpeshawar.edu.pk
- ⁴ Faculty of Civil Engineering and Resource Management, AGH University of Science and Technology, 30-059 Krakow, Poland; pkamin@agh.edu.pl
- ⁵ Mineral and Energy Economy Research Institute, Polish Academy of Sciences, Wybickiego St. 7A, 31-261 Krakow, Poland; olczak@min-pan.krakow.pl
- ⁶ Department of Civil Engineering, CECOS University of IT and Emerging Sciences, Peshawar 25000, Pakistan; beenish@cecos.edu.pk
- ⁷ Department of Physics, Mindanao State University-Iligan Institute of Technology, Iligan City 9200, Philippines; arnold.alguno@g.msuiit.edu.ph
- * Correspondence: ramez@iium.edu.my

Citation: Ahmad, M.; Amjad, M.; Al-Mansob, R.A.; Kamiński, P.; Olczak, P.; Khan, B.J.; Alguno, A.C. Prediction of Liquefaction-Induced Lateral Displacements Using Gaussian Process Regression. *Appl. Sci.* **2022**, *12*, 1977. <https://doi.org/10.3390/app12041977>

Academic Editors: Andrea Chiozzi, Elena Benvenuti and Željana Nikolić

Received: 31 December 2021

Accepted: 8 February 2022

Published: 14 February 2022

Publisher's Note: MDPI stays neutral with regard to jurisdictional claims in published maps and institutional affiliations.



Copyright: © 2022 by the authors. Licensee MDPI, Basel, Switzerland. This article is an open access article distributed under the terms and conditions of the Creative Commons Attribution (CC BY) license (<https://creativecommons.org/licenses/by/4.0/>).

Abstract: During severe earthquakes, liquefaction-induced lateral displacement causes significant damage to designed structures. As a result, geotechnical specialists must accurately estimate lateral displacement in liquefaction-prone areas in order to ensure long-term development. This research proposes a Gaussian Process Regression (GPR) model based on 247 post liquefaction in-situ free face ground conditions case studies for analyzing liquefaction-induced lateral displacement. The performance of the GPR model is assessed using statistical parameters, including the coefficient of determination, coefficient of correlation, Nash–Sutcliffe efficiency coefficient, root mean square error (RMSE), and ratio of the RMSE to the standard deviation of measured data. The developed GPR model predictive ability is compared to that of three other known models—evolutionary polynomial regression, artificial neural network, and multi-layer regression available in the literature. The results show that the GPR model can accurately learn complicated nonlinear relationships between lateral displacement and its influencing factors. A sensitivity analysis is also presented in this study to assess the effects of input parameters on lateral displacement.

Keywords: lateral displacement; liquefaction; Gaussian process regression; sensitivity analysis; machine learning

1. Introduction

Loss of life and property remains an unavoidable consequence of major earthquakes. Studies of the consequences of major earthquakes have attempted to analyze the damage and make recommendations for reducing loss in the event of future earthquakes throughout history [1–3]. Liquefaction-induced lateral displacement is one of the most prevalent and damaging of these effects. It can cause enormous blocks of soil to move by a few millimeters to 10 m or more, inflicting substantial damage to lifeline networks, buried utilities, and a variety of other subsurface and civil engineering projects. Liquefaction-induced lateral displacement is most common on gentle slopes built on loose sand with a groundwater table close to the surface of the ground; however, open faces such as stream channels can also be susceptible [4].

Various approaches have been presented to estimate the magnitude of lateral displacement to date, and from the technical perspective, they can be classified as: (1) numerical analysis based on finite element or finite difference approaches (e.g., Finn et al. [5], Liao et al. [6] and Arulanandan et al. [7]), (2) simplified analytical methods, e.g., Newmark [8], Towhata et al. [9], and Kokusho and Fujita [10], (3) empirical methods based on either laboratory testing set or analytical methods of lateral spreading case history records (e.g., Hamada et al. [11] and Youd et al. [12]) and (4) machine learning approaches (e.g., Wang and Rahman [13]). These different approaches are reviewed herein, with particular emphasis on empirical models and soft computing techniques.

1.1. Finite Element Analysis

To simulate different aspects of liquefaction and lateral spreading, including seismic loads, rapid loss of shear strength, redistribution of pore water pressure, and soil softening, Liao et al. [6] reported that very complex finite element and finite difference approaches are required. Very intricate numerical techniques, large computer skills, and extensive resources are necessary to create a realistic three-dimensional simulation inside the real-time domains. A number of well-known finite element method (FEM) and finite difference (FD) software programmes are used for liquefaction-induced lateral displacement assessments and earthquake soil dynamic analysis. Other finite element models provided by Hamada et al. [14] and Orense and Towhata [15] to determine the lateral ground deformations generated by earthquakes. Gu et al. [16,17] estimated liquefaction deformation using a planar strain model. It successfully anticipated the pattern of displacements at a wildlife site in California [17], but overestimated the magnitude of displacements by around 30%.

1.2. Simplified Analytical Models

1.2.1. Sliding Block Model

Newmark [8] proposed a model based on strategy of sliding block on a frictional sloping surface that predicted seismically induced ground deformations by integrating accelerations above the sliding block's yield acceleration to obtain its velocities. The angle of inclination and the factor of safety over sliding are associated to yield acceleration. When the driving force (seismic acceleration) equal to or greater than resisting force (yield acceleration), block will begin to slide. The total cumulative resulting deformation is then determined by integrating the sliding block velocity. Yegian et al. [18] used Newmark's concept to introduce their model for predicting the permanent ground displacement expressed as

$$D = N_{eq} T^2 a_p f \left(\frac{a_y}{a_p} \right) \quad (1)$$

where D is the lateral ground deformation, N_{eq} denote cycles number equivalent to uniform base motion, T denotes time interval (s), a_y denotes yield acceleration (g), a_p denotes peak acceleration (g), and f denotes dimensionless function that depends on base motion. Baziar et al. [19] also used Newmark's concept, assuming an equivalent sinusoidal base acceleration record, to propose their model for predicting the permanent ground displacement expressed as:

$$\log D = 1.46 \log I_a - 6.642 a_y + 1.546 \quad (2)$$

D denotes lateral ground deformation (cm), I_a presents arias intensity (m/s), and a_y presents yield acceleration (g).

1.2.2. Minimum Potential Energy Model

This model was proposed by Towhata et al. [9] depending on the results of shaking table testing. The final position of soil layers was found by the principle of minimal potential energy, using the Lagrangian equations of motion, and assuming the variation of lateral ground deformation with depth as a sine function and with neglecting inertial

effects during dynamic loading. Tokida et al. [20] used the same principle to establish equations for predicting the maximum lateral displacement at the center of a slide as:

$$D = 1.73 \times 10^{-5} L^{1.99} H^{0.298} T^{-0.275} \theta^{0.963} \text{ for } (10 \text{ m} \leq L \leq 100 \text{ m}) \quad (3)$$

$$D = 1.29 \times 10^{-5} L^{1.99} H^{0.28} T^{-0.243} \theta^{0.995} \text{ for } (100 \text{ m} < L \leq 1000 \text{ m}) \quad (4)$$

where D is horizontal displacement (m), L = length of slide (m), H represents average thickness of liquefied layer (m), T represents average thickness of liquefied surface layer (m), and θ is the slope of ground surface express in percentage.

1.2.3. Shear Strength Loss and Strain Re-Hardening Model

Bardet et al. [21] reported that in 1997, Byrne proposed a method to find the final position of a liquefying slope using the finite element software tool Fast Lagrangian Analysis of Continua. In liquefaction region, it is assumed that the liquefied material is initially free of shear, and is subjected to isotropic pressure. After such immediate melting of liquefied soil, the shear stress (τ) was supposed to rise with shear strain unless reached a certain residual shear strength (τ_{ST}). Although the liquefied soil regains shear strength, the shear modulus was supposed to take a constant value G_{LIQ} . The final position of the slope is determined using the dynamic equation of motion.

1.2.4. Viscous Models

Hadush et al. [22] reported that Aydan [23] considered the liquefied subsoil to act as a visco-elastic object and used an upgraded Lagrangian numerical approach to find the deformation velocities for the liquefied soil sub-layers. They also proposed a numerical method based on cubic interpolated pseudoparticles for liquefaction-induced lateral displacement analysis in the context of fluid dynamics. Liao et al. [6] reported that Hamada et al. [24] recommended to use viscous models to estimate the liquefaction-induced lateral displacement. Kokusho and Fujita [10] studied the role of water film in lateral flow failure during earthquakes, on the basis of field survey results collected from Niigata (1964) earthquake. It was reported that the water films produced under the fine soil sub layers did not actually have shear resistance, and a significant factor for the large lateral flow displacement.

1.3. Empirical Models and Soft Computing Techniques

Hamada et al. [11] provided a preliminary relation of measuring horizontal ground displacement in meter's relying on 60 case histories, majority of them are obtained in Niigata and Noshiro, Japan. It can be seen from Table 1 that the equations are very common and easy to apply that contains only two parameters of site geometry and not considered seismic and geotechnical parameters but it has been suggested for limited dataset making it insufficiently broad to be extended to additional lateral displacement sites.

Youd and Perkins [25] suggested "liquefaction severity index" (LSI) to estimate maximum horizontal ground displacement generated by an earthquake. The LSI (inches) was calculated using distance to seismic energy source (R) (km); and moment magnitude (M_w) with maximum range of horizontal ground displacement as 2.5 m. This model assumes that the value of LSI depends on only seismic parameters (R , M_w). At the time, the proposed equation drew the attention of engineers. Although this method may have been useful for assessing lateral spreads inside the western United States, but lacks applicability and hence didn't receive widespread use.

Bardet et al. [21] used multiple linear regression (MLR) for developing relation to estimate lateral ground deformation for free face and sloping ground situations, respectively, utilizing data gathered by Bartlett and Youd [26,27], including three kinds of input variables:

1. Seismic parameters—seismic source distance (R , km) and earthquake magnitude, (M).
2. Topographic characteristics (in percent)—gradient of ground surface (S) and free face ratio.

- Geotechnical parameters (in percent)—average mean particle size within T_{15} ($D50_{15}$, mm) and averaged fines contents in T_{15} (F_{15})

The MLR approach was used to create the Youd et al. [12] model, presented in 1992, was built on upgraded results of Bartlett and Youd [26,27] for estimating lateral ground displacement, D_H (m). As indicated in Table 1 the models include free face and sloping ground conditions equations. This model gained attraction amongst geotechnical engineers due to its utilization of a huge dataset from various earthquakes, as well as geometry of site, geotechnical data, and seismic characteristics. Although, it does have some limits in terms of applications. For example, the free face equation was used when $5 \leq W \leq 20\%$, Jafarian and Nasri [28] gathered the latest dataset of liquefaction-induced lateral ground deformation based on uncertainties of different boreholes, which outperformed Hamada et al. [11] Kanibir [29], Al Bawwab [30], Javadi et al. [31], Youd et al. [12], and Baziar and Azizkandi [32] models.

Table 1. Empirical and machine learning approaches for liquefaction-induced lateral displacement.

Method and Technique	Model	Reference	
Empirical model	$D_H = 0.75H^{1/2}\theta^{1/3}$	Hamada et al. [11]	
	$\log LSI = -3.49 - 1.86 \log R + 0.98M_w$	Youd and Perkins [25]	
	$\log(D_H + 0.01) = -17.372 + 1.248M_w - 0.923 \log R - 0.014R$ $+ 0.685 \log W + 0.3 \log T_{15} + 4.826 \log(100 - F_{15})$ $- 1.091D50_{15} \log(D_H + 0.01)$ $= -14.152 + 0.988M_w - 1.049 \log R - 0.011R$ $+ 0.318 \log S + 0.619 \log T_{15}$ $+ 4.287 \log(100 - F_{15}) - 0.705D50_{15}$	Bardet et al. [21]	
	$\log(D_H) = -16.713 + 1.532M - 1.406 \log R^* - 0.012R + 0.592 \log W$ $+ 0.540 \log T_{15} + 3.413 \log(100 - F_{15}) - 0.795 \log(D50_{15} + 0.1\text{mm})$ $\log(D_H) = -16.213 + 1.532M - 1.406 \log R^* - 0.012R + 0.338 \log S$ $+ 0.540 \log T_{15} + 3.413 \log(100 - F_{15}) - 0.795 \log(D50_{15} + 0.1\text{mm})$ $R^* = R_0 + 10^{0.98M - 5.64}$	Youd et al. [12]	
	$\log(D_H) = -17.95 + 1.605M_w - 1.8673R^* - (\log(R + 20))^{-3.3836}$ $+ 0.547 \log W + 0.4431 \log T_{15} + 4.1873 \log(100 - F_{15})$ $- 0.7666 \log(D50_{15} + 0.1\text{mm}) \log(D_H)$ $= -19.63 + 2.0137M_w - 2.6124 \log R^*$ $- (\log(R + 20))^{-2.7004} + 0.3147 \log S$ $+ 0.6985 \log T_{15} + 4.1954 \log(100 - F_{15})$ $- 0.6772 \log(D50_{15} + 0.1\text{mm})$	Jafarian and Nasri [28]	
Soft computing methods	ANN	$D_H = f(M, R, D50_{15}, T_{15}, F_{15}, W, S, N1_{60s})$ $D_H = f(M, R, D50_{15}, T_{15}, F_{15}, W, S)$	Wang and Rahman [13] Baziar and Ghorbani [33]
	GP	$D_H = -163.1 \frac{1}{M^2} + 57 \frac{1}{R \cdot F_{15}} - 0.0035 \frac{T_{15}^2}{W \cdot D50_{15}^2} + 0.02 \frac{T_{15}^2}{F_{15} \cdot D50_{15}^2}$ $- 0.26 \frac{T_{15}^2}{F_{15}^2} + 0.006T_{15}^2 - 0.0013W^2 + 0.0002M^2 \cdot W \cdot T_{15} + 3.7$ $D_H = -0.8 \frac{F_{15}}{M} + 0.0014F_{15}^2 + 0.16T_{15} + 0.112S + 0.04 \frac{S \cdot T_{15}}{D50_{15}}$ $- 0.026R \cdot D50_{15} + 1.14$	Javadi et al. [31]
	ANFIS	$D_H = f(M, R, D50_{15}, T_{15}, F_{15}, W, S)$	Javdanian [34]

Note: $N1_{60s}$: ($N1$)₆₀ value corresponds to J_s , J_s is the lowest factor of safety below water table using simplified approach; θ : larger slope of either ground surface or the base of liquefied soil (%); H : thickness of liquefied zone (m); R^* : modified source distance factor that is a function of earthquake magnitude.

Soft computing is made up of a variety of techniques that function together, such as: artificial neural network, genetic algorithm, neuro-computing etc. Wang and Rahman [13] reported that new area of machine learning has arisen for handling decisions, modeling, and control issues. Baziar and Ghorbani [33] and Wang and Rahman [13] both used artificial neural networks (ANN) to estimate horizontal ground displacement. Javadi et al. [31] computed lateral displacement for free face and sloping ground using genetic programming (GP) using upgraded case data from Youd et al. [12]. In comparison to the MLR approach, the proposed GP approach has some advantages. Table 1 shows the proposed equations for free

face and sloping ground. Adaptive neuro-fuzzy inference system (ANFIS) based approach was suggested by Jadanian [34] using 426 case histories data and shows an improvement to the Youd et al. [12], Kanibir [29], Bardet et al. [21], and Rezanian et al. [4] models.

Soft computing methodologies are more accurate than analytical formulas, according to all of these studies. The findings revealed that the ML models mentioned above are capable of obtaining the experimental observations with acceptable accuracy. However, this field continues to be further explored.

The Gaussian process regression (GPR) approach has been successfully applied in many domains, but its application in geotechnical engineering is limited based on literature surveys. Considering the improved performance of GPR, it is, however, used for the first time in this study to predict the liquefaction-induced lateral spread displacement for free face condition. To demonstrate the efficacy of the proposed GPR-based model, the results are compared with various well-known models for calculating the D_H .

2. Gaussian Process Regression

Gaussian process regression (GPR) is one of the appropriate and newly-proposed methods that have been employed for various machine learning examples. GPR is a stochastic, non-parametric technique for addressing complicated and non-linear challenges. GPR assumes that the target variable m is determined as follows:

$$m = f(n(k)) + \varepsilon \quad (5)$$

where f represents unidentified functional dependency, n represents the number input parameters, and ε represents Gaussian noise with variance σ_a^2 . It's a method of indicating precedence straight over function space. The mean and covariance of a Gaussian distribution are matrices and vectors, respectively. The GPR model can determine the prediction distributions, which is similar to ensuring input knowledge [35]. The GPR approach is based on the idea that surrounding data informs neighbours.

GPR makes use of a number of kernel functions. A restriction of GPR regression is the selection of a suitable kernel function. Pearson VII kernel function (*PUK*) is utilized for GPR proposed model in this work.

$$PUK = \left(1 / \left[1 + \left(2 \sqrt{\|x_i - x_j\|^2} \sqrt{2^{(1/\omega)} - 1} / \sigma \right)^2 \right]^\omega \right) \quad (6)$$

where ω and σ are the Person's width, and peak tailing factor, respectively.

3. Case-History Database

The case-study dataset used for this work was collected using three sources (Chu et al. [36], Youd et al. [12], and Cetin et al. [37]) which contains a total of 247 records of lateral displacement related to free face ground conditions.

The input parameters chosen by Youd et al. [12] have been largely acknowledged amongst researchers as a full and acceptable set for controlling lateral displacement. As a result, several other scholars have chosen the same characteristics as important indicators (e.g., Javadi et al. [31]; Jafarian and Nasri [28]; Baziar and Saeedi Azizkandi [32]). In addition, with inclusion of a ground's intensity measure, peak ground acceleration (PGA, a_{max}) is employed in the present study to increase data set, making it more competent and effective in accounting for earthquake causes. By considering the causative fault types of all earthquakes, Sadigh et al. [38] employed attenuation equation to predict the PGA.

In this research, the following seven key parameters have been used to evaluate lateral displacement: earthquake magnitude (M), peak ground acceleration (a_{max} , g), horizontal distance to seismic energy source (R , km), average particle size in T_{15} ($D_{50_{15}}$, mm), average fines material (particles < 0.075 mm) in T_{15} (F_{15} , %), accumulative thickness of saturated layers with adjusted SPT number (N_1)₆₀ < 15 (T_{15} , m), free-face ratio (W , %), while the output is liquefaction-induced lateral displacement (D_H , m).

In this work, training datasets are based on 80% of the data available (198 sets of data in free face characteristics). The testing dataset has been used to evaluate the proposed models' prediction abilities. The 49 historical records data are used as testing datasets in this study. The training and testing datasets were partitioned depending on statistical features of the datasets, such as mean and standard deviation. The model efficiency is enhanced by the statistical consistency of the training and testing datasets, which makes it easier to evaluate them. Table 2 shows the evaluation metrics of input and output variables in training and testing datasets for free face. Summary of liquefaction-induced lateral ground deformation database is presented in Appendix A, Table A1.

Table 2. Statistical parameters for free-face condition.

Dataset	Statistical Parameters	Seismic Parameter			Geotechnical Parameter			Topographic Parameter	Output
		<i>M</i>	<i>a_{max}</i>	<i>R</i>	<i>D50₁₅</i>	<i>F₁₅</i>	<i>T₁₅</i>	<i>W</i>	<i>D_H</i>
		-	g	km	mm	%	m	%	m
Training	Minimum	6.4	0.15	0.5	0.04	1	0.2	1.64	0
	Average	7.26	0.41	15.10	0.36	18.83	7.80	11.69	2.45
	Maximum	9.2	0.68	100	7.7	70	16.7	57.7	10.16
	Standard deviation	0.51	0.15	11.61	0.65	13.71	5.16	9.96	2.26
Testing	Minimum	6.4	0.15	0.5	0.07	2	0.5	2.11	0
	Average	7.3	0.38	16.10	0.39	13.96	7.98	10.04	2.17
	Maximum	9.2	0.68	60	1.98	66	16	48.98	8.39
	Standard deviation	0.49	0.13	10.61	0.42	12.14	5.20	9.78	2.21

4. Correlation Analysis

Correlation coefficients (ρ) have been used to test the significance of the relation between different factors (see Table 3). The equation for ρ is as:

$$\rho(u, v) = \frac{cov(u, v)}{\sigma_u \sigma_v} \tag{7}$$

where *cov* indicates covariance, σ_u represents standard deviation of *u*, and σ_v defines standard deviation of *v*. $|\rho| > 0.8$ signifies a strong relation among *u* and *v*, values from 0.3–0.8 represents a moderate relationship, while $|\rho| < 0.30$ signifies a weak relation [39]. According to Song et al. [40], a relation is considered as “strong” if $|\rho| > 0.8$. *M*, *a_{max}*, *R*, *D50₁₅*, *F₁₅*, *T₁₅* and *W* have moderate to weak relations, as seen in Table 3. As a result, no variables from the lateral displacement estimation model were eliminated. Table 3 reveals that the correlation coefficient has a maximum absolute value of 0.761 and there is no “strong” link between different pairs of components.

Table 3. Correlation between parameters.

Parameters	<i>M</i>	<i>a_{max}</i>	<i>R</i>	<i>D50₁₅</i>	<i>F₁₅</i>	<i>T₁₅</i>	<i>W</i>	<i>D_H</i>
<i>M</i>	1.000							
<i>a_{max}</i>	−0.341	1.000						
<i>R</i>	0.761	−0.722	1.000					
<i>D50₁₅</i>	0.033	−0.112	0.013	1.000				
<i>F₁₅</i>	−0.370	0.560	−0.371	−0.230	1.000			
<i>T₁₅</i>	0.208	−0.573	0.360	0.237	−0.591	1.000		
<i>W</i>	0.003	0.178	−0.046	0.025	0.245	−0.145	1.000	
<i>D_H</i>	0.179	−0.250	0.230	−0.078	−0.354	0.518	0.146	1.000

5. Construction and Evaluation of Prediction Model

Figure 1 illustrates the prediction model's creation process. In this case, 80% and 20% of the dataset were chosen as training and test sets, respectively, based on statistical integrity. Second, the predictive model was constructed using the trial-and-error approach

based on training set utilizing the optimum hyperparameters configurations. Iterative method was utilized to find optimum values for the hyperparameters after setting them to random values (within a reasonable range). The values of the key kernel parameters, omega (ω) and sigma (σ) are 0.4 while noise is 0.3 in the GPR model after multiple trials. Finally, the testing data was used to evaluate the proposed GPR model's performance using four common evaluation metrics: coefficient of determination (R^2), coefficient of correlation (r), mean absolute error (MAE), root mean square error ($RMSE$), ratio of the root mean square error (RSR) to the standard deviation of measured values, and Nash–Sutcliffe coefficient (NSE). The R^2 and NSE values that are higher, and RSR values that are lower, imply that proposed model's prediction accuracy is better. Waikato Environment for Knowledge Analysis software was used throughout the whole calculation process The Pearson VII function-based kernel [41] was employed in this study for the GPR model.

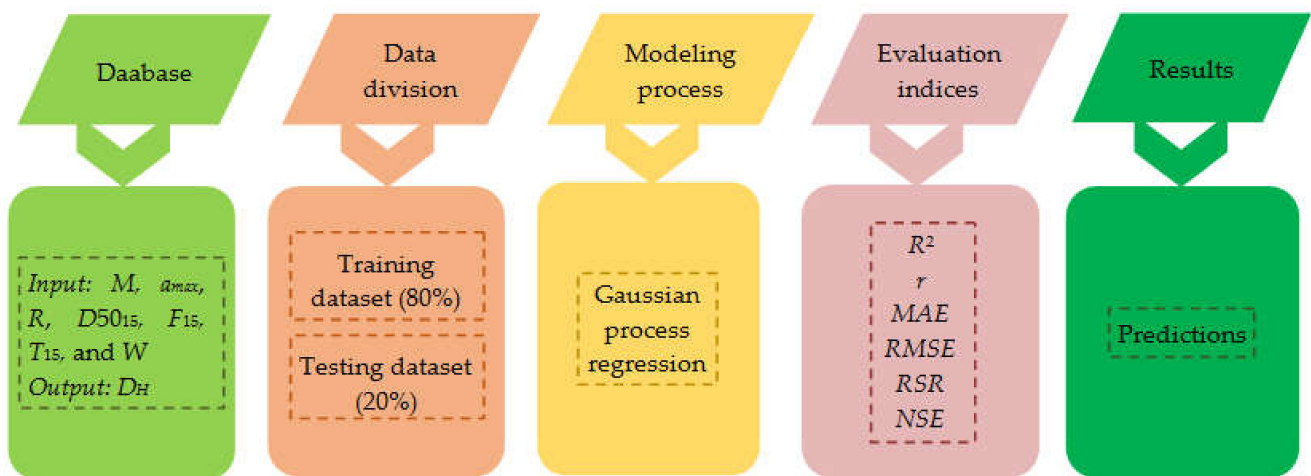


Figure 1. The flowchart for GPR based model to predict liquefaction induced lateral displacement.

The generated model's performance was assessed using R^2 , r , MAE , $RMSE$, RSR , and NSE .

$$R^2 = 1 - \frac{\sum_{i=1}^n (x_i - y_i)^2}{\sum_{i=1}^n (x_i - \bar{x})^2} \tag{8}$$

$$r = \frac{\sum_{i=1}^n (x_i - \bar{x})(y_i - \bar{y})}{\sqrt{\sum_{i=1}^n (x_i - \bar{x})^2} \sqrt{\sum_{i=1}^n (y_i - \bar{y})^2}} \tag{9}$$

$$MAE = \frac{1}{n} \sum_{i=1}^n (x_i - y_i) \tag{10}$$

$$RMSE = \sqrt{\frac{1}{n} \sum_{i=1}^n (x_i - y_i)^2} \tag{11}$$

$$RSR = \frac{\sqrt{\sum_{i=1}^n (x_i - y_i)^2}}{\sqrt{\sum_{i=1}^n (x_i - \bar{x})^2}} \tag{12}$$

$$NSE = 1 - \frac{\sum_{i=1}^n (x_i - y_i)^2}{\sum_{i=1}^n (x_i - \bar{x})^2} \tag{13}$$

where n denotes the set of data points, x_i and y_i denotes the actual and estimated output of data's i th sample, respectively; \bar{x} and \bar{y} represents the mean actual and estimated output of the dataset, respectively. The r value varies from -1 to 1 . A perfect distribution between actual and estimated values is represented by value of r equal to 1 , whereas a value of 0

shows no relation [42]. For $MAE = 0$, the model’s value is perfectly aligned with the real value, and the model is deemed “ideal.” The MAE value is between 0 and $+\infty$. The mean squared difference between outputs and targets is termed as $RMSE$, and its value ranges from 0 to $+\infty$. The NSE scale ranges from $-\infty$ to 1, with 1 representing the ideal match. A strong relation is indicated by an NSE score of more than 0.65 [43,44]. The RSR ranges from a perfect 0 to a significant positive number. A smaller RSR indicates low $RMSE$, indicates that the model is more predictive. The RSR and NSE categorization ranges are shown in Table 4 as very good, good, adequate, and inadequate [44].

Table 4. Statistical indicators for model performance evaluation.

Performance	RSR	NSE
Very Good	$0 \leq RSR \leq 0.5$	$0.75 < NSE \leq 1$
Good	$0.5 < RSR \leq 0.6$	$0.65 < NSE \leq 0.75$
Adequate	$0.6 < RSR \leq 0.7$	$0.5 < NSE \leq 0.65$
Inadequate	$RSR > 0.7$	$NSE \leq 0.5$

6. Result and Discussion

6.1. Performance of GPR Model

The GPR model’s efficiency were assessed using coefficient of correlation (r), mean absolute error (MAE), root mean square error ($RMSE$), ratio of root mean square error (RSR) and Nash-Sutcliffe coefficient (NSE). The trend line for GPR in training and testing phases has been drawn by comparing the observed regression in Figure 2 scatter plot, and the GPR findings have the maximum inclination to the line $y = x$ (i.e., $R^2 = 0.9402$ in training and $R^2 = 0.894$ in testing phases). Table 5 shows clearly that for the training model, $r = 0.9697$, $MAE = 0.3403$, $RMSE = 0.5597$, $RSR = 0.248$ and $NSE = 0.938$. Whereas for the testing model $r = 0.9455$, $MAE = 0.5443$, $RMSE = 0.8438$, $RSR = 0.387$ and $NSE = 0.851$. The trend line for GPR in training and testing phases has been drawn by comparing the observed regression in Figure 2 scatter plot, and the GPR findings have the maximum inclination to the line $y = x$ (i.e., $R^2 = 0.9402$ in training and $R^2 = 0.894$ in testing phases).

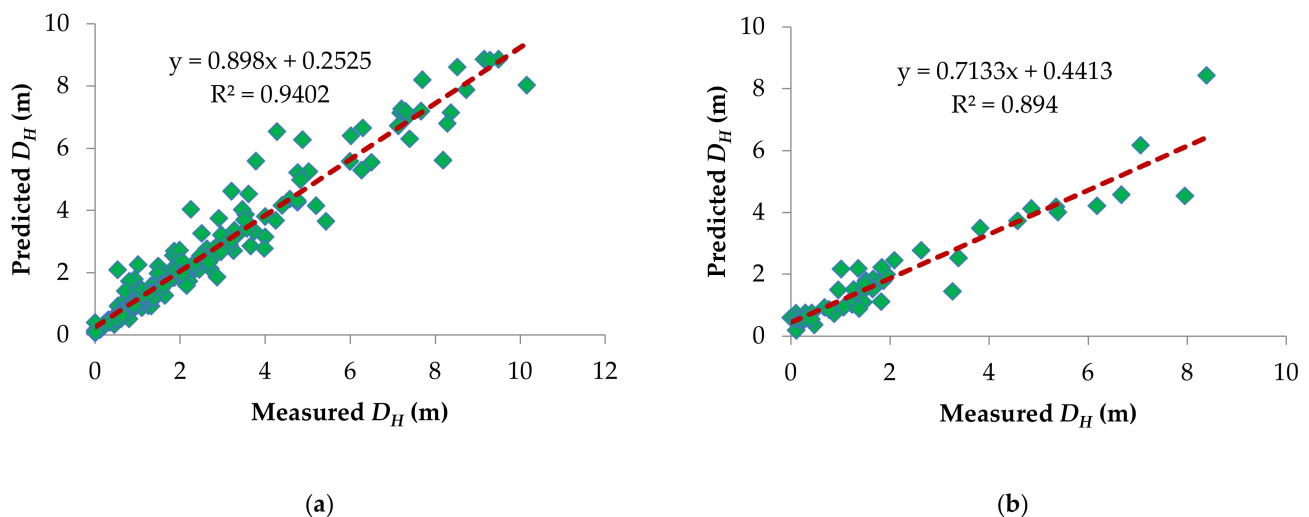


Figure 2. Scatter plot presenting the measured D_H values versus the predicted D_H (a) training and (b) testing model.

Table 5. Performance statistics of GPR model in comparison with extra available models in literature.

Model	Indicators	R^2	r	MAE (m)	RMSE (m)	RSR	NSE	Reference
GPR	Training model	0.9402	0.9697	0.3403	0.5597	0.248	0.938	Present study
	Testing model	0.894	0.9455	0.544	0.8438	0.387	0.851	
EPR	Training model	0.913	-	0.537	1.003	-	-	[4]
	Testing model	0.883	-	0.291	1.158	-	-	
ANN	Training model	0.875	-	0.702	1.074	-	-	[4]
	Testing model	0.872	-	0.82	1.21	-	-	
MLR	Training model	0.868	-	0.81	1.24	-	-	[4]
	Testing model	0.875	-	0.43	1.196	-	-	

Note: - represents that this performance statistic is not included in the reference.

The performance of the developed GPR model was compared to the evolutionary polynomial regression (EPR), MLR and ANN models in literature based on the R^2 , MAE, and RMSE criteria and the results are summarized in Table 5. Furthermore, in terms of the MAE and RMSE statistical measures in training, the lowest value was found for GPR (MAE = 0.3403 m, RMSE = 0.5597 m) compared to EPR (MAE = 0.537 m, RMSE = 1.003 m), ANN (MAE = 0.702 m, RMSE = 1.074 m), and MLR (MAE = 0.81 m, RMSE = 1.24 m). Whereas the prediction results in the testing, the MAE and RMSE values was found less for GPR (MAE = 0.544 m, RMSE = 0.8438 m) compared to EPR, ANN, and MLR except the MAEs values of EPR (=0.291 m) and MLR (=0.43 m) models. The superiority may be owing to the fact that the GPR model excellently captures the nonlinear relationships between lateral displacement and its influencing factors. It can therefore be concluded that, based on statistical indices, the GPR model had the best results. However, due to the use of different number of datasets, a comparison between these results is unwarranted. A project that uses different datasets is needed to gives generalized model to geotechnical earthquake engineering.

6.2. Sensitivity Analysis

The sensitivity results of the GPR model were examined using Yang and Zang's approach for determining the impact of input variables on D_H . This strategy, which has been used in a number of research [44–47], is as follows:

$$r_{ij} = \frac{\sum_{k=1}^n (x_{ik} \times x_{ok})}{\sqrt{\sum_{k=1}^n x_{ik}^2 \sum_{k=1}^n x_{ok}^2}} \quad (14)$$

x_{ik} and x_{ok} are the actual and estimated variables, respectively, and n represents number of datasets (i.e., 198 data samples). For each input variable, the r_{ij} value varies from zero to one, with the greatest r_{ij} values indicating the most efficient output factor (i.e., D_H). Figure 3 displays the r_{ij} values for all input factors. The accumulative thickness of saturated layers with adjusted SPT number, T_{15} ($r_{ij} = 0.843$) has the greatest effect on the D_H . Furthermore, Table 3 shows that the accumulative thickness of saturated layers with adjusted SPT number, T_{15} has the highest ρ of 0.518 in all other parameters validating the sensitivity analysis results.

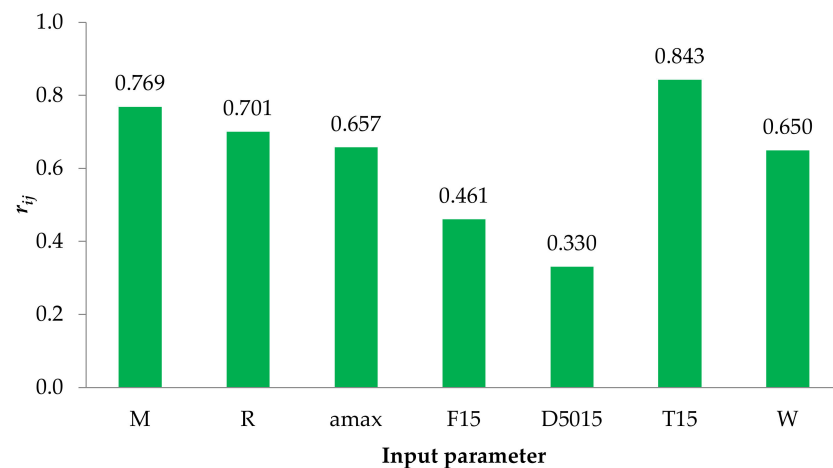


Figure 3. Sensitivity analysis of input variables.

7. Conclusions

The GPR model was used to estimate liquefaction-induced lateral displacement in this work. The predictive model was built using seven input parameters and one output parameter. Performance measures such as R^2 , r , $RMSE$, MAE , RSR , NSE , and visual inspection such as scatter plots were used to assess the effectiveness of the developed model. This study's findings can be summarized as follows:

1. With respect to the values of GPR with $R^2 = 0.9402$, $r = 0.9697$, $MAE = 0.3403$, $RMSE = 0.5597$, $RSR = 0.248$ and $NSE = 0.938$ in training phase whereas for testing phase it performed equally well with $R^2 = 0.894$, $r = 0.9455$, $MAE = 0.5443$, $RMSE = 0.8438$, $RSR = 0.387$ and $NSE = 0.851$. In comparison to the EPR, ANN, and MLR models in literature, the GPR model was found to be more accurate and stable than the other models.
2. The results of sensitivity analysis show that the degree of importance of different input parameters on lateral displacement is as $T_{15} > M > R > a_{max} > W > F_{15} > D5015$.
3. The developed Pearson VII kernel function-based GPR model makes predictions accurate and outperforms the others for this dataset and may be applied to a range of geotechnical engineering situations involving uncertainties.

The GPR approach has the advantage of becoming easily modified as new data becomes available, reducing need for expertise and time to modify an existing design aid or equation and/or suggest a new equation.

Author Contributions: Conceptualization, M.A. (Mahmood Ahmad); methodology, M.A. (Mahmood Ahmad), M.A. (Maaz Amjad); software, M.A. (Maaz Amjad) and M.A. (Mahmood Ahmad); validation, R.A.A.-M., P.K., P.O., M.A. (Maaz Amjad) and B.J.K.; formal analysis, M.A. (Mahmood Ahmad) and M.A. (Maaz Amjad); investigation, P.K., P.O., A.C.A. and B.J.K.; resources, P.K.; data curation, M.A. (Maaz Amjad) and M.A. (Mahmood Ahmad); writing—original draft preparation, M.A. (Maaz Amjad); writing—review and editing, M.A. (Maaz Amjad) and M.A. (Mahmood Ahmad); supervision, M.A. (Mahmood Ahmad), R.A.A.-M. and P.K.; project administration, M.A. (Mahmood Ahmad), A.C.A.; funding acquisition, R.A.A.-M., P.K., P.O. and A.C.A. All authors have read and agreed to the published version of the manuscript.

Funding: This research received no external funding.

Institutional Review Board Statement: Not applicable.

Informed Consent Statement: Not applicable.

Data Availability Statement: The data used to support the findings of this study are included within the article.

Conflicts of Interest: The authors declare no conflict of interest.

Appendix A

Table A1. Summary of Liquefaction-Induced Lateral Ground Deformation Database.

Earthquake	<i>M</i>	<i>R</i> (km)	<i>a</i> _{max} (g)	<i>F</i> ₁₅ (%)	<i>D</i> _{50/15} (mm)	<i>T</i> ₁₅ (m)	<i>W</i> (%)	<i>D</i> _{<i>H</i>} (m)
1906, San Francisco	7.9	27	0.24	23	0.25	7.2	22.02	1.84
1906, San Francisco	7.9	24	0.26	30	0.16	1.5	17.76	0.92
1964, Alaska	9.2	60	0.3	21	1.35	3.4	24.59	1.86
1964, Alaska	9.2	100	0.2	13	1	10.4	7.03	1.38
1964, Alaska	9.2	60	0.3	23	1.47	3.8	16.07	1.58
1964, Alaska	9.2	60	0.3	66	0.07	3.1	48.98	1.92
1964, Niigata	7.5	21	0.32	5	0.35	12.7	3.06	1.01
1964, Niigata	7.5	21	0.32	4	0.34	13.6	3.15	5.2
1964, Niigata	7.5	21	0.32	24	0.19	8.6	5.36	0.82
1964, Niigata	7.5	21	0.32	6	0.35	0.5	3.43	1.1
1964, Niigata	7.5	21	0.32	32	0.1	2.4	2.03	0.54
1964, Niigata	7.5	21	0.32	26	0.16	2.5	20.61	0.91
1964, Niigata	7.5	21	0.32	6	0.35	0.5	22.37	0.88
1964, Niigata	7.5	21	0.32	10	0.25	11.3	29.7	5.03
1964, Niigata	7.5	21	0.32	6	0.29	7.5	7.32	3.75
1964, Niigata	7.5	21	0.32	24	0.19	8.6	8.78	0.93
1964, Niigata	7.5	21	0.32	12	0.27	12.2	5.01	2.36
1964, Niigata	7.5	21	0.32	24	0.19	8.6	24.02	3.07
1964, Niigata	7.5	21	0.32	9	0.26	11.3	19.62	10.16
1964, Niigata	7.5	21	0.32	12	0.26	12.3	5.76	1.49
1964, Niigata	7.5	21	0.32	31	0.12	2.4	3.26	1.25
1964, Niigata	7.5	21	0.32	10	0.39	9	3.27	2.48
1964, Niigata	7.5	21	0.32	32	0.11	2.4	2.09	1.32
1964, Niigata	7.5	21	0.32	14	0.36	7.1	19.62	3.34
1964, Niigata	7.5	21	0.32	4	0.57	8.6	2.82	1.23
1964, Niigata	7.5	21	0.32	11	0.26	11.9	5.93	2.97
1964, Niigata	7.5	21	0.32	5	0.32	15.6	4.94	7.36
1964, Niigata	7.5	21	0.32	16	0.22	9.6	3.06	2.41
1964, Niigata	7.5	21	0.32	24	0.19	8.6	18.49	1.78
1964, Niigata	7.5	21	0.32	11	0.27	12	4.83	1.84
1964, Niigata	7.5	21	0.32	6	0.32	12.4	4.82	3.66
1964, Niigata	7.5	21	0.32	12	0.26	12.4	5.01	1.75
1964, Niigata	7.5	21	0.32	31	0.12	2.4	3.35	0.69
1964, Niigata	7.5	21	0.32	7	0.35	9.8	4.5	0.53
1964, Niigata	7.5	21	0.32	5	0.32	15.6	7.86	8.37
1964, Niigata	7.5	21	0.32	5	0.32	13.9	5.77	4.58
1964, Niigata	7.5	21	0.32	12	0.26	12	9.18	4.4
1964, Niigata	7.5	21	0.32	12	0.24	11.8	5.54	4
1964, Niigata	7.5	21	0.32	12	0.26	12.2	5.36	2.38
1964, Niigata	7.5	21	0.32	5	0.44	10.1	2.42	1.25
1964, Niigata	7.5	21	0.32	11	0.28	12.1	3.68	2.09
1964, Niigata	7.5	21	0.32	6	0.35	0.5	3.39	0.86
1964, Niigata	7.5	21	0.32	14	0.25	12.6	13.73	6.27
1964, Niigata	7.5	21	0.32	5	0.4	7.9	3.59	1.46
1964, Niigata	7.5	21	0.32	5	0.32	15.6	17.75	9.15
1964, Niigata	7.5	21	0.32	6	0.35	0.5	4.26	0.72
1964, Niigata	7.5	21	0.32	6	0.29	14.3	6.51	3.61
1964, Niigata	7.5	21	0.32	8	0.23	6.8	1.85	0.91
1964, Niigata	7.5	21	0.32	24	0.19	8.6	5.29	1.64
1964, Niigata	7.5	21	0.32	5	0.36	13.6	8.52	4.77
1964, Niigata	7.5	21	0.32	5	0.5	10.9	4.77	0.81
1964, Niigata	7.5	21	0.32	5	0.35	12.7	9.12	6
1964, Niigata	7.5	21	0.32	15	0.25	9.6	2.68	1.89
1964, Niigata	7.5	21	0.32	24	0.19	8.6	8.19	2.2
1964, Niigata	7.5	21	0.32	3	0.35	13.3	4.05	4.76
1964, Niigata	7.5	21	0.32	11	0.26	12	6.53	2.51

Table A1. Cont.

Earthquake	<i>M</i>	<i>R</i> (km)	<i>a</i> _{max} (g)	<i>F</i> ₁₅ (%)	<i>D</i> ₅₀₁₅ (mm)	<i>T</i> ₁₅ (m)	<i>W</i> (%)	<i>D</i> _H (m)
1964, Niigata	7.5	21	0.32	5	0.32	15.6	17.75	9.49
1964, Niigata	7.5	21	0.32	11	0.24	11.6	11.06	8.19
1964, Niigata	7.5	21	0.32	13	0.29	13.6	2.76	1.01
1964, Niigata	7.5	21	0.32	7	0.34	10.5	6.03	5.43
1964, Niigata	7.5	21	0.32	6	0.45	10.5	5.84	1.86
1964, Niigata	7.5	21	0.32	5	0.32	15.5	9.98	6.02
1964, Niigata	7.5	21	0.32	6	0.39	9.2	4.87	1.86
1964, Niigata	7.5	21	0.32	12	0.24	11.9	5.06	3.98
1964, Niigata	7.5	21	0.32	5	0.32	15.6	17.05	9.29
1964, Niigata	7.5	21	0.32	15	0.32	11.3	2.86	1.41
1964, Niigata	7.5	21	0.32	16	0.31	11	3.06	1.3
1964, Niigata	7.5	21	0.32	18	0.21	6.7	4.45	0.9
1964, Niigata	7.5	21	0.32	15	0.32	7	7.72	1.92
1964, Niigata	7.5	21	0.32	11	0.28	12.1	2.88	1.56
1964, Niigata	7.5	21	0.32	6	0.38	11.6	3.22	2.71
1964, Niigata	7.5	21	0.32	5	0.32	15.6	5.25	7.19
1964, Niigata	7.5	21	0.32	16	0.3	10.8	3.68	0.71
1964, Niigata	7.5	21	0.32	13	0.38	7.2	20.55	3.28
1964, Niigata	7.5	21	0.32	9	0.4	13	2.05	1.11
1964, Niigata	7.5	21	0.32	13	0.25	12.5	16.07	7.4
1964, Niigata	7.5	21	0.32	6	0.37	12.7	7.05	3.54
1964, Niigata	7.5	21	0.32	6	0.35	0.5	2.68	0.82
1964, Niigata	7.5	21	0.32	9	0.39	9.3	3.72	1.96
1964, Niigata	7.5	21	0.32	5	0.39	7.3	2.76	1.23
1964, Niigata	7.5	21	0.32	24	0.19	8.6	12.86	2.74
1964, Niigata	7.5	21	0.32	12	0.25	12.1	16.72	4.88
1964, Niigata	7.5	21	0.32	11	0.27	12.1	3.38	1.83
1964, Niigata	7.5	21	0.32	5	0.32	15.6	5.77	7.21
1964, Niigata	7.5	21	0.32	2	0.33	10.4	8.89	4.76
1964, Niigata	7.5	21	0.32	13	0.25	12.4	35	7.67
1964, Niigata	7.5	21	0.32	7	0.32	9.4	2.99	1.31
1964, Niigata	7.5	21	0.32	4	0.34	13.5	3.36	3.46
1964, Niigata	7.5	21	0.32	11	0.26	11.6	11.32	3.78
1964, Niigata	7.5	21	0.32	3	0.44	11.3	3.82	1.52
1964, Niigata	7.5	21	0.32	13	0.29	13	3.1	0.56
1964, Niigata	7.5	21	0.32	28	0.14	2.5	4.79	0.88
1964, Niigata	7.5	21	0.32	5	0.32	15.6	19.62	7.7
1964, Niigata	7.5	21	0.32	3	0.44	11.3	4.87	1.9
1964, Niigata	7.5	21	0.32	9	0.37	10	16.4	6.5
1964, Niigata	7.5	21	0.32	7	0.35	9.8	3.9	2.87
1964, Niigata	7.5	21	0.32	12	0.25	12.2	12.47	4.83
1964, Niigata	7.5	21	0.32	5	0.34	13.8	12.01	8.73
1964, Niigata	7.5	21	0.32	24	0.19	8.6	25.93	3.57
1964, Niigata	7.5	21	0.32	14	0.25	12.6	11.32	3.51
1964, Niigata	7.5	21	0.32	17	0.24	6.8	4.26	1.37
1964, Niigata	7.5	21	0.32	11	0.25	11.6	17.05	8.29
1964, Niigata	7.5	21	0.32	5	0.31	14.1	16.4	8.52
1964, Niigata	7.5	21	0.32	24	0.19	8.6	5.76	1.27
1964, Niigata	7.5	21	0.32	15	0.25	9.5	3.04	2.68
1964, Niigata	7.5	21	0.32	13	0.27	11.8	2.27	1.56
1964, Niigata	7.5	21	0.32	13	0.25	12.4	12.47	3.21
1964, Niigata	7.5	21	0.32	24	0.19	8.6	7.14	2.15
1964, Niigata	7.5	21	0.32	24	0.19	8.6	5.15	1.06
1964, Niigata	7.5	21	0.32	7	0.43	10.4	15.25	2.25
1964, Niigata	7.5	21	0.32	5	0.35	16.7	11.06	2.91
1964, Niigata	7.5	21	0.32	8	0.15	3.7	1.64	0.62
1964, Niigata	7.5	21	0.32	5	0.32	15.6	7.72	7.31
1964, Niigata	7.5	21	0.32	13	0.25	12.5	55.68	7.13

Table A1. Cont.

Earthquake	<i>M</i>	<i>R</i> (km)	<i>a</i> _{max} (g)	<i>F</i> ₁₅ (%)	<i>D</i> ₅₀₁₅ (mm)	<i>T</i> ₁₅ (m)	<i>W</i> (%)	<i>D</i> _H (m)
1964, Niigata	7.5	21	0.32	6	0.31	15.2	12.44	6.3
1964, Niigata	7.5	21	0.32	13	0.35	11.9	2.86	1.11
1964, Niigata	7.5	21	0.32	11	0.25	11.6	19.37	4.28
1964, Niigata	7.5	21	0.32	10	0.28	12.1	3.09	1.66
1964, Niigata	7.5	21	0.32	5	0.36	9.6	3.72	3.26
1964, Niigata	7.5	21	0.32	13	0.25	12.3	16.07	7.06
1964, Niigata	7.5	21	0.32	2	0.33	10.4	13.65	5.35
1964, Niigata	7.5	21	0.32	13	0.26	12.6	6.23	1.87
1964, Niigata	7.5	21	0.32	3	0.44	11.3	3.27	0.96
1964, Niigata	7.5	21	0.32	7	0.33	10.6	12.01	7.95
1964, Niigata	7.5	21	0.32	3	0.44	11.3	5.12	1.36
1964, Niigata	7.5	21	0.32	30	0.13	2.4	4.18	0.68
1964, Niigata	7.5	21	0.32	4	0.34	13.6	2.99	4.85
1964, Niigata	7.5	21	0.32	28	0.14	2.5	20.61	1.06
1964, Niigata	7.5	21	0.32	11	0.28	12.1	3.86	1.93
1964, Niigata	7.5	21	0.32	2	0.33	10.4	7.58	4.57
1964, Niigata	7.5	21	0.32	11	0.28	12.2	2.9	1.65
1964, Niigata	7.5	21	0.32	8	0.34	11.4	3.1	2.09
1964, Niigata	7.5	21	0.32	5	0.45	10	2.86	1.82
1964, Niigata	7.5	21	0.32	12	0.24	11.9	4.45	3.38
1964, Niigata	7.5	21	0.32	5	0.35	12.7	2.79	1.01
1964, Niigata	7.5	21	0.32	13	0.29	12.9	3.04	0.42
1964, Niigata	7.5	21	0.32	5	0.31	14.1	17.75	8.39
1964, Niigata	7.5	21	0.32	11	0.24	12.1	2.11	1.27
1964, Niigata	7.5	21	0.32	7	0.28	8.1	17.05	6.18
1964, Niigata	7.5	21	0.32	6	0.35	0.5	5.96	0.77
1964, Niigata	7.5	21	0.32	6	0.35	0.5	2.29	1.38
1964, Niigata	7.5	21	0.32	5	0.31	14.1	4.55	6.67
1964, Niigata	7.5	21	0.32	11	0.27	12	3.98	1.83
1964, Niigata	7.5	21	0.32	6	0.29	7.9	17.05	5.39
1964, Niigata	7.5	21	0.32	11	0.27	12.1	2.97	1.49
1971, San Fernando	6.4	0.5	0.68	47	0.08	5.3	19.96	2.93
1971, San Fernando	6.4	0.5	0.68	47	0.08	5.6	4.7	0.47
1971, San Fernando	6.4	0.5	0.68	47	0.08	6.5	5.08	0.52
1971, San Fernando	6.4	0.5	0.68	47	0.08	4.6	20.3	3.16
1971, San Fernando	6.4	0.5	0.68	47	0.08	3.6	20.34	3.18
1971, San Fernando	6.4	0.5	0.68	47	0.08	3	17.07	1.81
1971, San Fernando	6.4	0.5	0.68	47	0.08	2.3	13.59	2.14
1971, San Fernando	6.4	0.5	0.68	47	0.08	1.6	20.41	2.45
1971, San Fernando	6.4	0.5	0.68	47	0.08	4.8	19.61	2.78
1971, San Fernando	6.4	0.5	0.68	47	0.08	2.7	15.43	2.02
1971, San Fernando	6.4	0.5	0.68	47	0.08	2	13.59	1.46
1971, San Fernando	6.4	0.5	0.68	47	0.08	4	18.87	3.26
1971, San Fernando	6.4	0.5	0.68	47	0.08	2.7	20.47	3.16
1971, San Fernando	6.4	0.5	0.68	47	0.08	5.9	4.89	0.54
1971, San Fernando	6.4	0.5	0.68	47	0.08	4.5	19.26	1.99
1971, San Fernando	6.4	0.5	0.68	47	0.08	1	20.27	1
1971, San Fernando	6.4	0.5	0.68	47	0.08	3.1	18.26	2.04
1971, San Fernando	6.4	0.5	0.68	47	0.08	5.2	19.96	2.63
1979, Imperial Valley	6.5	2	0.49	20	0.12	3	8.57	2.63
1979, Imperial Valley	6.5	2	0.49	32	0.09	1.5	6.25	0.37
1979, Imperial Valley	6.5	2	0.49	23	0.11	2	7.89	2.04
1979, Imperial Valley	6.5	2	0.49	17	0.12	3.6	3.08	0.92
1979, Imperial Valley	6.5	2	0.49	15	0.12	3.8	6.56	2.02
1979, Imperial Valley	6.6	6	0.36	70	0.04	0.2	4.26	0.01
1979, Imperial Valley	6.6	6	0.36	54	0.12	1.8	10.66	0.01
1979, Imperial Valley	6.5	2	0.49	17	0.12	3.7	9.6	4
1979, Imperial Valley	6.5	2	0.49	22	0.11	2.6	3.68	0.31

Table A1. Cont.

Earthquake	<i>M</i>	<i>R</i> (km)	<i>a</i> _{max} (g)	<i>F</i> ₁₅ (%)	<i>D</i> ₅₀₁₅ (mm)	<i>T</i> ₁₅ (m)	<i>W</i> (%)	<i>D_H</i> (m)
1979, Imperial Valley	6.5	2	0.49	23	0.11	2.4	6.35	1.41
1979, Imperial Valley	6.5	2	0.49	23	0.11	2	6.15	1.1
1979, Imperial Valley	6.5	2	0.49	22	0.11	2.7	6.45	1.53
1979, Imperial Valley	6.5	2	0.49	23	0.11	2.9	7.02	1.43
1979, Imperial Valley	6.5	2	0.49	25	0.1	2.5	6.78	0.72
1979, Imperial Valley	6.5	2	0.49	15	0.12	4	6.56	1.48
1979, Imperial Valley	6.5	2	0.49	17	0.12	3.7	6.78	2.3
1979, Imperial Valley	6.5	2	0.49	21	0.11	1.6	4.8	0.67
1979, Imperial Valley	6.5	2	0.49	25	0.1	2.5	9.84	2.63
1979, Imperial Valley	6.5	2	0.49	22	0.11	1.8	6.67	1.13
1979, Imperial Valley	6.5	2	0.49	30	0.09	1.8	8.05	1.03
1979, Imperial Valley	6.5	2	0.49	22	0.11	2.7	8.05	2.12
1979, Imperial Valley	6.5	2	0.49	25	0.11	2.2	3.68	0.47
1979, Imperial Valley	6.5	2	0.49	16	0.12	3.8	9.37	4.25
1979, Imperial Valley	6.5	2	0.49	22	0.11	3	10.08	3.21
1979, Imperial Valley	6.5	2	0.49	16	0.12	3.7	3.72	1.23
1979, Imperial Valley	6.5	2	0.49	18	0.12	3.4	9.16	3.82
1979, Imperial Valley	6.5	2	0.49	19	0.12	3.3	6.15	1.51
1979, Imperial Valley	6.5	2	0.49	21	0.11	1.4	4.69	0.87
1979, Imperial Valley	6.5	2	0.49	25	0.11	2.2	3.52	0.47
1987, Superstition Hills	6.6	23	0.15	27	0.09	3.5	17.91	0.19
1987, Superstition Hills	6.6	23	0.15	22	0.09	3.3	41.38	0.21
1987, Superstition Hills	6.6	23	0.15	43	0.07	1.7	17.52	0.11
1987, Superstition Hills	6.6	23	0.15	44	0.07	3.6	7.5	0.01
1987, Superstition Hills	6.6	23	0.15	38	0.08	2.7	13.11	0.11
1987, Superstition Hills	6.6	23	0.15	25	0.09	3.4	41.38	0.24
1989, Loma Prieta	7	27.2	0.2	1	0.6	3.4	29.73	0.26
1989, Loma Prieta	7	27.2	0.2	2	0.8	2.7	33.54	0.29
1995, Hyogo-Ken Nanbu	6.8	7.5	0.35	12.6	0.47	14.2	13.95	1.18
1995, Hyogo-Ken Nanbu	6.8	6	0.38	13.4	0.94	12.5	9.25	1.01
1995, Hyogo-Ken Nanbu	6.8	8	0.34	14.6	1.98	16	6.67	0.45
1995, Hyogo-Ken Nanbu	6.8	8	0.34	14.6	1.98	16	16.82	0.93
1995, Hyogo-Ken Nanbu	6.8	7.5	0.35	12.6	0.47	14.2	10.4	0.89
1995, Hyogo-Ken Nanbu	6.8	5.5	0.39	10	1.36	15	14.56	1.34
1995, Hyogo-Ken Nanbu	6.8	5.5	0.39	10	1.36	15	30.21	2.83
1995, Hyogo-Ken Nanbu	6.8	6.5	0.37	10	1.88	12.5	5.16	0.34
1995, Hyogo-Ken Nanbu	6.8	5.5	0.39	10	1.36	15	56.8	2.48
1995, Hyogo-Ken Nanbu	6.8	8	0.34	14.6	1.98	16	18	0.97
1995, Hyogo-Ken Nanbu	6.8	8	0.34	14.6	1.98	16	20.69	0.9
1995, Hyogo-Ken Nanbu	6.8	7.5	0.35	12.6	0.47	14.2	18.56	1.33
1995, Hyogo-Ken Nanbu	6.8	8	0.34	14.6	1.98	16	14.63	0.66
1995, Hyogo-Ken Nanbu	6.8	6.5	0.37	10	1.88	12.5	9.84	1.03
1995, Hyogo-Ken Nanbu	6.8	5.5	0.39	10	1.36	15	14.34	1.31
1995, Hyogo-Ken Nanbu	6.8	6.5	0.37	10	1.88	12.5	14.63	1.47
1995, Hyogo-Ken Nanbu	6.8	6	0.38	13.4	0.94	12.5	15	1.48
1995, Hyogo-Ken Nanbu	6.8	5.5	0.39	10	1.36	15	9.79	1.47
1995, Hyogo-Ken Nanbu	6.8	8	0.34	14.6	1.98	16	8.45	0.41
1999, Chi-Chi	7.6	5	0.67	20.8	0.11	0.5	7.4	0
1999, Chi-Chi	7.6	5	0.67	20.8	0.11	0.8	13.7	0.45
1999, Chi-Chi	7.6	5	0.67	20.8	0.11	0.8	18.4	0.55
1999, Chi-Chi	7.6	5	0.67	20.8	0.11	0.8	25.2	0.8
1999, Chi-Chi	7.6	5	0.67	20.8	0.11	0.8	37.3	1.05
1999, Chi-Chi	7.6	5	0.67	20.8	0.11	0.8	49.9	2.05
1999, Chi-Chi	7.6	5	0.67	13	0.18	0.75	21.2	0.49
1999, Chi-Chi	7.6	5	0.67	20.8	0.11	1.1	11.9	0
1999, Chi-Chi	7.6	5	0.67	20.8	0.11	1.1	26.3	0
1999, Chi-Chi	7.6	5	0.67	30	0.13	0.45	12.2	0.4
1999, Chi-Chi	7.6	5	0.67	30	0.13	0.45	14.3	0.65

Table A1. Cont.

Earthquake	M	R (km)	a_{max} (g)	F_{15} (%)	D50 ₁₅ (mm)	T_{15} (m)	W (%)	D_H (m)
1999, Chi-Chi	7.6	5	0.67	30	0.13	0.45	24.6	1
1999, Chi-Chi	7.6	5	0.67	30	0.13	0.45	57.7	1.24
1999, Chi-Chi	7.6	5	0.67	31.4	0.1	1	8	0.35
1999, Chi-Chi	7.6	5	0.67	31.4	0.1	1	10.5	0.61
1999, Chi-Chi	7.6	5	0.67	31.4	0.1	1	19	0.96
1999, Chi-Chi	7.6	5	0.67	31.4	0.1	1	31.3	2.96
1999, Chi-Chi	7.6	5	0.67	48.5	0.1	1.8	9.6	0.35
1999, Chi-Chi	7.6	5	0.67	48.5	0.1	1.8	11.7	0.52
1999, Chi-Chi	7.6	5	0.67	48.5	0.1	1.8	13.3	0.62
1999, Chi-Chi	7.6	5	0.67	48.5	0.1	1.8	23.7	1.62
1999, Chi-Chi	7.6	5	0.67	13	0.18	0.5	5.7	0
1999, Chi-Chi	7.6	5	0.67	13	0.18	0.75	6.6	0.1
1999, Chi-Chi	7.6	5	0.67	13	0.18	0.75	7.9	0.17
1999, Chi-Chi	7.6	5	0.67	13	0.18	0.75	9	0.23
1999, Chi-Chi	7.6	5	0.67	13	0.18	0.75	15	0.29
1999, Kocaeli	7.4	0.5	0.57	11	7.7	1.2	8	0.9
1999, Kocaeli	7.4	0.5	0.57	31	0.55	1.7	6	0.1

References

- Huang, W.; Zou, M.; Qian, J.; Zhou, Z. Consistent damage model and performance-based assessment of structural members of different materials. *Soil Dyn. Earthq. Eng.* **2018**, *109*, 266–272. [CrossRef]
- Ma, Y.; Gong, J.X. Probability Identification of Seismic Failure Modes of Reinforced Concrete Columns based on Experimental Observations. *J. Earthq. Eng.* **2017**, *22*, 1881–1899. [CrossRef]
- Liu, C.; Fang, D.; Zhao, L. Reflection on earthquake damage of buildings in 2015 Nepal earthquake and seismic measures for post-earthquake reconstruction. *Structures* **2021**, *30*, 647–658. [CrossRef]
- Rezania, M.; Faramarzi, A.; Javadi, A.A. An evolutionary based approach for assessment of earthquake-induced soil liquefaction and lateral displacement. *Eng. Appl. Artif. Intell.* **2011**, *24*, 142–153. [CrossRef]
- Finn, W.; Ledbetter, R.; Wu, G. Liquefaction in silty soils: Design and analysis. 1994; pp. 51–76. In *Ground Failures under Seismic Conditions*; ASCE: Reston, VA, USA; p. 51.
- Liao, T.; McGillivray, A.; Mayne, P.; Zavala, G.; Elhakim, A. *Seismic Ground Deformation Modeling Final Report for MAE HD-7a (Year 1)*; Geosystems Engineering/School of Civil & Environmental Engineering, Georgia Institute of Technology: Atlanta, GA, USA, 2002.
- Arulanandan, K.; Li, X.S.; Sivathanan, K. (Siva) Numerical Simulation of Liquefaction-Induced Deformations. *J. Geotech. Geoenviron. Eng.* **2000**, *126*, 657–666. [CrossRef]
- Newmark, N.M. Effects of earthquakes on dams and embankments. *Geotechnique* **1965**, *15*, 139–160. [CrossRef]
- Towhata, I.; Sasaki, Y.; Tokida, K.I.; Matsumoto, H.; Tamari, Y.; Yamada, K. Prediction of Permanent Displacement of Liquefied Ground by Means of Minimum Energy Principle. *Soils Found.* **1992**, *32*, 97–116. [CrossRef]
- Kokusho, T.; Fujita, K. Site Investigations for Involvement of Water Films in Lateral Flow in Liquefied Ground. *J. Geotech. Geoenviron. Eng.* **2002**, *128*, 917–925. [CrossRef]
- Hamada, M. Study on liquefaction induced permanent ground displacements. *Report of Association for the Development of Earthquake Prediction* **1986**. [CrossRef]
- Youd, T.L.; Hansen, C.M.; Bartlett, S.F. Revised Multilinear Regression Equations for Prediction of Lateral Spread Displacement. *J. Geotech. Geoenviron. Eng.* **2002**, *128*, 1007–1017. [CrossRef]
- Wang, J.; Rahman, M.S. A neural network model for liquefaction-induced horizontal ground displacement. *Soil Dyn. Earthq. Eng.* **1999**, *18*, 555–568. [CrossRef]
- Hamada, M.; Towhata, I.; Yasuda, S.; Isoyama, R. Study on permanent ground displacement induced by seismic liquefaction. *Comput. Geotech.* **1987**, *4*, 197–220. [CrossRef]
- Orense, R.; Towhata, I. Prediction of liquefaction—induced permanent ground displacements: A three—dimensional approach. *Tech. Rep. NCEEER* **1992**, *1*, 335–349.
- Gu, W.H.; Morgenstern, N.R.; Robertson, P.K. Progressive failure of lower San Fernando dam. *J. Geotech. Eng.* **1993**, *119*, 333–349. [CrossRef]
- Gu, W.H.; Morgenstern, N.R.; Robertson, P.K. Postearthquake Deformation Analysis of Wildlife Site. *J. Geotech. Eng.* **1994**, *120*, 274–289. [CrossRef]
- Yegian, M.K.; Marciano, E.A.; Ghahraman, V.G. Earthquake-induced permanent deformations: Probabilistic approach. *J. Geotech. Eng.* **1991**, *117*, 35–50. [CrossRef]

19. Baziar, M.H.; Dobry, R.; Elgamal, A.-W.M. Engineering Evaluation of Permanent Ground Deformations Due to Seismically Induced Liquefaction. Tech. Rep. NCEER-92-0007. 1992; 306.
20. Tokida, K.; Matsumoto, H.; Azuma, T.; Towhata, I. Simplified Procedure to Estimate Lateral Ground Flow by Soil Liquefaction. *WIT Trans. Built Environ.* **1993**, *3*, 1–16.
21. Bardet, J.; Mace, N.; Tobita, T. *Liquefaction-Induced Ground Deformation and Failure, a Report to PEER/PG&E. Task 4A-Phase 1*; Civil Engineering Department, University of Southern California: Los Angeles, CA, USA, 1999.
22. Hadush, S.; Yashima, A.; Uzuoka, R.; Moriguchi, S.; Sawada, K. Liquefaction induced lateral spread analysis using the CIP method. *Comput. Geotech.* **2001**, *28*, 549–574. [CrossRef]
23. Aydan, Ö. The stress state of the earth and the earth's crust due to the gravitational pull. In Proceedings of the 35th US Rock Mechanics Symposium, Lake Tahoe, CA, USA, 4–7 June 1995; pp. 237–243.
24. Hamada, M.; Sato, H.; Kawakami, T. A consideration of the mechanism for liquefaction-related large ground displacement. In Proceedings of the Fifth US-Japan Workshop on Earthquake Resistant Design of Lifeline Facilities and Countermeasures Against Soil Liquefaction, Technical Report NCEER-94-0026, Snowbird, UT, USA, 29 September–1 October 1994; pp. 217–232.
25. Youd, T.L.; Perkins, D.M. Mapping of liquefaction severity index. *J. Geotech. Eng.* **1987**, *113*, 1374–1392. [CrossRef]
26. Bartlett, S.F.; Youd, T.L. Empirical prediction of lateral spread displacement. In Proceedings of the Fourth Japan-U.S. Workshop on Earthquake Resistant Design of Lifeline Facilities and Countermeasures for Soil Liquefaction, Honolulu, HI, USA, 27–29 May 1992; pp. 351–365.
27. Bartlett, S.F.; Leslie Youd, T. Empirical prediction of liquefaction-induced lateral spread. *J. Geotech. Eng.* **1995**, *121*, 316–329. [CrossRef]
28. Jounrnan, A.; Jafarian, Y.; Nasri, E. Evaluation of uncertainties in the existing empirical models and probabilistic prediction of liquefaction-induced lateral. *AJSR-Civil Environ. Eng.* **2016**, *48*, 107–110.
29. Kanibir, A. *Investigation of the Lateral Spreading at Sapanca and Suggestion of Empirical Relationships for Predicting Lateral Spreading*; Department of Geological Engineering, Hacettepe University: Ankara, Turkey, 2003.
30. Bawwab, W. Al Probabilistic assessment of liquefaction-induced lateral ground deformations. Ph.D. Thesis, Middle East Technical University, Ankara, Turkey, November 2005.
31. Javadi, A.A.; Rezania, M.; Nezhad, M.M. Evaluation of liquefaction induced lateral displacements using genetic programming. *Comput. Geotech.* **2006**, *33*, 222–233. [CrossRef]
32. Baziar, M.; Saeedi Azizkandi, A. Evaluation of lateral spreading utilizing artificial neural network and genetic programming. *Int. J. Civ. Eng. Trans. B Geotech. Eng.* **2013**, *11*, 100–111.
33. Baziar, M.H.; Ghorbani, A. Evaluation of lateral spreading using artificial neural networks. *Soil Dyn. Earthq. Eng.* **2005**, *25*, 1–9. [CrossRef]
34. Javdanian, H. Field data-based modeling of lateral ground surface deformations due to earthquake-induced liquefaction. *Eur. Phys. J. Plus* **2019**, *134*, 297. [CrossRef]
35. Williams, C.K.; Rasmussen, C.E. *Gaussian Processes for Machine Learning*; MIT Press: Cambridge, MA, USA, 2006; Volume 2, p. 4.
36. Chu, D.B.; Stewart, J.P.; Youd, T.L.; Chu, B.L. Liquefaction-Induced Lateral Spreading in Near-Fault Regions during the 1999 Chi-Chi, Taiwan Earthquake. *J. Geotech. Geoenviron. Eng.* **2006**, *132*, 1549–1565. [CrossRef]
37. Cetin, K.O.; Youd, T.L.; Seed, R.B.; Bray, J.D.; Stewart, J.P.; Durgunoglu, H.T.; Lettis, W.; Yilmaz, M.T. Liquefaction-Induced Lateral Spreading at Izmit Bay During the Kocaeli (Izmit)-Turkey Earthquake. *J. Geotech. Geoenviron. Eng.* **2004**, *130*, 1300–1313. [CrossRef]
38. Sadigh, K.; Chang, C.Y.; Egan, J.A.; Makdisi, F.; Youngs, R.R. Attenuation Relationships for Shallow Crustal Earthquakes Based on California Strong Motion Data. *Seismol. Res. Lett.* **1997**, *68*, 180–189. [CrossRef]
39. van Vuren, T. Modeling of transport demand—Analyzing, calculating, and forecasting transport demand. *Transp. Rev.* **2020**, *40*, 115–117. [CrossRef]
40. Song, Y.; Gong, J.; Gao, S.; Wang, D.; Cui, T.; Li, Y.; Wei, B. Susceptibility assessment of earthquake-induced landslides using Bayesian network: A case study in Beichuan, China. *Comput. Geosci.* **2012**, *42*, 189–199. [CrossRef]
41. Üstün, B.; Melssen, W.J.; Buydens, L.M.C. Facilitating the application of Support Vector Regression by using a universal Pearson VII function based kernel. *Chemom. Intell. Lab. Syst.* **2006**, *81*, 29–40. [CrossRef]
42. Ly, H.B.; Nguyen, T.A.; Pham, B.T. Estimation of Soil Cohesion Using Machine Learning Method: A Random Forest Approach. *Adv. Civ. Eng.* **2021**, *2021*, 8873993. [CrossRef]
43. Nash, J.E.; Sutcliffe, J.V. River flow forecasting through conceptual models part I—A discussion of principles. *J. Hydrol.* **1970**, *10*, 282–290. [CrossRef]
44. Ahmad, M.; Ahmad, F.; Wróblewski, P.; Al-Mansob, R.A.; Olczak, P.; Kamiński, P.; Safdar, M.; Rai, P.; Ahmad, M.; Ahmad, F.; et al. Prediction of Ultimate Bearing Capacity of Shallow Foundations on Cohesionless Soils: A Gaussian Process Regression Approach. *Appl. Sci.* **2021**, *11*, 10317. [CrossRef]
45. Ahmad, M.; Kamiński, P.; Olczak, P.; Alam, M.; Iqbal, M.; Ahmad, F.; Sasui, S.; Khan, B.; Ahmad, M.; Kamiński, P.; et al. Development of Prediction Models for Shear Strength of Rockfill Material Using Machine Learning Techniques. *Appl. Sci.* **2021**, *11*, 6167. [CrossRef]

46. Ahmad, M.; Hu, J.-L.; Ahmad, F.; Tang, X.-W.; Amjad, M.; Iqbal, M.; Asim, M.; Farooq, A.; Ahmad, M.; Hu, J.-L.; et al. Supervised Learning Methods for Modeling Concrete Compressive Strength Prediction at High Temperature. *Materials* **2021**, *14*, 1983. [CrossRef]
47. Chen, W.; Hasanipanah, M.; Nikafshan Rad, H.; Jahed Armaghani, D.; Tahir, M.M. A new design of evolutionary hybrid optimization of SVR model in predicting the blast-induced ground vibration. *Eng. Comput.* **2021**, *37*, 1455–1471. [CrossRef]

Article

A PROMETHEE Multiple-Criteria Approach to Combined Seismic and Flood Risk Assessment at the Regional Scale

Arianna Soldati ¹, Andrea Chiozzi ² , Željana Nikolić ³ , Carmela Vaccaro ^{2,4}  and Elena Benvenuti ^{1,*} ¹ Department of Engineering, University of Ferrara, 44122 Ferrara, Italy; arianna.soldati@edu.unife.it² Department of Environmental and Prevention Sciences, University of Ferrara, 44122 Ferrara, Italy; andrea.chiozzi@unife.it (A.C.); carmela.vaccaro@unife.it (C.V.)³ Faculty of Civil Engineering, Architecture and Geodesy, University of Split, 21000 Split, Croatia; zeljana.nikolic@gradst.hr⁴ OGS, Istituto Nazionale di Oceanografia e di Geofisica Sperimentale, Borgo Grotta Gigante 42/C, 34010 Sgonico, Italy

* Correspondence: elena.benvenuti@unife.it

Abstract: Social vulnerability is deeply affected by the increase in hazardous events such as earthquakes and floods. Such hazards have the potential to greatly affect communities, including in developed countries. Governments and stakeholders must adopt suitable risk reduction strategies. This study is aimed at proposing a qualitative multi-hazard risk analysis methodology in the case of combined seismic and flood risk using PROMETHEE, a Multiple-Criteria Decision Analysis technique. The present case study is a multi-hazard risk assessment of the Ferrara province (Italy). The proposed approach is an original and flexible methodology to qualitatively prioritize urban centers affected by multi-hazard risks at the regional scale. It delivers a useful tool to stakeholders involved in the processes of hazard management and disaster mitigation.

Keywords: risk assessment; multi hazard; seismic risk; flood risk; multiple-criteria decision analysis; PROMETHEE algorithm

Citation: Soldati, A.; Chiozzi, A.; Nikolić, Ž.; Vaccaro, C.; Benvenuti, E. A PROMETHEE Multiple-Criteria Approach to Combined Seismic and Flood Risk Assessment at the Regional Scale. *Appl. Sci.* **2022**, *12*, 1527. <https://doi.org/10.3390/app12031527>

Academic Editor: Igal M. Shohet

Received: 30 November 2021

Accepted: 27 January 2022

Published: 31 January 2022

Publisher's Note: MDPI stays neutral with regard to jurisdictional claims in published maps and institutional affiliations.



Copyright: © 2022 by the authors. Licensee MDPI, Basel, Switzerland. This article is an open access article distributed under the terms and conditions of the Creative Commons Attribution (CC BY) license (<https://creativecommons.org/licenses/by/4.0/>).

1. Introduction

Many areas in Europe and worldwide are increasingly subjected to catastrophic events. These events intensify the exposure of these territories to multi-risk events and make societies more vulnerable to entangled risks [1–7]. Globalization and climate changes are the main culprits of these multi-risk dynamics. Globalization, indeed, makes countries closely linked and interdependent, so communities are not only vulnerable to local extreme events but also to those occurring outside their national territories. Climate change increases, among others, the frequency and intensity of extreme meteorological phenomena, hydrological and flood risk, as well as the risk of fires. The awareness of this worrying trend has determined the need for adequate tools to address and mitigate these risks, as well as information campaigns to foster resilience and coping capacity of communities [5–7].

Understanding risks involving vast inhabited areas is therefore paramount, particularly when assessing potential losses produced by a combination of multiple hazards. Hereafter, a hazard refers to the probability of occurrence in a specified period of a potentially damaging event of a given magnitude in a given area [8]. Total risk is a measure of the expected human (casualties, injuries) and economic (damage to property, activity disruption) losses due to adverse natural phenomena. Such a measure is assumed to be the product of hazard, vulnerability, and exposure instances [9]. Many areas on Earth are subjected to the effects of coexisting multiple hazards, among which floods [3,8] and earthquakes are some of the most widespread [5–7]. Though inhabited environments are affected by multiple hazardous processes, most studies focus on a single hazard [8].

The choice to adopt a multi-risk analysis approach has the potential to play a fundamental role in increasing urban resilience, an essential factor for sustainable development, enabling cities to prepare, respond, and recover when hit by catastrophic events, and therefore prevent or contain economic, environmental, and social losses [1]. However, performing a multi-risk analysis with the tools and methodologies available today raises numerous challenges and difficulties [10–20]. For instance, an updated analysis of multi-hazard aggregated risk for infrastructures considering multiple potential threats has recently been proposed in reference [5].

Risk assessment is indeed carried out through independent procedures that adopt different estimation metrics. This makes comparisons difficult and precludes considering correlations or cascading effects [11]. On the contrary, the Multiple-Criteria Decision Analysis (MCDA) technique is a promising approach in multiple-hazard risk analysis, even if this route has been scarcely explored to date [21–24].

To pave the way for sustainable land-use plans and risk-mitigation strategies, we must analyze, quantify, and, especially, compare all concurrent risks [25]. To date, single-risk assessment is generally performed by means of independent procedures, whose results cannot be compared. The purpose of this paper is to devise an approach for the qualitative assessment of combined risks at the regional scale. In particular, the objective is to jointly analyze the flood and seismic risk for the Ferrara province area. The proposed approach is based on the suitable use of the Preference Ranking Organization Method for Enrichment Evaluations (PROMETHEE), a Multiple-Criteria Decision Analysis technique [26–29]. The province of Ferrara is in a flatland area in the northern part of Italy. Historically, it has been mainly hit by floods and seismic events. Though floods are exogeneous processes, whereas earthquakes are exogenic, we assume flood and seismic hazards to be the two relevant hazards for determining a priority list. This priority list is meant to be useful to stakeholders and public agencies called to rapidly implement investment plans aimed to prevent economic and life losses and foster the coping capacity of communities to manage the adverse conditions induced by natural disasters. Particularly, the present objective is to prioritize this among the different municipalities. Therefore, the adopted level of observation is at the scale of the area included within each municipality.

Assuming the municipalities of the province of Ferrara as the alternatives of the multiple-criteria analysis, the proposed approach defines a priority ranking among all the alternatives. The outcome is represented by qualitative risk maps. These maps are useful tools for stakeholders involved in community management and risk prevention.

Among the Multi-Risk Methodologies applied in Italian territories, we recall here the works by Gallina et al. [23,24] for the assessment of the impact of sea-level rise, coastal erosion, and storm surge induced by climate changes in coastal zones in North Italy. Flood and seismic risks have been multi-assessed through a Machine Learning framework recently devised by the authors for the Emilia Romagna region [30]. Up to now, the present contribution is the very first to use an MCDA approach for multi-risk analysis of combined flood and earthquake risks, while no other relevant contributions exist dealing with multi-hazard analyses of the Province of Ferrara.

2. Materials and Methods

2.1. Geographical Context and Single Risk Description

To introduce the concept of multi-risk assessment, it is first necessary to discuss the concept of single risk. Risk is basically defined as the product of three parameters: Hazard, vulnerability, and exposure [9]. A hazard represents the probability that an adverse event will occur in a specific area and in a specific time interval. Vulnerability, on the other hand, is an intrinsic characteristic of a system; it represents its propensity to suffer a certain level of damage following the occurrence of a hazard event. Finally, exposure indicates the presence of people, critical infrastructures, natural and cultural heritage, and much more still in hazard zones that are thereby subject to potential losses [4].

The concept of multi-risk follows as the overall risk from a multi-hazard and multi-vulnerability perspective. The term multi-hazard indicates several hazards affecting the same exposed elements (with or without space–time coincidence) or the occurrence of a hazard event that triggers another one giving rise to a domino or cascade effect. Furthermore, the term multi-vulnerability indicates those circumstances where several elements are sensitive to different possible vulnerabilities towards the various hazards affecting them or vulnerabilities that vary over time [10,11].

The territory of the province of Ferrara is located at the north-eastern extremity of the Padana Plain, a flat land area in the north part of Italy crossed by the Po River and bathed by the Adriatic Sea on the east side. It is characterized by minimum land slopes and its altimetry is mainly under the mean sea level, as almost half of its area is below the mean sea level, as shown in Figure 1. Moreover, the eastern part of the territory is affected by subsidence phenomena as well. These ground-level modifications, caused mainly by anthropogenic actions as well as by geological and neotectonic factors [31,32], produced a subsidence rate of up to -2.5 mm/year [31]. The main watercourses that flow through the Ferrara province are the Po River, which marks the northern border of the Reno River, and the Idice and Sillaro streams, which are not tributaries of the Po River, and cross the province in their last stretch. Furthermore, numerous artificial canals flow through the Ferrara Province, including the Cavo Napoleonico, which connects the Po and Reno rivers, and the Idrovia Ferrarese.

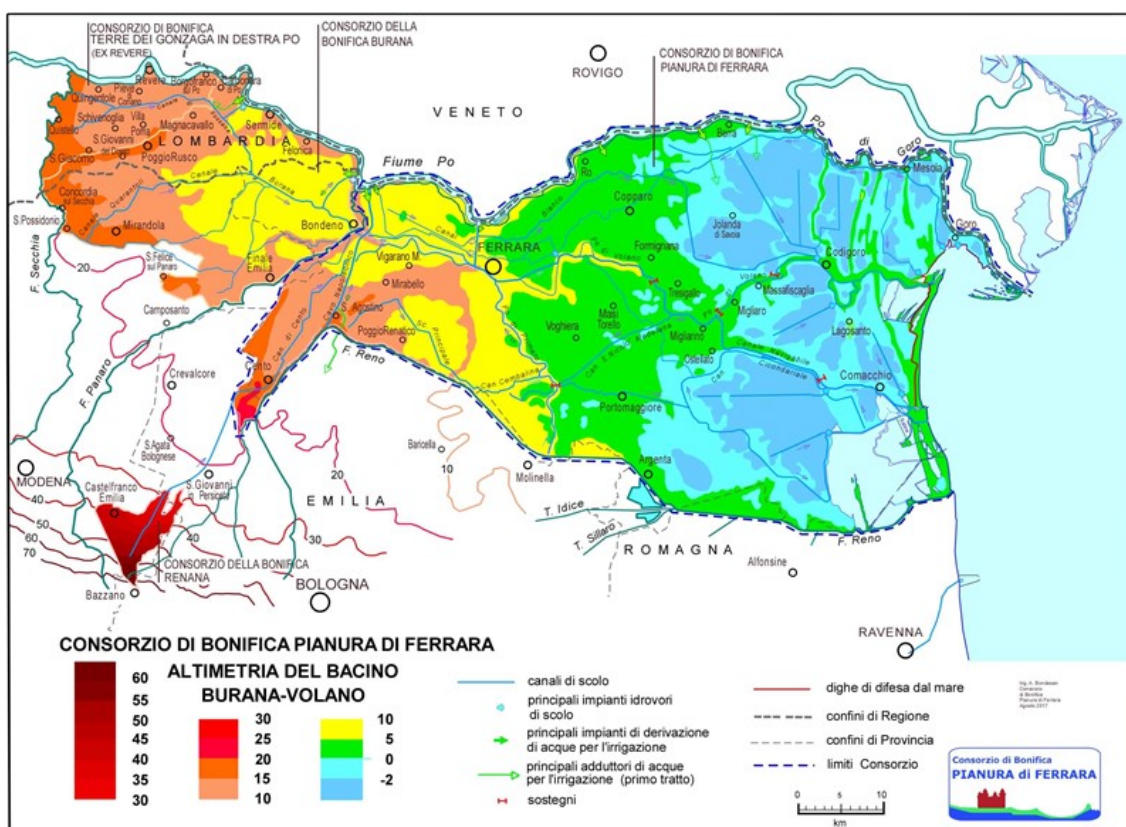


Figure 1. Altimetric map of Ferrara province (free source [https://www.bonificaferrara.it/images/Allegati/SITL/4d-3-altimetria\(100\).pdf](https://www.bonificaferrara.it/images/Allegati/SITL/4d-3-altimetria(100).pdf), accessed on 3 January 2022, made available by Consorzio di Bonifica Pianura di Ferrara). The minimum and maximum extremal values of the ground level over the sea in the legend are -2 m (dark blue) and 60 m (dark red), respectively.

The province of Ferrara includes 23 municipalities. Attention is hereafter restricted to the two main risks of the area under study, namely flood and seismic risks. Site effects associated with inherent geological morphology and instability issues such as liquefaction

were not considered, for simplicity. Desertification is another risk that has been emerging in recent years in the Po delta plain [10]. However, it has not been considered in the present contribution. Hereafter, flood risk refers to the risk that depends on the probability of occurrence of a flood, evaluated concerning the different typologies of watercourses that flow through the territory. The flood risk for the selected region was quantified by the Land Reclamation Authority of the province of Ferrara (Consorzio di Bonifica Pianura di Ferrara), and accounts for flood hazard, exposure, and vulnerability parameters.

Seismic risk depends on the peak ground acceleration (PGA) as well as on the vulnerability of the built environment and the exposure of people and economic activities. We exploited the map of seismic hazard provided by the Italian Institute of Volcanology and Geophysics (INGV), and the seismic classification of municipalities in Emilia (free source <https://ambiente.regione.emilia-romagna.it/en/geologia/seismic-risk/seismic-classification>, accessed on 26 January 2022), shown in Figure 2a. In Figure 2b, Italy is divided into different areas according to peak ground acceleration values [33] (free source <http://zonesismiche.mi.ingv.it/>, accessed on 26 January 2022).

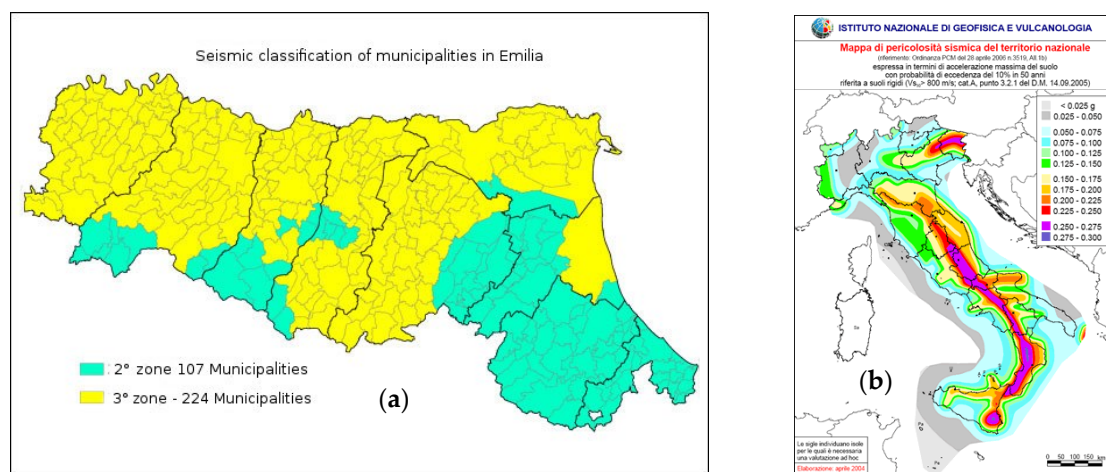


Figure 2. (a) Seismic classification of municipalities in Emilia (<https://ambiente.regione.emilia-romagna.it/en/geologia/seismic-risk/seismic-classification>, accessed on 26 January 2022). (b) Seismic Hazard Map of Italy (free source from INGV webpage <http://zonesismiche.mi.ingv.it/>, accessed on 26 January 2022).

Finally, we used the database made available by the Italian National Institute of Statistics (Istat). This database was used in 2018 by the Italian Superior Institute for Environmental Protection and Research (ISPRA) to produce seismic, hydrogeological, volcanic, and social vulnerability hazard maps for the entire Italian peninsula. The reader is referred to the pertinent report by Trigila et al. [34] to obtain a detailed description of ISPRA's methodology for the processing of the data.

2.2. The PROMETHEE Method

The proposed multi-hazard risk analysis procedure for the region under study is based on PROMETHEE [26–29], a Multiple-Criteria Decision Analysis method. It belongs to the class of aggregation methods based on outranking relationships. It is known for its simplicity and the ability to analyze information from multiple sources. PROMETHEE allows one to jointly compare data originally expressed in different units and scales. A flux diagram explaining the various steps of the PROMETHEE-based analysis can be found in reference [29].

PROMETHEE deals with maximization or minimization problems with k different criteria of the kind

$$\max(\text{ormin}) \{g_1(a), g_2(a), \dots, g_k(a) | a \in A\}, \quad (1)$$

where A is a finite set of possible alternatives and function $g_j(a)$ represents the performance of the j -th criterion. Let us consider two alternatives, $(a, b) \in A$. We have the following cases:

$$\begin{cases} \forall j : g_j(a) \geq g_j(b) \\ \exists k : g_k(a) > g_k(b) \end{cases} \Leftrightarrow aPb,$$

$$\forall j : g_j(a) = g_j(b) \Leftrightarrow aIb,$$

$$\begin{cases} \exists s : g_s(a) > g_s(b) \\ \exists r : g_r(a) < g_r(b) \end{cases} \Leftrightarrow aRb,$$
(2)

where P, I , and R denote preference (P), indifference (I), or incompatibility relations (R) of one alternative over the other, respectively.

By comparing all the alternatives for each criterion, a hierarchy of alternatives belonging to the starting space A will be obtained. When comparing two actions, $(a, b) \in A$. the result of this comparison is expressed in terms of the preference function $\wp : A \times A \rightarrow (0, 1)$ that represents the intensity of the preference of alternative a towards alternative b . Therefore, $\wp(a, b) = 0$ indicates no preference of a over b (or indifference), $\wp(a, b) \simeq 0$ indicates a weak preference of a over b , $\wp(a, b) \simeq 1$ indicates a strong preference of a over b , and $\wp(a, b) = 1$ indicates a strict preference of a over b . In practice, the preference function will often be a function of the difference between the evaluations of the two alternatives considered:

$$\wp(a, b) = P(g(a) - g(b)) = P(d),$$
(3)

where P is a non-decreasing function, equal to zero for negative values of d . PROMETHEE offers six types of preference functions (see Table 1).

Table 1. Types of preference function.

Generalized Criterion	Definition	Parameters to Fix
Type 1: usual criterion	$P(d) = \begin{cases} 0 & d \leq 0 \\ 1 & d > 0 \end{cases}$	-
Type 2: U-shape criterion	$P(d) = \begin{cases} 0 & d \leq q \\ 1 & d > q \end{cases}$	q
Type 3: V-shape criterion	$P(d) = \begin{cases} 0 & d \leq p \\ \frac{d}{p} & 0 \leq d \leq p \\ 1 & d > p \end{cases}$	p
Type 4: Level criterion	$P(d) = \begin{cases} 0 & d \leq q \\ \frac{1}{2} & q \leq d \leq p \\ 1 & d > p \end{cases}$	p, q
Type 5: V-shape with indifference criterion	$P(d) = \begin{cases} 0 & d \leq q \\ \frac{d-q}{p-q} & q \leq d \leq p \\ 1 & d > p \end{cases}$	p, q
Type 6: Gaussian criterion	$P(d) = \begin{cases} 0 & d \leq 0 \\ 1 - e^{-\frac{d^2}{2s^2}} & d > 0 \end{cases}$	s

Therefore, a preference index is defined as follows:

$$\begin{cases} \pi(a, b) = \sum_{j=1}^k P_j(a, b)w_j \\ \pi(b, a) = \sum_{j=1}^k P_j(b, a)w_j \end{cases},$$
(4)

where $\pi(a, b)$ expresses the degree to which a is preferred to b over all criteria and vice versa, and w_j is the weight of each criterion and expresses a measure of the importance of the relative criterion.

For all the criteria, a classification is available for the various alternatives necessary to define the so-called outranking flows, which are the fundamental units for the PROMETHEE methodology. Each alternative a faces $(n - 1)$ other alternatives that belong to the generic space A . The two following outranking flows are defined:

$$\begin{cases} \Theta^+(a) = \frac{1}{n-1} \sum_{x \in A} \pi(a, x) \\ \Theta^-(a) = \frac{1}{n-1} \sum_{x \in A} \pi(x, a) \end{cases} \quad (5)$$

where x represents the deviation of the specific preference function with respect to the same function of preference for the other alternatives. $\Theta^+(a)$ expresses how alternative a outranks all the others, otherwise $\Theta^-(a)$ expresses how alternative a is outranked by all the others. The higher $\Theta^+(a)$ (lower $\Theta^-(a)$) is, the more likely alternative a is strongest; otherwise, alternative a , compared to the others, is weakest when $\Theta^+(a)$ assumes small values. Once these two flows have been defined, it becomes very simple to make comparisons between alternatives and subsequently establish their order.

PROMETHEE offers several ways to view the results; the main ones are illustrated below:

- PROMETHEE I Partial Ranking: This is a partial ranking of the alternatives, based on positive and negative flows, and includes preferences, indifference, and incomparability. This scheme allows, therefore, to compare, where possible, the alternatives and establish their partial order of preference through the indices and the related outranking flows.
- PROMETHEE II Complete Ranking: This is useful when the decision maker needs a complete hierarchy among the alternatives of the problem. In this case, the alternatives will be compared in relation to their net flow $\Theta(a) = \Theta(a)^+ - \Theta^-(a)$. PROMETHEE II allows a complete classification of the alternatives; however, it is less realistic and poor in information as it eliminates any possible factor of incomparability between the different alternatives.
- PROMETHEE Table: This displays the Θ , Θ^+ , and Θ^- scores. The actions are ranked according to the PROMETHEE II complete ranking.
- PROMETHEE Rainbow: This is a diagram that allows one to highlight, for each alternative, the criteria that positively or negatively affect the final result.
- Profile of alternatives: This is a diagram that shows, for each alternative, the net flow Θ of each criterion.

2.3. Data Collection and Processing

Both flood and seismic risks have been included in PROMETHEE as criteria according to their components (hazard, exposure, and vulnerability), while the municipalities, i.e., the object on which to evaluate the criteria, are the alternatives. Risk parameters for each municipality are made available by the National Institute of Vulcanology and Geophysics (INGV), the Italian National Institute of Statistics (Istat), and the Land Reclamation Authorities of the Province of Ferrara. Accordingly, we have drawn from the aforementioned databases a simplified map of the flood risk. In particular, Figure 3 displays the flood hazard for the Province of Ferrara in terms of the probability of floods. In this map, the classification is based on Italian Government Decree n. 49/2010 [35]. Accordingly, frequent floods are defined as those having a high probability of occurrence, with a return period of $20 \leq T \leq 50$ years (P3); infrequent floods have an average probability of occurrence with a return period of $100 \leq T \leq 200$ years (P2); finally, low-probability floods have a return period of $200 < T \leq 500$ years (P1).

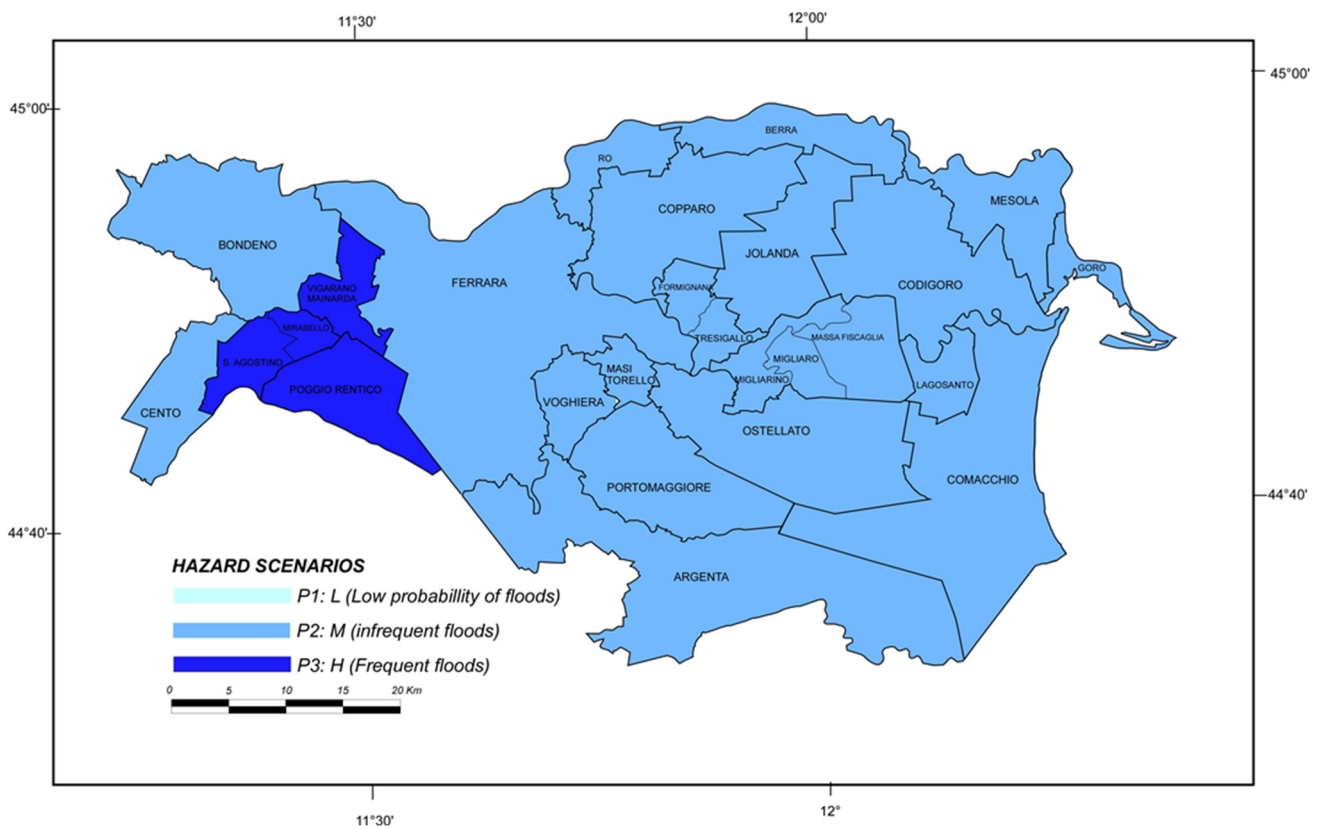


Figure 3. Map of the flood hazard for the province of Ferrara in terms of probability of flood.

Figure 4 provides a map of the seismic hazard for the province of Ferrara in terms of peak ground acceleration (PGA). The PGA-intervals are indicated in the legend.

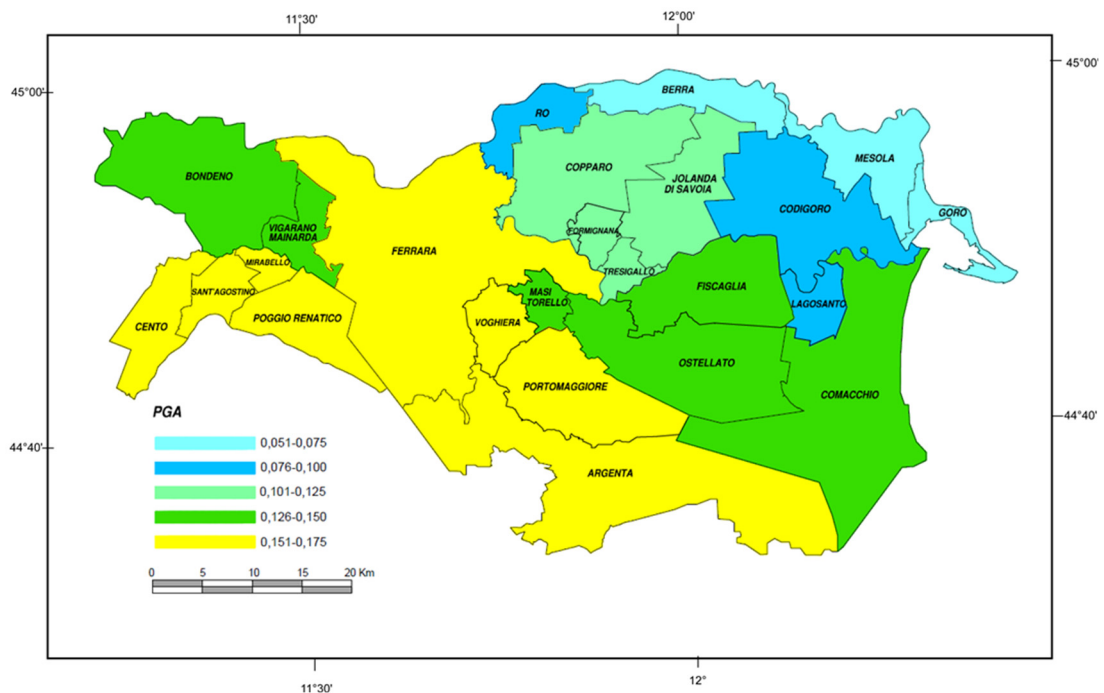


Figure 4. Map of the seismic hazard for the province of Ferrara in terms of peak ground acceleration.

As for exposure-related criteria, for each municipality, we adopted three parameters: Land use percentage, the number of strategic buildings, and population density. All of them

were drawn from the Istat database. The strategic buildings were defined based on the presence and number of halls, police stations, fire brigade buildings, schools, universities, water lifting plants, hospitals, and civil protection centers. This information was obtained from the website of the province of Ferrara (<http://www.provincia.fe.it/>, 1 October 2021), as per educational and public institutions and centers, and from the website of the Consorzio di Bonifica Pianura di Ferrara as per water lifting plants (<https://www.bonificaferrara.it/>, 1 October 2021).

Specifically, four classes of land use percentages were obtained based on the ratio between the urbanized area divided by the total area. In synthesis, we collected the municipalities into four land use classes (Figure 5), four classes in terms of the number of strategic buildings (Figure 6), and four classes of population density (Figure 7).

As for the vulnerability criteria, we adopted a single non-dimensionalized parameter, which accounts for the average age of buildings. Knowing the age of construction and the corresponding number of buildings, we computed the following vulnerability index:

$$I_v = \frac{A \alpha_1 + B \alpha_2 + C \alpha_3 + D \alpha_4}{A + B + C + D},$$

where *A*, *B*, *C* e *D* represent the number of buildings built between the end of 1800 and 1945; the number of buildings built between 1946 and 1980; the number of buildings built between 1981 and 2000, and finally, the number of buildings built from 2001 up to now. α_1 , α_2 , α_3 e α_4 are coefficients equal to 1, 0.75, 0.5, and 0.25, respectively. The vulnerability index I_v results in being mainly related to the age of buildings, and its map is shown in Figure 8.

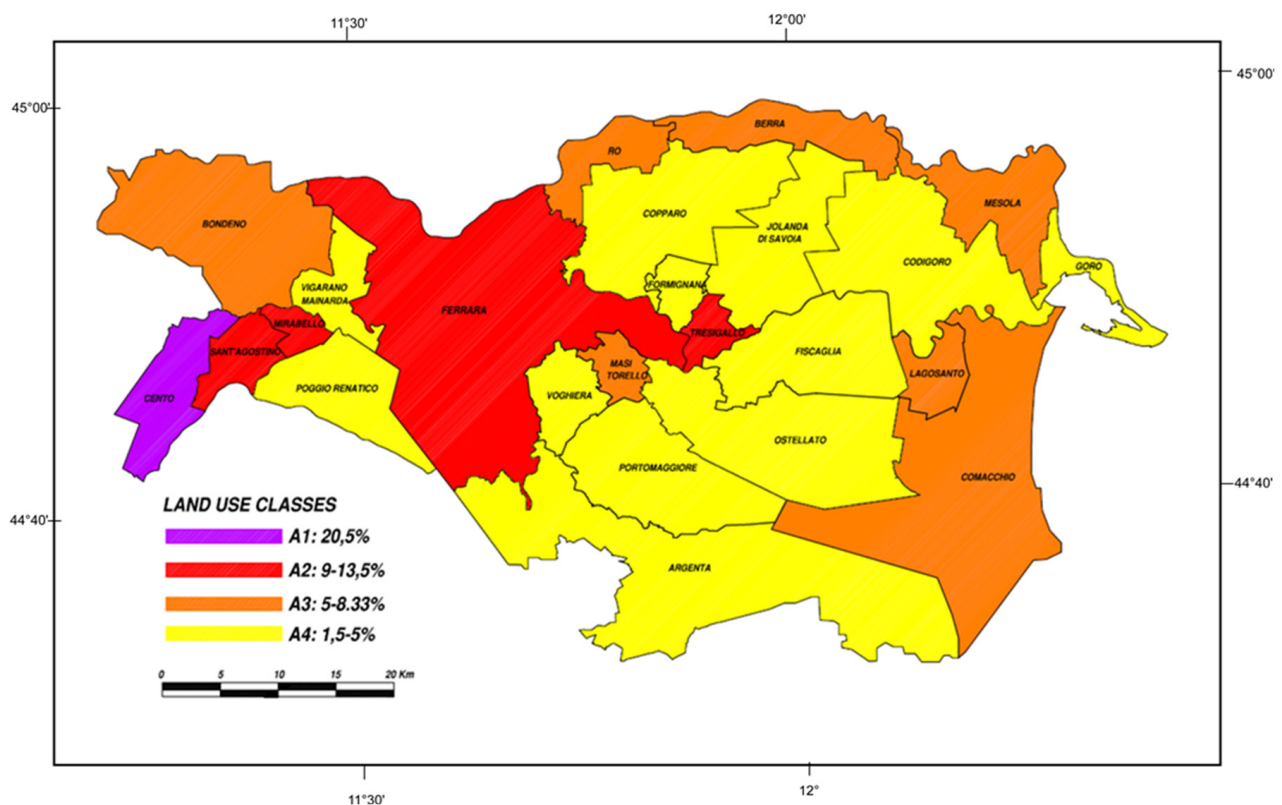


Figure 5. Land use map for the province of Ferrara.

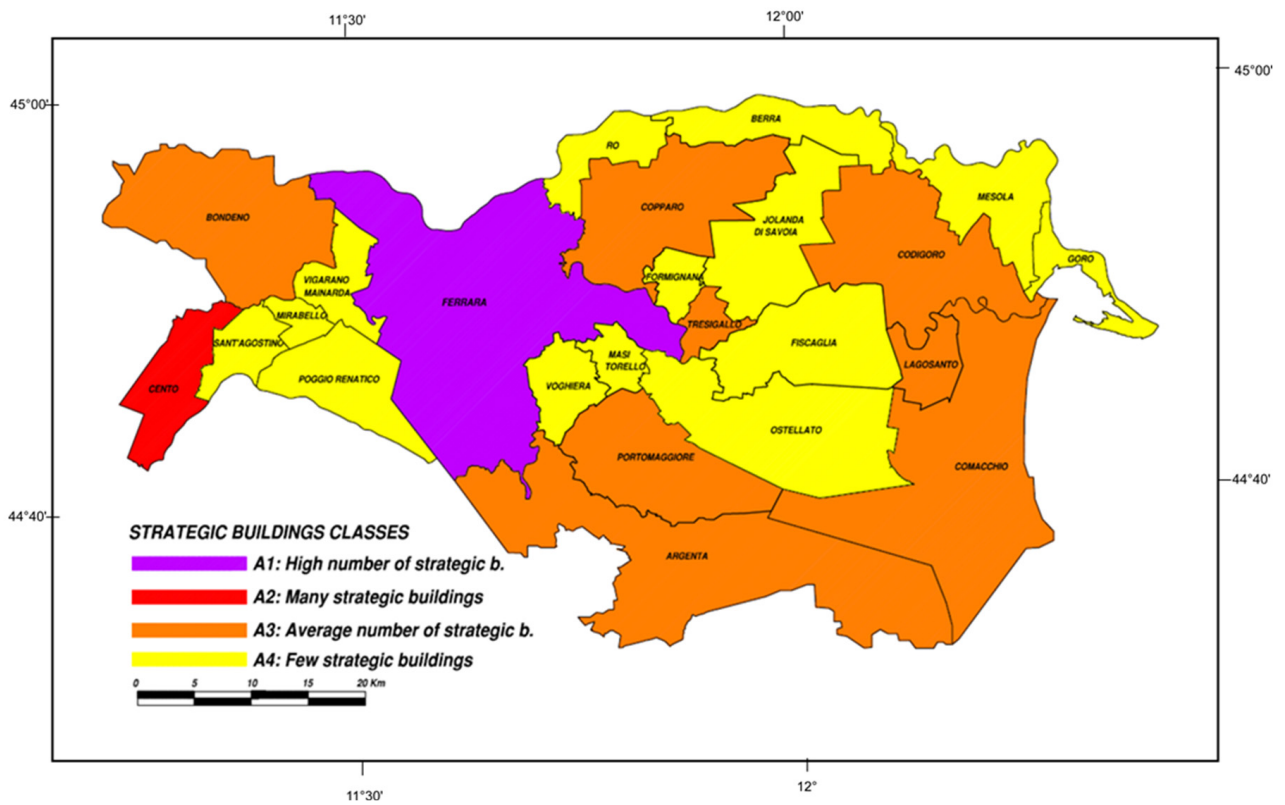


Figure 6. Map of strategic buildings incidence for the province of Ferrara.

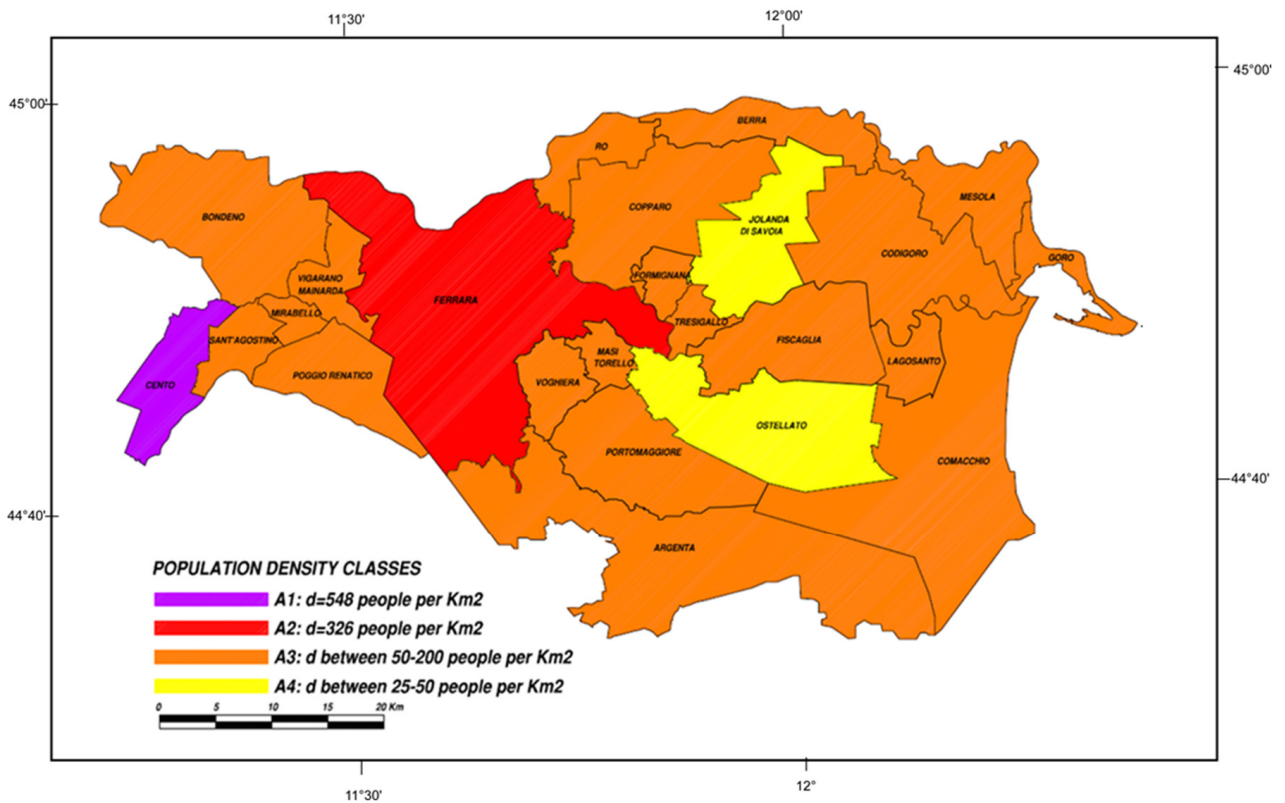


Figure 7. Map of the population density for the province of Ferrara.

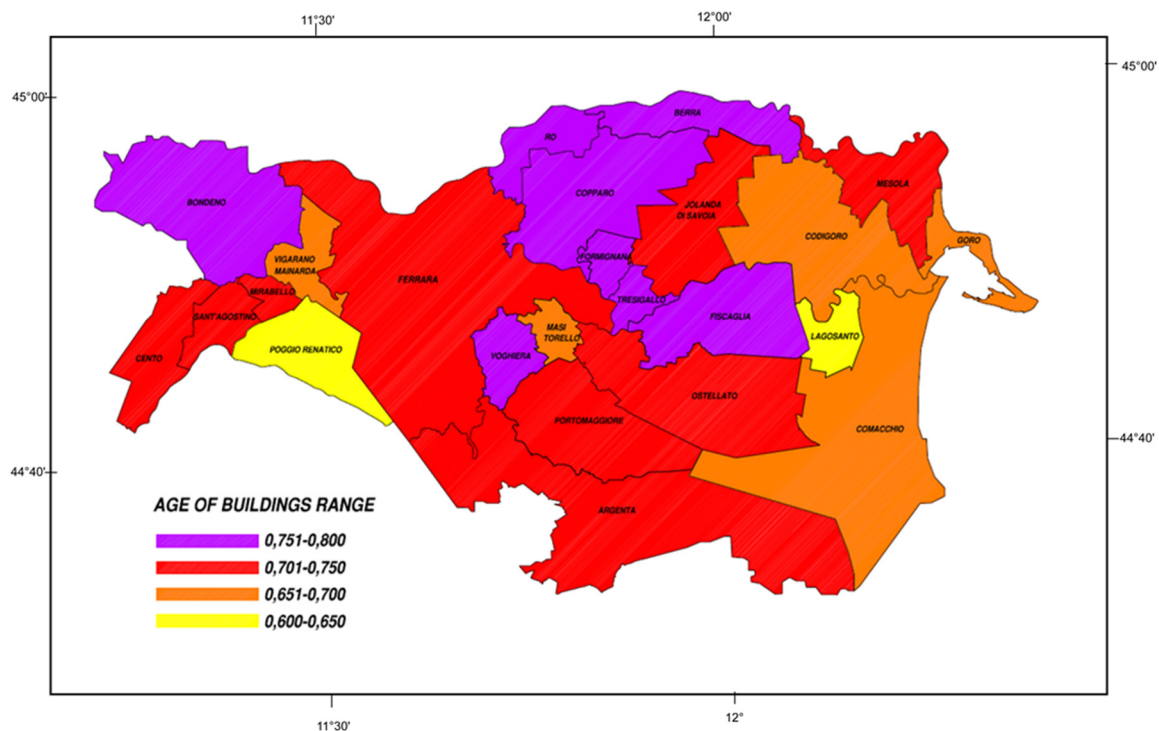


Figure 8. Map of the vulnerability parameter for the province of Ferrara computed as a function of the building age.

2.4. Normalization and Weight Assignment

All the data have been collected in an evaluation matrix, whose rows correspond to each alternative (i.e., each municipality), while each column corresponds to each selected criterion. In other words, the i, j -th element of the evaluation matrix expresses the value of the i -th alternative relating to the attribute of the j -th criterion and describes the performance of each alternative regarding each criterion.

It should be noted that criteria are represented through different scales and units. This precludes mutual comparisons. Thus, it is necessary to further homogenize the data contained in the evaluation matrix and proceed with comparisons through normalization. Through the preference function, the performance of the alternatives is transformed into a dimensionless value, ranging from 0 to 1. As a first attempt, we adopted the Type 1 preference function described in Table 1, which does not require the definition of any threshold. Subsequently, the linear preference function was also used.

Finally, we attributed weights to each criterion. Through this step, decision makers can make their preferences explicit, since it is not ensured that all the criteria take on the same importance. We first decided to attribute the same weight to each criterion. Then, a sensitivity analysis was performed with varying weights.

The risk maps shown in the following sections indicate three classes of risk levels, namely low, medium, high. It is emphasized that this classification must be intended as a pure ranking in terms of the relative urgency of investments. It does not at all intend to indicate the level of safety in absolute terms of the various municipalities. This classification answers the question as to whether the method can provide the priority level associated with a certain municipality and help to decide how to distribute investments over various municipalities.

2.5. Sensitivity Analysis

To verify the reliability of the results obtained, a sensitivity analysis was carried out. During this sensitivity analysis, we retraced the procedure by which the results were obtained and identified the steps most affected by uncertainties and subjectivity,

considering their influence on the final ranking. Specifically, the choice of the preference function and the choice of weights appeared to be the most subjective. As for the choice of the preference function, a previous study [26] recommends assuming a linear preference function endowed with the definition of p, q thresholds. Two approaches are adopted for the determination of p and q : The so-called zero-max method, which imposes that the indifference threshold q is assigned the value of zero while the preference threshold p is set to be equal to the maximum difference between the evaluations of the criteria.

The mean-std method requires the calculation of the average value and the standard deviation of a set of differences between the evaluations of the criteria. In the mean-std method, the indifference threshold is assigned the value of the difference between the average value and standard deviation, while the sum between the average value and standard deviation is assigned to the preference threshold. Following [26–28], we adopted the preference function of the linear type for the quantitative criteria, that is flood hazard, land use, the age of buildings, and population density. However, the algorithm was also run by choosing the usual preference function, which is the simplest possible one. The thresholds were computed as shown in Table 2. As for the sensitivity on the weights, the four scenarios described in Table 3 have been considered.

Table 2. Preference functions and the associated thresholds $p, q,$ and s .

	Criteria					
	Flood Hazard	PGA	Land Use	Strategic Buildings	Age of Buildings	Population Density
Min/Max	max	Max	max	max	max	max
Weight	1	1	1	1	1	1
Preference function	Usual	Linear	Linear	Usual	Linear	Linear
Thresholds	absolute	Absolute	absolute	absolute	absolute	absolute
q: Indifference, zero-max	n/a	0.000	0.0000	n/a	0.000	0.000
p: Preference (zero-max)	n/a	0.098	0.1896	n/a	0.158	523.00
s: Gaussian (zero-max)	n/a	n/a	n/a	n/a	n/a	n/a
q: Indifference (mean-std)	n/a	0.093	0.0261	n/a	0.0676	16.10
p: Preference (mean-std)	n/a	0.155	0.1081	n/a	0.766	238.60
s: Gaussian (mean-std)	n/a	n/a	n/a	n/a	n/a	n/a

Table 3. Sensitivity analysis on the weights of the criteria.

Sensitivity Analysis: Increase of Single Criteria Weights	
Scenario 0	All criteria have the same weight. $p = 17\%$
Scenario 1	Increase the weight of the i -th criterion by 50% compared to its initial value. $p_i = 25.5\%; p_{\text{other criteria}} = 14.9\%$
Scenario 2	Increase the weight of the i -th criterion by 50% compared to its previous value. $p_i = 38.2\%; p_{\text{other criteria}} = 12.3\%$
Scenario 3	Increase the weight of the i -th criterion by 50% compared to its previous value. $p_i = 57.4\%; p_{\text{other criteria}} = 8.5\%$

3. Results

In the following Section, we describe the outcomes of the multiple-criteria analysis for the usual and linear preference function as well as the results of the sensitivity analysis performed for varying weight changes.

3.1. Usual Preference Function

When the usual preference function is used, the algorithm assumes equal weights. We recall that, here, thresholds p and q are not required. Basically, what is provided to the analyst is an order of priority where the municipalities in the province of Ferrara are ordered from the most sensitive to combined flood and seismic risk to the one that is least affected. Table 4 shows the final ranking of the alternatives.

Table 4. Ranking of alternatives for the usual preference function.

Rank	Alternatives	Θ	Θ^+	Θ^-
1	Ferrara	0.6111	0.7302	0.119
2	Cento	0.5873	0.7222	0.1349
3	Tresigallo	0.4127	0.6111	0.1984
4	Vigarano Mainarda	0.2857	0.5873	0.3016
5	Mirabello + Sant'Agostino	0.2698	0.5794	0.3095
6	Argenta + Portomaggiore	0.2381	0.5238	0.2857
7	Bondeno	0.1825	0.4921	0.3095
8	Copparo	0.0238	0.4127	0.3889
9	Poggio Renatico	0.0238	0.4524	0.4286
10	Comacchio	0.0000	0.4048	0.4048
10	Formignana	0.0000	0.381	0.381
12	Voghiera	-0.0238	0.3651	0.3889
13	Lagosanto	-0.0317	0.3889	0.4206
14	Berra	-0.1587	0.3016	0.4603
15	Masi Torello	-0.1746	0.2937	0.4683
16	Ro	-0.1905	0.2857	0.4762
17	Fiscaglia	-0.2063	0.2778	0.4841
18	Mesola	-0.2857	0.2381	0.5238
19	Ostellato	-0.3571	0.1984	0.5556
20	Goro	-0.3651	0.1984	0.5635
21	Codigoro	-0.3651	0.2222	0.5873
22	Jolanda di Savoia	-0.4762	0.1429	0.619

This is not the only way to visualize the results: The PROMETHEE rainbow plot, shown in Figure 9, allows one to highlight, for each alternative, the criteria that positively or negatively affect the results. In Figure 9, the colors are representative of the criterion: Yellow indicates the criteria relating to exposure, red is used for seismic hazard, green for vulnerability, and blue for flood hazard. For example, for the municipality of Ferrara (first in the ranking), it can be observed that the criterion that has a negative effect is the one relating to the flood hazard, whereas the other criteria have a positive effect on the Ferrara municipality. On the contrary, in the municipality of Jolanda di Savoia (last in the ranking), the only criterion that has a positive influence is the one relating to vulnerability, while all the others have a negative influence.

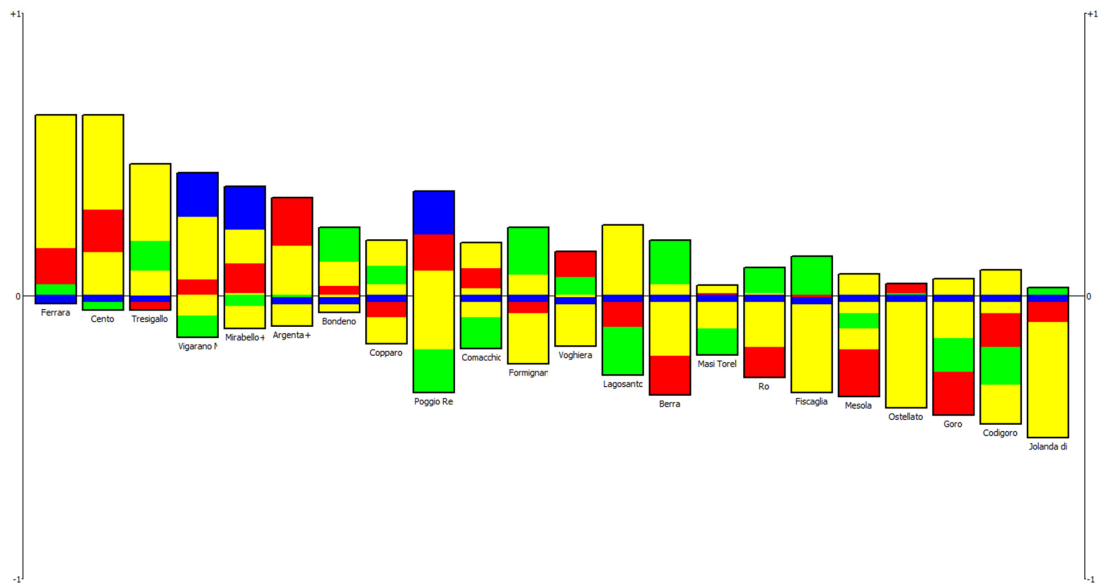


Figure 9. PROMETHEE rainbow plot for the usual preference function. On the vertical axis, the preference function Θ is reported. The yellow bar indicates the criteria relating to exposure, red is used for seismic hazard, green for vulnerability, and blue for hydraulic hazard.

Based on the ranking provided by PROMETHEE, it is possible to create a risk map of the municipalities of the province of Ferrara that highlights high-priority areas as those with a high level of combined flood and seismic risk, medium priority areas as the areas characterized by a medium combined-risk level, and, finally, low combined-risk areas.

This map is shown in Figure 10. It can be seen that the three risk levels are identified by three different colors: Red is used for high risk, orange for medium risk, and yellow for low risk.

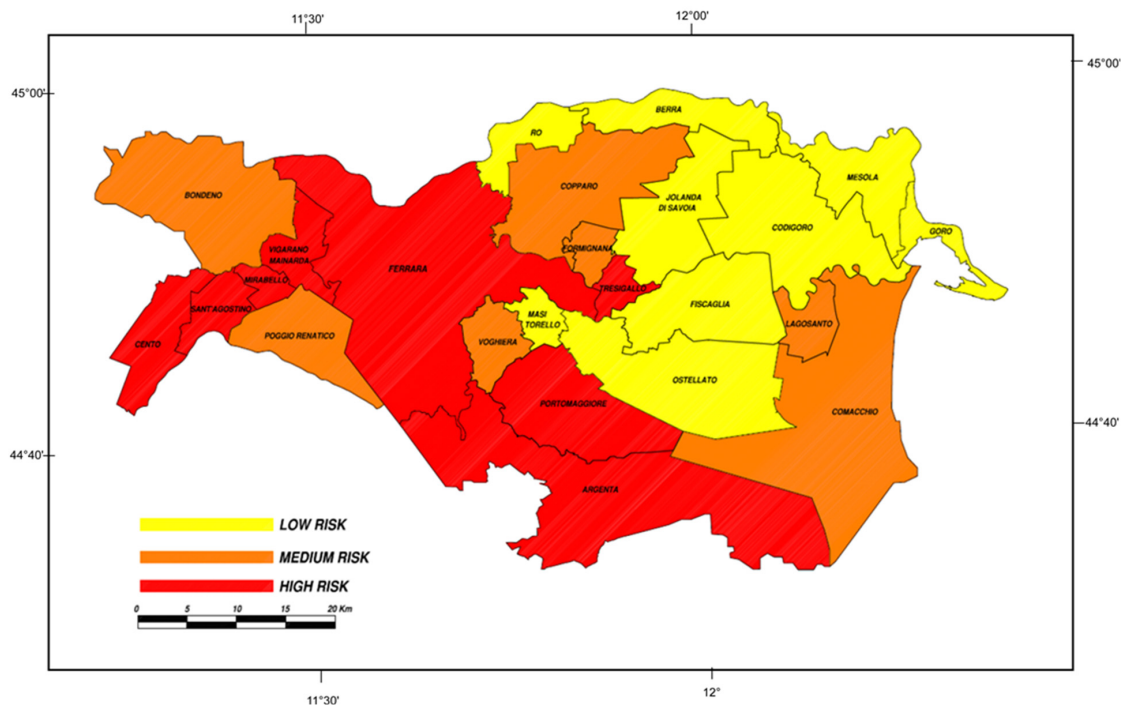


Figure 10. Multiple-risk map for the Ferrara province obtained for the usual preference function (Type 1 in Table 1). The risk levels strictly indicate the relative priority ranking for decision-makers and do not indicate the effective safety level of the various municipalities.

3.2. Linear Preference Function

The ranking of alternatives for the linear preference function and zero-max method is shown in Table 5, while the corresponding multi-risk map is shown in Figure 11. These maps were obtained by associating the quantitative criteria, i.e., flood hazard, land use, age of buildings, and population density, with a linear preference function, while thresholds q and p were determined with the zero-max method.

Table 5. Ranking of alternatives for the linear preference function and zero-max method.

Rank	Alternatives	Θ	Θ^+	Θ^-
1	Cento	0.459	0.5086	0.0496
2	Ferrara	0.3545	0.393	0.0385
3	Tresigallo	0.1821	0.2642	0.0821
4	Mirabello + Sant'Agostino	0.1444	0.2622	0.1179
5	Argenta + Portomaggiore	0.1352	0.2182	0.0829
6	Bondeno	0.1257	0.2069	0.0812
7	Vigarano Mainarda	0.112	0.255	0.143
8	Copparo	0.0505	0.1684	0.1179
9	Poggio Renatico	0.031	0.2216	0.1906
10	Comacchio	0.0224	0.1631	0.1406
10	Voghiera	-0.0422	0.0984	0.1406
12	Formignana	-0.0721	0.0937	0.1657
13	Fiscaglia	-0.0761	0.0868	0.1628
14	Lagosanto	-0.0898	0.1385	0.2283
15	Codigoro	-0.101	0.1155	0.2164
16	Ostellato	-0.1092	0.0736	0.1828
17	Ro	-0.1362	0.0589	0.195
18	Masi Torello	-0.1371	0.0557	0.1928
19	Berra	-0.1551	0.0688	0.2239
20	Jolanda di Savoia	-0.1947	0.0408	0.2355
21	Mesola	-0.2203	0.0353	0.2556
22	Goro	-0.283	0.0137	0.2968

For a linear preference function of the aforementioned quantitative criteria, and thresholds q and p determined by the mean-std method, we obtained the results shown in Table 6 and Figure 12.

By comparing the results obtained from the usual and the linear preference functions, it can be understood that changes of the preference function do not reflect large changes of the final risk maps. The only difference is that the risk levels of the municipality of Vigarano Mainarda swap with Bondeno, and Fiscaglia swaps with Lagosanto.

By comparing the maps in Figures 11 and 12, obtained with the thresholds chosen with the zero-max and mean-std methods, respectively, we observe that the risk levels of Lagosanto, Vigarano Mainarda, and Codigoro increase. Particularly, we observe that the choice of the preference function affects the final ranking of the alternatives especially when the thresholds are chosen according to the mean-std method.

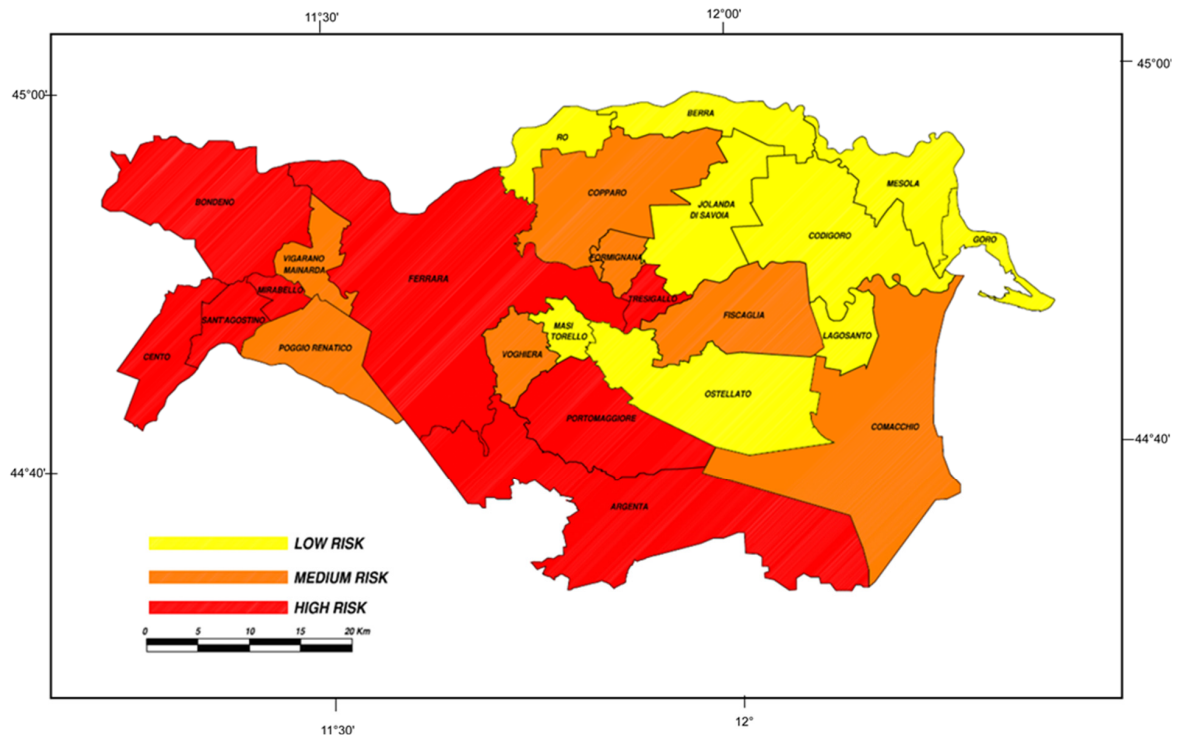


Figure 11. Multiple-risk map for the Ferrara province for the linear preference function with the thresholds chosen with the zero-max method. The risk levels strictly indicate the relative priority ranking for decision-makers and do not indicate the effective safety level of the various municipalities.

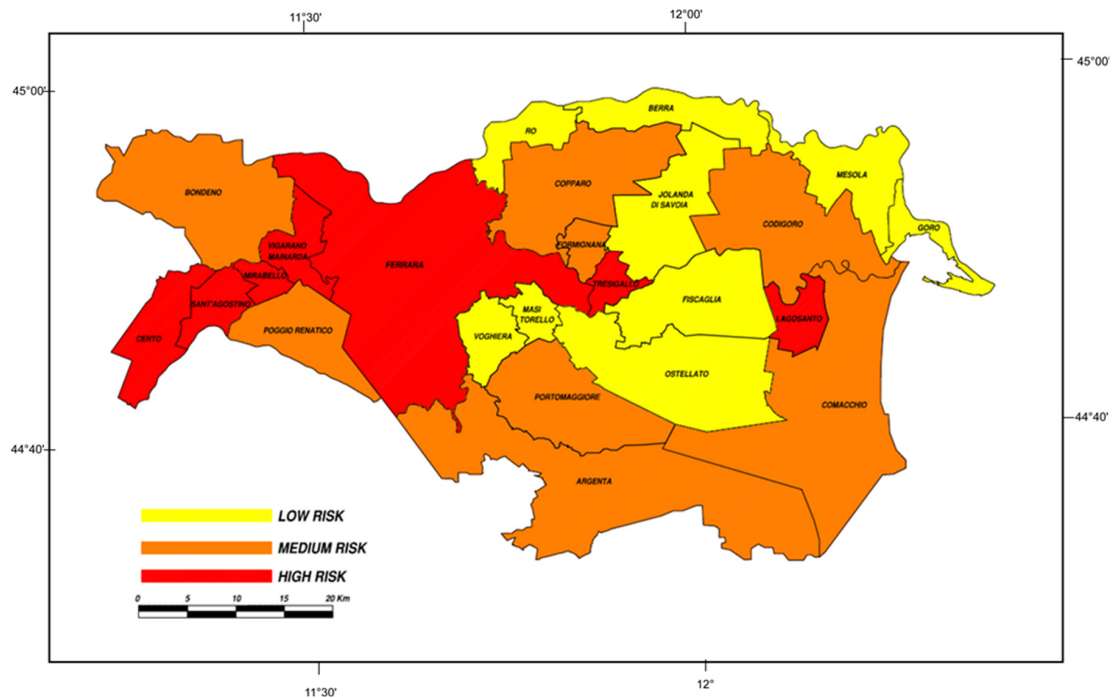


Figure 12. Multiple-risk map for the Ferrara province for the linear preference function with the thresholds chosen with the mean-std method. The risk levels strictly indicate the relative priority ranking for decision-makers and do not indicate the effective safety level of the various municipalities.

Table 6. Ranking of alternatives for the linear preference function and std-mean method.

Rank	Alternatives	Θ	Θ^+	Θ^-
1	Cento	0.4532	0.4849	0.0317
2	Ferrara	0.3769	0.4123	0.0354
3	Tresigallo	0.2051	0.2613	0.0562
4	Vigarano Mainarda	0.1219	0.2185	0.0966
5	Mirabello+ Sant'Agostino	0.078	0.1835	0.1056
6	Lagosanto	0.0597	0.1319	0.0722
7	Poggio Renatico	0.0523	0.167	0.1147
8	Argenta + Portomaggiore	0.0307	0.1133	0.0826
9	Copparo	0.0261	0.1107	0.0846
10	Bondeno	0.0222	0.1075	0.0853
11	Comacchio	0.0217	0.1075	0.0857
12	Codigoro	0.0125	0.1053	0.0928
13	Formignana	-0.1232	0.0146	0.1378
14	Masi Torello	-0.1275	0.0086	0.1361
15	Goro	-0.1278	0.0106	0.1384
16	Mesola	-0.1317	0.0069	0.1386
17	Berra	-0.1383	0.0046	0.1429
18	Voghiera	-0.1383	0.0041	0.1424
19	Ro	-0.1385	0.004	0.1425
20	Fiscaglia	-0.1497	0.002	0.1517
21	Ostellato	-0.1839	0	0.1839
22	Jolanda di Savoia	-0.2014	0	0.2014

Regardless of the preference function chosen, the maps obtained present a similar risk trend, i.e., the territory is divided into two parts: The municipalities of the western part of the territory of the province of Ferrara, plus Ferrara and Tresigallo, are characterized by a medium–high risk level; the upper-eastern part of the province is characterized by a medium–low risk level.

3.3. Sensitivity Analysis on the Choice of Weights

As introduced in Section 2, the sensitivity analysis on the weights was performed by first increasing the weight of each individual criterion at a time, and then assuming the simultaneous increase in the weights of the three “exposure”-related criteria, namely land use, population density, and strategic buildings. Specifically, the weights were changed according to Scenarios 0, 1, 2, and 3 described in Table 3.

For the sake of brevity, we present hereafter the results obtained by assuming the usual preference function. For the reader’s convenience, the results are reported as maps, as in the previous sections.

In the first part of the analysis, the criteria are changed according to the following order: Flood hazard, PGA, land use, strategic buildings, age of buildings, and population density. Hereafter, we omit the maps obtained for the changes of the weights relating to the criteria of strategic buildings and age of buildings, for brevity. Figures 13 and 14 illustrate the various risk maps obtained by increasing the weights.

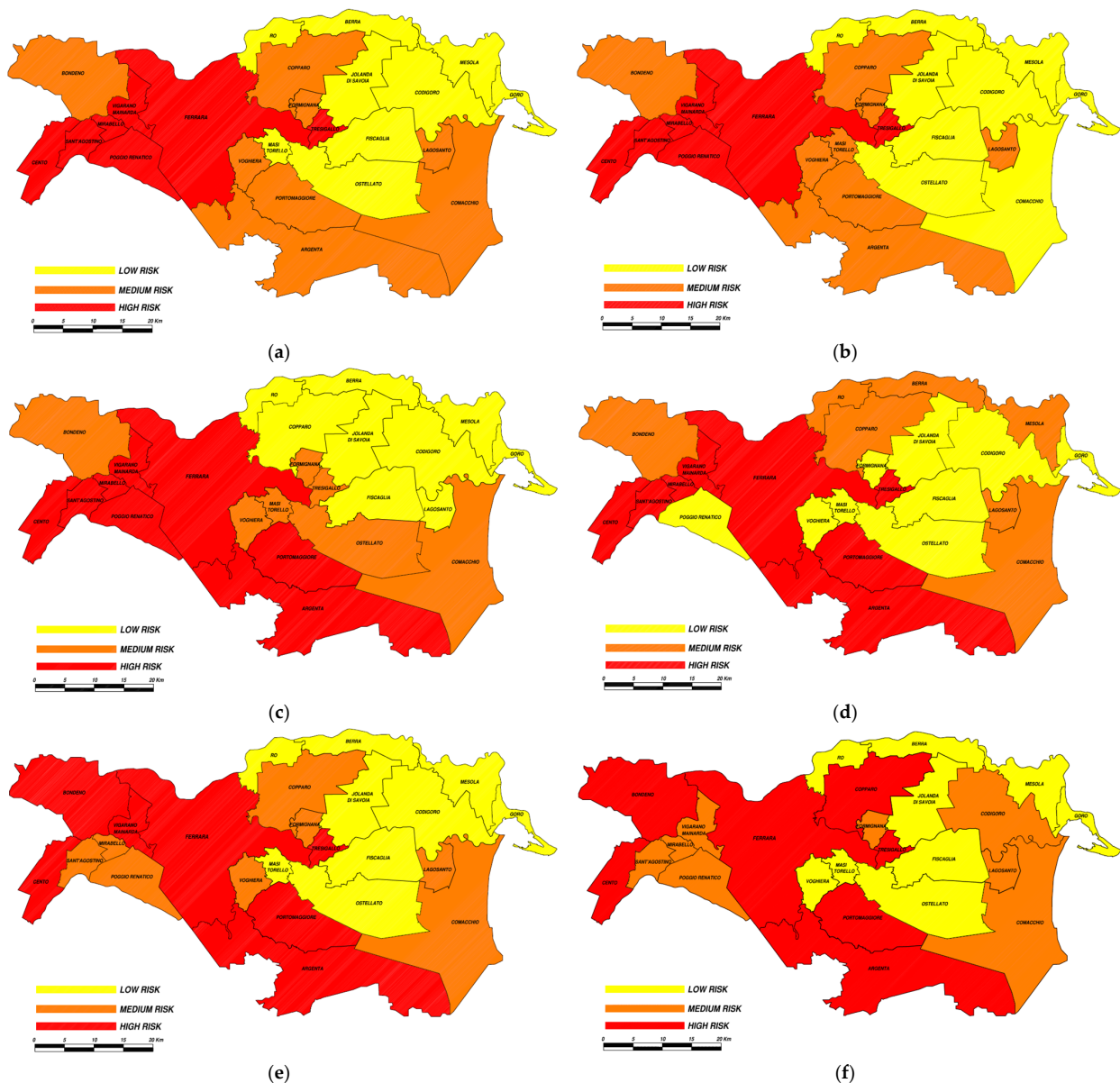


Figure 13. Weights sensitivity analysis, multi-risk maps; (a) flood hazard weight increase assuming Scenarios 2 or 3; (b) PGA weight increase assuming Scenario 1; (c) PGA weight increase assuming Scenario 2; (d) land use weight increase assuming Scenarios 2 or 3; (e) strategic buildings weight increase assuming Scenario 1; (f) strategic buildings weight increase assuming Scenarios 2 or 3. The risk levels strictly indicate the relative priority ranking for decision-makers and do not indicate the effective safety level of the various municipalities.

With Scenario 1 based on the variation of the flood hazard weight, the ranking of the municipalities remains almost unchanged, as the multi-risk map is identical to that of Scenario 0. On the other hand, the maps change when Scenarios 2 and 3 are adopted, as shown in Figure 13a. More marked differences can be observed when the weight of the PGA (Figure 13b,c) is changed. By increasing the weight of the land-use criterion, an increase in Scenario 1 does not reflect evident changes in the multi-risk map (Figure 13d). On the other hand, changes in Scenarios 2 and 3 affect the multi-risk map. Looking back at the strategic building criterion, we observe differences in the risk map when the first change of Scenario 1 is applied, compared to Scenario 0 (Figure 13e), and more so with the last two increases of Scenario 2 (Figure 13f). For the criterion of population density, the first increase in the weight according to Scenario 1 does not affect the map (see Figure 14a),

while the subsequent increases in the weight bring about noticeable modifications. In particular, the multi-risk map reported in Figure 14b assigns a comparatively low level of attention to the Argenta municipality, which, however, is associated with a medium seismicity level according to the territorial classification of Figure 2a. Depending on the stakeholders' expectations, this might suggest that weights should not be varied to the extent of downgrading the seismic risk level of certain municipalities classified at medium to high seismic risk.

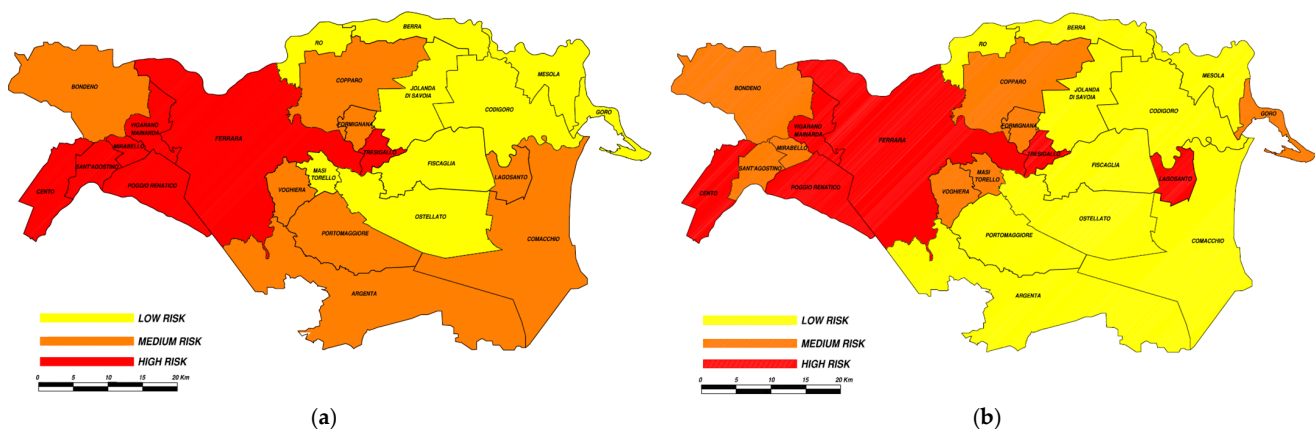


Figure 14. Weights sensitivity analysis, multi-risk maps; (a) Scenario 2, population density weight increase; (b) Scenario 3, population density weight increase. The risk levels strictly indicate the relative priority ranking for decision-makers and do not indicate the effective safety level of the various municipalities.

Lastly, results of the sensitivity on the weight choice for the criteria related to exposure are presented in Table 7. Proceeding as illustrated in Section 2, the first increase in the weight does not alter the risk map, which remains the same as in Scenario 0, whereas with the changes of Scenario 2, greater variations can be observed.

Therefore, concluding the sensitivity analysis of weights, it can be inferred that, in general, the results are sensitive to the increase in the weights of the criteria, determining a risk map that varies from case to case, causing the risk of some municipalities to decrease while that of others increased. However, these variations do not upset the overall trend, which highlights a territory divided into two parts, that of the municipalities of the western part of the territory of the province of Ferrara characterized by a medium–high risk level, and the municipalities of the north-eastern area characterized by a medium–low risk level.

3.4. Remarks on the Limitations of the Analysis

The proposed methodology requires the definition of several parameters, criteria, and weights, whose choice resulted in being strongly dependent on the expectations of stakeholders and end-users. Thus, the obtained results should be seen as a first attempt towards the proposal of an MCDA methodology that does not require great mathematical expertise, is flexible, and can be easily adapted to many situations. Nevertheless, further efforts are necessary in order for the tool to be readily exploited by public authorities and decision makers. Furthermore, it is worth highlighting other limitations inherent in the present analysis.

The first type of limitation is mainly related to the availability of data. Indeed, the choice of the criteria was based on the availability of the relevant information, which led, for some criteria, to a purely qualitative evaluation. Greater availability, accuracy, and ease of retrieval of the data would lead to the creation of a more complete and more precise analysis, and it could also contribute to the development of operational tools and software.

Table 7. Sensitivity analysis on the exposure factor, ranking of alternatives (EXP: EXPOSURE).

Scenario 1: WEIGHT = 0.22; OTHERS = 011					Scenario 2: WEIGHT = 0.32; OTHERS = 0.01			
Rank	Alternativa	Θ	Θ^+	Θ^-	Alternativa	Θ	Θ^+	Θ^-
1	Ferrara	0.7153	0.8064	0.0911	Cento	0.9452	0.9683	0.0231
2	Cento	0.7093	0.8061	0.0968	Ferrara	0.9168	0.9538	0.037
3	Tresigallo	0.5092	0.6746	0.1654	Tresigallo	0.696	0.7975	0.1015
4	Vigarano Mainarda	0.2908	0.5771	0.2863	Lagosanto	0.4603	0.6797	0.2193
5	Argenta + Portomaggiore	0.2279	0.534	0.306	Vigarano Mainarda	0.3006	0.5575	0.2569
6	Mirabello + Sant'Agostino	0.219	0.5413	0.3222	Argenta + Portomaggiore	0.2083	0.5536	0.3454
7	Bondeno	0.1597	0.4971	0.3375	Mirabello + Sant'Agostino	0.1207	0.4675	0.3468
8	Lagosanto	0.1359	0.488	0.352	Bondeno	0.1154	0.507	0.3915
9	Copparo	0.0416	0.4381	0.3965	Comacchio	0.1044	0.5017	0.3973
10	Comacchio	0.0356	0.4378	0.4022	Copparo	0.076	0.4873	0.4113
11	Poggio Renatico	-0.0499	0.4041	0.454	Mesola	-0.0919	0.3574	0.4493
12	Formignana	-0.0661	0.3555	0.4216	Masi Torello	-0.1448	0.3309	0.4757
13	Voghiera	-0.1127	0.3295	0.4422	Goro	-0.1563	0.3252	0.4815
14	Masi Torello	-0.1644	0.3064	0.4708	Codigoro	-0.1861	0.3564	0.5426
15	Berra	-0.2045	0.2863	0.4908	Poggio Renatico	-0.1924	0.3107	0.5031
16	Mesola	-0.2197	0.2787	0.4984	Formignana	-0.1938	0.3064	0.5002
17	Ro	-0.226	0.2756	0.5016	Voghiera	-0.2848	0.2607	0.5455
18	Goro	-0.2939	0.2416	0.5355	Berra	-0.2929	0.2569	0.5498
19	Codigoro	-0.3041	0.268	0.5721	Ro	-0.2949	0.2559	0.5507
20	Fiscaglia	-0.3385	0.2193	0.5578	Fiscaglia	-0.594	0.1063	0.7003
21	Ostellato	-0.4816	0.1451	0.6267	Ostellato	-0.7225	0.0418	0.7643
22	Jolanda di Savoia	-0.5829	0.0971	0.68	Jolanda di Savoia	-0.7893	0.0087	0.798

Secondly, this analysis neglected cascade effects, an aspect that deserves further investigation in the future [11].

Thirdly, the present contribution does not consider the impact of modeling assumptions on the seismic risk assessment. At the relevant scale of observations of the present analysis, specific structural aspects connected to the vulnerability levels of the buildings cannot be easily considered. In this regard, we recall that specific structural aspects and modeling assumptions play, among others, a key role for seismic risk evaluation at both the building and the urban scale [36]. A recent study focusing on South America has shown the uncertainties and biases that the use of simplified models or heterogenous data may produce in the determination of seismic vulnerability [36]. For completeness, seismic risk evaluation is extensively discussed, for instance, in the aforementioned contributions [36–39] and the references cited therein.

Finally, we recall that the seismic classification shown in Figure 2 has been merely used as a technical-administrative reference for establishing the priority of actions and measures aimed at preventing and mitigating seismic risk. It must not be used to determine the local seismic action or for the structural design of buildings, which, instead, rely upon more detailed maps highlighting, for instance, the presence of site effects due to the inherent geological structure of the ground or instability effects such as liquefaction. Therefore, the present analysis should be purposefully extended in order to consider the aforementioned local effects [40].

4. Conclusions

For the present case study, the application of the Multiple-Criteria Decision Analysis (MCDA) methodology through the PROMETHEE algorithm has proved an innovative

and promising operational tool. Its potential derives from the ability to both analyze information from various sources and jointly systematize data expressed in different units and scales. The application of this methodology has made it possible to rank the various municipalities in terms of the relative proneness to joint flood and seismic hazards. We recall that the objective of the methodology is not to quantify the safety level in absolute terms of the various municipalities. Its scope is, indeed, to provide useful information for decision makers and public authorities to define future intervention priorities. We further emphasize that, in the authors' opinion, the present study is original as it applies the PROMETHEE algorithm for the first time to a multi-risk assessment of seismic and flood hazards.

Depending on the territory to be studied, the relevant risks could be different, and therefore, different criteria must be used to express them. Nevertheless, the generalization to other multi-risk analyses and different case studies deserves further considerable efforts and thoughtful insights. Full validation of the present methodology is also of utmost importance and calls for new developments. However, the proposed methodology is flexible. This suggests that, with due precautions and adaptations, it is possible to apply it to different risk scenarios, such as scenarios including coastal floods and landslides, while keeping the same applicative scheme.

Finally, the obtained results have shown that the proposed methodology is an operational tool that, once further validated, can be used by end users, whether modelers or decision makers, to urgently allocate resources and increase the coping capacity of communities in the case of catastrophic events.

Author Contributions: Conceptualization, Ž.N., A.C., C.V. and E.B.; methodology, Ž.N., A.S. and A.C.; software, A.S.; validation, A.S., A.C. and C.V.; formal analysis A.S., A.C., Ž.N. and C.V.; resources E.B.; data curation, A.S.; writing—original draft preparation, A.S. and A.C.; writing—review and editing, A.C., C.V., Ž.N. and E.B.; visualization, A.S. and A.C.; supervision, E.B.; project administration, E.B.; funding acquisition, E.B. All authors have read and agreed to the published version of the manuscript.

Funding: This research was funded by the EUROPEAN UNION, Programme Interreg Italy-Croatia, Project "Preventing, managing and overcoming natural-hazards risks to mitigate economic and social impact"—PMO-GATE ID 10046122.

Institutional Review Board Statement: Not applicable.

Informed Consent Statement: Not applicable.

Data Availability Statement: Publicly available datasets and figures were analyzed in this study. This data can be found here: <https://www.bonificaferrara.it/images>, <https://www4.istat.it/it/mappa-rischi/documentazione>, <https://ambiente.regione.emilia-romagna.it/en/geologia/seismic-risk/seismic-classification>, <http://zonesismiche.mi.ingv.it>, <http://www.provincia.fe.it>. (accessed on 26 January 2022).

Acknowledgments: The authors are very grateful to Consorzio di Bonifica Pianura di Ferrara for making the flood maps freely available, and, particularly, to Eng. Alessandro Bondesan for his kind support in georeferencing the maps.

Conflicts of Interest: The authors declare no conflict of interest.

References


1. UN-ISDR. Sendai Framework for Disaster Risk Reduction 2015–2030. In Proceedings of the UN world Conference on Disaster Risk Reduction, Sendai, Japan, 14–18 March 2015; United Nations Office for Disaster Risk Reduction: Geneva, Switzerland. Available online: http://www.unisdr.org/files/43291_sendaiframeworkfordrren.pdf (accessed on 1 October 2021).
2. Poljanšek, K.; Ferrer, M.M.; De Groeve, T.; Clark, I. Preface. In *Science for Disaster Risk Management 2017: Knowing Better and Losing Less*; Publications Office of the European Union: Luxembourg, 2017; ISBN 978-92-79-60678-6. [CrossRef]
3. Topics Geo: Natural Catastrophes 2013: Analyses, Assessments, Positions, Münchener Rückversicherungs-Gesellschaft, Munich. 2014. Available online: https://www.munichre.com/content/dam/munichre/contentlounge/website-pieces/documents/302-08121_en.pdf/_jcr_content/renditions/original./302-08121_en.pdf (accessed on 26 January 2022).

4. UN-ISDR. Terminology: Basic Terms of Disaster Risk Reduction. 2009. Available online: <http://www.unisdr.org/we/inform/terminology> (accessed on 1 October 2021).
5. Urlainis, A.; Ornai, D.; Levy, R.; Vilnay, O.; Shohet, I.M. Loss and damage assessment in critical infrastructures due to extreme events. *Saf. Sci.* **2022**, *147*, 105587. [CrossRef]
6. Kanamori, H.; Hauksson, E.; Heaton, T. Real-time seismology and earthquake hazard mitigation. *Nature* **1997**, *390*, 461–464. [CrossRef]
7. Quesada-Román, A.; Villalobos-Chacón, A. Flash flood impacts of Hurricane Otto and hydrometeorological risk mapping in Costa Rica. *Geogr. Tidsskr.-Dan. J. Geogr.* **2020**, *120*, 142–155. [CrossRef]
8. Quesada-Román, A.; Ballesteros-Cánovas, J.A.; Granados-Bolaños, S.; Birkel, C.; Stoffel, M. Improving regional flood risk assessment using flood frequency and dendrogeomorphic analyses in mountain catchments impacted by tropical cyclones. *Geomorphology* **2022**, *396*, 108000. [CrossRef]
9. Kron, W. Reasons for the increase in natural catastrophes: The development of exposed areas. In *Topics 2000: Natural Catastrophes, the Current Position*; Munich Reinsurance Company: Munich, Germany, 1999; pp. 82–94.
10. Barredo, J.I. Major flood disasters in Europe: 1950–2005. *Nat. Hazards* **2007**, *42*, 125–148. [CrossRef]
11. Zuccaro, G.; De Gregorio, D.; Leone, M. Theoretical model for cascading effects analyses. *Int. J. Disaster Risk Reduct.* **2018**, *30*, 199–215. [CrossRef]
12. Zschau, J. Where are we with multihazards, multirisks assessment capacities? In *Science for Disaster Risk Management 2017: Knowing Better and Losing Less*; Poljansek, K., Marin Ferrer, M., De Groeve, T., Eds.; Publications Office of the European Union: Luxembourg, 2017; ISBN 978-92-79-60678-6. [CrossRef]
13. Fuchs, S.; Keiler, M.; Zischg, A. A spatiotemporal multi-hazard exposure assessment based on property data. *Nat. Hazard. Earth Syst. Sci.* **2015**, *15*, 2127–2142. [CrossRef]
14. Komentova, N.; Scolobig, A.; Garcia-Aristizabal, A.; Monfort, D.; Fleming, K. Multi-risk approach and urban resilience. *Int. J. Disast. Res. Built Environ.* **2016**, *7*, 114–132. [CrossRef]
15. Marzocchi, W.; Garcia-Aristizabal, A.; Gasparini, P.; Mastellone, M.L.; Di Ruocco, A. Basic principles of multi-risk assessment: A case study in Italy. *Nat. Hazards* **2012**, *62*, 551–573. [CrossRef]
16. Kappes, M.S.; Keiler, M.; von Elverfeldt, K.; Glade, T. Challenges of analyzing multi-hazard risk: A review. *Nat. Hazards* **2012**, *64*, 1925–1958. [CrossRef]
17. Bell, R.; Glade, T. Multi-hazard analysis in natural risk assessments. *WIT Trans. Ecol. Environ.* **2004**, *77*, 1–10.
18. Schmidt, J.; Matcham, I.; Reese, S.; King, A.; Bell, R.; Henderson, R.; Smart, G.; Cousins, J.; Smith, W.; Heron, D. Quantitative multi-risk analysis for natural hazards: A framework for multi-risk modelling. *Nat. Hazards* **2011**, *58*, 1169–1192. [CrossRef]
19. Neri, A.; Aspinall, W.P.; Cioni, R.; Bertagnini, A.; Baxter, P.J.; Zuccaro, G.; Andronico, D.; Barsotti, S.; Cole, P.D.; Esposti Ongaro, T.; et al. Developing an Event Tree for probabilistic hazard and risk assessment at Vesuvius. *J. Volcanol. Geotherm. Res.* **2008**, *178*, 397–415. [CrossRef]
20. Barthel, F.; Neumayer, E. A trend analysis of normalized insured damage from natural disasters. *Clim. Chang.* **2012**, *113*, 215–237. [CrossRef]
21. Skilodimou, H.D.; Bathrellos, G.D.; Chousianitis, K.; Youssef, A.M.; Pradhan, B. Multi-hazard assessment modeling via multi-criteria analysis and GIS: A case study. *Environ. Earth Sci.* **2019**, *78*, 47. [CrossRef]
22. Brans, J.P.; Mareschal, B. Promethee Methods. In *Multiple Criteria Decision Analysis: State of the Art Surveys*; Figueira, J., Greco, S., Ehrogott, M., Eds.; Springer: Berlin/Heidelberg, Germany, 2005.
23. Gallina, V.; Torresan, S.; Critto, A.; Sperotto, A.; Glade, T.; Marcomini, A. A review of multi-risk methodologies for natural hazards: Consequences and challenges for a climate change impact assessment. *J. Environ. Manag.* **2016**, *168*, 123–132. [CrossRef]
24. Gallina, V.; Torresan, S.; Zabeo, A.; Critto, A.; Glade, T.; Marcomini, A. A Multi-Risk Methodology for the Assessment of Climate Change Impacts in Coastal Zones. *Sustainability* **2020**, *12*, 3697. [CrossRef]
25. Peduzzi, P.; Dao, H.; Herold, C.; Mouton, F. Assessing global exposure and vulnerability towards natural hazards: The Disaster Risk Index. *Nat. Hazards Earth Syst. Sci.* **2009**, *9*, 1149–1159. [CrossRef]
26. Brans, J.P.; Vincke, P.; Mareschal, B. How to select and how to rank projects: The PROMETHEE method. *Eur. J. Oper. Res.* **1986**, *24*, 228–238. [CrossRef]
27. Mladineo, M.; Jajac, N.; Rogulj, K. A simplified approach to the PROMETHEE method for priority setting in management of mine action projects. *Croat. Oper. Res. Rev.* **2016**, *7*, 249–268. [CrossRef]
28. Crnjac, M.; Aljinovic, A.; Gjeldum, N.; Mladineo, M. Two-stage product design selection by using PROMETHEE and Taguchi method: A case study. *Adv. Prod. Eng. Manag.* **2019**, *14*, 39–50. [CrossRef]
29. Savic, M.; Nikolic, D.; Mihajlovic, I.; Zivkovic, Z.; Bojanov, B.; Djordjevic, P. Multi-Criteria Decision Support System for Optimal Blending Process in Zinc Production. *Miner. Process. Extr. Metall. Rev.* **2015**, *36*, 267–280. [CrossRef]
30. Rocchi, A.; Chiozzi, A.; Nale, M.; Nikolic, Z.; Riguzzi, F.; Mantovan, L.; Gilli, A.; Benvenuti, E. A Machine Learning Framework for Multi-Hazard Risk Assessment at the Regional Scale in Earthquake and Flood-Prone Areas. *Appl. Sci.* **2022**, *12*, 583. [CrossRef]
31. Carminati, E.; Martinelli, G. Subsidence rates in the Po Plain, northern Italy: The relative impact of natural and anthropogenic causation. *Eng. Geol.* **2002**, *66*, 241–255. [CrossRef]

32. Salvati, L.; Mavrakis, A.; Colantoni, A.; Mancino, G.; Ferrara, A. Complex Adaptive Systems, soil degradation and land sensitivity to desertification: A multivariate assessment of Italian agro-forest landscape. *Sci. Total Environ.* **2015**, *521–522*, 235–245. [CrossRef] [PubMed]
33. Stucchi, M.; Meletti, C.; Montaldo, V.; Akinci, A.; Faccioli, E.; Gasperini, P.; Malagnini, L.; Valensise, G. Pericolosità Sismica di Riferimento Per il Territorio Nazionale MPS04 [Data Set]. Istituto Nazionale di Geofisica e Vulcanologia (INGV). 2004. Available online: <https://data.ingv.it/en/dataset/70#additional-metadata> (accessed on 1 October 2021). [CrossRef]
34. Trigila, A.; Iadanza, C.; Bussetini, M.; Lastoria, B. *Dissesto Idrogeologico in Italia: Pericolosità e Indicatori di Rischio—Edizione 2018; Rapporti 287/2018*; ISPRA: Roma, Italy, 2018.
35. Decreto Legislativo n. 49/2010. Available online: https://www.mite.gov.it/sites/default/files/archivio/allegati/vari/documento_definitivo_indirizzi_operativi_direttiva_alluvioni_gen_13.pdf (accessed on 3 January 2022).
36. Dolce, M.; Prota, A.; Borzi, B.; da Porto, F.; Lagomarsino, S.; Magenes, G.; Moroni, C.; Penna, A.; Polese, M.; Speranza, E.; et al. Seismic risk assessment of residential buildings in Italy. *Bull. Earthquake Eng.* **2021**, *19*, 2999–3032. [CrossRef]
37. Hoyos, M.C.; Hernández, A.F. Impact of vulnerability assumptions and input parameters in urban seismic risk assessment. *Bull. Earthq. Eng.* **2021**, *19*, 4407–4434. [CrossRef]
38. Asadi, E.; Salman, A.M.; Li, Y.; Yu, X. Localized health monitoring for seismic resilience quantification and safety evaluation of smart structures. *Struct. Saf.* **2021**, *93*, 102127. [CrossRef]
39. Joyner, M.D.; Gardner, C.; Puentes, B.; Sasani, M. Resilience-Based seismic design of buildings through multiobjective optimization. *Eng. Struct.* **2021**, *246*, 113024. [CrossRef]
40. CTMS. Linee Guida per la Gestione del Territorio in Aree Interessate da Faglie Attive e Capaci (FAC). Commissione Tecnica Per la Microzonazione Sismica, Gruppo di Lavoro FAC. Dipartimento Della Protezione Civile e Conferenza Delle Regioni e Delle Province Autonome. 2015. Available online: http://www.protezionecivile.gov.it/resources/cms/documents/LineeGuidaFAC_v1_0.pdf (accessed on 3 January 2022).

Article

Risk Assessment of Riverine Terraces: The Case of the Chenyulan River Watershed in Nantou County, Taiwan

Ji-Yuan Lin ¹, Jen-Chih Chao ^{1,*}  and Yung-Ming Hsu ²

¹ Department of Landscape and Urban Design, Chaoyang University of Technology, Taichung 413310, Taiwan; jylin@cyut.edu.tw

² Department of Civil & Construction Engineering, Chaoyang University of Technology, Taichung 413310, Taiwan; s9911625@cyut.edu.tw

* Correspondence: jenchihchao@gmail.com; Tel.: +866-423323000 (ext. 7668)

Abstract: The purpose of this study is to establish a method of hazard assessment for the river terraces along the Chenyulan River and use 40 of them as protected objects. Using a geographic information system, the researchers extracted nine parameters for such terraces. These are length to attack shore, distance away from fault, distance from river channel, number of creeks and streams with possibility of debris flows, height above stream level, average slope degree, geology, number of erosion ditches, and distance from landslide area behind. Next, the weightings identified by analytic hierarchy process analysis were used as the basis for grading the various factors affecting river terraces. Hazard assessment for the river terraces then proceeded via totaling of the potential trends of the various factors and the protected objects, as well as comparison of historical disaster conditions and satellite images. The results showed that there were 8 high-risk river terraces, 14 medium-high-risk river terraces, 14 medium-low-risk river terraces and 4 low-risk river terraces. The evaluation of the current conditions of the settlement environment through parameter weighting has a certain accuracy and reference value in reducing the disaster impact of the riverine terrace settlement.

Keywords: geographic information system; hazard assessment; river terraces; risk assessment

Citation: Lin, J.-Y.; Chao, J.-C.; Hsu, Y.-M. Risk Assessment of Riverine Terraces: The Case of the Chenyulan River Watershed in Nantou County, Taiwan. *Appl. Sci.* **2022**, *12*, 1375. <https://doi.org/10.3390/app12031375>

Academic Editors: Andrea Chiozzi, Elena Benvenuti and Željana Nikolić

Received: 16 November 2021

Accepted: 19 January 2022

Published: 27 January 2022

Publisher's Note: MDPI stays neutral with regard to jurisdictional claims in published maps and institutional affiliations.



Copyright: © 2022 by the authors. Licensee MDPI, Basel, Switzerland. This article is an open access article distributed under the terms and conditions of the Creative Commons Attribution (CC BY) license (<https://creativecommons.org/licenses/by/4.0/>).

1. Introduction

Taiwan is located at the junction of the Eurasian continental plate and the Philippine Sea plate. Formed through the Penglai orogeny, the Nanao orogeny and crustal changes, it is a mountainous terrain with flat land accounting for only 25% of its total area. Due to population growth and rapid industrial and commercial development in Taiwan in recent years, the use of flat land has become saturated, and development of hillside areas, especially river terraces, has become common. The existence of river terraces indicates frequent geological changes, high erosion rates, abundant sources of silt, and strong river scour [1], but their formation is also affected to some extent by climate change and human activities [2]. As Taiwan is surrounded by the sea on all sides, it receives abundant rainfall throughout the year, about 2500 mm, more than two and a half times the world annual average of 970 mm. During the rainy season (from 1 May to 30 November each year), the region is prone to typhoons, each of which tends to increase the intensity of rainfall within a short period of time, and this can result in landslides and mudslides in mountainous areas, as well as rapid rises in the water levels in rivers, which often results in flooding and the erosion and collapse of riverbanks. To prevent loss of life, residents of river terraces have to evacuate when typhoons occur. On 7 August 2009, when Taiwan was struck by a moderate-strength typhoon, Morakot, heavy rainfall led to a series of disasters in southern Taiwan. Due to the collapse of Xiandu (Xianto) Mountain, Xiaolin Village was destroyed, and a short-term barrier lake that was formed endangered the lives and property of residents downstream.

Due to undercutting and erosion by rivers, river terraces remain above the water surface during normal floods and are distributed in steps on the slopes of the river valleys [3]. Chang and Shi defined river terraces as land along rivers, consisting of terraces and cliffs [4]. The terraces' surfaces were the riverbed or floodplain surfaces in a former period, while the cliffs below them, facing the valley axis, were formed by both down erosion and lateral erosion [2]. The terraces of Xiaolin Village were formed by ancient and recent landslides. Their geology is extremely unstable, and the village was destroyed largely due to its location on dangerous low-lying ones. According to our survey, among the 144 mountain settlements and aboriginal tribal villages in southern Taiwan, 92 are located on river terraces, similar to the situation of Xiaolin. Therefore, the hazard and risk assessment of river terraces demand special attention to avoid similar disasters.

Various explorations of the topographic evolution of river terraces and the reasons they are formed in different regions have been conducted [5–8]. Scholars have also investigated the risks to river-terrace settlements posed by rainfall-induced landslides, based on historical data regarding the potential risk range of debris flows and the areas where landslides occur [9–11]. The Chenyulan River, in particular, has been the subject of multiple studies focused on collapses' potential indicators and locations [12–14], due to the multiple disasters that have struck the terraces of its lower reaches. However, due in part to strong variation in the reasons for the formation of river terraces and the hazards they face, residents of river-terrace settlements tend to have low awareness of disaster risks and are thus unable to effectively mitigate them. The people who live in settlements on the river terraces in Chenyulan today could face disaster at any time. Therefore, levels of danger to such terraces are estimated by risk assessment, so that when a typhoon is about to strike Taiwan, local residents can be quickly moved to safe places and disaster-relief facilities.

This study focuses on factors that may harm river terraces, derived from special questionnaires to establish index weights, and uses a geographic information system (GIS) overlap to allocate these factors to particular river terraces. Then, the scores of these potential factors and preservation factors are summed to estimate the terraces' risk, and establish a risk map of the area, with the wider aim of disaster prevention and reduction in disaster losses. This study uses the analytical features of AHP multilevel evaluation to decompose the elements of the river terraces' environment and construct a model of potential factors of the river terraces. Using the GIS data and AHP model, a matrix of judgement is established based on the corresponding criteria to derive the corresponding element weights, and a spatial analysis of the river terraces' hazard trend map is used to provide a solution to reduce the impact caused by the disaster.

Study Area

Li's survey of the Chenyulan River noted that its inland river terraces, alluvial fans and landslides were highly developed, and that there were 46 fan-shaped terraces and alluvial fans. The large number of these features implies rapid geological change [1].

According to the Bureau of Soil and Water Conservation, part of Taiwan's Council of Agriculture, there are more than 1700 potential soil and rock flows [15]. Within our study area, as shown in Figure 1, there are 49 such potential flows.

2. Literature Review

The potential hazard factors affecting river terraces can be summarized into three latent-sensing categories. The first, in front of the terrace, comprises four factors: attack shore, distance from fault, distance from river, and potential stream-impact quantity. The second, of the river terrace itself, consists of three factors: minimum ratio, average slope and geology. Additionally, the third, behind the river terrace, includes two factors: number of erosion ditches and number of collapses from the rear. Each category is analyzed in the following sections.

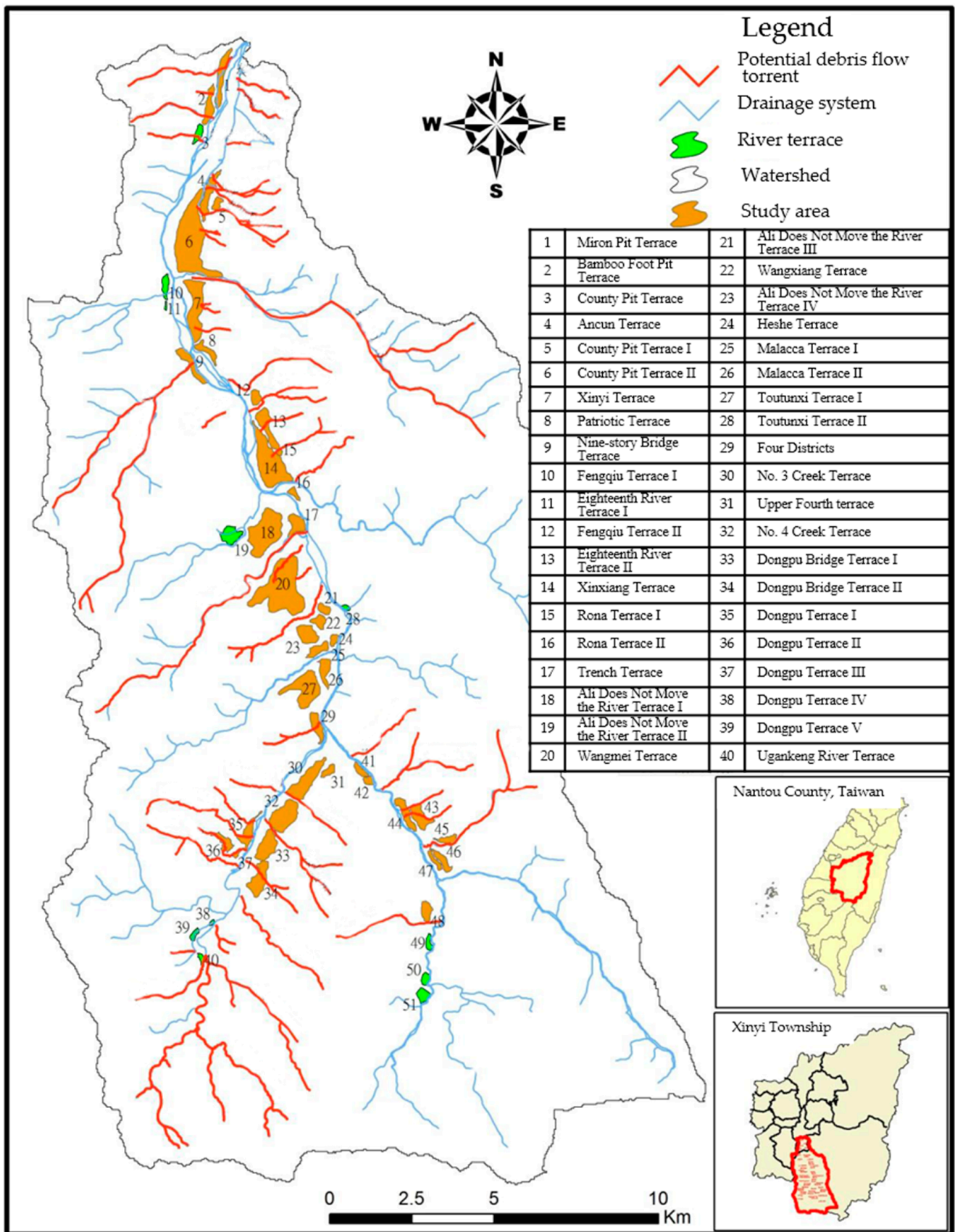


Figure 1. Study area.

2.1. The Front of the Terrace

2.1.1. The Attack Shore

Lin et al. showed that riverbank erosion mainly occurs at the bends in the river courses and tends to be most severe at the outer edges of such bends, called the attack shore (or cutting slope) [16]. The riverbank located on the attack shore has been eroded by the river for a long time, and the soil and rocks detached by such erosion are constantly being carried away by the river water, causing the toe to be gradually emptied; over time, this makes the riverbank steeper until it collapses. Roads and building foundations on the top are then damaged, or in some cases completely destroyed, due to loss of support. Lin et al. also noted that the movement of sandbars is mainly affected by five factors, i.e., the presence or absence of bends in rivers, the degree of such bends' curvature (known as meander), the presence or absence of confluent lateral structures, the way the river is scrubbed, and the supply of soil and sand [17]. Generally, convex-bank sandbars in curved sections of a river are more developed, and water flows mostly to the concave bank—i.e., the attacking shore—to erode it. Su concluded that, when the river flows through the attacking shore, flow velocity increases, and the centrifugal vortex water is formed there, washing it and transporting soil and sand to the convex bank [18].

2.1.2. Distance from Fault

Being located at the junction of the Eurasian continental plate and the Philippine Sea plate, Taiwan experiences frequent seismic activity. According to data collected by its Central Meteorological Bureau from 1991 to 2006, there are about 18,500 earthquakes in Taiwan each year, of which around 1000 are felt earthquakes. Major earthquakes often result in surface ruptures, rock folds and new faults. At present, scientists are unable to determine whether such faults cause earthquakes or vice versa, but their locations are identified in areas where seismic energy is strong [19]. Geological conditions in such areas are very fragmented due not only to the presence of fault gouges but also to broken zones near them and changes in the Earth's crust. The physical properties of the filler between the discontinuous surfaces of fault gouge or broken zone are usually poor, as is the degree of cementation, and this often causes engineering problems [16]. Lin observed that the rock mass on both sides of the Chenyulan fault is relatively broken, and weathered slate and metamorphic sandstone there, respectively provide fine-grained and coarse-grained material for earth-rock flows. The effects of faulting and river erosion also contribute to such flows [20]. The slopes of the terrain along both sides of the river are relatively steep, so the original weathered-soil layer collapsed due to heavy rain and formed debris flows. During these flows, the rock plate was broken, and the broken pieces in the rock mass were drawn into them.

2.1.3. Distance from River

Wang's study of the Shaolai River concluded that the collapse percentages of susceptibility increased with proximity to the river's course. Specifically, the percentage of collapses within 200 m from the river channel was 42.7%; between 200 m and 400 m, 26.6%; between 400 m and 600 m, accounted for 19.4% [21]. Beyond 1600 m from the river channel, there were no collapses at all. Therefore, it can be inferred that large increases in the collapsed areas of adjacent rivers may be related to heavy typhoon rain causing water levels to surge, which in turn eroded the slope foot of the Shaolai River and accelerated the collapse of the riverbank [22]. In short, a closer distance to the river entails a higher level of risk. It is also a principle of hydrology that when the slope is closer to the river, it is nearer to groundwater; thus, water seeping into the ground will cause seepage pressure in the slope. If the soil structure is highly permeable, this process will greatly increase the probability that the stability of the slope will be negatively affected [23]. As Chang et al. observed, distance from the river channel determines flood impact [24]. The smoothness of a river channel determines its flood-discharge capacity, and the reclamation-area ratio of a reclaimed lake determines the flood-regulation capacity of the lake in the protection zone.

2.1.4. Potential Stream-Impact Quantity

According to a comprehensive assessment by Taiwan's Bureau of Soil and Water Conservation [15], natural streams or pits are likely to cause debris-flow disasters, though this likelihood is affected by local conditions including the presence or absence of protected objects. The Bureau uses two main criteria for judging the probable impact of potential debris flows. The first is that the slope of the stream bed is greater than 10 degrees, and that the catchment area above this point is greater than three hectares. The second is that, at the downstream exit or overflow point of the stream, there are more than three households or important bridges or roads that need to be protected. Assessment should be divided into four levels—"high", "medium", "low", and "continuous observation"—based on the characteristics of the site.

2.2. *The River Terrace Itself*

2.2.1. Minimum Ratio

Specific height is defined as the height of the riverbank relative to that of the riverbed surface. Yoshiro divided Taiwan's terrain into eight types; from high to low, these were Highest Peneplain (HP), Old Piedmont (OP), Elevated Highland (EH), Young Piedmont (YP), Lateritic Highland (LH), Lateritic Terrace (LT), Fluvial Terrace (FT), and Fluvial Plain (FP) [25]. Through this perspective, the topographic evolution of the Taiwan River Valley can be explored. Lin subsequently provided a general description of the topographical features of Taiwan's important river systems, along with more detailed descriptions of the topographical categories defined by Tomita [25,26].

2.2.2. Average Slope

According to statistics from the Bureau of Soil and Water Conservation, the most frequent damage from debris flows occurs on Taiwan's mountain slopes above 30 degrees, and especially at 40 degrees or more, while the least damage is suffered where slopes are 15 degrees or less [15]. This is because steep slopes provide greater driving force and also reduce slope resistance, making them conducive not only to the development of shallow landslides but also to the fluidization of landslides and the formation of sloping debris flows [27]. Cheng used GIS and a conditional-probability method to analyze four factors—bare land, eroded gullies, slope, and lithology—and established that, among them, slope had the greatest influence [28]. Kao showed that unstable Index method achieved good accuracy in predicting slope collapses, with 92% of actual collapsed land falling within the areas it identified as being at medium or high risk [29,30]. Liulater used a neural network-like sensitivity analysis to establish that the most important factors in this type of damage were rainfall, slope, slope type, elevation, lithology, fault, slope direction, roads, folds, and erosion gullies [30]. After controlling for rainfall, however, the greatest influence was slope, irrespective of whether Kao's or Liu's analysis method was applied.

2.2.3. Geology

The right bank of the main channel of the Chenyulan River consists of Paleogene submetamorphic rock strata, with interbedded argillite, slate, meta sandstone and quartzite, among other types of rock; on the left bank are Miocene sedimentary rock strata, with interbedded sandstone, shale and sand shale. Other strata include platform accumulation, four-sided sandstone layers, and hsichun, shihti, alluvial, nanchung, kueichoulin and kankou formations [31]. The wider area is dominated by thick-bedded sandstone, shale (argillite), and sandstone and shale formed together. When thick-bedded sandstone is subjected to tectonic stress, the rock mass is often cut into large blocks because it is thick and strong, but the density of the fractured surface is low. This type of rock is also relatively easy to weather. When the degree of weathering is slight, shale often forms smaller cuttings; when the degree of weathering is severe, a weathered soil layer forms. Due to the sharp difference in water permeability and resistance between sand and shale interbeds, the interface between them is often a stratum-slip surface, and the exposed area of interbeds

often forms a single-sided mountain topography [32]. Chang and Lin investigated the Chenyulan River after Typhoon Huber and found that the contact between the upper mountain belt and the submetamorphic belt of Taiwan's geological structure was a fault. That is to say, near the Chenyulan River, the rock mass is abnormally broken, and a considerable amount of broken rock and soil accumulates on the surfaces of slopes and in the river itself, which may cause disasters [33].

2.3. Rear of the Terrace

2.3.1. Number of Erosion Ditches

Chang showed that erosion ditches are mainly caused by rain, surface runoff and wind, which causes the original soil to loosen or move; this process removes fine particles, and the resultant slope appears to be grooved [34]. Taiwan's Water Resources Agency, MOEA, on the other hand, defined an erosion ditch as a slender, linear drainage route from the top of a slope to its foot, usually caused by incision and erosion by concentrated runoff on the slope's surface. At the same time, the ditch wall is emptied and collapses, forming an obvious drainage pipe [35]. Chang suggested that the degree of slope erosion is a dynamic topographic effect on slope and is judged by the degree of contour curvature on a topographic contour map, supplemented by field surveys. Such curvature can also be used to determine the grade of a slope-erosion gully, i.e., a trough-shaped depression formed by the removal of vegetation by runoff on a hillside, excluding stream beds [36]. Hung noted that the debris-flow disasters caused by Typhoon Huber in the Chenyulan River Basin mainly occurred in the large erosion ditches (some of which are large enough to be named "Stream") and the flat reclaimed land of the community at the intersection and Provincial Highway 21 [37].

2.3.2. Number of Collapses from the Rear

When the combination of hydrological and geological conditions exceeds its damage threshold, a hillside will collapse. Hydrological conditions include rainfall intensity, rainfall delay, the soil's water content, pore water pressure, etc. Geological conditions include soil cohesion, anti-friction angle, soil slope, surface vegetation and whether there has been a recent earthquake or not. Tang conducted simulations of the Xiaolin Village disaster using PFC 3D. Their preliminary results show that just 60 s after the landslide was triggered, some of the houses in the village may have been covered by falling rocks or pushed to the opposite bank of the Qishan River [38]. Certainly, at its maximum sliding speed of 50 m per second, the kinetic energy of soil and rock is sufficient to cross the river entirely at this point, and a barrier lake was formed by this process in this vicinity. Ji investigated landslides in Caoling over a period from 1862 to 1999 and identified five large-scale ones linked to earthquakes or heavy rain. The landslides directly or indirectly caused disaster to the Caolingtian dyke breach, and a total of 170 people were killed and injured. Additionally, during the "921" earthquake of 1999, Caoling Mountain collapsed rapidly, its soil and rock moving up to 4 km, and the impact area of the collapse was nearly 500 hectares. Such cases of large-scale rock mass sliding are extremely rare, in Taiwan or anywhere else [39].

2.4. Preservation-Factor Assessment

Preservation factors include households, schools, hostels, public buildings (if residential), roads, bridges, farmland, orchards and other such sites. The Bureau of Soil and Water Conservation noted that the streams' debris-flow potential should be evaluated and prioritized according to the formula (natural potential factor affecting the risk level of debris flow \times 50%) + (preservation hazard factor \times 50%) [15]. The individual scores for the following three factors were added together to obtain the hazard degree score for each preservation object. (1) Building factor: The more buildings there are, the more people live in them, so the damage score is higher. (2) Traffic factor: Damage to the bridge is more harmful to the traffic, so a higher score is given. (3) Effective factors of on-site remediation: After many disasters, there have been many remediation facilities for potential debris flows.

If the remediation facilities are effective, damage to preservation objects by such flows can be reduced.

3. Methods

This study used Li’s Chenyulan River terrace map data, modified to reflect the current shape of river terraces there, and purposively selected 40 potential river terraces for further analysis [1]. An analytic hierarchy process was used to analyze the strength of the mutual influences of the various elements, as well as of the high-level elements on the low-level elements; the levels of risk to each focal river terrace were derived through weighting the latent perception factors [40].

3.1. Questionnaire Design

In this study, following the methodology laid out by the Bureau of Soil and Water Conservation, the priority-order score of the potential unearthed rock flows was calculated according to the formula set forth in Section 2.4 above. Therefore, the risk-scoring method for the river terraces in this study equals (the potential factor of river terraces × 50%) + (the preservation hazard factor of the river terraces × 50%) [15]. The questionnaire design can be divided into the two hierarchical-structure diagrams—one for latent factors and the other for preservation factors, shown in Figures 2 and 3.

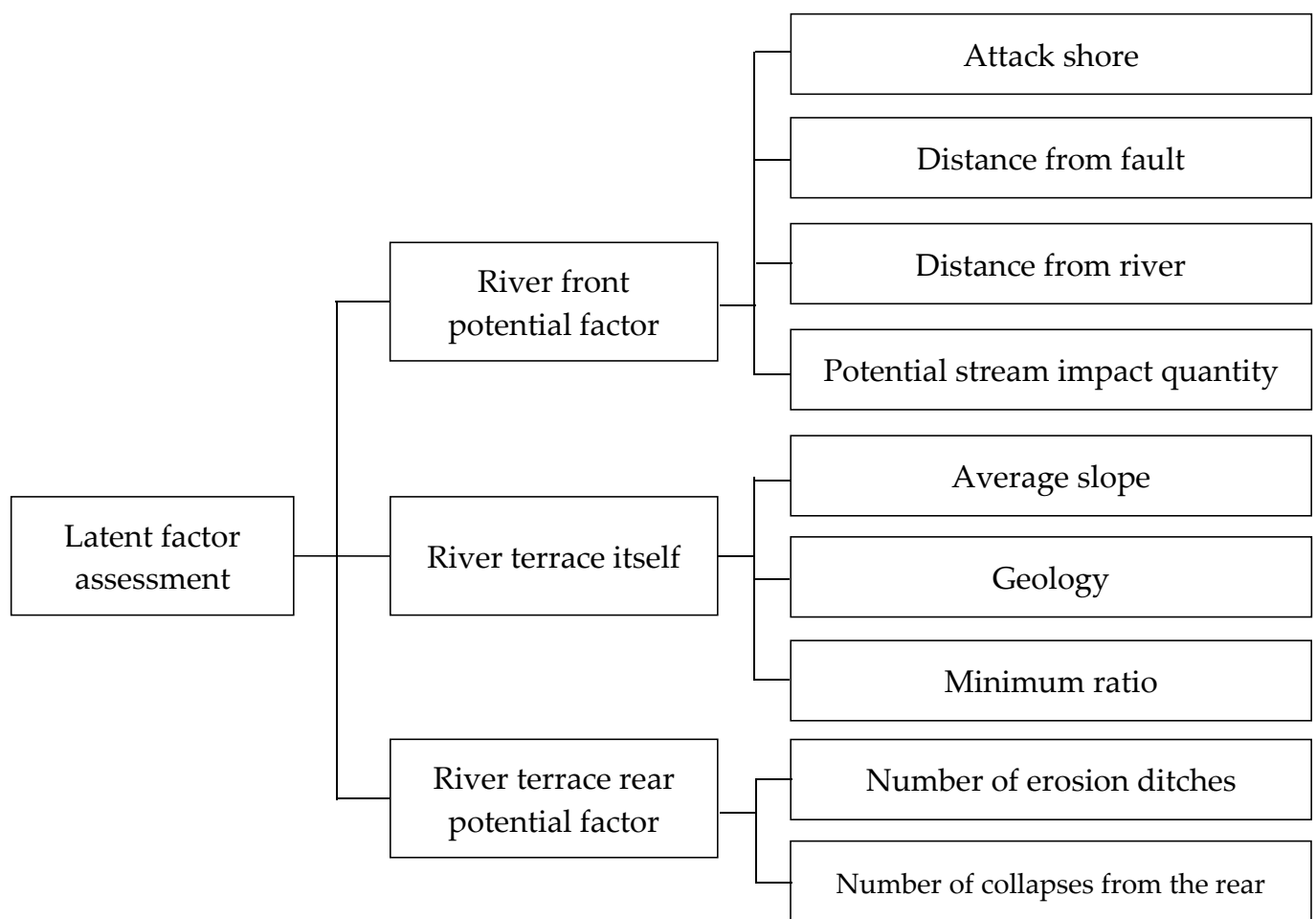


Figure 2. Evaluation conditions of latent factors and hierarchy of related factors.

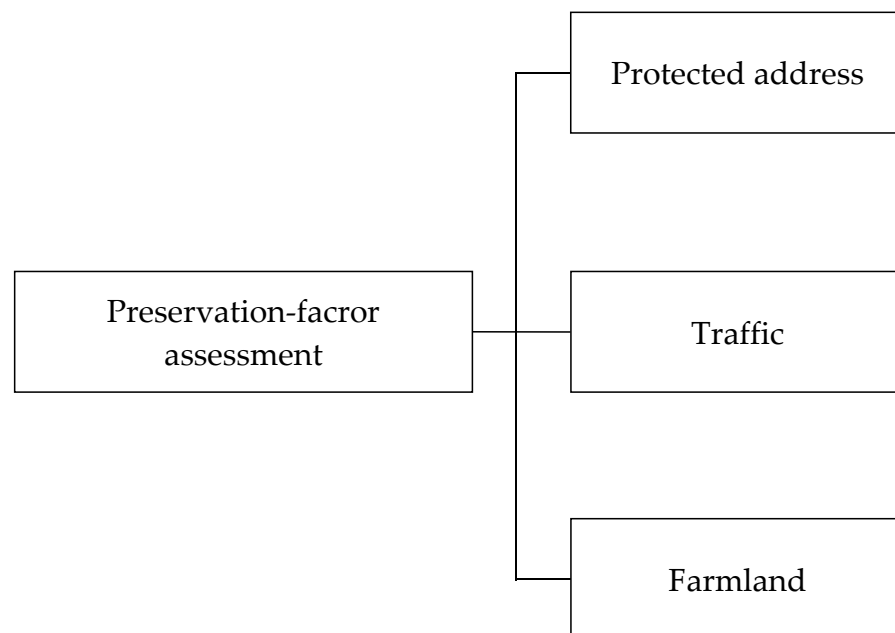


Figure 3. Evaluation conditions of preservation factors and hierarchy of related factors.

3.2. Questionnaire Survey Subjects

The participants in the questionnaire survey were mainly professors from the fields of land, water conservancy, soil and water conservation, geology, and environment and disaster prevention, employed by National Taiwan University, Chung Hsing University, Kaohsiung University, Tamkang University, Hua Fan University, Pingtung University of Science and Technology, and Chaoyang University of Science and Technology.

3.3. Statistical Results of Questionnaire Recovery

A total of 23 questionnaires were sent out and 17 were returned, resulting in a response of 79.9%. After eliminating five questionnaires due to repeated answers or omitted, unanswered items, which led them to have a consistency index (C.I.) and a consistency ratio (C.R.) greater than 0.1, 12 valid questionnaires remained for analysis. The C.R. value achieved a margin < 0.1 , indicating a strong degree of consistency among the pairwise comparisons, and proved it did not require a statistically significant sample size [40]. Shrestha et al. pointed out that AHP is usually used to survey people who have knowledge about the topic under investigation and a large sample size is not needed [41].

4. Results

Based on AHP principles, the scale indicates the level of relative importance from equal, moderate, strong, very strong to extreme level by 1, 3, 5, 7, and 9, respectively. The intermediate values between two adjacent comparisons are denoted by 2, 4, 6, and 8. The diagonal of the matrix of the comparison is equal to 1, since each criterion is compared to itself. When the number of alternatives is n , a total of $n(n - 1)/2$ comparisons are made [40]. As shown in Table 1, our expert respondents' ranking of our three categories of latent-sensing factors was in front of river terrace (0.352) > river terrace itself (0.342) > behind river terrace (0.306).

In the experts' evaluation of the preservation factors of river terraces, as shown in Table 2, the ranking was households (0.599) > traffic (0.292) > farmland (0.109).

Table 1. Evaluation results, river terraces' latent-sensing factors.

Level	Evaluation Project	Inter-Level Weight	Overall Weight	Rank	
Level one	Latent factor assessment	1.000	1.000		
Level two	Latent factor assessment	In front of river terrace	0.352	0.352	
		River terrace itself	0.342	0.342	
		Behind river terrace	0.306	0.306	
Level three	In front of river terrace	Attack shore	0.379	0.133	3
		Distance from fault	0.096	0.034	9
		Distance from river	0.288	0.101	7
		Potential impact of debris-flow quantity	0.237	0.083	8
Level three	River terrace itself	Average slope	0.321	0.110	6
		Geology	0.354	0.121	4
		Minimum ratio	0.325	0.111	5
Level three	Behind river terrace	Number of erosion ditches	0.563	0.172	1
		Distance from the collapse	0.438	0.134	2

Table 2. Evaluation results of river terraces' preservation factors.

Level	Evaluation Project	Inter-Level Weight	Overall Weight
Level one	Preservation factor assessment	1.000	1.000
Level two	Preservation factor assessment	Protected address	0.599
		Traffic	0.292
		Farmland	0.109

4.1. Distribution Method

Due to the large gaps between the various factors, to avoid extreme values, we first used statistical methods to find the average value and standard deviation of each factor and set reasonable parameter ranges X_{\max} and X_{\min} . If a parameter was greater than X_{\max} , X_{\max} was used, and if one was less than X_{\min} , X_{\min} was used. Then, an interval mapping method was conducted with AHP weightings to determine the score for each factor. In this study, the maximum and minimum range (0.1–1) of the interval mapping method was multiplied by the overall weight of each factor in the AHP to obtain the maximum and minimum range values.

4.2. Factor-by-Factor Allocation

First, we assumed that each factor was normally distributed, and its average value and standard deviation were ascertained, using one standard deviation to determine its reduction range. In this way, the extreme value of each parameter had less influence when calculating the weight, as shown in Table 3.

Table 3. Average value and standard deviation of each factor.

Factors	Average Value	Standard Deviation	$X_{\max}-X_{\min}$
Minimum height ratio (m)	58.6	64.4	0–123
Attack shore length (m)	213.9	375.1	0–589
Distance from river (m)	182.2	202.3	0–384.4
Average slope (degrees)	10.4	4.5	5.9–14.8
Distance from fault (m)	388.6	455.2	0–843.7
Number of potential streams affected	2.2	2.1	1.1–5.3
Number of erosion ditches	3.2	2.5	0.7–5.6
Distance from the collapse (m)	654.2	388.7	285.5–1022.9
Protected address	91.1	130.1	0–221.1

According to Juang et al., to improve the learning rate and accuracy of a similar neural network, the inconsistency of the difference between the numerical ranges of the parameters should be calculated, as before analysis, the input parameters must be normalized to avoid

the problem of temporary instability of the network and difficulty in convergence [42]. Accordingly, this study utilized a modified version of the interval-mapping method in Juang et al.'s normalization formula, and the maximum and minimum values obtained were between 0.1 and 1.

$$X_{norm} = (X + a)/b \tag{1}$$

Among them:

$$a = (X_{max} - 10X_{min})/9 \tag{2}$$

$$b = (X_{max} - X_{min})/0.9 \tag{3}$$

In the above three formulae, X_{norm} is the normalized value; X is the actual input parameter value; X_{max} is the maximum actual input parameter; X_{min} is the minimum actual input parameter.

For ease of calculation, a full score was held to be 100 points. In this study, the maximum and minimum range of the interval mapping method (0.1–1) is multiplied by the overall AHP weight of each factor and then multiplied by 100 to obtain the factors' respective maximum and minimum ratio ranges, as shown in Table 4. Substituting the data of each factor into Equation (1), the calculation formula of each factor can be calculated, and the factor weight of each river terrace calculated.

Table 4. Weight distribution of each factor.

Factors	Maximum Weighting	Minimum Weighting	
Latent susceptibility factors	Minimum height ratio (m)	11.1	1.11
	Attack shore length (m)	13.3	1.33
	Distance from river (m)	10.1	1.01
	Average slope (degrees)	11.0	1.1
	Distance from fault (m)	3.4	0.34
	Number of potential streams affected	8.3	0.83
	Geology	12.1	1.21
	Number of erosion ditches	17.2	1.72
	Distance from the collapse (m)	13.4	1.34
	Total	100	10
Preservation factors	Protected address	59.9	5.99
	Traffic	29.3	2.93
	Farmland	10.9	1.09
Total	100	10	

In its geological aspects, this research is based on the results of a survey by the Civil Engineering Research Institute of the Ministry of Construction of Japan regarding where earth-rock flows occur, along with the characteristics of Taiwan geology. Adopting a predetermined risk standard of geological lithology, this study divides such geology into three broad categories, based on the maximum, minimum and intermediate values. Among the preservation factors, traffic and farmland were deemed to be either "present" or "not present" and also allocated based on the minimum values.

5. Discussion

5.1. Risk Assessment of River Terraces

The evaluation results for each river terrace are shown in Table 5. The average value (57.70) and standard deviation (13.346) were calculated by statistical methods, with the average value as the center plus or minus one standard deviation. After adjusting with the concept of rounding to integers, the boundaries were 70, 55 and 40. Thus, risk was divided into four categories: high risk (70–100), medium–high risk (55–69), medium risk (41–54) and low risk (0–40). These categories are also presented in map form in Figure 4.

After the risk assessment, 8 of the 40 focal river terraces were deemed to be high risk, 14 at medium-high risk, another 14 at medium risk, and the remaining 4 at low risk.

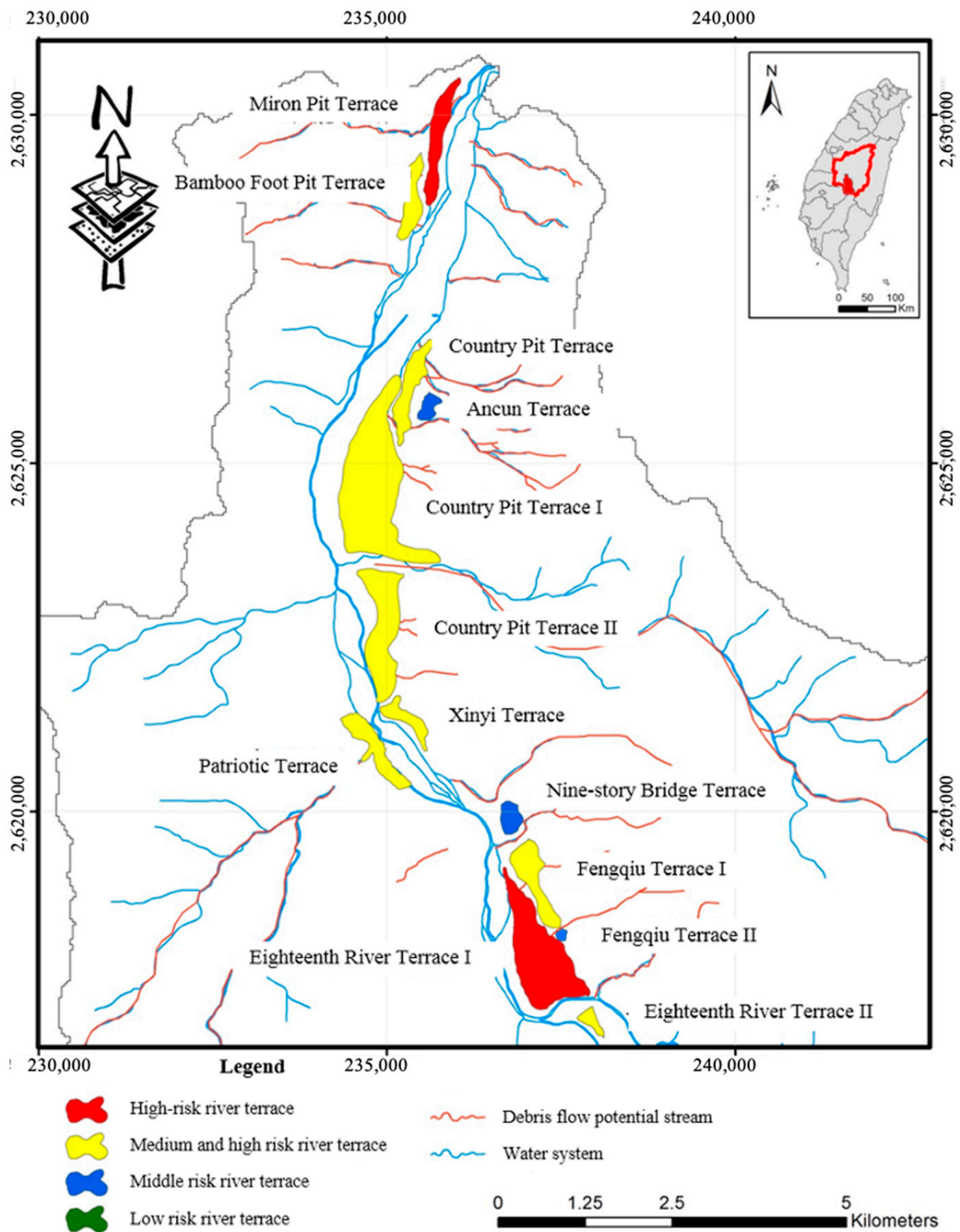


Figure 4. The distribution map of the danger degree of the river terrace.

Table 5. Risk assessment of river terraces.

No.	River Terrace Name	Risk	Hazard Classification
1	Miron Pit Terrace	67	Medium high
2	Bamboo Foot Pit Terrace	59	Medium high
3	County Pit Terrace	72	High
4	Ancun Terrace	49	Medium
5	County Pit Terrace I	79	High
6	County Pit Terrace II	85	High
7	Xinyi Terrace	81	High
8	Patriotic Terrace	78	High
9	Nine-story Bridge Terrace	49	Medium
10	Fengqiu Terrace I	66	Medium high
11	Eighteenth River Terrace I	76	High
12	Fengqiu Terrace II	45	Medium high
13	Eighteenth River Terrace II	53	Medium high
14	Xinxiang Terrace	53	Medium high
15	Rona Terrace I	55	Medium
16	Rona Terrace II	70	High
17	Trench Terrace	38	Low
18	Ali Does Not Move the River Terrace I	35	Low
19	Ali Does Not Move the River Terrace II	65	Medium high
20	Wangmei Terrace	50	Medium
21	Ali Does Not Move the River Terrace III	39	Low
22	Wangxiang Terrace	49	Medium
23	Ali Does Not Move the River Terrace IV	68	Medium high
24	Heshe Terrace	78	High
25	Malacca Terrace I	59	Medium high
26	Malacca Terrace II	42	Medium
27	Toutunxi Terrace I	67	Medium high
28	Toutunxi Terrace II	59	Medium high
29	Four Districts	44	Medium
30	No. 3 Creek Terrace	65	Medium high
31	Upper Fourth terrace	37	Low
32	No. 4 Creek Terrace	41	Medium
33	Dongpu Bridge Terrace I	55	Medium high
34	Dongpu Bridge Terrace II	52	Medium
35	Dongpu Terrace I	50	Medium
36	Dongpu Terrace II	62	Medium high
37	Dongpu Terrace III	47	Medium
38	Dongpu Terrace IV	63	Medium high
39	Dongpu Terrace V	57	Medium high
40	Ugankeng River Terrace	49	Medium

5.2. Verification

Three comparison methods were used in this research to verify our approach. These were: (1) unsupervised classification using the SPOT-3 satellite multi-spectral state (XS) image map of Chen Youlanxi in each period to determine changes in river-terrace area; (2) comparison of river terraces in various periods with satellite images and aerial photos; (3) comparison of historical disaster data from the Chenyulan River, covering a total of 87 floods linked to 42 discrete weather events from August 1959 through October 2009 [43].

5.3. Historical Disaster Comparison

5.3.1. Dangerous River Terraces

As noted above, eight river terraces were deemed high-risk by our approach because they scored above 70 points. This indicated that the frequency of disasters there is high, damage to buildings and crops is noteworthy, and the area affected is relatively large. From historical disaster data, it can be seen that debris flows struck these eight terraces at 1.36 times the average rate; dike destruction (by number of occurrences) and land loss (in

hectares) were both 5 times the average; houses totally destroyed, 4.44 times the average; damaged houses, 4.09 times the average; number of deaths, 2.74 times the average.

5.3.2. County Pit I

County Pit I is a high-risk river terrace located on the right bank of the lower reaches of Chenyulan River. Figure 5 was obtained by extracting and overlapping images from five periods and shows little change in this area before and after Typhoon Hebo, whereas after Typhoon Tochigi, a shrinking trend in its land area can be observed. After the 72nd flood, the terrace's area was obviously reduced, but after Typhoon Morakot five years later, it had increased.

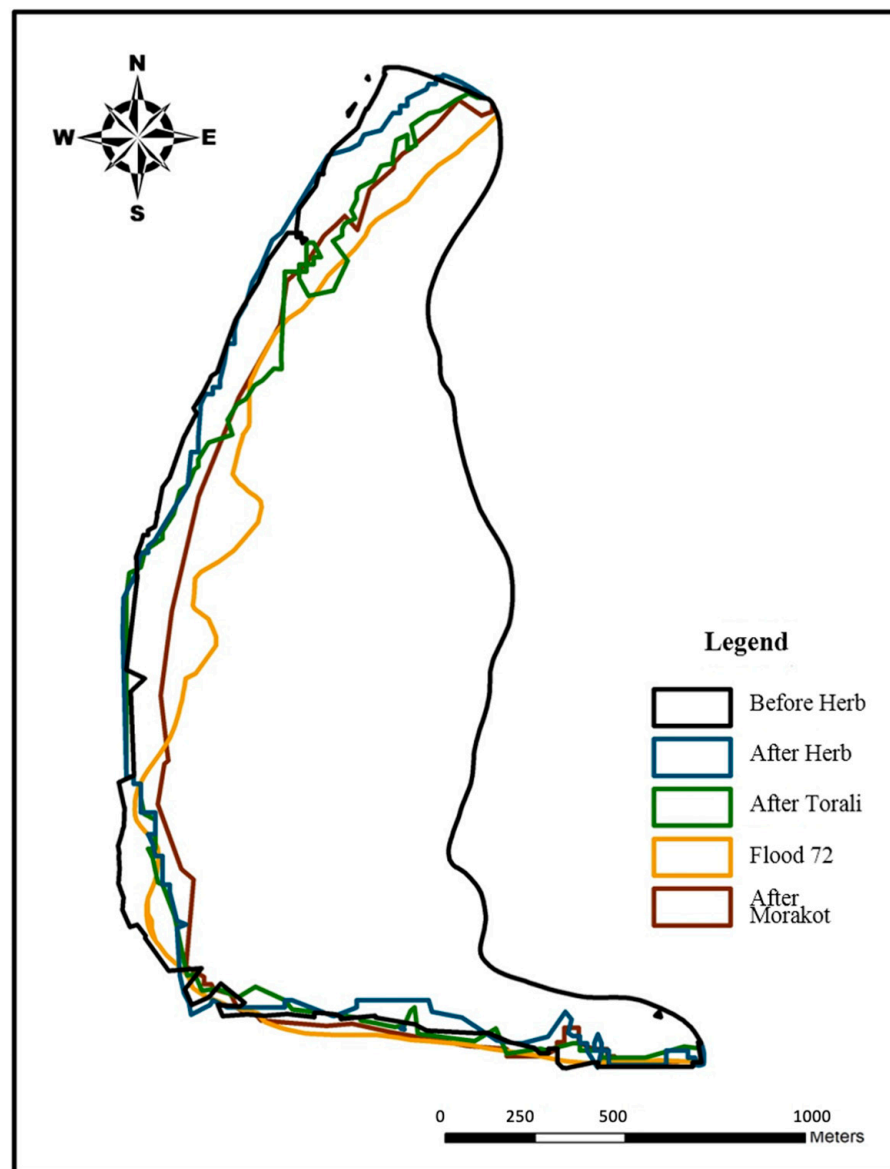


Figure 5. Area changed to County Pit I across five flooding events.

County Pit Terrace I was destroyed by Typhoon Mintouli in 2004, which in turn caused the embankment of Junkengxi Terrace I to be washed away. The disaster area was very large, as shown in aerial photographs obtained from the Fourth River Bureau, Water Resources Department, Ministry of Economic Affairs (Figures 6–9).



Figure 6. The County Pit embankment in 2003 (the year before it was destroyed).



Figure 7. The former area of the County Pit embankment, marked in blue, in 2004.



Figure 8. The Shang'an embankment in 2003 (before its destruction).



Figure 9. The former area of the Shang'an embankment, marked in blue, in 2004.

5.3.3. Toutunxi Terrace I

Toutunxi I is a medium-high-risk river terrace located on the right bank of the middle reaches of Heshhe River. A schematic diagram of its changes, based on image extraction and overlap from five flooding events, is presented in Figure 10. It is obvious from Figure 10 that the area of the terrace was broadly unchanged after Typhoon Toraji and the 72nd flood, but after Typhoon Morakot, it was significantly reduced.

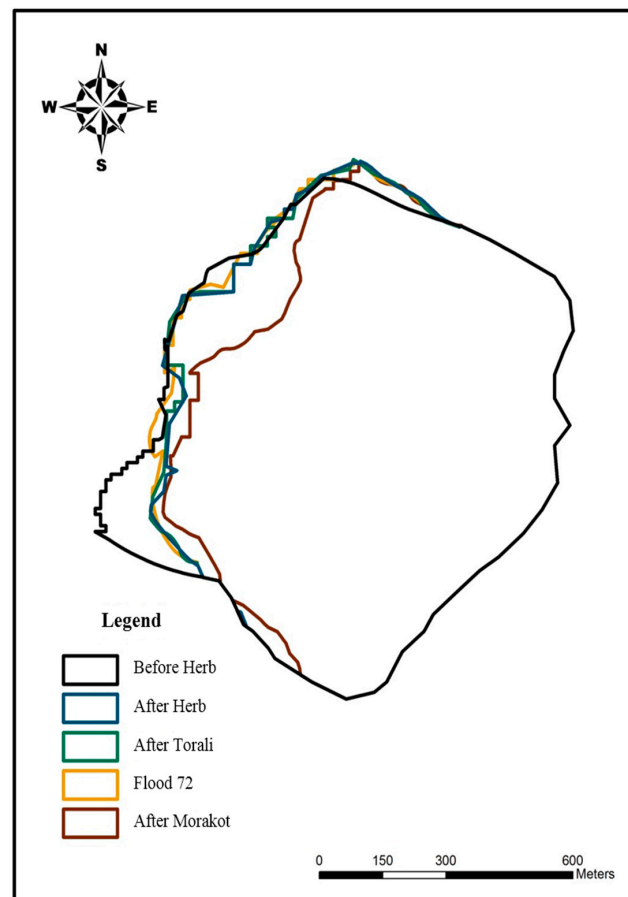


Figure 10. Area changed to Toutunxi Terrace I across five flooding events.

During Typhoon Morakot in 1998, three large landslides in the upper reaches of Toutunxi Creek indirectly formed soil and rock flows, which caused both banks of the downstream terraces to be washed away. In a satellite image from before this disaster (Figure 11, left), the channel of the Toukeng River is not obvious, being then only 20–30 m wide, but one taken after it (Figure 11, right) shows the channel clearly, as it had widened to 120 m.

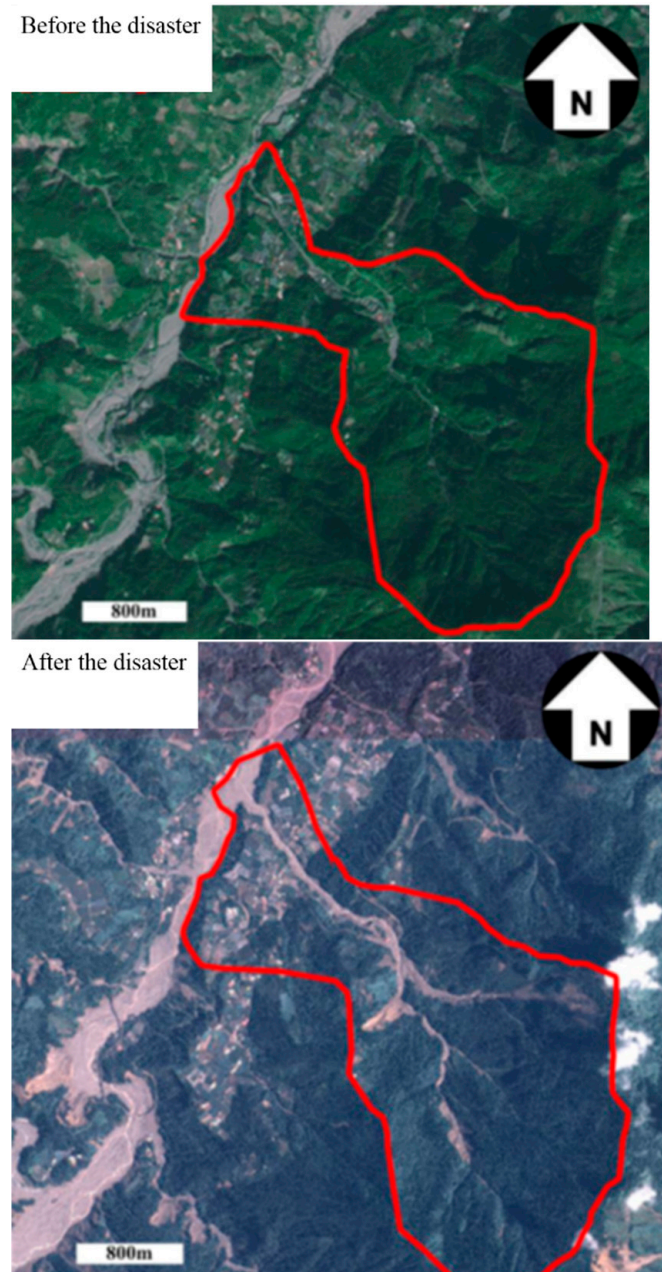


Figure 11. The confluence of Toutunxi Creek and the Toukeng River before and after Typhoon Morakot in 1998, with study area marked in red.

6. Conclusions

The latent-susceptibility factors selected in this study through the literature were the length of the attacking bank, distance from fault, distance from river course, number of potential debris flows, minimum specific height, average slope, geology, number of erosion ditches, distance to collapsed land, etc. The three preservation factors selected were the preservation of households, transportation and farmland; the risk to particular river

terraces was established from the latent-susceptibility factors and preservation factors. The results of the AHP analysis indicated that, among the latent-susceptibility factor conditions, those affecting the front of the river terrace were considered more important than those affecting the river terrace itself or the area behind it. Additionally, the results indicated that the preservation of households was deemed more important than traffic or farmland factors. The research also established that, of the 40 focal river terraces, the highest-risk ones were County Pit Terrace, County Kengxi Terraces I and II, Xinyi Terrace, Patriotic Terrace, Eighteenth Terrace I, Rona Terrace II and Heshe Terrace. In this study, a potential factor assessment framework was established to examine whether the research results were contradictory by comparing SPOT satellite images and historical hazards. Unlike other risk assessments of riverine terraces [10,11], the current environmental conditions of riverine terraces can be used to assess the risk of disasters. This study's risk-level designation has important implications for both disaster prevention and the evacuation of local residents when disasters occur, and, if generally adopted, it should mitigate loss of life and property. However, this study was not without its limitations. Chief among these was that it relied on the 5m × 5m DTM of Taiwan surveyed and mapped by the Chengda Satellite Center in 2004 to conduct its river-terrace risk assessments and stability analyses. The use of a more recent DTM would undoubtedly increase the accuracy of the analysis results. Additionally, when conducting stability analysis, due to limited drilling data from the Chenyulan River Basin, such data from Toutunxi River Terrace I were used as a proxy for it. Thus, more geological data would, therefore, improve our approach's ability to identify potential river-terrace collapses.

Author Contributions: Conceptualization, J.-Y.L.; data curation, Y.-M.H.; writing—original draft, Y.-M.H.; writing—review and editing, J.-C.C.; supervision, J.-Y.L. All authors have read and agreed to the published version of the manuscript.

Funding: This study is part of the research results of the Ministry of Science and Technology number NSC100-2218-E-005-001. I would like to thank the staff for their hard work during the planning period and to express their greatest gratitude to the National Science Council for their support research. Funding has enabled this study to be successfully completed.

Institutional Review Board Statement: Not applicable.

Informed Consent Statement: The authors declare no conflict of interest.

Data Availability Statement: The data presented in this study are available in the article.

Acknowledgments: We would like to thank the anonymous reviewers for their helpful suggestions and feedback.

Conflicts of Interest: The authors declare no conflict of interest.

References

1. Li, X.D. From the point of view of topography, Chen Youlan's He Bo Feng disaster. *Geotech. Technol.* **1996**, *17*–24. Available online: <http://www.geotech.org.tw/purchase-inner.php?id=131> (accessed on 15 November 2021).
2. Liu, M.X. Topographical Research on the River Steps in the Northwest of Taiwan. Ph.D. Thesis, Department of Geography, National Taiwan Normal University, Taipei, Taiwan, 2004.
3. Du, H.Y.; Chen, H.H.; Cao, B.X. *Geomorphology and Quaternary Geology*; one edition of Three Brushes; Geological Publishing House: Beijing, China, 1991.
4. Chang, R.J.; Shi, Z.T. An overview of the study of the rivers. *J. Chin. Geogr. Soc.* **1990**, *18*, 1–8.
5. Ger, M.L. A Study of the Relations between the Terraces and Subsurface Structure in the Hsinshue Area. Ph.D. Thesis, Department of Geography, National Taiwan Normal University, Taipei, Taiwan, 2005.
6. Wang, F.T. Comparison of River Terraces in Hua-Tung Coast Area: A Case Study in Streams of Shuilian, Shuimuding and Sanxian. Master's Thesis, Department of History and Geography, University of Taipei, Taipei, Taiwan, 2016.
7. Chang, T.Y. Fluvial Terrace Landscape in Tai-Yuan Basin and Its Implications. Master's Thesis, Department of Natural Resources and Environmental Studies, National Dong Hwa University, Hualien County, Taiwan, 2016.
8. Wu, T.Y. Holocene Landscape Evolution of the Jinlun, Dazhu and Dawu River Basins in the Southeastern Taiwan. Master's Thesis, Department of Geography, National Kaohsiung Normal University, Kaohsiung, Taiwan, 2019.

9. Chen, Y.C. Application of Geographic Information System in Risk Assessment of River Terrace in Chenyulan River Watershed, Nantou County. Master's Thesis, Department of Civil and Construction Engineering, Chaoyang University of Technology, Taichung, Taiwan, 2010.
10. Zhuang, Z.Z. Apply Artificial Intelligence and Weight of Evidence to Assess Vulnerability for River Terrace Communities. Master's Thesis, Department of Land Management and Development, Chang Jung Christian University, Tainan, Taiwan, 2020.
11. Lin, J.R. Risk Assessment of Rainfall-induced Landslides for River Terrace Communities. Master's Thesis, Department of Land Management and Development, Chang Jung Christian University, Tainan, Taiwan, 2020.
12. Chang, C.F. Effects of Watershed Runoff Factors on Debris Flow Occurrence—Using the Watershed of Chenyoulan Stream as An Example. Master's Thesis, Department of Bioenvironmental Systems Engineering, National Taiwan University, Taipei, Taiwan, 2015.
13. Lin, S.Y. Study on the Factors of Landslide Susceptibility Analysis in Chen- You-Lan Watershed. Master's Thesis, Department of Soil and Water Conservation, National Chung Hsing University, Taichung, Taiwan, 2018.
14. Thi-To, N.N. Early Warning of Landslide Hazard by Integrating Spatial Statistical Analysis Methods to Calculate the Landslide Susceptibility Index in the Chen-Yu-Lan River Watershed. Taiwan. Ph.D. Thesis, Department of Earth Sciences, National Cheng Kung University, Tainan, Taiwan, 2019.
15. Debris Flow Disaster Prevention Information, Soil and Water Conservation Bureau. Available online: <https://246.swcb.gov.tw/?lang=en> (accessed on 15 November 2021).
16. Lin, M.L.; Wu, W.L.; Zhou, K.X.; Yang, Z.S.; Wang, J.P. Discussion on Geographical Location Types and Remediation Cases of Taiwan Slope Disasters. *CECI Eng. Technol.* **2008**, *77*. Available online: <https://www.ceci.org.tw/Upload/Download/F8950026-85C8-4386-9075-13CCB737881D.pdf> (accessed on 15 November 2021).
17. Lin, D.G.; Lai, Y.C.; Liu, W.T. Design and analysis of natural ecological method for river and stream improvement. In Proceedings of the Natural Ecological Practices Conference, Taitpi, Taiwan, November 2002. Available online: <https://www.m.ishare.iask.sina.com.cn/f/34860363.html> (accessed on 15 November 2021).
18. Su, K.H. Investigating the Slope Failure of Interbedded Sandstone and Mudstone Slope: Case of Highway R174 on 50 k + 650. Master's Thesis, Institute of Resources and Environment, University of Kang Ning, Taipei, Taiwan, 2007.
19. Central Weather Bureau. Available online: <https://www.cwb.gov.tw/eng/> (accessed on 15 November 2021).
20. Lin, C.W. Geological Factors to Influence the Landslides in The Hoshe Area, Nantou Hsien. *Sino-Geotech.* **1996**, *57*, 5–16.
21. Wang, M.H. Application of SPOT Satellite Images and GIS for Landslide Potential Analysis-A Case Study of Shao-Lai River. Master's Thesis, Department of Civil and Construction Engineering, Chaoyang University of Technology, Taichung, Taiwan, 2008.
22. Chu, Y.T.; Hsu, M.L. The Relationship between Discharge and Suspended Sediment Concentration at Typhoon Events in Yu-Feng Catchment. *J. Geogr. Sci.* **2007**, *49*, 1–22.
23. Huang, T.H. The Study of Slope Landslide Disaster Management-Take Tainan County for Example. Master's Thesis, Department of Land Management and Development, Chang Jung Christian University, Tainan, Taiwan, 2004.
24. Zhang, L.; Weng, Y.; Chen, X.H. Research on evaluation model for vulnerability of flood control based on SVM. *Yangtze River* **2009**, *40*.
25. Lin, C.K. Topography of Taiwan, *Taiwan Provincial General Records 1957*, 1. (Land Records, Geography, Volume 1), published by the Taiwan Provincial Literature Committee, 424 pp. Available online: https://tm.ncl.edu.tw/article?u=006_001_0000395034&lang=chn (accessed on 15 November 2021).
26. Lin, C.C. Topography of Taiwan, Draft of the General Gazetteer of Taiwan Province, Taiwan Provincial Literature Committee. *1*, 1957.
27. Wang, L.C. The Characteristics of Topography and Occurrence of Hillslope Debris Flows in Shitou area. Master's Thesis, Department of Earth Sciences, National Cheng Kung University, Tainan, Taiwan, 2005.
28. Cheng, Y.C. Application of Geographic Information System to Regional Slope Stability Analysis—Tianxiang-Tailuege Section of Zhongheng Highway. Master's Thesis, Department of Materials Science and Engineering, National Cheng Kung University, Tainan, Taiwan, 1992.
29. Kao, C.L. A Study on the Failure Potential of Slopes along 31~75 K Section of the 14th Provincial Highway. Master's Thesis, Department of Civil and Construction Engineering, Chaoyang University of Technology, Taichung, Taiwan, 2003.
30. Liu, H.F. Evaluation of Slope Failures along the 14th Provincial Highway Using Artificial Neural Networks. Master's Thesis, Department of Civil and Construction Engineering, Chaoyang University of Technology, Taichung City, Taiwan, 2005.
31. Hou, C.F. Application of SPOT Remote Sensing Images and GIS on Landslide potential Analysis Using Chen Yu Lan Creek Basin. Master's Thesis, Department of Civil and Construction Engineering, Chaoyang University of Technology, Taichung, Taiwan, 2006.
32. Luo, S.Y.; Huang, H.Y. Chenyulan. Available online: http://www1.geo.ntnu.edu.tw/~shensm/Course/CourseWork/TaiGeom_Stu90/24.25%E9%99%B3%E6%9C%89%E8%98%AD%E6%BA%AA/ (accessed on 15 November 2021).
33. Jeng, F.S.; Lin, M.L. Engineering Deficiencies Exposed by Typhoon Herb. *Sino-Geotech.* **1996**, *57*, 65–74.
34. Chang, W.C. Research on the Sustainability of Debris Flow Influenced Areas in Yilan County with the Application of the Fuzzy Backpropagation Neural Network Deduction Pattern. Master's Thesis, Department of Civil Engineering, National Ilan University, Ilan, Taiwan, 2006.
35. Taiwan's Water Resources Agency, MOEA. Available online: <https://eng.wra.gov.tw/> (accessed on 15 November 2021).
36. Chang, S.J. Hillside Survey Planning, Evaluation and Slump Prediction and Management. Master's Thesis, Department of Geography, National Taiwan Normal University, Taipei, Taiwan, 1993.

37. Hung, J.J. Typhoon Herb, The New-Central-Cross-Island-Highway and Slope Failures in Central Taiwan. *Sino-Geotechnics* **1996**, *57*, 25–30.
38. Tarn, H.R. The Transportation and Deposition of Catastrophic Landslides in Taiwan: Insight from Granular Discrete Element Simulation. Ph.D. Thesis, Department of Geosciences, National Taiwan University, Taipei, Taiwan, 2010.
39. Chi, C.C. Investigation and Interpretation of Rock Slide Potential. *Nation Sci. Technol. Cent. Disaster Reduct.* **2010**, *62*. Available online: <https://www.ncdr.nat.gov.tw/Epaper/MessageView?itemid=5061&mid=39> (accessed on 15 November 2021).
40. Saaty, T.L.; Vargas, T.L. Comparison of eigenvalue, logarithmic least squares and least squares methods in estimating ratios. *Mathematical Modelling* **1984**, *5*, 309–324. [CrossRef]
41. Shrestha, R.K.; Alavalapati, J.R.; Kalmbacher, R.S. Exploring the potential for silvopasture adoption in south-central Florida: An application of SWOT-AHP method. *Agric. Syst.* **2004**, *81*, 185–199. [CrossRef]
42. Juang, C.H.; Chen, C.J. A rational method for development of limit state for liquefaction evaluation based on shear wave velocity measurements. *Int. J. Numer. Anal. Methods Geomech.* **2000**, *24*, 1–27. [CrossRef]
43. Lai, M.F. Application of GIS to Spatial Characteristic of Rainfall—Chenyulan River Watershed as an Example. Master's Thesis, Department of Civil and Construction Engineering, Chaoyang University of Technology, Taichung, Taiwan, 2010.

Article

Quantifying the Occurrence of Multi-Hazards Due to Climate Change

Diamando Vlachogiannis ^{*}, Athanasios Sfetsos , Iason Markantonis , Nadia Politi , Stelios Karozis 
and Nikolaos Gounaris

Environmental Research Laboratory (EREL), INRASTES, NCSR “Demokritos”, Agia Paraskevi, 15341 Attiki, Greece; ts@ipta.demokritos.gr (A.S.); jasonm@ipta.demokritos.gr (I.M.); nadiapol@ipta.demokritos.gr (N.P.); skarozis@ipta.demokritos.gr (S.K.); gounaris@ipta.demokritos.gr (N.G.)
^{*} Correspondence: mandy@ipta.demokritos.gr; Tel.: +30-210-650-3417

Abstract: This paper introduces a climatic multi-hazard risk assessment for Greece, as the first-ever attempt to enhance scientific knowledge for the identification and definition of hazards, a critical element of risk-informed decision making. Building on an extensively validated climate database with a very high spatial resolution ($5 \times 5 \text{ km}^2$), a detailed assessment of key climatic hazards is performed that allows for: (a) the analysis of hazard dynamics and their evolution due to climate change and (b) direct comparisons and spatial prioritization across Greece. The high geographical complexity of Greece requires that a large number of diverse hazards (heatwaves—TX, cold spells—TN, torrential rainfall—RR, snowstorms, and windstorms), need to be considered in order to correctly capture the country’s susceptibility to climate extremes. The current key findings include the dominance of cold-temperature extremes in mountainous regions and warm extremes over the coasts and plains. Extreme rainfall has been observed in the eastern mainland coasts and windstorms over Crete and the Aegean and Ionian Seas. Projections of the near future reveal more warm extremes in northern areas becoming more dominant all over the country by the end of the century.

Citation: Vlachogiannis, D.; Sfetsos, A.; Markantonis, I.; Politi, N.; Karozis, S.; Gounaris, N. Quantifying the Occurrence of Multi-Hazards Due to Climate Change. *Appl. Sci.* **2022**, *12*, 1218. <https://doi.org/10.3390/app12031218>

Academic Editor: Jason K. Levy

Received: 15 December 2021

Accepted: 21 January 2022

Published: 24 January 2022

Publisher’s Note: MDPI stays neutral with regard to jurisdictional claims in published maps and institutional affiliations.

Keywords: climate change; multi-hazards; WRF-ARW; EC-Earth GCM; Greece

1. Introduction

A new era has unequivocally emerged that has brought climate change and its impacts to the foreground of scientific research. There is growing evidence that weather and climate extremes (i.e., hazards) are increasing in frequency, intensity, spatial coverage and duration, indicating the need for a more meticulous investigation and a better physical understanding of the processes governing the state of the climate and its future evolution [1–3]. The adverse impacts of extreme events, evidenced in the reported data of disaster implications, e.g., [4–6], are also an active subject of climate research of paramount importance [7–11]. Noteworthy, anthropogenic effects are emerging as the underlying cause of the weather and climate extremes [1,12–18].

Over recent years, research works have consistently reported that climate change aggravates climate hazards, amplifying the risks of various impacts (river and coastal floods, wildfires, droughts, landslides, etc.) [19–23]. Several studies on temperature and precipitation extremes have provided important findings on the regional variability of the impacts of climate change across Europe, e.g., [24–29]. Forzieri et al. [30] reported that the risks of wildfires, windstorms and inland flooding would increase in Europe, with varying degrees of change across regions, while the most dramatic rise is predicted to be in damages in southern Europe caused by heatwaves, droughts and coastal floods. The report of PESETA IV [31] consolidated those findings and indicated “a clear north–south divide, with the southern regions in Europe being much more impacted by the effects of extreme heat, water scarcity, drought, forest fires and agriculture losses”. The estimated



Copyright: © 2022 by the authors. Licensee MDPI, Basel, Switzerland. This article is an open access article distributed under the terms and conditions of the Creative Commons Attribution (CC BY) license (<https://creativecommons.org/licenses/by/4.0/>).

patterns of climate-change developments urge for more efficient risk management of climate-related extremes and disasters in order to significantly advance climate-change adaptation, particularly in the most vulnerable regions. This consequently implies the need for a reliable quantification of the probability of extremes in the current and future climate. Identifying the climate vulnerabilities of key societal systems should be based on a detailed knowledge of projected climate-change hazards and the factors affecting the likelihood of each one for the selected assessment of the region of interest.

According to the report of the United Nations Office for Disaster Risk Reduction [32], the term “multi-hazard” is used to promote risk reduction and disaster management, and denotes hazardous events that may occur simultaneously or cumulatively over time. One of the most challenging research questions is the harmonization of risk metrics to allow the comparison of risks across hazards, regions, time, assets, or sectors [33]. Establishing a harmonized risk understanding would pave the way to a multi-hazard risk assessment, introducing interactions and cascading effects as well as providing some analytical interpretations of the compound and systemic risks. This would lead to more credible scenarios for describing future disaster events in terms of their magnitude and probability based on the validated scientific knowledge that can benefit from high-resolution climate projections.

The single-hazard risk assessment is a proven methodology, but shifting to multi-hazards is not a linear or easily understood process, as a multi-hazard risk analysis is not just the sum of single hazard risk examinations and thus, comparability of the single-hazard results is strongly needed [34]. Due to the diversity of the hazard characteristics’ complex relationships, triggering effects, climate-changing mechanisms, compounds and interactions could be potentially established [35–37].

In this work, the occurrence of hazards due to climate change was determined for Greece using data that were dynamically downscaled to a very high resolution by the Advanced Weather Research and Forecasting (WRF-ARW) model [38], initially produced by the EC–Earth Global Climate Model (GCM) [39]. The hindcast period covered the years from 1980 to 2004, while for the future projections, two different periods, i.e., 2025–2049 (near future) and 2075–2099 (far future), were studied using the Intergovernmental Panel on Climate Change (IPCC) Representative Concentration Pathways (RCPs), RCP4.5 and RCP8.5, following the recommendations of the EU National Risk Assessment [33] and similar studies in the US [40]. The RCP scenarios demonstrated a significant convergence in their emission pathways in the near future and considerable deviations towards the end of the century [41].

It has been established that high-resolution, dynamic-downscaling models applied to regional climate assessments can be implemented to assess the climate-change impacts on extremes, especially in areas with complex topography and local scale effects [42–45]. Here, we sought to provide the first step towards a comprehensive multi-hazard risk assessment for the country based on high-resolution model data to support training and preparatory activities for disaster risk reduction (DRR). The analysis focused on four critical climate hazards for Europe: heat and cold extremes, flash floods, and windstorms, each one described by a climate indicator (Section 2.2).

The scope of this work was to carry out a very detailed assessment of the most significant hazards that have occurred in Greece in the past and to predict their evolution in the future considering the impact of climate change. This is a highly valuable process as disaster management should also take into account the (non-)stationary characteristics of climate change. The current study examined these parameters for Greece using very-high-resolution climate simulations at 5 km. Furthermore, one of the goals was to identify a common categorization framework across different climate hazards, which allowed a direct and coherent prioritization of the hazards and their evolution due to climate change considering complex patterns due to local geographic conditions. The produced hazard data could readily be applied to the generation of multiple scenarios with various likelihoods of occurrence in order to obtain a more complete picture of risk [32], accounting for climate-change projections (IPCC). In addition, this work was based on the recommenda-

tions set by the UNDRR/ISC Sendai Hazard Definition and Classification Review Technical Report [46] and intended to introduce the climate dimensions and dynamic evolution of risk harmonization that was missing from such assessments [33].

Section 2 focuses on the details of the data used and the methodology that was developed to estimate the probability of the occurrence of extreme values of the variables. Section 3 presents the results and discussion of the analysis applied to the quantification of risks and the likelihood of hazard evolution due to climate change. Finally, the final section concludes the paper.

2. Materials and Methods

2.1. Area of the Study and Model Datasets

The study area included the country of Greece. The country presents several climatic variations, always in the Mediterranean climate frame, due to the influence of its vivid geomorphologic complexity (interplay of mountainous regions and plains, extended coastline, and numerous islands) on the different atmospheric-pressure dependencies from the Atlantic, central Mediterranean area, Eurasia and North Africa. This enhances the need for higher-resolution climate modeling to resolve the topography features more effectively.

In the present work, climate data of EC–Earth (1.125° horizontal resolution originally) downscaled by the WRF-ARW version 3.6.1 model to $5 \times 5 \text{ km}^2$ were employed at a temporal resolution of 6-h. The hindcast climate simulations have been extensively evaluated in our previous works, whereby exhaustive quantitative validation of the highly resolved fields of temperature, precipitation, wind speed and solar radiation were performed for our observations [45,47–50]. The WRF-ARW modeling domain covering Greece comprises a grid of 185×185 cells in the horizontal and 40 levels in the vertical that are arranged according to terrain, following the hydro-static-pressure vertical coordinates (up to ~50 mbars). A more detailed description of the WRF model setup and physical parameterization schemes can be found in [47].

For the simulations of future years under the influence of climate change, the two IPCC greenhouse-gas-emission scenarios, RCP4.5 and RCP8.5, were selected as they constitute the most commonly used scenarios by impact-assessment modelers. In particular, RCP4.5 represents an increase in the radiative forcing of the atmosphere of 4.5 W/m^2 relative to the pre-industrial era with a profile of greenhouse-gas emissions increasing until the mid-century (~2050) and stabilizing thereafter until the end of the century (2100). On the other hand, RCP8.5 is considered to be the most extreme scenario with greenhouse-gas emissions increasing sharply until the end of the century, implying at its end a radiative forcing of 8.5 W/m^2 relative to the pre-industrial era. The future time periods in the RCP4.5 and RCP8.5 simulations were selected in order to study the projected climate-change effects on hazard dynamics, both in the middle and near the end of the 21st century. For the present analysis, the model-downscaled data that were used and the corresponding 25-year-period slots are presented in Table 1.

Table 1. The global (EC–Earth) model datasets downscaled by WRF model used in the study and corresponding periods.

Dataset	Period
EC–EARTH–WRF	1980–2004 (historical)
EC–EARTH–WRF RCP4.5	2025–2049 (near future)
EC–EARTH–WRF RCP8.5	2025–2049 (near future)
EC–EARTH–WRF RCP4.5	2075–2099 (far future)
EC–EARTH–WRF RCP8.5	2075–2099 (far future)

2.2. Statistical Tools and Data Processing

All model-data processing and figure drawing were executed with R software and the ARC.GIS (MAP) 10.0 environment. Figure 1 depicts the basic steps of the process followed for the assessment of the extreme values of the variables, namely those of temperature

(maximum and minimum), precipitation rate, snowfall and wind speed. Firstly, the maximum and minimum temperature values were retrieved for the summer and winter seasons, respectively, while data were extracted throughout the year from the gridded datasets to determine the extremes of the precipitation rate, snowfall and wind speed. In this manner, at each grid cell and for each period (see Table 1), the 25 maximum values of each variable were obtained. The process was applied to all three time periods of interest and both RCP scenarios (see Table 1).

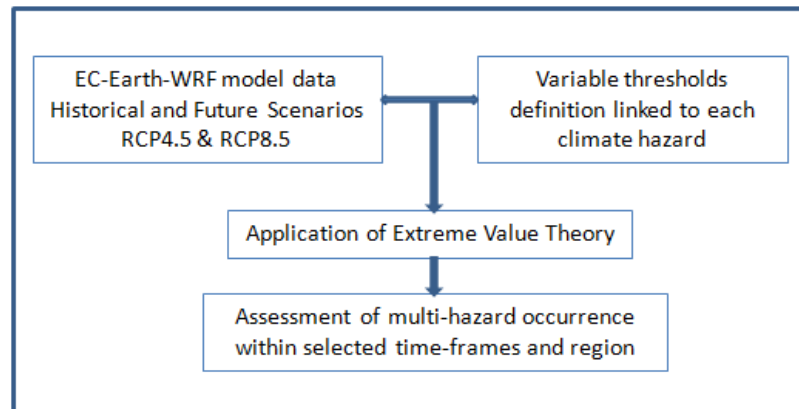


Figure 1. Schematic representation of the main methodological steps for determining a quantified climatic multi-hazard assessment.

Then, the modeled values of the variables of interest to this study were categorized in terms of likelihood, i.e., probability of occurrence, according to Table 2. The likelihood categories, six in total, and the threshold values of Table 2 were retrieved from the EU-CIRCLE project report [51] for the characterization of the hazard (maximum (summer) temperature, minimum (winter) temperature, precipitation rate, snow rate and wind speed). The probability of occurrence of each variable was calculated for all six categories. As the study was aimed at determining the likelihood of extremes, the focus was placed only on the specific categories characterizing the highest threshold values and hence, the probabilities of occurrence were calculated as totals of the three classes “High”, “Very High” and “Exceptional”.

In this work, the method for calculating the probability of exceeding a value was based on the Extreme Value Theory (EVT). The determination of the extreme values of the studied variables required the selection and definition of the underlying distribution functions. The estimations were made using the R package “Extremes” [52], fitting a Generalized Extreme Value distribution (GEV) to block maxima data (annual maxima) under the assumption of non-stationarity [53]. The GEV distribution has three parameters: the shape factor ξ , the scale or dispersion parameter σ and the location or mode parameter μ . The GEV-distribution function, $G(y)$, is given by:

$$\text{For } \xi \neq 0, G(y) = \exp\left(-\left[1 + \xi\left(\frac{y - \mu}{\sigma}\right)\right]^{-1/\xi}\right) \quad (1)$$

$$\text{For } \xi = 0, G(y) = \exp\left(-\exp\left(-\frac{y - \mu}{\sigma}\right)\right) \quad (2)$$

The GEV has three types depending on shape parameter ξ , as follows:

1. When $\xi = 0$, GEV is known also as Type I Extreme Value Distribution (or Gumbel Distribution, light tail)
2. When $\xi > 0$, GEV is known also as Type II Extreme Value Distribution (or Frechet Distribution, heavy tail)

3. When $\xi < 0$, GEV is known also as Type III Extreme Value Distribution (or Weibull Distribution, upper finite end point).

Table 2. Likelihood categories and threshold values for maximum and minimum temperature, maximum precipitation rate, maximum snow rate and maximum wind speed. In bold, the threshold values to which the probability of occurrence was applied in the current study.

Variables	Likelihood Categories					
	Very Low	Low	Medium	High	Very High	Exceptional
Daily Minimum Temperature [°C]	0<	0–(–2)	(–2)–(–5)	(–5)–(–10)	(–10)–(–15)	<(–15)
Daily Maximum Temperature [°C]	<30	30–33	33–35	35–39	39–42	>42
Daily Maximum Precipitation rate [mm/h]	<2.5	2.5–7.6	7.6–10.0	10–50	50–100	>100
Daily Maximum Snowfall [mm/h]	<2.5	2.5–12.7	12.7–25.4	25.4–76.2	76.2–127	>127
Daily Maximum wind speed value [m/s]	0–3	3–12	12–15	15–20	20–30	>30

The final step of the applied methodology included the calculation of the most frequently appearing hazard at each grid cell, time period and RCP scenario. In this manner, we performed the spatial assessment of the occurrence of multi-hazards in the historical period and in the two studied future periods according to the two RCP projections in order to illustrate the areas susceptible to hazards over long time scales.

3. Results and Discussion

In this part, we present the results of the previously described applied approach. For reasons of clarity, each subsection provides the results pertinent to each studied hazard. Figure 2a presents the highly resolved topography of the EC-Earth global model down-scaled by WRF to the high horizontal resolution of $5 \times 5 \text{ km}^2$. Additionally, highlighted in Figure 2b are the regions of the country, where some important findings are more extensively discussed.

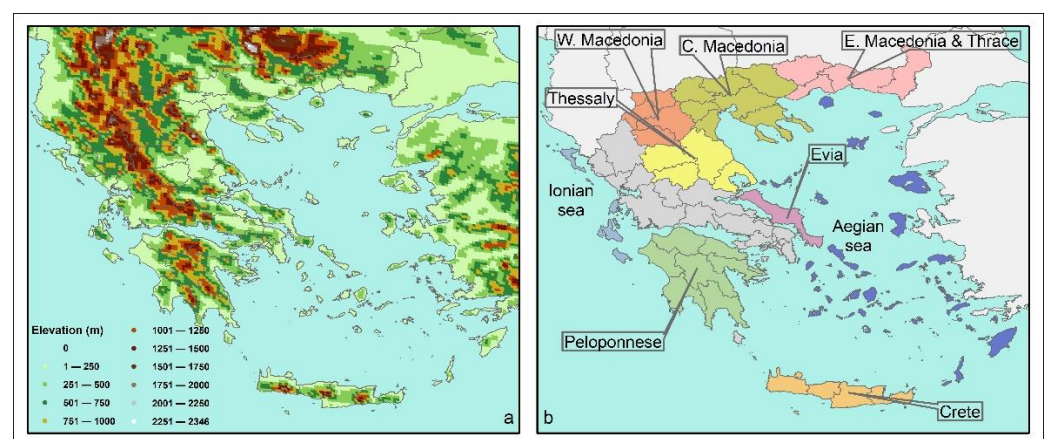


Figure 2. (a) EC-Earth-WRF topography of the simulated domain of Greece with horizontal resolution ($5 \times 5 \text{ km}^2$). (b) Highlighted regions of the country of particular interest for discussion.

3.1. Maximum Temperature

Figure 3a shows the probability of the occurrence of TX exceeding the threshold value (i.e., the probability of exceedance) of 35 °C during the summer season of the historical period of 1980–2004. Figure 3b–e depict the differences in the probability of exceedance

between the future projections and the historical values (i.e., future–historical) for both RCPs and the studied periods. During the historical period, we may deduce that the majority of areas show low probabilities of exceedance below 2.5% (Figure 3a). On the other hand, the highest occurrence of maximum temperature values with the probability of exceedance above 10% is seen in the plains of the regions of Thessaly, central Macedonia, Peloponnese, the western mainland, the eastern Aegean islands and southern Crete, which are well known as summer hot-spot areas [54].

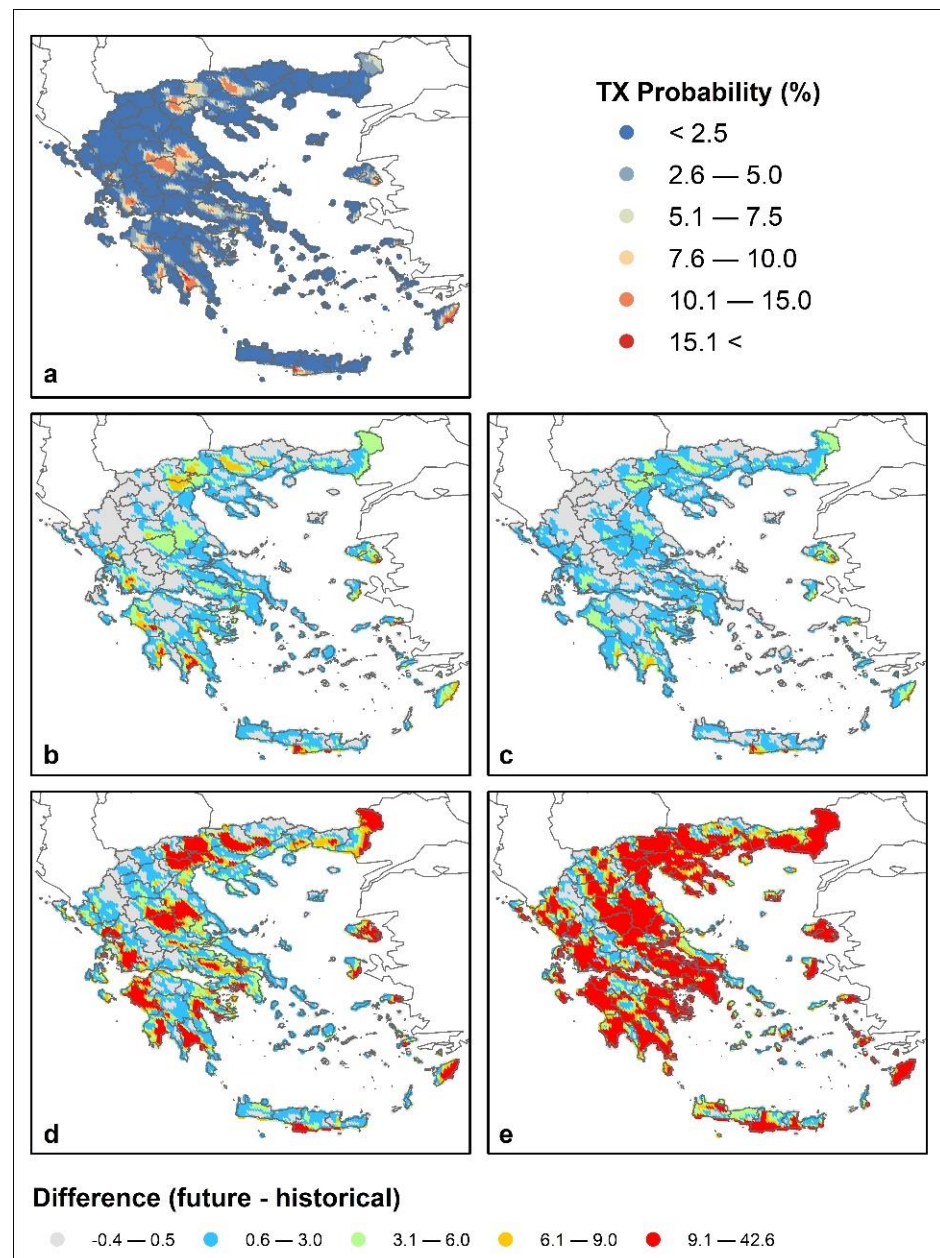


Figure 3. (a) Spatial distribution of probability of TX exceedance above 35 °C calculated using EC–Earth–WRF downscaled data for the historical summer period 1980–2004. Differences (future–historical) in the probability of TX exceedance for: (b) RCP4.5 in near future (2025–2049), (c) RCP8.5 in near future (2025–2049), (d) RCP4.5 in far future (2075–2099) and (e) RCP8.5 in far future (2075–2099).

Overall, in the near future, more areas compared to the historical period were found to be exposed to extreme TX values (Figure 3b,c). In addition, it appears that the probability increase in hot-spot areas is higher in RCP4.5, with these values exceeding 3%. The

differences in the referenced areas become much larger, exceeding 10%, and even extend spatially into the far future and more profoundly in RCP8.5 (Figure 3d,e). In fact, the probability of exceedance according to RCP8.5 in the far future increases not only in the plains areas with low topographic heights but also in areas with heights in the range of 500 to 1000 m (Figure 3e).

This could be considered an important change predicted by the worst-case emissions scenario that would cause adverse conditions near the end of the century. Nevertheless, in the near future, insignificant changes are expected over the high mountainous regions according to both RCPs concerning the historical period (Figure 3b,c). In the far future, the insignificant changes are still found over the highest mountains with RCP4.5 (Figure 3d) but the RCP8.5 scenario diminishes these (around zero values), showcasing detectable differences in the probability of exceedances of 3–6% with respect to the historical period, even over the highest summits of the mainland (Figure 3e).

3.2. Minimum Temperature

Figure 4a presents the probability of TN exceeding -5°C towards lower values during the winters of the historical period. Overall, the probability values remain below 5% in most areas of the mainland and the islands. Over the higher topographic heights of the central and northeastern mainland (see Figure 2a), the probability increases to noticeable levels in the range of 20 to 40% that are consistent with the occurrence of very low temperatures and the extreme winter climatology of the country [54]. The differences in the probabilities of exceedance of TN between the two future and historical periods (future–historical) are shown in Figure 4b–e for both RCPs. We may observe that under all scenarios and periods, areas that have historically had very low probability values of extremely cold temperatures preserve these characteristics in the future.

In general, we observe a strong decrease in the probabilities of exceedance of TN over the mountainous areas of the central and northeastern mainland in both future periods with respect to the historical period, which denotes a reduction in the future occurrence of extreme values of TN and thus, fewer winter extremes. In the near-future period, the highest decreases in the central mountainous areas are more intense in RCP4.5 (Figure 4b) than in RCP8.5 (Figure 4c) while in eastern Macedonia, Thrace and Peloponnese there are no noticeable differences between the two scenarios. Stronger decreases in the occurrence of winter extremes are estimated for both scenarios in the far future (Figure 4d,e). The impacted areas according to RCP4.5 remain the same during both periods (Figure 4b,d) but they extend more spatially in the far future with RCP8.5 (Figure 4c,e).

3.3. Precipitation Rate

Figure 5a presents, for the historical period, the probability of precipitation extremes calculated as the probability of precipitation rates exceeding 10 mm/h. The pattern with persisting probabilities over the majority of the domain of less than 0.025% does not yield noticeable spatial variability. Yet, increased probabilities of extreme precipitation with values greater than 0.075% are observable in the very high mountainous areas of the central and eastern mainland and over the summits of Crete and Peloponnese. In addition, some areas known for high-precipitation rates such as the Ionian islands and parts of central and eastern Macedonia and Rhodes reasonably exhibit distinguishable contours of the probability of exceeding 10 mm/h up to 0.075%.

The differences between the future projections and historical simulations indicate a reduction in future extreme precipitation mostly in the eastern parts of the mainland, central Aegean islands and mountainous areas of Crete (Figure 5b–e). The maximum decrease is obtained in the near future (Figure 5b,c). Additionally, with reference to the historical period and both RCPs, we may observe minute and insignificant changes in extreme precipitation rates, more extensively in the regions of Thessaly and central Macedonia and predominantly in the near future (Figure 5b,c). However, interesting patterns of increased probabilities of extreme precipitation can be seen in highly mountainous areas primarily in

the western and northeastern mainland (in the range of 0.051–0.285%) and more vividly for RCP8.5 (Figure 5d,e). The RCP4.5 projections do not show a noticeable change between the two future periods. On the contrary, according to RCP8.5, the far-future period shows on average an increase in the probability of rainfall extremes compared with the near future, both in magnitude and spatial extent. Overall, the patterns of differences showcase increased probabilities of extreme precipitation rates in the studied future periods even at low topographic heights, which may highlight a bothersome climate-change effect for the agricultural economy.

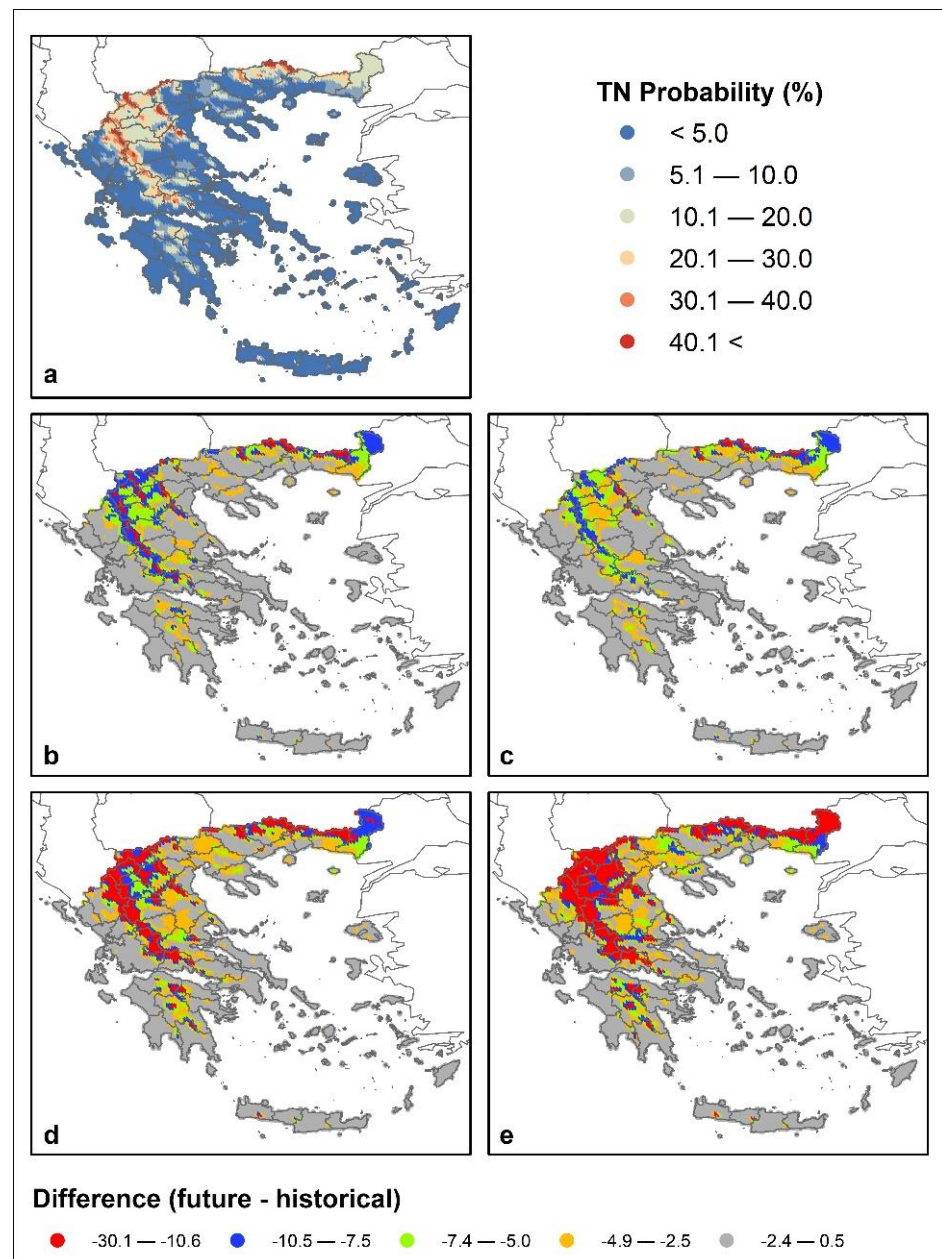


Figure 4. (a) Spatial distribution of probability of TN exceedance below -5°C calculated using EC–Earth–WRF downscaled data for the historical winter period 1980–2004. Differences (future–historical) in the probability of TN exceedance for: (b) RCP4.5 in near future (2025–2049), (c) RCP8.5 in near future (2025–2049), (d) RCP4.5 in far future (2075–2099) and (e) RCP8.5 in far future (2075–2099).

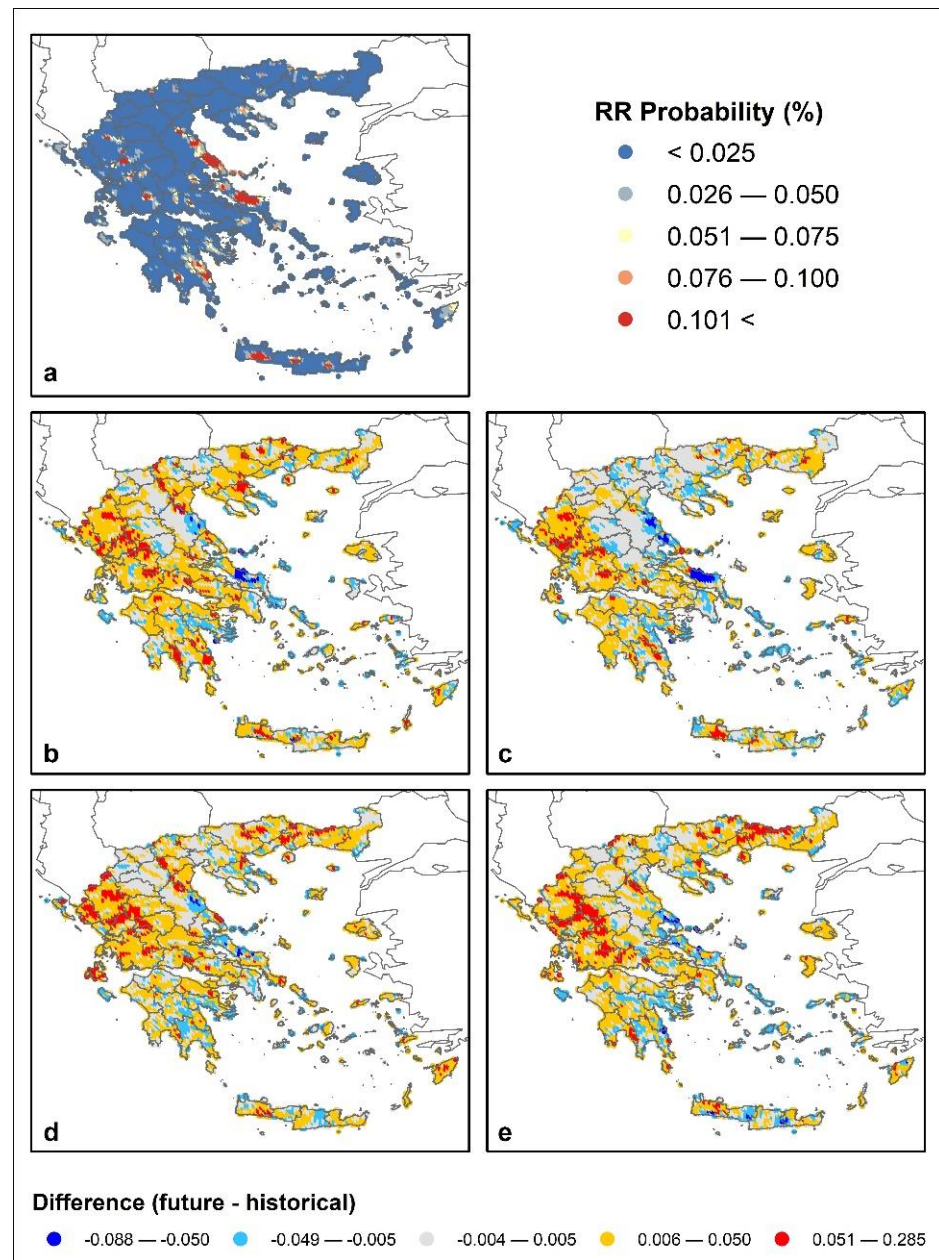


Figure 5. (a) Spatial distribution of probability of RR exceedance above 10 mm/h calculated using EC–Earth–WRF downscaled data for the historical period 1980–2004. Differences (future–historical) in the probability of RR exceedance for: (b) RCP4.5 in near future (2025–2049), (c) RCP8.5 in near future (2025–2049), (d) RCP4.5 in far future (2075–2099) and (e) RCP8.5 in far future (2075–2099).

3.4. Wind

During the historical period, the areas of high wind-speed (exceeding 15 m/s) probability are found to be consistent with other studies in the literature [45,55,56] (Figure 6a) and in accordance with the known synoptic atmospheric systems associated with the prevailing wind patterns. More particularly, the areas of the northeastern Aegean Sea are impacted by north-easterlies and the central Aegean by the Etesians, whereas the topography of Crete significantly amplifies the patterns of the extreme winds.

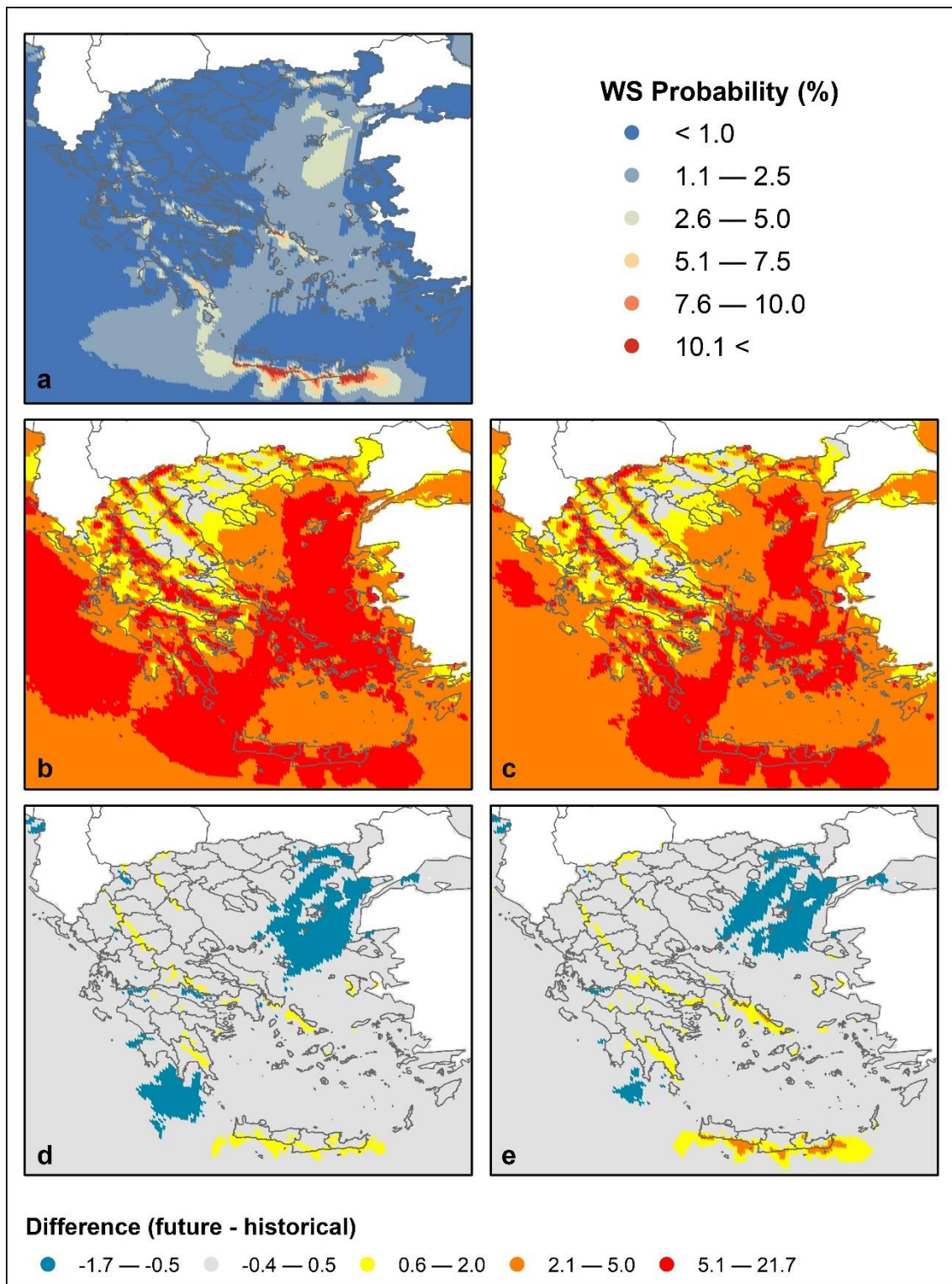


Figure 6. (a) Spatial distribution of probability of wind speed exceedance over the threshold (15 m/s) calculated using EC–Earth–WRF downscaled data for the historical period 1980–2004. Differences (future–historical) in the probability of wind speed exceedance for: (b) RCP4.5 in near future (2025–2049), (c) RCP8.5 in near future (2025–2049), (d) RCP4.5 in far future (2075–2099) and (e) RCP8.5 in far future (2075–2099).

In the near future and under both scenarios, the probability of the occurrence of windstorms is amplified almost all over the domain and mostly over the sea areas and mountain ridges (Figure 6b,c). The Ionian and central Aegean Seas are projected to exhibit the highest changes in the probabilities in the RCP4.5 scenario.

In the far future, both scenarios show a decrease in the probability of extreme winds over the northeastern Aegean and south Ionian Seas (Figure 6d,e). On the other hand, the mountainous areas, the central Aegean Sea and Crete present an increase in the probability of extreme winds. The increases in extreme winds associated with the Etesians over the Aegean Sea projected by both RCPs are in agreement with the findings of [57].

3.5. Multi-Hazard Probability Maps

Figure 7 depicts the spatial distribution of the probability of occurrence of the most dominant hazard calculated for the historical period and both future periods and scenarios. The dominant-hazard map for the historic period indicates the dominance of extreme TX over plains and coastal areas and the dominance of extreme TN at topographic heights higher than ~500 m a.m.s.l (Figure 7a). Over the seas, the islands of the central Aegean and the southeastern corners of Evia and Peloponnese, the extreme winds become dominant. However, extreme temperatures preside in the islands of the Ionian and eastern Aegean Seas, while in the northern parts of some of them, the extremely low temperatures or extreme winds dominate. In the case of Crete in particular, we observe the dominance of the three hazards with extreme TX and TN over the plains and high mountainous regions, respectively, and windstorms over the remaining areas of the island. Moreover, the dominance of extreme rainfall is observed in parts of the eastern coasts of the central mainland and Peloponnese.

The projected changes according to RCP4.5 in the near future yield a more extended dominance of extreme TX, particularly in the areas of Peloponnese, the central-eastern mainland and in the north of the country over the plains of central and eastern Macedonia and Thrace (Figure 7b). The same effect is observed in the central Aegean islands and northern parts of Crete. In addition, the extreme rainfall is seen to prevail more extensively in eastern coastal areas of the mainland. On the other hand, according to RCP8.5, the dominance of extreme TX becomes more profound in Thessaly and the plains areas of northern Greece (Figure 7c). Moreover, an interesting pattern of prevailing extreme winds is revealed in parts of the mainland and mostly in the Peloponnese where in the historical period the dominance of extreme temperatures was evident. Furthermore, RCP8.5 presents extremely windier conditions for the Ionian islands and Crete. This result agrees with the findings of Karozis et al. [56] that highlighted the reduction in the persisting anticyclonic activities over Greece and the Balkans in the near future, a change that denotes less frequent stagnant atmospheric conditions. The same study indicated a possible reduction in the passage of cyclones over Greece originating from the cyclogenesis region of the Central Mediterranean and the Adriatic Sea that could explain the reduced extreme-rainfall findings.

In the far future, the projected changes due to RCP4.5 show the dominance of extreme TX in areas of low altitude and more vividly in western Greece, Peloponnese, Thessaly and the northern mainland (Figure 7d). Additionally, in Crete and the central Aegean islands the extreme winds become less dominant and extreme TX predominates. In addition, the extreme rainfall is noted to persist in the far future over coastal parts of the eastern mainland. All the same, the extreme TN dominates in the mountainous areas. The high occurrence of extreme-winter-cold events under high-emission scenarios agrees with other climate-model projections that estimated increases in mid-latitude westerlies and northerly cold-air flow due to the influence of the upper-tropospheric equator-to-pole temperature difference in the storm-track response to climate change [58].

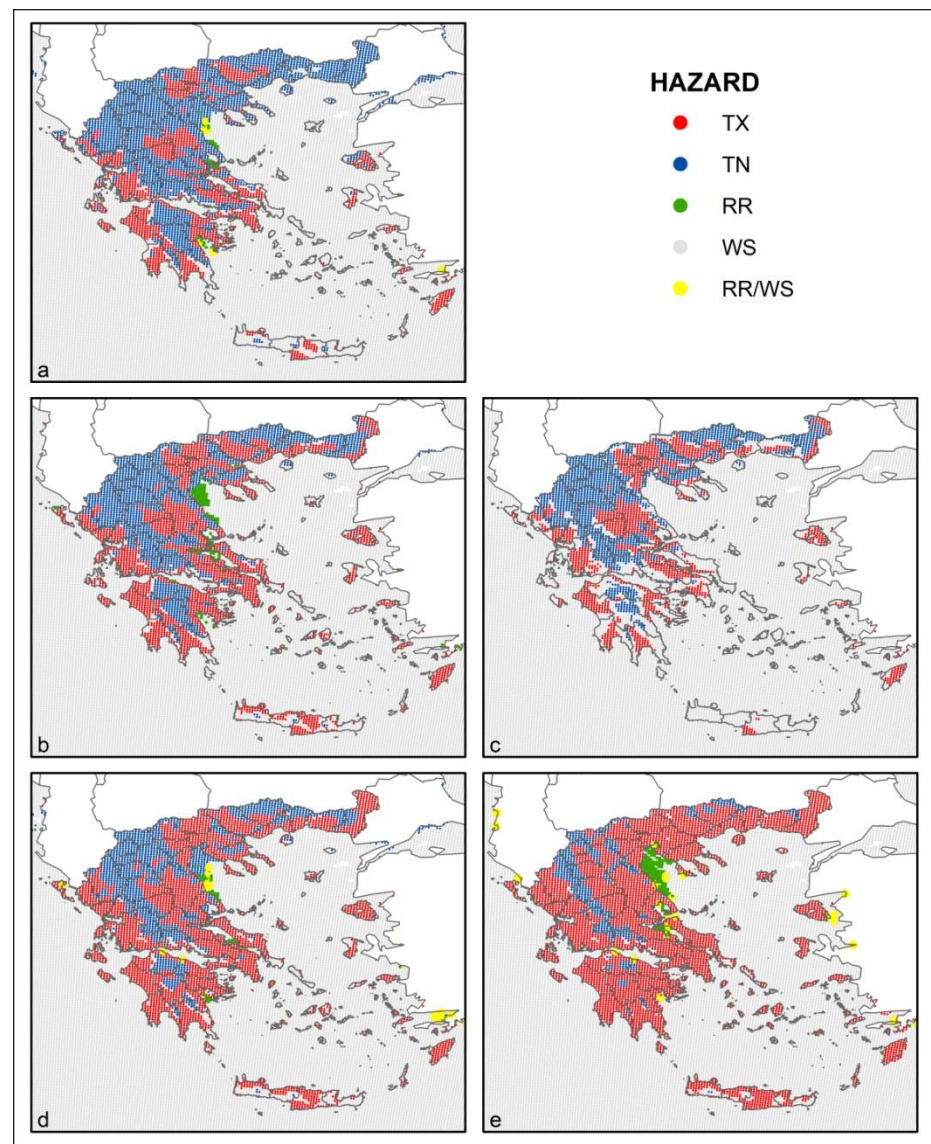


Figure 7. Dominant-hazard maps using EC–Earth–WRF downscaled data for: (a) the historical period 1980–2004, (b) RCP4.5 in near future (2025–2049), (c) RCP8.5 in near future (2025–2049), (d) RCP4.5 in far future (2075–2099) and (e) RCP8.5 in far future (2075–2099).

Furthermore, the RCP8.5 projections of the far future showcase the extended dominance of extreme TX in the islands and mainland except for the highest altitudes (circa 1500 m a.m.s.l.) (Figure 7e). The future intensification of extreme-temperature events is in agreement with other studies due to non-linear interactions, which are presently not quantified, between Arctic teleconnections and other remote and regional feedback processes [59,60]. Furthermore, the extreme winds remain the dominant hazard over the seas while the eastern coasts of the mainland would mostly experience extreme rainfall events that only persist locally in the far future. This outcome is associated with the Arctic amplification and possible connection to the weakening of mid-latitude storm tracks [61].

Figure 8 presents the multi-hazard occurrence in Greece for the examined periods. The value indicates the cumulative annual probability that at least one of the studied extreme hazards will occur. It demonstrates that patterns of highly exposed areas in Greece over the historic period will be spatially shifted in the far future as the increase in hotter climate regimes will be dominating the risk landscape.

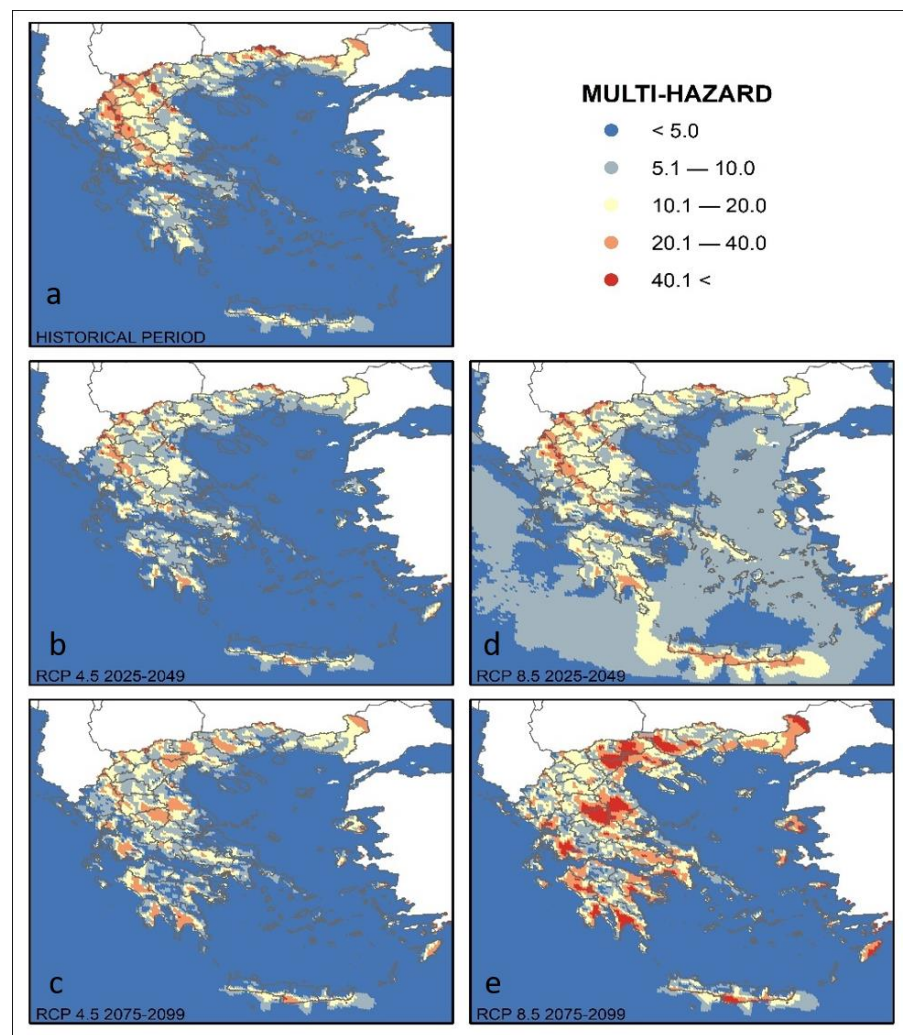


Figure 8. Annual percentage of multi-hazard using EC–Earth–WRF downscaled data for: (a) the historical period 1980–2004, (b) RCP4.5 in near future (2025–2049), (c) RCP8.5 in near future (2025–2049), (d) RCP4.5 in far future (2075–2099) and (e) RCP8.5 in far future (2075–2099).

In the historic period (Figure 8a), mountainous areas in the northern parts appear to be the most exposed regions in Greece, with TN and RR being the most significant risks (Figure 7a). The plains areas in the mainland and Crete exhibit lower risk levels through a combination of TX and extreme winds. The coastal zones and the Aegean islands appear to lie at the lower risk level.

In the near future, the RCP4.5 scenario (Figure 8b) appears to demonstrate the smallest variability in the risk levels when compared to RCP8.5 (Figure 8c). The mountainous areas will be exposed to lower risk levels by a factor between 5 and 14% compared to present times, contrasting a similar increase due to TX in the lowlands and western Greece. These relative changes were determined to be statistically significant at the 95% confidence level using the student t-test. The southern parts of the Eastern Aegean islands and Crete will also experience increased level of hazards. For the RCP8.5 scenario, in the near future, a greater number of regions are projected to be exposed to higher levels of risk due to both higher TX values and stronger winds (Figure 8c). These appear to be located in the southern and the western parts of the mainland and the Aegean Sea. For the far future (Figure 8d,e), both scenarios will exhibit similar patterns of risk changes compared to the present period, although RCP8.5 will be associated with higher hazard risk, often exceeding a 5% increase. Plains, agricultural lands and islands will be especially exposed to increased risk.

4. Conclusions

The study presented here aimed to elucidate the highly dynamic changing patterns of climate risk in Greece, a European climate hot spot [62]. The findings highlighted the areas that are exposed to multiple climate hazards in the country, considering the influence of the highly complex topography. In addition, the generated multi-hazard risk maps could be used to support disaster-risk-prevention activities such as avoiding future human, natural and material losses and generating economic benefits by reducing climate-related risks. The introduced method could be easily transferred to other geographical regions provided that the climate simulations are available. In addition, based on the perceived risk values or values identified in national risk assessments, the likelihood categories of the hazards (Table 2) could be adjusted accordingly. It should be mentioned that a limitation in the approach emanates from the complex topography of a domain or parts of it. In such a case, it may be required to downscale the climate data to even higher than a 5 km resolution over the complex topography areas, where there is the need to study the occurrence of (multi-)hazard(s) in more detail and accuracy.

Overall, the analysis demonstrated that climate change is a highly non-stationary process and the exposed areas, risk level and dominant risk will be significantly changed in the future under both RCP4.5 and RCP8.5 scenarios. More particularly, the impact of global warming on the country will become more evident in the far future (end of the century) when the extreme maximum temperature will dominate all other hazards.

According to the RCP4.5 scenario, a gradual expansion of the extreme maximum temperature can be anticipated from the coastal regions to the higher altitude areas, and this trend will become more persistent towards the end of the century. Under the RCP8.5 scenario, the extreme wind speed was found to be the dominant hazard in the near future, while afterwards, near the end of the century, the extreme maximum temperature becomes the most significant hazard.

Author Contributions: Conceptualization, D.V. and A.S.; methodology, D.V. and A.S.; software, I.M., S.K. and N.P.; validation, A.S. and N.P.; formal analysis, D.V. and N.G.; investigation, D.V.; resources, D.V.; writing—original draft preparation, D.V.; writing—review and editing, A.S.; supervision, D.V. All authors have read and agreed to the published version of the manuscript.

Funding: This research received no external funding.

Institutional Review Board Statement: Not applicable.

Informed Consent Statement: Not applicable.

Data Availability Statement: Data used in this study can be obtained by request to the authors.

Acknowledgments: This work was supported by computational time granted from the Greek Research & Technology Network (GRNET) in the National HPC facility—ARIS—under project ID HRCOG (pr004020 and pr006028).

Conflicts of Interest: The authors declare no conflict of interest.

References

1. IPCC; Masson-Delmotte, V.; Zhai, P.; Pirani, A.; Connors, S.L.; Péan, C.; Berger, S.; Caud, N.; Chen, Y.; Goldfarb, L.; et al. *Climate Change 2021: The Physical Science Basis. Contribution of Working Group I to the Sixth Assessment Report of the Intergovernmental Panel on Climate Change*; Cambridge University Press: Geneva, Switzerland, 2021. Available online: <https://www.ipcc.ch/report/ar6/wg1/> (accessed on 1 December 2021).
2. Fischer, E.M.; Sippel, S.; Knutti, R. Increasing probability of record-shattering climate extremes. *Nat. Clim. Chang.* **2021**, *11*, 689–695. [CrossRef]
3. Guerreiro, S.B.; Fowler, H.J.; Barbero, R.; Westra, S.; Lenderink, G.; Blenkinsop, S.; Lewis, E.; Li, X.F. Detection of continental-scale intensification of hourly rainfall extremes. *Nat. Clim. Chang.* **2018**, *8*, 803–807. [CrossRef]
4. WMO Climate and Weather Related Disasters Surge Five-Fold over 50 Years, but Early Warnings Save Lives. Available online: <https://news.un.org/en/story/2021/09/1098662> (accessed on 30 September 2021).

5. NOAA National Centers for Environmental Information (NCEI) Billion-Dollar Weather and Climate Disasters: FAQ | National Centers for Environmental Information (NCEI). Available online: <https://www.ncdc.noaa.gov/billions/> (accessed on 30 September 2021).
6. European Environment Agency Economic Losses from Climate-Related Extremes in Europe. Available online: <https://www.eea.europa.eu/data-and-maps/indicators/direct-losses-from-weather-disasters-4/assessment> (accessed on 30 September 2021).
7. Gampe, D.; Zscheischler, J.; Reichstein, M.; O'Sullivan, M.; Smith, W.K.; Sitch, S.; Buermann, W. Increasing impact of warm droughts on northern ecosystem productivity over recent decades. *Nat. Clim. Chang.* **2021**, *11*, 772–779. [CrossRef]
8. van Vliet, M.T.H.; van Beek, L.P.H.; Eisner, S.; Flörke, M.; Wada, Y.; Bierkens, M.F.P. Multi-model assessment of global hydropower and cooling water discharge potential under climate change. *Glob. Environ. Chang.* **2016**, *40*, 156–170. [CrossRef]
9. Schewe, J.; Gosling, S.N.; Reyer, C.; Zhao, F.; Ciais, P.; Elliott, J.; Francois, L.; Huber, V.; Lotze, H.K.; Seneviratne, S.I.; et al. State-of-the-art global models underestimate impacts from climate extremes. *Nat. Commun.* **2019**, *10*, 1005. [CrossRef]
10. Monier, E.; Paltsev, S.; Sokolov, A.; Chen, Y.-H.H.; Gao, X.; Ejaz, Q.; Couzo, E.; Schlosser, C.A.; Dutkiewicz, S.; Fant, C.; et al. Toward a consistent modeling framework to assess multi-sectoral climate impacts. *Nat. Commun.* **2018**, *9*, 660. [CrossRef]
11. Sillmann, J.; Sippel, S.; Russo, S. *Climate Extremes and Their Implications for Impact and Risk Assessment*; Elsevier: Amsterdam, The Netherlands, 2019; pp. 1–9. [CrossRef]
12. Otto, F.E.L.; Van Oldenborgh, G.J.; Eden, J.; Stott, P.A.; Karoly, D.J.; Allen, M.R. The attribution question. *Nat. Clim. Chang.* **2016**, *6*, 813–816. [CrossRef]
13. Hoegh-Guldberg, O.; Jacob, D.; Taylor, M.; Bindi, M.; Abdul Halim, S.; Achlatis Australia, M.; Alexander, L.V.; Allen, M.R.; Berry, P.; Boyer, C.; et al. Impacts of 1.5 °C global warming on natural and human systems. In *Global Warming of 1.5 °C. An IPCC Special Report on the Impacts of Global Warming of 1.5 °C above Pre-Industrial Levels and Related Global Greenhouse Gas Emission Pathways, in the Context of Strengthening the Global Response to the Threat of Climate Change, Sustainable Development, and Efforts to Eradicate*; IPCC Secretariat: Geneva, Switzerland, 2018; pp. 175–311.
14. Lehmann, J.; Coumou, D.; Frieler, K. Increased record-breaking precipitation events under global warming. *Clim. Change* **2015**, *132*, 501–515. [CrossRef]
15. Ribes, A.; Zwiers, F.W.; Azais, J.M.; Naveau, P. A new statistical approach to climate change detection and attribution. *Clim. Dyn.* **2017**, *48*, 367–386. [CrossRef]
16. King, A.D. Attributing Changing Rates of Temperature Record Breaking to Anthropogenic Influences. *Earth's Futur.* **2017**, *5*, 1156–1168. [CrossRef]
17. Van Der Wiel, K.; Kapnick, S.B.; Jan Van Oldenborgh, G.; Whan, K.; Philip, S.; Vecchi, G.A.; Singh, R.K.; Arrighi, J.; Cullen, H. Rapid attribution of the August 2016 flood-inducing extreme precipitation in south Louisiana to climate change. *Hydrol. Earth Syst. Sci.* **2017**, *21*, 897–921. [CrossRef]
18. Diffenbaugh, N.S.; Singh, D.; Mankin, J.S.; Horton, D.E.; Swain, D.L.; Touma, D.; Charland, A.; Liu, Y.; Haugen, M.; Tsiang, M.; et al. Quantifying the influence of global warming on unprecedented extreme climate events. *Proc. Natl. Acad. Sci. USA* **2017**, *114*, 4881–4886. [CrossRef] [PubMed]
19. Marsooli, R.; Lin, N.; Emanuel, K.; Feng, K. Climate change exacerbates hurricane flood hazards along US Atlantic and Gulf Coasts in spatially varying patterns. *Nat. Commun.* **2019**, *10*, 3785. [CrossRef] [PubMed]
20. Ali, H.; Modi, P.; Mishra, V. Increased flood risk in Indian sub-continent under the warming climate. *Weather Clim. Extrem.* **2019**, *25*, 100212. [CrossRef]
21. Coogan, S.C.P.; Robinne, F.N.; Jain, P.; Flannigan, M.D. Scientists' warning on wildfire—A Canadian perspective. *Can. J. For. Res.* **2019**, *49*, 1015–1023. [CrossRef]
22. Mezósi, G.; Bata, T.; Meyer, B.C.; Blanka, V.; Ladányi, Z. Climate Change Impacts on Environmental Hazards on the Great Hungarian Plain, Carpathian Basin. *Int. J. Disaster Risk Sci.* **2014**, *5*, 136–146. [CrossRef]
23. Cook, B.I.; Mankin, J.S.; Anchukaitis, K.J. Climate Change and Drought: From Past to Future. *Curr. Clim. Chang. Rep.* **2018**, *4*, 164–179. [CrossRef]
24. Pereira, S.C.; Carvalho, D.; Rocha, A. Temperature and Precipitation Extremes over the Iberian Peninsula under Climate Change Scenarios: A Review. *Climate* **2021**, *9*, 139. [CrossRef]
25. Savi, S.; Comiti, F.; Strecker, M.R. Pronounced increase in slope instability linked to global warming: A case study from the eastern European Alps. *Earth Surf. Processes Landf.* **2021**, *46*. [CrossRef]
26. Tjrdeman, E.; Hannaford, J.; Stahl, K. Human influences on streamflow drought characteristics in England and Wales. *Hydrol. Earth Syst. Sci.* **2018**, *22*, 1051–1064. [CrossRef]
27. Cammalleri, C.; Naumann, G.; Mentaschi, L.; Bisselink, B.; Gelati, E.; De Roo, A.; Feyen, L. Diverging hydrological drought traits over Europe with global warming. *Hydrol. Earth Syst. Sci.* **2020**, *24*, 5919–5935. [CrossRef]
28. Sieck, K.; Nam, C.; Bouwer, L.M.; Rechid, D.; Jacob, D. Weather extremes over Europe under 1.5 and 2.0 °C global warming from HAPPI regional climate ensemble simulations. *Earth Syst. Dyn.* **2021**, *12*, 457–468. [CrossRef]
29. Suarez-Gutierrez, L.; Li, C.; Müller, W.A.; Marotzke, J. Internal variability in European summer temperatures at 1.5 °C and 2 °C of global warming. *Environ. Res. Lett.* **2018**, *13*, 064026. [CrossRef]
30. Forzieri, G.; Bianchi, A.; Silva, F.B.; Marin Herrera, M.A.; Leblois, A.; Lavalle, C.; Aerts, J.C.J.H.; Feyen, L. Escalating impacts of climate extremes on critical infrastructures in Europe. *Glob. Environ. Chang.* **2018**, *48*, 97–107. [CrossRef]

31. Feyen, L.; Ciascar, J.; Gosling, S.; Ibarreta, D.; Soria, A.; Dosio, A.; Naumann, G.; Russo, S.; Formetta, G.; Forzieri, G.; et al. *JRC Science for Policy Report*; Joint Research Centre: Petten, The Netherlands, 2020.
32. The United Nations Office for Disaster Risk Reduction Proposed Updated Terminology on Disaster Risk Reduction: A Technical Review. Available online: <http://www.unisdr.org/we/inform/terminology> (accessed on 8 October 2021).
33. EUR 30596 EN. *JRC Recommendations for National Risk Assessment for Disaster Risk Management in EU: Where Science and Policy Meet*; Publications Office of the European Union: Luxembourg, 2021; Version 1; p. 273. Available online: <https://data.europa.eu/doi/10.2760/43449> (accessed on 1 December 2021).
34. Kappes, M.S.; Keiler, M.; von Elverfeldt, K.; Glade, T. Challenges of analyzing multi-hazard risk: A review. *Nat. Hazards* **2012**, *64*, 1925–1958. [CrossRef]
35. Tilloy, A.; Malamud, B.D.; Winter, H.; Joly-Laugel, A. A review of quantification methodologies for multi-hazard interrelationships. *Earth-Science Rev.* **2019**, *196*, 102881. [CrossRef]
36. Gallina, V.; Torresan, S.; Critto, A.; Sperotto, A.; Glade, T.; Marcomini, A. A review of multi-risk methodologies for natural hazards: Consequences and challenges for a climate change impact assessment. *J. Environ. Manag.* **2016**, *168*, 123–132. [CrossRef]
37. Sperotto, A.; Molina, J.L.; Torresan, S.; Critto, A.; Marcomini, A. Reviewing Bayesian Networks potentials for climate change impacts assessment and management: A multi-risk perspective. *J. Environ. Manag.* **2017**, *202*, 320–331. [CrossRef]
38. Skamarock, W.C.; Skamarock, W.C.; Klemp, J.B.; Dudhia, J.; Gill, D.O.; Barker, D.M.; Wang, W.; Powers, J.G. *A Description of the Advanced Research WRF Version 3*. NCAR Technical Note -475+STR; University Corporation for Atmospheric Research: Boulder, CO, USA, 2008.
39. Doblas Reyes, F.; Acosta Navarro, J.C.; Acosta Cobos, M.C.; Bellprat, O.; Bilbao, R.; Castrillo Melguizo, M.; Fuckar, N.; Guemas, V.; Lledó Ponsati, L.; Menegoz, M. *Using EC-Earth for Climate Prediction Research*; European Centre for Medium-Range Weather Forecasts (ECMWF): Reading, UK, 2018; Volume 154, pp. 35–40.
40. Kc, B.; Shepherd, J.M.; King, A.W.; Johnson Gaither, C. Multi-hazard climate risk projections for the United States. *Nat. Hazards* **2021**, *105*, 1963–1976. [CrossRef]
41. Jay, A.D.R.; Reidmiller, C.W.; Avery, D.; Barrie, B.J.; DeAngelo, A.; Dave, M.; Dzaugis, M.; Kolian, K.L.M.; Lewis, K.; Reeves, D. Winner, Overview. In *Impacts, Risks, and Adaptation in the United States: Fourth National Climate Assessment, Volume II*; Reidmiller, D.R., Avery, C.W., Easterling, D.R., Kunkel, K.E., Lewis, K.L.M., Maycock, T.K., Stewart, B.C., Eds.; U.S. Global Change Research Program: Washington, DC, USA, 2018; pp. 33–71. [CrossRef]
42. Lhotka, O.; Kyselý, J.; Plavcová, E. Evaluation of major heat waves' mechanisms in EURO-CORDEX RCMs over Central Europe. *Clim. Dyn.* **2018**, *50*, 4149–4262. [CrossRef]
43. Cardoso, R.M.; Soares, P.M.M.; Lima, D.C.A.; Miranda, P.M.A. Mean and extreme temperatures in a warming climate: EURO CORDEX and WRF regional climate high-resolution projections for Portugal. *Clim. Dyn.* **2019**, *52*, 129–157. [CrossRef]
44. Tian, L.; Jin, J.; Wu, P.; Niu, G.Y.; Zhao, C. High-resolution simulations of mean and extreme precipitation with WRF for the soil-erosive Loess Plateau. *Clim. Dyn.* **2020**, *54*, 3489–3506. [CrossRef]
45. Katopodis, T.; Markantonis, I.; Vlachogiannis, D.; Politi, N.; Sfetsos, A. Assessing climate change impacts on wind characteristics in Greece through high-resolution regional climate modelling. *Renew. Energy* **2021**, *179*, 427–444. [CrossRef]
46. UNDRR International Science Council Sendai. *Hazard Definition & Classification Review: Technical Report*; UNDRR: Panama City, Panama, 2020.
47. Politi, N.; Vlachogiannis, D.; Sfetsos, A.; Nastos, P.T. High-resolution dynamical downscaling of ERA-Interim temperature and precipitation using WRF model for Greece. *Clim. Dyn.* **2021**, *57*, 1–27. [CrossRef]
48. Politi, N.; Sfetsos, A.; Vlachogiannis, D.; Nastos, P.T.; Karozis, S. A sensitivity study of high-resolution climate simulations for Greece. *Climate* **2020**, *8*, 44. [CrossRef]
49. Politi, N.; Nastos, P.T.; Sfetsos, A.; Vlachogiannis, D.; Dalezios, N.R. Evaluation of the AWR-WRF model configuration at high-resolution over the domain of Greece. *Atmos. Res.* **2018**, *208*, 229–245. [CrossRef]
50. Katopodis, T.; Markantonis, I.; Politi, N.; Vlachogiannis, D.; Sfetsos, A. High-resolution solar climate atlas for greece under climate change using the weather research and forecasting (WRF) model. *Atmosphere* **2020**, *11*, 761. [CrossRef]
51. Habermann Nadine; Thanasis Sfetsos; Ralh Hedel; Albert Chen EU-CIRCLE, Report on Climate Related Critical Event Parameters: Deliverable 3.2. Available online: <https://www.eu-circle.eu/wp-content/uploads/2018/10/D3.2.pdf> (accessed on 8 November 2021).
52. Gilleland, E.; Katz, R.W. New software to analyze how extremes change over time. *Eos Trans. Am. Geophys. Union* **2011**, *92*, 13–14. [CrossRef]
53. Cooley, D. Return periods and return levels under climate change. In *Extremes in a Changing Climate*; Springer: Berlin/Heidelberg, Germany, 2013; pp. 97–114.
54. Hellenic Meteorological Service Climate Atlas of Greece, 1971–2000. Available online: <http://climatlas.hnms.gr/sdi/> (accessed on 18 November 2021).
55. Katopodis, T.; Vlachogiannis, D.; Politi, N.; Gounaris, N.; Karozis, S.; Sfetsos, A. Assessment of climate change impacts on wind resource characteristics and the wind energy potential in Greece. *J. Renew. Sustain. Energy* **2019**, *11*, 066502. [CrossRef]
56. Karozis, S.; Sfetsos, A.; Gounaris, N.; Vlachogiannis, D. An assessment of climate change impact on air masses arriving in Athens, Greece. *Theor. Appl. Climatol.* **2021**, *145*, 501–517. [CrossRef]

57. Dafka, S.; Toreti, A.; Zanis, P.; Xoplaki, E.; Luterbacher, J. Twenty-First-Century Changes in the Eastern Mediterranean Etesians and Associated Midlatitude Atmospheric Circulation. *J. Geophys. Res. Atmos.* **2019**, *124*, 12741–12754. [CrossRef]
58. Harvey, B.J.; Shaffrey, L.C.; Woollings, T.J. Deconstructing the climate change response of the Northern Hemisphere wintertime storm tracks. *Clim. Dyn.* **2015**, *45*, 2847–2860. [CrossRef]
59. Russo, S.; Dosio, A.; Graversen, R.G.; Sillmann, J.; Carrao, H.; Dunbar, M.B.; Singleton, A.; Montagna, P.; Barbola, P.; Vogt, J.V.; et al. Magnitude of extreme heat waves in present climate and their projection in a warming world. *J. Geophys. Res. Atmos.* **2014**, *119*, 12500–12512. [CrossRef]
60. Coumou, D.; Di Capua, G.; Vavrus, S.; Wang, L.; Wang, S. The influence of Arctic amplification on mid-latitude summer circulation. *Nat. Commun.* **2018**, *9*, 2959. [CrossRef]
61. Chang, E.K.M.; Ma, C.G.; Zheng, C.; Yau, A.M.W. Observed and projected decrease in Northern Hemisphere extratropical cyclone activity in summer and its impacts on maximum temperature. *Geophys. Res. Lett.* **2016**, *43*, 2200–2208. [CrossRef]
62. Cos, J.; Doblas-Reyes, F.; Jury, M.; Marcos, R.; Bretonnière, P.-A.; Samsó, M. The Mediterranean climate change hotspot in the CMIP5 and CMIP6 projections. *Earth Syst. Dyn. Discuss.* **2021**, 1–26. [CrossRef]

Article

A Machine Learning Framework for Multi-Hazard Risk Assessment at the Regional Scale in Earthquake and Flood-Prone Areas

Alessandro Rocchi ¹, Andrea Chiozzi ², Marco Nale ¹, Zeljana Nikolic ³, Fabrizio Riguzzi ⁴,
Luana Mantovan ¹, Alessandro Gilli ¹ and Elena Benvenuti ^{1,*}

- ¹ Department of Engineering, University of Ferrara, 44122 Ferrara, Italy; alessandro.rocchi@edu.unife.it (A.R.); marco.nale@unife.it (M.N.); luana.mantovan@edu.unife.it (L.M.); alessandro.gilli@edu.unife.it (A.G.)
- ² Department of Environmental and Prevention Sciences, University of Ferrara, 44122 Ferrara, Italy; andrea.chiozzi@unife.it
- ³ Faculty of Civil Engineering, Architecture and Geodesy, University of Split, 21000 Split, Croatia; zeljana.nikolic@gradst.hr
- ⁴ Department of Mathematics and Computer Science, University of Ferrara, 44122 Ferrara, Italy; fabrizio.riguzzi@unife.it
- * Correspondence: elena.benvenuti@unife.it

Abstract: Communities are confronted with the rapidly growing impact of disasters, due to many factors that cause an increase in the vulnerability of society combined with an increase in hazardous events such as earthquakes and floods. The possible impacts of such events are large, also in developed countries, and governments and stakeholders must adopt risk reduction strategies at different levels of management stages of the communities. This study is aimed at proposing a sound qualitative multi-hazard risk analysis methodology for the assessment of combined seismic and hydraulic risk at the regional scale, which can assist governments and stakeholders in decision making and prioritization of interventions. The method is based on the use of machine learning techniques to aggregate large datasets made of many variables different in nature each of which carries information related to specific risk components and clusterize observations. The framework is applied to the case study of the Emilia Romagna region, for which the different municipalities are grouped into four homogeneous clusters ranked in terms of relative levels of combined risk. The proposed approach proves to be robust and delivers a very useful tool for hazard management and disaster mitigation, particularly for multi-hazard modeling at the regional scale.

Keywords: risk assessment; multi hazard; seismic risk; hydraulic risk; machine learning; principal component analysis

Citation: Rocchi, A.; Chiozzi, A.; Nale, M.; Nikolic, Z.; Riguzzi, F.; Mantovan, L.; Gilli, A.; Benvenuti, E. A Machine Learning Framework for Multi-Hazard Risk Assessment at the Regional Scale in Earthquake and Flood-Prone Areas. *Appl. Sci.* **2022**, *12*, 583. <https://doi.org/10.3390/app12020583>

Academic Editor: Salvador García-Ayllón Veintimilla

Received: 21 November 2021

Accepted: 1 January 2022

Published: 7 January 2022

Publisher's Note: MDPI stays neutral with regard to jurisdictional claims in published maps and institutional affiliations.



Copyright: © 2022 by the authors. Licensee MDPI, Basel, Switzerland. This article is an open access article distributed under the terms and conditions of the Creative Commons Attribution (CC BY) license (<https://creativecommons.org/licenses/by/4.0/>).

1. Introduction

The frequency of natural extreme events is increasing worldwide [1–9], and human activities often interact with devastating effects, affecting people and natural environments, and producing great economic losses, especially in developing countries. On the other hand, in some developed countries, disasters have been decreasing since the beginning of the 20th century [3,4]. Understanding risk involving vast inhabited areas is, therefore, paramount, particularly when assessing potential losses produced by a combination of multiple hazards, which are defined as the probability of occurrence in a specified period of a potentially damaging event of a given magnitude on a given area [5]. In fact, total risk is a measure of the expected human (casualties and injuries) and economic (damage to property and activity disruption) losses due to a particular adverse natural phenomenon. Such a measure is conceptually assumed as the product of hazard, vulnerability, and exposure instances [6]. Exposure of people to the consequences of extreme natural phenomena

could be reduced if predictive models based on new approaches and deeper knowledge of effective factors were employed [7].

Many areas on Earth are subjected to the effects of coexisting multiple hazards, among which floods and earthquakes are some of the most widespread [8,9] and even if it is well established that inhabited environments are affected by multiple hazardous processes, most studies focus on a single hazard [10]. However, hazards usually interact with each other and contribute to the overall risk in a complex way. For this reason, the development of multi-hazard risk assessment approaches is of first importance [11] and multi-hazard mapping is receiving increasing attention [12,13]. In particular, Schmidt et al. proposed a multi-hazard risk assessment methodology in New Zealand, devising an adaptable computational tool allowing its users to input the natural phenomena of interest [11]. Still, relatively scarce are the studies exploiting machine learning techniques to assess multi-hazard risks [14–16], albeit machine learning is especially useful when dealing with the huge amount of data encountered in risk analysis, particularly at the regional scale.

In this study, machine learning is used to construct a risk assessment framework in which the combined effects of two major natural events (flood and earthquakes) are analyzed for the Emilia Romagna test region (Italy). A large input dataset containing, for each municipality of the test region, a wide number of quantitative variables related to hazard, exposure, and vulnerability instances for both flood and earthquake hazards is adopted. Then, the number of variables is suitably reduced by means of Principal Component Analysis (PCA) [17–19], and the municipalities are subsequently grouped into four approximately risk-wise homogeneous clusters using a K-means clustering algorithm [20,21]. Finally, a qualitative overall risk level is assigned to each cluster. The proposed methodology represents a robust tool for the qualitative multi-hazard risk assessment at the regional scale, which enables suitable extraction of risk-related information from a large input dataset and provides a useful instrument that assists stakeholders in decision-making processes, especially with respect to intervention prioritization.

2. Materials and Methods

The proposed multi-hazard risk assessment approach is based on the analysis of available data using logical, mathematical, and statistical tools. It was applied to the Emilia Romagna region, which is located in the Northern part of Italy. Our analysis focused on seismic and hydraulic risks associated with this territory. A map of the seismic classification of municipalities in Emilia is shown in Figure 1. A hot-spot of hydraulic risk in Emilia Romagna, Ferrara possesses an altimetry below the sea level over a large part of its territory, as illustrated in Figure 2.

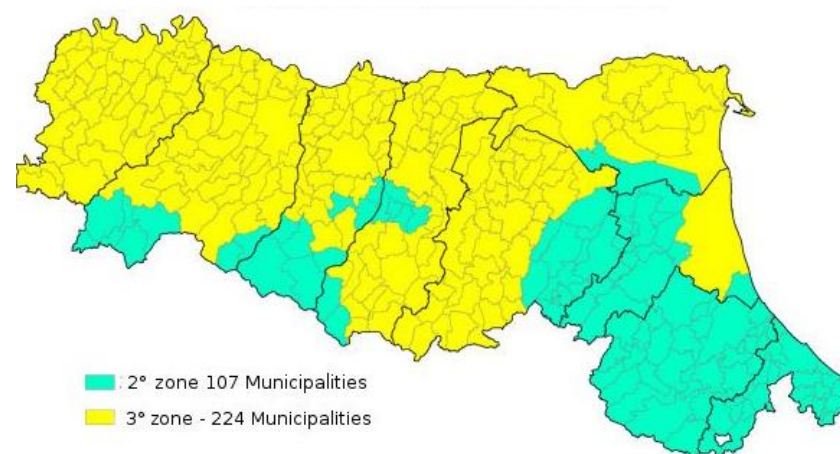


Figure 1. Seismic classification of municipalities in Emilia (<https://ambiente.regione.emilia-romagna.it/en/geologia/seismic-risk/seismic-classification>, accessed on 15 October 2021).

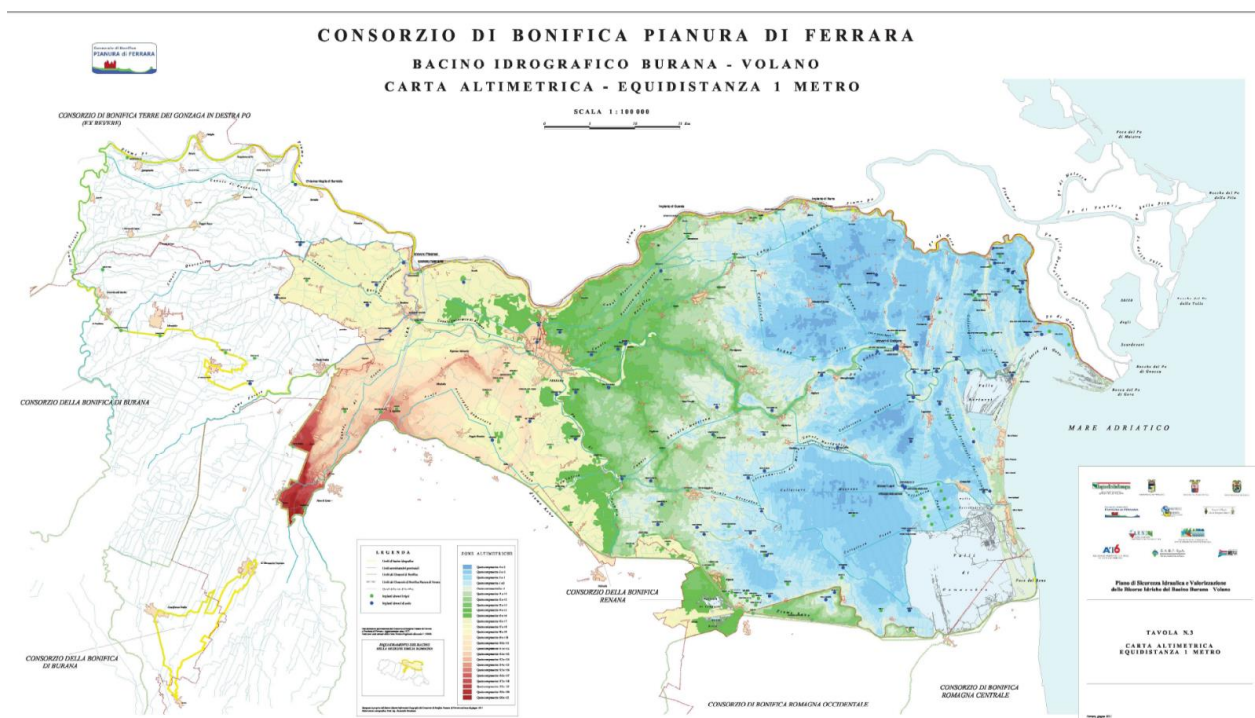


Figure 2. Ferrara territory altimetry (The map can be downloaded from <https://www.bonificaferrara.it> and has been released from “Consorzio di Bonifica Pianura di Ferrara”; accessed on 15 October 2021).

To evaluate the overall combined risk for the different municipalities in the test region, several intermediate steps were necessary. At first, the reliability of the method was tested on a smaller data sample given by the municipalities in the Province of Ferrara (Italy), then on a slightly larger one, considering municipalities from other provinces in the test region, and then, finally, expanding the data sample to each municipality of the Emilia Romagna region. This type of approach improved control on both the algorithm and its calibration, as well as the initial dataset, leading to a significant reduction in terms of computational time. In what follows, we omit the description of the intermediate steps and directly present the analysis for the whole test region.

2.1. Dataset

Choosing the correct amount of data is paramount. The data employed for our analysis have been obtained from the Italian National Institute of Statistics (ISTAT) database, which was used in 2018 by the Italian Superior Institute for Environmental Protection and Research (ISPRA) to produce seismic, hydrogeological, volcanic, and social vulnerability hazard maps for the entire Italian peninsula as shown in the report by Trigila et al. [22]. These maps constitute a fundamental tool of support to national risk mitigation policies, allowing the identification of intervention priorities, the allocation of funds, and the planning of soil protection interventions.

The input dataset was organized as a matrix in which the rows corresponded to each of the 331 municipalities of the Emilia-Romagna region and the columns corresponded to quantitative variables associated with different aspects of seismic and flood risk. Hence, we had 331 rows or observations and hundreds of columns or variables. For instance, we adopted as variables the number of buildings sharing certain features (such as building material, the period of construction, or the state of conservation), superficial extension, number of inhabitants, population density, seismic peak ground acceleration, etc. Overall, all the variables can be grouped into three macro-categories: variables related to vulner-

ability instances, variables related to exposure instances, and variables related to hazard instances for both seismic and hydraulic risks.

Since hydraulic risk, as a combination of hydraulic vulnerability, exposure, and hazard, has previously been evaluated for each observation by the Italian National Institute of Geophysics and Vulcanology (INGV), it was represented in the proposed analysis as a unique variable, which condensed all the variables related to hydraulic risk.

The relative importance between some variables and the relation among them is quantified by means of the PCA method, which will be described in the next subsections.

For instance, some of the crucial variables were identified as follows:

- agMAX_50: maximum value of the peak ground acceleration about the grid data point;
- DENSPOP: Population density (n. of inhabitants/kmq);
- E1-E31: Type of Buildings (e.g., residential, masonry, and state of conservation);
- IDR_AreaP1/P2/P3: Hydraulic risk surface, respectively, low/medium/high;
- IDR_PopP1/P2/P3: Population living in, respectively, low/medium/high hydraulic risk surface.

An extensive table reporting the explanations of all acronyms associated with the relevant variables is reported in Appendix A.

2.2. Initial Exploratory Analysis

Exploratory analysis is a typical analytical approach in statistics that is suitable for defining and synthesizing the main characteristics of a group of data. This type of approach enables preliminarily evaluating, searching, and finally, analyzing possible notable patterns within the data, in a phase where possible interactions among variables are not known yet. Again, graphics techniques for data visualization are quite useful in this step, producing diagrams such as box plots, scatter plots, histograms, etc. More analytical techniques, such as PCA, are very useful. The whole proposed analysis has been implemented and performed in a MATLAB computing environment [23].

2.2.1. Standardization

The first step of the exploratory analysis is data standardization. As usual [15,16], the metric of standard deviation was adopted to test the machine learning model's accuracy and to measure confidence in the obtained statistical conclusions. This allows us to compare variable data with different units of measure, scaling all the variables such that each scaled variable will have mean value equal to 0 and standard deviation equal to 1, referred to the data distribution for each variable. To attain this outcome, for each variable x of the dataset, mean μ and the standard deviation σ have been calculated. Then the z-score formula has been applied:

$$z = \frac{x - \mu}{\sigma}. \quad (1)$$

2.2.2. PCA

Once the entire dataset was standardized, PCA was applied. One of the main targets of PCA is to reduce the dimensionality of the initial dataset without losing the amount of information belonging to it. A dimensionality reduction technique is a process that takes advantage of linear algebraic operations to convert an n -dimensional dataset to an $n-k$ dimensional one. Clearly, this transformation comes at the cost of a certain loss of information, but it also gives the benefit of being able to graphically visualize the data, while keeping good accuracy.

The idea behind PCA is to find the best subspace, which explicates the highest possible variance in the dataset. Using linear transformations, starting from an initial standardized matrix in the n -dimensional space, changes in variables are carried out that makes possible to identify observations in the space generated from the principal components, which have the particularity to catch the maximum possible variance of the initial dataset, thus reducing the loss of information.

Given p random standardized variables $\tilde{X}_1, \tilde{X}_2, \dots, \tilde{X}_p$, collected into the matrix \tilde{X} , the analysis allows determining $k < p$ variables Y_1, Y_2, \dots, Y_k , each of them a linear combination of the p starting variables, having maximum variance. To find Y_i , also known as the i -th principal component, we need to find the vector V_i such that

$$Y_i = \tilde{X}V_i \quad (2)$$

by maximizing the variance relative to the first principal component. In other words, vectors V_i are the eigenvectors of the covariance matrix C of \tilde{X} , i.e., the $n \times p$ matrix whose generic element C_{hk} is equal to $COV(\tilde{X}_h, \tilde{X}_k)$.

The j -th element of Y_i represents the *score* of the i -th principal component for j -th statistical unit. The j -th element of V_i represents the *weight* that the j -th variable \tilde{X}_j has in the definition of the i -th principal component. Vectors V_i can be collected as columns in the matrix of weights V .

Lastly, axis rotations are applied, which mean a change of position of the dimensions obtained during the factor's extraction phase, keeping the initial variance fixed as much as possible. The axis can be rigidly rotated (orthogonal rotation) or interrelated (oblique rotation). The result is a new matrix of rotated factors.

Once the dimension of the dataset has been reduced, it is possible to plot the observations in the new space generated by the principal components, space where the coordinates of the observations have undergone linear transformation, in accordance with the variables as mentioned before.

The scatter plot represented in Figure 3, depicts the observations after variable reduction. One can notice the presence of elements defined as outliers, i.e., abnormal values, far from the average observations. These disturbing elements could generate unbalanced compensations inside the analytical model, and that is why they will be handled with care, modifying the algorithm's settings whenever possible or, in extreme cases, removed from the dataset. In this case, the outliers were almost all the administrative centers of Emilia-Romagna region, far away, in terms of the quantitative variables, from the rest of the observations.

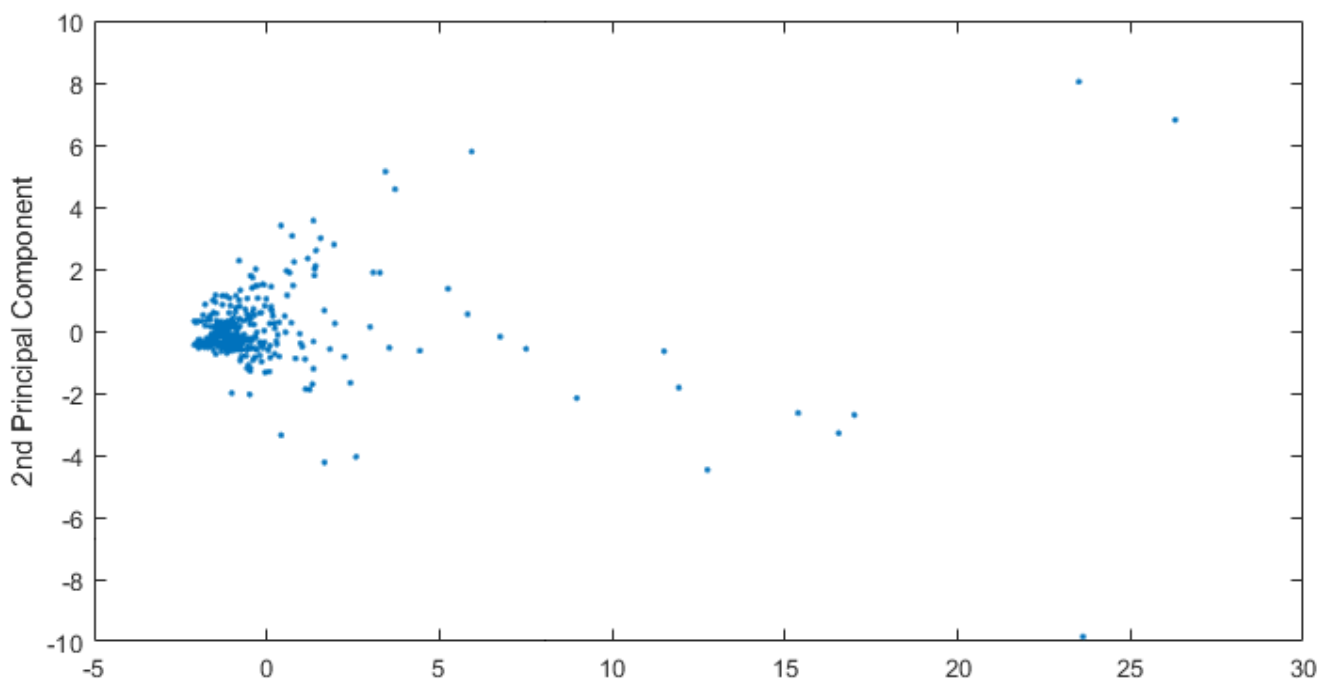


Figure 3. Observations scatter plot which depicts the observations after variable reduction.

It is a good rule to consider the principal components that catch at least 80% of the variance of the starting dataset. The more the considered variables, the higher the number of principal components necessary to reach that quote. Whenever the amount of variance reached is not sufficient, an additional reduction in variables is performed by iterating the process.

One of PCA's main purposes is to delete the noise due to non-useful data, which is evaluated in terms of how much information and how much variance they carry inside the dataset. Figure 4 represents variance for each principal component before variable reduction. Loading plots have been generated as histograms representing the weight of the variables transformed after the PCA and are reported in Figures 5 and 6. The variables reported along the abscissa have been selected among all the available data for being the most meaningful as per the multi-risk evaluation. For instance, AGMAX_50 denotes the maximum ground acceleration (fiftieth percentile) calculated on a grid with a 0.02° step, with the maximum and minimum of the values of the grid points falling within the municipal area. IDR_POPP3 indicates the resident population at risk in areas with high hydraulic hazard (P3). From Figures 5 and 6, the variables with the highest coefficients have been extrapolated, the higher the coefficient of the variable, the higher the weight of the variable on the principal component. Along the first principal component, the difference between observations will be led by the different values referred to the variables with highest coefficient in the histogram depicted in Figure 5.

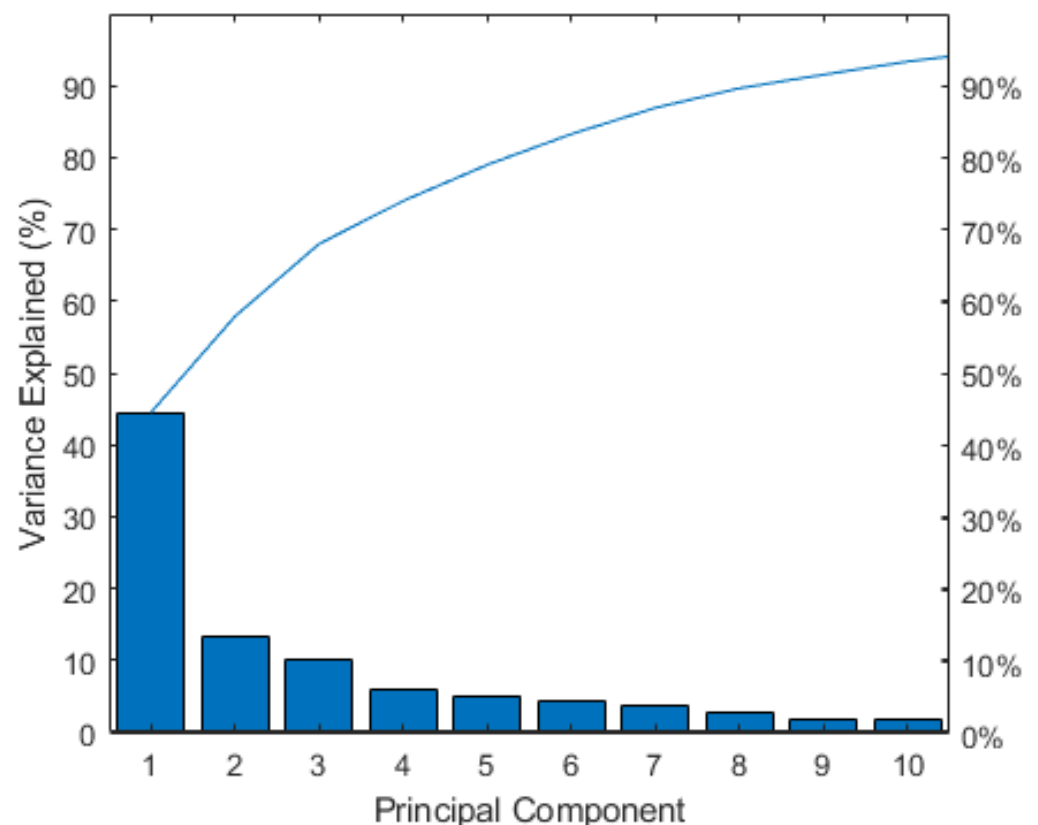


Figure 4. Variance for each principal component before variable reduction.

We chose to assess the weight of the coefficient of the variables referring to the first two principal components only, because they explicated more than 70% of the variance and are the most significant of the combined risk assessment. Figure 7 depicts the variance explicated by the first 10 principal components after the PCA.

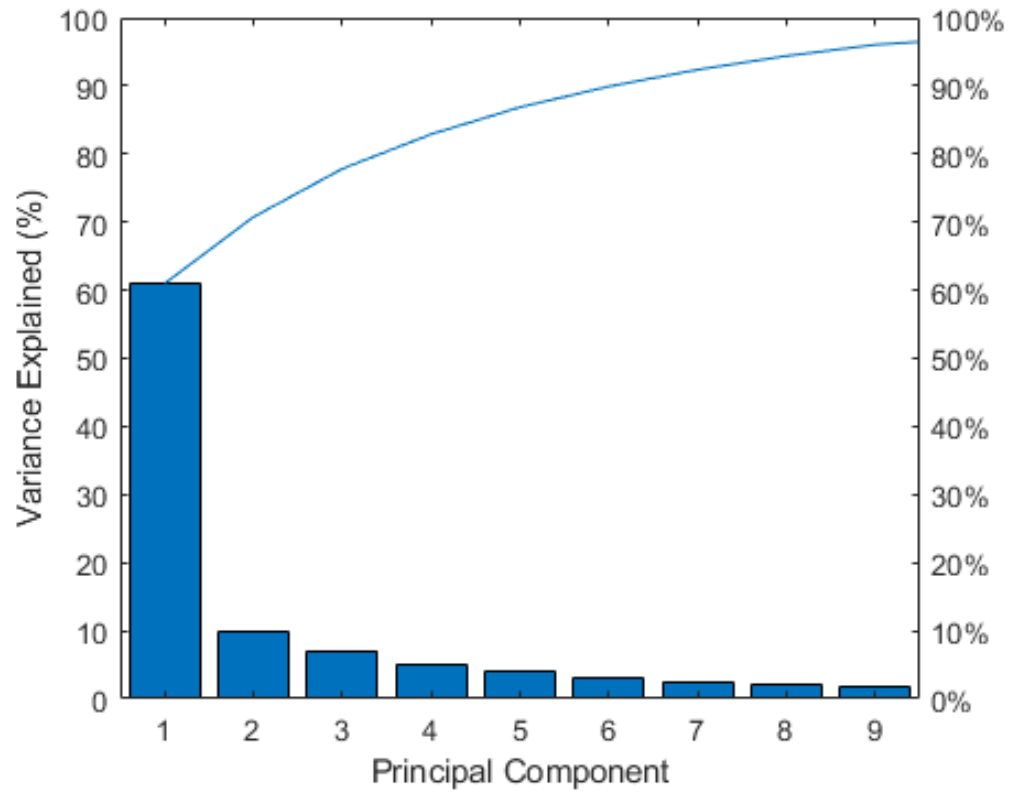


Figure 7. Variance of the first 10 principal components after variable reduction.

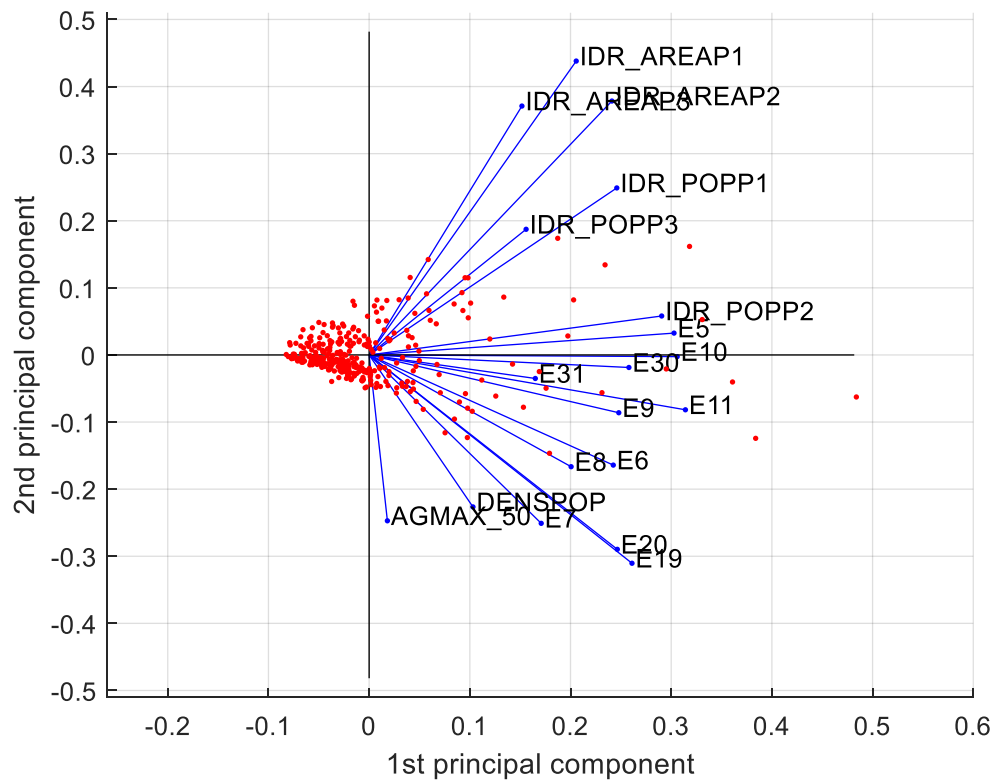


Figure 8. Biplot along the first two principal components.

This plot allows catching at an early stage any pattern within the dataset, such as the separation between observations and deep relation among variables. In general:

- the projection of the values on each principal component shows how much weight those values have on that principal component;
- when two vectors are close, in terms of angle, the two represented variables have a positive correlation;
- if two vectors create a 90 angle, the respective variables are not correlated;
- when they diverge and create an angle of almost 180, they are negatively correlated.

Outliers differ from the other observations in terms of vulnerability and the population at hydraulic risk. It is reasonable because, remembering the outliers are the provincial administrative centers, they present higher values in terms of population and built environment. Moreover, along the vertical axis the observations differ in terms of seismic hazard and exposition.

Moreover, vulnerability and exposure to hydraulic risk variables are quite correlated and differentiate the observations along the horizontal axis, whereas seismic hazard and exposition variables are not correlated with the variables representing surfaces at hydraulic risk. These remarks will come in handy later, at a post-clustering stage, a level of multi-risk will be attributed to each cluster.

2.3. K-Means Clustering Algorithm

The PCA allowed us to reduce the dimensionality of the dataset and plot the observations, i.e., the municipalities of the Emilia Romagna region, in the new sub-space identified by the principal components, while retaining the majority of information, which identified the observations in the initial n -dimensional space before the linear transformations.

To suitably group the observations according to homogeneous levels of overall risk, we used an unsupervised machine learning algorithm, known as *k-means clustering*.

In general, cluster analysis is a technique to group data where the main purpose is to gather observations according to the features selected by the user. The analysis allows splitting a set of observations into clusters according to similar or non-similar features. Cluster analysis does not require knowing the classes in advance, as in the case of supervised algorithms.

In the k -means clustering algorithm, we assumed N observations x_1, x_2, \dots, x_n and partitioned them into k clusters, each defined by a centroid c_1, c_2, \dots, c_k . We assigned the x_i observation to the cluster, such that the distance among the observation and the cluster center was minimum.

The algorithm began by randomly choosing k centroids. After measuring the distance of each observation to each centroid, the observation was assigned to the closest cluster. Then, centroids were updated, as the average of the observations in each centroid. The procedure was repeated iteratively, each time minimizing the distance between observation and centroid.

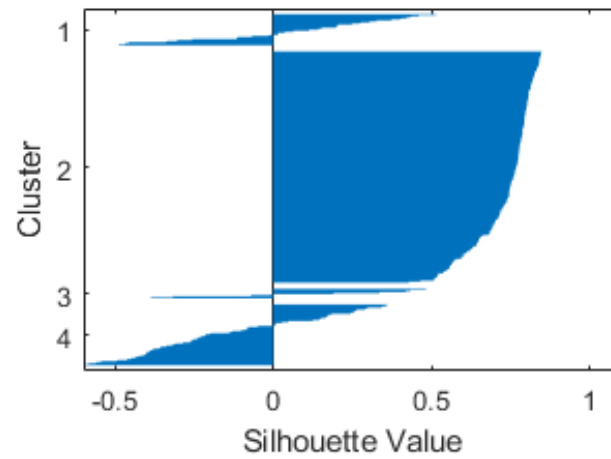
Different choices for such distance function are possible and readily available in many scientific computing software packages such as MATLAB: the squared Euclidean distance, one minus the cosine of the included angle between points (treated as vectors), or one minus the sample correlation between points (treated as sequences of values).

In particular, the squared Euclidean metric does not allow keeping the outlier in the dataset because of the square of the distance. By doing so, the algorithm will place a specific cluster just for the outlier, influenced by its distance from the other observations. Later, we will propose a comparison among the distances in terms of the quality of clustering.

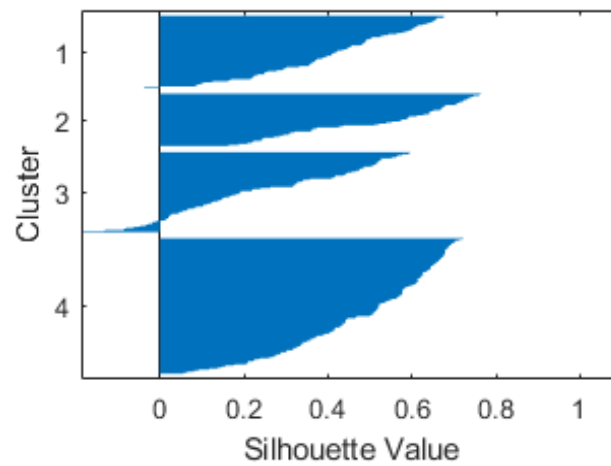
To legitimate the clusterization carried out with the k -means algorithm, the *silhouette method* was employed. The technique provided a succinct graphical representation of how well each observation has been classified. The silhouette value is a measure of how similar an object is to its own cluster (cohesion) compared to other clusters (separation). The silhouette ranges from -1 to $+1$, where a high value indicates that the object is well matched to its own cluster and poorly matched to neighboring clusters. If most objects have a high value, then the clustering configuration is appropriate. If many points have a low or negative value, then the clustering configuration may have too many or too few

clusters. The silhouette can be calculated with any distance metric, such as the Euclidean distance or the so-called Manhattan distance.

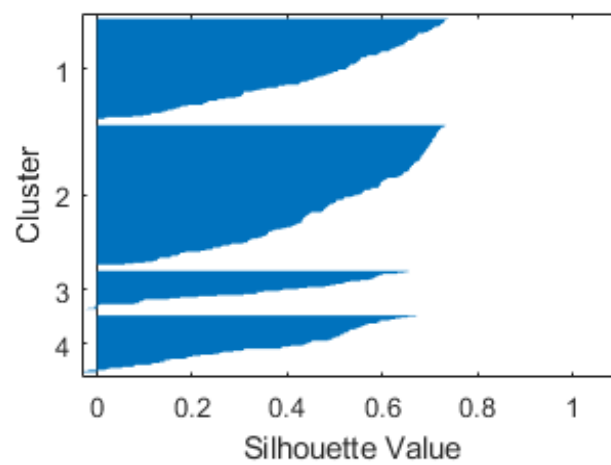
To decide which metrics to adopt, a comparison based on the silhouette of each method was performed (see Figure 9). Correlation metrics appear to be the most reliable, whereas the squared Euclidean would be as good if it were not for the outliers.



(a)



(b)



(c)

Figure 9. Silhouette for different metrics: squared Eculidean (a), cosine (b), and correlation (c).

A four clusters grouping was chosen for the proposed analysis. Figure 10 represents the final clusterization of Emilia-Romagna municipalities. Cluster evaluation was conducted considering the weight and the distribution of the variables. All the outliers belonged to cluster 4, which was developed both on the horizontal axis, led by seismic vulnerability and hydraulic risk variables, and slightly on the vertical one, led by seismic hazard and by hydraulic risk variables. The great majority of the municipalities presented similar quantitative values of variables, in particular, those belonging to clusters 2 and 3. Silhouette values relative to this clusterization were good, reinforcing the reliability of the method proposed.

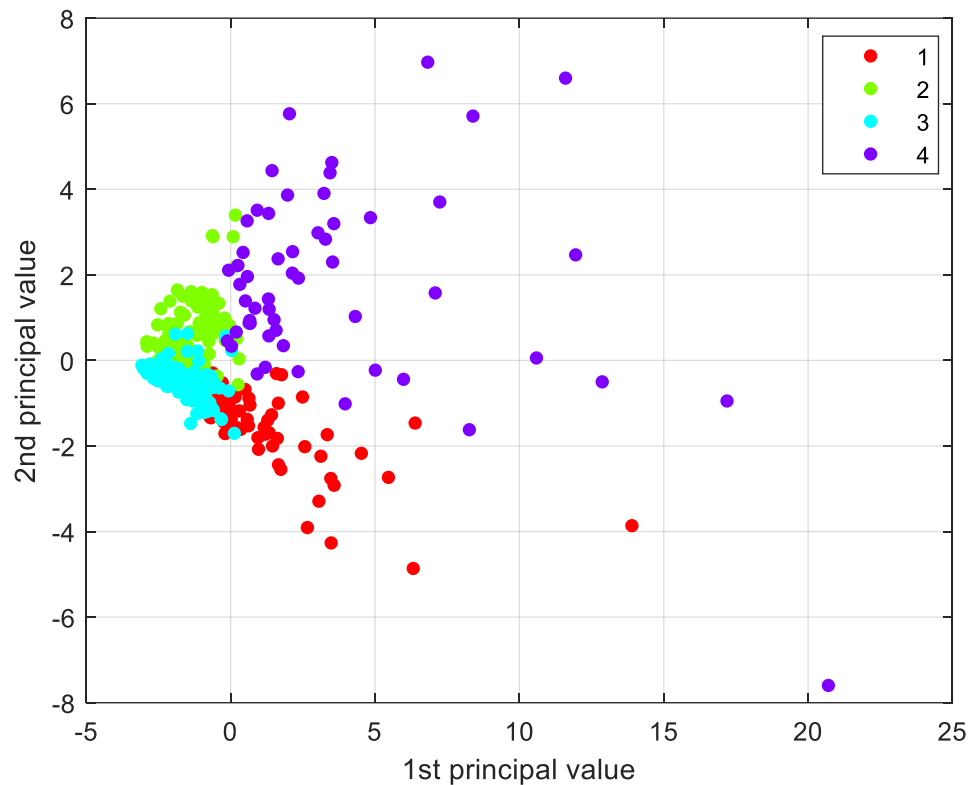


Figure 10. Grouping of the Emilia Romagna municipalities into four clusters.

3. Results

In this section, we show how to assign to each observation and, more generally, to each cluster, a label which identifies the associated level of overall risk.

3.1. Variables Label Assignment

First, we set intervals in an objective way, in order to suitably define labels for the variables. To this aim, we set interval extremals in correspondence of quartile percentages Q1, Q2, and Q3 as indicated in Table 1.

Table 1. Labels and intervals for cluster definition.

Intervals	Label
first element: Q1	Low
Q1: Q2	Medium-to-low
Q2: Q3	Medium-to-high
Q3: last element	High

The chosen labels referred, respectively, to the presence of low, medium-to-low, medium-to-high and high amounts regarding that specific variable. Such subdivision was allowed because the variables were quantitative types and sorted by normal distribution. Furthermore, sorting out variables, the information within them was unaffected.

We analyzed the variable with the greater value from the previous analysis, as a component that defined a risk, with the risk as the combined result of three factors, hazard, exposure, and vulnerability. We illustrate how to assign a label to each cluster for each variable considered, among the most relevant ones.

We first considered the variable $a_{g,max}$, i.e., the peak ground acceleration for the site, with a return period of 475 years. The first step was the extrapolation of observables in the initial dataset. Subsequently, we associated each observation with the respective cluster indexes and the respective values of $a_{g,max}$. Then, we rearranged the observables in ascending order of $a_{g,max}$, and defined the quartile as the extreme point of the interval. The cluster composition in terms of $a_{g,max}$ is reported in Table 2, together with the resulting assigned labels.

Table 2. Quartile distribution of the $a_{g,max}$ variable in the four clusters.

	%Q1	%Q2	%Q3	%Q4	Label
CL1	74	20	6	0	Low
CL2	0	25	25	50	Medium-to-high
CL3	3	18	68	11	Medium-to-low
CL4	7	16	13	64	High

The labels were assigned based on the percentage prevalence of the cluster for each quartile. A prevalence allocated in the fourth quartile for one of the clusters indicated that the selected cluster gathered the most dangerous municipalities in terms of $a_{g,max}$. On the other hand, a prevalence in the first quartile indicated that the cluster gathered the less dangerous municipalities in terms of seismic hazard.

The same operation was carried out for the hydraulic risk component IDR_POPP2, the prevailing seismic vulnerability variable, i.e., the percentage of buildings under poor maintenance conditions E_30, and the main exposure variable, i.e., density population DENS_POP (see Tables 3–5).

Table 3. Quartile distribution of the IDR_POPP2 variable in the four clusters.

	%Q1	%Q2	%Q3	%Q4	Label
CL1	17	20	54	9	Medium-to-low
CL2	46	41	12	1	Low
CL3	3	5	18	74	Medium-to-high
CL4	4	5	9	82	High

Table 4. Quartile distribution of the E_30 variable in the four clusters.

	%Q1	%Q2	%Q3	%Q4	Label
CL1	41	27	22	9	Low
CL2	25	30	29	15	Medium-to-low
CL3	18	29	37	16	Medium-to-high
CL4	0	4	11	86	High

Table 5. Quartile distribution of the $a_{g,max}$ variable in the four clusters.

	%Q1	%Q2	%Q3	%Q4	Label
CL1	16	29	40	14	Medium-to-low
CL2	46	28	19	7	Low
CL3	0	0	3	97	High
CL4	5	25	27	43	Medium-to-high

3.2. Overall Risk Definition

Once the variables were rearranged, the incidence of clusters for each variable were calculated and a label for each variable and cluster was assigned (based on the distribution of the cluster indexes within the variable); each cluster was assigned an overall risk label based on their score for each rearranged variable (Table 6).

Table 6. Overall risk quantification for each cluster of municipalities.

	Hydraulic Risk	Seismic Exposition	Seismic Vulnerability	Seismic Hazard	Label
CL1	Medium-to-low	Low	Medium-to-low	Low	Low
CL2	Low	Medium-to-low	Low	Medium-to-high	Low-to-medium
CL3	Medium-to-high	Medium-to-high	High	Medium-to-low	Medium-to-high
CL4	High	High	Medium-to high	High	High

The significance of the assigned risk labels was strictly dependent on the starting population, i.e., from the region under study and do not have absolute value.

This means that the obtained labels cannot be extrapolated to a larger scale without losing their significance. As shown in Figure 11, it is also possible to represent the population of each risk cluster by the main administrative province in the Emilia Romagna region. Obviously, frequency values for each province depend on the number of municipalities, which constitute each province. Therefore, this plot allows analyzing risk clusters from the same province, but comparing clusters from different provinces may be inappropriate. It is worth noting that the proposed methodology has recognized Piacenza as the province with most low-risk municipalities, while the main cluster featuring Parma, Modena, Bologna, Forlì-Cesena, and Rimini is the low-to-medium risk cluster. Most municipalities of the Reggio-Emilia province are associated with low and low-to-medium clusters. Finally, each of the provinces of Ferrara and Ravenna result being equally split in two main clusters, namely the low and the high-risk clusters in the former case, and the low-to-medium and high-risk clusters in the latter case.

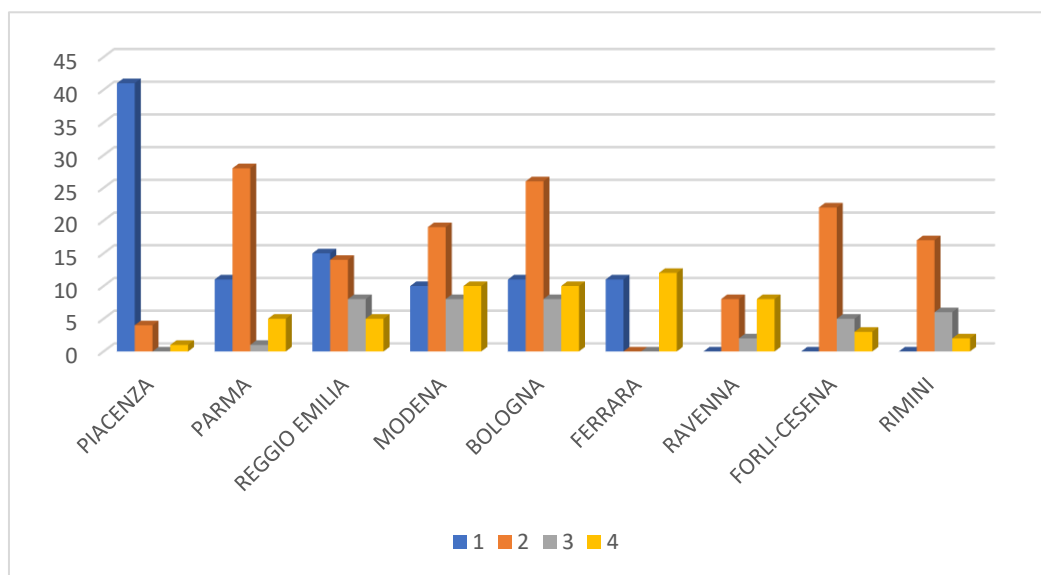


Figure 11. Population of each risk cluster by province in the Emilia Romagna region. In the *y*-axis, the number of municipalities has been reported.

4. Discussion

Ensuring ethical, inclusive, and unbiased machine learning tools is one of the new epistemic frontiers in the application of artificial intelligence technologies to disaster risk management. We recall that this paper discusses an individual application of machine learning tools to a multi-risk assessment of a Northern Italy case study. For this purpose, we had at our disposal a massive amount of data from the ISTAT database containing indicators and data on seismic, hydrogeological, and volcanic risk as well as demographic, housing, territorial and geographical information, obtained through the integration of various institutional sources such as Istat, INGV, ISPRA, Italian Ministry for Cultural Heritage. Like all big data technologies, the adopted machine learning model proved effective in reducing CPU time and model-development costs, owing to its ability to process quantities and sources of data that could not have been otherwise simply elaborated [24,25]. We expect that the model can be used to devise mitigation measures, prepare emergency response, and plan flood recovery measures. The proposed tool has, indeed, the potential for being an operational instrument for land use managers and planners. However, misuse should be avoided, and, for this purpose, crucial issues such as applicability, bias, and ethics should be carefully considered [24–26]. The ethical issues pertaining to a possible misuse of Artificial Intelligence technologies are several [25], including the loss of human decision making, the potential for criminal and malicious use, the emergence of problems of control and use of data and systems, the dependence of the outcomes on users' bias, and the possible prioritization of the "wrong" problems with respect to stakeholder expectations.

Prioritization in disaster multi-risk management, additionally, is markedly affected by needs and expectations of private users, public agencies, and final stakeholders. For instance, a water level management company will be expectedly more inclined to consider flood risk as the most important risk to cope with, while any public agency that is called to reduce the seismic vulnerability of a certain region will tend to consider seismic risk as a priority. Thus, the labeling of the clusterization will be intrinsically permeated with the end-user's intentions. A further aspect is that one should understand that publicizing the results of a multi-risk algorithm might inadvertently touch sensitive aspects from a privacy point of view [27].

In many cases, criticalities rely upon an inherent disconnect between the algorithm's designers and the communities where the research is conducted [26], while users may complain about a lack of transparency and accountability. Furthermore, immature machine learning tools might be used in safety-critical situations for which they are not yet ready.

As suggested by Gevaert et al. [26], disaster-risk-management specialists constantly seek expertise on how to clearly communicate the results and uncertainties of machine learning algorithms to reduce inflated expectations. Furthermore, sensitive groups should be identified and audited for overcoming bias. Therefore, we suggest that, before being systematically applied, the present machine learning methodology is validated against established computational modeling tools. We also believe that the obtained results are very promising, but further efforts are necessary to assess the proneness of the proposed machine learning tool to the aforementioned ethical and bias issues.

5. Conclusions

The purpose of this work is to illustrate a sound methodology for the qualitative multi-risk analysis at the regional scale by means of machine learning techniques that allow dealing with large and heterogeneous amounts of data. The initial dataset, made of variables carrying information about hazard, exposure, and vulnerability for both seismic and hydraulic risk for each municipality of the Emilia Romagna region, has been suitably normalized and reduced through the PCA, whereas observations have been clustered through a machine-learning algorithm.

Then, risk labels were individually assigned to clusters for each variable. Finally, based on the score of each variable an overall risk label was assigned to each cluster. Results confirmed previous risk classifications for the case study analyzed. Both provinces with a moderate risk level and high-risk level have been correctly detected by the proposed approach. The reliability of the obtained results is dependent on the existence of valid quantitative initial data for the region under study. In fact, the proposed methodology does not allow qualitative data, whether they are fundamental or not.

In conclusion, the proposed analysis delivers useful information: municipalities with major priority of intervention are identified so that stakeholders can take advantage of this tool to prioritize any preventive measures. Moreover, the procedure also allows identifying the most important variables to consider in a combined seismic and hydraulic multi-risk analysis. In other words, this tool allows evaluating the variables most suited to categorize the observations in terms of combined risk. Indeed, from the analysis, variables have emerged relative to different types of risks, which better communicate with each other and carry most information. By contrast, the methodology also allows identifying variables, which do not collaborate with variables of different nature and, therefore, cannot be usefully employed.

Author Contributions: Conceptualization, A.R., M.N., A.C., and E.B.; methodology, A.R., M.N., A.C., F.R., and E.B.; software, A.R., M.N., L.M., A.G., and F.R.; validation, A.R., A.C., M.N., F.R., L.M., A.G., and Z.N.; formal analysis A.R., A.C., M.N.; resources, E.B., and Z.N.; data curation, A.R., M.N., L.M., and A.G.; writing—original draft preparation, A.R., A.C., E.B., and F.R.; writing—review and editing, A.C., F.R., Z.N., and E.B.; visualization, A.R., M.N., and F.R.; supervision, A.C., M.N., Z.N., and E.B.; project administration, E.B., and Z.N.; funding acquisition, E.B., and Z.N. All authors have read and agreed to the published version of the manuscript.

Funding: This research was funded by: (1) the EUROPEAN UNION, Programme Interreg Italy-Croatia, Project “Preventing, managing and overcoming natural-hazards risks to mitigate economic and social impact”—PMO-GATE ID 10046122.

Institutional Review Board Statement: Not applicable.

Informed Consent Statement: Not applicable.

Data Availability Statement: The Istat dataset used for the simulations is public and downloadable from the web page <https://www4.istat.it/it/mappa-rischi/documentazione> (accessed on 15 October 2021).

Acknowledgments: The support of Eng. Alessandro Bondesan from Consorzio di Bonifica Pianura di Ferrara is gratefully acknowledged.

Conflicts of Interest: The authors declare no conflict of interest.

Appendix A

We provide hereafter a table with the acronyms of the variables used for Figures 5–7:

Table A1. Description of the variables used in Figures 5–7.

DENSPOP	Population Density
AGMAX_50	Maximum ground acceleration (50th percentile) calculated on a grid with a 0.02° step, maximum (MAX) and minimum (MIN) of the values of the grid points falling within the municipal area.
IDR_POPP3	Resident population at risk in areas with high hydraulic hazard-P3
IDR_POPP2	Resident population at risk in areas with medium hydraulic hazard-P2
IDR_POPP	Resident population at risk in areas with low hydraulic hazard-P1
IDR_AREAP1	Areas with low hydraulic hazard P1 (low probability of floods or extreme event scenarios)–D.Lgs. 49/2010 (km ²)
IDR_AREAP2	Areas with average hydraulic hazard P2 (return time between 100 and 200 years)–D.Lgs. 49/2010 (km ²)
IDR_AREAP3	Areas with high hydraulic hazard P3 (return time between 20 and 50 years)–D.Lgs. 49/2010 (km ²)
E5	Residential buildings in load-bearing masonry
E6	Residential buildings in load-bearing reinforced concrete
E7	Residential buildings in other load-bearing materials (steel, wood, . . .)
E8	Residential buildings made before 1919
E9	Residential buildings made between 1919 and 1945
E10	Residential buildings made between 1946 and 1960
E11	Residential buildings made between 1961 and 1970
‘E19	Residential buildings with three floors
E20	Residential buildings with more than three floors
E30	Residential buildings with a poor state of conservation
‘E31	Residential buildings with a very poor state of conservation

References

- Fuchs, S.; Keiler, M.; Zischg, A. A spatiotemporal multi-hazard exposure assessment based on property data. *Nat. Hazards Earth Syst. Sci.* **2015**, *15*, 2127–2142. [CrossRef]
- Kron, W. Reasons for the increase in natural catastrophes: The development of exposed areas. In *Topics 2000: Natural Catastrophes, the Current Position*; Munich Reinsurance Company: Munich, Germany, 1999; pp. 82–94.
- Zschau, J. Where are we with multihazards, multirisks assessment capacities? In *Science for Disaster Risk Management: Knowing Better and Losing Less*; Poljansek, K., Marin Ferrer, M., De Groeve, T., Clark, I., Eds.; European Union: Luxembourg, 2017; pp. 98–115.
- Barthel, F.; Neumayer, E. A trend analysis of normalized insured damage from natural disasters. *Clim. Chang.* **2012**, *113*, 215–237. [CrossRef]
- Munich, R.E.; Kron, W.; Schuck, A. Analyses, assessments, positions. In *Topics Geo: Natural Catastrophes*; Münchener Rückversicherungs-Gesellschaft: Munich, Germany, 2014.
- Peduzzi, P.; Dao, H.; Herold, C.; Mouton, F. Assessing global exposure and vulnerability towards natural hazards: The Disaster Risk Index. *Nat. Hazards Earth Syst. Sci.* **2009**, *9*, 1149–1159. [CrossRef]
- Bell, R.; Glade, T. Multi-hazard analysis in natural risk assessments. *WIT Trans. Ecol. Environ.* **2004**, *77*, 1–10.
- Barredo, J.I. Major flood disasters in Europe: 1950–2005. *Nat. Hazards* **2007**, *42*, 125–148. [CrossRef]
- Kanamori, H.; Hauksson, E.; Heaton, T. Real-time seismology and earthquake hazard mitigation. *Nature* **1997**, *390*, 461–464. [CrossRef]
- Kappes, M.S.; Keiler, M.; von Elverfeldt, K.; Glade, T. Challenges of analyzing multi-hazard risk: A review. *Nat. Hazards* **2012**, *64*, 1925–1958. [CrossRef]
- Schmidt, J.; Matcham, I.; Reese, S.; King, A.; Bell, R.; Henderson, R.; Smart, G.; Cousins, J.; Smith, W.; Heron, D. Quantitative multi-risk analysis for natural hazards: A framework for multi-risk modelling. *Nat. Hazards* **2011**, *58*, 1169–1192. [CrossRef]

12. Gruber, F.E.; Mergili, M. Regional-scale analysis of high-mountain multi-hazard and risk indicators in the Pamir (Tajikistan) with GRASS GIS. *Nat. Hazards Earth Syst. Sci.* **2013**, *13*, 2779–2796. [CrossRef]
13. Tyagunov, S.; Vorogushyn, S.; Jimenez, C.M.; Parolai, S.; Fleming, K. Multi-hazard fragility analysis for fluvial dikes in earthquake- and flood-prone areas. *Nat. Hazards Earth Syst. Sci.* **2018**, *18*, 2345–2354. [CrossRef]
14. Yousefi, S.; Pourghasemi, H.R.; Emami, S.N.; Pouyan, S.; Eskandari, S.; Tiefenbacher, J.P. A machine learning framework for multi-hazards modeling and mapping in a mountainous area. *Sci. Rep.* **2020**, *10*, 12144. [CrossRef] [PubMed]
15. Boniolo, F.; Dorigatti, E.; Ohnmacht, A.J.; Saur, D.; Schubert, B.; Menden, M.P. Artificial intelligence in early drug discovery enabling precision medicine. *Expert Opin. Drug Discov.* **2021**, *16*, 991–1007. [CrossRef]
16. Pouyan, S.; Pourghasemi, H.R.; Bordbar, M.; Rahmani, S.; Clague, J.J. A multi-hazard map-based flooding, gully erosion, forest fires, and earthquakes in Iran. *Sci. Rep.* **2021**, *11*, 14889. [CrossRef] [PubMed]
17. Pearson, K. On Lines and Planes of Closest Fit to Systems of Points in Space. *Phil. Mag.* **1901**, *2*, 559–572. [CrossRef]
18. Hotelling, H. Analysis of a complex of statistical variables into principal components. *J. Edu. Psychol.* **1933**, *24*, 417–441. [CrossRef]
19. Jolliffe, I.T. *Principal Component Analysis*; Springer: New York, NY, USA, 2002.
20. MacQueen, J.B. Some methods for classification and analysis of multivariate observations. In *Proceedings of the 5th Berkeley Symposium on Mathematical Statistics and Probability, Berkeley, CA, USA, 1967*; University of California Press: Berkeley, CA, USA, 1967; pp. 281–297.
21. Ding, C.; Xie, H. K-means clustering via principal components analysis. In *Proceedings of the 21st International Conference on Machine Learning, Banff, AB, Canada, 4–8 July 2004*; ACM Press: New York, NY, USA, 2004.
22. Trigila, A.; Iadanza, C.; Bussettini, M.; Lastoria, B. *Dissesto Idrogeologico in Italia: Pericolosità e Indicatori di Rischio—Edizione 2018; Rapporti 287/2018*; ISPRA: Roma, Italy, 2018.
23. Mantovan, L.; Gilli, A. Supplementary Material, Open Access. Available online: <https://github.com/alessandrogilli/analisi-multirischio> (accessed on 15 October 2021).
24. Wagenaar, D.; Curran, A.; Balbi, M.; Bhardwaj, A.; Soden, R.; Hartato, E.; Sarica, G.M.; Ruangpan, L.; Molinaro, G.; Lallemand, D. Invited perspectives: How machine learning will change flood risk and impact assessment. *Nat. Hazards Earth Syst. Sci.* **2020**, *20*, 1149–1161. [CrossRef]
25. Stahl, B.C. Ethical Issues of AI. Artificial Intelligence for a Better Future: An Ecosystem Perspective on the Ethics of AI and Emerging Digital Technologies. In *SpringerBriefs in Research and Innovation Governance*; Springer: Berlin/Heidelberg, Germany, 2021; pp. 35–53.
26. Gevaert, C.M.; Carman, M.; Rosman, B.; Georgiadou, Y.; Soden, R. Fairness and accountability of AI in disaster risk management: Opportunities and challenges. *Patterns* **2021**, *2*, 100363. [CrossRef] [PubMed]
27. GFDRR. *Machine Learning for Disaster Risk Management*; GFDRR: Washington, WA, USA, 2018.

Article

Population Bias on Tornado Reports in Europe

Răzvan Pîrloagă^{1,2,*} , Dragoș Ene¹  and Bogdan Antonescu¹ 

¹ Remote Sensing Department, National Institute of Research and Development for Optoelectronics INOE 2000, Str. Atomîștilor 409, 077125 Măgurele, Romania; dragos.ene@inoe.ro (D.E.); bogdan.antonescu@inoe.ro (B.A.)

² Faculty of Physics, University of Bucharest, 077125 Măgurele, Romania

* Correspondence: razvan.pirloaga@inoe.ro

Abstract: Tornadoes are associated with damages, injuries, and even fatalities in Europe. Knowing the spatial distribution of tornadoes is essential for developing disaster risk reduction strategies. Unfortunately, there is a population bias on tornado reporting in Europe. To account for this bias, a Bayesian modeling approach was used based on tornado observations and population density for relatively small regions of Europe. The results indicated that the number of tornadoes could be 53% higher than are currently reported. The largest adjustments produced by the model are for Northern Europe and parts of the Mediterranean regions.

Keywords: tornadoes; climatology; Bayesian

Citation: Pîrloagă, R.; Ene, D.; Antonescu, B. Population Bias on Tornado Reports in Europe. *Appl. Sci.* **2021**, *11*, 11485. <https://doi.org/10.3390/app112311485>

Academic Editor: Ben J. Anthony

Received: 2 November 2021

Accepted: 2 December 2021

Published: 3 December 2021

Publisher's Note: MDPI stays neutral with regard to jurisdictional claims in published maps and institutional affiliations.



Copyright: © 2021 by the authors. Licensee MDPI, Basel, Switzerland. This article is an open access article distributed under the terms and conditions of the Creative Commons Attribution (CC BY) license (<https://creativecommons.org/licenses/by/4.0/>).

1. Introduction

Tornadoes in Europe can be associated with severe damage and can result in injuries and fatalities. Despite this, until recently their threat has been underestimated. Antonescu et al. [1] showed that European tornadoes reported between 1995–2015 resulted in 4462 injuries and 316 fatalities and damages estimated at more than €1 billion. They also indicated that the density of tornado reports was the highest over Belgium, Germany, the Netherlands, and the southeastern United Kingdom. For these countries, there is a reporting bias, as central and western Europe have a high population density compared with other regions in Europe (e.g., Eastern Europe). Coastal areas were also hot-spots for tornado reports (e.g., western Italy, eastern Spain), as these areas tend to have higher population density compared with inland areas and also because of the waterspouts that move from the Mediterranean Sea inland [2].

This difference in the population density (i.e., different regions of Europe, coastal area versus inland area) introduces a bias in the reporting of tornadoes. This is because tornadoes (and also other types of severe weather events like hail or extreme winds) are “targets of opportunity” [3]. Thus, an observer needs to witness the event and then to report it and systems need to exist for collecting and verifying the reports (i.e., tornado database). Very few countries in Europe have developed and maintained such databases, which resulted in a lack of information about tornadoes [2]. One reason for not developing tornado databases is that they do not seem justified. Compared with the United States, the impact of tornadoes in European countries (given their relative small area) is relatively low, and thus there is no need to develop tornado databases for individual countries [4]. Only when considered from a pan-European perspective does the impact of tornadoes in Europe start to emerge. The collection of tornado reports and other types of severe weather reports at the pan-European level started in 2006 with the development of the European Severe Weather Database (ESWD) by the European Severe Storms Laboratory [5]. Currently, ESWD contains more than 16,500 tornado reports collected between 1800–2020.

Given the differences in population density across Europe, the real number of tornadoes is an unknown quantity. Even in relatively high populated areas, tornadoes might not be reported because of their small spatial extent and short life time, obstruction of the

observer view point (e.g., forest, hills, buildings) or if the tornado occurred during the nighttime. As indicated in previous studies for the United States [6] and Canada [7], the population density is the key factor, besides the meteorological factors, in determining the bias in tornado reports.

Several studies have addressed the issue of population bias on tornado reports. Anderson et al. [6] used a hierarchical Bayesian model to account for the population bias on tornado occurrence using historical tornado reports for the United States from the Storm Prediction Center between 1953–2001. Their results for the central and eastern United States indicated that F0–F1 tornado reports vary less with population density compared with F2–F5 tornadoes. Starting from the hypothesis that the number of tornado reports in Canada is significantly lower than the actual number of tornadoes, Cheng et al. [7] also used a Bayesian modeling approach that considered the population bias on tornado reports. Their model also included the occurrence of cloud-to-ground lightning, as cloud-to-ground lightning can be used to quantify convective storms activity and thus can be used as precursor for tornadoes. Their results showed that in areas with low population density, the probability of tornado occurrence is significantly higher compared with the observed tornado climatology for Canada. More recently, Potvin et al. [8] developed a Bayesian hierarchical modeling framework for correcting the reporting bias in the United States tornado database. Compared with other covariates (e.g., distance from the nearest city, terrain ruggedness index, road density) population density explained more of the variance in the number of reported tornadoes. Their model indicated that approximately 45% of the tornadoes that occurred in the study domain were reported.

The aim of this article is to analyze the effects of population bias on tornado reports in Europe using a Bayesian modeling approach. The expected tornado counts over Europe can be used to better understand the societal and economic impact of tornadoes and to be included in national disaster risk reduction strategies. This article is structured as follows. Section 2 details the tornado and the population density datasets. Section 3 describes the Bayesian modeling approach. The results and discussions are presented in Sections 4 and 5, respectively. Finally, Section 6 summarizes the results.

2. Tornado and Population Datasets

Tornado reports were obtained from the European Severe Weather Database. The ESWD collects information on severe storms over Europe (i.e., tornadoes, severe wind, large hail, heavy rain, heavy snowfall, damaging lightning) using a citizen-science approach [9] and through collaborations with national weather services and volunteer severe weather spotter networks. Before the inclusion in the ESWD, each report is verified and receives a quality control level. In this article, tornado reports with a quality control level Q0+ (i.e., validated with meteorological data such as radar and/or satellite imagery) have been used. Unlike the United States tornado database that contains only reports for tornadoes, the ESWD also contains reports for waterspouts [2]. The ESWD include information about the surface type (e.g., land, forest, sea, lake) over which tornadoes have been observed and the surface types crossed during the event. Thus, all the waterspouts that moved inland were included in the analyses presented in this article.

Data on population density in Europe were obtained from Eurostat [10]. The data were extracted for NUTS3 regions. NUTS (Nomenclature of territorial units for statistics) classification is a system for dividing the economic territory of European Union and the United Kingdom. The NUTS 2021 [11] classification valid from 1 January 2021 contains 1166 regions at NUTS3 level. NUTS3 level represent small regions for specific diagnoses. For example, for Romania there are 42 NUTS3 regions (41 counties and Bucharest, the capital city). In previous studies, for the United States, it was argued that the rural population density at the county level is a more appropriate measure for tornado reporting compared with total population density [12]. Here, we follow [6] and use the total population density as population tends to be distributed over much of the counties and not concentrated in isolated towns. Based on the data availability and overlap with the tornado dataset, for

each NUTS3 region the population density was average for the period 2006–2019 and the area for the period 2006–2015. These data together with the number of tornadoes reported between 2006–2020 at NUTS3 level were included in the Bayesian model.

3. Hierarchical Bayesian Model

3.1. Model

The Bayesian model used in this article starts with the hypothesis that the population density is the main influence on tornado reporting and thus, that tornadoes are underreported in Europe. As indicated by [6,7], the occurrence of tornadoes can be described as a series of conditional models linked using the Bayes’ rule. Considering the t_n as number of observed tornadoes and T_n as the true number of tornadoes ($T_n \geq t_n$), a binomial model can be specified in which

$$t_n | T_n, p_n(\beta) \sim \text{Binomial}[T_n, p_n(\beta)] \tag{1}$$

where $p_n(\beta)$ represents the probability to observe a tornado and n indicates the NUTS3 region. The probability to observe a tornado is a function of β , which is related to population density (x_n). Anderson et al. (2007) used an exponential model for p_n assuming that the probability of detection increases with population density

$$p_n(\beta) = \exp(-\beta/x_n) \tag{2}$$

The true number of tornadoes (T_n) in the n NUTS3 region is modeled as Poisson process, which is conditioned on the climatological frequency λ

$$T_n | \lambda \sim \text{Poisson}(\lambda a_n) \tag{3}$$

where a_n is the area of the NUTS3 region and λ (i.e., Poisson intensity) is a measure the tornado frequency per unit area [6].

3.2. Estimation

For the Bayesian approach, the prior distribution for β and λ need to be specified. These prior distributions are non-informative (i.e., large variance) because there is no prior knowledge that can inform the distributions. Thus, the population parameter β is specified as

$$\exp(\beta) \sim N(\mu_\beta, \sigma_\beta^2) \tag{4}$$

The distribution of $\exp(\beta)$ is a normal distribution characterized by the mean μ_β and variance σ_β^2 . In the model developed in [6], μ_β was set to 0.5 and σ_β^2 to 10,000. For the climatological frequency parameter λ , a prior gamma distribution was used

$$\lambda \sim \text{gamma}(q, r) \tag{5}$$

Following [6], the shape parameter q was set to 0.001 and the scale parameter r to 0.001 corresponding to a prior mean of 1 and a prior variance of 1000 (non-informative). Using the Bayes’ rule

$$\underbrace{p(\beta, \lambda, T_1, \dots, T_N | t_1, \dots, t_N)}_{\text{Posterior model}} \propto \prod_{n=1}^N \underbrace{p(t_n | T_n, \beta)}_{\text{Data model (Equation (1))}} \times \underbrace{p(T_n | \lambda)}_{\text{Explanatory model (Equation (3))}} \times \underbrace{p(\beta) p(\lambda)}_{\text{Parameter model (Equations (4) and (5))}} \tag{6}$$

A Markov Chain Monte Carlo analysis of the Bayesian model was applied to obtain a sequence of realizations from the posterior model ([6,7]) using the WinBUGS software [13]

(Available online at <https://www.mrc-bsu.cam.ac.uk/software/bugs/the-bugs-project-winbugs/>, accessed on 23 October 2021).

4. Results

Based of the data from ESWD a total number of 2319 tornadoes were observed in Europe between 2006–2020 over the NUTS3 regions considered in this article. The predicted number of tornadoes by the model considering the population bias is 3563 tornadoes (Table 1). Thus, 65% of tornadoes predicted by the model were reported.

Table 1. Posterior parameters and model predictions.

	Mean	Standard Deviation
β	14.91	1.050
λ	0.0006008	0.00001669
	Total (15 yr)	Mean (yr ⁻¹)
$\sum T_n$	3563	237.5
$\sum t_n$	2319	154.6

The difference between predicted and observed number of tornadoes is low (<0.027 tornadoes 10,000 km⁻² yr⁻¹) over parts of the United Kingdom, the Netherlands, Belgium, Germany, and Italy (Figure 1). As indicated previously [1,14], these are regions characterized by both a high number of tornado reports and high population density. For some NUTS3 regions there were no tornadoes reported during the study period, for example, parts of north-western and southeastern France, central Romania, central Italy, Albania, Northern Macedonia, southern Bulgaria, Finland. For these regions the predicting values of tornado counts are less than 2 tornadoes over the 15 years study period. The highest difference between predicted and observed tornadoes (between 0.33–0.41 tornadoes 10,000 km⁻² yr⁻¹) is over Iceland and northern parts of the United Kingdom, Norway, Sweden, and Finland (Figure 1). This is not surprising given that the population density of these regions is low compared with other regions of Europe and also given that the number of observed tornadoes by NUTS3 regions in this area is less than 10 tornadoes over the entire study period.

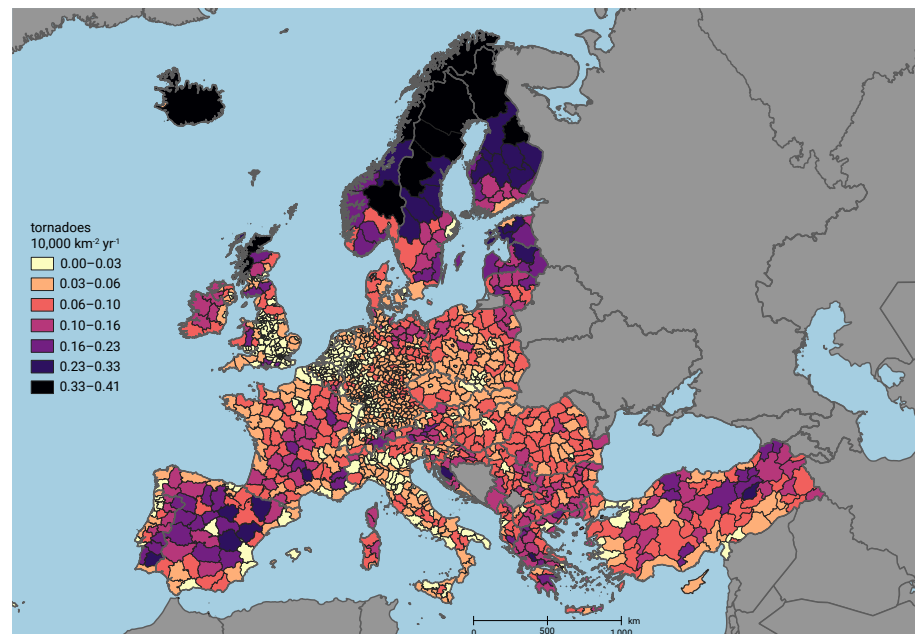


Figure 1. Difference between posterior adjusted number of tornadoes and the number of observed tornadoes normalized by the area of NUTS3 regions and year (shaded according to the scale, 10,000 km⁻² yr⁻¹).

Low values for standard deviation (<0.13 tornadoes $10,000 \text{ km}^{-2} \text{ yr}^{-1}$) of the tornado occurrence from the posterior distribution are found over most of Europe (Figure 2), with the exception of an area stretching from eastern Germany over Austria, Croatia, Bulgaria, and Greece characterized by values between 0.13 – 0.30 tornadoes $10,000 \text{ km}^{-2} \text{ yr}^{-1}$. In these regions the NUTS3 areas are characterized by relatively small area and low population density and also a low number of observed tornadoes during the study period.

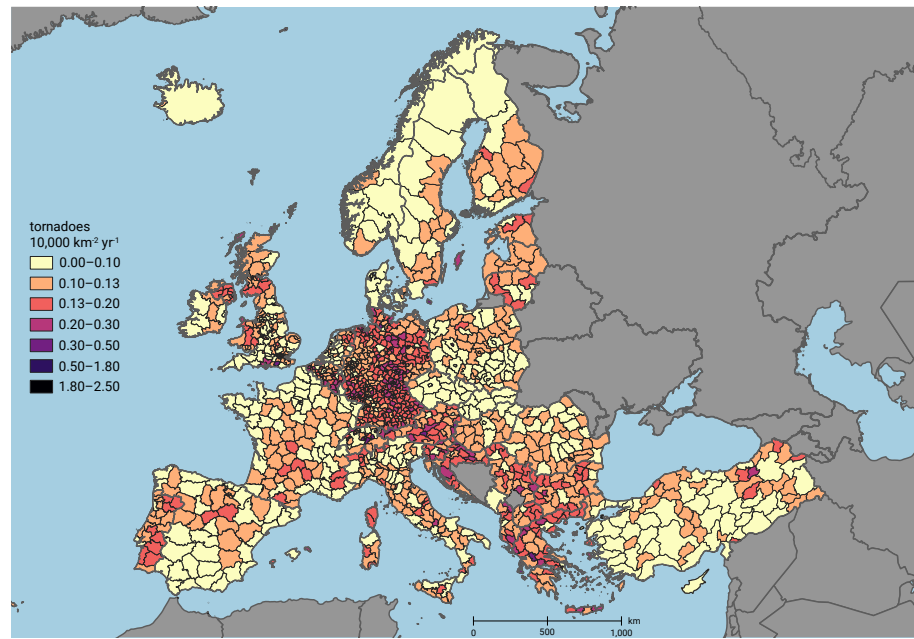


Figure 2. As in Figure 1, but for the standard deviation of tornado occurrence from posterior distribution.

5. Discussion

The Bayesian model used in this article only included the population effects, but previous studies using a similar approach have also included meteorological data [7]. These are large areas where the data collection is unreliable and thus can reduce the predictive capacity of the model. In their study of the probability of tornado occurrence across Canada, Cheng et al. [7] included the cloud-to-ground lightning climatology to account for the spatial variability of tornadoes. For Europe, an indication regarding the predictive capacity of the model can be obtained by comparing the results from Figure 1 with lightning density over Europe between 2008–2012 developed by Anderson and Klugmann [15] using data from the Arrival Time Differing NETWORK. Over northern Norway, Sweden, and Finland, where NUTS3 have a large area and the collection of data is not as reliable as for other regions of Europe, the Bayesian model is introducing large adjustments. For these regions, the lightning density (Figure 4 from [15]) is lower (<0.4 flashes $\text{km}^{-2} \text{ yr}^{-1}$) compared with almost any other regions in Europe. Thus, the adjustments in the number of tornadoes are less realistic for the regions from a meteorological point of view. For the Baltic states (i.e., Estonia, Latvia, Lithuania) the corrections from the model are realistic due to the relatively large lightning density (i.e., 0.4 – 2.5 flashes $\text{km}^{-2} \text{ yr}^{-1}$) in this region. The predictive capacity of the model in these areas can be improved by improving data collection (e.g., ref. [16] used satellite data to obtain information on unreported tornadoes that occurred in forested regions) or by considering as covariate meteorological factors related to tornado occurrence [17].

Future research will develop the model by considering meteorological covariates such as lightning density (e.g., from Arrival Time Difference long-range lightning detection network [18]) and tornadic environments (e.g., ERA5 reanalysis data [19]).

6. Conclusions

In this article, a Bayesian model was applied to adjust the number of observed tornadoes over Europe. The hypothesis was that the number of observed tornadoes in Europe is lower than the real number due to the differences in population density. The model indicated that the average annual number of tornadoes during the study period (2006–2020) was 237.5 compared with an annual average of 154.6 observed tornadoes. The largest adjustments occur over northern Europe (e.g., Iceland, Norway, Sweden, Finland), but also parts of the Mediterranean region (e.g., Spain, Greece).

The corrected distribution of tornadoes in Europe can be used to better understand the risk posed by European tornadoes. Compared with the previous distribution of tornadoes in Europe, the distribution obtained in this article is more relevant for risk reduction strategies, as it is including a correction for the population bias on tornado reporting. Furthermore, the current results can be used by decision-makers and emergency managers to develop disaster risk reduction strategies for tornadoes. Very few countries in Europe have developed tornado preparedness and response programs.

Author Contributions: Conceptualization, B.A.; methodology, R.P.; formal analysis, R.P., D.E. and B.A.; original draft preparation, R.P., D.E. and B.A.; visualization, R.P.; funding acquisition, B.A. All authors have read and agreed to the published version of the manuscript.

Funding: This research was funded by the Romanian Ministry of Education and Research, CNCS-UEFISCDI (Project No. PN-III-P1-1.1-TE-2019-0649) within PNCDI III.

Institutional Review Board Statement: Not applicable.

Informed Consent Statement: Not applicable.

Data Availability Statement: Data used in this study can be obtained by request to the authors.

Acknowledgments: This work was supported by the Romanian National Core Program (Contract No. 18N/2019) and by a grant of the Romanian Ministry of Education and Research, CNCS-UEFISCDI (Project No. PN-III-P1-1.1-TE-2019-0649) within PNCDI III. Further support was provided by the European Regional Development Fund through the Competitiveness Operational Programme 2014–2020, Action 1.1.3 Creating synergies with H2020 Programme, project H2020 Support Centre for European project management and European promotion, MYSMIS code 107874, project Strengthen the participation of the ACTRIS-RO consortium in the pan-European research infrastructure ACTRIS, ACTRIS-ROC, MYSMIS code 107596 (contract No.337/2021). The authors thank Cristina Marin for her comments on an earlier version of the manuscript.

Conflicts of Interest: The authors declare no conflict of interest.

References

1. Antonescu, B.; Schultz, D.M.; Holzer, A.; Groenemeijer, P. Tornadoes in Europe: An underestimated threat. *Bull. Am. Meteorol. Soc.* **2017**, *98*, 713–728. [CrossRef]
2. Antonescu, B.; Schultz, D.M.; Lomas, F.; Kühne, T. Tornadoes in Europe: Synthesis of the Observational Datasets. *Mon. Weather Rev.* **2016**, *144*, 2445–2480. [CrossRef]
3. Brooks, H.E. Severe thunderstorm and climate change. *Atmos. Res.* **2013**, *123*, 129–138. [CrossRef]
4. Doswell, C.A. Societal impacts of severe thunderstorms and tornadoes: Lessons learned and implications for Europe. *Atmos. Res.* **2003**, *67–68*, 135–152. [CrossRef]
5. Groenemeijer, P.; Púčik, T.; Holzer, A.M.; Antonescu, B.; Riemann-Campe, K.; Schultz, D.M.; Kühne, T.; Feuerstein, B.; Brooks, H.E.; Doswell, C.A.; et al. Severe convective storms in Europe: Ten years of research and education at the European Severe Storms Laboratory. *Bull. Am. Meteorol. Soc.* **2017**, *98*, 2641–2651. [CrossRef]
6. Anderson, C.J.; Winkle, C.K.; Zhou, Q.; Royle, J.A. Population influences on Tornado Reports in the United States. *Weather Forecast.* **2007**, *22*, 571–579. [CrossRef]
7. Cheng, V.Y.S.; Arhonditsis, G.B.; Sills, D.M.L.; Auld, H.; Shephard, M.W.; Gough, W.A.; Klaassen, J. Probability of tornado occurrence across Canada. *J. Clim.* **2013**, *26*, 9415–9428. [CrossRef]
8. Potvin, C.K.; Broyles, C.; Skinner, P.S.; Brooks, H.E.; Rasmussen, E. A Bayesian hierarchical modeling framework for correcting reporting bias in the U.S. tornado database. *Weather Forecast.* **2019**, *34*, 15–30. [CrossRef]
9. Muller, C.L.; Chapman, L.; Johnston, S.; Kidd, C.; Illingworth, S.; Foody, G.; Overeem, A.; Leigh, R.R. Crowdsourcing for climate and atmospheric sciences: Current status and future potential. *Int. J. Climatol.* **2015**, *35*, 3185–3203. [CrossRef]

10. Eurostat Database. Available online: <https://ec.europa.eu/eurostat/data/database> (accessed on 1 November 2021).
11. Nomenclature of Territorial Units for Statistics (NUTS). Available online: <https://ec.europa.eu/eurostat/documents/345175/629341/NUTS2021.xlsx> (accessed on 1 November 2021).
12. Changnon, S.A. Trends in tornado frequencies: Fact or fallacy. In Proceedings of the Preprints 12th Conference on Severe Local Storms, San Antonio, TX, USA, 12–15 January 1982; pp. 42–44.
13. Lunn, D.J.; Thomas, A.; Best, N.; Spiegelhalter, D. WinBUGS—A Bayesian modelling framework: Concepts, structure, and extensibility. *Stat. Comput.* **2000**, *10*, 325–337. [CrossRef]
14. Groenemeijer, P.; Kühne, T. A climatology of tornadoes in Europe: Results from the European Severe Weather Database. *Mon. Weather Rev.* **2014**, *142*, 4775–4790. [CrossRef]
15. Anderson, G.; Klugmann, D. A European lightning density analysis using 5 years of ATDnet data. *Nat. Hazards Earth Syst. Sci.* **2014**, *14*, 815–829. [CrossRef]
16. Shikhov, A.; Chernokulsky, A. A satellite-derived climatology of unreported tornadoes in forested regions of northeast Europe. *Remote Sens. Environ.* **2018**, *204*, 553–567. [CrossRef]
17. Taszarek, M.; Allen, J.T.; Púčik, T.; Hoogewind, K.A.; Brooks, H.E. Severe convective storms across Europe and the United States. Part II: ERA5 environments associated with lightning, large hail, severe wind, and tornadoes. *J. Clim.* **2020**, *33*, 10263–10286. [CrossRef]
18. Enno, S.E.; Sugier, J.; Alber, R.; Seltzer, M. Lightning flash density in Europe based on 10 years of ATDnet data. *Atmos. Res.* **2020**, *235*, 104769. [CrossRef]
19. Hersbach, H.; Bell, B.; Berrisford, P.; Hirahara, S.; Horányi, A.; Muñoz-Sabater, J.; Nicolas, J.; Peubey, C.; Radu, R.; Schepers, D.; et al. The ERA5 global reanalysis. *Q. J. R. Meteorol. Soc.* **2020**, *146*, 1999–2049. [CrossRef]

MDPI
St. Alban-Anlage 66
4052 Basel
Switzerland
Tel. +41 61 683 77 34
Fax +41 61 302 89 18
www.mdpi.com

Applied Sciences Editorial Office
E-mail: applsci@mdpi.com
www.mdpi.com/journal/applsci





Academic Open
Access Publishing

www.mdpi.com

ISBN 978-3-0365-8016-6